Design of a bifunctional alkoxy-NHC ligand for assembling tantalum-rhodium heterobimetallic molecular and silica-supported complexes

Ravi Srivastava

N°d'ordre NNT : xxx

THESE de DOCTORAT DE L'UNIVERSITE DE LYON
opérée au sein de
l'Université Claude Bernard Lyon 1

Ecole Doctorale de Lyon
Nº ED206

Spécialité de doctorat : **Chimie**
Discipline : **Chimie Industrielle Durable**

Soutenue publiquement le 16/03/2020
par
M. Ravi Srivastava

Design of a bifunctional alkoxy-NHC ligand for assembling tantalum-rhodium heterobimetallic molecular and silica-supported complexes

---

Jury:

Dr. Marine Desage-El Murr	**Rapportrice**	CNRS - UMR 7177 Strasbourg
Dr. Vincent César	**Rapporteur**	CNRS - UPR 8241 Toulouse
Prof. Regina Palkovits	**Examinatrice**	RWTH Aachen University
Dr. Stéphane Bellemin-Laponnaz	**Examinateur**	CNRS - UMR 7504 Strasbourg
Dr. Nathanaelle Schneider	**Examinatrice**	CNRS - UMR 9006 Palaiseau
Prof. Abderrahmane Amgoune	**Examinateur**	Université Claude Bernard Lyon 1
Prof. Walter Leitner	**Co-directeur de thèse**	RWTH Aachen University
Dr. Clément Camp	**Co-encadrant de thèse**	CNRS - UMR 5265 Lyon

Invitée:

Dr. Alessandra E. Quadrelli	**Directrice de thèse**	CNRS - UMR 5265 Lyon

“Design of a bifunctional alkoxy-NHC ligand for assembling tantalum-rhodium heterobimetallic molecular and silica-supported complexes”

Der Fakultät für Mathematik, Informatik und Naturwissenschaften der RWTH Aachen University vorgelegte Dissertation zur Erlangung des akademischen Grades eines Doktors der Naturwissenschaften

von

Ravi Srivastava, M. Sc.

aus

Bhatpurva, Deoria (Uttar Pradesh), Indien

UNIVERSITE Claude BERNARD – LYON 1

Président de l'Université	M. Frédéric FLEURY
Président du Conseil Académique	M. Hamda BEN HADID
Vice-Président du Conseil d'Administration	M. Didier REVEL
Vice-Président du Conseil des Etudes et de la Vie Universitaire	M. Philippe CHEVALLIER
Vice-Président de la Commission de Recherche	M. Fabrice VALLEE
Directeur Général des Services	M. Damien VERHAEGHE

COMPOSANTES SANTE

Faculté de Médecine Lyon-Est-Claude Bernard	Doyen : M. Gilles RODE
Faculté de Médecine et Maïeutique Lyon Sud Charles Mérieux	Doyenne : Mme Carole BURILLON
UFR d'Odontologie	Doyenne : Mme Dominique SEUX
Institut des Sciences Pharmaceutique et Biologiques	Directrice : Mme Christine VINCIGUERRA
Institut des Sciences Techniques de la Réadaptation	Directeur : M. Xavier PERROT
Département de Formation et Centre de Recherche en Biologie Humaine	Directrice : Mme Anne-Marie SCHOTT

COMPOSANTES & DEPARTMENTS DE SCIENCES & TECHNOLOGIE

UFR Biosciences	Directrice : Mme Kathrin GIESELER
Département Génie Electrique et des Procédés (GEP)	Directrice : Mme Rosaria FERRIGNO
Département Informatique	Directeur : M. Behzad SHARIAT
Département Mécanique	Directeur : M. Marc BUFFAT
UFR - Faculté des Sciences	Administrateur Provisoire : M. Bruno ANDRIOLETTI
UFR (STAPS)	Directeur : M. Yannick VANPOULLE
Observatoire de Lyon	Directeur : Mme Isabelle DANIEL
Ecole Polytechnique Universitaire Lyon 1	Directeur : Emmanuel PERRIN
Ecole Supérieure de Chimie, Physique, Electronique (CPE Lyon)	Directeur : Bernard BIGOT
Institut Universitaire de Technologie de Lyon 1	Directeur : M. Christophe VITON
Institut de Science Financière et d'Assurances	Directeur : M. Nicolas LEBOISNE
ESPE	Administrateur Provisoire : M. Pierre CHAREYRON

This doctoral research project was part of Erasmus mundus joint doctoral (EMJD) program offered by Sustainable Industrial Chemistry (SINCHEM) consortium under the aegis of ERASMUS^{+} action program. The research work was carried out in two different universities. The synthesis and characterisation of the organometallic complexes was carried at "University Claude Bernard Lyon 1" in surface organometallic chemistry team at C2P2, CPE Lyon. The computational calculations for the dinitrogen activation was carried out at "RWTH Aachen University" in Institute of technical and macromolecular chemistry (ITMC).

Table of Contents

List of Abbreviations.....**i**

ABSTRACT.....**iii**

RÉSUMÉ.....**v**

ZUSAMMENFASSUNG.....**vii**

Summary.....**ix**

Résumé.....**xxii**

Chapter 1. Bibliography.....

1.1) Introduction.....

1.1.1) An overview of heterobimetallic Early-Late transition metal complexes.....**1**

1.1.2) Surface Organometallic Chemistry (SOMC): An approach to realize well defined surface-supported complexes.....

1.1.2.1) Presentation.....**9**

1.1.2.2) Silica-supported heterobimetallic species prepared through SOMC.....**15**

1.1.2.3) Molecular silanols as homogeneous molecular models of silica.....**16**

1.2) Objectives of this PhD work: synthesis of silica-supported early-late heterobimetallic complex bridged by a bifunctional N-heterocyclic carbene (NHC).....**19**

References.....

Chapter 2. Synthesis and characterization of bifunctional N-heterocyclic carbene (NHC).....

2.1) Introduction.....

2.1.1) Bifunctional ligands for the assembly of early/late heterobimetallic complexes.....**31**

2.1.2) Recent literature on bifunctional NHC.....**33**

2.1.3) Ligand design.....**37**

2.2) Results and Discussion.....

2.2.1) One pot, fast and scalable Synthesis of a new imidazolium salt and its characterization.....**39**

2.2.2) Synthesis and Characterization of free NHC ligand.....**43**

Conclusion.....**51**

References.....

Experimental section .....

Chapter 3. Synthesis and Characterisation of metal-NHC complexes.....

3.1) Introduction.....

3.1.1) Examples of early-late tantalum-rhodium heterobimetallic complexes and the synthetic...

protocols involved therein.....**63**

3.2) Results and Discussion.....

3.2.1) Synthesis and Characterization of monometallic tantalum-NHC species.....

3.2.1.1) Synthesis of tantalum-alkylidene NHC complex.....**67**

3.2.1.2) Decomposition of tantalum-alkylidene NHC complex at room temperature.....**69**

3.2.1.3) Synthesis of tantalum imido alkylidene NHC complex.....**73**

3.2.2) Synthesis and characterization of monometallic rhodium-NHC species.....**75**

3.3) Synthesis of Ta-Rh bimetallic complex.....

3.3.1) Insertion of Rh into the tantalum-NHC complex.....**86**

3.3.2) Reaction between the rhodium-NHC complex and $Ta(CH^tBu)(CH_2{}^tBu)_3$.....**92**

3.3.3) Synthesis of $[Ta(\mu\text{-}L)(N^tBu)(CH_2{}^tBu)_2Rh(COD)Cl]$ by using tantalum imido alkylidene.....

$Ta(\mu\text{-}L)(N^tBu)(CH_2{}^tBu)_2$ as the tantalum precursor.....**92**

Conclusion.....**96**

References.....

Experimental section.....

Chapter 4. Development of POSS based homogeneous molecular model of the bimetallic complex and the synthesis of silica-supported early-late heterobimetallic complexes.....

4.1) Introduction.....

4.1.1) Recent advances in silica-supported heterobimetallic complexes.....**117**

4.1.2) Two different routes to synthesize the silica supported bimetallic complexes.....**120**

4.2) Results and Discussion.....

4.2.1) Synthesis and Characterization of POSS based heterobimetallic complex.....**121**

4.2.2) Synthesis, characterization and reactivity of tris(tert-butoxy) silanol heterobimetallic.....

derivatives.....**126**

4.2.3) Surface OrganoMetallic Chemistry (SOMC).....

4.2.3.1) Synthesis and characterization of the silica support: $SBA_{15\text{-}700}$.....**132**

4.2.3.2) Synthesis and characterisation of silica-supported tantalum-NHC species.....**133**

4.2.3.3) Preparation and characterization of silica-supported Ta/Rh heterobimetallic species....

.....**137**

Conclusion.....**144**

References.....

Experimental section .....

Chapter 5. Computational studies using bimetallic complex for N_2 activation to NH_3.....

5.1) Introduction.....

5.1.1) General introduction on N_2 activation to outline different molecular mechanisms.....**159**

5.1.2) State of the art for the activation of N_2 molecule by homogeneous bimetallic complexes...

.....**163**

5.1.3) Aim of the chapter.....**167**

5.2) Results and Discussion.....

5.2.1) Structure optimisation of tris(tert-butoxy) silanolate derivative of bimetallic complex.....

.....**168**

5.2.2) Computation of catalytic cycle for dinitrogen conversion to ammonia using rhodium as..

late metal.....**170**

5.2.3) Computation of catalytic cycle for dinitrogen conversion to ammonia using cobalt as late

metal.....**174**

5.2.4) Computation of catalytic cycle for dinitrogen conversion to ammonia using iridium as....

late metal.....**176**

5.2.5) Computation of catalytic cycle for dinitrogen conversion to ammonia at tantalum.....

center.....**177**

Conclusion.....**179**

References.....

Concluding remarks.....**185**

Acknowledgement.....**191**

Annexure.....

Appendix 1.....195

Appendix 2.....200

Appendix 3.....228

Appendix 4.....241

List of Abbreviations

NHC: N-heterocyclic carbene

ELHB: Early-late heterobimetallic

SOMC: Surface organometallic chemistry

SBA: Santa Barbara amorphous

EXAFS: Extended X-ray absorption fine structure

DRIFT: Diffuse reflectance infrared Fourier transform

FTIR: Fourier-transform infrared spectroscopy

XRD: X-ray diffraction spectroscopy

DFT: Density functional theory

BuH: n-butane

NpH: Neopentane

HETCOR: Heteronuclear correlation spectroscopy

CP-MAS: Cross-polarization magic angle spinning

TON: Turnover number

POSS: Polyhedral oligosilsesquioxane

ESI: Electrospray ionization

SSNMR: Solid-state nuclear magnetic resonance

GC: Gas chromatography

MS: Mass spectroscopy

COSY: Homonuclear correlation spectroscopy

HSQC: Heteronuclear single quantum correlation

HMBC: Heteronuclear multiple bond correlation

TMS: Tetramethylsilane

SPS: Solvent purification system

IRC: Intrinsic reaction coordinate

SVP: Split valence polarization

ABSTRACT

Early-Late heterobimetallic (ELHB) transition metal complexes offer unique perspectives in small molecules activation reactions due to the bifunctionality of the metal atoms involved. One identified strategy in order to direct and stabilize ELHB assemblies is to take profit of bifunctional bridging ligands featuring two distinct coordination motifs: one hard, able to form strong bonds with electrophilic early metal centers and one soft nucleophilic site featuring a strong affinity for electron rich late metal centers. In most examples of bifunctional ligands reported to date in the literature, the late-metal donor is a phosphine-derived moiety. N-Heterocyclic carbenes (NHCs) have evolved as a substitute to phosphine ligands due to their relatively easy synthesis and ability to form stable and strong metal complexes when compared to phosphines. Moreover, a versatile range of functionalized NHCs could be synthesized by incorporating wide variety of functional groups in the NHC backbone. Surprisingly, very few ELHB complexes supported by bifunctional NHC ligands have been reported to date. Hence, the aim of this PhD work is to report the synthesis of tantalum-rhodium ELHB complexes utilizing the bifunctional NHC ligands. The efficient, scalable, simple and versatile synthesis of a new unsymmetrical hydroxyl-tethered NHC has been developed. The exact structure of the free ligand platform has been investigated in detail: the analyses reveal that this ligand adopts a neutral hydroxyl-carbene form that features an unusual OH-carbene hydrogen-bonding interaction. This ligand platform was successfully used to yield rare examples of Ta-NHC complexes, as well as a series of Rh-NHC monometallic species. The potential of these derivatives for the preparation of Ta/Rh heterobimetallic assemblies was then explored through either i) the protonolysis reaction between the free hydroxyl pendant group in the monometallic Rh complex and the alkyl moiety from tantalum precursors or ii) the incorporation of Rh into Ta-NHC complexes through carbene transmetallation from Ta to Rh. Mitigated results were obtained in the case of tantalum alkylidene derivatives, likely due to the high reactivity of this chemical motif. However, well-defined NHC-based Ta/Rh heterobimetallic entities were obtained in the case of Ta-imido or Ta-siloxy alkyl derivatives. This showcases the utility of this bifunctional alcoxy-carbene motif to promote the assembly of the two metals, due to the preferred coordination of the "soft" carbene ligand moiety to Rh while the "hard" alkoxy ligand group is selective to Ta. The insight obtained from the reactivity in solution with molecular silanols was utilized to develop rare examples of silica-supported tantalum-rhodium ELHB complexes. Finally, as a prospective exploration of a potential reaction of interest; computational study for nitrogen activation to NH_3 was carried out using the homogeneous bimetallic complex. The first few steps of the catalytic cycle involve the transfer of hydride from the rhodium center to the tantalum bound η^2-N_2 and are energetically favorable i.e., the transition states and the local minima energies are below 30 kcal.mol^{-1}. This work opens attractive perspectives for small molecules activation by ELHB species, and future work will focus on the implementation of the N_2 activation in laboratory using the silica-supported complexes.

RESUMÉ

Les complexes de métaux de transitions hétérobimétalliques “Early-Late“ (*ELHB*) offrent des perspectives uniques pour les réactions d’activation de petites molécules grâce à la bifonctionnalité des atomes métalliques mis en jeu. Une des stratégies identifiées afin de diriger et de stabiliser ces assemblages hétérobimétalliques “Early-Late” est de tirer parti de ligands pontants bifonctionnels se caractérisant par la présence de deux fonctions coordinnantes distinctes : une fonction dite “dure”, capable de former des liaisons fortes avec des métaux précoces électrophiles ; et une fonction dite “molle”, exhibant une forte affinité pour les métaux tardifs riches en électrons. Dans la plupart des exemples de ligands bifonctionnels reportés dans la littérature à ce jour, le site donneur pour les métaux tardifs est de type phosphine. Les Carbènes N-Hétérocycliques (NHCs) sont devenus un substitut aux ligands phosphines grâce à leur synthèse relativement aisée ainsi qu’à leur propension à former des complexes métalliques stables et robustes comparés aux phosphines. De plus, une gamme étendue de NHCs fonctionnalisés peut être obtenue par l’introduction d’une grande diversité de groupements fonctionnels sur le squelette du NHC. De manière surprenante, très peu de complexes *ELHB* supportés par des ligands NHC bifonctionnels ont été reportés dans la littérature jusqu’à présent. Par conséquent, l’objectif de ce travail de thèse est de reporter la synthèse de complexes *ELHB* à base de Tantale-Rhodium comportant des ligands NHC bifonctionnels. Une méthode efficace, extensive, simple et polyvalente d’un ligand NHC asymétrique présentant un bras hydroxyde a été développée. La structure exacte de ce ligand libre a été examinée : les analyses ont relevées que ce ligand adopte une forme neutre carbène-hydroxyde contenant une liaison hydrogène atypique $C_{carbène}$-HO. Cette plateforme moléculaire a été utilisée avec succès pour la synthèse presque inouïe de complexes Ta-NHC, ainsi qu’une série de complexes Rh-NHC monométalliques. Le potentiel de ces dérivés pour la préparation d’assemblages hétérobimétalliques Ta/Rh a été exploré, soit par i) la réaction de protonolyse entre le groupement hydroxyle libre contenu dans le complexe monométallique de rhodium et le groupement alkyle des précurseurs de tantale, ou par ii) l’incorporation de Rh dans le complexe Ta-NHC *via* une transmétallation du carbène depuis le tantale vers le rhodium. Des résultats mitigés ont été obtenus dans le cas des dérivés de tantale- alkylidènes, probablement dus à la forte réactivité de cette entité chimique. Cependant, des édifices *ELHB* bien définis, à base de Ta/Rh et supportés par un NHC ont été obtenus dans le cas des dérivés de Tantale-imido ou siloxy-alkyle. Cela valorise l’utilité de ce motif alcoxy-carbène à promouvoir l’assemblage de ces deux métaux *via* la coordination préférentielle du ligand “mou” carbénique sur le Rh tandis que le groupement coordinant hydroxyle “dur” est sélectif vis-à-vis du tantale. Les informations obtenues à partir de la réactivité en solution avec des silanols moléculaires ont été utilisées pour développer des exemples rares de complexes *ELHB* tantale-rhodium supportés sur silice. Finalement, en tant que perspective exploratoire d’une réaction potentielle d’intérêt, une étude computationnelle de l’activation de diazote et sa conversion en ammoniac a été réalisée en utilisant le complexe bimétallique homogène. Les premières étapes du cycle catalytique impliquent le transfert d’hydrures depuis le rhodium vers la liaison η^2-N_2–tantale, ses étapes sont énergétiquement favorables c’est-à-dire que les états de transition ainsi que les minima locaux d’énergie sont en deçà de 30 kcal·mol^{-1}. Ces travaux ouvrent des perspectives intéressantes pour l’activation de petites molécules par des espèces *ELHB*. De futurs travaux se concentreront sur la mise en œuvre de l’activation de N_2 au laboratoire en utilisant des complexes supportés sur silice.

ZUSAMMENFASSUNG

Die Kombination von frühen und späten hetero-bimetallischen Übergansmetallkomplexen (ELHB) bietet durch die Bifunktionalität der involvierten Metallatome einzigartige Möglichkeiten in der Aktivierung von kleinen Molekülen. Eine Strategie zur Stabilisierung von ELHBs nutzt die Eigenschaften von bifunktionalen, verbrückenden Liganden aus, die zwei verschiedene Koordinationsmotive besitzen: Ein hartes, das es ermöglicht starke Bindungen mit den elektrophilen Frühmetallzentren einzugehen und eine weiche, nukleophile Seite für eine starke Affinität zu elektronenreichen Spätmetallzentren. In den meisten Beispielen von zum heutigen Zeitpunkt literaturbekannten bifunktionellen Liganden fungiert eine vom Phosphan abgeleitete Gruppe als Spätmetalldonor. N-Heterocyclische Carbene (NHCs) haben sich als Substitution zu den Phosphanliganden hervorgetan auf Grund ihrer leichten Synthese und der Bildung von stabileren Metallkomplexen im Vergleich zu den Phosphanen. Eine große Bandbreite an funktionalisierten NHCs konnte schon synthetisiert werden durch die Einbringung der verschiedensten funktionellen Gruppen in das NHC-Rückgrat. Überraschenderweise sind bis jetzt nur sehr wenige ELHB-Komplexe bekannt, die von einem bifunktionalen NHC-Liganden stabilisiert werden. Daher ist das Ziel dieser Doktorarbeit die Synthese von Tantal-Rhodium ELHB-Komplexen mit bifunktionellen NHC-Liganden. Die effiziente, skalierbare, einfache und vielseitige Synthese eines neuen, unsymmetrischen Hydroxyl-verknüpftem NHC wurde entwickelt. Die genaue Struktur des freien Ligandengrundgerüsts wurde im Detail analysiert und ergab, dass dieser Ligand eine neutrale Hydroxyl-Carben-Form annimmt, die eine ungewöhnliche OH-Carben Wasserstoff-Bindungs-Wechselwirkung beinhaltet. Diese Liganden-Plattform wurde erfolgreich zur Herstellung seltener Tantal-NHC-Komplexe und einer Reihe von monometallischen Rh-NHC Spezies genutzt. Das Potential dieser Derivate für die Herstellung von bimetallischen Ta/Rh-Komplexen wurde dann erforscht durch entweder i) die Protonoloyse zwischen der freien Hydroxyl-Gruppe in dem monometallischen Rh-Komplex und der Alkyl-Gruppe der Tantal-Vorstufe oder ii) das Einfügen von Rh in Tantal-NHC-Komplexe durch Carben-Transmetallierung von Ta zu Rh. Die Herstellung von Tantal-Alkyliden gestaltete sich als Herausforderung, durch die hohe Reaktivität dieses chemischen Motivs. Trotzdem wurden definierte NHC-basierte heterobimetallische Ta/Rh-Verbindungen erhalten für Ta-Imido und Ta-Siloxyl-Alkyl-Derivate. Dies zeigt beispielhaft die Nützlichkeit der bifunktionalen Alkoxy-Carben-Motive zur Verbindung zweier Metalle durch die selektive Koordination des „weichen“ Carben-Liganden am Rh und des „harten“ Alkoxy-Liganden am Ta. Durch die Einblicke in die Reaktivität der Komplexe in Lösung mit molekularen Silanolen konnten seltene Beispiele von Silika unterstützten Ta/Rh ELHB-Komplexen entwickelt werden. Schließlich wurde, für eine Erkundung einer potentiellen Anwendung, eine rechnerische Studie über die Stickstoff-Aktivierung zur Ammoniak Synthese an den homogenen, bimetallischen Komplexen durchgeführt. Die ersten Schritte des Katalysezyklus beinhalten den Transfer eines Hydrids vom Rh-Zentrum zu dem am Ta gebundenem η^2-N_2 und sind energetisch günstig, d.h. die Übergangszustände und lokalen Minima liegen weniger als 30 kcal mol-1 auseinander. Diese Arbeit eröffnet attraktive Perspektiven für die Aktivierung von kleinen Molekülen durch ELHB-Spezies und die zukünftige Arbeit wird sich auf die Implementierung der N_2-Aktivierung im Labor mit Silika unterstützten Komplexen fokussieren.

Summary

Cooperativity and synergy between metals of a bimetallic complex presents distinctive prospects in stoichiometric as well as catalytic transformations.[1] Both metal centers of a bimetallic complex can operate simultaneously on the same substrate. They can also work in tandem where the second metal takes the output from the catalytic cycle of the first metal and coverts it into the final product.[2,3] One of the extreme forms of bimetallic complexes is *early-late heterobimetallic (ELHB)* species, that combine electronically different metals.[4,5] These complexes have proven active in a number of stoichiometric and catalytic chemical transformations like C-H activations,[6] small molecules activations,[7] hydrosilylation reactions,[8] and several reports demonstrate better reactivity with early/late heterobimetallic catalysts than with their monometallic analogues.[7,9–12] However, the synthesis of ELHB complexes is a challenging task due to the different chemical properties of the metal atoms involved. One identified strategy in order to direct and stabilize ELHB assemblies is to take profit of bifunctional bridging ligands featuring two distinct coordination motifs: one hard electrophilic site, able to form strong bonds with electrophilic early metal centers and one soft nucleophilic site featuring a strong affinity for electron rich late metal centers. In most examples of bifunctional ligands reported to date in the literature, the late-metal donor is a phosphine-derived moiety.[13–16] N-Heterocyclic carbenes (NHCs) ligands have been a preferred ligand of choice and a substitute to the phosphine ligands due to their ability to form stable and strong metal complexes when compared to phosphines,[17] and currently play an important role in organometallic catalysis.[18] Moreover, a versatile range of functionalized NHCs could be synthesized by incorporating wide variety of functional groups in the NHC backbone.[19–22] Surprisingly, very few ELHB complexes supported by bifunctional NHC ligands have been reported to date.[23–28] Hence, we designed a bifunctional N-heterocyclic carbene (NHC) linker to assemble two different metals. We envisaged a NHC molecule which can bind to a late metal center through its carbenic carbon and to an early electrophilic metal with the pendant alcoholic group present in one of its arms. The aim of this PhD work is to report the synthesis of tantalum-rhodium ELHB complexes utilizing this bifunctional NHC ligand.

The first step of the thesis was to synthesize the targeted bifunctional hydroxyl-NHC ligand needed to assemble the heterobimetallic complex. A one-pot, scalable and straightforward synthetic procedure was developed leading to the desired unsymmetrical unsaturated imidazolium salt precursor, namely 1-mesityl-3-(2-hydroxyisobutyl)imidazolium hexafluorophosphate **1** (**Scheme S1**). The deprotonation of the imidazolium salt **1** by KHMDS

leads to the targeted bifunctional hydroxyl-NHC ligand **2**. The ^{13}C NMR spectrum depicts the characteristic carbene signal as a broad resonance at 202.6 ppm in THF-d_8. A carbene-alcohol interaction was evidenced on the basis of the NMR, IR and X-ray crystal structure data.[29] In particular, in the solid-state the observed distance between the hydroxyl hydrogen and the carbene carbon (1.97 Å) of an adjacent ligand is characteristic of intermolecular hydrogen bonding.

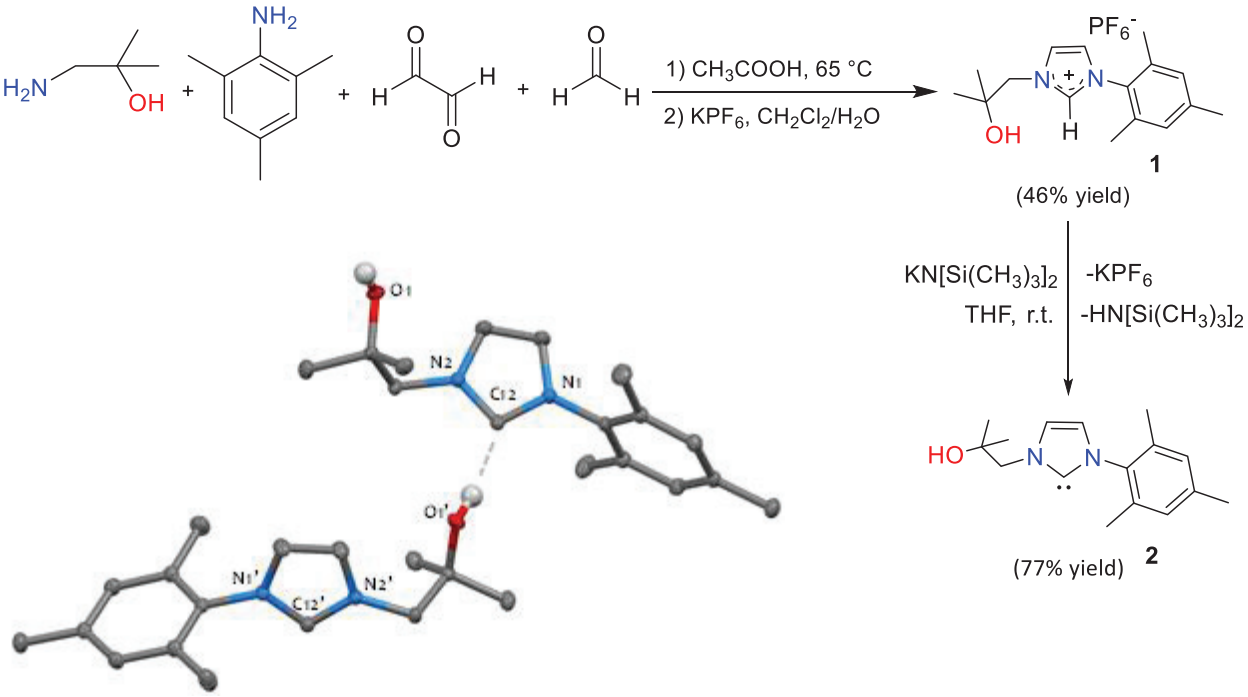

Scheme S1. One-pot straightforward synthesis of the unsymmetrical imidazolium salt 1. KHMDS addition to **1** leads to the selective deprotonation of the imidazolium proton (to yield the free carbene **2**) rather than the deprotonation of hydroxyl proton.

With the ligand in hands, the next step was to study its coordination properties in solution towards early and late metals. To this aim, a series of monometallic tantalum and rhodium species were prepared. The tantalum-NHC complex **3** was synthesized by addition of 1.0 equivalent of the free carbene to the tantalum tris(neopentyl) neopentylidene precursor. The ^{13}C NMR of the complex in C_6D_6 shows the $NHC_{carbene}$ signal at 203.1 ppm which is upfield as compared to the free carbenes[30] suggesting a weak interaction between the carbene and the tantalum metal centre. The crystal structure of the complex validates this metal-NHC

interaction. However, the Ta-C_{NHC} bond length is long (2.355 Å)[31] and suggests that it should be possible to transmetallate to a metal with higher affinity for the carbene. Complex **3** is stable in solid state at -40°C for months but decomposes within hours at room temperature (to yield complex **4** by C-H activation of the mesityl group at the tantalum center which was confirmed by the crystal structure of complex **4**). This process is not unusual since such orthometallation reactions have been reported with tantalum metal.[32]

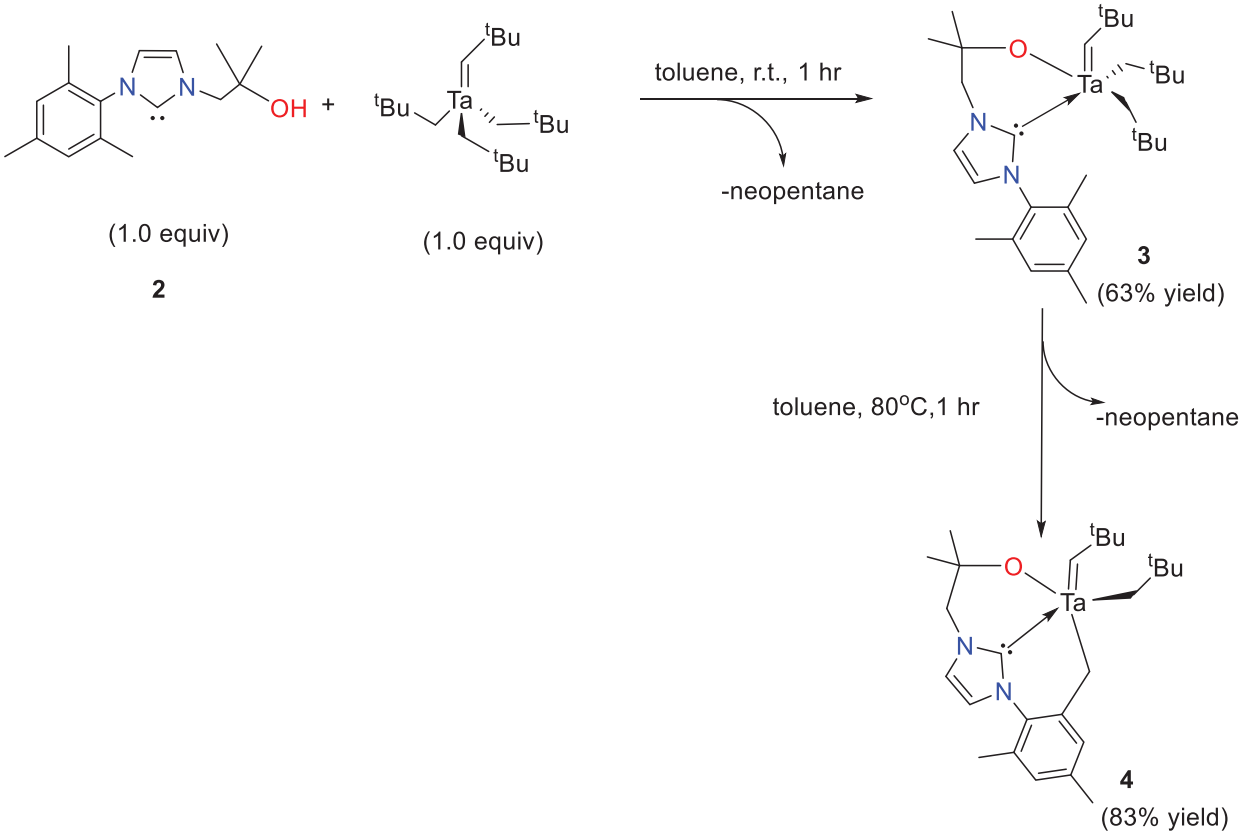

Scheme S2. The tantalum-NHC complex **3** was prepared by addition of 1.0 equivalent of the bifunctional NHC ligand to the tantalum precursor. Complex **3** decomposes at room temperature to yield **4** by C-H activation of the ligand mesityl group.

The addition of $[Rh(COD)Cl]_2$ to the tantalum complex **3** lead to the formation of a trimetallic complex **11** as shown in **scheme S3**. The formation of this trimetallic species is confirmed by elemental analysis result (mol%Rh: mol%Ta = 1.9) as well as HRMS-[ESI] (expected for $[M\text{-}Cl]^+$ 1107.3309, found 1107.3320). Unfortunately, multiple attempts to grow single crystals of **11** suitable for X-ray crystallographic studies failed.

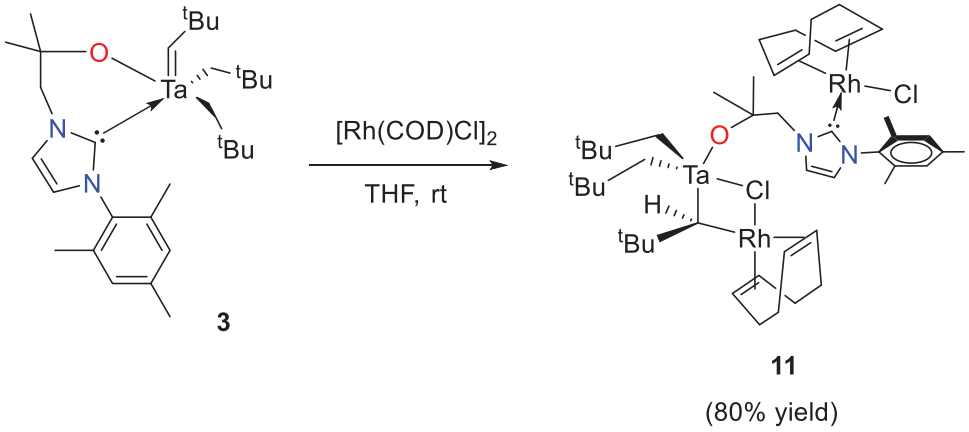

Scheme S3: The tantalum precursor **3** and $[Rh(COD)Cl)]_2$ molecule react in 1:1 ratio in THF to yield the trimetallic complex **11**.

This study established the feasibility of the envisioned Ta to Rh NHC transmetallation. However the clean formation of the targeted heterobimetallic species was not successful since over-metallation at the Ta alkylidene moiety was observed. Another route to synthesize the desired bimetallic complex involves the synthesis of the rhodium-NHC complex first followed by a protonolysis reaction with the tantalum tris(neopentyl) neopentylidene precursor. The rhodium-NHC complex **6** was successfully synthesized by the addition of a THF solution of the ligand to the rhodium precursor $[Rh(COD)Cl]_2$ at room temperature (**Scheme S4**). The formation of the compound was confirmed by ^1H, ^{13}C, elemental analysis and X-ray crystallography. In particular the ^1H NMR spectrum of the isolated compound in $CDCl_3$ showed that the hydroxyl proton was intact (observed as sharp singlet at 3.5 ppm), which is further confirmed by the IR data (characteristic ν_{OH} signal at 3368 cm^{-1}). The reaction between complex **6** and $Ta(CH^tBu)(CH_2{}^tBu)_3$ resulted in the observation of mixture of products probably due to the availability of multiple reaction sites at the tantalum center for the hydroxyl group of complex **6**.

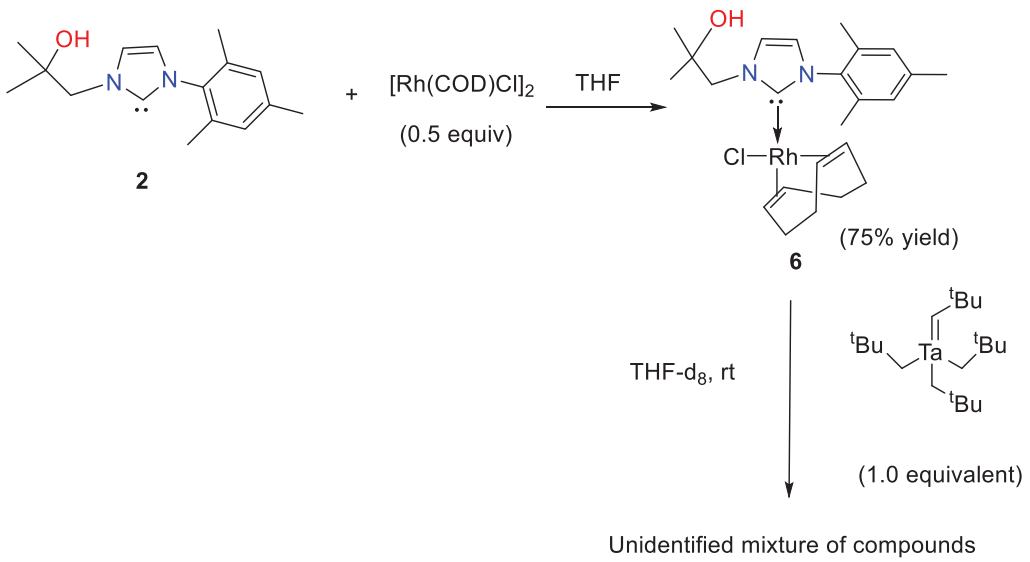

Scheme S4. The scheme represents the synthesis of the rhodium-NHC complex **6**. Treatment of **6** with $Ta(CH^tBu)(CH_2{}^tBu)_3$ resulted in the formation of a mixture of species.

This first set of studies revealed that the presence of the highly reactive alkylidene moiety at tantalum was hampering the clean formation of the targeted Ta/Rh heterobimetallic species. Therefore a third synthetic route was developed and consisted first in adding a silanol moiety onto the alkylidene to tune the reactivity of the Ta site. The next part of the work consisted of developing silica-supported heterogeneous Ta/Rh heterobimetallic complexes via Surface OrganoMetallic Chemistry (SOMC) approach.[33] Firstly, Polyhedral Oligosilsesquioxane (POSS) based homogeneous molecular model of the silica-supported complex was developed. The treatment of the tantalum-NHC complex **3** with the mono-hydroxyl Polyhedral Oligomeric Silsesquioxane derivative, POSS-OH **14**, yielded the intermediate *tris*-alkyl complex **16** resulting from the 1,2-addition of the hydroxyl group across the tantalum alkylidene motif without elimination of neopentane. The addition of $[Rh(COD)Cl]_2$ to complex **16** leads to desired bimetallic complex **17** (**Scheme S5**). The incorporation of rhodium metal was confirmed by ^1H and ^{13}C NMR studies. However, despite multiple attempts, single crystals of compound **17** could not be obtained.

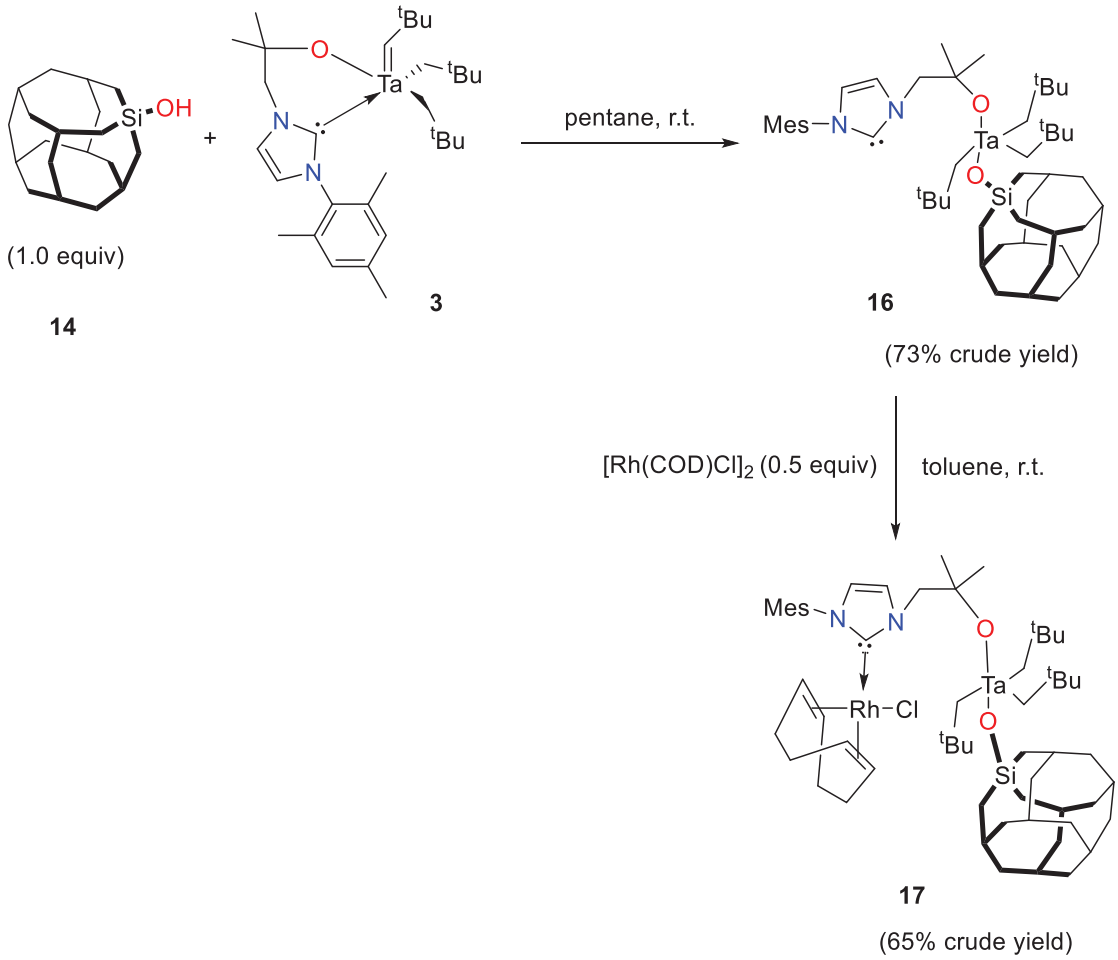

Scheme S5. The scheme represents the preparation of the POSS-supported Ta-NHC complex **16**, followed by rhodium addition to lead to the desired Ta/Rh heterobimetallic complex **17**.

Obtaining the crystal structure of the complex was important in order to perform computational studies on the bimetallic complex for small molecule activation. Hence the *tris*(tert-butoxy)silanolate analogue of complex **17** was synthesized using an analogous procedure (**Scheme S6**). The ^{13}C NMR spectrum of the tantalum complex **18** displays a signal at 219.4 ppm which is characteristic of the free NHC carbene which is not involved in an interaction with the metal center. Complex **18** undergoes metallation with $[Rh(COD)Cl]_2$ to yield the desired bimetallic complex **19**. The crystal structure of the complex, (Scheme S6) confirms the incorporation of rhodium metal which is attached to the NHC ligand, as expected.

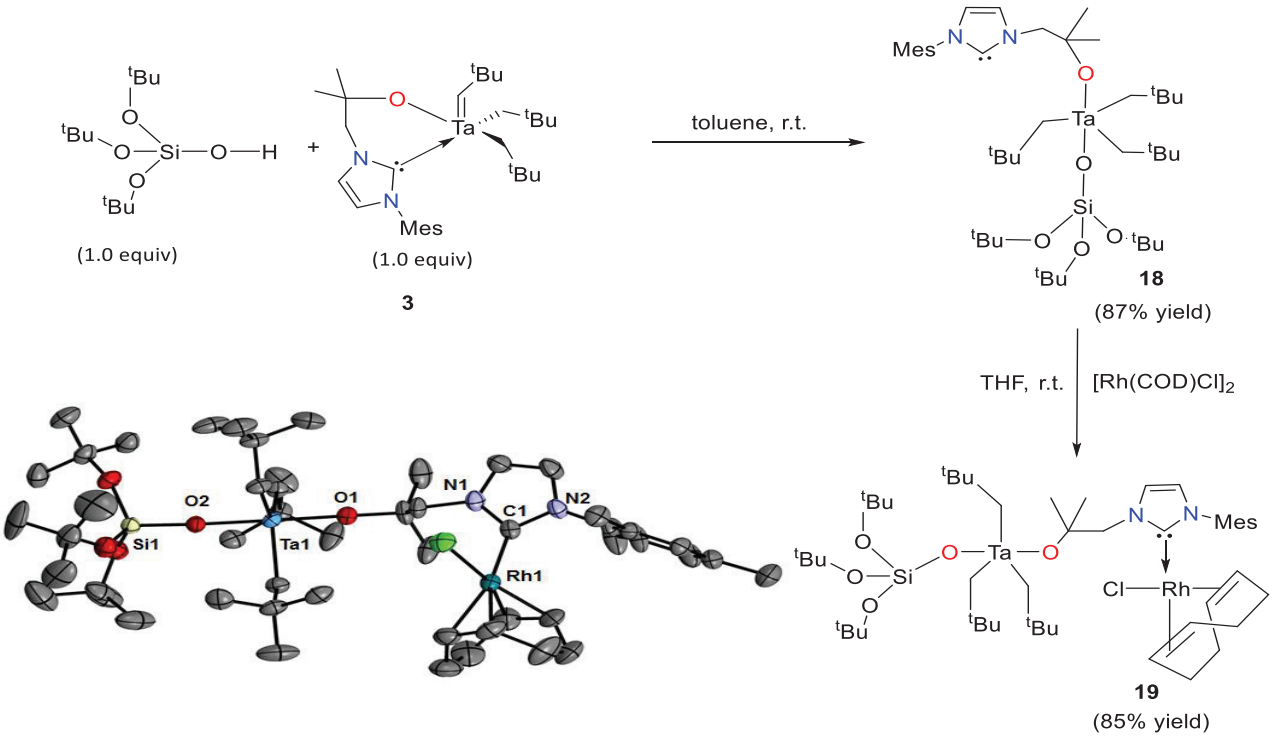

Scheme S6. The addition of 1 equivalent of *tris*(tert-butoxy)silanol to a toluene solution of complex **3** leads to the tantalum complex **18**. Metallation of the Ta complex **18** at room temperature with $[Rh(COD)Cl]_2$ yields the bimetallic complex **19**.

After streamlining the synthetic protocol for preparing the homogenous bimetallic complex **19**, the next step was to implement this protocol to access the analogous silica supported bimetallic complex. For this purpose, the Ta-NHC complex **3** was added to silica surface dehydroxylated at 700°C ($SBA\text{-}15_{700}$) to yield the corresponding supported tantalum-NHC complex. The ^{13}C CP-MAS solid state NMR spectrum displays the expected ligand signals except that of the $NHC_{carbene}$ carbon. Therefore the corresponding ^{13}C labelled tantalum-NHC complex **3** was synthesized and grafted over silica. The ^{13}C NMR spectrum of the labelled carbene species shows two carbene signals: one signal at δ = 219.81 ppm which is reminiscent of a free carbene (as also observed for complex **18**) and second signal at δ = 201.97 ppm which is characteristic of a carbene interacting with a Ta center. This indicates that two surface species are obtained upon immobilization of **3** onto silica: one (supported complex 21) in which the NHC is bound to Ta, and a second one (supported complex 21') in which the NHC ligand is unbound to Ta. The corresponding bimetallic supported complex **22** was obtained by the reaction of this material containing supported complexes **21** & **21'** with $[Rh(COD)Cl]_2$ (**Scheme S7**).

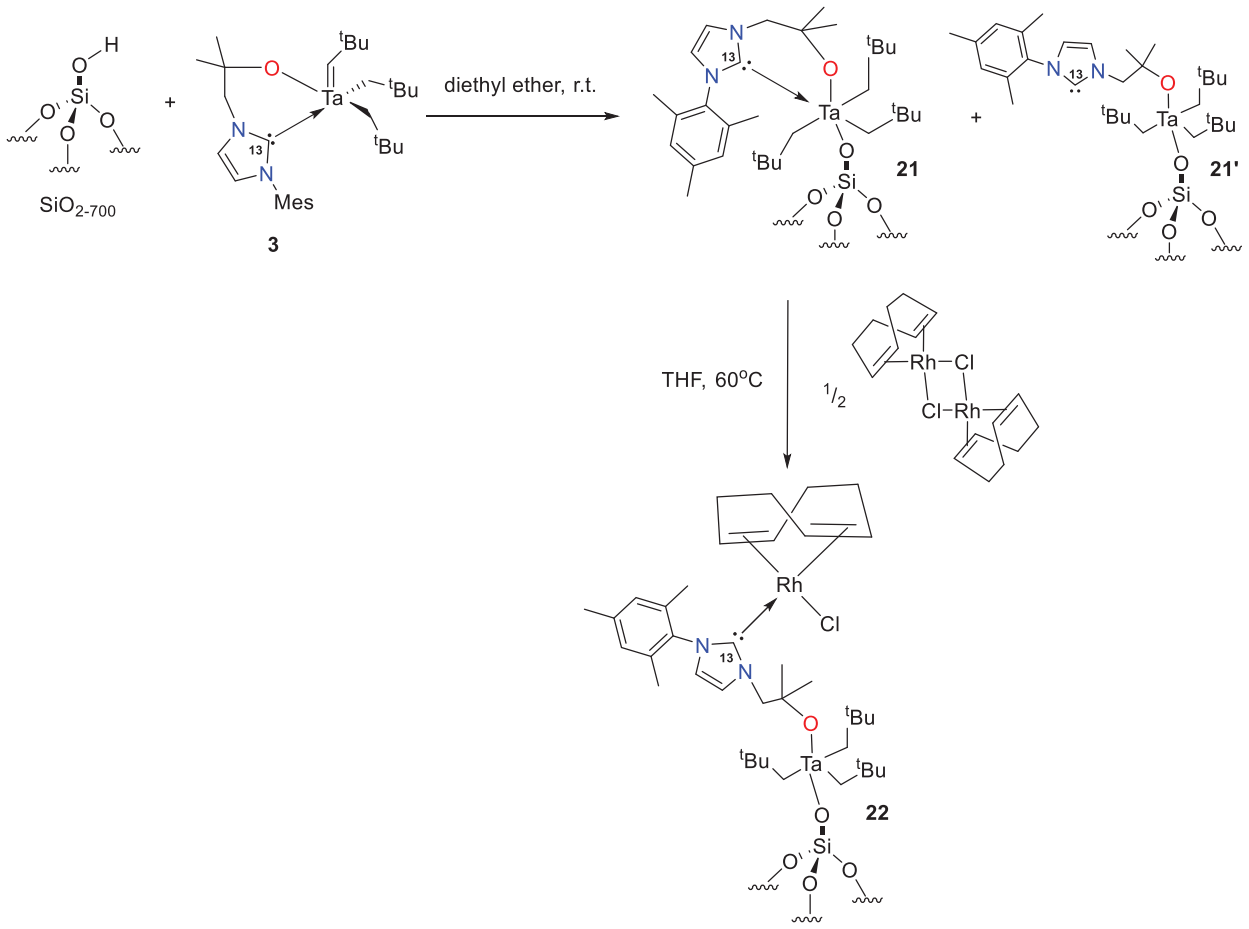

Scheme S7. Immobilization of the Ta complex **3** at the surface of silica and post-treatment with $[Rh(COD)Cl]_2$ to lead to the silica supported Ta/Rh heterobimetallic complex **22**.

The characterization of the grafted complex **22** by elemental analysis indicates that 85% of the NHC carbene is transmetallated to the rhodium metal.

We then shifted our attention to study the catalytic behavior of the bimetallic complex for small molecule activation. As a model reaction we studied the catalytic conversion of nitrogen activation to ammonia computationally using complex **17**. We hypothesized a reaction mechanism in which the nitrogen reduction takes place at the tantalum center whereas the rhodium center supplies the hydrides for the reduction. The catalytically active species so obtained is depicted in **Figure S1**. B97D3-BJ dispersion corrected density functional and def2-SVP basis set was used to perform all the calculations.

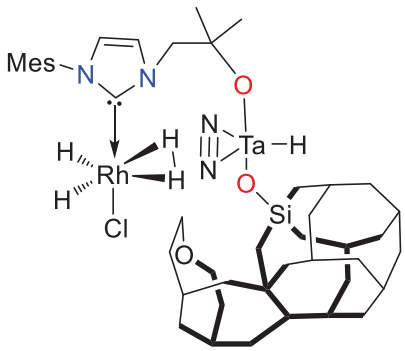

Figure S1. Computed complex N_2/hydrido Ta/Rh complex, exhibiting a dinitrogen bonded in a side-on fashion to Ta.

We were able to calculate the energy demand of first few local minima. Unfortunately, the transition state for the first step which involves the transfer of hydride from rhodium to the tantalum bound nitrogen could not be located. However, the transition state for the next step which involves the transfer of a second hydride to the nitrogen center was located 18 kcalmol^{-1} higher in energy than the starting material (**Figure S2**). This barrier is significantly lower than the energy requirements of the catalytic cycle where the two metals do not interact with each other. This preliminary result is promising as it validates our hypothesis of utilizing two chemically different elements in synergy with each other to establish cooperative reactivity for small molecules activation. Future work will be required to implement these results in laboratory using the silica supported bimetallic complex **22**.

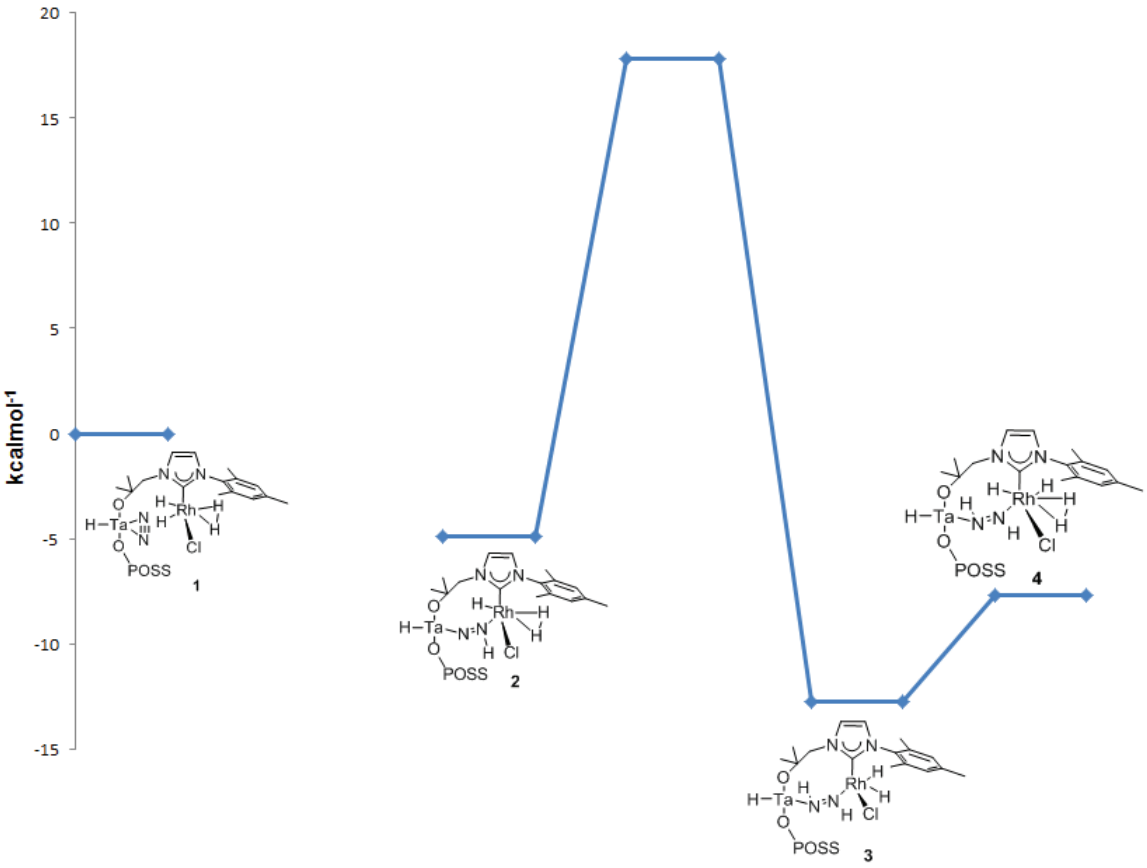

Figure S2. Gibbs energy profile (B97D3-BJ/def2-SVP) of the POSS based bimetallic complex with the nitrogen molecule bonded to the tantalum centre. Although we could not locate the transition state TS1-2, the computations show that TS2-3 lays 17.85 kcalmol^{-1} higher than the catalytically active species.

In conclusion, the tantalum-rhodium early-late heterobimetallic species was successfully assembled by using a bifunctional N-heterocyclic carbene as a bridge between the two transition metal centers, both in solution and at the surface of silica material. Preliminary computational studies regarding N_2 conversion to ammonia are promising, and showed that the nitrogen reduction could benefit from the proximity of the two metals. Future work will focus on the implementation of the N_2 activation in laboratory using the silica-supported complexes.

REFERENCES

1 P. Buchwalter, J. Rosé and P. Braunstein, *Chem. Rev.*, 2015, **115**, 28–126.

2 C. M. Thomas, *Comments Inorg. Chem.*, 2011, **32**, 14–38.

3 C. Cornelissen, G. Erker, G. Kehr and R. Fröhlich, *Organometallics*, 2005, **24**, 214–225.

4 L. H. Gade, *Angew. Chem. Int. Ed.*, 2000, **39**, 2658–2678.

5 B. G. Cooper, J. Wesley Napoline and C. M. Thomas, *Catal. Rev. Sci. Eng.*, 2012, **541**, 1–401.

6 S. Lassalle, R. Jabbour, P. Schiltz, P. Berruyer, T. K. Todorova, L. Veyre, D. Gajan, A. Lesage, C. Thieuleux and C. Camp, *J. Am. Chem. Soc.*, 2019, jacs.9b08311.

7 T. A. Hanna, A. M. Baranger and R. G. Bergman, *J. Am. Chem. Soc.*, 1995, **117**, 11363–11364.

8 W. Zhou, S. L. Marquard, M. W. Bezpalko, B. M. Foxman and C. M. Thomas, *Organometallics*, 2013, **32**, 1766–1772.

9 E. Bodio, M. Picquet and P. Le Gendre, in *Topics in Organometallic Chemistry*, 2015, **59**, 139–186.

10 N. Wheatley and P. Kalck, *Chem. Rev.*, 2002, **99**, 3379–3420.

11 M. J. Hostetler and R. G. Bergman, *J. Am. Chem. Soc.*, 1990, **112**, 8621–8623.

12 M. J. Hostetler, M. D. Butts and R. G. Bergman, *J. Am. Chem. Soc.*, 1993, **115**, 2743-2752.

13 L. M. Slaughter and P. T. Wolczanski, *Chem. Commun.*, 1997, 2109–2110.

14 J. P. Krogman, B. M. Foxman and C. M. Thomas, *J. Am. Chem. Soc.*, 2011, **133**, 14582–14585.

15 T. Miyazaki, Y. Tanabe, M. Yuki, Y. Miyake and Y. Nishibayashi, *Organometallics*, 2011, **30**, 2394–2404.

16 L. J. Clouston, V. Bernales, R. K. Carlson, L. Gagliardi and C. C. Lu, *Inorg. Chem.*, 2015, **54**, 9263–9270.

17 R. H. Crabtree, *J. Organomet. Chem.*, 2005, **690**, 5451–5457.

18 E. Peris, *Chem. Rev.*, 2018, **118**, 9988–10031.

19 M. N. Hopkinson, C. Richter, M. Schedler and F. Glorius, *Nature*, 2014, **510**, 485–496.

20 F. Cisnetti, C. Gibard and A. Gautier, *J. Organomet. Chem.*, 2015, **782**, 22–30.

21 H. V. Huynh, *Chem. Rev.*, 2018, **118**, 9457–9492.

22 A. J. Arduengo, H. V. R. Dias, R. L. Harlow and M. Kline, *J. Am. Chem. Soc.*, 1992, **114**, 5530–5534.

23 P. K. Majhi, S. C. Serin, G. Schnakenburg, D. P. Gates and R. Streubel, *Eur. J. Inorg. Chem.*, 2014, **2014**, 4975–4983.

24 J. Ruiz, L. García, M. Vivanco, Á. Berros and J. F. Van der Maelen, *Angew. Chem. Int. Ed.*, 2015, **127**, 4286–4290.

25 J. Ruiz and A. F. Mesa, *Chem. - A Eur. J.*, 2012, **18**, 4485–4488.

26 T. Okayama, T. Watanabe, Y. Hatayama, S. Ishihara and Y. Yamaguchi, *Inorganica Chim. Acta*, 2016, **448**, 1–6.

27 D. A. Valyaev, M. A. Uvarova, A. A. Grineva, V. César, S. N. Nefedov and N. Lugan, *Dalt. Trans.*, 2016, **45**, 11953–11957.

28 M. A. Huertos, J. Pérez, L. Riera, J. Díaz and R. López, *Chem. - A Eur. J.*, 2010, **16**, 8495–8507.

29 J. A. Cowan, J. A. C. Clyburne, M. G. Davidson, R. L. W. Harris, J. A. K. Howard, P. Küpper, M. A. Leech and S. P. Richards, *Angew. Chemie Int. Ed.*, 2002, **41**, 1432–1434.

30 D. Tapu, D. A. Dixon and C. Roe, *Chem. Rev.*, 2009, **109**, 3385–3407.

31 P. A. Petrov, T. S. Sukhikh and M. N. Sokolov, *Dalt. Trans.*, 2017, **46**, 4902–4906.

32 L. P. Spencer, C. Beddie, M. B. Hall and M. D. Fryzuk, *J. Am. Chem. Soc.*, 2006, **128**, 12531–12543.

33 C. Copéret, A. Fedorov and P. A. Zhizhko, *Catal. Letters*, 2017, **1**, 1–13.

Résumé

Les effets de coopérativité et de synergie entre métaux d'un complexe bimétallique offrent des perspectives particulières pour les transformations stœchiométriques comme catalytiques.[1] Les deux centres métalliques de l'entité bimétallique peuvent être impliqués simultanément sur un même substrat. Ils peuvent également fonctionner en tandem où le second métal réagit sur le composé issu du cycle catalytique du premier métal pour le convertir en produit final.[2,3] Une des catégories extrêmes de complexes bimétaliques est les espèces *early-late* hétérobimétalliques (*ELHB*) combinant des métaux électroniquement distincts .[4,5] Ces complexes se sont avérés actifs pour un grand nombre de transformations stœchiométriques et catalytiques tel que l'activation C–H,[6] les activations de petite molécules,[7] ainsi que les réactions d'hydrosylilation.[8] De plus, de nombreux rapports démontrent une meilleure réactivité des catalyseurs *ELHB* par rapport à leur analogues monométaliques.[7,9–12] Cependant, la synthèse des complexes *ELHB* est une tâche ardue en raison de propriétés chimiques complétement différentes des atomes métalliques mis en jeu. Une stratégie connue en vue de stabiliser et diriger les assemblages *ELHB* est d'avoir recours à des ligands bifonctionnels contenant deux motifs de coordinations distincts : un site électrophile dit « dur », capable de former des liaisons fortes avec des centres métalliques précoces et un site nucléophile dit « mou » ayant une forte affinité pour les métaux tardifs électroniquement riche. Dans la plupart des exemples de ligands bifonctionnels reportés à ce jour dans la littérature, le donneur métallique « dur » est un groupement de type phosphine.[13–16] Les Carbènes N-Hétérocycliques (*NHCs*) sont devenus un ligand un de choix et un substitut aux ligands phosphines grâce à leur synthèse relativement aisée ainsi qu'à leur propension à former des complexes métalliques stables et robustes comparés aux phosphines.[17] Aussi, les *NHCs* occupent un rôle important en catalyse organométallique.[18] De plus, une gamme étendue de *NHCs* fonctionnalisés peut être obtenue par l'introduction d'une grande diversité de groupements fonctionnels sur le squelette du *NHC*.[19–22] De manière surprenante, très peu de complexes *ELHB* supportés par des ligands *NHC* bifonctionnels ont été reportés dans la littérature jusqu'à présent.[23–28] Par conséquent, nous avons conçu un connecteur NHC bifonctionnel pour assembler deux métaux différents. Nous avons envisagé une molécule NHC qui peut se lier à un centre métallique tardif *via* son carbone carbénique et à un métal électrophile précoce avec la présence d'une fonction alcool sur l'un de ses bras. L'objectif de ce travail de thèse est de reporter la synthèse de complexes *ELHB* tantale-rhodium utilisant ce ligand *NHC* bifonctionnel.

La première étape de cette thèse a été de synthétiser le ligand bifonctionnel hydroxyle-NHC nécessaire pour l'assemblage du complexe hétérobimétalique. Une procédure de synthèse *one pot*, extensible et simple a été développée pour produire le précurseur de sel d'imidazolium insaturé et asymétrique souhaité, à savoir le 1-mésityl-3-(2-hydroxyisobutyl)imidazolium hexafluorophosphate **1** (**Scheme S1**). La déprotonation du sel d'imidazolium **1** par la KHMDS conduit au ligand bifonctionnel hydroxyl-NHC ciblé. Le spectre de RMN du ^{13}C montre le signal caractéristique du carbène sous la forme d'une résonnance élargie à 206,6 ppm dans le THF-d_8. Une interaction alcool-carbène a été mis en évidence sur la base de données RMN, IR et DRX sur monocristal.[29] En particulier, à l'état solide, la distance observée entre l'hydrogène de l'hydroxyle et le carbone carbénique (1.97 Å) d'un ligand adjacent est typique d'une liaison hydrogène intermoléculaire.

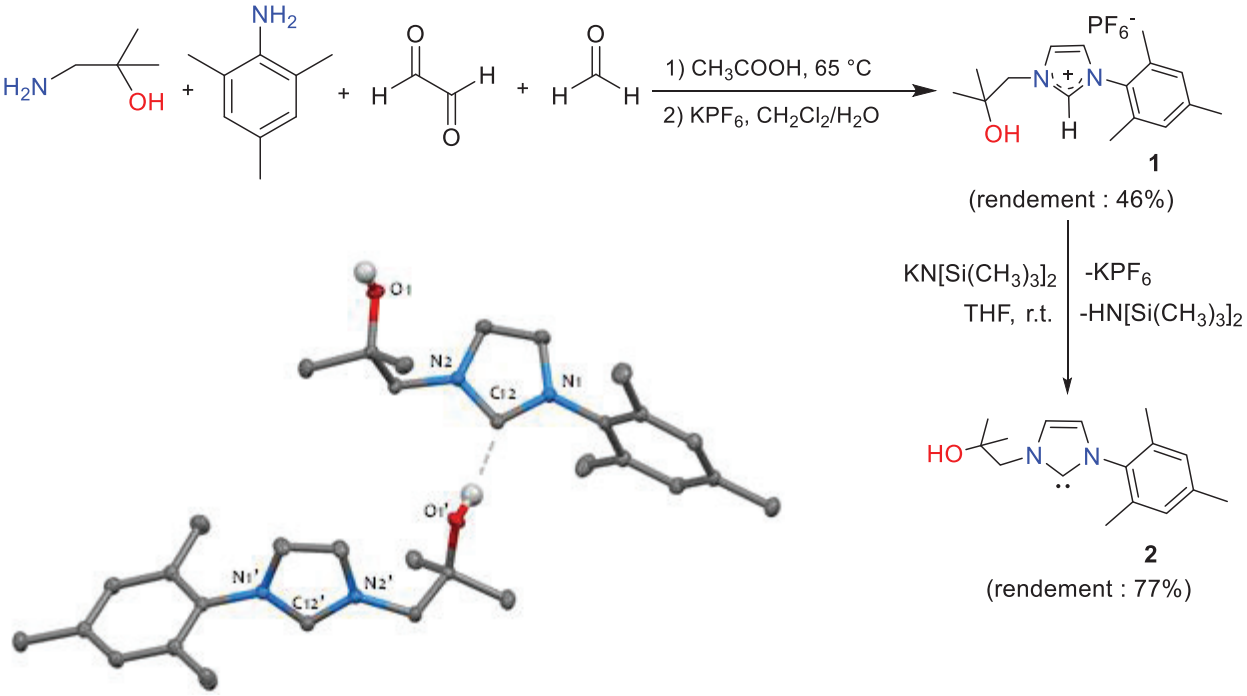

Schéma S3. Synthèse simple *one pot* du sel asymétrique **1**. Addition de KHMDS sur **1** pour déprotonner sélectivement le proton de l'imidazolium (afin de produire la carbène libre **2**)

Une fois le ligand en mains, la prochaine étape a été d'étudier ces propriétés de coordination en solution vis à vis des métaux précoces et tardifs. Pour ce faire, une série d'espèces monométalliques de tantale et de rhodium a été préparée. Le complexe de tantale-NHC **3** a été synthétisé par l'addition d'un équivalent du carbène libre sur le précurseur de tantale tris(néopentyl)néopentylidene. La RMN du ^{13}C du complexe dans le C_6D_6 montre le signal du

$NHC_{carbène}$ à 203,1 ppm qui est blindé comparé aux carbènes libres,[30] suggérant ainsi une interaction faible entre le carbène et le centre métallique de tantale. La structure cristalline du complexe confirme cette interaction métal-NHC. Cependant, la longueur de liaison Ta-C_{NHC} est longue (2.355 Å)[31] et suggère une potentielle transmétallation vers un métal avec une plus grande affinité sur le carbène. Le complexe **3** est stable à l'état solide à -40°C pendant des mois mais se décompose en quelques heures à température ambiante (pour former le complexe **4** par une activation C-H du groupement mésityle sur le centre tantale, ce qui a été confirmé par la structure cristalline du complexe **4**). Cette réactivité n'est pas inhabituelle puisque de telles réactions d'orthométallation ont été reporté avec du tantale.[32]

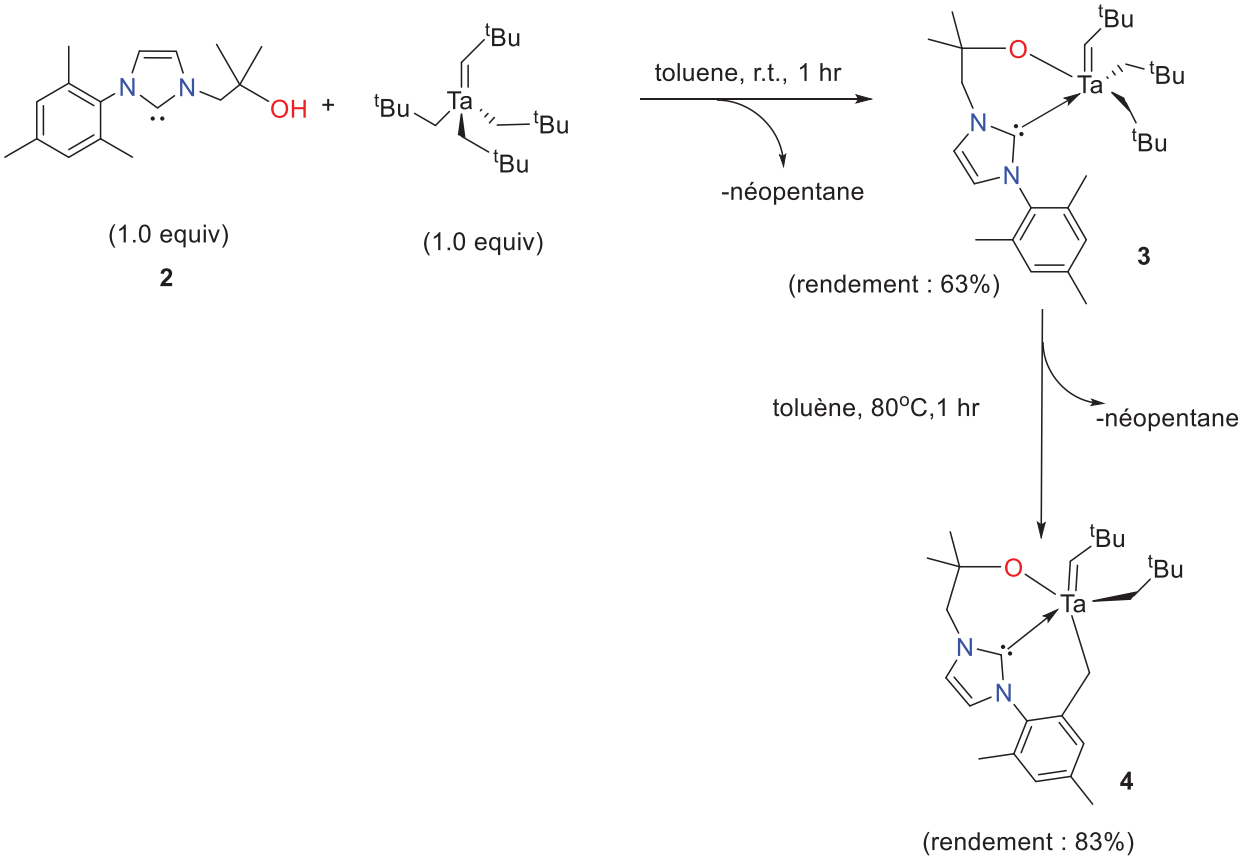

Schéma S4. Le tantale-NHC complexe **3** a été préparé par l'addition de 1,0 équivalent du ligand NHC bifonctionnel sur le précurseur de tantale. Complexe **3** se décompose à température ambiante pour former **4** par C-H activation du groupement mésityle du ligand.

L'addition de $[Rh(COD)Cl)]_2$ sur le complexe de tantale **3** amène à la formation d'un complexe trimétallique **5** comme montré sur le **schéma S3**. La formation de cette espèce trimétallique est confirmé par analyse élémentaire (mol% Rh : mol% Ta = 1.9) ainsi que par *HRMS-[ESI]* (attendu pour $[M\text{-}Cl]^+$ 1107.3309, trouvé 1107.3320). Malheureusement, de nombreuses tentatives pour faire croître des monocristaux de **11** adaptés à des études DRX n'ont pas abouti.

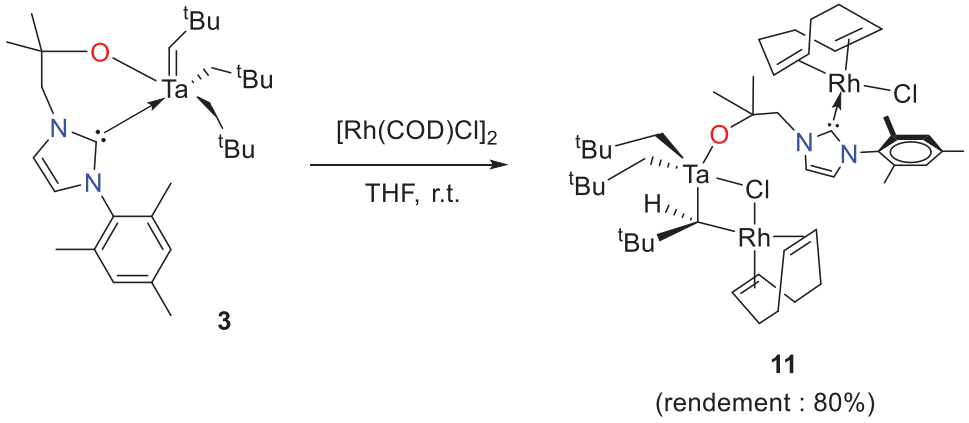

Schéma S3: Le précurseur de tantale **3** et la molécule |Rh(COD)Cl]$_2$ réagissent selon un ratio 1:1 dans le THF pour produire le complexe trimétallique **11**.

Cette étude a établi la faisabilité de la transmétallation envisagée du Ta vers le Rh-NHC. Cependant, la formation de l'espèce hétérobimétallique ciblée n'a pas abouti puisque une surmétallation sur la fonctionnalité Ta-alkylidène a été observée. Une autre voie réactionnelle pour synthétiser le complexe bimétallique désiré implique d'abord la synthèse du complexe rhodium-NHC suivi d'une réaction de protonolyse avec le précurseur de tantale tris(néopentyl) néopentylidène. Le complexe de rhodium-NHC **6** a été synthétisé avec succès *via* l'addition d'une solution du ligand dans le THF sur le précurseur de rhodium [Rh(COD)Cl]$_2$ à température ambiante **(Schéma S4)**. La formation du composé a été confirmée par RMN-^{1}H, ^{13}C, par analyse élémentaire et par DRX. En particulier, le spectre RMN ^{1}H du composé isolé dans le $CDCl_3$ a montré que le proton hydroxyle était intact (observé en tant qu'un singulet étroit à 3,5 ppm), ce qui est ultérieurement confirmé par les données IR (signal ν_{OH} caractéristique à 3368 cm^{-1}). La réaction entre le complexe **6** et Ta(CH^{t}Bu)(CH$_2$^{t}Bu)$_3$ a abouti à l'observation d'un mélange de produits probablement dû à la disponibilité de nombreux sites réactionnels sur le centre tantale vis-à-vis du groupement hydroxyle du complexe **6**.

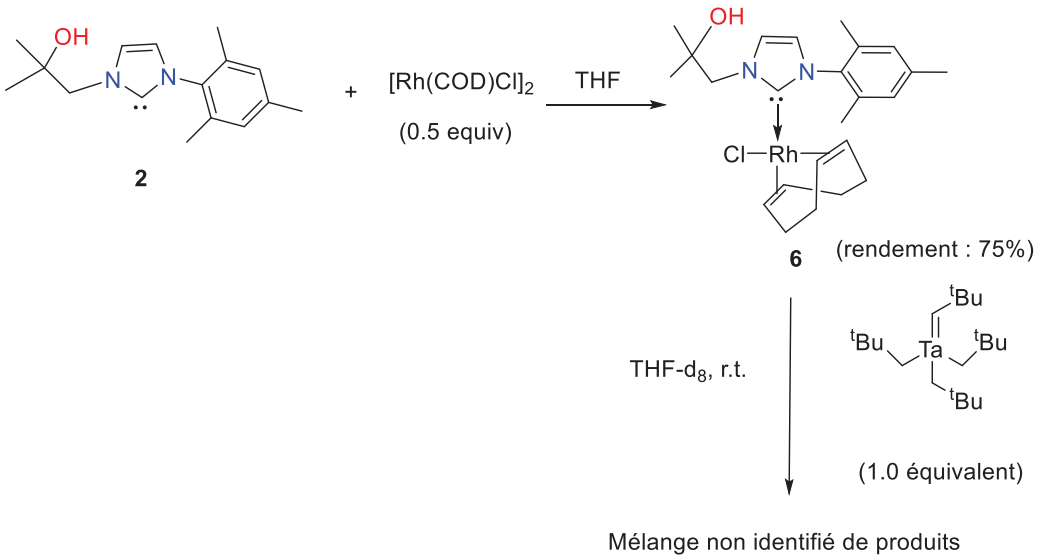

Schéma S4. Le schéma représente la synthèse du complexe de rhodium-NHC **6**. Le traitement de **6** avec Ta(CH^{t}Bu)(CH$_2$^{t}Bu)$_3$ a résulté en la formation d'un mélange d'espèces.

Ce premier ensemble d'études a révélé que la présence des fonctionnalités alkylidène hautement réactives sur le Ta a entravé la formation propre de l'espèce hétérobimétallique Ta/Rh ciblée. Ainsi, un troisième chemin réactionnel a été développé. Il consista premièrement en l'addition d'un groupement silanol sur l'alkylidène pour moduler la réaction du site Ta. La partie suivante du travail consista à developper des complexes hétérobimétalliques Ta/Rh hétérogènes supportés sur silice *via* une approche de chimie organométallique de surface (SOMC).[33] En premier lieu, un modèle moléculaire homogène à base d'Oligosilesquioxane Polyhédrique (POSS) (ayant pour but de modéliser le complexe supporté sur silice), a été développé. Le traitement du complexe de tantale-NHC **3** avec un dérivé de type mono-hydroxyle silsesquioxane polyhédrique oligomérique, POSS-OH **14**, a produit l'intermédiaire *tris*-alkyl - complexe **16** – issu de l'addition 1,2 du groupement hydroxyle le long du motif tantale-alkylidène sans l'élimination de néopentane. L'addition de [Rh(COD)Cl]$_2$ sur le complexe **16** amène à la formation du complexe bimétallique **17** désiré (**Schéma S5**). L'incorporation du rhodium métallique a été confirmée par des études de RMN ^{1}H et ^{13}C. Cependant, en dépit de nombreuses tentatives, il n'a pas été possible d'obtenir le composé **17** sous la forme de monocristaux.

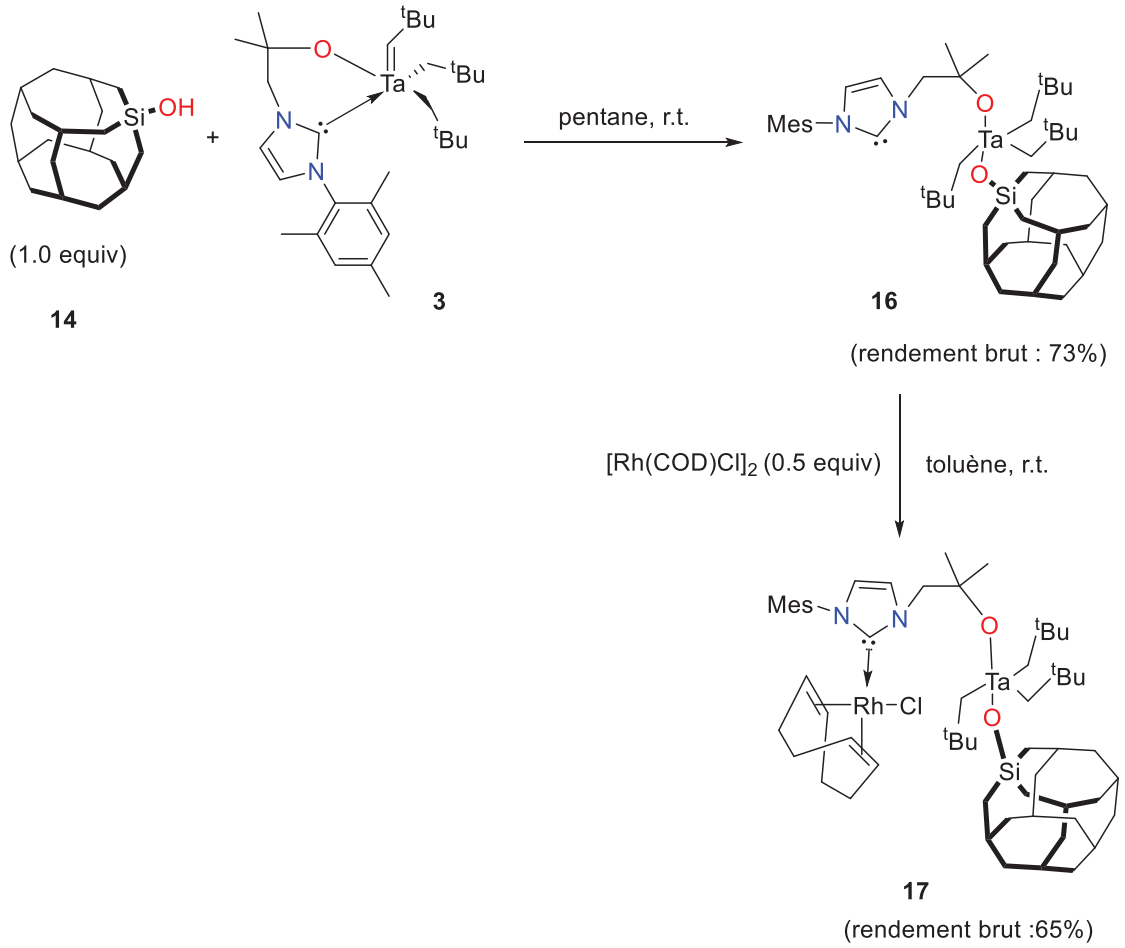

Schéma S5. Le schéma présente la préparation du complexe Ta-NHC supporté sur POSS **16**, suivi par l'addition du rhodium conduisant au complexe hétérobimétallique Ta/Rh souhaité **17**.

Obtenir la structure cristalline du complexe a été important pour réaliser l'étude computationnelle du complexe bimétallique pour l'activation de petites molécules. Par conséquent, l'analogue tris(*tert*-butoxy)silanolate **18** a été synthétisé en suivant une procédure similaire (**Schéma S6**). Le spectre de RMN du carbone ^{13}C du complexe **18** exhibe un signal à 219,4 ppm qui est spécifique des carbènes NHC libres n'interagissant pas avec un centre métallique. Le complexe **18** peut subir une métallation avec le complexe $[Rh(COD)Cl]_2$ pour produire le complexe bimétallique **19**. La structure cristalline du complexe (**Schéma S6**) confirme l'incorporation du rhodium qui est lié au ligand NHC comme attendu.

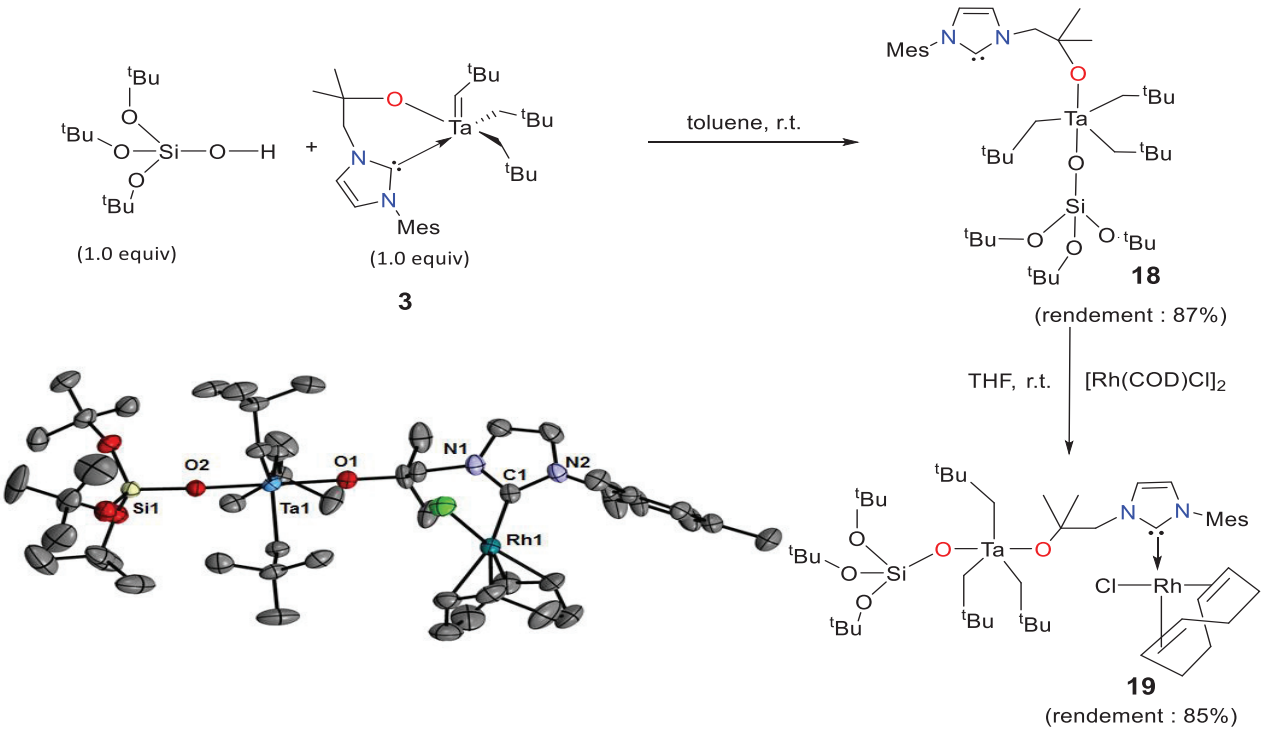

Schéma S6. Addition d'un équivalent de tris(*tert*-butoxy)silanol à une solution de complexe **3** dans du toluène, qui mène au complexe de tantale **3**. La métallation du complexe de tantale **18** à température ambiante avec $Rh(COD)Cl]_2$ conduit au complexe bimétallique **19**.

Après avoir optimisé le protocole de synthèse pour la préparation du complexe homogène **19**, l'étape suivante a été de mettre en place un protocole pour avoir accès à un analogue moléculaire de complexe bimétallique supporté sur silice. A cet effet, le complexe Ta-NHC **3** a été greffé sur de la silice dont la surface a été déshydroxylée à 700 °C ($SBA\text{-}15_{700}$) pour mener au complexe de tantale-NHC supporté correspondant. Le spectre de RMN du carbone ^{13}C à l'état solide dénote les signaux attendus du ligand sauf le carbone carbénique. C'est pourquoi le complexe **3** correspondant marqué au ^{13}C a été synthétisé et greffé sur silice. Le spectre de RMN du carbone ^{13}C de l'espèce carbénique marqué montre deux signaux de carbène : un premier signal à δ = 219,81 ppm qui est une signature du carbène libre (aussi observé pour le complexe **18**) ainsi qu'un second à δ = 201,97 ppm qui est spécifique d'un carbène en interaction avec le tantale. Cela indique que deux espèces de surface sont obtenues lors de l'immobilisation de **3** sur silice : un (complexe supporté **21**) dans lequel le NHC est lié au tantale, et un second (complexe supporté **21'**) où le ligand NHC n'est pas greffé sur le centre métallique. Le complexe bimétallique supporté **22** correspondant a été obtenu par réaction du

matériau contenant les complexes suportés **21** et **21'** avec le complexe $[Rh(COD)Cl]_2$ (**Schéma S7**).

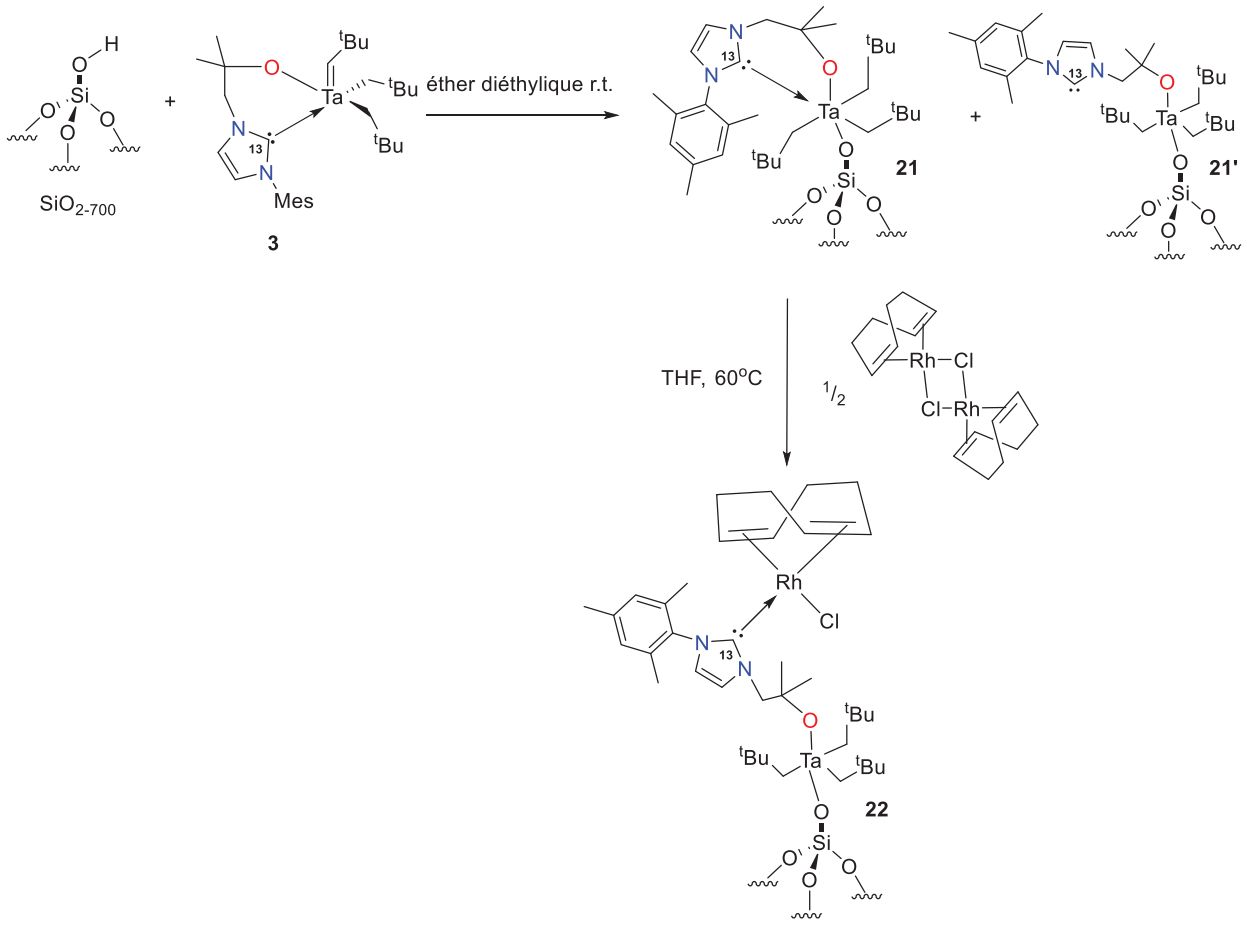

Schéma S7. Immobilisation du complexe de tantale **3** sur la surface d'une silice et traitement *a posteriori* par du $[Rh(COD)Cl]_2$, ce qui conduit au complexe hétérobimétallique supporté sur silice **14**.

La caractérisation du complexe greffé **22** par analyse élémentaire indique que 85% du carbène NHC est transmétallé sur le rhodium.

Nous avons ensuite tourné notre attention vers l'étude du comportement catalytique du complexe bimétallique pour l'activation de petites molécules. Comme réaction modèle, nous avons choisi, par une approche computationnelle, la conversion catalytique du diazote en ammoniac en utilisant le complexe **17**. Nous avons fait l'hypothèse d'un mécanisme réactionnel où la réduction du diazote se déroule sur le tantale tandis que le rhodium permet la délivrance d'hydrure pour cette réduction. L'espèce catalytique active ainsi obtenu est

présentée sur la **Figure S1**. La fonctionnelle de densité électronique avec correction à la dispersion B97D3-BJ et la base def2-SVP ont été utilisées pour tous les calculs.

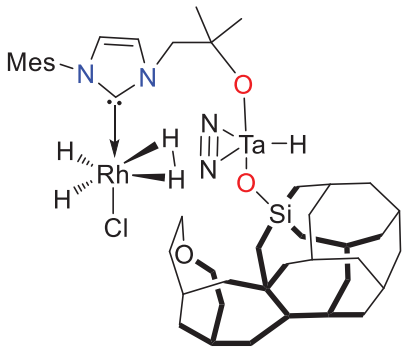

Figure S1. Complexe calculé N2/hydrido Ta/Rh, présentant un diazote lié de manière side-on (η^2) au tantale.

Nous avons été capables de calculer la demande énergétique des premiers minima locaux d'énergie. Malheureusement, l'état de transition de la première étape qui implique le transfert d'un premier hydrure depuis le rhodium sur le tantale portant le diazote n'a pas pu être localisé. Cependant, l'état de transition de l'étape suivante impliquant le transfert d'un deuxième hydrure sur l'azote a pu être déterminé 18 kcal·mol^{-1} au-dessus de l'énergie du complexe de départ (**Figure S2**). Cette barrière énergétique est substantiellement plus basse que l'énergie nécessaire au cycle catalytique où les deux métaux n'interagissent pas l'un avec l'autre. Ce résultat préliminaire est prometteur en cela qu'il valide notre hypothèse d'utiliser deux éléments différents en synergie pour accomplir l'activation coopérative de petites molécules. Des travaux ultérieurs nécessiteront l'application de ces résultats au laboratoire en utilisant le complexe bimétallique supporté **22**.

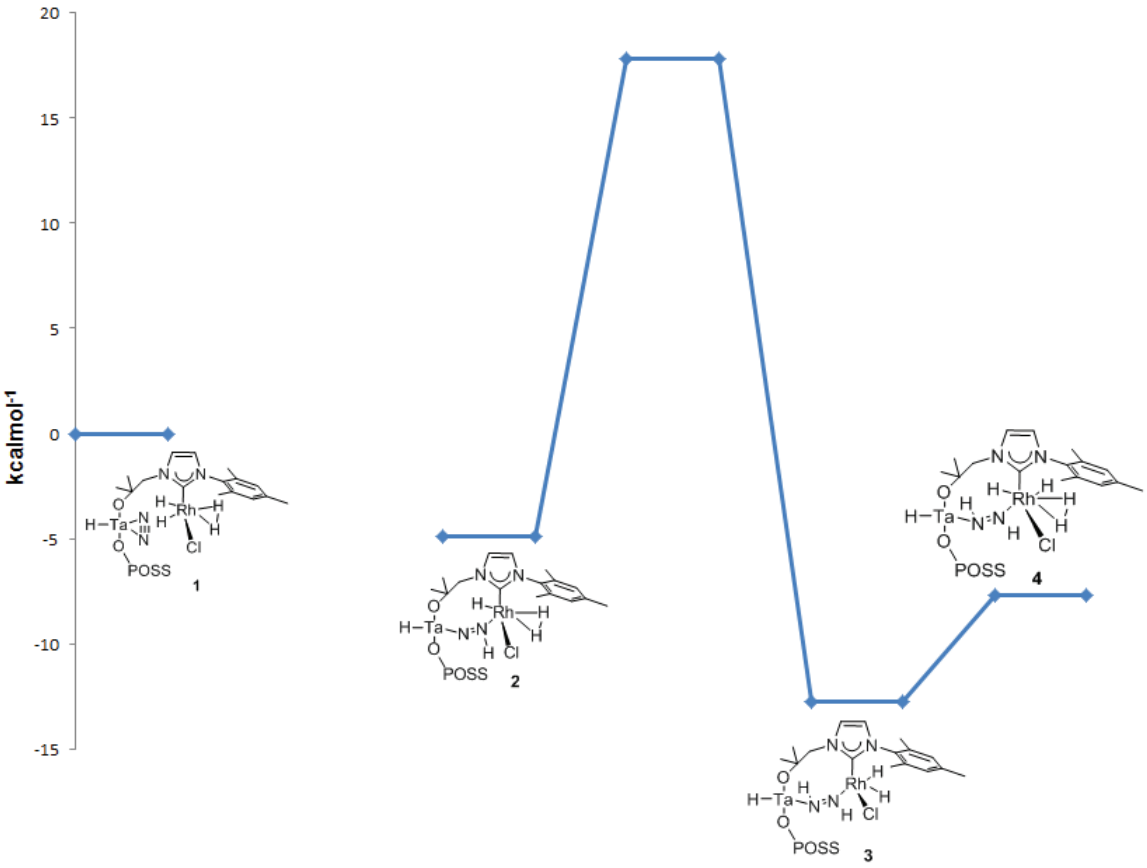

Figure S2. Profil énergétique en enthalpie libre de Gibbs (B97D3-BJ/def2-SVP) du complexe bimétallique sur POSS avec le diazote lié au tantale. Même si nous n'avons pas pu localiser l'état de transition TS12, les calculs théoriques montre que l'état de transition TS23 se situe 17,85 kcal·mol^{-1} au-dessus de l'espèce catalytiquement active.

En conclusion, l'espèce hétérobimétallique *early-late* tantale-rhodium a été synthétisée efficacement en utilisant un carbène N-hétérocyclique bifonctionnel comme pont entre les deux métaux de transition, en solution mais aussi sur la surface d'une silice. Les études computationnelles préliminaires concernant la conversion de N_2 en ammoniac sont prometteuses et montrent que la réduction du diazote peut bénéficier de la proximité des deux métaux. De travaux ultérieurs se concentreront sur la mise en pratique au laboratoire de l'activation de N2 en utilisant les complexes supportés sur silice.

REFERENCES

1 P. Buchwalter, J. Rosé and P. Braunstein, *Chem. Rev.*, 2015, **115**, 28–126.

2 C. M. Thomas, *Comments Inorg. Chem.*, 2011, **32**, 14–38.

3 C. Cornelissen, G. Erker, G. Kehr and R. Fröhlich, *Organometallics*, 2005, **24**, 214–225.

4 L. H. Gade, *Angew. Chemie - Int. Ed.*, 2000, **39**, 2658–2678.

5 B. G. Cooper, J. Wesley Napoline and C. M. Thomas, *Catal. Rev. Sci. Eng.*, 2012, **541**, 1–401.

6 S. Lassalle, R. Jabbour, P. Schiltz, P. Berruyer, T. K. Todorova, L. Veyre, D. Gajan, A. Lesage, C. Thieuleux and C. Camp, *J. Am. Chem. Soc.*, 2019, jacs.9b08311.

7 T. A. Hanna, A. M. Baranger and R. G. Bergman, *J. Am. Chem. Soc.*, 1995, **117**, 11363–11364.

8 W. Zhou, S. L. Marquard, M. W. Bezpalko, B. M. Foxman and C. M. Thomas, *Organometallics*, 2013, **32**, 1766–1772.

9 E. Bodio, M. Picquet and P. Le Gendre, in *Topics in Organometallic Chemistry*, 2015, **59**, 139–186.

10 N. Wheatley and P. Kalck, *Chem. Rev.*, 2002, **99**, 3379–3420.

11 M. J. Hostetler and R. G. Bergman, *J. Am. Chem. Soc.*, 1990, **112**, 8621–8623.

12 M. J. Hostetler, M. D. Butts and R. G. Bergman, *J. Am. Chem. Soc.*, 1993, **115**, 2743-2752.

13 L. M. Slaughter and P. T. Wolczanski, *Chem. Commun.*, 1997, 2109–2110.

14 J. P. Krogman, B. M. Foxman and C. M. Thomas, *J. Am. Chem. Soc.*, 2011, **133**, 14582–14585.

15 T. Miyazaki, Y. Tanabe, M. Yuki, Y. Miyake and Y. Nishibayashi, *Organometallics*, 2011, **30**, 2394–2404.

16 L. J. Clouston, V. Bernales, R. K. Carlson, L. Gagliardi and C. C. Lu, *Inorg. Chem.*, 2015, **54**, 9263–9270.

17 R. H. Crabtree, *J. Organomet. Chem.*, 2005, **690**, 5451–5457.

18 E. Peris, *Chem. Rev.*, 2018, **118**, 9988–10031.

19 M. N. Hopkinson, C. Richter, M. Schedler and F. Glorius, *Nature*, 2014, **510**, 485–496.

20 F. Cisnetti, C. Gibard and A. Gautier, *J. Organomet. Chem.*, 2015, **782**, 22–30.

21 H. V. Huynh, *Chem. Rev.*, 2018, **118**, 9457–9492.

22 A. J. Arduengo, H. V. R. Dias, R. L. Harlow and M. Kline, *J. Am. Chem. Soc.*, 1992, **114**, 5530–5534.

23 P. K. Majhi, S. C. Serin, G. Schnakenburg, D. P. Gates and R. Streubel, *Eur. J. Inorg. Chem.*, 2014, **2014**, 4975–4983.

24 J. Ruiz, L. García, M. Vivanco, Á. Berros and J. F. Van der Maelen, *Angew. Chem. Int. Ed.*, 2015, **127**, 4286–4290.

25 J. Ruiz and A. F. Mesa, *Chem. - A Eur. J.*, 2012, **18**, 4485–4488.

26 T. Okayama, T. Watanabe, Y. Hatayama, S. Ishihara and Y. Yamaguchi, *Inorganica Chim. Acta*, 2016, **448**, 1–6.

27 D. A. Valyaev, M. A. Uvarova, A. A. Grineva, V. César, S. N. Nefedov and N. Lugan, *Dalt. Trans.*, 2016, **45**, 11953–11957.

28 M. A. Huertos, J. Pérez, L. Riera, J. Díaz and R. López, *Chem. - A Eur. J.*, 2010, **16**, 8495–8507.

29 J. A. Cowan, J. A. C. Clyburne, M. G. Davidson, R. L. W. Harris, J. A. K. Howard, P. Küpper, M. A. Leech and S. P. Richards, *Angew. Chemie Int. Ed.*, 2002, **41**, 1432–1434.

30 D. Tapu, D. A. Dixon and C. Roe, *Chem. Rev.*, 2009, 109, 3385–3407.

31 P. A. Petrov, T. S. Sukhikh and M. N. Sokolov, *Dalt. Trans.*, 2017, **46**, 4902–4906.

32 L. P. Spencer, C. Beddie, M. B. Hall and M. D. Fryzuk, *J. Am. Chem. Soc.*, 2006, **128**, 12531–12543.

33 C. Copéret, A. Comas-Vives, M. P. Conley, D. P. Estes, A. Fedorov, V. Mougel, H. Nagae, F. Núñez-Zarur and P. A. Zhizhko, *Chem. Rev.*, 2016, **116**, 323–421.

Chapter 1

Bibliography

1.1) INTRODUCTION

Catalysis is widely accepted as an essential tool of sustainable development, improving chemical industry's competitiveness, while minimizing its environmental impact. The direct activation of strong sigma bonds (C-H, Si-H, C-C, C-X) and small molecules (N_2, CH_4, CO, CO_2, H_2) by organometallic catalysts could substantially impact the feedstock pool for tomorrow's industry, allowing for the catalytic conversion of abundant raw materials into valuable organic compounds or the direct functionalization of organic products in an atom-efficient fashion. Most of the organometallic catalysts known to date rely on monometallic species. However, «if you look at the diverse chemistry of mononuclear complexes, imagine what the future would hold in polymetallic systems for cooperative reactivity in catalysis».[1] A current frontier area in organometallic catalysis is cooperative activity between two distinct metal centers in order to foster new transformations not possible with monometallic species. This PhD thesis is contributing to the development of this research theme.

1.1.1) An overview of early-late heterobimetallic complexes (ELHB) and their application in small molecules activation

In several instances, bimetallic complexes have shown enhanced reactivity in comparison to monometallic analogues.[2,3] This increase in reactivity is attributed to synergistic effects of both the metals on the substrate.

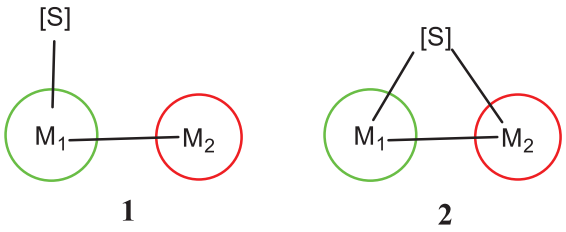

Figure 1.1. A schematic diagram showing the possible coordination pathways of a substrate with a bimetallic species.

As shown in **Figure 1.1**, case 1 represents the coordination of the substrate with only one of the two metal centers. However, the second metal works as a spectator ligand affecting the chemical environment around metal 1 and thus the extent of interaction with the substrate. This metal center can play the role of an "electron tuning" center and drastically impact the reactivity of the substrate binding site. The electronic effect will be more directly visible in case 2, where the substrate binds across both the metals simultaneously. The variety of electronic environments that could be generated is enormous given the range of possible

combinations of metals offered by the periodic table.[4] This have been exploited in a wide range of homogeneous[5,6] and heterogeneous[7,8] reactions.

This field of research started to gain importance when Tauster and co-workers showed that noble metals absorbed over titania were more active in hydrogen and carbon monoxide adsorption as compared to analogues supported over silica or alumina.[9] The increased electronic interaction between the Lewis basic noble metal and the empty d-orbitals of the Ti centers from titania lead to this improved reactivity. Later, titania-supported Co, Fe and Ru nanoparticles were used as heterogeneous catalysts in Fischer-Tropsch synthesis.[10] The growing interest in the strong metal support interaction in these heterogeneous systems lead to the development of homogenous models of these catalysts.[11–15] Casey and co-workers reported the preparation of Zr-Ru bimetallic complex $Cp_2Zr[Ru(CO)_2Cp]_2$, containing a direct metal-metal bond.[16] This bimetallic Zr-Ru complex was highly active in CO activation ($\nu_{bridgingCO}$ = 1380 cm^{-1}). The polarity of this direct metal-metal bond, can lead to enhanced reactivity, and is increased if both metals in the bimetallic system are chemically diverse, as in so-called *early-late heterobimetallic (ELHB)* complexes. In these classes of heterobimetallic complexes, one of the metal comes from left hand side of the transition metal series called *"early metal"* and the second metal belongs to other extreme of the transition metal series called *"late metal"*. ELHB complexes offer a wide scope of stoichiometric and catalytic transformations through various mechanisms, as illustrated in examples below.

Among the various bifunctional activation mechanisms[17] possible with those systems, the heterolytic cleavage of strong sigma bonds across polar metal-metal bonds, in a synergistic manner (as shown in **Figure 1.2**), is of particular interest, notably in the context of transfer hydrogenation/dehydrogenation chemistries. The reverse process (cooperative bimetallic reductive elimination) has for instance been speculated for the amine-borane dehydrogenation catalyzed by a Zr/Ru heterobimetallic complex.[18]

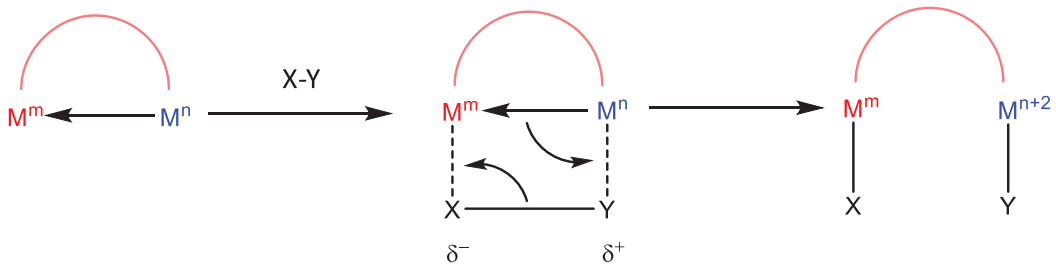

Figure 1.2. General representation of the heterolytic bond cleavage of a substrate across the metal-metal bond of a heterobimetallic complex.

In their seminal work on ELHB complexes Bergman and co-workers reported the preparation of $Cp_2Zr(\mu\text{-}N^tBu)IrCp^*$ bimetallic complex which was active in stoichiometric CO_2 activation. The same complex also reacted with various heterocumulenes and yielded a range of compounds (**Scheme 1.1**).[19]

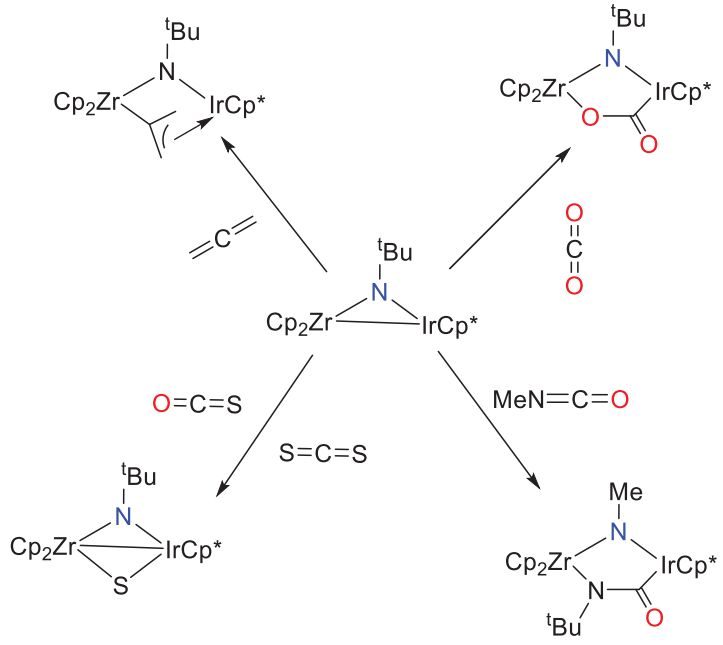

Scheme 1.1. The Zr-Ir heterobimetallic complex, $Cp_2Zr(\mu\text{-}N^tBu)IrCp^*$ was exploited in the activation of unsaturated small molecules by Bergman and co-workers.

Later the same group reported an interesting Ta-Ir heterobimetallic complex $[Cp_2Ta(\mu\text{-}CH_2)_2Ir(CO)L]$ (L = CO, PPh_3) which was active in alkene hydrogenation. As shown in **Scheme 1.2,** the iridium center is the catalytically active site whereas the tantalum center acts as a spectator ligand.[20] Of particular interest, DFT calculations performed recently on this system demonstrated that the heterobimetallic system operates though a mechanism which is different from that of analogous monometallic iridium catalysts, and which opens new perspectives for reactivity.[21]

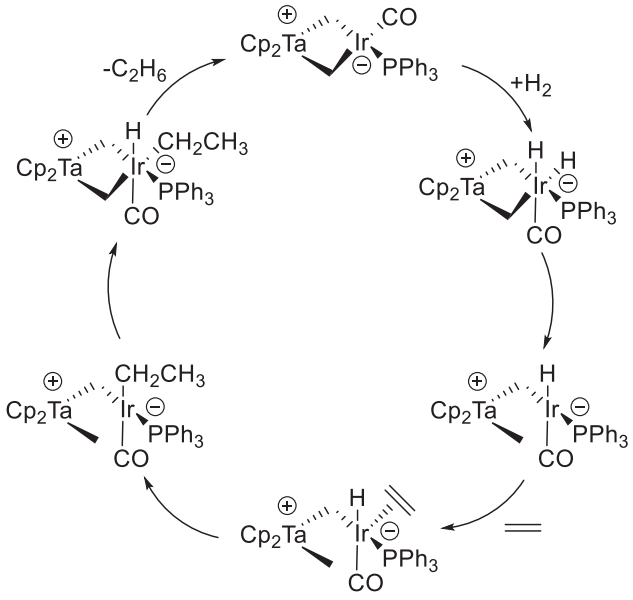

Scheme 1.2. The mechanism proposed for alkene hydrogenation shows reactivity centered at the iridium site while the tantalum center plays an "electron tuning" role.

More recently Thomas and coworkers reported an interesting Zr/Co heterobimetallic complex which was active in the stoichiometric reduction of CO_2[22] and catalytic ketone hydrosilylation.[23] The reaction mechanism in the latter case establishes that the Co atom acts as both a stabilizing center as well as an electron reservoir for the electrophilic Zr center which is the substrate binding site, which facilitates single electron reactivity to generate a ketyl radical intermediate (**Scheme 1.3**). This complex is also an active catalyst for Kumada coupling, and DFT studies revealed the crucial impact of the Co-Zr bond in this reactivity.[24] This system is therefore a rare well-documented example of an early/late heterodinuclear catalyst offering unique reactivity compared with mononuclear analogous complexes.

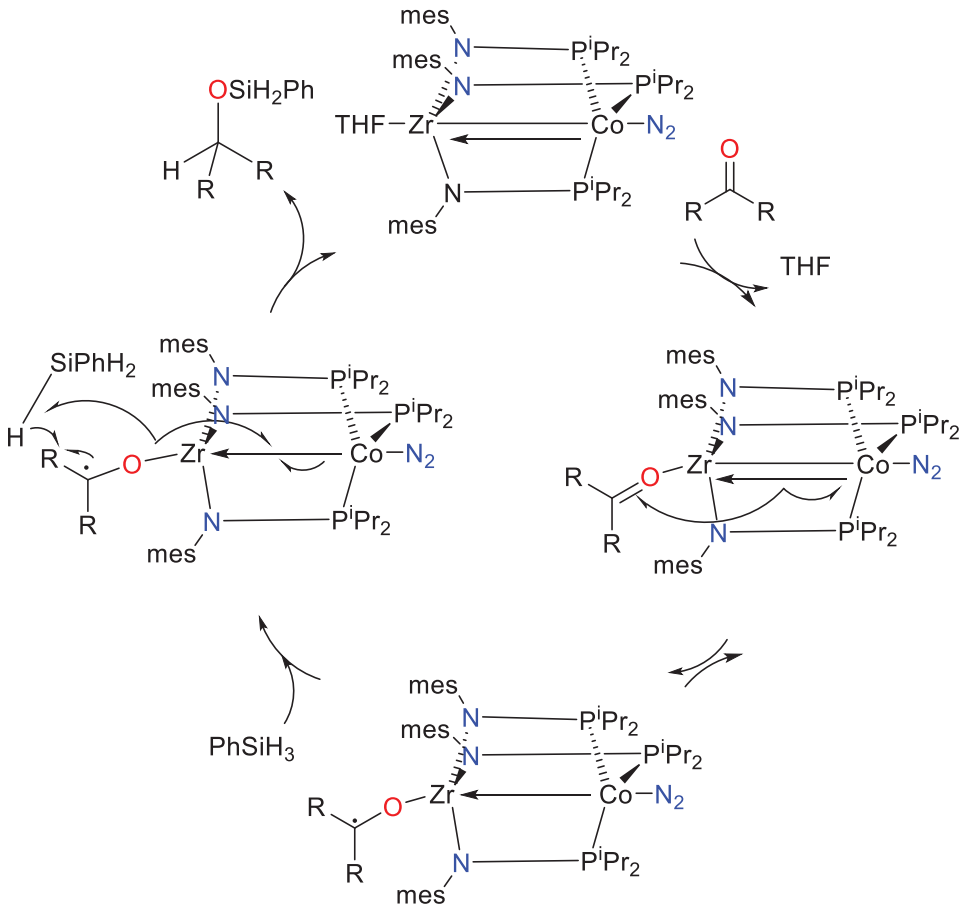

Scheme 1.3. Ketone hydrosilylation mechanism at a Zr/Co ELHB complex. In this system the Co metal center acts as an electron reservoir for the electron poor Zr center, which is the substrate-binding site.[23]

Other ELHB complexes have been used in a few catalytic reactions, including hydroformylation,[25–27] or hydrogenation/dehydrogenation[28,29] reactions.

The versatile properties of these complexes lead to the development of different pathways for synthesizing them. Designing ELHB complexes is a careful craft. The nature of the metal centers is crucial in deciding the reactivity of the complex, the distance between both the metal centers should be considered in case there is a requirement of direct metal-metal bond, the ligands surrounding the metal centers are also an important aspect of the design as they are helpful in the stability and the assembly of these complexes. A very common pathway to synthesize ELHB complexes is through salt metathesis reactions.[30–36] This route involves the reaction between an early transition metal halide with an alkali metal salt of a late transition metal complex (**Scheme 1.4**).

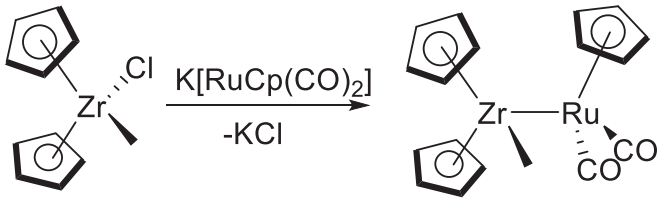

Scheme 1.4. Preparation of an ELHB complex using a salt metathesis reaction.[37]

However, the salt metathesis route suffers from several drawbacks, such as single electron transfers between the two metals if the redox potentials are not well adjusted, the formation of "ate" complexes or ion pairs and the stoichiometric generation of alkali halide salts which can be difficult to separate from the complex. Condensation of neutral organometallic precursors which would react to each other by simultaneous release of a neutral organic molecule presents an alternative pathway.[38–40] For instance, Bergmann and coworkers reported the synthesis of a Ta-Ir complex $Cp_2Ta(\mu\text{-}CH_2)_2Rh(CO)_2$ by indenyl ligand displacement reaction[20] (**Scheme 1.5**).

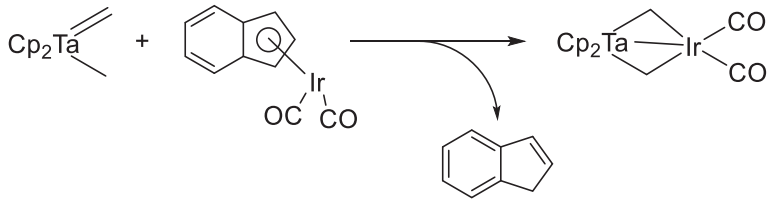

Scheme 1.5. Synthesis of a Ta-Ir heterobimetallic complex by the ligand displacement reaction.

In our group we also developed an original alkane elimination synthetic route based on the reaction between a nucleophilic metal alkyl derivative ($Ta(CH^tBu)(CH_2{}^tBu)_3$) and a Brønsted acidic metal hydride (Cp^*IrH_4) to prepare a novel heterobimetallic tantalum/iridium hydrido complex, [{$Ta(CH_2{}^tBu)_3$}{$IrH_2(Cp^*)$}] (see **Scheme 1.6**)

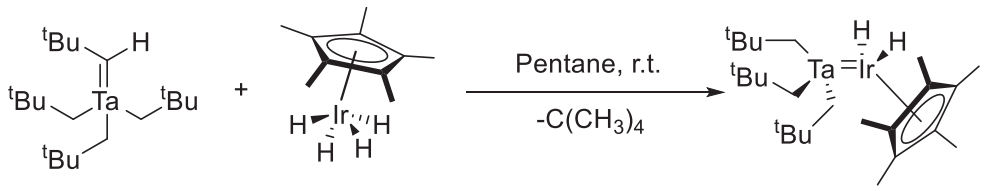

Scheme 1.6. Synthesis of a Ta-Ir heterobimetallic complex by an alkane elimination reaction.[41]

The most popular strategy to synthesize ELHB species is to use a bifunctional ligand which features two chemically different coordination sites with a specific affinity for each class of metals (early *vs* late).[37,42–44] For instance, Ferguson *et al* reported the synthesis of the Zr-Ni bimetallic complex $Cp^*Zr(p\text{-}OCH_2Ph_2P)_3NiPMe_3$ where both the metals are assembled together by an (alkoxymethyl)diphenylphosphine bridge[45] (**Scheme 1.7**).

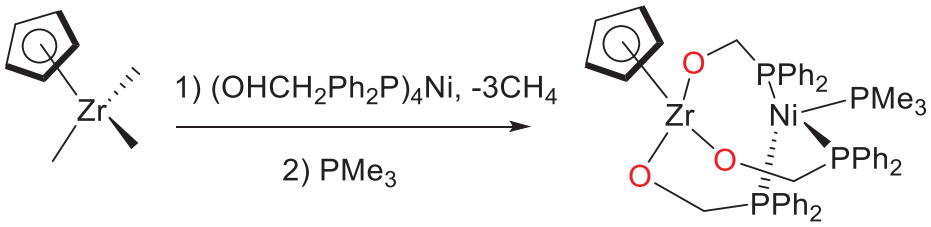

Scheme 1.7. One of the classical ways to synthesize ELHB species is to use a bidentate ligand which contains both a hard, oxophilic coordination site with high affinity for the early metal center as well as a soft nucleophilic donor with good affinity for the late metal center.

Although we note a stimulating resurgence of interest for this field in the past few years, catalytic applications of early/late heterobinuclear metal complexes are still very limited to date. This can, in part, be explained by the common practice of using bulky polydentate bridging ligands in order to direct the assembly of the two metals and stabilize the resulting edifices but this also prevents substrates to bind across the two metals and thus limits the range of accessible metal-metal synergistic effects. One possible strategy to overcome this limitation and access low-coordinate systems would be to target a Surface OrganoMetallic Chemistry (SOMC) approach.

1.1.2) Surface OrganoMetallic Chemistry (SOMC): an approach to realize well-defined surface-supported complexes

1.1.2.1) Presentation

Grafting organometallic complexes over metal oxide surfaces (e.g. silica), has been utilized as an important technique to access original organometallic species with structures not attainable in solution and exhibiting unique reactivity.[46–48] This concept was exploited to develop innovative heterogeneous catalysts with well-defined active sites that can be described with the precision of molecular organometallic chemistry, bridging the gap between homogeneous and heterogeneous catalysis. This methodology forms a scientific domain of research on its own, called “Surface OrganoMetallic Chemistry (SOMC)”.[49] The successful immobilization of organometallic species onto a solid support requires to precisely master the surface chemistry of the material. Most of the time, grafting exploits the reactivity of the

hydroxyl groups present at the surface of metal oxides, which is why a precise control of the chemical nature and density of these surface groups is critical for controlling catalyst immobilization. In the case of silica, different types of surface silanol groups (Si-OH), shown on **Scheme 1.8**, are found depending on the temperature at which the support is pretreated (usually under high vacuum).

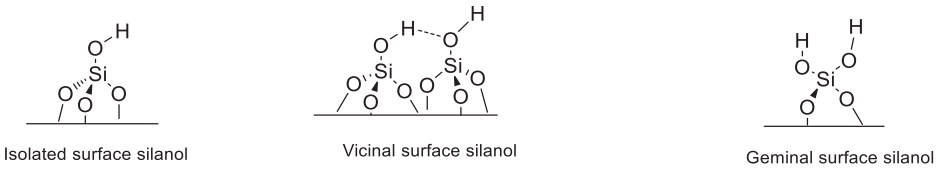

Scheme 1.8. Different types of silanol sites found at the surface of silica materials.

Not only the nature, but also the total amount of these surface silanols also depends on the temperature of the pretreatment, as the silanols condense together by the dehydroxylation reaction depicted below:

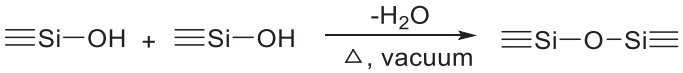

Zhuravlev modelled the silica surface by experimental and theoretical methods to predict the type and the concentration of silanols present over the silica surface at different temperatures.[50] As shown on **Figure 1.3**, high concentration and diversity of silanol groups are found for silica treated at 200°C. On the contrary, silica dehydroxylated at 700°C, used in this work, solely features isolated surface silanols at a density below 1/nm². Therefore the latter silica support allow the preparation of well-defined monopodal supported species, which are, most of the time, uniform in composition and distribution and are isolated from each other.

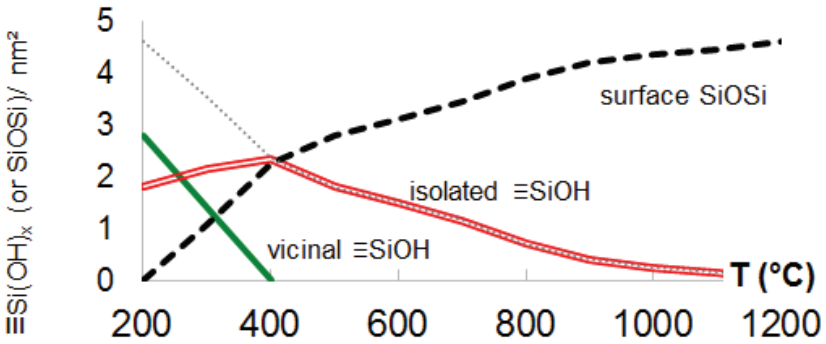

Figure 1.3. The graph shows the nature and quantity of surface silanols present over silica surface dehydroxylated at different temperatures.[50]

These isolated silica mobilized complexes exhibit higher lifetimes (higher activity and selectivity too) due to the decrease in intermolecular interactions which are available very readily in the homogeneous medium. The basic protocol for grafting an organometallic complex over silica surface involves following steps **a)** A coordination sphere for the metal where oxygen can fit in as a ligand is conceived. **b)** Organometallic complex is grafted on the silica surface with the proposition that surface siloxy group will act as the previously conceived -oxy ligand. **c)** Set of reactions are performed to get results and then the organometallic complex is modified for the improvement of the reaction.[51] The scheme below (**Scheme 1.9**) represents a general procedural scheme for the grafting of complexes over surface:

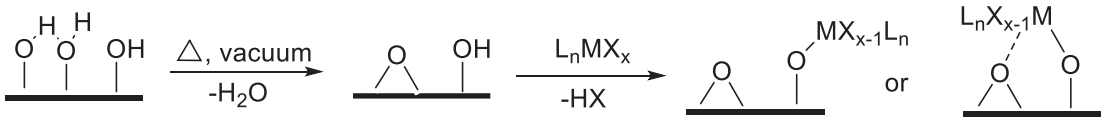

Scheme 1.9: The treatment of silica at elevated temperature under high vacuum yields isolated silanols which in turn was utilized to graft the complex. Besides metal-silanolate interaction, secondary interaction between siloxane bridge and the metal center have also been reported.[51]

A detailed representation of silica grafted complex is shown below in **Figure 1.4**:

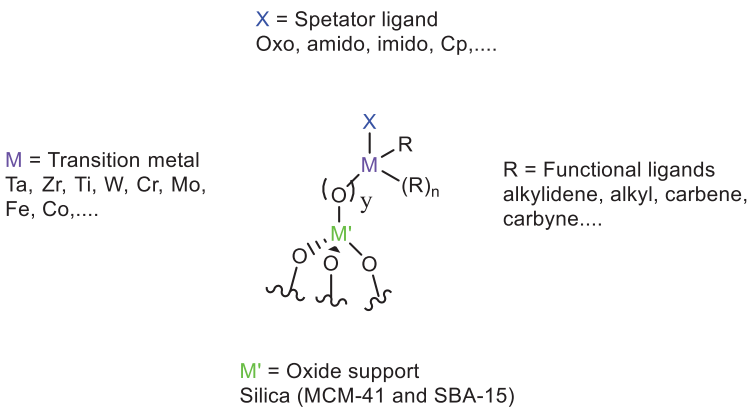

Figure 1.4: A comprehensive representation of grafted complex over metal oxide surface.[52]

One major limitation regarding direct grafting of an organometallic complex onto the surface of an oxide material (for e.g. silica) is the necessity to form a robust bond with one (or more) oxygen atom from a siloxy (≡Si-O-) surface group. While this methodology works well for oxophilic early transition metals (groups 3-6 and f-elements),[53–62] the grafting of late transition

metals is not as straightforward. Late transition metals complexes grafted over silica are reported to undergo aggregate formation into metal nanoparticles under reducing conditions particularly under hydrogenation conditions.[49,63–65] One way to reduce the aggregate formation involves the application of multidentate ligands to stabilize the mononuclear organometallic complexes.[66] However this strategy is only limited to iridium complexes [IrH(OSi)(POCOP)][67] stabilized by bulky (POCOP) pincer ligands and ruthenium complexes [Ru(OSi)(CH_2SiMe_3)(CO)(NNN)][68,69] stabilized by NNN pincer type ligands. Recently Thieuleux *et al* have reported functionalized silica supported late metal-NHC complexes linked/anchored through a flexible linker to surface.[70,71] The metal center is stabilized by secondary interactions with the surface functionality of the support. However these functionalized silica supports needs perfect dilution conditions during the sol-gel process to yield equidistant organic functionality. Moreover the metal NHC complexes are obtained through a multistep process involving a series of functionalization and metalation reactions and are limited to iridium and ruthenium NHC complexes only. In our quest to design a universal process extendable to a wide range of late transition metal complexes, we hypothesize a silica supported early-late bimetallic complex which will contain direct bond between early transition metal and silica surface whereas the late transition metal will not bond directly with the silica surface albeit it will be attached with the silica grafted early transition metal moiety with a bifunctional NHC. As it will be seen later in this chapter that our choice for early transition metal in the design of a silica supported early-late heterobimetallic complex is tantalum. Hence, we discuss the chemistry of silica supported tantalum complex here in detail. Schrock *et al* reported tantalum tris(neopentyl) neopentylidene complex Ta(CH^{t}Bu)($CH_2{}^t$Bu)$_3$ which is the most studied tantalum complex grafted over silica.[72] The tantalum alkylidene complex reacted with the silica silanol moieties[73] as shown in **Scheme 1.10** to yield (SiO)-Ta(CH^{t}Bu)($CH_2{}^t$Bu)$_2$.

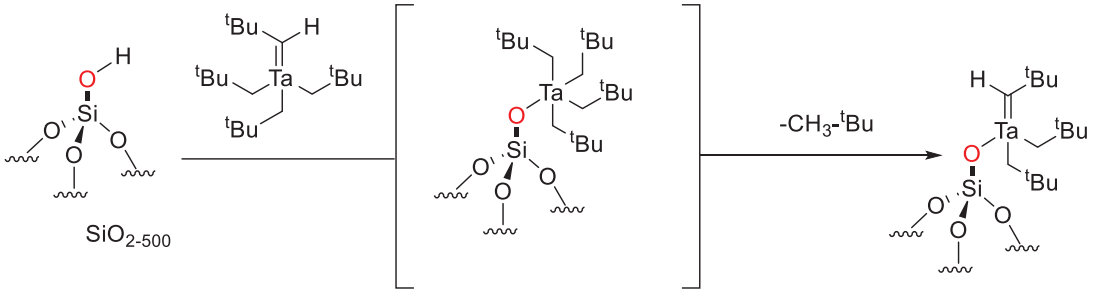

Scheme 1.10. The synthesis of Ta(CH^{t}Bu)($CH_2{}^t$Bu)$_3$ and its grafting over silica dehydroxylated at 500°C.

The addition of silanol to the Ta(CH^{t}Bu)(CH$_2$^{t}Bu)$_3$ complex yielded the sterically crowded tantalum tetra-alkyl monopodal species over silica which decomposed by releasing neopentane to yield the silica supported complex. The silica supported tantalum complex is characterized firsthand by IR spectroscopy which showed the disappearance of silanol moiety (observed at 3747 cm^{-1}) and appearance of peaks in region 3000-2700 cm^{-1} corresponding to the ν_{C-H} stretching frequencies of metalloligand framework. The detailed characterization of the grafted complex is done by solid state NMR and EXAFS study. The alkylidene carbon of the silica-supported tantalum species is observed as a doublet in the solid state ^{13}C NMR spectrum at 247 ppm with $^1J_{C-H}$ = 80 Hz whereas the Ta-*C*H$_2$^{t}Bu moiety is observed at 95 ppm.[73] The EXAFS data showed Ta-alkylidene bond distance at 1.898(8) Å and the Ta-alkyl bond distance at 2.150(4) Å respectively. The amount of the tantalum atom grafted at silica surface is obtained from elemental analysis.

The (SiO)-Ta(CH^{t}Bu)(CH$_2$^{t}Bu)$_2$ complex has been studied extensively for alkane metathesis reaction.[74] It was found that the active species in the alkane metathesis reaction are the tantalum hydride moieties. The formation of tantalum metal hydride species over the silica surface have been represented in **Scheme 1.11**.[52,75,76]

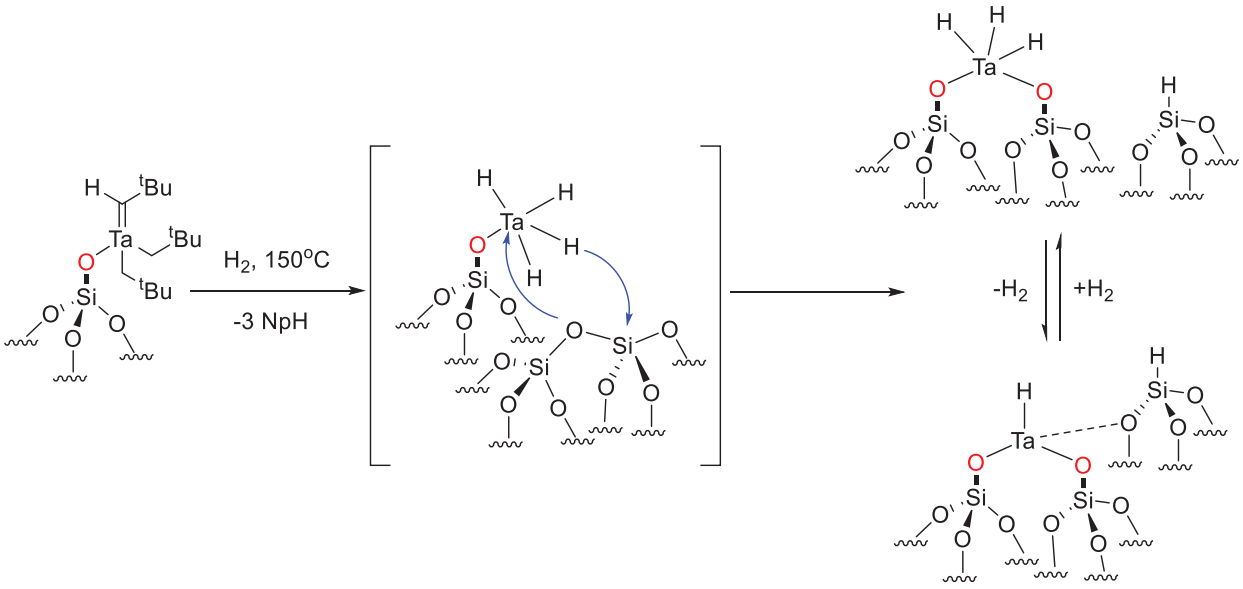

Scheme 1.11: Formation of tantalum hydride species over the silica surface.

The hydrogenolysis of the neopentyl and neopentylidene groups occurred at 150°C. The tantalum center in the intermediate tetrahydride species is highly electron deficient and thus further stabilization is provided by the siloxane (Si-O-Si) bridges through secondary electronic

interactions. At such high temperature the nearest siloxane bridge ultimately opened up forming bipodal tantalum tris hydride complex over the silica surface along with silicon hydride species. The IR spectrum of the complex supported the formation of metal hydride over the silica surface which is evident by the decrease in ν(C-H) intensity in the region 3000-2700 cm^{-1} and observation of the peak in 1800 cm^{-1} region corresponding to ν(Ta-H) and in 2300-2200 cm^{-1} region to ν(Si-H). The tris hydride complex evolved reversibly into monohydride species. The complex is further characterized by solid state NMR and EXAFS.

The highly reactive tantalum hydride species are reported to activate chemically inert C-H bonds of alkanes in the so-called alkane metathesis reactions to form higher and lower homologues.[49,77–79] Recently the focus has shifted to prepare long chain homologues (C9 to C20) from short chain alkanes; as the longer chain alkanes possess ideal fuel composition for diesel engine and currently operationalized Fischer-Tropsch process do not ensure the tight molecular weight control.[80] The silica supported Ta-H species also activated small molecules like N_2. Quadrelli *et al* has reported the formation of Ta (V) amido imido complex $[(\equiv SiO)_2Ta(=NH)(NH_2)]$ over the silica surface upon reaction with dry N_2 and H_2 at 250°C. The exact nature of the species over the silica surface is confirmed by $^{15}N_2$ labelling studies, EXAFS, IR and SS NMR studies.[81] (**Scheme 1.12**) Computational studies on N_2 activation to NH_3 showed that the reaction started with the formation of side on bonded η^2-N_2 on the tantalum center. Subsequent transfer of hydrides to the N_2 molecule led to the N_2 reduction.[82]

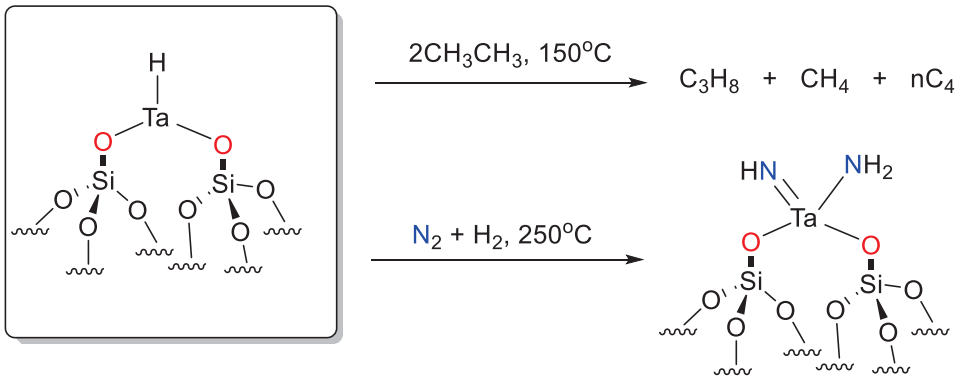

Scheme 1.12: The reactivity of Ta-H species in alkane metathesis and N_2 activation reactions.

The unique and attractive chemistry which has been developed with Ta, in particular for N_2 activation, led us to choose this element for the preparation of the organometallic species described in this project. In particular we projected to use $Ta(CH^tBu)(CH_2{}^tBu)_3$ as an entry point to this chemistry.

1.1.2.2) Silica supported heterobimetallic species prepared through SOMC

There has been a plethora of silica grafted monometallic complexes reported in last two decades.[55,70,83–85] But recently the focus has shifted on grafting bimetallic complexes over silica surface to promote advanced catalysis, although silica-supported *d*-block heterobimetallic species are remarkably rare to date. Vizza and co-workers have immobilized rhodium complexes at the surface of a silica support pre-functionalized with Pd nanoparticles. They successfully showed that the two metal centers interact synergistically in the catalytic conversion of benzene to cyclohexane.[86] Indeed, they proved that the grafted rhodium complex in the absence of Pd was inactive in the chemical transformation whereas the Pd/SiO_2 catalyst without Rh exhibited four times lower catalytic activity as compared to the material containing the two metals. A handful of early/early transition metals species (groups 4, 5 and 6) obtained through stepwise grafting of two independent monometallic molecular precursors have also been prepared. Scott and co-workers developed a synthetic route to access Ti-V bimetallic species on silica. They established a two-step process for the synthesis of the bimetallic complex wherein $VOCl_3$ is grafted first over the silica surface with concomitant release of HCl; following which $Ti(O^iPr)_4$ was added to the grafted complex.[87] Basset and coworkers also used the SOMC technique to prepare original W-Ti and W-Zr catalysts. To do so, in the first step of the synthetic procedure, only 0.5 equivalent of the organometallic precursor is added to the silica support, leaving half of the silica surface silanols groups untouched. The latter are thus available to react with another organometallic precursor in a second step (see **Scheme 1.13**). The as-synthesized heterobimetallic materials were characterized by 2D-HETCOR CP-MAS SSNMR (along with other usual characterization techniques) to establish the proximity between both the metal center. The authors have shown that these bimetallic species exhibit an unprecedented turnover number (of 9784) in alkane metathesis reaction, higher than that of monometallic analogues.[88]

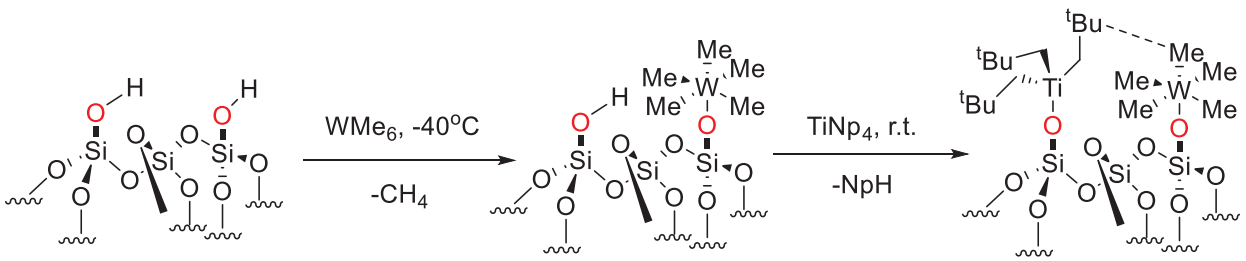

Scheme 1.13. A representation of the reaction protocol established by Basset and coworkers for the synthesis of a silica-supported W-Ti *early-early heterobimetallic complex*. A similar methodology was used to prepare the W-Zr analogue.[88]

Very recently, a novel heterobimetallic tantalum/iridium hydrido complex, [{Ta(CH$_2$^{t}Bu)$_3$}{IrH$_2$(Cp*)}] was isolated in our group. This molecular precursor was used to synthesize well-defined silica-supported low-coordinate heterobimetallic hydrido species (shown on **Scheme 1.14**). The SOMC methodology prevents undesired dimerization as encountered in solution and therefore allows access to unique low-coordinate species not attainable in solution. These original supported Ta/Ir complexes exhibit drastically enhanced catalytic performances in H/D exchange reactions with respect to (i) monometallic analogues as well as (ii) homogeneous systems. In particular, the *tris*-hydride species promotes the H/D exchange between fluorobenzene and C_6D_6 or D_2 as deuterium sources with excellent productivity (TON up to 1422; TOF up to 23.3 h^{-1}) under mild conditions (25°C, subatmospheric D_2 pressure) without any additives.

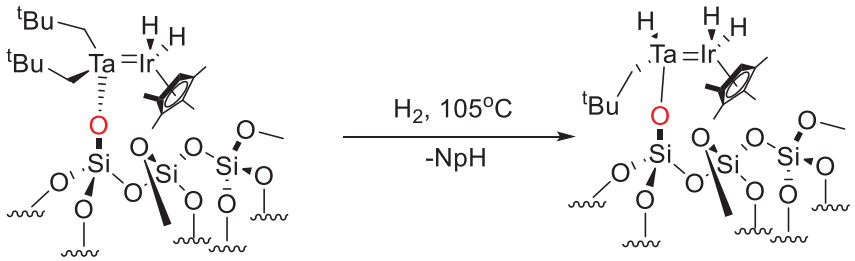

Scheme 1.14. Preparation of a silica-supported Ta/Ir catalyst by Camp and coworkers, which is highly active in arene H/D exchange under mild conditions.[89]

These few examples highlight the numerous possibilities offered by this research area, which is still in its infancy.

1.2.3) Molecular silanols as homogeneous molecular models of silica

Synthesizing and characterizing silica supported complexes is a challenge. First of all, these species are highly air-sensitive, therefore the synthesis and characterization must be realized under strict inert atmosphere conditions. Secondly the characterization of these materials requires solid-state techniques, which can be limiting. In contrast to liquid state chemistry where precise structural data can be gained through single-crystal XDR, analogous technique is not available for the SOMC species. NMR characterization in the solid state is also very challenging. Hence, the development of homogeneous molecular models of the supported species can provide precise and quick insights for SOMC that can be used to model the surface species, or anticipate the reactivity of molecular organometallic derivatives with the support before proceeding to immobilization for instance.

Polyhedral OligoSilSesquioxanes (POSS) molecules are one such homogeneous molecular models of silica. POSS are complex organosilicon compounds formed by hydrolytic condensation of organosilanes. The cubic framework of POSS derivatives is made up of Si-R moieties which are present at the corners of the cubic assembly and connected through oxygen atoms. A variety of derivatives mimicking the various silanol sites of silica (mono, di, tri, isolated, geminal, vicinal etc.) can be synthesized (see **Figure 1.5**).[90] These silicon-oxygen frameworks have close physical and chemical properties with silica and thus can serve as good molecular models for silica. For instance, Feher *et al* analyzed the X-ray data of POSS and showed that the crystal structure of trisilanol (c-$C_6H_{11})_7Si_7O_9(OH)_3$ is similar to the (111) β-cristobalite face of silica and exhibit similar conformation of the silicon atoms and Si-Si distances.[91] Furthermore the IR signal of isolated silanols present at the silica surface is observed as a sharp resonance at 3747 cm^{-1} while POSS-based monosilanols show a sharp OH stretch around 3700 cm^{-1}, demonstrating a good spectroscopic similarity. The acidity analogy is less good since the pK_A of POSS hydroxyls (in the range of 8-9) are slightly higher to what found for silica (ca. 7), but still better than simpler models such as Ph_3SiOH (pK_A = 10.8).

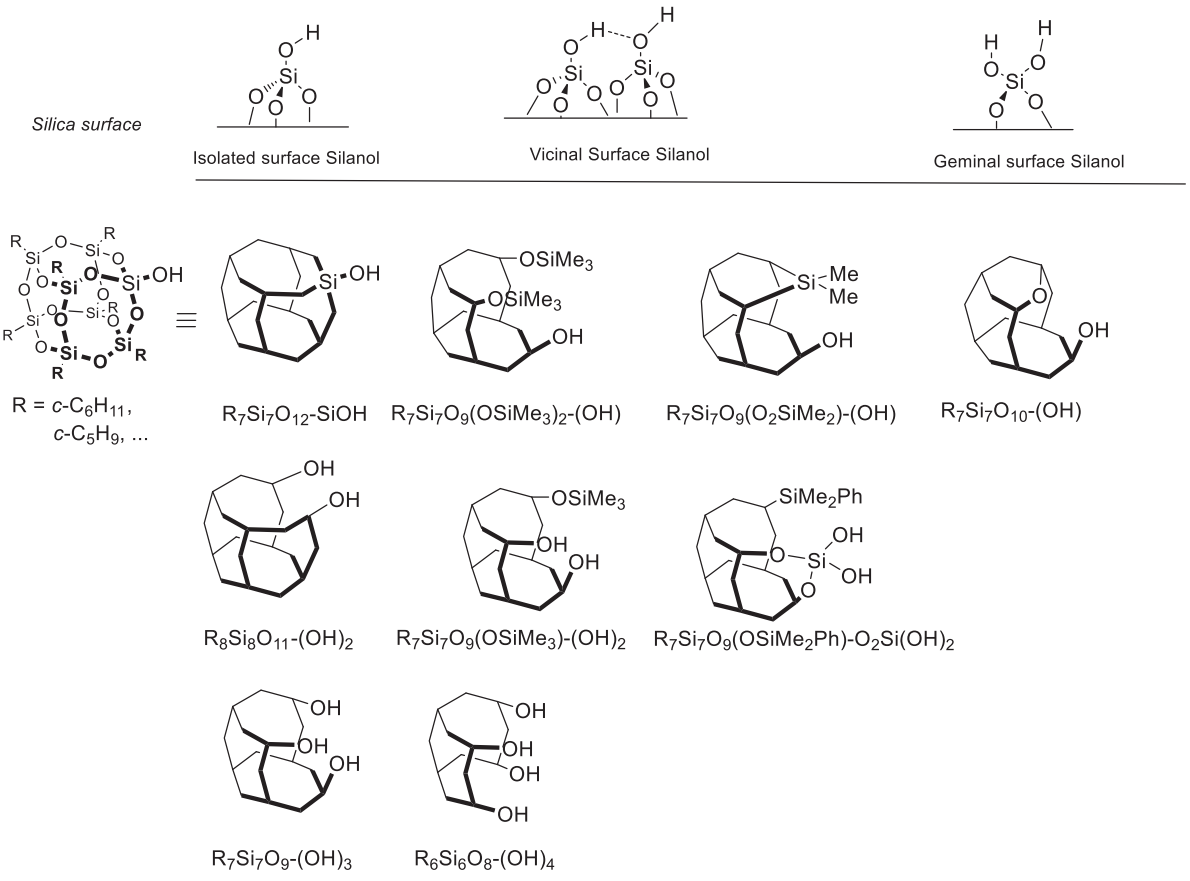

Figure 1.5. A comparison of silica surface silanols with their POSS analogues. The figure is reproduced from Quadrelli, E. A. *et al*.[90]

To illustrate the interest of POSS as molecular models for silica-grafted organometallic species, we selected following two examples, based on Ta and Ir species which are relevant to this work. To better investigate the reactivity of the tantalum tris-neopentyl neopentylidene complex with silica, Chabanas and co-workers investigated the reactivity of the same organometallic derivative with a mono-hydroxyl POSS ligand. This study revealed the formation of a peralkyl intermediate resulting from the 1,2-addition of ligand hydroxyl group to the alkylidene bond. This first step is followed by intramolecular α-H elimination. Quite interestingly, analogous reactivity is found with silica and leads to the corresponding alkylidene species (see **Scheme 1.15**). The spectroscopic data (NMR and IR) for both species are very similar[92] and the EXAFS data recorded for the supported species are well-complemented by the X-ray crystallographic data obtained from the homogeneous analogue. This seminal study perfectly demonstrated the interest of POSS derivative to (i) mimic the reactivity of silica and investigate grafting reaction mechanisms and (ii) provide spectroscopic models and structural information on the grafted species.

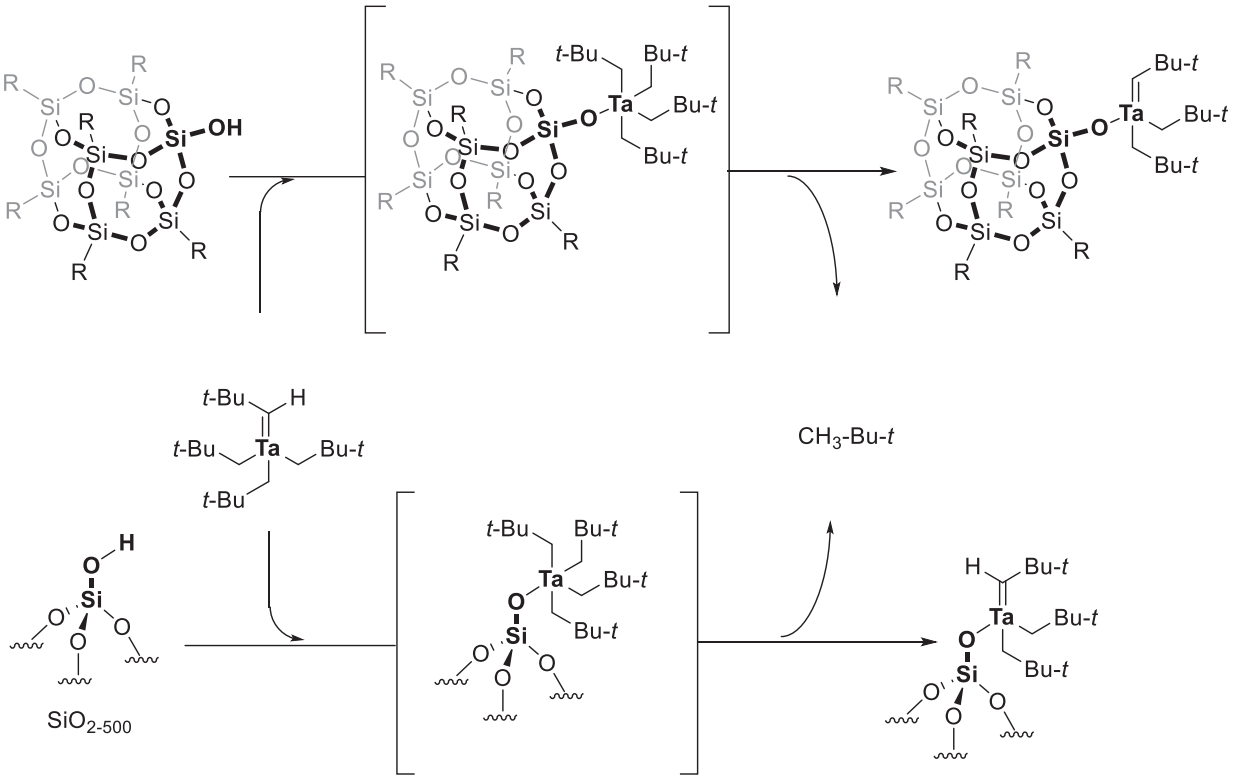

Scheme 1.15. Analogy of the immobilization of Ta(CH^{t}Bu)(CH$_2$^{t}Bu)$_3$ on silica and on a POSS derivative. The figure is taken from Chabanas *et al.*[92]

In 2014, Mezetti and co-workers reported the use of POSS molecular models to decipher the data obtained in the immobilization of the iridium pincer complex [IrH_2(POCOP)] on silica, as shown in **Figure 1.6**. The close analogy of both the ^{31}P NMR signal of the phosphine moieties and the ^{1}H NMR data for the hydride ligand between the silica grafted iridium complex and the corresponding POSS analogue confirms the fact that POSS can serve as a good molecular model for silica.

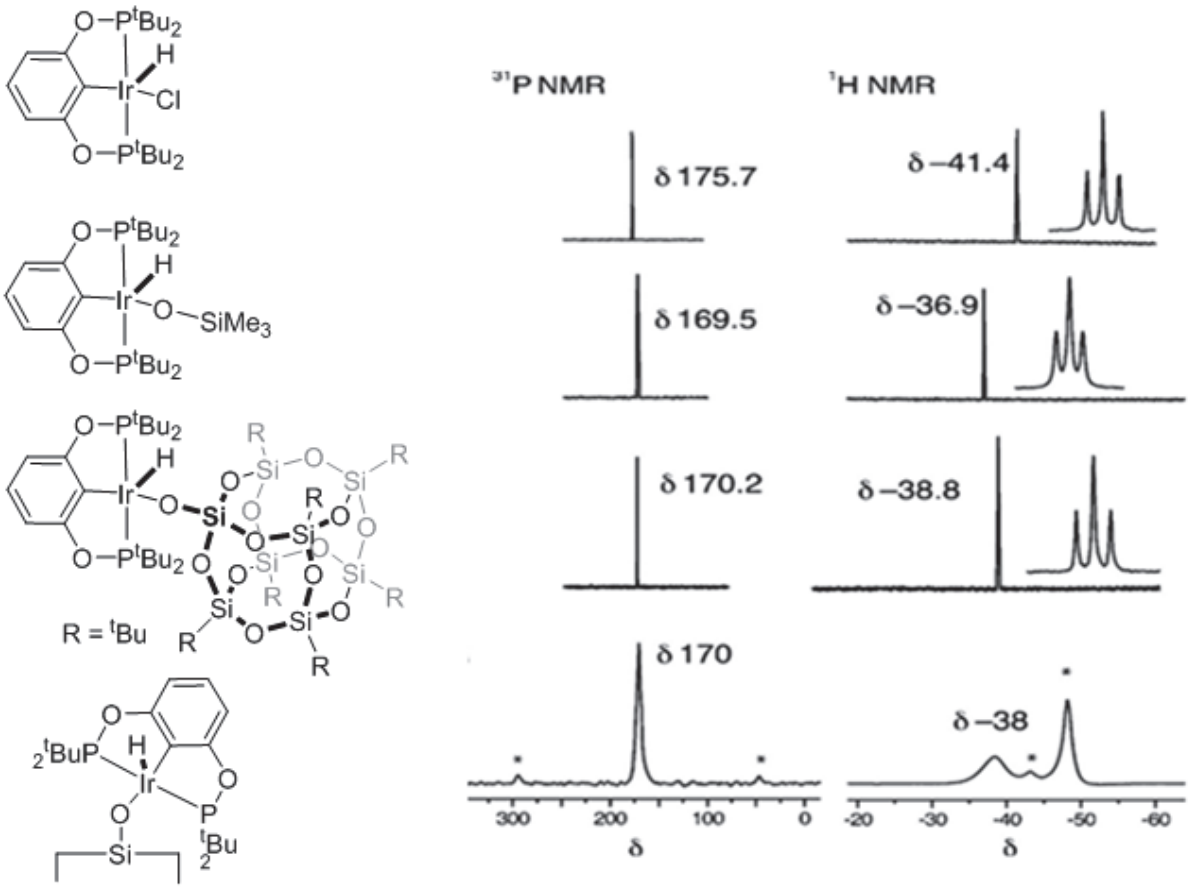

Figure 1.6. Silica supported iridium pincer complex and its soluble homogeneous analogues. The figure is taken from Mezetti *et al*.[93]

Thus we observe from the above discussed examples that POSS species have been used successfully to complement the data obtained from the silica grafted complexes.

1.3) Objectives of this PhD work: synthesis of silica-supported early-late heterobimetallic complex bridged by a bifunctional N-Heterocyclic carbene (NHC)

The central objective of this project is the development of original well-defined early/late heterobimetallic complexes supported at the surface of a mesoporous silica support. Its chemical foundation is to take advantage of (1) metal-metal and (2) metal-support cooperative effects, if possible in combination, to achieve unprecedented and highly reactive active sites ultimately leading to new bond activation pathways / new catalytic transformations.

As mentioned earlier, examples of silica functionalized with early/late heterobimetallic complexes are exceedingly rare. This can be partly explained by the fact that the methodologies employed for immobilizing both metal categories (early *vs* late) are often orthogonal. To knock down this barrier we propose in this work new modular synthetic approaches directly inspired and requiring skills from molecular organometallic chemistry and from SOMC.

To do so, molecular complexes will be specifically designed to serve (i) as precursors for grafting onto solid supports, (ii) as models for the immobilized species. A common methodology to direct and stabilize heterobimetallic assemblies consists in using bifunctional ligands featuring two distinct coordination motifs: one « hard », able to form strong bonds with abundant early TM, and one « soft » with a strong affinity for « late » TM. While a wide range of early-late heterobimetallic complexes have been reported, most of them feature phosphorus-based donors at the late metal center. In this thesis we propose to develop a straightforward synthetic procedure for the assembly ELHB complexes using functionalized N-Heterocyclic carbine (NHC) derivatives. More specifically, in Chapter 2 we will explore the synthesis of a new bifunctional NHC ligand containing an alcohol functional group in one of its pendant arms. A representation of this bifunctional NHC is shown below:

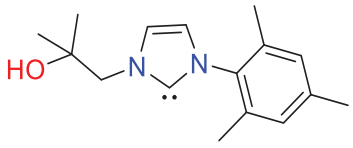

This ligand will be used to construct original monometallic and heterobimetallic complexes based on tantalum and rhodium, as described in Chapter 3. We chose to use tantalum as the early metal center since tantalum is reported to be active in a wide range of attractive reactions including C-H bond activations[94,95] and N_2 activation[96–98]. Moreover the host laboratory has a strong expertise in silica supported tantalum monometallic complexes and

has demonstrated the great potential of these species for stoichiometric and catalytic transformations. We chose rhodium as the late transition metal because of the stability of rhodium-NHC complexes and their ability to act as catalysts in a plethora of reactions such as alkene hydrosilylation[99–101] or C-H bonds functionalizations.[102,103] These two metals will form an important entry point to this chemistry. Once the proof of concept is validated, it will open new avenues to explore this chemistry with different early-late metal combinations.

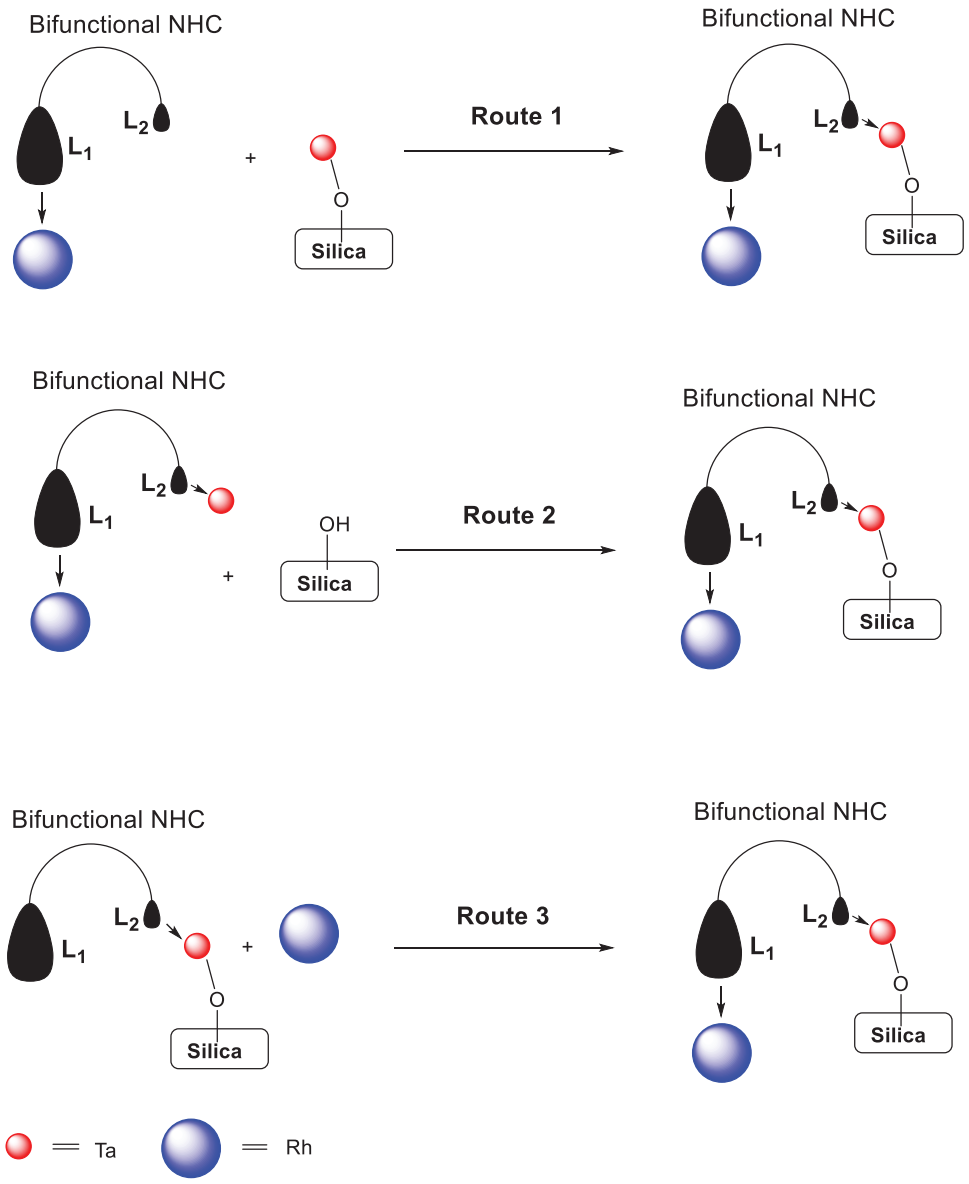

Scheme 1.16. The scheme depicts the possible synthetic routes to prepare the targeted silica-supported early-late heterobimetallic species, using a bifunctional alkoxy NHC as bridging ligand.

In order to access silica-supported ELHB species, direct surface functionalization by pre-assembled heterobimetallic entities will be explored (**Scheme 1.16**, route 2). A possible alternative strategy will consist first into grafting a well-chosen oxophilic metal precursor directly onto the surface of a silica material, and then to use this early transition metal site as a reactive center in order to introduce a late metal in close proximity to the first one (**Scheme 1.16**, routes 1 and 3). This is the purpose of Chapter 4.

The general representation of the targeted silica supported tantalum-rhodium early-late heterobimetallic species is reproduced below:

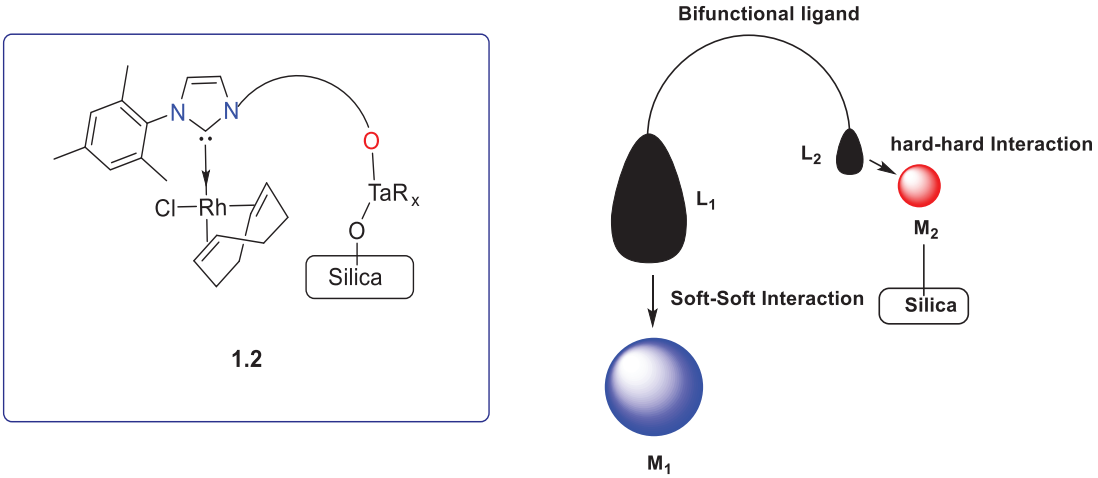

As reported earlier in this chapter, the characterization data of the silica supported complexes can be difficult to decipher. Hence the development of molecular models of silica grafted complexes is essential in understanding the structure and chemistry of the grafted complexes. Another objective of this thesis is thus to utilize POSS ligands as molecular models of the silica grafted complexes (Chapter 4). Computational studies will also be used to model the surface species and predict their reactivity (Chapter 5). Thus this project will consist of three main pillars: the synthesis of early-late heterobimetallic complexes in solution, the preparation of silica-supported ELHB species and the modelling of the supported species through the development of homogeneous molecular analogues of the silica grafted complexes and the use of computational methods.

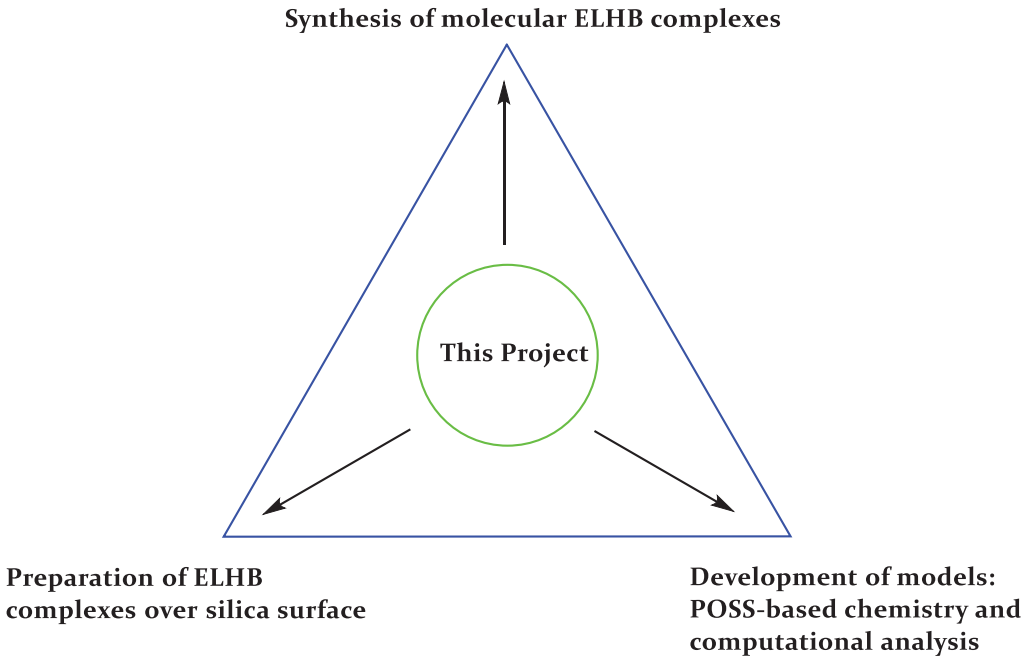

Figure 1.8: Pictorial diagram highlighting major dimensions of this thesis.

REFERENCES

1 J. A. Gladysz, Z. T. Ball, G. Bertrand, S. A. Blum, V. M. Dong, R. Dorta, F. E. Hahn, M. G. Humphrey, W. D. Jones, J. Klosin, I. Manners, T. J. Marks, J. M. Mayer, B. Rieger, J. C. Ritter, A. P. Sattelberger, J. M. Schomaker and V. W.-W. Yam, *Organometallics*, 2012, **31**, 1–18.

2 N. Nakata, M. Sakashita, C. Komatsubara and A. Ishii, *Eur. J. Inorg. Chem.*, 2010, **2010**, 447–453.

3 A. Sevin, Y. Hengtai and P. Chaquin, *J. Organomet. Chem.*, 1984, **262**, 391–405.

4 P. Buchwalter, J. Rosé and P. Braunstein, *Chem. Rev.*, 2015, **115**, 28–126.

5 J. T. Mague, *J. Organomet. Chem.*, 1982, **230**, 99–260.

6 M. Oishi, M. Kino, M. Saso, M. Oshima and H. Suzuki, *Organometallics*, 2012, **31**, 4658–4661.

7 M. Ichikawa, L. Rao, T. Ito and A. Fukuoka, *Faraday Discuss. Chem. Soc.*, 1989, **87**, 321–336.

8 J. R. Shapley, W. S. Uchiyama and R. A. Scott7, *J . Phys. Chem*, 1990, **94**, 1190–1196.

9 S. J. Tauster, S. C. Fung and R. L. Garten, *J. Am. Chem. Soc.*, 1978, **100**, 170–175.

10 B. H. Davis, in *Industrial and Engineering Chemistry Research*, 2007, **46**, 8938–8945.

11 S. J. Tauster, in *Preprints Symposia*, 1985, **30**, 132.

12 H. R. Sadeghi and V. E. Henrich, *J. Catal.*, 1988, **109**, 1–11.

13 J. C. Kennedy and A. K. Datye, *J. Catal.*, 1998, **179**, 375–389.

14 K. Hayek, M. Fuchs, B. Klötzer, W. Reichl and G. Rupprechter, *Top. Catal.*, 2000, **13**, 55–66.

15 E. Kikuchi, M. Matsumoto, T. Takahashi, A. Machino and Y. Morita, *Appl. Catal.*, 1984, **10**, 251–260.

16 Charles P. Casey and Gregory T. Whiteker, *Inorg. Chem.*, 1990, **29**, 876-879.

17 B. G. Cooper, J. Wesley Napoline and C. M. Thomas, *Catal. Rev. Sci. Eng.*, 2012, **541**, 1–401.

18 T. Miyazaki, Y. Tanabe, M. Yuki, Y. Miyake and Y. Nishibayashi, *Organometallics*, 2011, **30**, 2394–2404.

19 T. A. Hanna, A. M. Baranger and R. G. Bergman, *J. Am. Chem. Soc.*, 1995, **117**, 11363–11364.

20 M. J. Hostetler, M. D. Butts and R. G. Bergman, *J. Am. Chem. Soc.*, 1993, **115**, 2743–2752.

21 Y. Zhang, S. P. Roberts, R. G. Bergman and D. H. Ess, *ACS Catal.*, 2015, **5**, 1840–1849.

22 J. P. Krogman, B. M. Foxman and C. M. Thomas, *J. Am. Chem. Soc.*, 2011, **133**, 14582–14585.

23 W. Zhou, S. L. Marquard, M. W. Bezpalko, B. M. Foxman and C. M. Thomas, *Organometallics*, 2013, **32**, 1766–1772.

24 C. R. King, N. Rollins, A. Holdaway, M. M. Konnick, R. A. Periana and D. H. Ess, *Organometallics*, 2018, **37**, 3045–3054.

25 B. E. Bosch, I. Brümmer, K. Kunz, G. Erker, R. Fröhlich and S. Kotila, *Organometallics*, 2000, **19**, 1255–1261.

26 R. S. Dickson, T. De Simone, E. M. Campi and W. Roy Jackson, *Inorganica Chim. Acta*, 1994, **220**, 187–192.

27 T. Shribman, S. Kurz, U. Senff, F. Lindberg, E. Hey-Hawkins and M. S. Eisen, *J. Mol. Catal. A Chem.*, 1998, **129**, 191–198.

28 H. Kato, H. Seino, Y. Mizobe and M. Hidai, *J. Chem. Soc. Dalt. Trans.*, 2002, 1494–1499.

29 P. Braunstein, J. Durand, X. Morise, A. Tiripicchio and F. Ugozzoli, *Organometallics*, 2000, **19**, 444–450.

30 J. Sundermeyer, D. Runge and J. S. Field, *Angew. Chemie*, 1994, **106**, 679–682.

31 K. Mashima, H. Yonekura, T. Yamagata and K. Tani, *Organometallics*, 2003, **22**, 3766–3772.

32 T. P. Brewster, T. H. Nguyen, Z. Li, W. T. Eckenhoff, N. D. Schley and N. J. Deyonker, *Inorg. Chem.*, 2018, **57**, 1148–1157.

33 J. Abys and W. M. Risen, *J. Organomet. Chem.*, 1981, **204**, 5–9.

34 C. P. Casey and R. Morris Bullock, *J. Mol. Catal.*, 1982, **14**, 283–292.

35 T. G. Ostapowicz and M. D. Fryzuk, *Inorg. Chem.*, 2015, **54**, 2357–2366.

36 J. A. R. Schmidt and J. Arnold, *J. Am. Chem. Soc.*, 2001, **123**, 8424–8425.

37 L. H. Gade, *Angew. Chemie - Int. Ed.*, 2000, **39**, 2658–2678.

38 C. Moise, J.-F. Reynoud, J. C. Leblanc and R. Broussier, *J. Organomet. Chem.*, 1982, **240**, 5-7.

39 T. Bartik, B. Happ, A. Sieker, S. Stein, A. Sorken, K.-H. Thiele, C. Kriebel and G. Pulyi, *Zeitschrift fur Anorg. und Allg. Chemie*, 1992, **608**, 173–183.

40 K. G. J Am, *Organometallics*, 1987, **6**, 5818-5838.

41 S. Gautron, N. Lassauque, C. Le Berre, L. Azam, R. Giordano, P. Serp, G. Laurenczy, D. Thiébaut and P. Kalck, *Top. Catal.*, 2006, **40**, 83–90.

42 S. M. Baxter, G. S. Ferguson and P. T. Wolczanski, *Catal. Rev.*, 1988, **110**, 42.

43 H. Hellmann, J. Bader, H. Birkner and O. Schumacher, *Justus Liebigs Ann. Chem.*, 1962, **659**, 49–63.

44 M. H. Chisholm, D. L. Clark, J. C. Huffman and C. A. Smith, *Organometallics,* 1987, **6**, 1280-1291.

45 G. S. Ferguson and P. T. Wolczanski, *Organometallics*, 1985, **4**, 1601–1605.

46 J. M. Basset, F. Lefebvre and C. Santini, *Coord. Chem. Rev.*, 1998, **178–180**, 1703–1723.

47 B. Rhers, A. Salameh, A. Baudouin, E. A. Quadrelli, M. Taoufik, C. Copéret, F. Lefebvre, J. M. Basset, X. Solans-Monfort, O. Eisenstein, W. W. Lukens, L. P. H. Lopez, A. Sinha and R. R. Schrock, *Organometallics*, 2006, **25**, 3554–3557.

48 R. Anwander, *Chem. Mater.*, 2001, **13**, 4419–4438.

49 C. Copéret, M. Chabanas, R. Petroff Saint-Arroman and J. M. Basset, *Angew. Chemie - Int. Ed.*, 2003, **42**, 156–181.

50 L. T. Zhuravlev, *Colloids Surfaces A Physicochem. Eng. Asp.*, 2000, **173**, 1–38.

51 C. Copéret, A. Comas-Vives, M. P. Conley, D. P. Estes, A. Fedorov, V. Mougel, H. Nagae, F. Núñez-Zarur and P. A. Zhizhko, *Chem. Rev.*, 2016, **116**, 323–421.

52 J. D. A. Pelletier and J. M. Basset, *Acc. Chem. Res.*, 2016, **49**, 664–677.

53 R. Duchateau, U. Cremer, R. J. Harmsen, S. I. Mohamud, H. C. L. Abbenhuis, R. A. Van Santen, A. Meetsma, S. K. H. Thiele, M. F. H. Van Tol and M. Kranenburg, *Organometallics*, 1999, **18**, 5447–5459.

54 F. Quignard, A. Choplin and J. M. Basset, *J. Chem. Soc. Chem. Commun.*, 1991, 1589–1590.

55 J. Jarupatrakorn and T. D. Tilley, *J. Am. Chem. Soc.*, 2002, **124**, 8380–8388.

56 J. A. N. Ajjou and S. L. Scott, *Organometallics*, 1997, **16**, 86–92.

57 N. Merle, F. Le Qu??m??ner, Y. Bouhoute, K. C. Szeto, A. De Mallmann, S. Barman, M. K. Samantaray, L. Delevoye, R. M. Gauvin, M. Taoufik and J. M. Basset, *J. Am. Chem. Soc.*, 2017, **139**, 2144–2147.

58 F. Quignard, O. Graziani and A. Choplin, *Appl. Catal. A Gen.*, 1999, **182**, 29–40.

59 R. M. Gauvin, L. Delevoye, R. A. Hassan, J. Keldenich and A. Mortreux, *Inorg. Chem.*, 2007, **46**, 1062–1070.

60 M. Adachi, K. Yoshii, Y. Z. Han and K. Fujimoto, *Bull. Chem. Soc. Jpn.*, 1996, **69**, 1509–1516.

61 K. R. Kloetstra, M. Van Laren and H. Van Bekkum, *J. Chem. Soc. - Faraday Trans.*, 1997, **93**, 1211–1220.

62 F. Allouche, G. Lapadula, G. Siddiqi, W. W. Lukens, O. Maury, B. Le Guennic, F. Pointillart, J. Dreiser, V. Mougel, O. Cador and C. Copéret, *ACS Cent. Sci.*, 2017, **3**, 244–249.

63 P. Laurent, L. Veyre, C. Thieuleux, S. Donet and C. Copéret, *Dalt. Trans.*, 2013, **42**, 238–248.

64 Y. Liang and R. Anwander, *Dalt. Trans.*, 2013, **42**, 12521–12545.

65 F. Héroguel, D. Gebert, M. D. Detwiler, D. Y. Zemlyanov, D. Baudouin and C. Copéret, *J. Catal.*, 2014, **316**, 260–269.

66 M. Rimoldi and A. Mezzetti, *Catal. Sci. Technol.*, 2014, 4, 2724–2740.

67 M. Rimoldi, D. Fodor, J. A. Van Bokhoven and A. Mezzetti, *Chem. Commun.*, 2013, **49**, 11314–11316.

68 J. Ternel, L. Delevoye, F. Agbossou-Niedercorn, T. Roisnel, R. M. Gauvin and C. M. Thomas, *Dalt. Trans.*, 2010, **39**, 3802–3804.

69 E. K. Huang, W.-M. Cheung, K.-W. Chan, F. L.-Y. Lam, X. Hu, Q.-F. Zhang, I. D. Williams and W.-H. Leung, *Eur. J. Inorg. Chem.*, 2013, **2013**, 2893–2899.

70 M. K. Samantaray, J. Alauzun, D. Gajan, S. Kavitake, A. Mehdi, L. Veyre, M. Lelli, A. Lesage, L. Emsley, C. Copéret and C. Thieuleux, *J. Am. Chem. Soc.*, 2013, **135**, 3193–3199.

71 I. Romanenko, D. Gajan, R. Sayah, D. Crozet, E. Jeanneau, C. Lucas, L. Leroux, L. Veyre, A. Lesage, L. Emsley, E. Lacôte and C. Thieuleux, *Angew. Chemie - Int. Ed.*, 2015, **54**, 12937-12941.

72 R. R. Schrock and J. D. Fellmann, *J. Am. Chem. Soc.*, 1978, **100**, 3359–3370.

73 E. Le Roux, M. Chabanas, A. Baudouin, A. De Mallmann, C. Copéret, E. A. Quadrelli, J. Thivolle-Cazat, J. M. Basset, W. Lukens, A. Lesage, L. Emsley and G. J. Sunley, *J. Am. Chem. Soc.*, 2004, **126**, 13391–13399.

74 J. M. Basset, C. Copéret, D. Soulivong, M. Taoufik and J. Thivolle Cazat, *Acc. Chem. Res.*, 2010, **43**, 323–334.

75 S. Soignier, M. Taoufik, E. Le Roux, G. Saggio, C. Dablemont, A. Baudouin, F. Lefebvre, A. De Mallmann, J. Thivolle-Cazat, J. M. Basset, G. Sunley and B. M. Maunders, *Organometallics*, 2006, **25**, 1569–1577.

76 Y. Chen, E. Abou-Hamad, A. Hamieh, B. Hamzaoui, L. Emsley and J. M. Basset, *J. Am. Chem. Soc.*, 2015, **137**, 588–591.

77 M. C. Haibach, S. Kundu, M. Brookhart and A. S. Goldman, *Acc. Chem. Res.*, 2012, **45**, 947–958.

78 R. Ahuja, S. Kundu, A. S. Goldman, M. Brookhart, B. C. Vicente and S. L. Scott, *Chem. Commun.*, 2008, 253–255.

79 T. Agapie, M. W. Day and J. E. Bercaw, *Organometallics*, 2008, **23**, 6123-6142.

80 A. S. Goldman, A. H. Roy, Z. Huang, R. Ahuja, W. Schinski and M. Brookhart, *Science*, 2006, **312**, 257–261.

81 P. Avenier, M. Taoufik, A. Lesage, X. Solans-Monfort, A. Baudouin, A. De Mallmann, L. Veyre, J. M. Basset, O. Eisenstein, L. Emsley and E. A. Quadrelli, *Science*, 2007, **317**, 1056–1060.

82 H.-P. Jia and E. A. Quadrelli, *Chem. Soc. Rev.*, 2014, **43**, 547–564.

83 Y. Qiao, N. Said, M. Rauser, K. Yan, F. Qin, N. Theyssen and W. Leitner, *Green Chem.*, 2017, **19**, 977–986.

84 C. Copéret, D. P. Estes, K. Larmier and K. Searles, *Chem. Rev.*, 2016, **116**, 8463–8505.

85 C. Copéret, *Chem. Rev.*, 2010, **110**, 656–680.

86 P. Barbaro, C. Bianchini, V. D. Santo, A. Meli, S. Moneti, R. Psaro, A. Scaffidi, L. Sordelli and F. Vizza, *J. Am. Chem. Soc.*, 2006, **128**, 7065–7076.

87 G. L. Rice and S. L. Scott, *Chem. Mater.*, 1998, **10**, 620–625.

88 M. K. Samantaray, S. Kavitake, N. Morlans, E. Abou-Hamad, A. Hamieh, R. Dey and J. M. Basset, *J. Am. Chem. Soc.*, 2017, **139**, 3522–3527.

89 S. Lassalle, R. Jabbour, P. Schiltz, P. Berruyer, T. K. Todorova, L. Veyre, D. Gajan, A. Lesage, C. Thieuleux and C. Camp, *J. Am. Chem. Soc.*, 2019, jacs.9b08311.

90 E. A. Quadrelli and J. M. Basset, *Coord. Chem. Rev.*, 2010, **254**, 707–728.

91 F. J. Feher, T. A. Budzichowski, R. L. Blanski, K. J. Weller and J. W. Ziller, *Organometallics*, 1991, **10**, 2526–2528.

92 M. Chabanas, E. A. Quadrelli, B. Fenet, C. Copéret, J. Thivolle-Cazat, J. M. Basset, A. Lesage and L. Emsley, *Angew. Chemie - Int. Ed.*, 2001, **40**, 4493–4496.

93 M. Rimoldi and A. Mezzetti, *Inorg. Chem.*, 2014, **53**, 11974–11984.

94 J. F. Hartwig, *J. Am. Chem. Soc.*, 2016, **138**, 2–24.

95 T. R. Helgert, X. Zhang, H. K. Box, J. A. Denny, H. U. Valle, A. G. Oliver, G. Akurathi, C. E. Webster and T. K. Hollis, *Organometallics*, 2016, **35**, 3452–3460.

96 M. P. Shaver and M. D. Fryzuk, *Adv. Synth. Catal.*, 2003, **345**, 1061–1076.

97 M. D. Fryzuk, S. A. Johnson, B. O. Patrick, A. Albinati, S. A. Mason and T. F. Koetzle, *J. Am. Chem. Soc.*, 2001, **123**, 3960–3973.

98 R. J. Burford and M. D. Fryzuk, *Nat. Rev. Chem.*, 2017, **1**, 0026.

99 J. P. Morales-Cerón, P. Lara, J. López-Serrano, L. L. Santos, V. Salazar, E. Álvarez and A. Suárez, *Organometallics*, 2017, **36**, 2460–2469.

100 C. Karmel, B. Li and J. F. Hartwig, *J. Am. Chem. Soc.*, 2018, **140**, 1460-1470.

101 S. Leelasubcharoen, P. A. Zhizhko, L. G. Kuzmina, A. V Churakov, J. A. K. Howard and G. I. Nikonov, *Organometallics*, 2009, **28**, 4500–4506.

102 R. Dorta, E. D. Stevens and S. P. Nolan, *J. Am. Chem. Soc.*, 2004, **126**, 5054–5055.

103 T. Nakamura, K. Suzuki and M. Yamashita, *J. Am. Chem. Soc.*, 2017, **139**, 17763–17766.

Chapter 2

Synthesis and Characterisation of Bifunctional N-heterocyclic carbene (NHC)

2.1) INTRODUCTION

2.1.1) Bifunctional ligands for the assembly of early/late heterobimetallic edifices

Accessing early-late heterobimetallic edifices in a controlled fashion is a challenging task. Smart and dedicated synthetic methodologies are required to avoid the formation of statistical mixtures, oligomers or nanoparticles, ligand redistribution and unwanted redox processes. This is particularly true when the two metal centers exhibit quite different chemical properties which are often incompatible. Two chemically different metals can combine together through different chemical pathways to give "*early-late*" heterobimetallic complexes. The stabilization of these early-late heterobimetallic edifices can be achieved by an appropriate choice of ancillary ligands. Among them, bifunctional ligands featuring two distinct coordination motifs are particularly well poised to interact with both metal centers simultaneously. The highly Lewis acidic early transition metal centers have a high affinity for hard σ and π donor ligands, for example alkoxy, amido, imido and oxo ligands. These hard ligands not only fulfill the electronic demands of the early transition metals but they also help stabilize the high oxidation states of these elements. On the other hand the late metal centers are soft and nucleophilic and form strong bonds with Lewis basic ligands for example P and S donor ligands.[1]

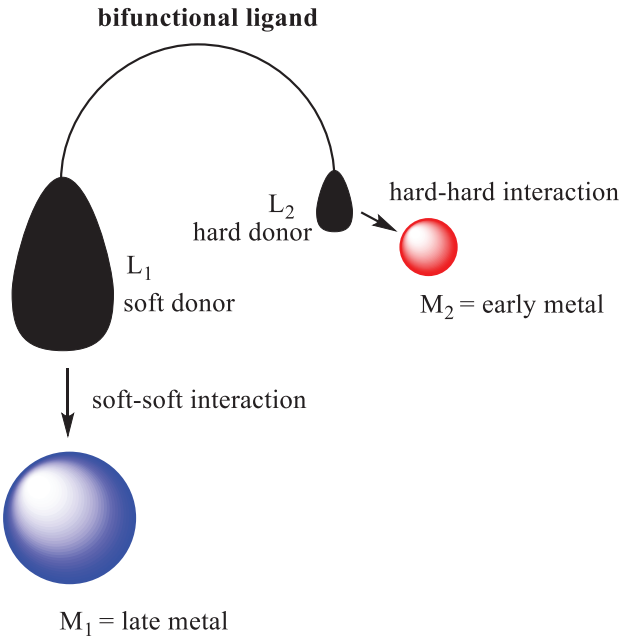

Figure 2.1: An interaction between soft and Lewis basic metal center with a soft donor ligand on the left hand side of the figure and hard and Lewis acidic metal center with a hard ligand on the right hand side of the figure leads to the assembly of early-late heterobimetallic complexes supported by bifunctional ligands.

Figure 2.1 shows a pictorial representation of the targeted bifunctional ligand design, featuring a hard and a soft donor to stabilize an early/late heterobimetallic complex.

To date, this synthetic approach is the most commonly used methodology to prepare well-defined early/late heterobimetallic complexes. **Figure 2.2** shows some representative examples where bifunctional ligands are used to drive the assembly of early-late heterobimetallic species.

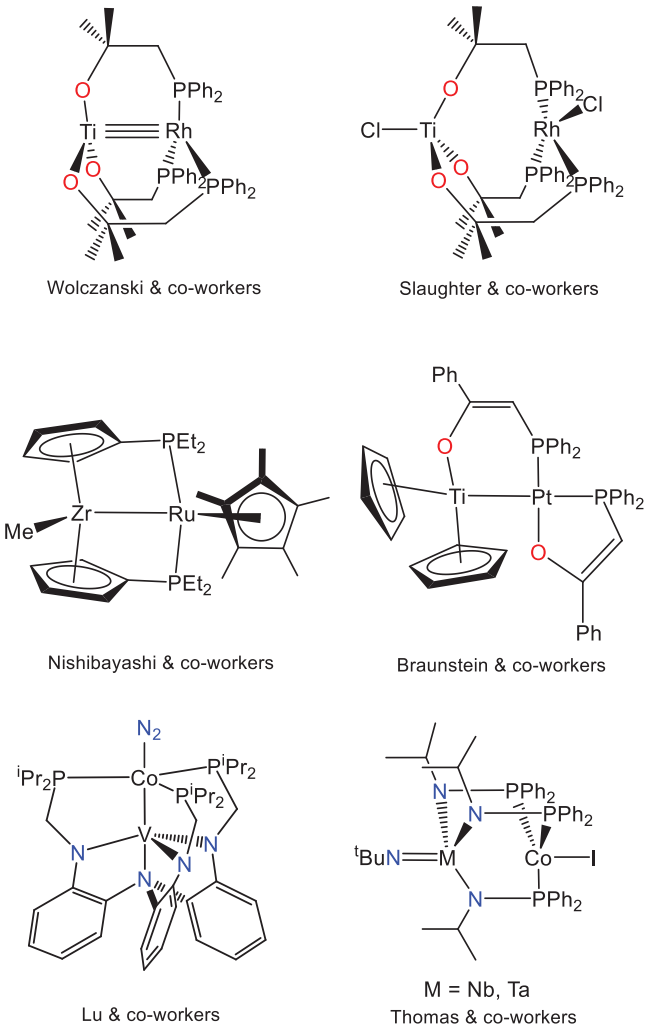

Figure 2.2: Some representative examples of early-late heterobimetallic complexes held together by hard-soft bifunctional ligands.[1–6]

Note that in most examples reported to date in the literature, the late-metal donor is a phosphorus-derived moiety. Encouraged by the flagship role played by N-heterocyclic carbene (NHC) derivatives of organometallic complexes in homogeneous catalysis;[7–13] we and others have identified functionalized NHC ligands as promising alternatives. Indeed, recently,

bifunctional N-heterocyclic carbenes (NHC) have emerged as a potential ligand framework to isolate polymetallic assemblies.

2.1.2) Bifunctional N-heterocyclic carbenes (NHCs)

A wide range of functional groups can be installed onto carbenic heterocycles and a large variety of bifunctional NHCs have been reported to date. The substitution of the imidazole-2-ylidene scaffold can be performed either at the N1 (FG1 – Figure 2.3) or the C4 (FG2 – Figure 2.3) position.

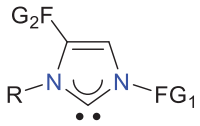

Figure 2.3: Schematic representation of a substituted NHC heterocycle.

Providing an exhaustive list of metal complexes bearing bifunctional NHCs ligands is therefore out of the scope of this thesis. To illustrate the diversity of the field and of accessible structures, selected examples of rhodium complexes featuring N-functionalized imidazole-2-ylidene ligands are shown on **Figure 2.4**.

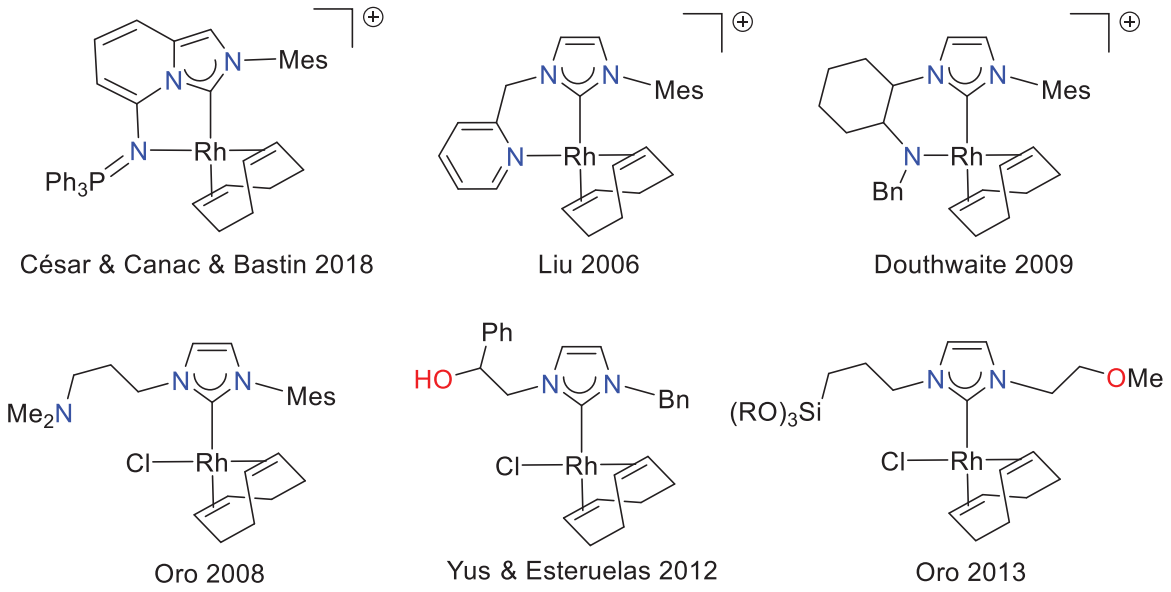

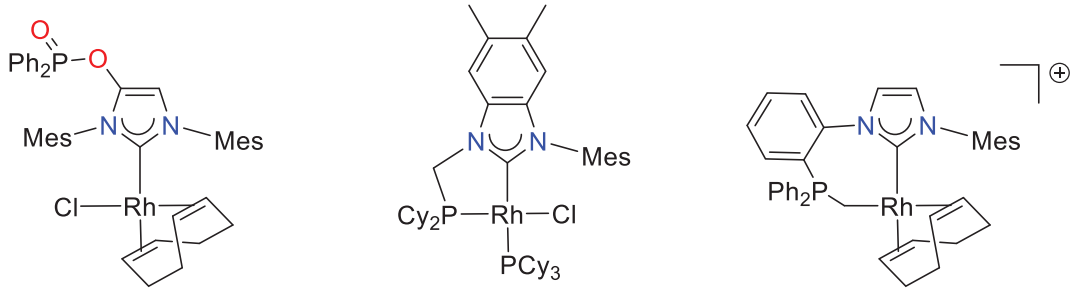

César & Lavigne 2009 | Hahn 2011 | Chauvin & Canac 2008

Figure 2.4: Selected examples of rhodium complexes featuring bifunctional NHC ligands, relevant to the present work.[14–22]

Among the various motivations invoked for developing bifunctional NHCs, the search for chelation and hemilability are the most prominent. Indeed, chelation of the pendant arm group may help stabilize the metal center in different oxidation states and provide greater stability of the resulting metal-bifunctional NHC complexes. While the carbene part of the ligand is assumed to be the site that is strongly bound to the metal, the pendant arm of the ligand can behave as a hemilabile ligand and occasionally de-coordinate in solution to open a coordination site. This hemilabile behavior has proven very helpful in increasing the catalytic properties in some instances.[23–27] For example, Matute and co-workers reported bis cationic Ir(III) complex containing hemilabile alkoxy functional group in the pendant arm which was active in acceptorless alcohol dehydrogenation (AAD) reaction.[13] It was observed that the alkoxy functional group opens a vacant site at the iridium center where the substrate conversion takes place. The subsequent re-coordination of the pendant alkoxy group leads to the release of final product. The introduction of a functional group is also used to implement an additional function that can be useful in catalysis such as a proton relay[28] or a redox non-innocent moiety.[29] This additional functionality can also be activated in the presence of an external chemical/photo/redox stimulus and can be used to switch the catalytic activity.[30–33]

The scientific community also developed tailor-made bifunctional NHC ligands to access a range of **late-late** homobimetallic and heterobimetallic complexes. Representative examples are shown in **Figure 2.5**. These systems were not only targeted for applications in catalysis, but also for the preparation of functionalized coordinated polymers and materials, etc. Note that in most of these examples the functionalization is performed at the backbone of the NHC. This is mostly motivated by the possibility to modulate the electronic properties of the carbenic ligand or facilitate electronic communication between the two metals.

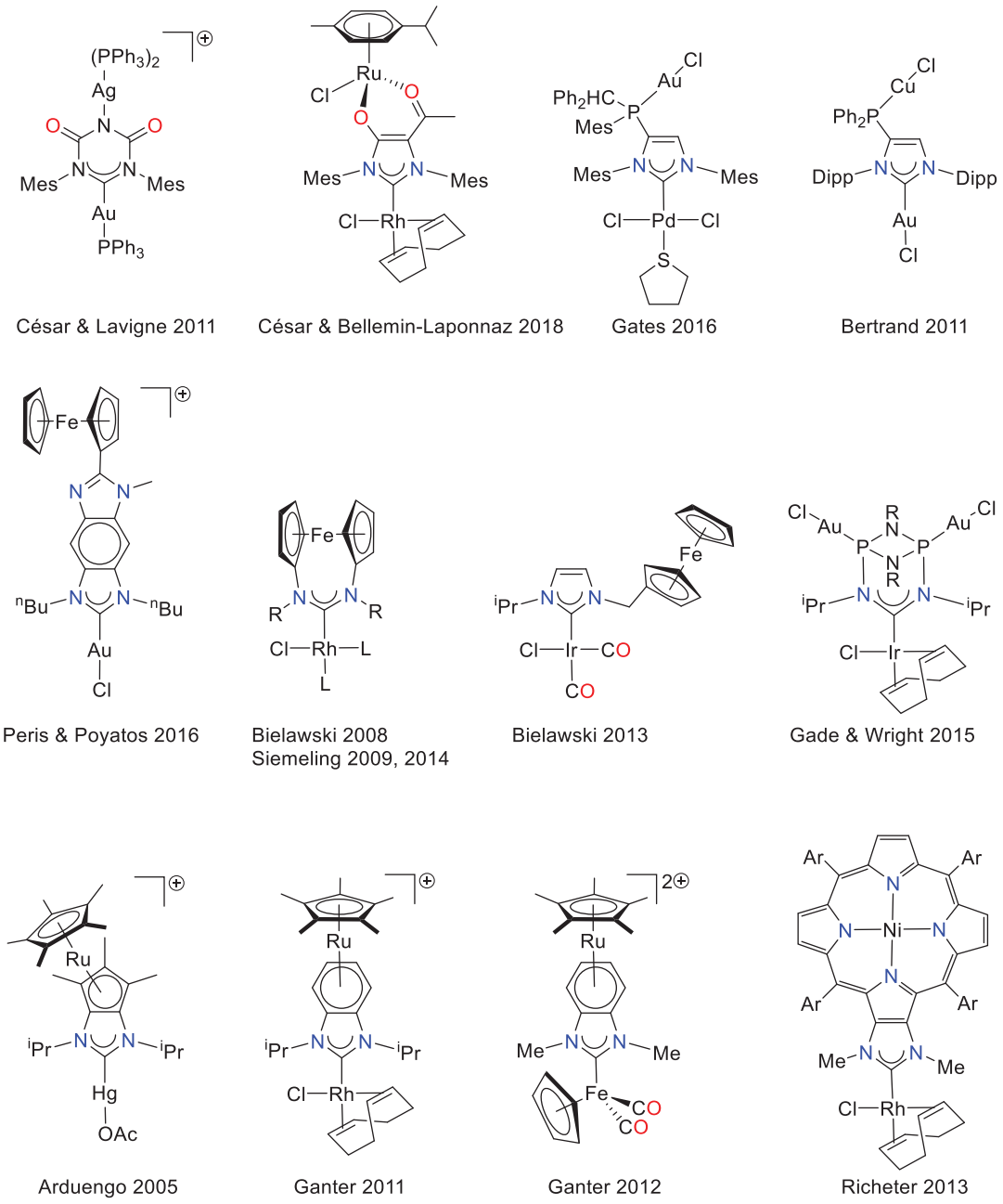

Figure 2.5: Relevant examples of late-late heterobimetallic complexes bearing bifunctional NHC ligands.[14,34–44]

While a range of late-late heterobimetallic systems are known, very few examples of NHC-containing early-late heterobimetallic complexes have been described so far. The structures of the systems known to date, to the best of our knowledge, are depicted on **Figure 2.6**.

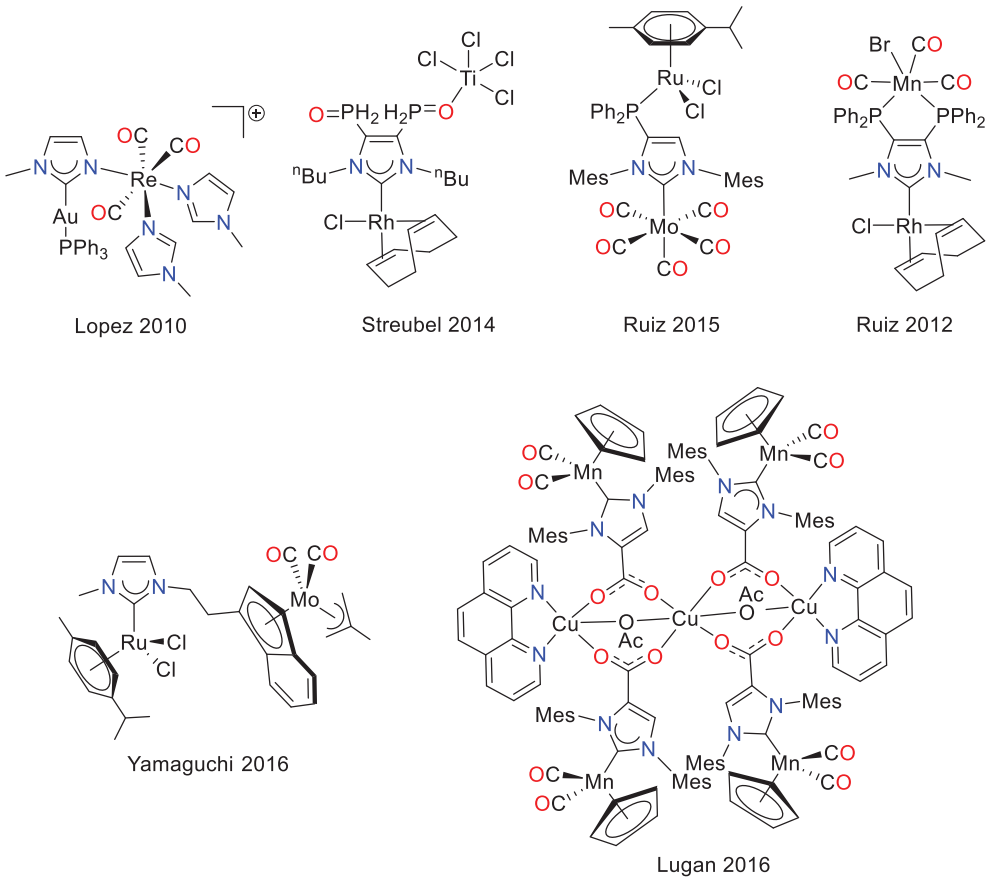

Figure 2.6: Early/late heterobimetallic complexes supported by bifunctional NHC ligands reported to date in the literature.[45–50]

Overall, these encouraging examples show the feasibility of the targeted methodology and highlight the diversity of metal combinations and ligand structures that could be achieved. However, the number of systems is still limited, and their applications in catalysis have not been fully explored. This is therefore an open, active and stimulating field of research.

2.1.3) **Ligand design**

While the carbene center is expected to bind preferentially with the late soft transition metal, several hard ligands (like alkoxy, amido, imido etc.) are available for installation in the NHC moiety to bind to the early metal. We focused our attention into alkoxy groups since the latter are known to form robust complexes with oxophilic early transition metals. In contrast, the late metal center should have reduced affinity for the oxygenated groups. Bifunctional NHCs featuring oxygen donor groups (alkoxides or aryloxides) have proven useful to stabilize a large range of monometallic species from across the *d*-block of the periodic table, as shown in **Figure 2.7**. Regarding early metals, pioneering work by the groups of Arnold, Bellemin-Laponnaz and Dagorne have shown that group 3 and group 4 as well as lanthanide and actinide alkyl/amido species could be isolated. Note that the M-NHC bonding in these species is not inert, as classically seen with late metals. Small molecules activation across the M-NHC bond has been reported by Arnold,[51,52] and a rare example of a zirconium to carbene alkyl transfer has been observed by Bellemin-Laponnaz and Dagorne. More recent work from the groups of Hohloch and Buchmeiser[53] has shown that aryloxy-carbenes were also good platforms to support group 5 and group 6 imido and alkylidene species (**Figure 2.7**). Regarding late metals, a series of NHC species featuring an oxygenated side arm have been developed and successfully applied in catalysis. One interesting example has been reported recently by Martin-Matute[13] which described alcohol/alkoxy-functionalized Ir-NHC species active in catalytic acceptorless alcohol dehydrogenation. Mechanistic studies conducted on these iridium complexes showed the direct involvement of the alkoxy group. The reactivity and hemilability of the side arm might be at the origin of the high catalytic performance exhibited by the Ir-NHC complex.

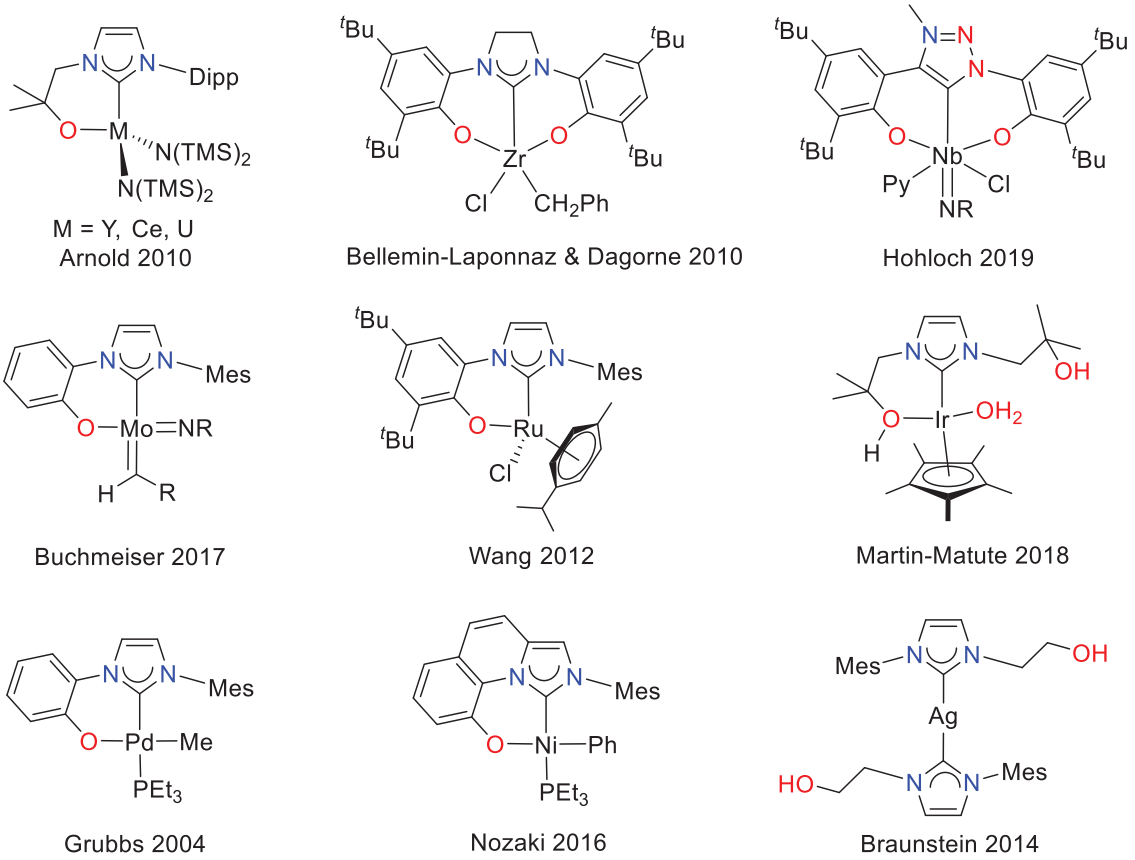

Figure 2.7: Representative examples of the diversity of metal phenoxy-NHC, alkoxy-NHC or hydroxy-NHC complexes reported from literature.[13,51,53–59]

Buoyed by the promising potential of these alkoxy-NHC complexes we hypothesized to utilize the specific bifunctional alcohol-NHC ligand, shown in **Figure 2.8**, to assemble early-late heterobimetallic complexes. We chose the unsaturated imidazolylidene backbone and the bulky N-mesityl group attached on one side of the ligand to provide good electronic and steric stabilization of the resulting NHC complexes. On the other arm we envisioned to implement a tertiary alcohol group. Compared to phenols, alcohols exhibit higher pK_a, and the corresponding alkoxide bases are more electron donating. In order to get stable 6-member metallacyclic complexes, 2 carbons were inserted as spacer between the heterocycle and the hydroxyl group. Finally, in order to avoid β-H elimination processes or putative enolization or conjugation phenomena with the imidazolyl moiety, we choose to introduce two methyl substituents on the cabon center bearing the hydroxyl group. This should also result in better steric protection of the ligand O-terminus. This chapter describes the synthesis and characterization of this new ligand platform.

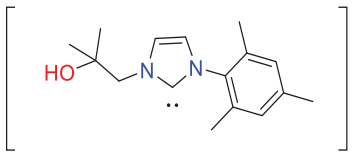

Figure 2.8: Structure of the targeted bifunctional NHC ligand containing a hydroxyl group in one of its arms.

2.2) RESULTS AND DISCUSSION

2.2.1) One-pot, fast and scalable synthesis of a new imidazolium salt and its characterization

The synthesis of bifunctional alkoxy-NHCs can be done via different chemical routes. Arnold and coworkers reported pioneering work on bifunctional alkoxy-NHCs.[15] They described the one pot synthesis of a bis-imidazolium salt precursor by ring opening of phenyloxirane with two equivalents of tert-butylimidazole. (**Scheme 2.1**) This synthesis required harsh reaction conditions: the ring opening of the epoxide is performed upon heating the neat precursors for 24 hours at 100°C. Since then, the ring-opening of epoxides with unsubstituted or alkyl substituted imidazoles has then be described in several occurrences.[16,60–63]

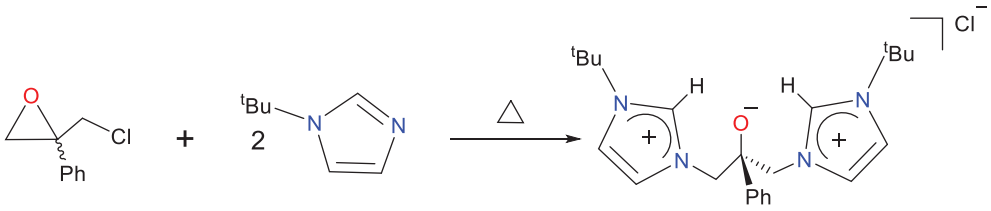

Scheme 2.1: Synthesis of an alkoxy bis-imidazolium salt from ring opening of phenyloxirane at elevated temperatures as reported by Arnold and coworkers.[60–62,64,65]

Inspired by this synthetic approach, we investigated the treatment of 1-mesitylimidazole with 1,2-epoxy-2-methylpropane. In this particular case, however, no reaction was observed and the starting materials were recovered, even after prolonged heating (**Scheme 2.2**). We attribute this result to the lower nucleophilicity of aryl imidazoles compared to their unsubstituted or alkyl-substituted counterparts. Indeed, the ring-opening reaction of epoxides with aryl imidazoles does not appear facile since, to the best of our knowledge, no such precedent is reported in the literature.

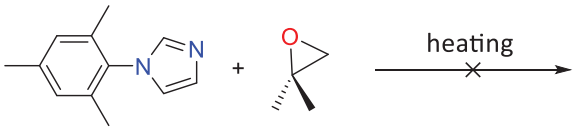

Scheme 2.2: 1-mesitylimidazole does not ring-open 1,2-epoxy-2-methylpropane.

Interestingly, Mauduit and co-workers recently reported a one-pot synthesis of bidentate hydroxyalkyl and carboxyalkyl-N-heterocyclic carbenes (**Scheme 2.3**). This relatively easy synthetic procedure involves mixing all the components in one step, and heating at 60°C for few minutes to yield the asymmetric imidazolium salt in good yield.[66]

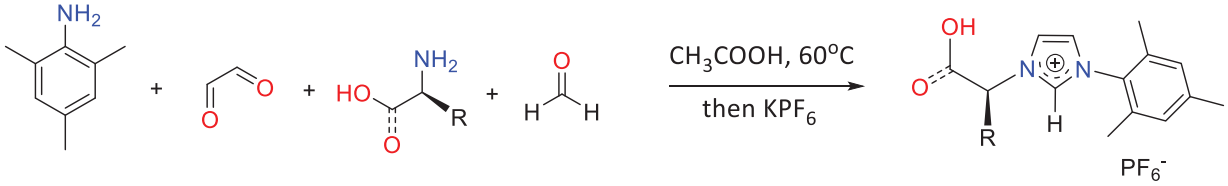

Scheme 2.3: One pot synthesis of asymmetric imidazolium salts using a primary amines, glyoxal and formaldehyde, as reported by Mauduit and coworkers.[66]

We therefore followed an analogous synthetic procedure to synthesize the unsymmetrical unsaturated imidazolium precursor. 2,4,6-trimethylaniline and 1-amino-2-methyl-2-propanol were mixed together in one pot with glyoxal and formaldehyde, heated at 60°C for 10 minutes to yield the imidazolium salt 1-mesityl-3-(2-hydroxyisobutyl)imidazolium acetate. A salt exchange is then performed upon vigorously stirring a DCM/H_2O biphasic mixture in the presence of excess KPF_6 at room temperature to yield the desired 1-mesityl-3-(2-hydroxyisobutyl)imidazolium hexafluorophosphate salt $[H_2L][PF_6]$ **1** (**Scheme 2. 4**). The use of the non-coordinating hexafluorophosphate counter anion facilitates the work-up and purification steps required to isolate the imidazolium salt.

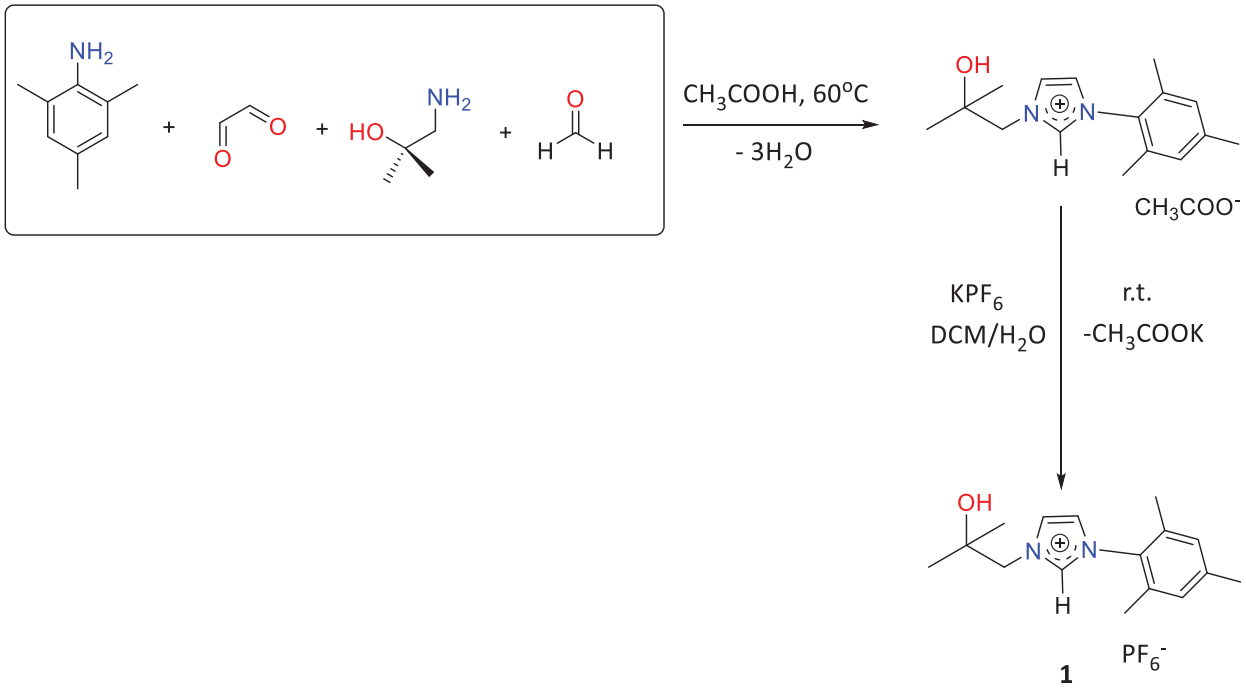

Scheme 2. 4: Synthesis of the hydroxyl-imidazolium hexafluorophosphate salt, **1**.

As anticipated, the crude mixture contains the desired asymmetric imidazolium species, but also the two symmetrically substituted imidazoliums, as a mixture. Therefore purification by flash chromatography using a 9:1 mixture of DCM/acetone was required to isolate compound **1** as a brown colored salt. The impurities elute first followed by the desired compound as shown in the **Figure 2.9**.

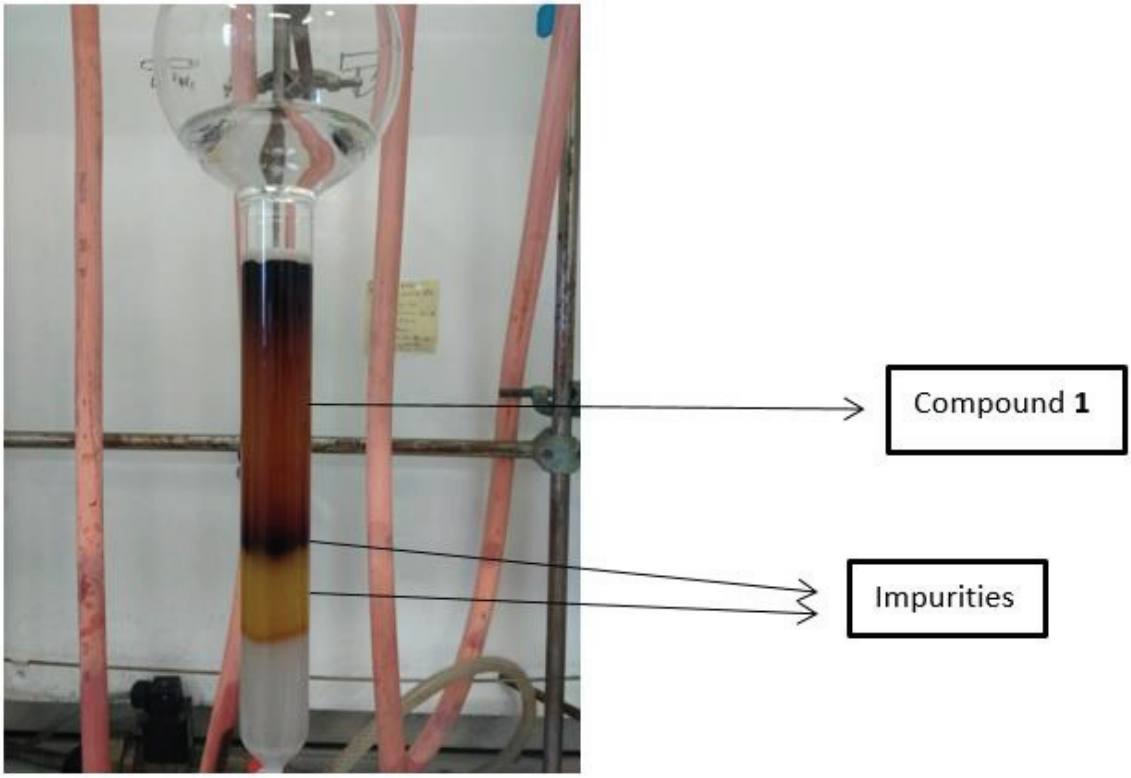

Figure 2.9: Purification *via* column chromatography of the hydroxyl-imidazolium hexafluorophosphate salt, **1**.

The structure of the salt **2.1** was confirmed by multiple nuclei NMR spectroscopy (^{1}H, ^{13}C, ^{31}P and ^{19}F), IR spectroscopy, ESI mass spectrometry and X-Ray crystallography. The ^{1}H NMR (Figure S1, Appendix 1) spectrum of the salt **2.1** in CD_2Cl_2 shows a highly downfield signal at 8.53 ppm corresponding to the imidazolium proton. The imidazolium salt backbone protons are observed as doublets at 7.64 and 7.25 ppm respectively. The free hydroxyl group is observed as a sharp singlet at 2.32 ppm. The sharp nature of the hydroxyl peak and corresponding upfield shift of the hydroxyl proton is indicative of a free hydroxyl which is not involved in hydrogen-bonding with neighboring groups. This is also confirmed by the presence of a sharp signal at 3585.4 cm^{-1} in the IR spectrum, corresponding to ν_{OH}. The X-Ray crystal structure of **1**, shown in **Figure 2.10**, confirms these attributions.

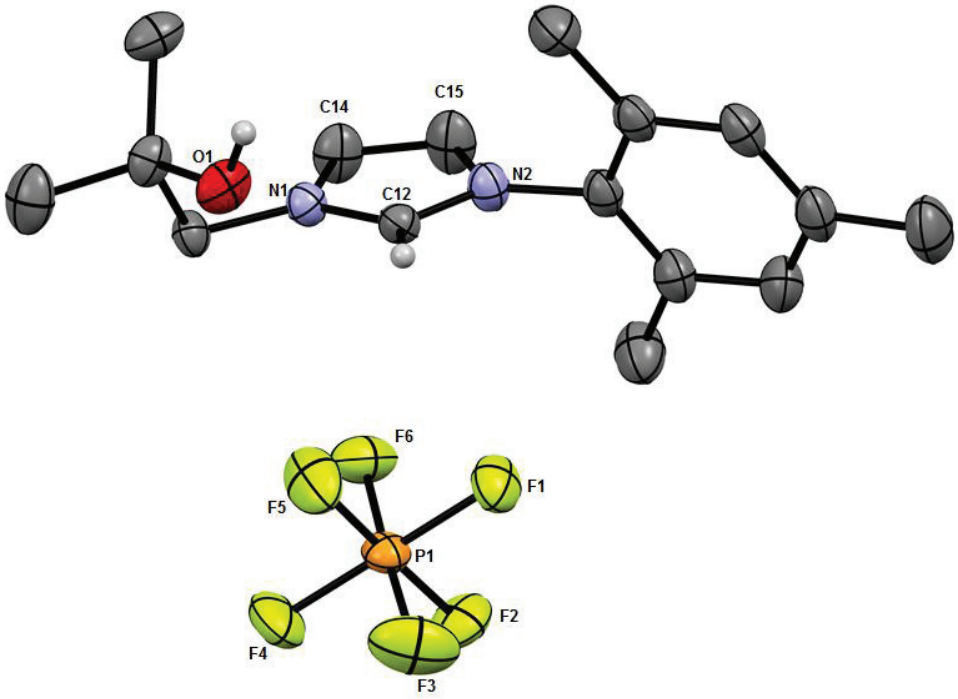

Figure 2.10: Molecular structure of **1** as determined by X-ray diffraction. Hydrogen atoms have been omitted for clarity and thermal ellipsoids are set at 50% probability level. Selected bond distances (Å) and angles (°) for **1**: N1-C12 1.332(3); N2-C12 1.326(3); N1-C12- N2 108.9(2).

2.2.2) Synthesis and characterization of the free NHC ligand

Predicting the locus of deprotonation of **1** when treated with one equivalent of base is not straightforward since there are two acidic centers: the hydroxyl moiety and the imidazolium moiety. Previous studies have shown that zwitterionic alkoxy-imidazolium tautomer forms are generally favored versus neutral hydroxyl-carbene forms. For instance, Davidson and coworkers reported the reaction of 2,6-di-tert-butyl-4-methylphenol with 1,3-dimesitylimidazol-2-ylidene (IMes) which gives the corresponding imidazolium aryloxide adduct (**Figure 2.11**-a).[67] In contrast, Movassaghi and coworkers described the formation of a methanol-carbene complex when IMes is treated with anhydrous MeOH (**Figure 2.11**-b).[68] In other cases it has been observed that the hydroxyl group undergoes an oxidative addition at the free carbene center forming bicyclic adducts behaving as masked carbenes (**Figure 2.11**-c), a phenomenon typically observed for saturated carbenes.[69] Overall, the net result of the reaction strongly depends on the nature of both the carbene and the hydroxyl groups.

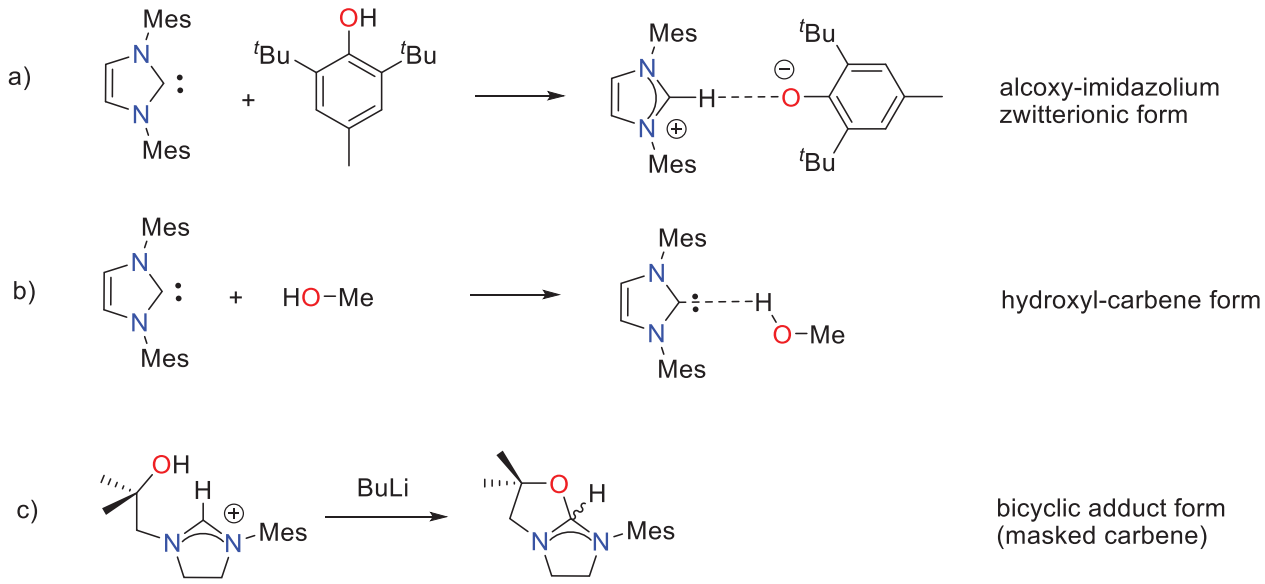

Figure 2.11: Three classes of compounds can be obtained from the interaction of free carbenes with hydroxyl groups: a) alcoxy-imidazolium zwitterions;[64,67] b) hydroxyl carbene adducts;[68] c) bicyclic adducts.[70–72]

Here, the reaction of potassium bis(trimethylsilyl)amide (KHMDS, 1.0 equivalent) with the imidazolium salt **1** leads to the deprotonation of the imidazolium proton selectively, thus yielding free N-heterocyclic carbene **2** (**Scheme 2.5**). Compound **2** sublimes (10^{-5} mbar, 120°C) which is in agreement with its neutral formulation, but is more easily purified upon recrystallization in THF and can be isolated in up to 77% yield.

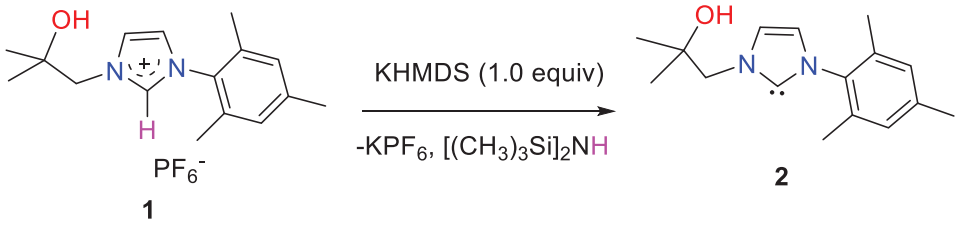

Scheme 2.5: Synthesis of the free NHC carbene by selective deprotonation of the imidazolium ring proton of the imidazolium salt 1 rather than the hydroxyl proton.

^{1}H NMR monitoring of the transformation of **1** into **2**, performed in C_6D_6 solution, shows the disappearance of the imidazolium resonance at $\delta = 8.5$ ppm, while the remaining hydroxyl proton resonance is shifted from $\delta = 2.3$ ppm in **1** to $\delta = 6.5$ ppm in **2**. This suggests that it is imidazolium proton which has reacted with the base (KHMDS) rather than the hydroxyl proton. Yet such significant downfield shift for the hydroxyl proton is unusual, and is suggestive of an interaction between the hydroxyl proton and a neighboring group (the free

carbene in this case). Indeed, Movassaghi and coworkers reported similar phenomenon for the Imes-MeOH adduct[68] (Figure 2.11-b). The two imidazolylidene backbone protons are observed as two distinct doublets at 6.13 and 6.06 ppm respectively in C_6D_6 (**Figure 2.12**). The singlet signal at 3.44 ppm integrating for two protons, which corresponds to the N-CH_2 group, excludes the formation of a bicyclic adduct, since in the latter two separate signals for these diastereotopic protons would be expected.

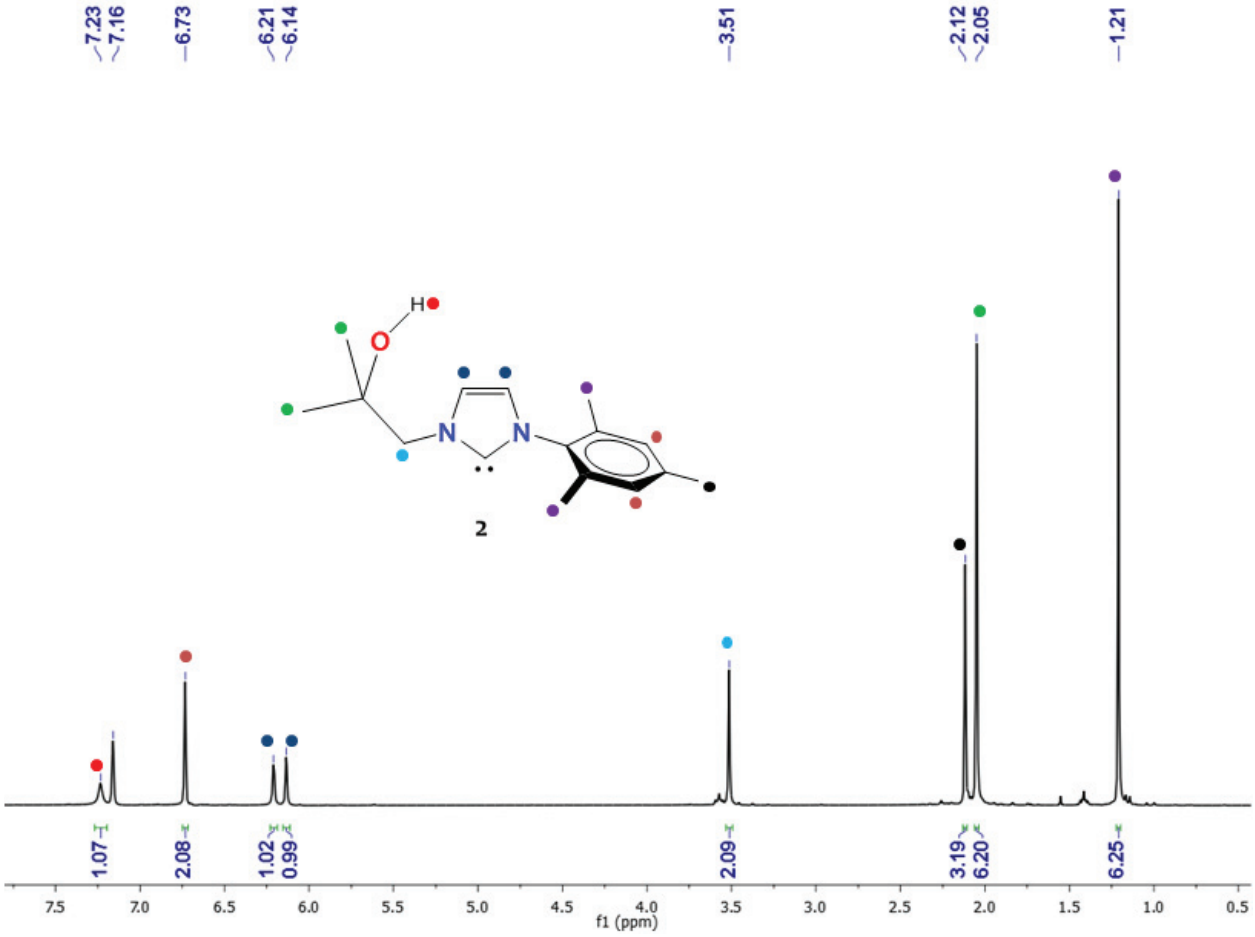

Figure 2.12: The ^{1}H NMR spectrum of the free NHC carbene **2** in C_6D_6 (293 K, 300 MHz).

This carbene-alcohol interaction is also reflected in the absence of a clear hydroxyl group stretching band in the IR spectrum of **2**. Instead a very broad and ill-defined feature centered around 2800 cm^{-1} is seen (**Figure 2.13**) which is unexpected.

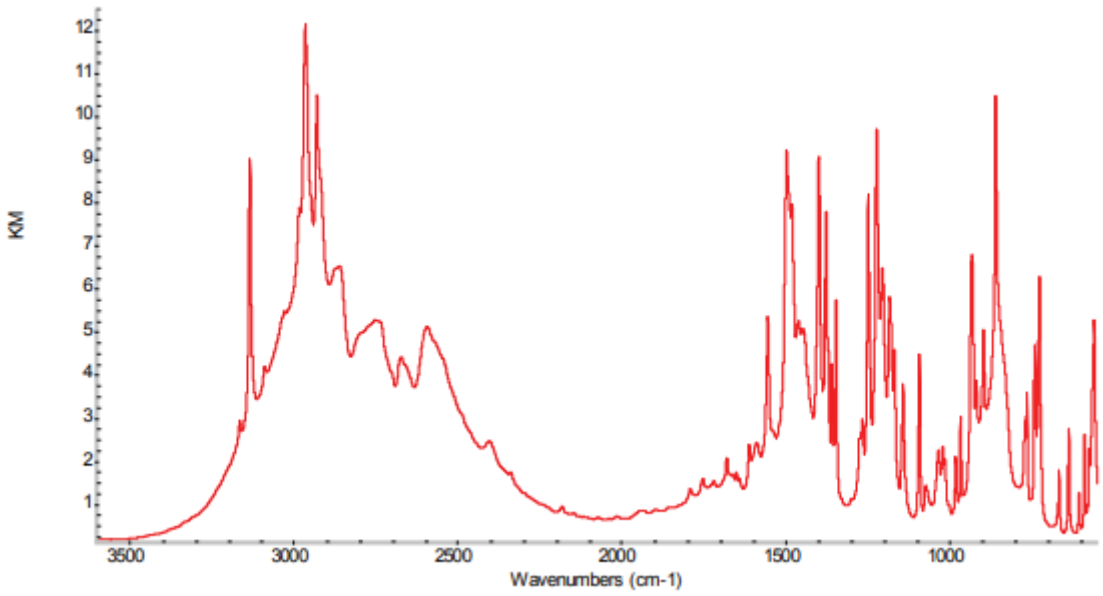

Figure 2.13: DRIFT spectrum (25°C, KBr solid dispersion under argon) for the free NHC carbene **2**.

The downfield shift of the hydroxyl proton seen in the ^{1}H NMR spectrum of **2** and the corresponding broad signal in the IR spectrum indicate that there is an unusual interaction between this hydroxyl group and a nearby available moiety, most likely the NHC. More evidence of this carbene-alcohol interaction was provided by ^{13}C NMR spectroscopy. The ^{13}C NMR spectrum of the ligand **2** does not contain any signal corresponding to the free carbene in solution. Hence the ^{13}C-labeled carbene was synthesized using the same protocol from ^{13}C-labelled formaldehyde. The solution ^{13}C NMR spectrum for the labelled compounds, **2-^{13}C**, recorded in THF-d_8 solution, shows an unusually broad peak at 202 ppm (**Figure 2.14**). Such signal broadening depicts an interaction between the NHC carbenic carbon with hydroxyl protons in solution. The upfield shift of the carbene signal (as compared to other imidazolylidenes which are in the range of 210-220 ppm) further validates the presence of an alcohol-carbene interaction.[73,74]

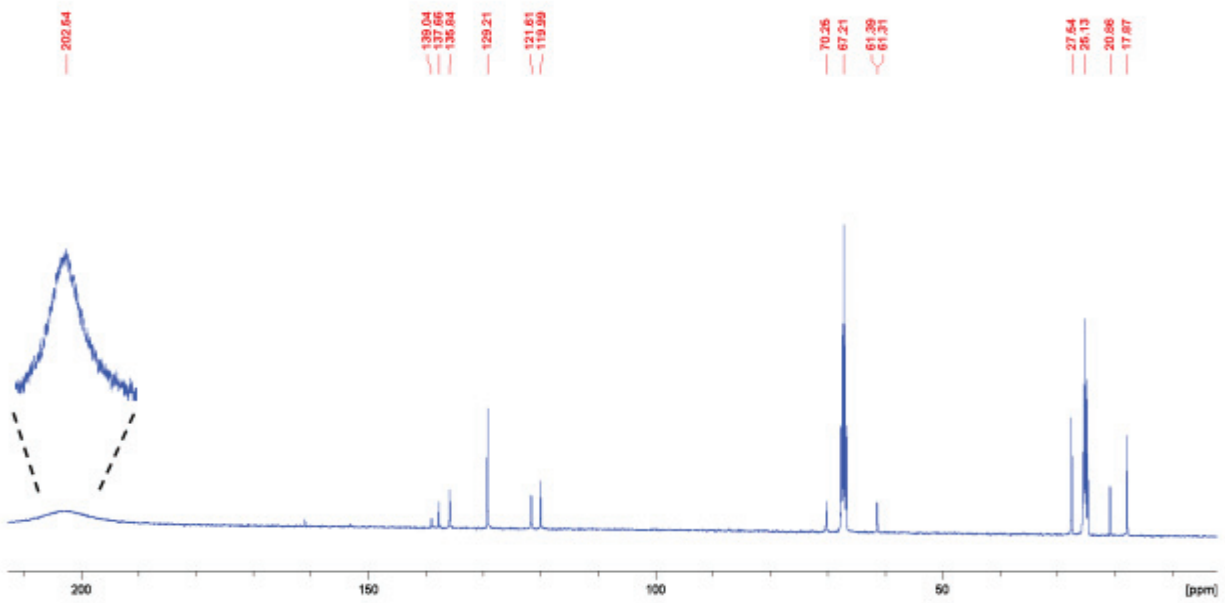

Figure 2.14: $^{13}C\{^{1}H\}$ NMR spectrum (293K, 75 MHz, THF-d_8) of the ^{13}C labelled ligand **2-^{13}C**. The insert shows the zoom on the carbene signal.

Finally, the solid-state ^{13}C CP-MAS NMR spectrum of **2** is particularly diagnostic and features a sharp resonance at δ=201.7 ppm (**Figure 2.15**), more consistent with an imidazolylidene carbon than an imidazolium. This ^{13}C carbene resonance is shifted upfield in comparison with that for free imidazol-2-ylidenes reported in the literature (typical range: 210–220 ppm) which further indicates that the carbene is engaged in electronic donation to the hydroxyl proton. The sharpening of the carbenic signal in the solid-state is likely the result of reduced fluxionality, as compared to what happen in solution.

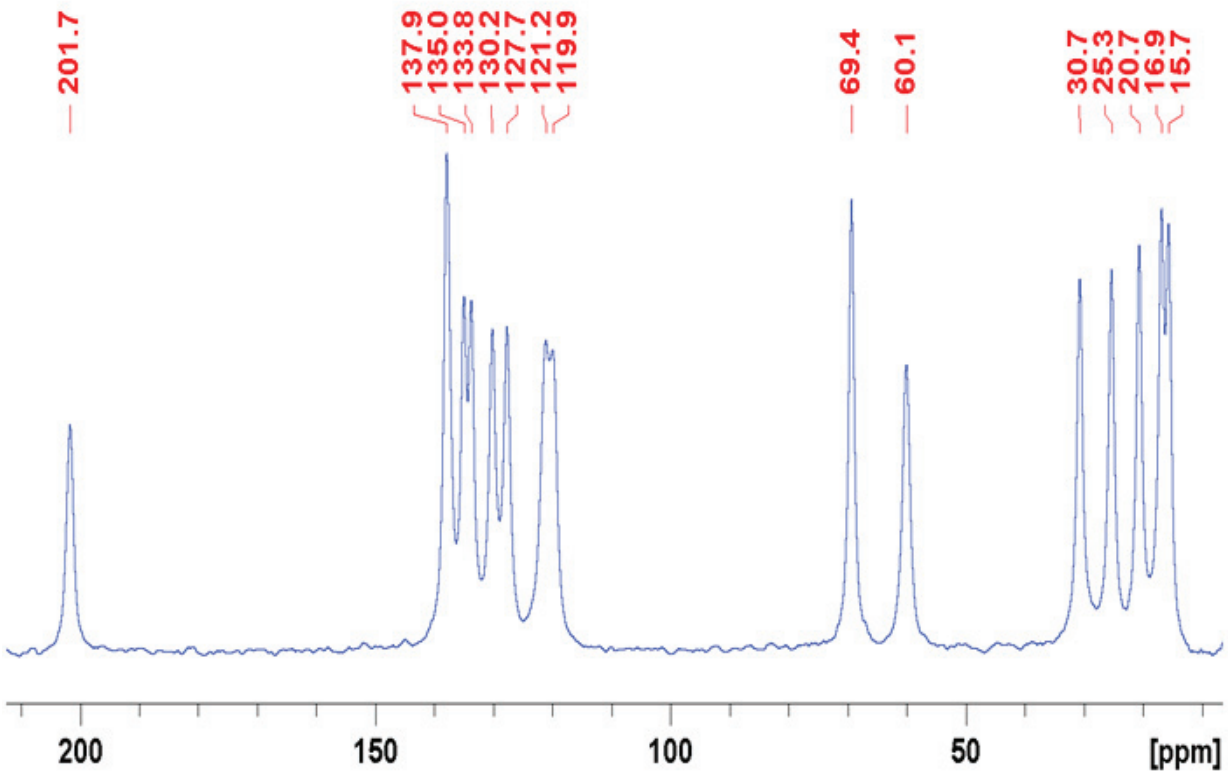

Figure 2.15: Solid-state ^{13}C CP-MAS NMR spectrum of ligand **2** (unlabeled). The carbene signal is sharp as compared what seen in the corresponding THF-d_8 solution ^{13}C NMR spectrum.

The X-ray crystal structure was recorded to obtain more insight into the structure of **2** (**Figure 2.16**). The N-C-N angle of 102.5°(1) is typical of free carbenes.[7,9,75–77] This angle is strained as compared to what classically seen for imidazoliums (typical range 107-110°),[11,69,78–81] and in particular to the corresponding angle in the imidazolium salt **1** (108.9(2)°). The N-$C_{carbene}$ bond lengths (1.360(2) Å and 1.362(2) Å) in **2** are significantly longer than the corresponding distances in **1** (1.332(3) Å and 1.326(3) Å). This again supports the finding that the imidazolium proton is deprotonated to give the free N-heterocyclic carbene with the hydroxyl group intact in the pendant arm. It is also observed that the mesityl ring is perpendicular to the plane of the imidazole ring which is expected as bulky ortho methyl groups will force the mesityl ring to twist and protrude out of the plane. In addition, the crystal structure shows that the hydroxyl hydrogen is pointing towards the carbene carbon of an adjacent molecule.

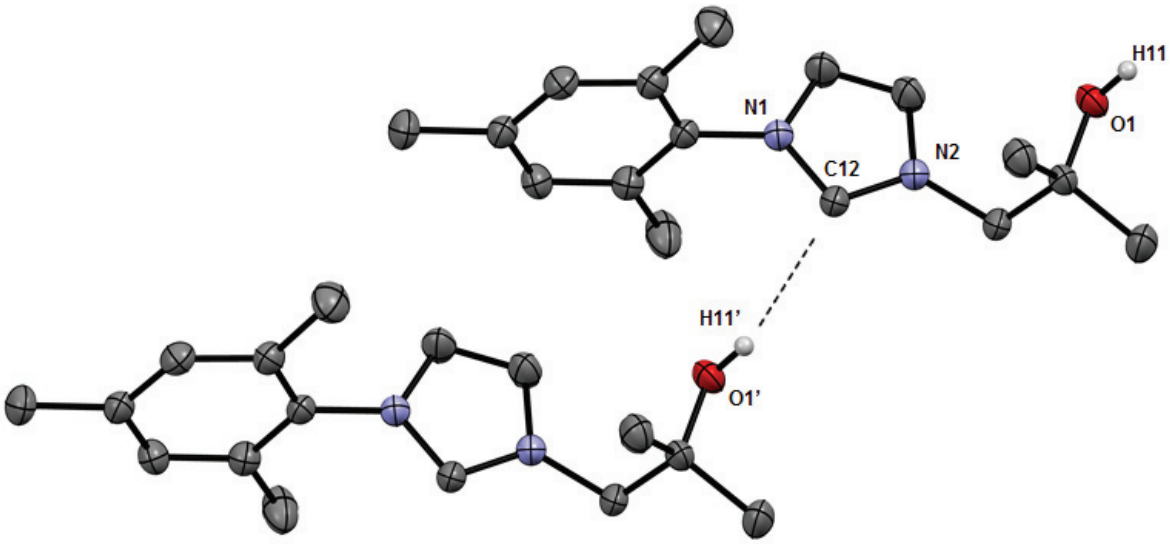

Figure 2.16: Solid-state molecular structure of **2** as determined by single crystal X-ray diffraction. Hydrogen atoms have been omitted for clarity and thermal ellipsoids are set at 50% probability level. The close distance between the hydroxyl proton and the carbene centre (1.97 Å) depicts the presence of an alcohol-carbene interaction. Selected bond distances [Å] and angles [°]: N1-C12 1.360(2), N2-C12 1.362(2), C12-O1' 2.866(2) Å, N1-C12-N2 102.5(1), O1'-H11'-C12 166(2).

The distance between the hydroxyl hydrogen and the carbene carbon (1.97(2) Å) and the O-H-C angle (166(2)°) are characteristics of hydrogen bonding.[68,73] The measured distance between the hydroxyl oxygen and the NHC carbon atom of a neighboring molecule is very short (2.866(2) Å). The solid-state structure of **2** is a rare example of a carbene-alcohol hydrogen-bonded complex engaged into intermolecular H-bonding, as represented in **Figure 2.17**.

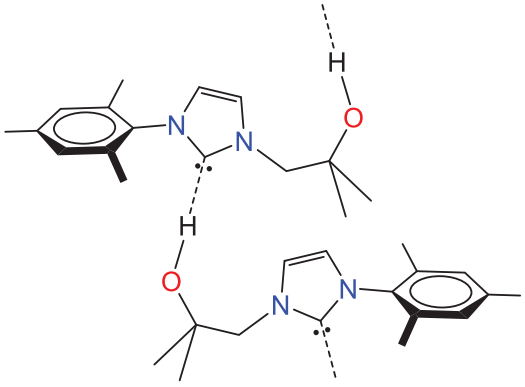

Figure 2.17: Schematic representation of the intermolecular H-bonding pattern in the solid-state structure of **2**.

Overall, the X-ray structure for **2** unambiguously confirms that i) the imidazolium proton is deprotonated (versus the hydroxyl proton) and that ii) an intermolecular hydroxyl-carbene interaction occurs in the solid-state. This reinforces the results obtained by ^{1}H, ^{13}C NMR and IR spectroscopy which are in favor of a hydroxyl-carbene formulation for **2**.

CONCLUSION

A bifunctional N-heterocyclic carbene (NHC) with an alcohol group in one of its pendant arm was synthesized as a competent bifunctional ligand to assemble early-late heterobimetallic complexes. Generally, the alkoxy-NHC ligands are synthesized by ring opening of epoxides by imidazoles at elevated temperatures. This synthetic protocol did not work in our case presumably because of lower nucleophilicity of the chosen aryl imidazole for the epoxide ring. Hence we adopted a simple, one-pot synthetic procedure to isolate a hydroxyl functionalized imidazolium salt from the condensation of 2,4,6-trimethylaniline and 1-amino-2-methyl-2-propanol with glyoxal and formaldehyde. This procedure allows the preparation of the targeted imidazolium pro-ligand in one step on a multi-gram scale. The structure of the imidazolium salt is supported by multinuclei NMR and X-Ray crystallographic studies. The deprotonation of the imidazolium salt with a base (KHMDS in this case) is selective to the imidazolium proton (versus the hydroxyl one), and results in the formation of the free carbene. However, a strong interaction between the hydroxyl moiety and the carbenic carbon is observed, as highlighted by the downfield shift of the alcoholic proton in the ^{1}H NMR studies as well as the observation of a broad ^{13}C carbene resonance at approximately 200 ppm by NMR. The existence of this interaction is further supported in the solid-state by IR spectroscopy and X-ray crystallographic studies, which established the presence of an intermolecular hydrogen bonding between the carbene and the hydroxyl group of an adjacent ligand. Note that while the activation of hydroxyl groups by NHCs is suspected to be involved in several organocatalytic processes, little is known about the exact nature of the alcohol-NHC interactions involved.[74,82–85] This study provides a well-defined and fully-characterized example of such hydroxyl-carbene hydrogen-bonding type of interaction. The isolation of the desired bifunctional hydroxyl-carbene ligand in reasonable yields is a step forward towards the realization of early and late monometallic and heterobimetallic complexes.

REFERENCES

1 L. M. Slaughter and P. T. Wolczanski, *Chem. Commun.*, 1997, **21**, 2109–2110.

2 C. M. Thomas, *Comments Inorg. Chem.*, 2011, **32**, 14–38.

3 T. Miyazaki, Y. Tanabe, M. Yuki, Y. Miyake and Y. Nishibayashi, *Organometallics*, 2011, **30**, 2394–2404.

4 P. Braunstein, X. Morise, M. Bénard, M.-M. Rohmer and R. Welter, *Chem. Commun.*, 2003, 610–611.

5 L. J. Clouston, V. Bernales, R. K. Carlson, L. Gagliardi and C. C. Lu, *Inorg. Chem.*, 2015, **54**, 9263–9270.

6 C. M. Thomas, *Comments Inorg. Chem.*, 2011, **32**, 14–38.

7 D. J. Nelson and S. P. Nolan, *Chem. Soc. Rev. Chem. Soc. Rev*, 2013, **42**, 6723–6753.

8 S. Kuwata and F. E. Hahn, *Chem. Rev.*, 2018, **118**, 9642-9677.

9 H. V. Huynh, *Chem. Rev.*, 2018, **118**, 9457–9492.

10 E. Peris, *Chem. Rev.*, 2018, **118**, 9988–10031.

11 D. Zhao, L. Candish, D. Paul and F. Glorius, *ACS Catal.*, 2016, **6**, 5978–5988.

12 A. Bartoszewicz, R. Marcos, S. Sahoo, A. K. Inge, X. Zou and B. Martin-Matute, *Chem. - A Eur. J.*, 2012, **18**, 14510–14519.

13 G. González Miera, E. Martínez-Castro and B. Martín-Matute, *Organometallics*, 2018, **37**, 636–644.

14 K. Azouzi, C. Duhayon, I. Benaissa, N. Lugan, Y. Canac, S. Bastin and V. César, *Organometallics*, 2018, **37**, 4726–4735.

15 M. V. Jiménez, J. J. Pérez-Torrente, M. I. Bartolomé, V. Gierz, F. J. Lahoz and L. A. Oro, *Organometallics*, 2008, **27**, 224–234.

16 I. Peñafiel, I. M. Pastor, M. Yus, M. A. Esteruelas and M. Oliván, *Organometallics*, 2012, **31**, 6154–6161.

17 G. Lázaro, M. Iglesias, F. J. Fernández-Alvarez, P. J. SanzMiguel, J. J. Pérez-Torrente and L. A. Oro, *ChemCatChem*, 2013, **5**, 1133–1141.

18 L. Benhamou, V. César, H. Gornitzka, N. Lugan and G. Lavigne, *Chem. Commun.*, 2009, 4720.

19 A. Raja Naziruddin, A. Hepp, T. Pape and F. Ekkehardt Hahn, *Organometallics*, 2011, **30**, 50.

20 Y. Canac, C. Lepetit, M. Abdalilah, C. Duhayon and R. Chauvin, *J. Am. Chem. Soc.*, 2008, **130**, 8406–8413.

21 C.-Y. Wang, Y.-H. Liu, S.-M. Peng and S.-T. Liu, *J. Organomet. Chem.*, 2006, **691**, 4012–4020.

22 G. Dyson, J.-C. Frison, A. C. Whitwood and R. E. Douthwaite, *Dalt. Trans.*, 2009, **0**, 7141.

23 A. T. Normand and K. J. Cavell, *Eur. J. Inorg. Chem.*, 2008, 2781–2800.

24 J. C. C. C. and and I. J. B. Lin, *Organometallics,* 2000, **19**, 5113-5121.

25 K. Riener, M. J. Bitzer, A. Pöthig, A. Raba, M. Cokoja, W. A. Herrmann and F. E. Kühn, *Inorg. Chem.*, 2014, **53**, 12767–12777.

26 V. Leigh, W. Ghattas, H. Mueller-Bunz and M. Albrecht, *J. Organomet. Chem.*, 2014, **771**, 33–39.

27 A. Mariconda, F. Grisi, C. Costabile, S. Falcone, V. Bertolasi and P. Longo, *New J. Chem.*, 2014, **38**, 762–769.

28 G. Song, Y. Su, R. A. Periana, R. H. Crabtree, K. Han, H. Zhang and X. Li, *Angew. Chemie Int. Ed.*, 2010, **49**, 912–917.

29 D. L. J. Broere, D. K. Modder, E. Blokker, M. A. Siegler and J. I. van der Vlugt, *Angew. Chemie Int. Ed.*, 2016, **55**, 2406–2410.

30 S. Semwal and J. Choudhury, *Angew. Chemie Int. Ed.*, 2017, **56**, 5556–5560.

31 J. B. Geri and N. K. Szymczak, *J. Am. Chem. Soc.*, 2015, **137**, 12808–12814.

32 S. Kuwata and T. Ikariya, *Chem. Commun.*, 2014, **50**, 14290–14300.

33 B. Maji and J. Choudhury, *Chem. Commun.*, 2019, **55**, 4574–4577.

34 N. Vujkovic, V. César, N. Lugan and G. Lavigne, *Chem. - A Eur. J.*, 2011, **17**, 13151–13155.

35 Z. Han, J. I. Bates, D. Strehl, B. O. Patrick and D. P. Gates, *Inorg. Chem.*, 2016, **55**, 5071–5078.

36 A. J. Arduengo, D. Tapu and W. J. Marshall, *Angew. Chemie Int. Ed.*, 2005, **44**, 7240–7244.

37 D. Mendoza-Espinosa, B. Donnadieu and G. Bertrand, *Chem. - An Asian J.*, 2011, **6**, 1099–1103.

38 E. Peris, *Chem. Rev.*, 2018, 118, 9988–10031.

39 D. M. Khramov, E. L. Rosen, V. M. Lynch and C. W. Bielawski, *Angew. Chemie Int. Ed.*, 2008, **47**, 2267–2270.

40 T. Roth, V. Vasilenko, C. G. M. Benson, H. Wadepohl, D. S. Wright and L. H. Gade, *Chem. Sci.*, 2015, **6**, 2506–2510.

41 B. Hildebrandt, W. Frank and C. Ganter, *Organometallics*, 2011, **30**, 3483–3486.

42 B. Hildebrandt, S. Raub, W. Frank and C. Ganter, *Chem. - A Eur. J.*, 2012, **18**, 6670–6678.

43 J.-F. Lefebvre, M. Lo, J.-P. Gisselbrecht, O. Coulembier, S. Clément and S. Richeter, *Chem. - A Eur. J.*, 2013, **19**, 15652–15660.

44 K. Arumugam, J. Chang, V. M. Lynch and C. W. Bielawski, *Organometallics*, 2013, **32**, 4334–4341.

45 P. K. Majhi, S. C. Serin, G. Schnakenburg, D. P. Gates and R. Streubel, *Eur. J. Inorg. Chem.*, 2014, **2014**, 4975–4983.

46 J. Ruiz, L. García, M. Vivanco, Á. Berros and J. F. Van der Maelen, *Angew. Chemie*, 2015, **127**, 4286–4290.

47 J. Ruiz and A. F. Mesa, *Chem. - A Eur. J.*, 2012, **18**, 4485–4488.

48 T. Okayama, T. Watanabe, Y. Hatayama, S. Ishihara and Y. Yamaguchi, *Inorganica Chim. Acta*, 2016, **448**, 1–6.

49 D. A. Valyaev, M. A. Uvarova, A. A. Grineva, V. César, S. N. Nefedov and N. Lugan, *Dalt. Trans.*, 2016, **45**, 11953–11957.

50 M. A. Huertos, J. Pérez, L. Riera, J. Díaz and R. López, *Chem. - A Eur. J.*, 2010, **16**, 8495–8507.

51 P. L. Arnold, Z. R. Turner, A. I. Germeroth, I. J. Casely, R. Bellabarba and R. P. Tooze, *Dalt. Trans.*, 2010, **39**, 6808.

52 Z. R. Turner, R. Bellabarba, R. P. Tooze and P. L. Arnold, *J. Am. Chem. Soc.*, 2010, **132**, 4050–4051.

53 M. Baltrun, F. A. Watt, R. Schoch, C. Wölper, A. G. Neuba and S. Hohloch, *Dalt. Trans.*, 2019, **48,** 14611-14625.

54 C. Romain, K. Miqueu, J.-M. Sotiropoulos, S. Bellemin-Laponnaz and S. Dagorne, *Angew. Chemie Int. Ed.*, 2010, **49**, 2198–2201.

55 C. Lienert, W. Frey and M. R. Buchmeiser, *Macromolecules*, 2017, **50**, 5701–5710.

56 A. W. W. and and R. H. Grubbs, Organometallics, 2004, **23**, 3105-3107.

57 P. Buchwalter, J. Rosé and P. Braunstein, *Chem. Rev.*, 2015, **115**, 28–126.

58 R. Nakano and K. Nozaki, *J. Am. Chem. Soc.*, 2015, **137**, 10934–10937.

59 Y. Kong, Y. Tang, Z. Wang, S. Xu, H. Song and B. Wang, *Macromol. Chem. Phys.*, 2013, **214**, 492–498.

60 P. L. Arnold, I. J. Casely, Z. R. Turner and C. D. Carmichael, *Chem. - A Eur. J.*, 2008, **14**, 10415–10422.

61 P. L. Arnold, A. J. Blake and C. Wilson, *Chem. - A Eur. J.*, 2005, **11**, 6095–6099.

62 P. L. Arnold. and and S. T. Liddle, *Organometallics*, 2006, **25**, 1485-1491.

63 R. Torregrosa, I. M. Pastor and M. Yus, *Tetrahedron*, 2007, **63**, 469–473.

64 P. L. Arnold, A. C. Scarisbrick, A. J. Blake and C. Wilson, *Chem. Commun.*, 2001, 2340–2341.

65 T. Watanabe, T. Matsuo and H. Kawaguchi, *Angew. Chem., Int. Ed*, 2000, **37**, 6580.

66 C. Jahier-Diallo, M. S. T. Morin, P. Queval, M. Rouen, I. Artur, P. Querard, L. Toupet, C. Crévisy, O. Baslé and M. Mauduit, *Chem. - A Eur. J.*, 2015, **21**, 993–997.

67 J. A. Cowan, J. A. C. Clyburne, M. G. Davidson, R. L. W. Harris, J. A. K. Howard, P. Küpper, M. A. Leech and S. P. Richards, *Angew. Chemie Int. Ed.*, 2002, **41**, 1432–1434.

68 M. Movassaghi and M. A. Schmidt, *Org. Lett.*, 2005, **7**, 2453–2456.

69 P. L. Arnold, I. J. Casely, Z. R. Turner and C. D. Carmichael, *Chem. - A Eur. J.*, 2008, **14**, 10415–10422.

70 Szilárd Csihony, Darcy A. Culkin, Alan C. Sentman, Andrew P. Dove, Robert M. Waymouth and James L. Hedrick, *J. Am. Chem. Soc.*, 2005, **127**, 9079-9084.

71 P. Arnold, I. Casely, S. Zlatogorsky and C. Wilson, *Helv. Chim. Acta*, 2009, **92**, 2291–2303.

72 T. M. Trnka, J. P. Morgan, M. S. Sanford, T. E. Wilhelm, M. Scholl, T. L. Choi, S. Ding, M. W. Day and R. H. Grubbs, *J. Am. Chem. Soc.*, 2003, **125**, 2546–2558.

73 J. A. Cowan, J. A. C. Clyburne, M. G. Davidson, R. L. W. Harris, J. A. K. Howard, P. Küpper, M. A. Leech and S. P. Richards, *Angew. Chemie - Int. Ed.*, 2002, **41**, 1432–1434.

74 M. Movassaghi and and M. A. Schmidt, *Org. Lett.*, 2005, **7**, 2453-2456.

75 A. J. Arduengo, J. R. Goerlich and W. J. Marshall, *Angew. Chem., Int. Ed. Engl*, 1995, **117**, 2518.

76 A. J. Arduengo, H. V. R. Dias, R. L. Harlow and M. Kline, *J. Am. Chem. Soc.*, 1992, **114**, 5530–5534.

77 M. N. Hopkinson, C. Richter, M. Schedler and F. Glorius, *Nature*, 2014, **510**, 485-496.

78 A. B. Chaplin, *Organometallics*, 2014, **33**, 3069-3077.

79 S. H. Wiedemann, J. C. Lewis, J. A. Ellman and R. G. Bergman, *J. Am. Chem. Soc.*, 2006, **128**, 2452–2462.

80 D. Mendoza-Espinosa, B. Donnadieu and G. Bertrand, *J. Am. Chem. Soc.*, 2010, **132**, 7264–7265.

81 D. Mendoza-Espinosa, A. Alvarez-Hernández, D. Angeles-Beltrán, G. E. Negrón-Silva, O. R. Suárez-Castillo and J. M. Vásquez-Pérez, *Inorg. Chem.*, 2017, **56**, 2092-2099.

82 E. M. Phillips, M. Riedrich and K. A. Scheidt, *J. Am. Chem. Soc.*, 2010, **132**, 13179–13181.

83 T. Kato, S. Matsuoka and M. Suzuki, *Chem. Commun.*, 2016, **52**, 8569–8572.

84 S. Marrot, F. Bonnette, T. Kato, L. Saint-Jalmes, E. Fleury and A. Baceiredo, *J. Organomet. Chem.*, 2008, **693**, 1729–1732.

85 S. Naumann and M. R. Buchmeiser, *Catal. Sci. Technol.*, 2014, **4**, 2466–2479.

EXPERIMENTAL SECTION

All the manipulations were performed under purified argon atmosphere unless mentioned otherwise. Either schlenk line technique or an MBraun glovebox was used to provide the inert argon atmosphere. All the glassware, cannulae, silica filters, glass syringes and needles were dried overnight (15 hr) at 110°C in the oven and assembled while hot under vacuum to perform the reaction. Pentane, toluene, tetrahydrofuran (THF) and diethyl ether were collected from Solvent purification system (SPS). Here all these solvents were already pre-dried by a passage through the activated alumina column. Then the solvents were dried over Na/benzophenone until the color changes to dark purple. Following which they were distilled under vacuum and then degassed to yield ready-to-use dry solvents. Dichloromethane (DCM) was dried over CaH_2 and vacuum distilled and degassed. Deuterated solvents like THF-d_8, C_6D_6, toluene-d_8 were dried over Na/benzophenone, vacuum distilled and degassed before using. $CDCl_3$ and CD_2Cl_2 were dried over CaH_2, vacuum distilled and then degassed prior to using them for NMR spectrum acquisition. All other reagents used were commercially available and they were used as received. Bruker AV-300, AVQ-400 and AV-500 spectrometers were used to record the NMR. All the chemical shifts were measured relative to the corresponding residual peak of the deuterated solvents; which in turn were assigned relative to an external TMS standard set at 0.00 ppm. ^{19}F and ^{31}P chemical shifts were assigned relative to the external standard $BF_3.OEt_2$ and Ph_3PO respectively. ^{1}H, ^{13}C, COSY, HSQC and HMBC NMR spectrum were thoroughly analyzed to assign the ^{1}H and ^{13}C peaks. IR spectrum was recorded using a Nicolet 6700 FT-IR spectrometer. Samples for recording IR spectrum were prepared in a DRIFT cell equipped with KBr dome under argon atmosphere. Samples were either send to the school of Human sciences, Science centre, London Metropolitan University or to Mikroanalytisches Labor Pascher, Germany for elemental analysis. X-Ray diffraction was performed at Centre de Diffractometrie Henri Longchambon-ISA, Université de Lyon. All the details regarding X-Ray diffraction are provided in the supporting information.

Synthesis of $[H_2L][PF_6]$ (1):

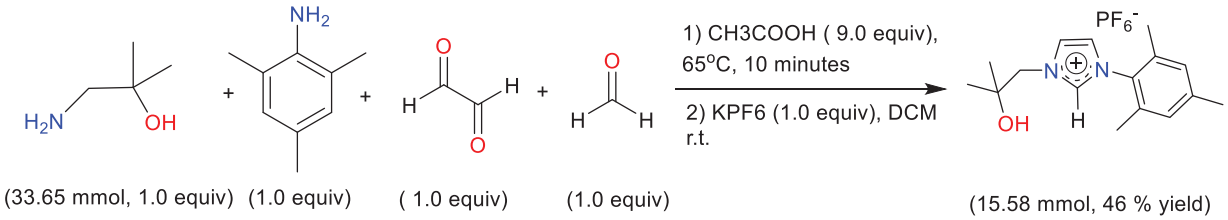

(33.65 mmol, 1.0 equiv) (1.0 equiv) (1.0 equiv) (1.0 equiv) (15.58 mmol, 46 % yield)

In a 100 mL round bottom flask (**I**) 1-amino-2-methylpropanol (0.813 g, 9.12 mmol, 1.0 equiv) was weighed and 1,3,5-trimethylaniline (1.23 g, 1.0 equiv) was added to it followed by addition of acetic acid (2.3 ml, 4.5 equiv). Instantaneously a brown reaction mixture is formed. The brownish reaction mixture was heated to 60°C for five minutes. In another 50 mL round bottom flask (**II**) 37 weight % solution of formaldehyde in water (0.72 ml, 1.0 equiv) was weighed and 40 weight % solution of glyoxaldehyde in water (1.05 ml, 1.0 equiv) was added to it. Then 4.5 equiv (2.3 ml) of acetic acid was added to the flask (**II**) and it was heated to 60°C also for 5 minutes. Then the contents of flask (**II**) were transferred to flask (**I**). This resulted in the formation of yellow solid which changes to brown and dissolves again. The resultant mixture was heated for 10 minutes. The solution was then cooled down to room temperature and 40 mL each of diethyl ether and distilled water was added to it. The aqueous layer was then extracted thrice with 40 mL of diethyl ether (3×40 mL) each time. Freshly prepared brine solution (50 mL) was added to the aqueous layer and extracted again thrice with 40 mL of diethyl ether (3×40 mL). The aqueous layer was then transferred to 500 mL round bottom flask and potassium hexafluorophosphate (1.66 g, 1.0 equiv) was added to it followed by addition of 110 mL of dichloromethane. The reaction mixture was vigorously stirred for 1 hr at room temperature. After that DCM layer was separated from the aqueous phase using a separating funnel and dried over Magnesium Sulphate. The resultant brownish solution was filtered and evaporated to yield brown solid. Following which the product mixture was purified by column chromatography (60M silica gel, eluent: DCM/Acetone = 9/1) to yield **1** as light brown solid (1.38 g, 3.43 mmol, 37.71 %). Single crystals suitable for X-ray diffraction were grown by slow evaporation of a CH_2Cl_2 solution of **1**.

TLC (silica gel, CH_2Cl_2/acetone = 9:1): R_f = 0.34; m.p. 168.2(5)°C;

^{1}H NMR (293 K, 300 MHz, CD_2Cl_2): δ = 8.53 (s, 1H; CH_{imid}), 7.64 (s, 1H; CH_{imid}), 7.25 (s, 1H; CH_{imid}), 7.08 (s, 2H; m-CH_{mes}), 4.29 (s, 2H; NCH_2), 2.37 (s, 3H; p-$CH_{3,mes}$), 2.32 (s, 1H; OH), 2.05 (s, 6H; o-$CH_{3,mes}$), 1.28 ppm (s, 6H; $C(CH_3)_2$);

$^{13}C\{^1H\}$ NMR (293 K, 75.4 MHz, CD_2Cl_2): δ = 142.05 (C_{Ar}), 137.20 (N-C_{imid}-N), 134.70 (C_{Ar}), 130.89 (C_{Ar}), 130.18 (C_{Ar}), 125.25 (C_{imid}), 123.35 (C_{imid}), 69.78 (OC), 60.22 (NCH_2), 26.61 (o-$CH_{3,mes}$), 21.23 (p-$CH_{3,mes}$), 17.32 ppm ($OC(CH_3)_2$);

$^{19}F\{^1H\}$ NMR (293 K, 282.2 MHz, CD_2Cl_2): δ = 72.05 ppm (d, $^2J_{P-F}$ = 711 Hz);

$^{31}P\{^1H\}$ NMR (293 K, 121.4 MHz, CD_2Cl_2): δ = 144.38 ppm (sept., $^2J_{F-P}$ = 711 Hz);

DRIFT (25 °C, solid on diamond): $\tilde{\nu}$ = 3585.4 (m, ν_{O-H}), 3149.3 (w, ν_{Ar-H}), 2973.6 (w, ν_{C-H}), 1562.9 (w), 1548.5 (w), 1453.7 (w), 1377.2 (w), 1202.5 (m), 1149.3 (m), 830.7 (s, ν_{P-F}), 768.9 (m), 758.2 (m), 671.4 (m), 638.6 (m), 578.8 (m), 555.8 cm^{-1} (s); MS (ESI): m/z: 259.2 $[M]^+$.

Note: ^{13}C labelled imidazolium salt was synthesized using the labelled formaldehyde solution and following the procedure as described above.

Synthesis of N-heterocyclic carbene [HL]:

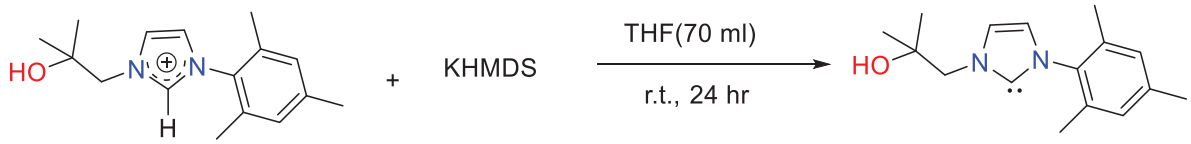

(2.0 g, 49.5 mmol, 1.0 equiv) (0.99 g, 1.0 equiv) (863 mg, 67 %)

A 250 mL Schlenk and a magnetic bar were assembled while hot and three cycles of vacuum Argon were given. Precursor **1** (2.0 g, 49.5 mmol, 1.0 equiv) was then transferred into the schlenk and dissolved in approximately 80 ml of THF. After that KHMDS (0.99 g, 49.5 mmol, 1.0 equiv) was added into another schlenk, dissolved in 50 mL of THF and then transferred to the first Schlenk. The reaction mixture was stirred at room temperature for 19 hr which resulted in precipitation of KPF_6. The solution phase was cannula filtered into another Schlenk to remove KPF_6. The supernatant was evaporated under vacuum till dryness to give orange solid. It was dissolved again in approximately 30 ml of THF followed by cannula filtration into another Schlenk and kept at -20°C for recrystallization. This yielded orange crystals which were collected and dried to yield 1 (0.863 g, 67%) as shiny orange crystalline powder. Single crystal suitable for crystal structure was grown in similar fashion.

^1H NMR (300 MHz, C_6D_6, 293 K): δ =7.13 (s, 1H; CH_{imid}), 6.74 (s, 2H; m-CH_{Mes}), 6.15 (s, 1H; CHimid), 6.12 (s, 1H; OH), 3.48 (s, 2H; NCH_2), 2.12 (s, 3H; p-$CH_{3,Mes}$), 2.06 (s, 6H; o-$CH_{3,Mes}$), 1.21 ppm (s, 6H; CH_3); ^1H NMR (300 MHz, THF-d_8, 293 K): δ =6.98 (s, 1H; CH_{imid}), 6.93 (s, 2H; m-CH_{Mes}), 6.78 (s, 1H; CH_{imid}), 6.38 (s, 1H; OH), 3.88 (s, 2H; NCH_2), 2.29 (s, 3H; p-$CH_{3,Mes}$), 2.01 (s, 6H; o-$CH_{3,Mes}$), 1.13 ppm (s, 6H; CH_3);

$^{13}C\{^1H\}$ NMR (101 MHz,THF-d_8, 293 K): δ =139.0 (C_{Ar}), 137.7 (C_{Ar}), 135.8 (C_{Ar}), 129.2 (CH_{Ar}), 121.6 (C_{imid}), 120.0 (C_{imid}), 70.2 (*C*(Me_2)OH), 61.4 (NCH_2), 27.5 (CH_3), 20.9 (CH_3), 17.9 ppm (CH_3); the ^{13}C carbene resonance could not be located in the unlabeled compound in solution;

^{13}C MAS NMR (75 MHz, 293 K): δ =201.7 (NCN), 137.9 (C_{Ar}), 135.0 (C_{Ar}), 133.7 (C_{Ar}), 130.2 (C_{Ar}), 127.7 (C_{Ar}), 121.2 (C_{imid}), 119.9 (C_{imid}), 69.4 (*C*(Me_2)OH), 60.1 (NCH_2), 30.7 (CH_3), 25.3 (CH_3), 20.7 (CH_3), 16.9 (CH_3), 15.7 ppm (CH_3);

DRIFT (25°C, KBr solid solution under argon): $\tilde{\nu}$ =3134.9 (s, $\nu_{C\text{-}Himid}$), 2967.82 (s, $\nu_{C\text{-}H}$), 2929.9 (s, $\nu_{C\text{-}H}$), 2861.1 (s, $\nu_{C\text{-}H}$), 2751.1 (m, br), 2594.9 (m, br), 1554.5 (m), 1497.2 (s), 1398.4 (s), 1376.4 (s), 1358.9 (m), 1346.4 (m), 1266.1 (m), 1247.7 (s), 1222.2 (s), 1203.9 (s), 1182.8 (m), 1167.7 (m), 1141.9 (m), 1092.4 (m), 965.2 (m), 930.9 (s), 917.9 (m), 895.7 (m), 858.8 (s),763.9 (m), 740.3 (m), 725.2 (s), 558.6 cm^{-1} (s);

Elemental analysis calculated (%) for $C_{16}H_{22}N_2O$: C 74.38, H 8.58, N 10.84; found: C 74.24, H 8.71, N 10.85.

Further data (^1H, ^{13}C NMR, IR, X-ray crystallographic details) are reported in appendix 1.

Chapter 3

Synthesis and Characterisation of metal-NHC complexes

3.1) INTRODUCTION

3.1.1) Examples of early-late tantalum-rhodium heterobimetallic complexes and the synthetic protocols involved therein

Bergman *and coworkers* reported seminal work on heterobimetallic complexes of tantalum combined with group 9 metals (rhodium and iridium).[1,2] These bimetallic complexes contain bridging methylene groups between both the metal centers. The metal centers are also held together by direct metal-metal single bond. The synthesis of the tantalum-rhodium heterobimetallic complex is performed under inert atmosphere in a ***base promoted reaction*** between the tantalum and rhodium precursors (**Scheme 3.1**).[3] The mechanism of the synthetic process cannot be ascertained since the isolation and characterization of the intermediates has not been achieved.

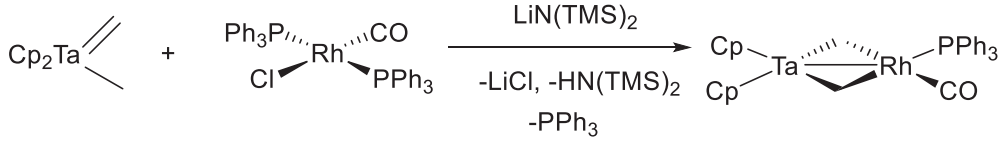

Scheme 3.1. Bergman and coworkers reported pioneering work on Ta-Rh heterobimetallic complexes.

The crystal structure of the complex cannot be obtained either. However, they have synthesized the similar iridium analogues $[Cp_2Ta(\mu\text{-}CH_2)_2Ir(CO)PPh_3$ and $[Cp_2Ta(\mu\text{-}CH_2)_2Ir(CO)_2PPh_3$.[4] The crystal structure of the iridium analogue $[Cp_2Ta(\mu\text{-}CH_2)_2Ir(CO)_2PPh_3$ shows that the four membered metallacycle is planar with M-CH_2-M bond angles between 80-83° and the Ta-Ir bond distance is observed at 2.881 Å. The Ta-CH_2 bond distance in the bimetallic complex (2.126 and 2.156 Å) is in between the Ta-CH_2 (2.039 Å) and Ta-CH_3 (2.268 Å) bond distances observed in the $Cp_2Ta(CH_2)CH_3$ precursor. The bridging CH_2 signals are observed at δ = 5.53 and 4.51 ppm respectively by ^{1}H NMR. The ^{13}C NMR spectrum of the complex shows the bridging methylene signals at 98.83 and 98.11 ppm respectively. The spectroscopic properties of the tantalum-rhodium bimetallic complex $[Cp_2Ta(\mu\text{-}CH_2)_2Rh(CO)PPh_3$ are similar to that of tantalum-iridium analogue $[Cp_2Ta(\mu\text{-}CH_2)_2Ir(CO)PPh_3]$. The bimetallic complexes are catalytically active in alkene hydrogenation reaction and H/D exchange reaction. The turnover rate for alkene hydrogenation is reported to be faster with the tantalum-rhodium heterobimetallic complex $[Cp_2Ta(\mu\text{-}CH_2)_2Rh(CO)L]$ (L = CO, PPh_3) than with the corresponding iridium analogue. For example, ethylene hydrogenation is 8 times faster with Ta-Rh (5 mol% catalyst loading) catalyst when compared

with Ta-Ir complex.[3] Later Ess *et al* carried-out Density Functional Theory (DFT) calculations on the Ta-Ir complex and proposed that the mechanistic route for the hydrogenation of alkenes with the bimetallic complex involved different elementary steps with lower activation barrier as compared to the steps involved with the monometallic iridium complex.[5] This highlights the ability of the bimetallic systems to promote original reaction pathways. The mechanism of alkene hydrogenation has been discussed in chapter 1 **[See scheme 1.2]**

Later, Findlay *et al* reported the synthesis of a Ta-Rh heterobimetallic complex bridged through two phosphido ligands (**Scheme 3.2**), utilizing a similar strategy as discussed in the previous example.[6] The bimetallic complex is synthesized by in-situ reaction between the tantalum precursor $Cp_2Ta(PHEt_2)(PEt_2)$ with 0.5 equivalent of $[Rh(\mu\text{-}Cl)(C_2H_4)_2]_2$ in THF.

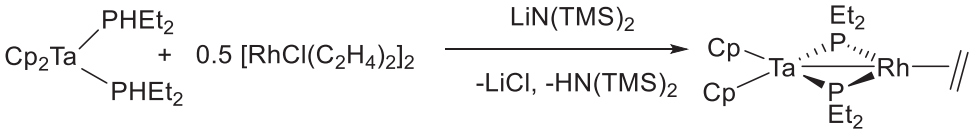

Scheme 3.2. Findlay *et al* reported the synthesis of a Ta-Rh heterobimetallic complex bridged by phosphido ligands.

The ^1H NMR spectrum of the complex shows a doublet ($^2J_{Rh-H}$ = 1.7 Hz) at 3.16 ppm corresponding to the coordinated alkene. The Cp protons are observed as a singlet at 4.37 ppm. The crystal structure of the complex (dTa-Rh: 2.858 Å) depicts that the tantalum center adopts a bent structure, which is expected for a bi-substituted metallocene whereas the rhodium center is in a tricoordinated ligand environment.

Fryzuk *et al* employed a ***salt metathesis reaction*** to synthesize the tantalum-rhodium complex $Cp_2Ta(\mu\text{-}H)_2Rh(dippp)$ [dipp = 1,3-bis(diisopropylphosphino)-propane] by reacting the tantalum dihydride complex $[Cp_2TaH_2]^-K$ with [Rh{Cl(dipp)}], as shown in **Scheme 3.3**. The crystal structure of the complex depicted the square planar arrangement around the rhodium center.

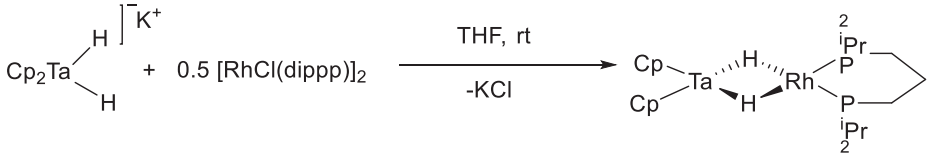

Scheme 3.3. Fryzuk *et al* synthesized the hydride bridged Ta-Rh bimetallic complex which was catalytically active in H/D exchange reaction.

The metallacycle is planar with a short Ta-Rh bond distance of 2.723 Å, which is smaller than the sum of covalent radii of tantalum and rhodium atoms (2.12 Å), thus indicating direct interaction between both the metals. The bimetallic catalyst undergoes H/D exchange reaction readily with D_2 in contrast with the monometallic tantalum complex which is inactive for this transformation.[7] Please note that the reactivity of the monometallic Rh analogue is not reported by the authors.

Arnold *et al* synthesized tantalum-rhodium bimetallic complex supported by an anionic triazacyclononane ligand. The complex is synthesized through ***salt metathesis reaction*** where the ligand exchange took place from Li to Rh.[8] (**Scheme 3.4**) They prepared the lithium precursor by the alkylation of ($^{i}Pr_2$-tacn)Ta(=NAr)-Cl_2 {Ar = 2,6-$^{i}Pr_2C_6H_3$, tacn= anionic traiazacyclononae ligand} with Me_3SiCH_2Li. The transmetallation of Li to Rh promoted a hapticity change of the chelate ligand which lead to the Ta-Rh bimetallic complex.

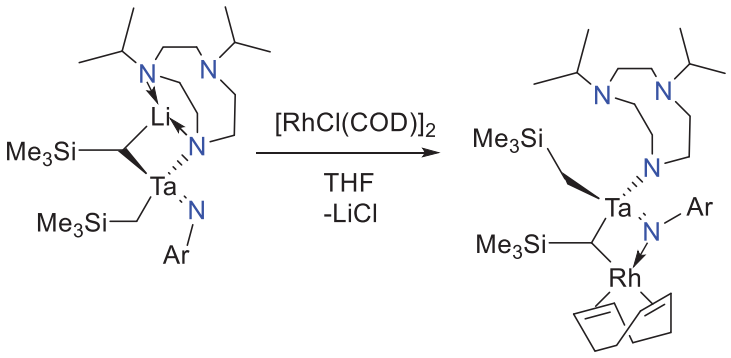

Scheme 3.4. Arnold *and co-workers* reported a salt metathesis reaction to prepare a Ta-Rh heterobimetallic complex.

The ^{1}H NMR spectrum of the complex shows the shift of the alkylidene proton from δ = 4.2 ppm in the Ta-Li precursor to δ = 5.5 ppm in the Ta-Rh product. A significant shift in ^{13}C NMR signal of the alkylidene carbon from δ = 57.4 ppm in the Ta reactant to δ = 93.5 ppm in the Ta/Rh product is observed, as a result of Rh ligation to the alkylidene.

Han *et al* reported the synthesis of a Ta-Rh heterometallic complex assembled together by a tripodal amido-phosphine ligand.[9] The ***bifunctional ligand*** $P(CH_2NHAr_3)$ chelates with the early transition metal center through the three amido donor atoms. The conformational restriction of the metalloligand framework renders the phosphine ligand free to interact with the late transition metal rhodium center, as shown in **Scheme 3.5**.

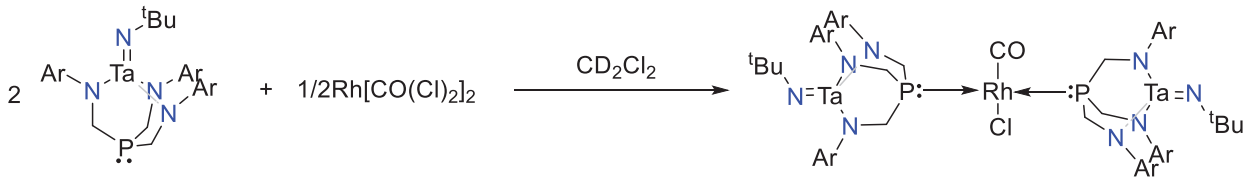

Scheme 3.5. Han *et al* employed the tripodal amido-phosphine ligand to synthesize the trimetallic Ta_2Rh complex**.**

Finally, Mashima and coworkers reported a tantalacyclopentadiene compound which could interact with a rhodium moiety in a η^4-fashion **(Scheme 3.6**). The interaction of the ligand brings both the metal centers close to each other.

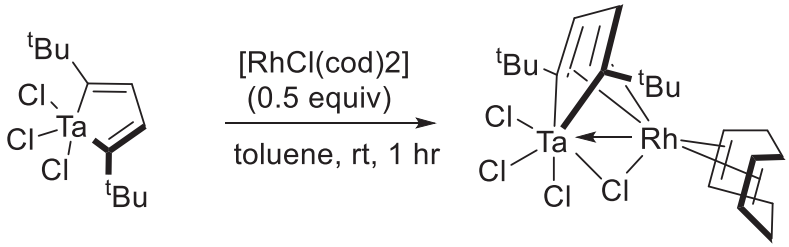

Scheme 3.6. Reported by Mashima *et al* in 2016, the scheme represents a unique way of synthesizing a tantalum-rhodium heterobimetallic complex where a conjugated diene interacts with a tantalum as well as a rhodium center.[10]

As we can see from the above examples, different ligand frameworks have been utilized to assemble tantalum-rhodium heterobimetallic complexes. However, to the best of our knowledge bifunctional N-heterocyclic carbenes have not been used to assemble tantalum-rhodium species. Herein we report the synthesis of tantalum-rhodium heterobimetallic complexes held together by a bifunctional NHC ligand. In the process, three different routes will be explored to synthesize the bimetallic complex. Two chemically different tantalum precursors will be studied to establish the proof of synthetic concept. Monometallic tantalum-NHC and rhodium-NHC complexes will be synthesized and characterized first. Cationic and neutral chelate Rh-NHC complexes will be synthesized as well and their chemical and catalytic properties will be explored.

3.2 RESULTS AND DISCUSSION

3.2.1) Synthesis and characterization of monometallic tantalum-NHC complexes

3.2.1.1) Synthesis of tantalum-alkylidene NHC complex:

The tantalum-NHC complex **3** is prepared by addition of 1.0 equivalent of the N-heterocyclic carbene **2** onto equimolar amount of the tantalum *tris*-neopentyl neopentylidene complex (**Scheme 3.7**). One equivalent of 2,2-dimethylpropane (C_5H_{12}, neopentane) is released during the reaction. The amount of neopentane released during the reaction is calculated by ^{1}H NMR monitoring of the reaction using 1,2,4,5-tetramethylbenzene (durene) as internal standard. Complex **3** is isolated by recrystallizing a concentrated pentane solution of the complex at -40°C which yields yellow crystals of the complex.

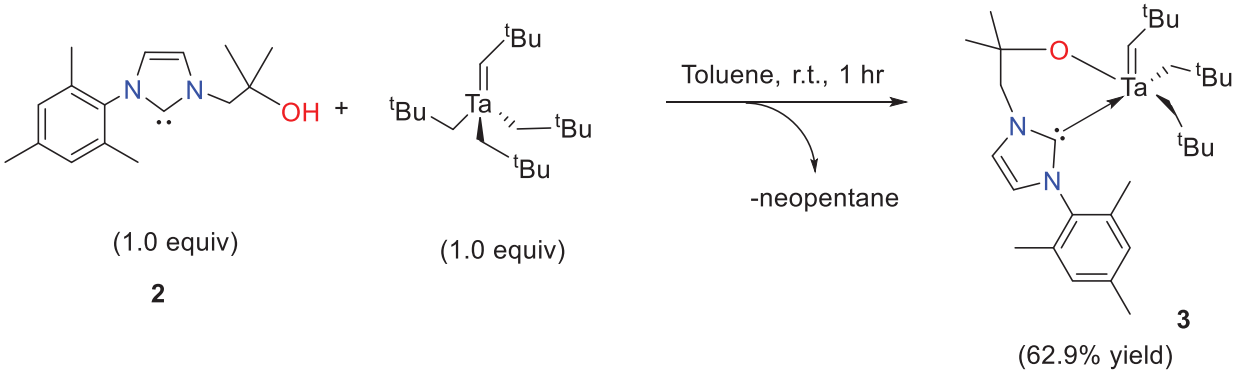

Scheme 3.7: Synthesis of the tantalum-NHC complex **3**.

The ^{13}C NMR spectrum of the complex (Figure S2) shows the NHC carbenic carbon signal at δ = 203.1 ppm which is upfield as compared to the free carbenes.[11–16] This suggests an interaction between the carbene and the tantalum metal centre in solution. The alkylidene carbon signal is observed downfield at δ = 250.1 ppm which is characteristic for tantalum (V) alkylidenes.[17–22] The proton NMR spectrum (Figure S1) in C_6D_6 contains a resonance at δ = 4.85 ppm corresponding to the alkylidene proton which is significantly downfield as compared to the corresponding alkylidene proton in the precursor Ta(CH^{t}Bu)(CH$_2$^{t}Bu)$_3$.[17] The comparatively larger $^1J_{C\text{alkylidene},H\alpha}$ (94 Hz) in **3** against the precursor (90 Hz) suggests the presence of a weak agostic α Ta···CH interaction. The presence of two doublets ($^2J_{HH}$ = 12.2 Hz) at δ = 1.05 and 0.76 ppm respectively in the ^{1}H NMR spectrum is attributed to the two non-equivalent Ta-CH$_2$ moieties. Further details regarding the structure of complex **3** are provided by X-ray crystallographic studies. Single crystals suitable for recording crystallographic data are grown

from a saturated pentane solution of the complex at -40°C. The complex contains a chelate NHC ring and adopts a pseudo-square pyramidal structure. The two neopentyl groups and the chelate NHC ring form the base of the pyramid while the neopentylidene group occupies the axial position. (**Figure 3.1**) The crystal structure shows that there is an interaction between the carbene and the tantalum metal centre in the solid-state. The Ta1-C6 bond distance (2.355 Å) is long and falls in the upper range of Ta-C_{NHC} bond distances reported so far.[23–26] The weak Ta-carbene bond implies that it could be transmetallated to a metal with a higher affinity for the $NHC_{carbene}$.

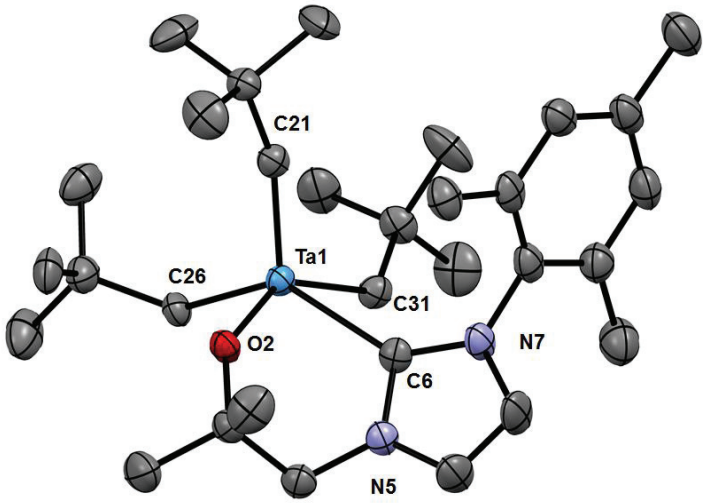

Figure 3.1: Molecular structure of **1** as determined by X-ray diffraction. Hydrogen atoms have been omitted for clarity and thermal ellipsoids are set at 50% probability level. Selected bond lengths (Å) and angles (°) are: Ta1-O2 1.907(3), Ta1-C21 1.921(5), Ta1-C26 2.218(4), Ta1-C31 2.253(5), Ta1-C6 2.355(5), N5-C6 1.365(6), N7-C6 1.364(6), O2-Ta1-C6 76.74(15), N5-C6-N7 102.6(4), Ta1-C21-C22 156.8(4).

The alkoxy-NHC ligand is bound in a chelate fashion to the tantalum centre. The ligand C_{NHC}-Ta-O bite angle is 76.74° which relates closely with the existing bite angles for early transition metal NHC complexes.[27,28] Ta1=C21 bond distance is considerably shorter and falls in the range of previously reported Ta (d°) alkylidene complexes.[29,30] The large Ta1=C21-C22 angle (156.8°) validates the presence of a α-Ta····C-H agostic interaction.[29,31] The two carbenes in complex **3** are arranged *cis* to each other, as in the well-known Grubbs catalysts.[32–34] The Ta-O (1.907(3) Å) and Ta-$C_{neopentyl}$ bond lengths are as expected, with the Ta-$C_{neopentyl}$ bond distance located trans to the alkoxy ligand (2.253(5) Å) being slightly elongated compared with that located trans to the NHC ligand (2.218(4) Å).

3.2.1.2) Decomposition of the complex 3 at room temperature

Complex **3** is stable in solid state at -40°C for months but decomposes within hours at room temperature to yield complex **4**. (**Scheme 3.8**) It was observed that heating a solution of the complex **3** in toluene at 80°C leads to the decomposition of the complex within minutes. The change in color from yellow to dark red is accompanied by release of 1.0 equivalent of neopentane. Compound **4** was recrystallized from a concentrated pentane solution of the complex at -40°C to yield reddish brown crystals of **4**.

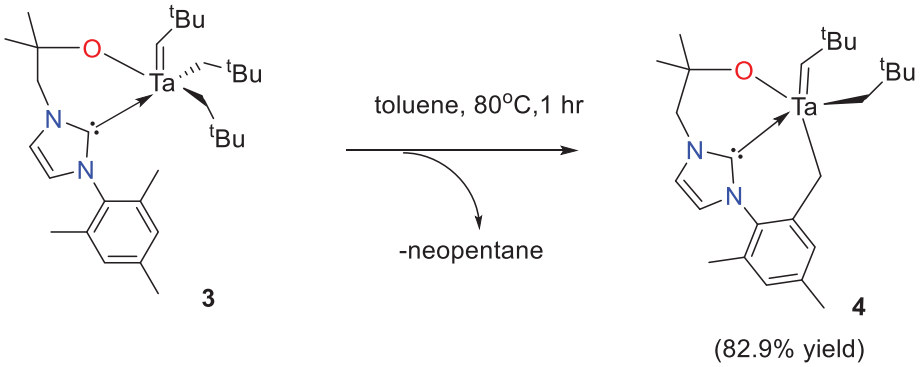

Scheme 3.8: Thermal decomposition of complex **3** due to C-H activation of the ortho-methyl group of the mesityl ring by the tantalum centre with simultaneous release of 1.0 equivalent of neopentane.

The asymmetric nature of the complex **4** is reflected in the solution proton NMR spectrum of the complex (Figure 3.3). The proton NMR spectrum of the complex in C_6D_6 contains two distinct doublets at δ = 2.4 and 2.5 ppm ($^2J_{HH}$ = 13.7 Hz) respectively which integrate to one proton each. These diastereotopic proton signals correspond to the Ta-*CH*$_2$-Ar methylenic moieties of complex **2** which reflect the orthometallation of the mesityl methyl group with the tantalum center. The asymmetric nature of the complex is also depicted by the observation of two different singlets for the *meta* protons of the mesityl ring at δ = 7.07 and 6.48 ppm respectively. In contrast the *meta* protons in the precursor **3** are observed as a singlet at δ = 6.75 ppm integrating to two protons in C_6D_6 (**Figure 3.2**). The ligand backbone N-CH_2 protons are also observed as two separate doublets at δ = 3.29 and 3.03 ppm respectively. Thus the NMR spectrum supports the formation of an orthometallated asymmetric complex as evident by the crystal structure (see below). The ^{13}C NMR spectrum of complex **4** displays two signals at δ = 252.3 ppm and 205.2 ppm depicting that the carbene and the alkylidene groups are essentially intact which concurs with the proposed structure of the compound (Figure S4).

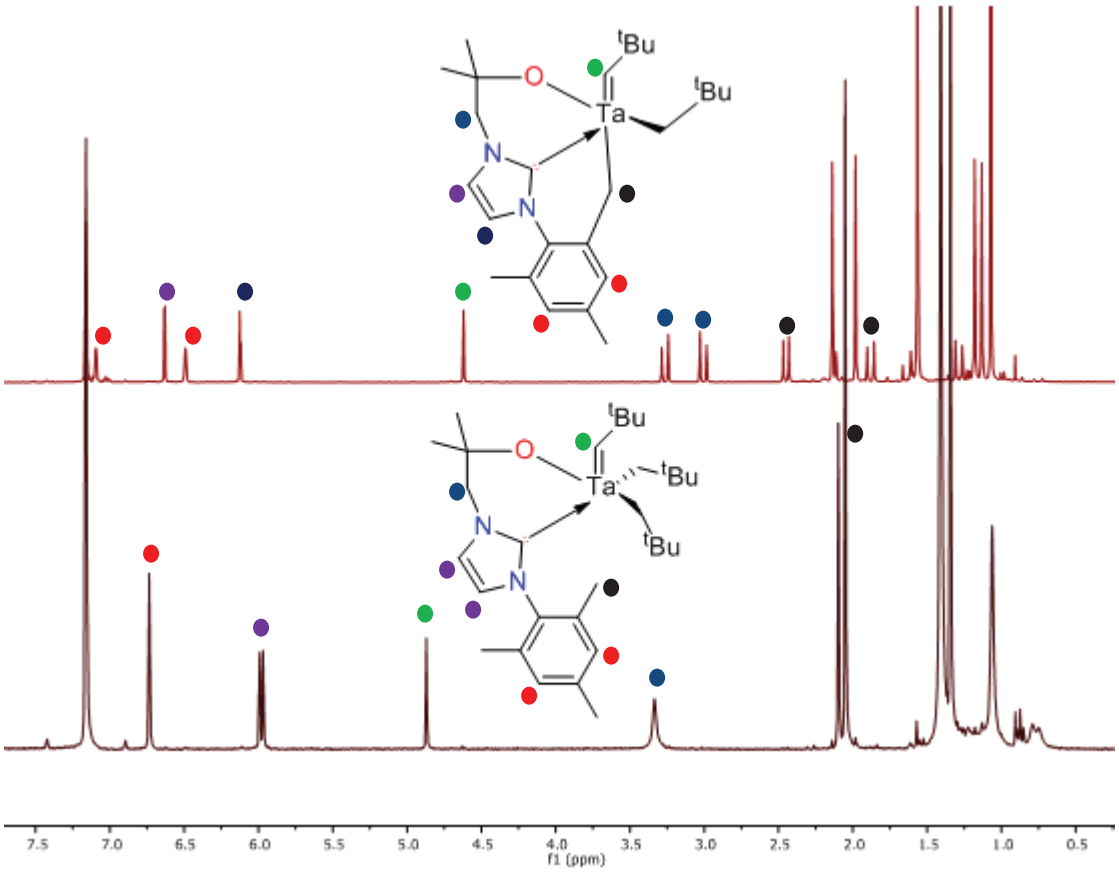

Figure 3.2: Comparison of the ^{1}H NMR spectra of complex **3** *vs* complex **4** in C_6D_6 solution. Upon cyclometallation, a more complicated ^{1}H NMR pattern is obtained for **4** which is exemplified by the appearance of distinct doublets for the tantalum-methylene moieties.

Single crystals of complex **4** suitable for X-Ray crystallography are grown from a saturated pentane solution of the complex **4** at -40°C. The complex adopts a pseudo square pyramidal geometry as shown below. (**Figure 3.3**)

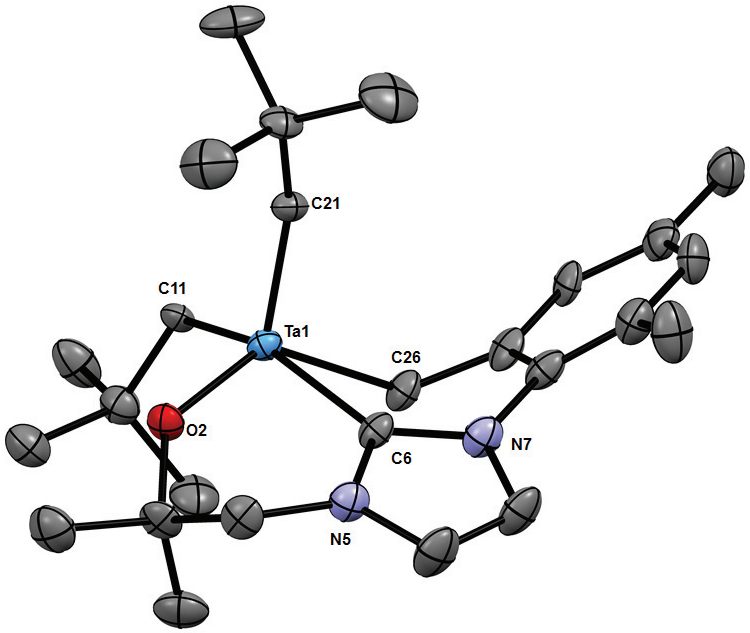

Figure 3.3: Molecular structure of **4** as determined by X-ray diffraction. Hydrogen atoms have been omitted for clarity and thermal ellipsoids are set at 50% probability level. Selected bond lengths (Å) and angles (°) are: Ta1-C11 2.236(6), Ta1-C21 1.921(8), Ta1-C26 2.237(6), Ta1-C6 2.260(6), Ta1-O2 1.893(5), N5-C6-N7 103.1(6), C6-Ta1-C26 155.4(3), O2-Ta1-C7 80.8(2).

The base of the square pyramid is occupied by the pincer NHC ligand and the neopentyl groups. The axial position is occupied by the alkylidene group. The crystal structure unambiguously shows the ortho-metallation of the methyl group (C26) of the mesityl ring. The shorter tantalum carbene bond length (2.260(6) Å) in **4** as compared to that **3** (2.235(5) Å) suggests the formation of stable pincer complex (of the type CCO pincer) at the tantalum centre. The alkylidene moiety is characterized by the large Ta1-C21-C22 angle of 153.1(5)° and the short Ta1=C21 bond (1.921(8) Å). This bond length is significantly shorter than that of the other Ta-C alkyl bonds length (2.236(6) Å) and compares well with that of previously reported Ta(V) alkylidene complexes.[17,35,36] The large Ta1=C21-C22 angle (153.8°) is characteristics of an α-Ta····C-H agostic interaction.

Intramolecular C-H bond activation of alkyl and aryl ligand substituents has been reported for a number of transition metal NHC complexes.[37–40] Orthometallated products have also been reported for early transition metal complexes with diverse ligands.[41,42] In particular, tantalum complexes are known to promote intramolecular C-H activation process leading to cyclometallated complexes which is similar to what observed here.[26,43–45]

In order to get more insights on this phenomenon, we monitored the conversion of complex **3** into **4** by ^{1}H NMR spectroscopy. The amount of each species in the reaction mixture is

quantified with regard to durene, used as internal standard. A NMR tube containing a C_6D_6 solution of complex **3** and durene is heated at 45°C and the amount of each species is monitored with time, as shown on **Figure 3.4**. The amount of complex **3** decreases with the progress of reaction and simultaneous increase in amount of complex **4** and neopentane is observed. The plot of $\ln[3]_t/[3]_0$ shows that the kinetics of the reaction is of 1st order. (See Figure S5)

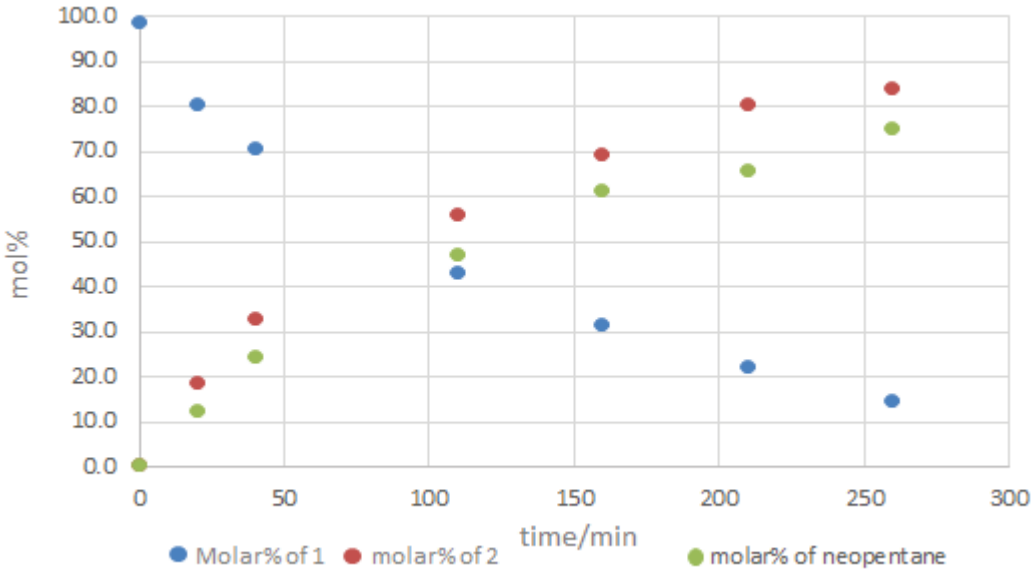

Figure 3.4: The decomposition of complex **3** into **4** is monitored by ^{1}H NMR spectroscopy. The relative amount of each species along with neopentane is plotted here as a function of time.

Two pathways, in agreement with this kinetic study, can be proposed for the decomposition of complex **3** into **4**: route 1) through σ bond metathesis between the mesityl methyl C-H group and the neopentyl group and route b) which involve 1,2-addition of the methyl C-H bond to the tantalum alkylidene group to form a tantalum peralkyl intermediate (rate determining step) followed by rapid α-H abstraction by the neopentyl group to restore the alkylidene moiety.[46] (**Scheme 3.9**)

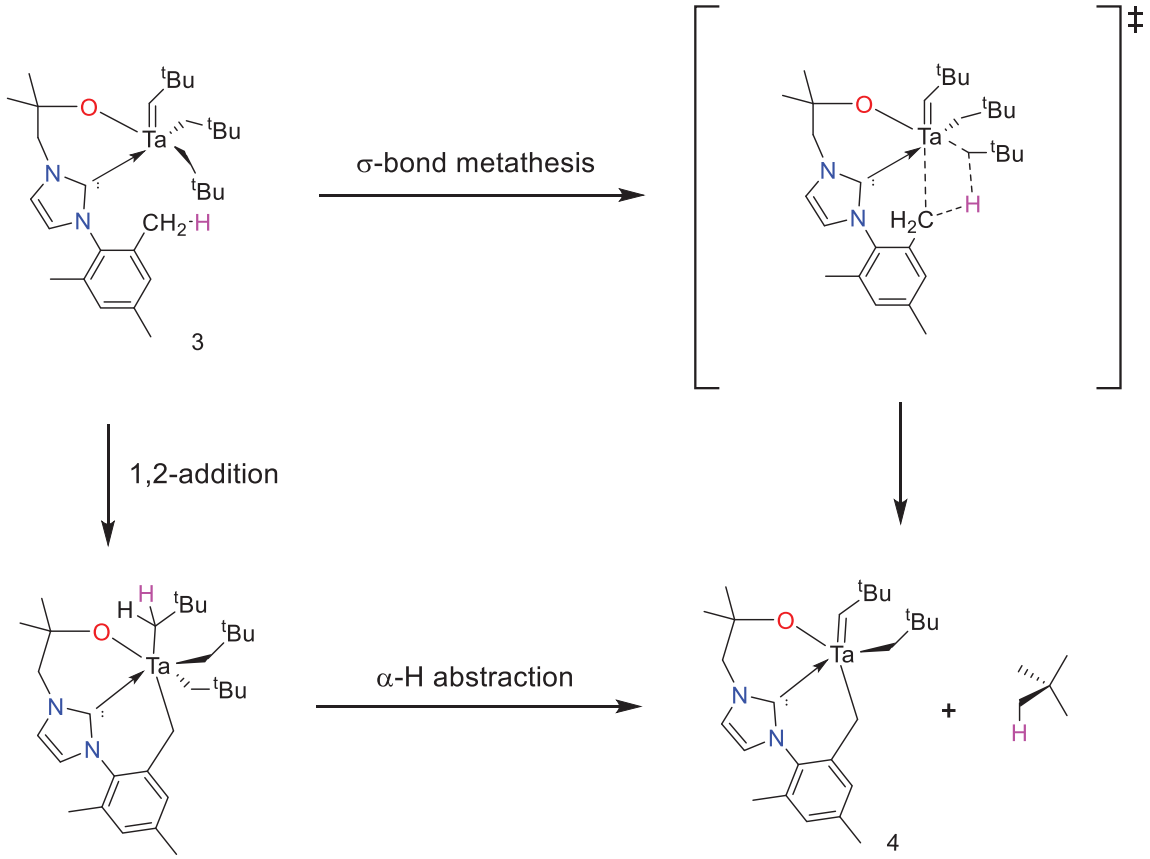

Scheme 3.9: The decomposition of complex **3** into **4** could take place through the following two pathways: a) σ bond metathesis and b) addition-elimination reaction.

3.2.1.3) Synthesis of tantalum imido alkylidene NHC complex:

The tantalum *tris*(neopentyl) *tert*-butylamido complex Ta(N^{t}Bu)(CH$_2$^{t}Bu)$_3$ [47] is treated with 1 equivalent of the bifunctional NHC ligand **2** at room temperature to yield Ta(N^{t}Bu)(L)(CH$_2$^{t}Bu)$_2$ **5** (**Scheme 3.10**). One equivalent of neopentane is released during this protonolysis reaction. The ^{13}C NMR spectrum of complex **5** in C_6D_6 (Figure S7) shows the characteristic carbene resonance at δ = 196.7 ppm. The deshielded value of the carbene signal in **5** as compared to values reported for free carbenes[12,16,48] suggest an electronic interaction between the metal and the carbine moiety in solution. The metal-carbene interaction is also supported by the crystal structure of the complex in the solid-state.

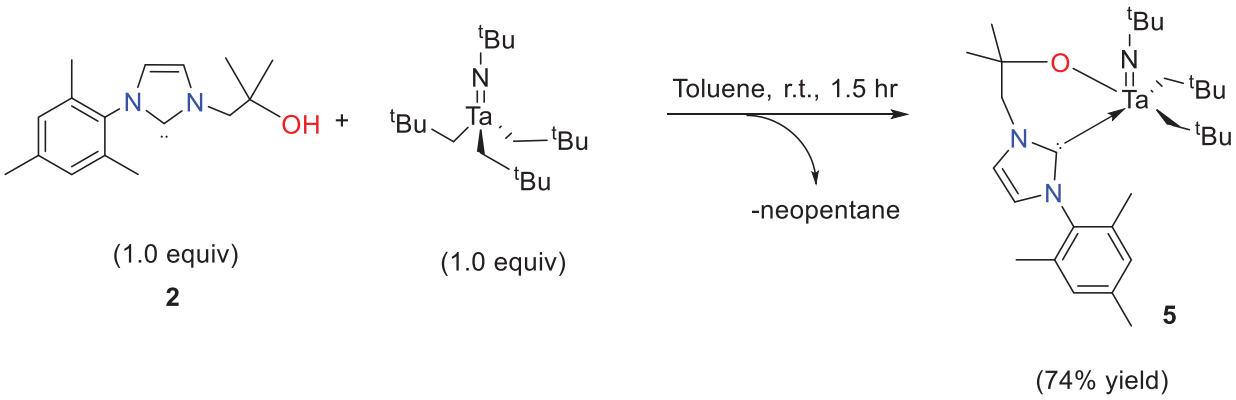

(1.0 equiv)
2

(1.0 equiv)

(74% yield)

Scheme 3.10: Synthesis of the imido alkoxy-NHC tantalum complex **5**.

The ^{1}H NMR spectrum of **5** in C_6D_6 solution (Figure S6) is in agreement with the proposed structure, and shows notably two doublets ($^2J_{HH}$ = 13.7 Hz) at upfield shifts of δ = 0.94 and 0.80 ppm corresponding to the tantalum methylene moieties. More details into the structure of the complex is provided by the X-ray crystal structure of **5**. Single crystals suitable for recording X-ray crystallographic data are grown by cooling a saturated pentane solution of complex **5** at -40^{0}C. Complex **5** adopts pseudo-square pyramidal geometry at the tantalum center. (**Figure 3.5**) The chelate NHC ligand and the two neopentyl groups occupy the base of the square pyramid whereas the axial position is occupied by the imido functional group. The chelate NHC bite angle C_{NHC}-Ta-O is 75.69(16)^0 which compares well with those reported for early transition metal chelate NHC complexes.[27,49] The Ta-C_{NHC} bond distance is 2.447(5) Å which is the longest tantalum NHC bond distance reported till date, an analysis of literature shows that the Ta-C_{NHC} bond distances typically lie between 2.22-2.41 Å.[25,26,50,51] This suggests that the Ta-NHC association might be loose and labile, and could eventually be displaced by another metal center featuring higher affinity for the NHC moiety.

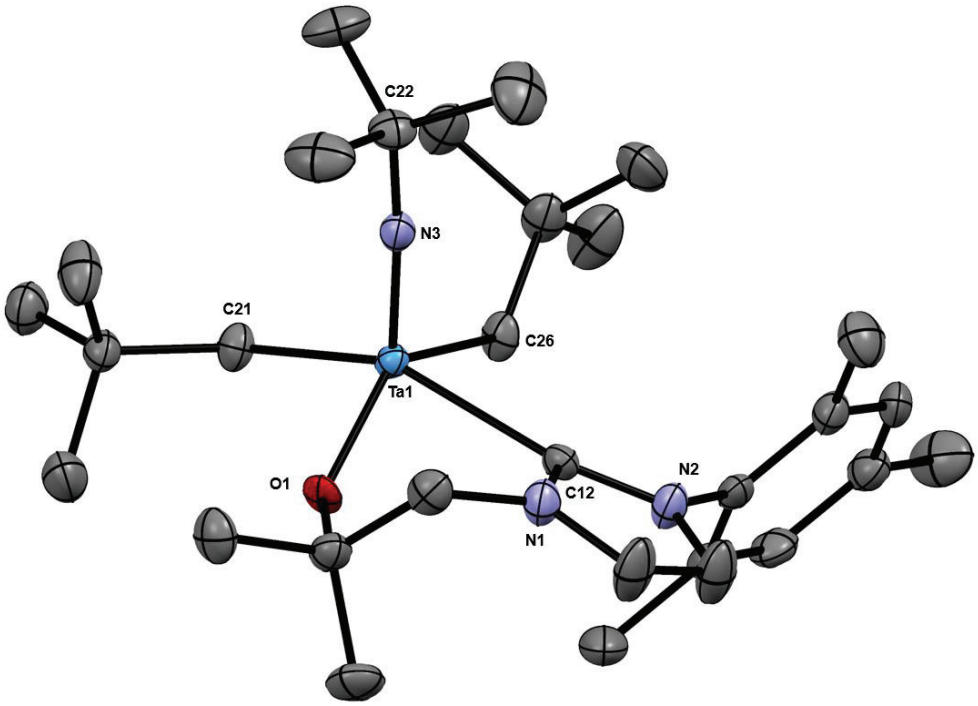

Figure 3.5: Molecular structure of **5** as determined by X-ray diffraction. Hydrogen atoms have been omitted for clarity and thermal ellipsoids are set at 50% probability level. Selected bond lengths (Å) and angles (°) are: Ta1-N3 1.753(5); Ta1-O1 1.953(3); Ta1-C12 2.447(5); Ta1-C21 2.213(6); Ta1-C26 2.232(5); N1-C12 1.356(7); N2-C12 1.367(6); O1-Ta1-C12 75.69(16); N1-C12-N2 103.5(5).

The metrical parameters for the Ta=N^{t}Bu moiety (Ta-N3-C22 angle = 173.5(4)°; Ta=N3 bond length = 1.753(5) Å) are typical of tantalum imido motifs reported in the literature. The Ta-O (1.953(3) Å) and Ta-$C_{neopentyl}$ (Ta-C21 = 2.213 Å and Ta-C26 = 2.232 Å) bond lengths are as expected.[45,52]

3.2.2) Synthesis and characterization of monometallic rhodium-NHC complexes

A THF solution of the bifunctional NHC ligand **2** was stirred at room temperature with the rhodium precursor $[Rh(COD)Cl)]_2$ for 24 hours to yield complex **6** (**Scheme 3.11**). Complex **6** is recrystallized by slow diffusion of pentane into a concentrated THF solution of the complex to yield shiny orange crystals.

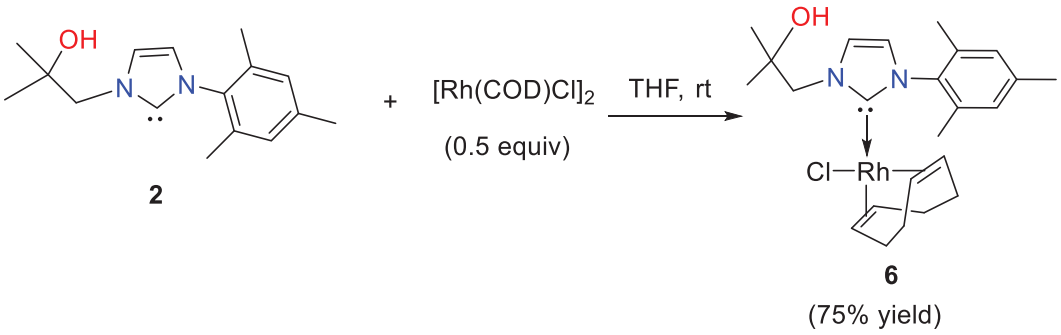

Scheme 3.11: Complex **6** is synthesized by simply adding a THF solution of the ligand to the rhodium precursor.

The ^{1}H NMR spectrum of the complex **6** (Figure S8), recorded in $CDCl_3$ solution, displays the expected cyclooctadiene (COD) sp^2 protons signals at δ = 4.87 and 4.83 ppm respectively integrating to two protons each. The imidazole backbone protons are observed as two distinct doublets ($^{2}J_{HH}$ = 1.6 Hz) at δ = 7.35 and 6.75 ppm respectively. The hydroxyl proton of the ligand is observed at δ = 3.5 ppm. The presence of the hydroxyl group is also supported by the stretching frequency signal at 3368 cm^{-1} in the IR spectrum of the complex. (Figure S27)

The ^{13}C NMR spectrum of complex **6** (Figure S9) displays a signal at δ = 181.9 ppm which supports the rhodium metallation of the carbene. The fine structure of this signal (doublet, $^{2}J_{Rh\text{-}C}$ = 52 Hz) further supports the coordination of Rh to the carbonic carbon from the ligand in solution.[53–55] The olefinic carbon atoms of the cyclooctadiene ligand feature two doublet resonances at δ = 97.1 ppm ($^{1}J_{Rh\text{-}C}$ = 7 Hz), which correspond to the olefinic carbon atoms situated *trans* to the carbene moiety, and at δ = 68.3 ppm ($^{1}J_{Rh\text{-}C}$ = 14 Hz), which has been attributed to those situated *cis* to the NHC ligand.[56–58] To gain more insight into the structure of the complex; single crystals were grown by slow diffusion of pentane into a concentrated THF solution of the complex at -40°C. Complex **6** adopts a pseudo-square planar geometry which is typical of 16 valence electrons complexes. (**Figure 3.6**)

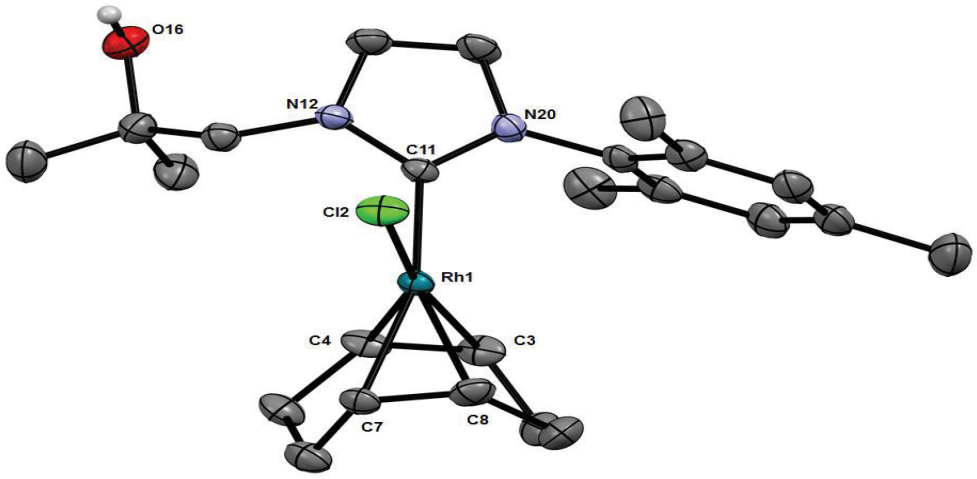

Figure 3.6: Molecular structure of **6** as determined by X-ray diffraction. Hydrogen atoms have been omitted for clarity and thermal ellipsoids are set at 50% probability level. Selected bond lengths (Å) and angles (°) are: Rh1-C11 2.042(4), Rh1-C3 2.105(4), Rh1-C4 2.088(4), Rh1-C7 2.209(4), Rh1-C8 2.185(4), Rh1-Cl2 2.3846(1), N12-C11 1.354(5), N20-C11 1.358(5), and N12-C11-N20 104.4(4).

The NHC ring is oriented nearly perpendicular to the pseudo D_{4h} plane (dihedral angle 70.2(2)°), and the Rh-C_{NHC} bond distance (2.042(4) Å) is in the range of reported values for related Rh-NHC complexes.[59–62] The Rh-C_{COD} bond distances in *trans* position with respect to the NHC ligand (2.209(4) and 2.185(4) Å) are slightly elongated compared with those *trans* to the chloride (2.105(4) and 2.088(4) Å), which is in agreement with the strong sigma donation of the NHC. The *trans* effect is also reflected by the increased olefinic C3=C4 (1.401(7) Å) bond distance compared with C7=C8 (1.379(6) Å). In the solid-state, a clear intermolecular O-H···Cl hydrogen-bonding interaction is observed between the free hydroxyl pendant group of the bifunctional NHC-OH ligand and the chloride ligand of an adjacent molecule, as reflected by the short H···Cl separation (2.35(5) Å) and the O-H···Cl angle (167(5)°), which is almost linear.

Overall, ligand **2** is well-suited to stabilize monometallic rhodium species. We have demonstrated the preferred coordination of the "soft" carbene ligand moiety to Rh while the "hard" hydroxyl group remains unbound to Rh and remains available for further reactivity. However, as will be described later in the section 3.3.2 of this chapter, the reaction between tantalum derivatives and the neutral rhodium-NHC complex **6** yielded mixtures of unidentifiable compounds instead of well-defined bimetallic Ta-Rh species. This prompted us to synthesize a larger series of cationic and neutral rhodium-NHC complexes in order to find

monometallic rhodium precursors better suited for the preparation of heterobimetallic species.

The cationic rhodium analogue, [Rh(HL)(COD)][BF_4] **7**, is isolated in excellent yield from treatment of **6** with the corresponding $AgBF_4$ salt, as shown on **Scheme 3.12**. The driving force of the reaction is the precipitation of AgCl. The ^{1}H NMR spectrum of **7**, recorded in $CDCl_3$ solution (Figure S10) shows the hydroxyl proton signal at δ = 5.75 ppm which is downfield as compared to corresponding neutral monometallic complex **6** where it is observed at δ = 3.17 ppm. The downfield shift may be due to a metal-hydroxyl interaction in solution.[63–65] Note that binding of the hydroxyl group to Rh is confirmed in the solid-state (see below). The IR spectrum of complex **7** (Figure S38) depicts a sharp signal at 3349.4 cm^{-1} corresponding to OH stretching. The incorporation of BF_4^- is confirmed by ^{11}B and ^{19}F NMR (Figure S12 and S13). Two signals are observed in ^{19}F NMR; one weak signal at δ = 150.27 ppm corresponding to the $^{10}BF_4^-$ species and a strong signal at δ = 150.32 ppm corresponding to $^{11}BF_4^-$.

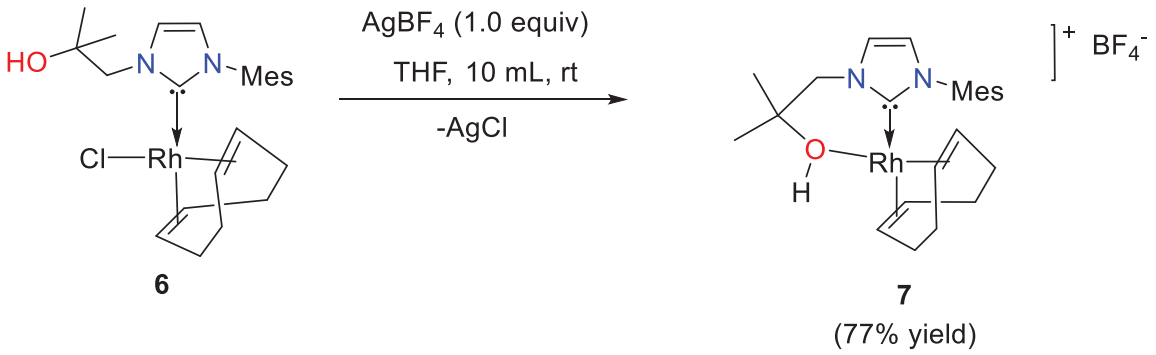

Scheme 3.12: Treatment of **6** with $AgBF_4$, at room temperature under dark conditions, leads to the formation of the cationic species **7**.

The ^{13}C NMR spectrum of **7** (Figure S11) displays a characteristic C_{NHC} signal at 174.5 ppm as a doublet due to coupling with the bound rhodium center ($^2J_{Rh\text{-}CNHC}$ = 52 Hz). The Rh-COD signals are observed as two separate doublets at δ = 99.95 ppm ($^2J_{Rh\text{-}COD}$ = 7 Hz) and 67.91 ppm ($^2J_{Rh\text{-}COD}$ = 16 Hz) respectively. Single crystals suitable for X-Ray crystallography to get more insight into the exact structure of complex were grown by cooling a saturated solution of the complex in THF at -40°C. The complex adapts a square-planar geometry at rhodium centre as shown below. (**Figure 3.7**)

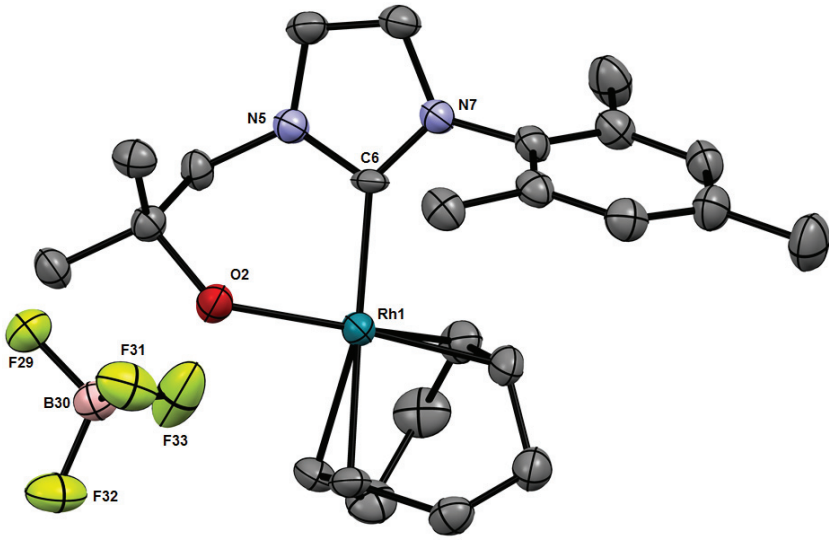

Figure 3.7: Molecular structure of complex **7** as determined by X-ray diffraction. Hydrogen atoms have been omitted for clarity and thermal ellipsoids are set at 50% probability level. Selected bond lengths (Å) and angles (°) are: Rh1-C6 2.029(4), Rh1-C25 2.095(4), Rh1-C26 2.109(3), Rh1-C21 2.178(4), Rh1-C22 2.199(6), Rh1-O2 2.152(1), N5-C6 1.355(4), N7-C6 1.347(6), N5-C6-N7 104.9(3).

The alkoxy-NHC ligand interacts with the rhodium centre in a chelate fashion with a ligand bite angle O2-Rh1-C_{NHC} of 84.1 (6)° which relates closely to chelate NHC complexes of late transition metals.[66,67] The Rh1-O2 bond distance of 2.152 (1) Å is also in the range of reported rhodium-oxygen bond distances.[67,68] The Rh-C_{COD} bond distances in *trans* position with respect to the NHC ligand (2.178(4) and 2.199(6) Å) are slightly elongated compared with those *trans* to the alkoxy group (2.095(4) and 2.109(3) Å), which is in agreement with the strong sigma donation of the NHC. The *trans* effect is also reflected by the increased olefinic C25=C26 (1.393(7) Å) bond length as compared with the cis C21=C22 (1.358(8) Å) bond length. Deprotonation of the cationic rhodium complex **7** by one equivalent of potassium *bis*(trimethylsilyl)amide (KHMDS) yields the alkoxy-NHC complex [Rh(L)(COD)], **8** in good isolated yield (**Scheme 3.13**).

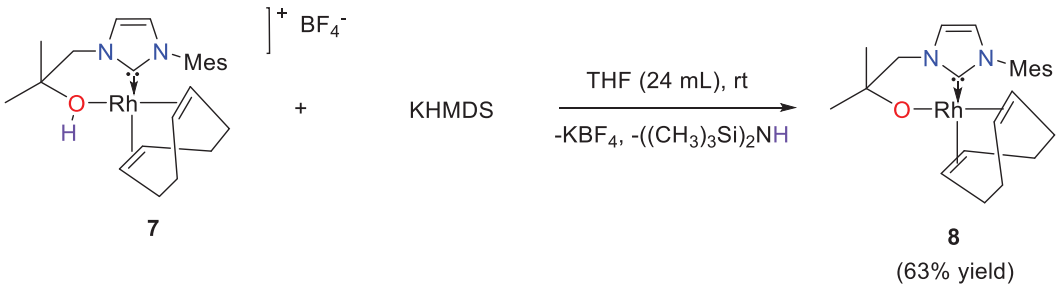

Scheme 3.13: One equivalent of KHMDS is added to complex **5** at room temperature to yield complex **8**.

The ^{1}H NMR spectrum of the resulting complex **8** (Figure S14) displays all the expected resonances. The imidazole backbone protons are observed as doublets ($^{3}J_{HH}$ = 1.7 Hz) at δ = 6.89 and 6.64 ppm respectively. The N-CH_2 protons are observed as a singlet at δ = 4.05 ppm integrating for two protons. As expected, it does not contain a peak corresponding to the hydroxyl proton which is also verified by the absence of hydroxyl stretching frequency in IR spectroscopy (Figure S40). The absence of fluorine and boron signals in the corresponding NMR spectra is in agreement with the absence of BF_4^-groups in the complex. Single crystals suitable for X-ray diffraction were grown by slow diffusion of pentane into the concentrated THF solution of the complex. The solid-state structure obtained by X-ray diffraction is shown on **Figure 3.8**. It is observed that the complex adopts a typical square planar geometry at the rhodium centre. The O2-Rh1-C_{NHC} ligand bite angle is 89.8 (2)° which is considerably higher than the corresponding angle (84.1 (6)°) in cationic rhodium complex **7**. The closeness of the ligand bite angle to the ideal 90° bite angle observed in square planar complexes suggests the enhanced stability of the chelate ring which is more relaxed after the deprotonation. This is also reflected in the significant decrease in rhodium oxygen bond length in complex **8** (2.031(4) Å) as compared to the corresponding bond length in the cationic complex **5** (2.152(2) Å), as expected.

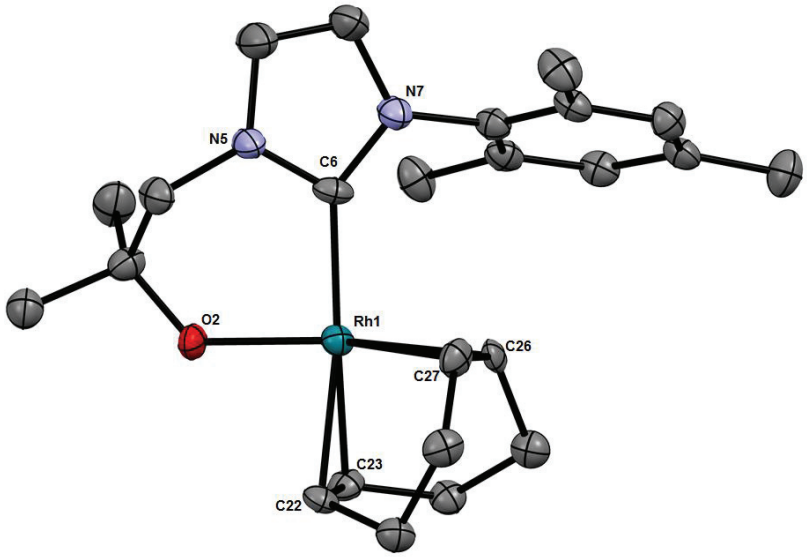

Figure 3.8: Molecular structure of the complex **8** as determined by X-ray diffraction. Hydrogen atoms have been omitted for clarity and thermal ellipsoids are set at 50% probability level. Selected bond lengths (Å) and angles (°) are: Rh1-C6 2.027(8), Rh1-C22 2.195(8), Rh1-C23 2.173(7), Rh1-C26 2.135(5), Rh1-C27 2.096(6), Rh1-O2 2.031(4), N5-C6 1.362(8), N7-C6 1.385(9), N1-C5-N2 102.6(5).

The conversion of complex **6** into **8** *via* complex **7** is a two-step process. Treatment of compound **6** with 1 equivalent of KHMDS quantitatively affords compound **8** as well, as an alternative and more direct synthetic route to **8** (**Figure 3.9**).

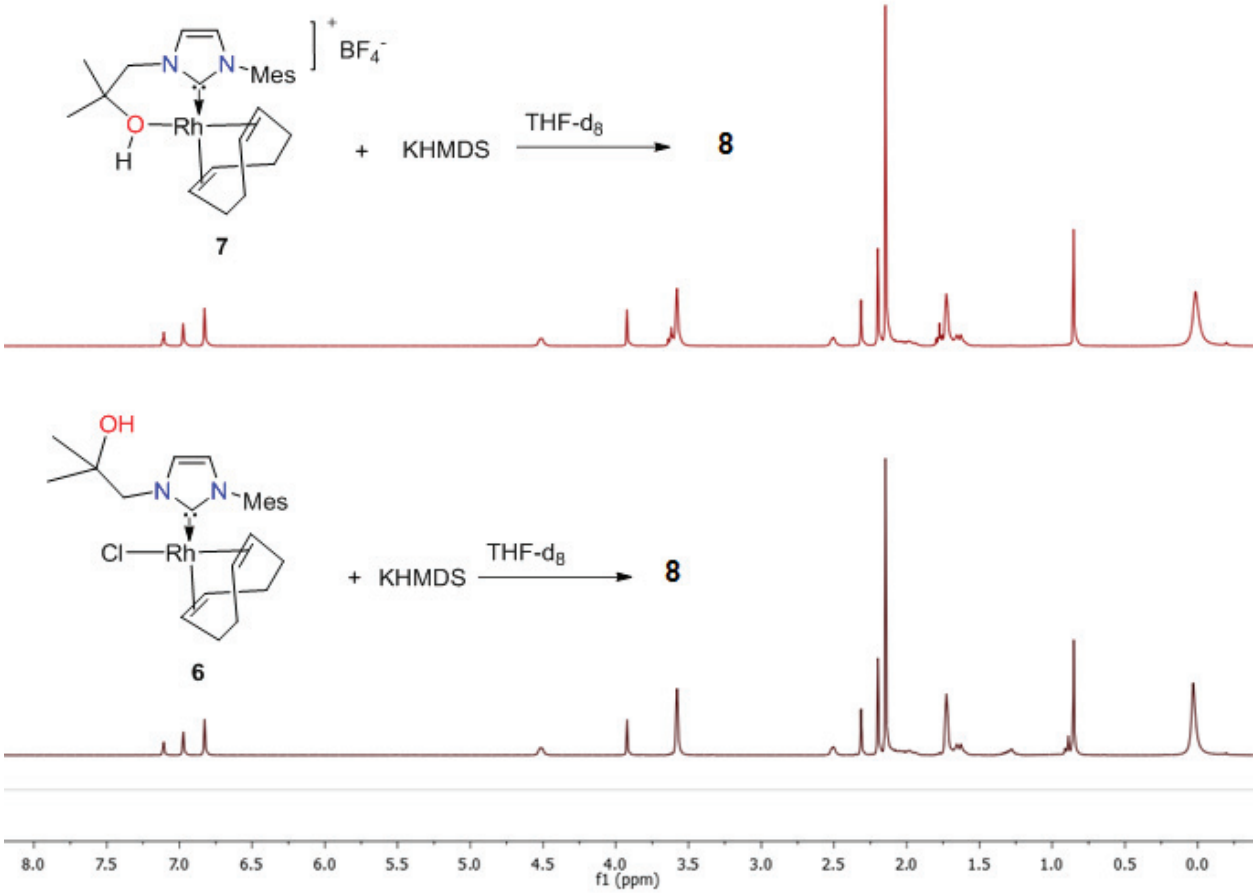

Figure 3.9: Comparison of the NMR spectra (THF-d_8) of the crude reaction mixtures obtained from the KHMDS deprotonation of the cationic rhodium NHC complex **7** (top) or the neutral rhodium-NHC complex **6** (bottom). The proton NMR study confirms that both synthetic routes lead to same chemical compound: complex **8**.

The latter reactivity indicates that the hydroxyl groups in **6** and **7** are reactive towards bases and might react with basic metal derivatives to lead to the formation of heterobimetallic assemblies. Accordingly, in an attempt to synthesize a tantalum/rhodium heterobimetallic species, complex **7** is treated with 1 equivalent of $Ta(CH^tBu)(CH_2{}^tBu)_3$ at room temperature in THF. After completion of the reaction, the reaction mixture is concentrated and stored at -40°C to yield a new product, **9**, as a yellow microcrystalline powder. The IR spectrum of complex **9** does not contain hydroxyl group stretching signal (**Figure 3.10**), which shows that the site of reaction is the hydroxyl proton as anticipated.

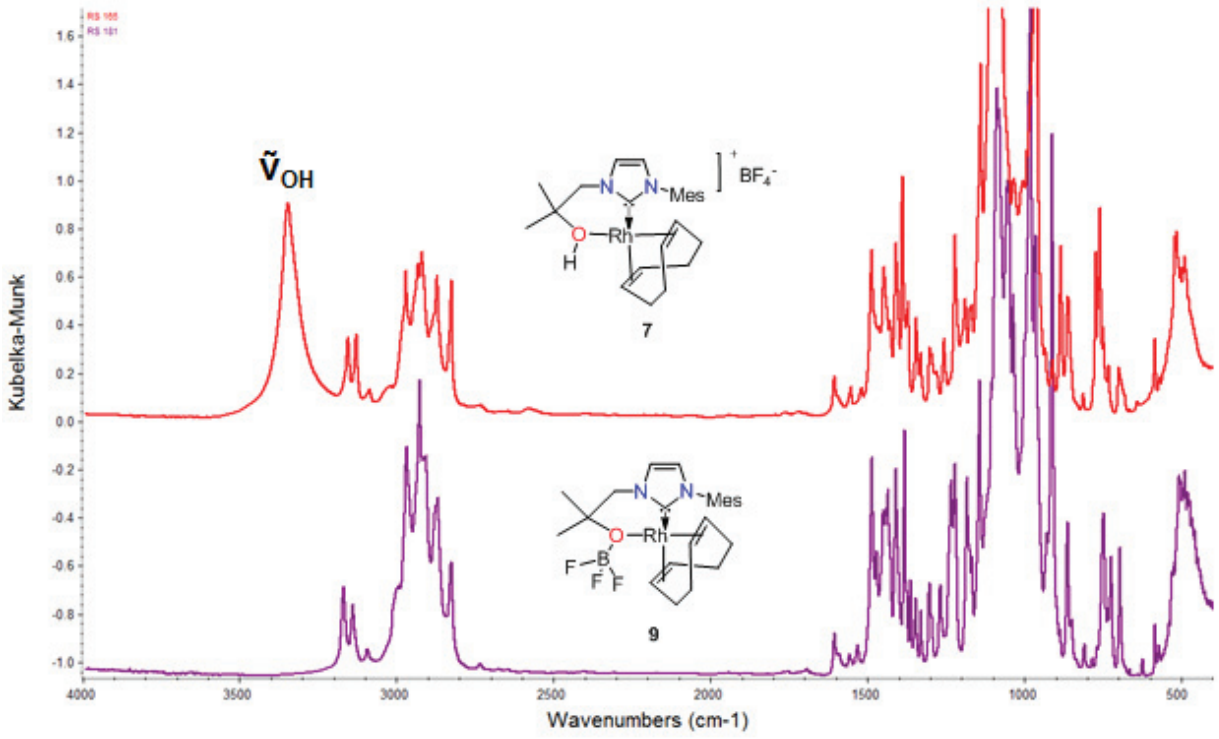

Figure 3.10: IR spectra of the rhodium cationic complex **7** (top) depict the characteristic IR stretching frequency of the hydroxyl group. In contrast we note the absence of such hydroxyl group stretching signal in complex **9** (bottom).

However, detailed NMR studies reveal that the obtained product is not a Ta/Rh heterobimetallic species. The ^{1}H NMR spectrum of **9** (Figure S17), recorded in THF-d_8, shows the disappearance of the hydroxyl group, as expected, but quite surprisingly there was no NMR signal observed for the neopentyl groups attached to the tantalum centre. Rather, the reaction leads to the unexpected formation of the monometallic complex [Rh(L•BF_3)(COD)], **9**. The COD sp^2 signals are observed at δ = 5.32 and 5.30 ppm respectively. The backbone imidazole protons are observed as doublets ($^{3}J_{HH}$ = 1.75 Hz) at δ = 7.03 and 6.73 ppm. The presence of a BF_3 moiety is confirmed by the ^{19}F NMR spectrum for **9** which displays a quartet centered at δ = 141.51 ppm. To get more insights into the structure of complex **9**, single crystals suitable for X-Ray crystallography were grown by slow diffusion of diethyl ether into a DCM solution of the compound at -40°C (**Figure 3.11**).

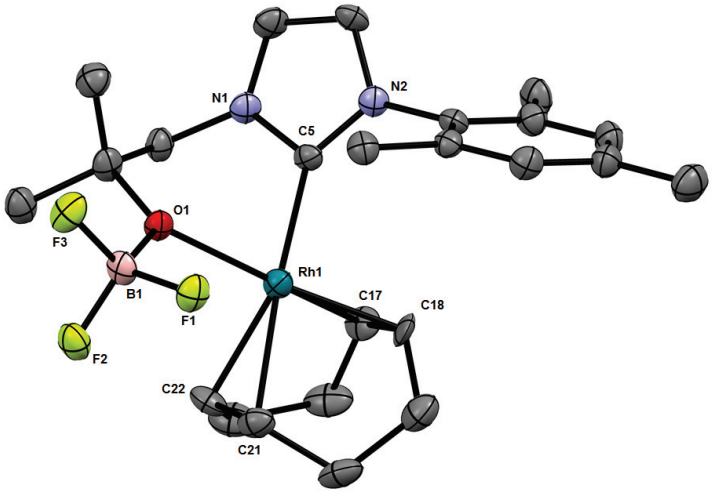

Figure 3.11: Solid-state molecular structure of complex **9** as determined by X-ray diffraction. Hydrogen atoms have been omitted for clarity and thermal ellipsoids are set at 50% probability level. Selected bond lengths (Å) and angles (°) are: Rh1-C5 2.012(5), Rh1-C17 2.102(7), Rh1-C18 2.078(7), Rh1-C21 2.226(5), Rh1-C22 2.175(5), Rh1-O1 2.213(5), O1-B1 1.479(9) N1-C5 1.359(6), N2-C5 1.346(7), N1-C5-N2 104.6(4).

Indeed, the crystal structure confirms that there was no incorporation of tantalum into the rhodium cationic complex but instead addition of a BF_3 moiety which interacts with the oxygen atom of the chelated alcoxy group, in agreement with the NMR data. The complex adopts a typical square-planar geometry at the rhodium centre. The alkoxy-NHC ligand interacts with the rhodium centre in a chelate fashion with a constrained ligand bite angle O1-Rh1-C_{NHC} of 82.0 (2)°. The Rh1-O1 bond distance of 2.213 (5) Å is much longer than the corresponding bond in complex **7**. This indicates that addition of BF_3 strongly reduces the nucleophilicity of the O-donor site of the bifunctional NHC ligand. The Rh-C_{COD} bond distances in *trans* position with respect to the NHC ligand (2.226(5) and 2.175(5) Å) are slightly elongated compared with those *trans* to the OBF_3 group (2.102(7) and 2.078(7) Å). The *trans* effect is also reflected by the increased olefinic C17=C18 (1.406(7) Å) bond distance compared with C21=C22 (1.357(7) Å), as observed for the whole series of these (COD)Rh-NHC species.

The absence of tantalum center in complex **9**, as well as one fluorine atom, leads us to enquire more about the nature of the tantalum by-product formed during the reaction process. For this purpose, a NMR scale reaction is performed between the rhodium cationic complex **7** and $Ta(CH^tBu)(CH_2{}^tBu)_3$ in THF-d_8. As the reaction progressed, the ^1H NMR signal corresponding to the acidic hydroxyl proton in **7** disappears, as a result of the reaction with the basic tantalum alkylidene carbon, without the release of neopentane. This is reflected by the disappearance of the tantalum alkylidene proton and the absence of neopentane signal in the

^{1}H NMR spectrum as well as the absence of a Ta-alkylidene carbon signal in the ^{13}C NMR spectrum. Furthermore, the ^{19}F NMR spectrum of the solution displays a singlet at 73.69 ppm (Figure S21) which is characteristic of tantalum fluorides[69] and corroborates the formation of a tantalum neopentyl fluoride derivative of general formula $[Ta(CH_2{}^tBu)_4F]_n$. Despite the low nucleophilicity of the tetrafluoroborate anion, strong electrophiles can abstract fluoride from BF_4^- [70,71] especially early transition metals.[72,73] Here the tantalum alkyl alkylidene derivative acts both as a base to deprotonate the hydroxyl group in **7** and as an electrophile to abstract a fluoride from the BF_4^- anion. Multiple attempts to obtain the crystal structure of the tantalum alkyl fluoride co-product failed because of the very high solubility of this species in non-polar solvents. Based on all these observations, the following reaction scheme can be proposed (**Scheme 3.14**):

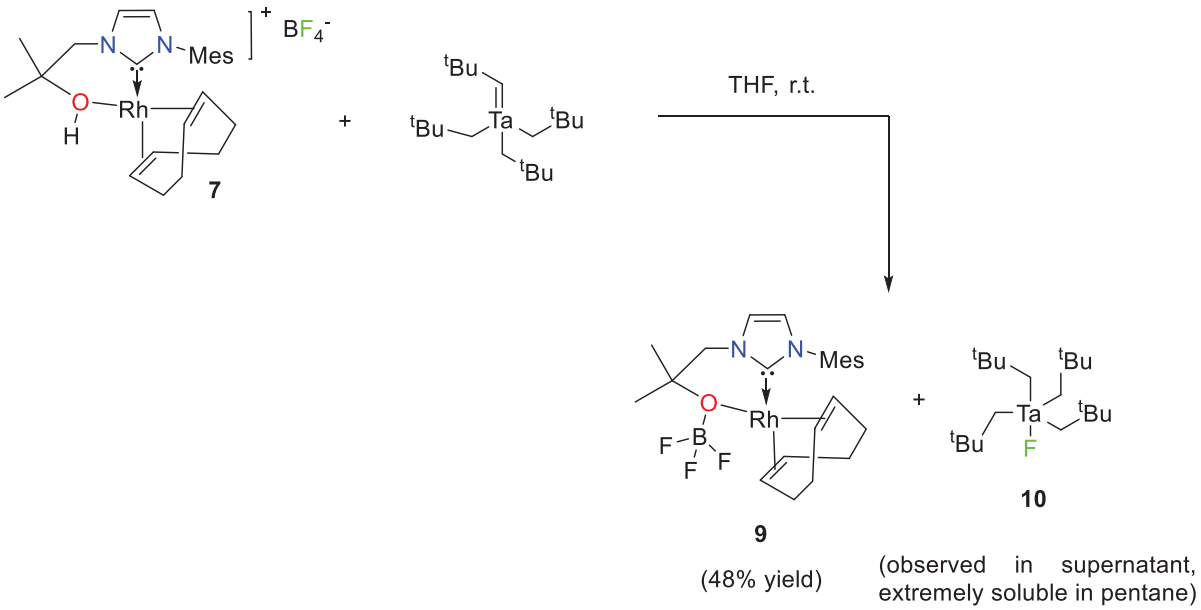

Scheme 3.14: Synthesis of compound **9** from **7** upon deprotonation and fluoride abstraction by $Ta(CH^tBu)(CH_2{}^tBu)_3$.

Compound **9** can be seen as a boron trifluoride adduct of **8**, and accordingly is more conveniently prepared upon treatment of **8** with BF_3•THF (Scheme 3.12). This finding opens attractive perspectives as it provides another possible route to synthesize heterobimetallic complexes where BF_3 could be replaced by other Lewis-acidic metal centers, for instance by boron analogues like aluminum, gallium etc.

The synthetic routes to this family of rhodium-NHC complexes are summarized in the scheme below (**Scheme 3.15**):

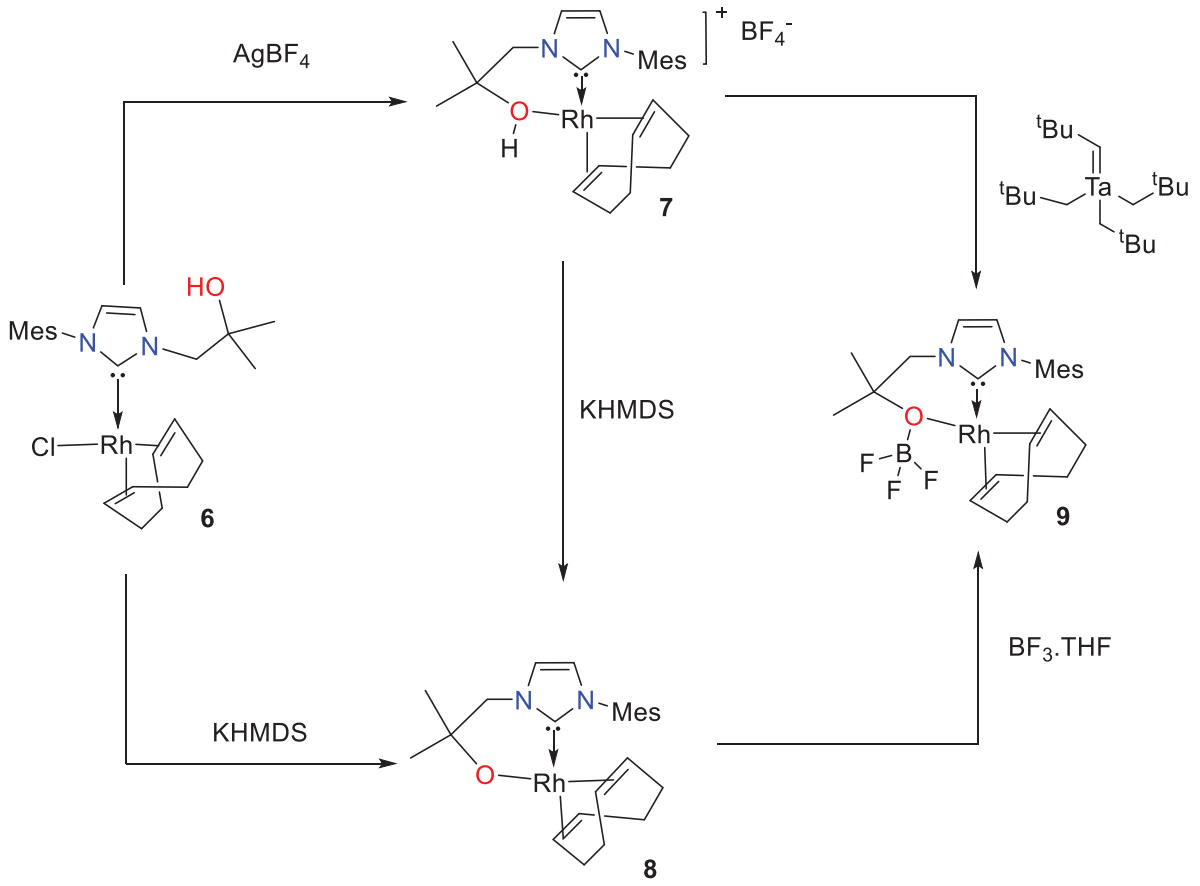

Scheme 3.15: The scheme discusses the chemical behavior of monometallic rhodium-NHC species. Addition of one equivalent of $AgBF_4$ to the complex **6** leads to cationic complex **7**, whereas adding KHMDS to the complex **6** leads to complex **8**. Complex **8** can also be synthesized by adding one equivalent of KHMDS to complex **7**. Addition of $Ta(CH^tBu)(CH_2{}^tBu)_3$ to complex **7** or, alternatively, treatment of complex **8** with BF_3•THF lead to the same complex, **9**.

The reaction between tantalum schrock and neutral complex 8 at room temperature led to mixture of compounds. Since, it is observed that the abstraction of F^- (from complex **7**) by tantalum alkylidene species lead to the Ta-F complex and hence we synthesized PF_6^- and $CF_3SO_3^-$ analogues of the complex **7**. The reaction between both these rhodium species and tantalum schrock did not yield the desired bimetallic complex. Note that preliminary studies have shown that complex **6**, **7**, **8** and **9** act as catalysts for alkene hydrosilylation. These preliminary results, which are out of the scope of the present chapter, are reported in the appendix.

3.3) Synthesis of Ta-Rh bimetallic complexes

Once the synthesis and characterization of several monometallic tantalum and rhodium complexes supported by the alkoxy-NHC or hydroxyl-NHC ligand was established, we then investigated the possibility of synthesizing the projected Ta-Rh heterobimetallic assemblies. To this aim, several synthetic routes can be envisioned. First we will present the reactivity of Ta-NHC complexes with Rh precursors. Then we will report the reactivity of Rh-NHC complexes towards Ta precursors.

3.3.1) Insertion of Rh into the tantalum-NHC complex 3

Since the characterization of the tantalum-NHC complex **3** established that the Ta-NHC interaction is weak and might be labile, we first investigated the possibility of transmetallation of the Ta-NHC motif to rhodium. To this aim, a yellow toluene solution of $[Rh(COD)Cl]_2$ is added to a dark orange toluene solution of the tantalum complex **1**. It is observed that complex **1** and the rhodium dimer precursor does not react in the expected complex 1:1 Ta:Rh ratio. (**Scheme 3.16**) The optimization of the reaction stoichiometry provides the following observations:

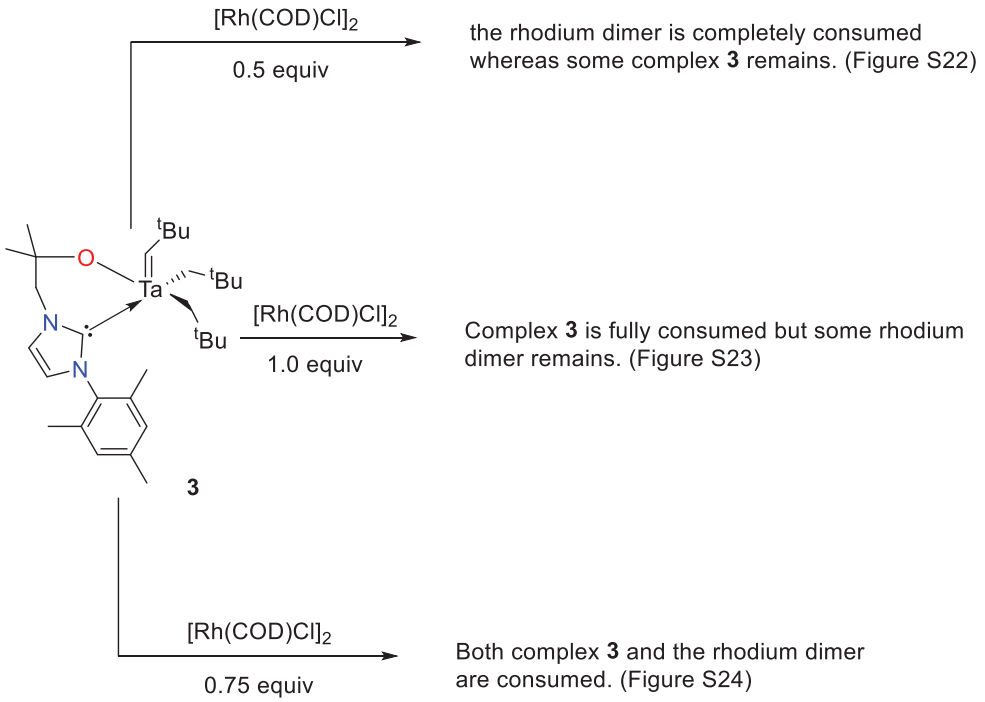

Scheme 3.16: Optimization of the stoichiometry for the reaction between complex **3** and $[Rh(COD)Cl]_2$ shows that both precursors are fully consumed when a 1:1.5 Ta:Rh ratio is used.

Once optimized, the precursors are mixed in the ratio of 1:0.75 (i.e. 1:1.5 Ta:Rh ratio) and stirred at room temperature for 4 hr. Toluene is removed to yield the mixture of compounds as shown in **Scheme 3. 17.**

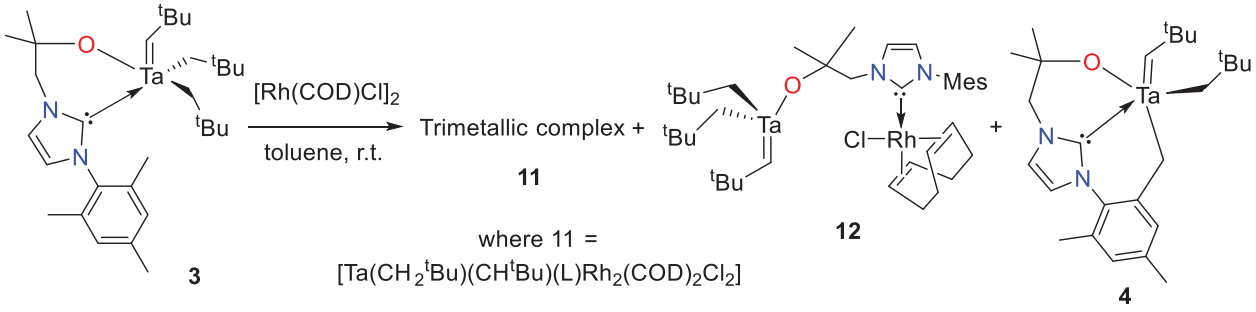

Scheme 3. 17: Reaction of $[Rh(COD)Cl]_2$ with the tantalum-NHC complex **3** performed in toluene leads to a mixture of species.

Unfortunately, all attempts to separate **11, 12** and **4** upon fractional crystallization of the crude mixture were unsuccessful. In particular, the heterometallic species **11** and **12** have similar solubility and co-crystallized in the same reaction conditions (Figure S25). The cyclometallated complex **4** results from the thermal decomposition of **1** as reported in section 3.2.1.2.[74]

Although the heterobimetallic complex [Ta(μ-L)(CH^{t}Bu)(CH$_2$^{t}Bu)$_2$Rh(COD)Cl], **12**, cannot be isolated, its formation is supported on the basis of NMR data. The NMR data closely match with that of the imido analogue, [Ta(μ-L)(N^{t}Bu)(CH$_2$^{t}Bu)$_2$Rh(COD)Cl], which we shall discuss in section 3.3.3.[74] In particular the ^{1}H NMR spectrum for **12** displays a singlet at δ = +3.93 ppm attributed to the Ta neopentylidene α-H. This signal correlates in the ^{1}H-^{13}C HSQC NMR (Figure S27) experiment to the characteristic neopentylidene ^{13}C resonance found at δ = +238.2 ppm (singlet); this highly deshielded value is typical of Ta(V) alkylidenes.[75,76] The ^{13}C resonance corresponding to the NHC carbene carbon appears as a doublet at δ = +184.5 ppm ($^1J_{Rh\text{-}C}$ = 52 Hz) which confirms Rh coordination to the NHC ligand. Furthermore, the solid-state structure of **12** is obtained by single crystal crystallography and is shown in **Figure 3.12**. The alkoxy-NHC ligand bridges the two metals: the "hard" alkoxy arm binds to Ta while the "soft" carbene ligand moiety is coordinated to Rh. Both metal centers are separated by 7.236(1) Å. The tantalum metal center adopts a pseudo-tetrahedral geometry which is typical for 4-coordinate d^0 Ta(V) complexes.[77,78]

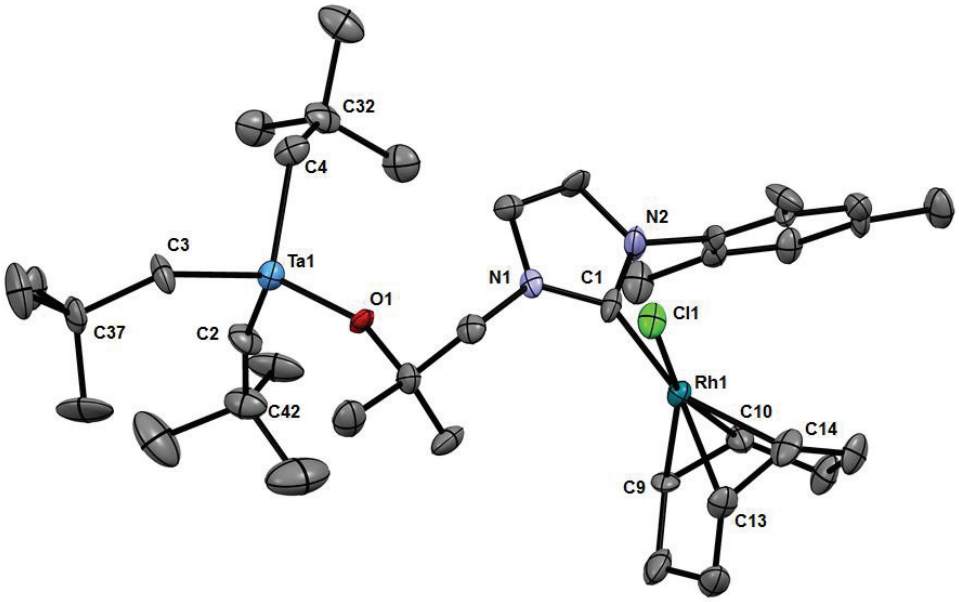

Figure 3.12: Solid-state molecular structure of **12** as determined by X-ray diffraction. Hydrogen atoms have been omitted for clarity and thermal ellipsoids are set at 50% probability level. Selected bond lengths (Å) and angles (°) for 10: Ta1-O1 1.837(7); Ta1-C2 1.902(11); Ta1-C3 2.138(11); Ta1-C4 1.155(11); Rh1-C1 2.039(11); Rh1-Cl1 2.389(3); Rh1-C9 2.084(10); Rh1-C10 2.114(11); Rh1-C13 2.184(13); Rh1-C14 2.203(11); N1-C1 1.376(12); N2-C1 1.365(15); N1-C1-N2 102.6(9); Ta1-C2-C42 163.9(10); Ta1-C3-C37 132.8(8); Ta1-C4-C32 130.7(8).

The Rh centre adopts a square-planar coordination geometry which is characteristic for 4-coordinate 16-valency electrons Rh(I) species. The Rh-carbene bond length (2.039(11) Å) is comparable to that found in related Rh(I)-NHC species.[55,62] As a result of the greater *trans* influence of the NHC donor, the Rh-COD distances trans to the carbene (2.184(13) and 2.203(11) Å) are longer than those in the cis arrangement (2.084(10) and 2.114(11) Å).

Gratifyingly, we discovered that the outcome of this reaction is strongly dependent of the solvent used. Indeed, the reaction of $[Rh(COD)Cl]_2$ with the tantalum-NHC complex **3**, performed in a 1:1 ratio in THF at room temperature, yields cleanly the trimetallic complex of general formula $[Ta(CH_2{}^tBu)(CH{}^tBu)(\mu\text{-}L)Rh_2(COD)_2Cl_2]$, **11** (**Scheme 3.18**). The nuclearity of complex **11** was determined by elemental analysis which shows that it is a trimetallic complex $[TaRh_2]$ (mol%Rh: mol%Ta = 1.9), HRMS ESI (expected for $[M\text{-}Cl]^+$ 1107.3309, found 1107.3320) as well as the NMR characterization which is in agreement with the proposed general formula for **11**.

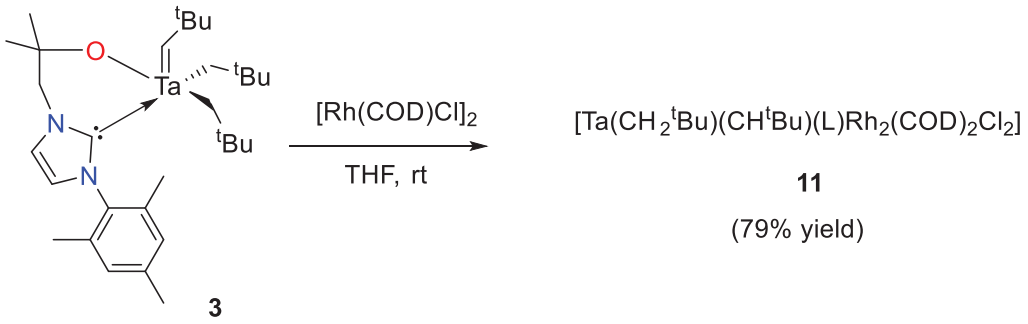

Scheme 3.18: Reaction of $[Rh(COD)Cl]_2$ with the tantalum-NHC complex **3** performed in THF.

The ^1H and ^{13}C NMR patterns for **11** are very complex, and denote the formation of a highly asymmetric species in solution. The $^{13}C\{^1H\}$ NMR spectrum for **11** displays a characteristic signal at δ = +184.6 ppm which corresponds to the NHC carbene carbon. This signal appears as a doublet ($^1J_{Rh\text{-}C}$ = 53.1 Hz), which is characteristic signal for rhodium coordination to the NHC moiety. (**Figure 3.13**)

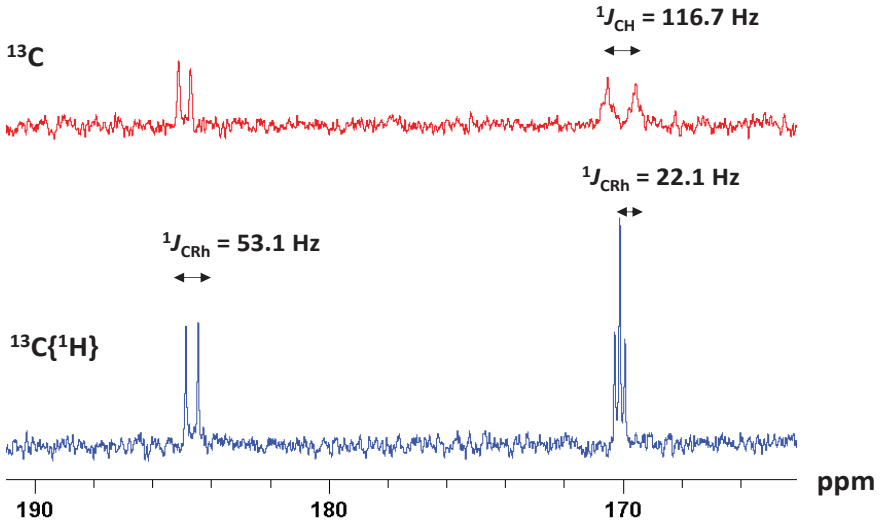

Figure 3.13: ^{13}C NMR and $^{13}C\{^1H\}$ NMR spectra of **11** showing characteristic signals at δ = +184.6, +170.2 and +170.0 ppm demonstrating transmetallation and rhodium coordination to both the NHC and the alkylidene ligands.

The reaction of added rhodium metal with the tantalum alkylidenic carbon is evident by the observation of the neopentylidene ^{13}C NMR resonance at a highly upfield chemical shift of δ = +170.0 ppm as compared to δ = 250.1 ppm in the starting material **3**. The chemical shift is highly upfield when compared with other classically reported Ta(V) alkylidenes too.[17]

More insight into the structure of the complex **11** can be obtained from the $^{1}J_{CH}$ and $^{1}J_{RhC}$ splitting constant values of the bridging ligand. The $C_{alkylidene}$ peak is a doublet of doublets which merges together and appears as a pseudo-triplet. The low splitting constant ($^{1}J_{CRh}$= 22.1 Hz) is in close consonance with the $^{1}J_{CRh}$ value (20 Hz) observed for bridging methylene ligands of analogous Ti-Rh heterobimetallic complex.[79,80] This characteristic signal evolves to a doublet of pseudo-triplets in the proton coupled ^{13}C NMR spectrum due to coupling with the neopentylidene α-H ($^{1}J_{C-H}$ = 116.7 Hz, **Figure 3.13**) and correlates in the ^{1}H-^{13}C HSQC NMR experiment (Figure S30) to characteristic neopentylidene α-H ^{1}H resonances found at δ = 4.80 ppm.

The observed value of $^{1}J_{C-H}$ is again reminiscent of the bridging sp^{3} methylene center ($^{1}J_{C-H}$ =128 Hz) in the Ti-Rh analogue $Cp_2TiRh(COD)(\mu\text{-}CH_2)(\mu\text{-}Cl)$.[80] However, it is important to mention here that the exact nature of bonding between the bridging methylene ligand and the metal centers in the $Cp_2TiRh(COD)(\mu\text{-}CH_2)(\mu\text{-}Cl)$ is defined only with the help of crystal structure which showed that the Ti-CH_2 bond length (2.02 Å) lies between the double bond (1.85-1.88 Å) and single bond (2.15 Å) lengths. Also, the utilization of ^{13}C NMR chemical shift to arrive at the proposed structure is not supported by the other literature reports as the analogous Ta-Ir bridging methylene complex reported by Bergman depicts the ^{13}C methylene signals in the range δ = 90-110 ppm.[2,3,81] Unfortunately, all attempts to grow single crystals of **11** suitable for X-ray diffraction were unsuccessful always recrystallizing to a brownish yellow powder; therefore a definite structure for this compound cannot be given. Based on the available information and literature[8,80] following structure for complex **11** is proposed: (**Figure 3.14**)

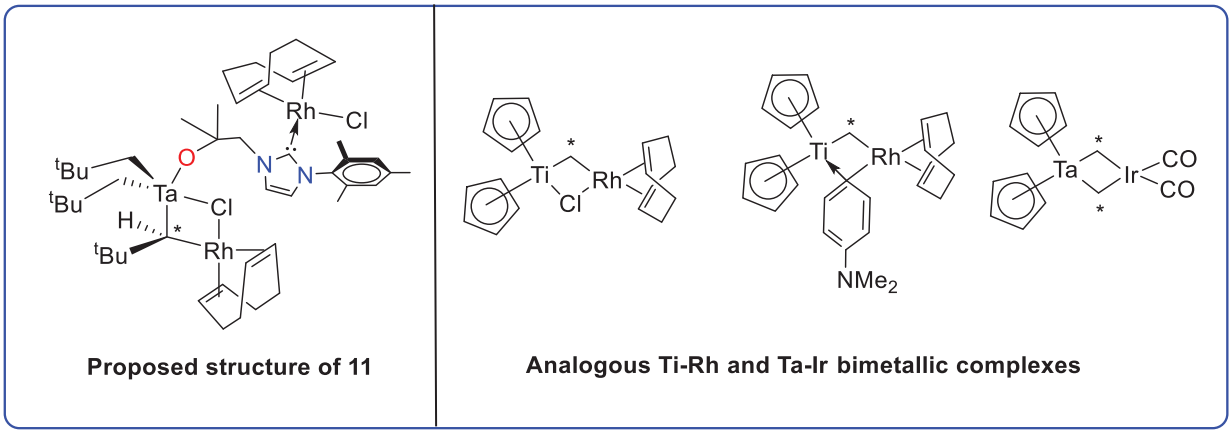

Proposed structure of 11

Analogous Ti-Rh and Ta-Ir bimetallic complexes

S.No.	Complex 11	$Cp_2TiRh(COD)(\mu\text{-}CH_2)(\mu\text{-}Cl)$	$Cp_2TiRh(COD)(\mu\text{-}CH_2)(\mu\text{-}Ar)$	$Cp_2Ta(CH_2)_2Ir(CO)_2$
δ (^{13}C)	170.0 ppm	186.5 ppm	189.4 ppm	100.0
$^1J_{Rh\text{-}C}$	22.1 Hz	20 Hz	23.5 Hz	-
$^1J_{C\text{-}H}$	116.7 Hz	128 Hz	129 Hz	-

Figure 3.14: Proposed structure of the polymetallic complex **11**, inferred on the basis of the NMR data and elemental analysis results, compared with analogous systems from the literature. The NMR data for the bridged alkylidene ligand (represented by asterisk *) in these molecules are shown in table below for a comparison.

The remaining ^1H and ^{13}C resonances for complex **11** (Figure S28) indicate the existence of an asymmetric compound. For example two singlets at 6.89 and 6.68 ppm integrating to one proton each corresponds to the *meta* mesitylene protons again supporting the asymmetric nature of the complex. Two pairs of diastereotopic doublets integrating to one proton each are also observed at (δ = 6.16, 6.12, 4.55 and 4.50 ppm, $^2J_{HH}$ = 14.1 Hz) for the N-CH_2 fragments of the NHC ligand.

From this first set of experiments we can draw two main conclusions: 1) the NHC-Ta adduct is labile and NHC transmetallation from Ta to Rh occurs readily; 2) the neopentylidene fragment in **3** is highly reactive, and presumably reacts with $[Rh(COD)Cl]_2$ to yield species of higher nuclearity, or, alternatively, the neopentylidene moiety reacts with the ligand mesityl group to

form a cyclometallated species. This hampers clean formation of a heterobimetallic species through simple Ta to Rh NHC transmetallation from **3**.

3.3.2) Reaction between rhodium-NHC complex and Ta(CH^{t}Bu)(CH$_2$^{t}Bu)$_3$.

Another route to synthesize the envisioned Ta/Rh heterobimetallic complex is the reaction of Ta(CH^{t}Bu)(CH$_2$^{t}Bu)$_3$ with Rh-NHC species featuring a reactive hydroxyl group. As already discussed in section 3.2.2 of this chapter, this reaction is not successful in the case of cationic Rh complexes since the Ta precursor reacts with the counter-anions (especially BF_4^-) in these species. We also investigated treatment of the rhodium-NHC complex **4** with Ta(CH^{t}Bu)(CH$_2$^{t}Bu)$_3$. Unfortunately, this leads to an unidentifiable mixture of compounds (**Scheme 3.19**). We attribute this behavior to the ability of Ta–alkylidene moiety to compete with the Ta–alkyls in the protonolysis reaction with the ligand hydroxyl group.

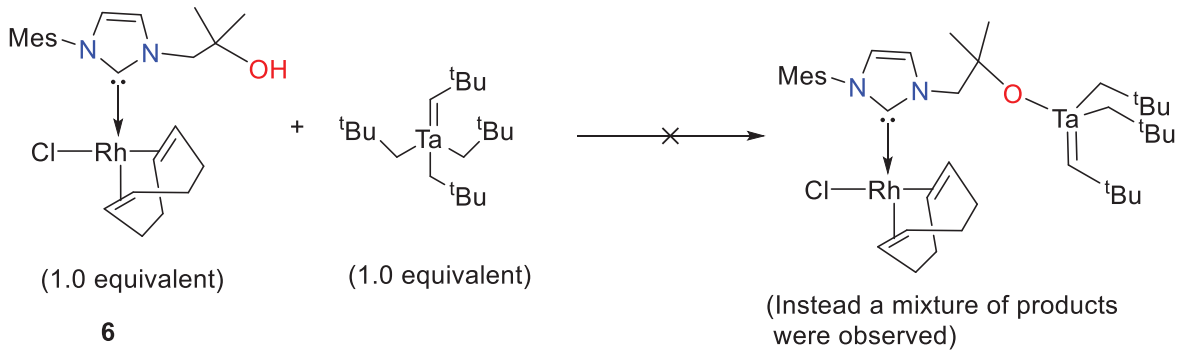

Scheme 3.19: The reaction between the Rh-NHC complex **6** and tantalum alkylidene precursor lead to a mixture of products.

3.3.3) Synthesis of [Ta(μ-L)(N^{t}Bu)(CH$_2$^{t}Bu)$_2$Rh(COD)Cl] by using tantalum imido alkylidene Ta(μ-L)(N^{t}Bu)(CH$_2$^{t}Bu)$_2$ **3** as the tantalum precursor.

We could conclude from sections 3.3.2 and 3.3.3 that the targeted Ta-Rh heterobimetallic complexes could not be synthesized because of the high reactivity of the tantalum alkylidene motif towards a) [Rh(COD)Cl]$_2$ or b) the hydroxyl moiety of rhodium-NHC complex **6** or c) the BF_4^- anion. In order to overcome this limitation, we sought to use the tantalum imido alkylidene Ta(N^{t}Bu)(CH$_2$^{t}Bu)$_3$ complex and its derivative Ta(μ-L)(N^{t}Bu)(CH$_2$^{t}Bu)$_2$ **5** (reported in section 3.2.1.3). Indeed, these species contain a less reactive tantalum imido group in place of a tantalum alkylidene moiety. Using these derivatives, the desired Ta-Rh heterobimetallic

complexes are synthesized and isolated in good yields following the synthetic routes presented on **Scheme 3.20**.

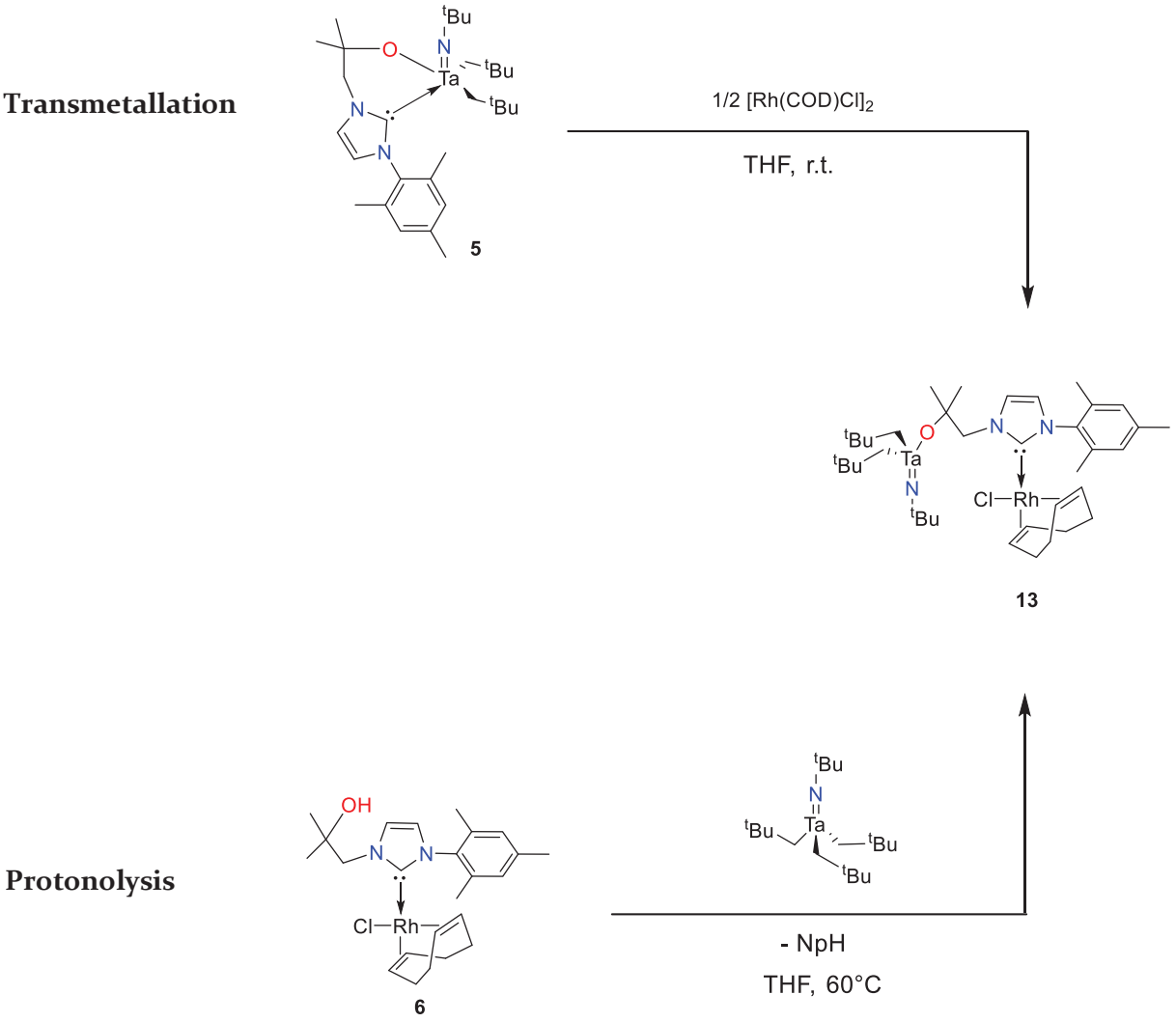

Scheme 3.20: Synthesis of the heterobimetallic complex [Ta(μ-L)(N^{t}Bu)(CH$_2$^{t}Bu)$_2$Rh(COD)Cl] through two different routes.

Both synthetic routes afforded the same heterobimetallic Ta-Rh complex, Ta(μ-L)(N^{t}Bu)(CH$_2$^{t}Bu)$_2$Rh(COD)(Cl) **13** demonstrating the versatility of this approach. The transmetallation route which involves the insertion of rhodium metal into the tantalum-C_{NHC} bond is kinetically faster (2h r.t.) when compared to the protonolysis route which involves the reaction of hydroxyl group with the neopentyl ligand of the tantalum imido complex (24h 60°C). Thus the transmetallation route is preferred for synthetic purposes. Compound **13** is isolated in 68% yield and is fully characterized by ^{1}H and ^{13}C NMR spectroscopy, DRIFT spectroscopy, elemental analysis and X-ray diffraction structural determination.

The rhodium coordination to the NHC moiety in solution is confirmed by $^{13}C\{^{1}H\}$ NMR (Figure S32) which displays a characteristic signal at δ=184.0 ppm featuring a $^{1}J_{Rh\text{-}C}$ coupling constant of 52 Hz. This peak is shifted upfield from that of **5** but it is analogous to that of **6**. Contrary to **6**, four different COD olefinic resonances are observed for **13** at δ=96.5 and 96.4 ppm ($^{1}J_{Rh\text{-}C}$ = 14 Hz) and δ=68.4 and 66.7 ppm ($^{1}J_{Rh\text{-}C}$ = 14 Hz) respectively, which is indicative of a rigid unsymmetrical structure in which the rotation around the Rh-C bond is hindered as a result of Ta ligation. More insights into the structure of complex **13** are obtained by the X-ray crystallographic studies of the complex. Single crystals of **13** suitable for X-ray diffraction are obtained upon recrystallization in pentane at -40°C (**Figure 3.15**). The crystal structure confirms that Rh has indeed been inserted into the Ta-NHC bond.

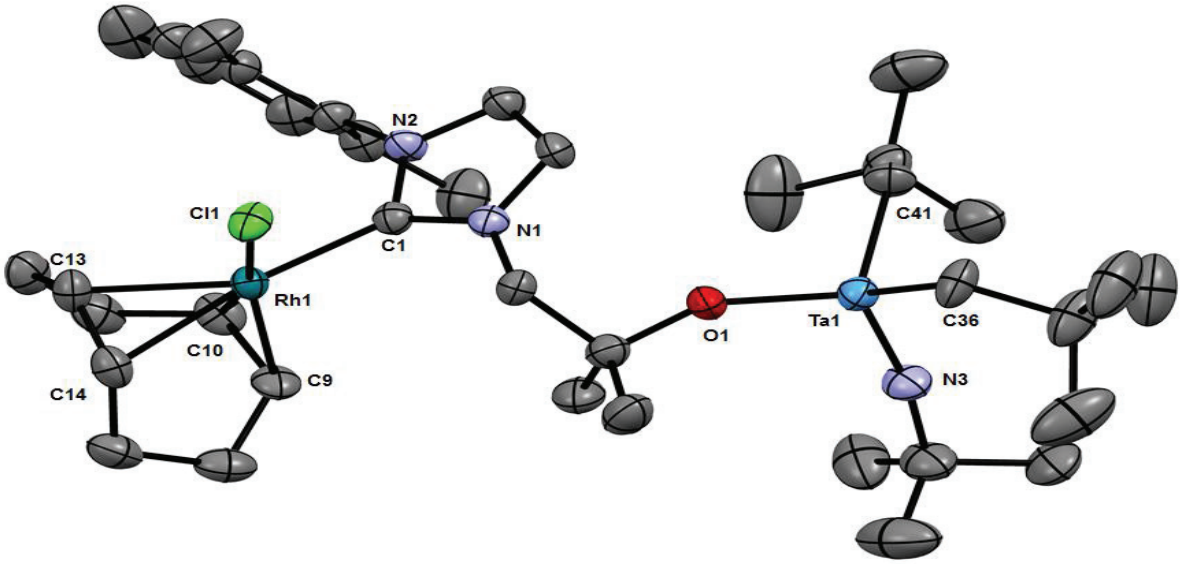

Figure 3.15: Solid-state molecular structure of **13** as determined by X-ray diffraction. Hydrogen atoms have been omitted for clarity and thermal ellipsoids are set at 50% probability level. Selected bond lengths (Å) and angles (°) for 10 : Ta1-N3 = 1.774(7); Ta1-O1 = 1.871(5); Ta1-C36 = 2.135(8); Ta1-C41 = 2.130(8); Rh1-C1 = 2.033(8); Rh1-C9 = 2.095(8); Rh1-C10 = 2.110(7); Rh1-C13 = 2.154(8); Rh1-C14 = 2.190(8); Rh1-Cl1 = 2.364(2); N1-C1 = 1.367(9); N2-C1 = 1.360(9), N1-C1-N2 = 102.9(6).

The tantalum atom displays a tetrahedral coordination, as expected for a 4-coordinate d^0 Ta(V) center. The Ta-O bond distance is significantly shorter in **13** (1.871(5) Å) than in **5** (1.953(3) Å), that we attribute to the lower coordination number, but also to the released steric strain from the chelate alkoxy-NHC ligand. The Ta=N (1.774(7) Å) and Ta-C (2.135(8) and 2.130(8) Å) bond distances are as expected. The rhodium center adopts a pseudo square-planar geometry, which is characteristic of d^8 Rh(I) species. The metrical parameters around the Rh

center in **13** are fairly similar to that found in **12**. Both metals are separated by 7.374(1) Å. This complex adds to the short list of well-defined Ta-Rh heterobimetallic species[7–9,82] and to a limited list of NHC supported early/late transition metal complexes.[83–85]

CONCLUSION

The hydroxyl-NHC ligand platform is successfully used to synthesize a series of well-defined Ta and Rh monometallic complexes. We have demonstrated the preferred coordination of the "soft" carbene ligand moiety to Rh while the "hard" alkoxy ligand group is selective to Ta. Rare examples of Ta-NHC complexes are reported and in particular, the first tantalum complex displaying both a Fischer-type and a Schrock-type carbene ligand. The X-ray crystal structures of the Ta complexes show that the bifunctional ligand interacts with the tantalum atoms in a chelate manner, though the interaction is weak as reflected by the long bond distance between the NHC-carbene and the Ta centers. This observation is promising for transmetallation with other metals, with the objective of accessing early/late heterobimetallic species. The crystal structure of rhodium NHC complex shows that the hydroxyl group is unbound to the metal and available for reaction with the tantalum precursor. Attempts to synthesize the heterobimetallic complexes by two different routes are made a) by reacting tantalum NHC complexes with $[Rh(COD)Cl]_2$ or b) upon treating rhodium NHC complexes with tantalum alkyl precursors. In the case of stable tantalum imido derivatives, this allowed the clean preparation of a rare Ta/Rh heterobimetallic assembly through either a) the protonolysis reaction between the free hydroxyl pendant group in the monometallic complex Rh(HL)(COD)Cl, and the alkyl moiety from the tantalum precursor $Ta(N^tBu)(CH_2{}^tBu)_3$ or b) the incorporation of Rh into the alkoxy-NHC Ta complex $Ta(N^tBu)(L)(CH_2{}^tBu)_2$ through carbene transmetallation from Ta to Rh. This proof of concept result showcases the utility and versatility of this bifunctional alcoxy-carbene motif for the straightforward generation of well-defined NHC-based early-late heterobimetallic entities. However, in the case of Ta alkylidenes, both synthetic approaches failed to provide the targeted complexes. Intractable mixtures of species are formed in several places, and the alkylidene motif is found to be too reactive, leading to trimetallic assemblies or the activation of the BF_4^- counter anion for instance. Hence a possible way going forward would be to consume the alkylidene motif with a reactive proton source to reach a peralkyl species before introduction of the rhodium precursor. This possible route is developed and discussed in the next chapter.

REFERENCES

1 M. J. Hostetler, M. D. Butts and R. G. Bergman, *Organometallics*, 1993, **12**, 65–75.

2 M. D. Butts and R. G. Bergman, *Organometallics*, 1994, **13**, 2668–2676.

3 M. J. Hostetler, M. D. Butts and R. G. Bergman, *J. Am. Chem. Soc.*, 1993, **115**, 2743–2752.

4 M. J. Hostetler, M. D. Butts and R. G. Bergman, *Inorganica Chim. Acta*, 1992, **198–200**, 377–392.

5 Y. Zhang, S. P. Roberts, R. G. Bergman and D. H. Ess, *ACS Catal.*, 2015, **5**, 1840–1849.

6 A. E. Findlay, S. Leelasubcharoen, L. G. Kuzmina, J. A. K. Howard and G. I. Nikonov, *Dalt. Trans.*, 2010, **39**, 9264.

7 T. G. Ostapowicz and M. D. Fryzuk, *Inorg. Chem.*, 2015, **54**, 2357–2366.

8 J. A. R. Schmidt and J. Arnold, *J. Am. Chem. Soc.*, 2001, 123, 8424–8425.

9 H. Han, M. Elsmaili and S. A. Johnson, *Inorg. Chem.*, 2006, **45**, 7435–7445.

10 K. Yamamoto, K. Higashida, H. Nagae, H. Tsurugi and K. Mashima, *Helv. Chim. Acta*, 2016, **99**, 848–858.

11 D. Tapu, D. A. Dixon and C. Roe, *Chem. Rev.*, 2009, 109, 3385–3407.

12 A. J. Arduengo, H. V. R. Dias, R. L. Harlow and M. Kline, *J. Am. Chem. Soc.*, 1992, **114**, 5530–5534.

13 H. V. Huynh, *Chem. Rev.*, 2018, **118**, 9457–9492.

14 M. N. Hopkinson, C. Richter, M. Schedler and F. Glorius, *Nature*, 2014, 510, 485–496.

15 S. Díez-González and S. P. Nolan, *Coord. Chem. Rev.*, 2007, **251**, 874–883.

16 P. de Frémont, N. Marion and S. P. Nolan, *Coord. Chem. Rev.*, 2009, 253, 862–892.

17 R. R. Schrock and J. D. Fellmann, *J. Am. Chem. Soc.*, 1978, **100**, 3359–3370.

18 J. K. C. Abbott, T. Li and Z. L. Xue, *J. Am. Chem. Soc.*, 2009, **131**, 8246–8251.

19 R. R. Schrock and C. Copéret, *Organometallics*, 2017, **36**, 1884–1892.

20 S. Halbert, C. Copéret, C. Raynaud and O. Eisenstein, *J. Am. Chem. Soc.*, 2016, **138**, 2261–2272.

21 J. M. Boncella, M. L. Cajigal and K. A. Abboud, *Organometallics*, 1996, **15**, 1905–1912.

22 A. Ligands, L. Li, M. Hung and Z. Xue, *Compr. Organomet. Chem.*, 1995, **117**, 243.

23 P. A. Petrov, T. S. Sukhikh and M. N. Sokolov, *Dalt. Trans.*, 2017, **46**, 4902–4906.

24 M. Bortoluzzi, E. Ferretti, F. Marchetti, G. Pampaloni and S. Zacchini, 2016, **45**, 6939.

25 Z. Wei, W. Zhang, G. Luo, F. Xu, Y. Mei and H. Cai, *New J. Chem.*, 2016, **40**, 6270–6275.

26 L. P. Spencer, C. Beddie, M. B. Hall and M. D. Fryzuk, *J. Am. Chem. Soc.*, 2006, **128**,

12531–12543.

27 P. L. Arnold, T. Cadenbach, I. H. Marr, A. A. Fyfe, N. L. Bell, R. Bellabarba, R. P. Tooze and J. B. Love, *Dalt. Trans.*, 2014, **43**, 14346–14358.

28 M. Oishi, M. Oshima and H. Suzuki, *Inorg. Chem.*, 2014, **53**, 6634–6654.

29 A. J. Schultz, J. M. Williams, R. R. Schrock, G. A. Rupprecht and J. D. Fellmann, *J. Am. Chem. Soc.*, 1979, **101**, 1593–1595.

30 A. J. Schultz, R. K. Brown, J. M. Williams and R. R. Schrock, *J. Am. Chem. Soc.*, 1981, **103**, 172-176.

31 A. J. Schultz, R. K. Brown, J. M. Williams and R. R. Schrock, *J. Am. Chem. Soc.*, 1981, **103**, 169–176.

32 B. F. Straub, *Angew. Chemie Int. Ed.*, 2005, **44**, 5974–5978.

33 T. M. Trnka, J. P. Morgan, M. S. Sanford, T. E. Wilhelm, M. Scholl, T. L. Choi, S. Ding, M. W. Day and R. H. Grubbs, *J. Am. Chem. Soc.*, 2003, **125**, 2546–2558.

34 M. Scholl, S. Ding, C. W. Lee and R. H. Grubbs, *Org. Lett.*, 1999, **1**, 953–956.

35 R. J. Goddard, R. Hoffmann and E. D. Jemmis, *J. Am. Chem. Soc.*, 1980, **102**, 7667–7676.

36 J. A. Van Doom, H. Van Der Heijden and A. G. Orpen, *Organometallics*, 1994, **13**, 4271-4277.

37 M. E. Garner, B. F. Parker, S. Hohloch, R. G. Bergman and J. Arnold, *J. Am. Chem. Soc.*, 2017, **139**, 12935–12938.

38 M. J. Chilvers, R. F. R. Jazzar, M. F. Mahon and M. K. Whittlesey, *Adv. Synth. Catal.*, 2003, **345**, 1111–1114.

39 D. Giunta, M. Hölscher, C. W. Lehmann, R. Mynott, C. Wirtz and W. Leitner, *Adv. Synth. Catal.*, 2003, **345**, 1139–1145.

40 R. Dorta, E. D. Stevens and S. P. Nolan, *J. Am. Chem. Soc.*, 2004, **126**, 5054–5055.

41 C. Camp and J. Arnold, *Dalt. Trans.*, 2016, **45**, 14462–14498.

42 R. Jiao, M. Xue, X. Shen, Y. Zhang, Y. Yao and Q. Shen, *Eur. J. Inorg. Chem.*, 2011, **2011**, 1448–1453.

43 M. P. Shaver and M. D. Fryzuk, *Organometallics*, 2005, **24**, 2606–2611.

44 X. Yu, S. Bi, I. A. Guzei, Z. Lin and Z. L. Xue, *Inorg. Chem.*, 2004, **43**, 7111–7119.

45 B. M. Kriegel, R. G. Bergman and J. Arnold, *Dalt. Trans.*, 2014, **43**, 10046.

46 M. Chabanas, E. A. Quadrelli, B. Fenet, C. Copéret, J. Thivolle-Cazat, J.-M. Basset, A. Lesage and L. Emsley, *Angew. Chemie Int. Ed.*, 2001, **40**, 4493.

47 L. L. Anderson, J. A. R. Schmidt, J. Arnold and R. G. Bergman, *Organometallics*, 2006, **25**, 3394–3406.

48 A. J. Arduengo, J. R. Goerlich and W. J. Marshall, *Angew. Chem., Int. Ed. Engl*, 1995, **117**,

2518.

49 P. L. Arnold, I. J. Casely, Z. R. Turner and C. D. Carmichael, *Chem. - A Eur. J.*, , DOI:10.1002/chem.200801321.

50 T. R. Helgert, X. Zhang, H. K. Box, J. A. Denny, H. U. Valle, A. G. Oliver, G. Akurathi, C. E. Webster and T. K. Hollis, *Organometallics*, 2016, **35**, 3452–3460.

51 T. R. Helgert, T. K. Hollis, A. G. Oliver, H. U. Valle, Y. Wu and C. E. Webster, *Organometallics*, 2014, **33**, 40.

52 C. Camp, L. Maron, R. G. Bergman and J. Arnold, *J. Am. Chem. Soc.*, 2014, **136**, 17652–17661.

53 M. Srebro and A. Michalak, *Inorg. Chem*, 2009, **48**, 5361–5369.

54 I. Peñ, I. M. Pastor, M. Yus, M. A. Esteruelas and M. O. Oliván, *Organometallics*, , DOI:10.1021/om300498e.

55 A. Di Giuseppe, R. Castarlenas, J. J. Pérez-Torrente, F. J. Lahoz and L. A. Oro, *Chem. - A Eur. J.*, 2014, **20**, 8391–8403.

56 I. Peñafiel, I. M. Pastor, M. Yus, M. A. Esteruelas and M. Oliván, *Organometallics*, 2012, **31**, 6154–6161.

57 A. Raja Naziruddin, A. Hepp, T. Pape and F. Ekkehardt Hahn, *Organometallics*, 2011, **30**, 50.

58 V. Gierz, A. Urbanaite, A. Seyboldt and D. Kunz, *Organometallics*, 2012, **31**, 7532–7538.

59 G. González Miera, E. Martínez-Castro and B. Martín-Matute, *Organometallics*, 2018, **37**, 636–644.

60 I. Peñafiel, I. M. Pastor, M. Yus, M. A. Esteruelas and M. Oliván, *Organometallics*, 2012, **31**, 6154–6161.

61 G. Lázaro, F. J. Fernández-Alvarez, M. Iglesias, C. Horna, E. Vispe, R. Sancho, F. J. Lahoz, M. Iglesias, J. J. Pérez-Torrente and L. A. Oro, *Catal. Sci. Technol.*, 2014, **4**, 62–70.

62 J. P. Morales-Cerón, P. Lara, J. López-Serrano, L. L. Santos, V. Salazar, E. Álvarez and A. Suárez, *Organometallics*, 2017, **36**, 2460–2469.

63 E. Peris, *Chem. Rev.*, 2018, **118**, 9988–10031.

64 M. V. Jiménez, J. J. Pérez-Torrente, M. I. Bartolomé, V. Gierz, F. J. Lahoz and L. A. Oro, *Organometallics*, 2008, **27**, 224–234.

65 G. González Miera, E. Martínez-Castro and B. Martín-Matute, *Organometallics*, 2018, **37**, 636–644.

66 J. P. Morales-Cerón, P. Lara, J. López-Serrano, L. L. Santos, V. Salazar, E. Álvarez and A. Suárez, *Organometallics*, 2017, **36**, 2460–2469.

67 E. Peris, *Chem. Rev.*, 2018, **118**, 9988–10031.

68 E. Lindner, Q. Wang, H. A. Mayer, R. Fawzi and M. Steimann, *Organometallics*, 1993, **12**, 1865–1870.

69 R. Bini, C. Chiappe, F. Marchetti, G. Pampaloni and S. Zacchini, *Inorg. Chem.*, 2010, **49**, 339–351.

70 A. J. Cresswell, S. G. Davies, P. M. Roberts and J. E. Thomson, *Chem. Rev.*, 2015, **115**, 566–611.

71 E. Tomat, L. Cuesta, V. M. Lynch and J. L. Sessler, *Inorg. Chem.*, 2007, **46**, 6224–6226.

72 Charles H. Winter, Xiao-Xing Zhou, and Mary Jane Heeg, *Chem. Commun.*, 1992, **31**, 1808-1815.

73 R. Hage, R. Prins, J. G. Haasnoot, J. Reedijk and J. G. Vos, *J. Chem. Soc. Dalt. Trans.*, 1987, 1389–1395.

74 R. Srivastava, R. Moneuse, J. Petit, P.-A. Pavard, V. Dardun, M. Rivat, P. Schiltz, M. Solari, E. Jeanneau, L. Veyre, C. Thieuleux, E. A. Quadrelli and C. Camp, *Chem. - A Eur. J.*, 2018, **24**, 4361–4370.

75 M. Chabanas, E. A. Quadrelli, B. Fenet, C. Copéret, J. Thivolle-Cazat, J. M. Basset, A. Lesage and L. Emsley, *Angew. Chemie - Int. Ed.*, 2001, **40**, 4493–4496.

76 J. S. Freundlich, R. R. Schrock, C. C. Cummins and W. M. Davis, *J. Am. Chem. Soc.*, 1994, **116**, 6476-6477.

77 J. A. R. Schmidt, S. A. Chmura and J. Arnold, *Organometallics*, 2001, **20**, 1062–1064.

78 S. C. Hunter, S. J. Chen, C. A. Steren, M. G. Richmond and Z. L. Xue, *Organometallics*, 2015, **34**, 5687–5696.

79 J. Won Park, L. M. Henling, W. P. Schaefer, R. H. Grubbs, M. Beckman, W. J. Am, A. J. J Chem Soc, Y. J. Am, van Koten and R. H. Pure Appl, *Organometallics*, 1991, **10**, 171-175.

80 P. B. Mackenzie, R. J. Coots, R. H. Grubbs and M. Beckman, *Organometallics*, 1989, **8**, 8-14.

81 M. J. Hostetler and R. G. Bergman, *J. Am. Chem. Soc.*, 1990, **112**, 8621–8623.

82 A. E. Findlay, S. Leelasubcharoen, L. G. Kuzmina, J. A. K. Howard and G. I. Nikonov, *Dalt. Trans.*, 2010, **39**, 9264.

83 M. A. Huertos, J. Pérez, L. Riera, J. Díaz and R. López, *Chem. - A Eur. J.*, 2010, **16**, 8495–8507.

84 D. Mendoza-Espinosa, B. Donnadieu and G. Bertrand, *J. Am. Chem. Soc.*, 2010, **132**, 7264–7265.

85 P. K. Majhi, S. C. Serin, G. Schnakenburg, D. P. Gates and R. Streubel, *Eur. J. Inorg. Chem.*, 2014, **2014**, 4975–4983.

EXPERIMENTAL SECTION

All the manipulations were performed under purified argon atmosphere unless mentioned otherwise. Either schlenk line technique or an MBraun glovebox was used to provide the inert argon atmosphere. All the glassware, cannulae, silica filters, glass syringes and needles were dried overnight (15 hr) at 110°C in the oven and assembled while hot under vacuum to perform the reaction. Pentane, toluene, tetrahydrofuran (THF) and diethyl ether were collected from Solvent purification system (SPS). Here all these solvents were already pre-dried by a passage through the activated alumina column. Then the solvents were dried over Na/benzophenone until the color changes to dark purple. Following which they were distilled under vacuum and then degassed to yield ready-to-use dry solvents. Dichloromethane (DCM) was dried over CaH_2 and vacuum distilled and degassed. Deuterated solvents like THF-d_8, C_6D_6, toluene-d_8 were dried over Na/benzophenone, vacuum distilled and degassed before using. $CDCl_3$ and CD_2Cl_2 were dried over CaH_2, vacuum distilled and then degassed prior to using them for NMR spectrum acquisition. Tantalum precursors; $[Ta(CH^tBu)(CH_2{}^tBu)_3]$ was prepared according to available literature procedures.[17] All other reagents used were commercially available and they were used as received. Bruker AV-300, AVQ-400 and AV-500 spectrometers were used to record the NMR. All the chemical shifts were measured relative to the corresponding residual peak of the deuterated solvents; which in turn were assigned relative to an external TMS standard set at 0.00 ppm. ^{19}F and ^{31}P chemical shifts were assigned relative to the external standard $BF_3.OEt_2$ and Ph_3PO respectively. ^1H, ^{13}C, COSY, HSQC and HMBC NMR spectrum were thoroughly analyzed to assign the ^1H and ^{13}C peaks. IR spectrum was recorded using a Nicolet 6700 FT-IR spectrometer. Samples for recording IR spectrum were prepared in a DRIFT cell equipped with KBr dome under argon atmosphere. Samples were either send to the school of Human sciences, Science centre, London Metropolitan University or to Mikroanalytisches Labor Pascher, Germany for elemental analysis. X-Ray diffraction was performed at Centre de Diffractometrie Henri Longchambon-ISA, Université de Lyon. All the details regarding X-Ray diffraction are provided in the supporting information.

Synthesis of Tantalum-NHC complex [Ta(L)(CH^{t}Bu)(CH$_2$^{t}Bu)$_2$]:

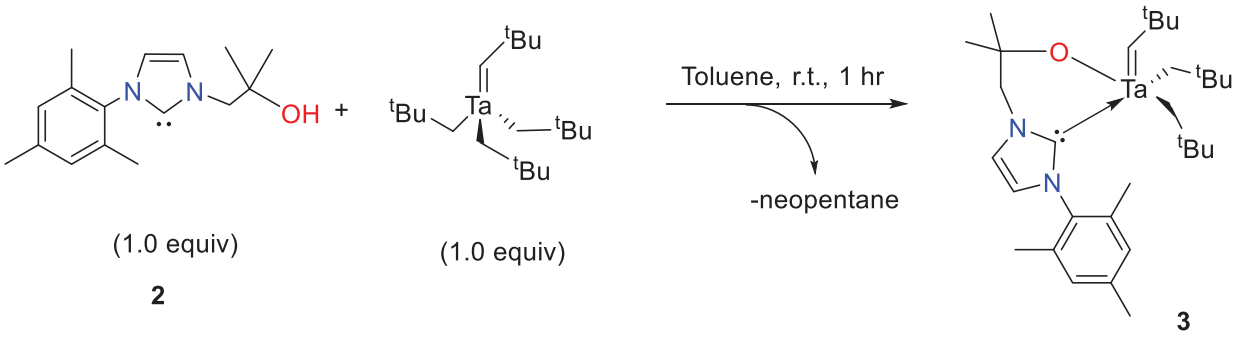

(1.0 equiv)

2

(1.0 equiv)

3

A 15 mL orange toluene suspension of ligand (0.5 g, 1.935 mmol, 1.0 equiv) was added drop wise to a 10 mL reddish brown toluene solution of Tantalum precursor (0.902 g, 1.935 mmol, 1.0 equiv). The reaction mixture was stirred for 1.0 hr. Then the solvent was evaporated to give yellow powder which was dissolved in 4.0 mL of pentane, filtered and stored at -40°C to yield orange crystals. The compound was recovered and dried to give compound **3** (0.793 g, 1.21 mmol, 62.9 %). Single crystals suitable for crystal structure were grown in similar manner.

^{1}H NMR (300 MHz, C$_6$D$_6$, 293 K): δ =6.74 (s, 2H; m-CH$_{Mes}$), 6.03 (d, $^3J_{HH}$=1.7 Hz, 1H; CH$_{imid}$), 5.99 (d, $^3J_{HH}$=1.7 Hz, 1H; CH$_{imid}$), 4.85 (s, 1H; TaCH^{t}Bu), 3.36 (s, 2H; NCH$_2$), 2.10 (s, 3H; p-CH$_{3,Mes}$), 2.05 (s, 6H; o-CH$_{3,Mes}$), 1.40 (s, 18H; CH$_2$^{t}Bu), 1.33 (s, 9H; CH^{t}Bu), 1.07 (s, 6H; CH$_3$), 1.05 (br d,$^2J_{HH}$=12.2 Hz, 2H; TaCH2), 0.76 ppm (br d, 2JHH=12.2 Hz, 2H; TaCH$_2$);

^{13}C{^{1}H} NMR (101 MHz, C$_6$D$_6$, 293 K): δ =250.4 (Ta=CHtBu), 203.1 (Ta=C$_{imid}$), 138.8 (C$_{Ar}$), 137.2 (C$_{Ar}$), 135.1 (C$_{Ar}$), 129.8 (CH$_{Ar}$), 122.1 (CH$_{imid}$), 121.5 (CH$_{imid}$), 88.9 (Ta-CH$_2$^{t}Bu), 75.5 (OC), 63.3 (NCH$_2$), 44.3 (Ta-CH*C*(Me)$_3$), 36.3 (Ta-CH$_2$*C*(CH$_3$)$_3$), 35.2 (Ta- CH$_2$*C*(Me)$_3$), 35.2 (Ta-CH*C*(CH$_3$)$_3$), 27.0 (CH$_3$), 21.0 (CH$_{3,Mes}$), 19.6 ppm (CH$_{3,Mes}$);

DRIFT (25°C, KBr solid solution under argon): $\tilde{\nu}$ =3171.9 (w, ν$_{C-H}$), 3138.6 (w, ν$_{C-H}$), 2950.7 (s, ν$_{C-H}$), 2937.4 (s, ν$_{C-H}$), 2893.0 (m, ν$_{C-H}$), 2859.1 (m, ν$_{C-H}$), 2786.2 (m, ν$_{C-H}$), 2718.3 (m, ν$_{C-H}$), 1608.0 (w), 1553.6 (w), 1488.9 (m), 1466.9 (m), 1457.4 (m), 1405.7 (m), 1374.1 (m), 1356.9 (s), 1328.4 (w), 1277.6 (w), 1254.8 (m), 1224.6 (s), 1208.5 (s), 1190.2 (m), 1170.7 (w), 1140.2 (m), 1102.1 (w), 1035.5 (w), 1006.7 (s), 963.4 (s), 925.9 (w), 858.0 (m), 800.7 (m), 793.9 (m), 729.8 (s), 689.5 (m), 641.4 (w), 606.5 (m), 591.9 (m), 582.6 cm^{-1} (m). **Due to thermal instability of the compound; elemental analysis was not performed.**

Synthesis of [Ta(L*)(CH^{t}Bu)(CH$_2$^{t}Bu)]:

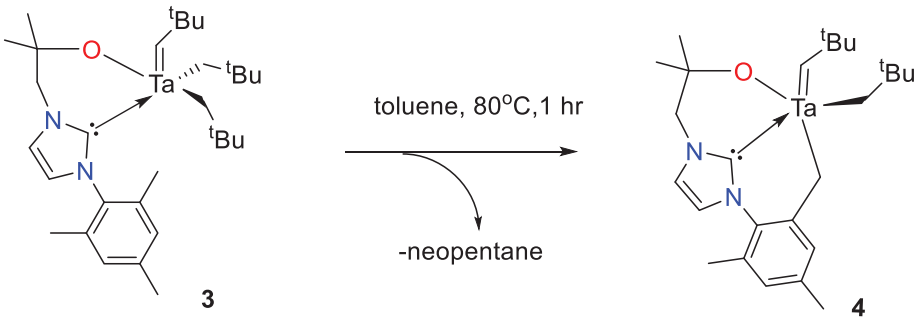

An intense yellow toluene solution (20 mL) of Ta-NHC complex **3** (0.407 g, 0.625 mmol, 1.0 equiv) was heated at 80°C for 1 hr. The color of the solution changes to dark red. Vacuum evaporation of the solvent lead to dark brown solid compound (0.3 g, 83 %). Single crystals suitable for crystal structure were grown by slow recrystallization of the compound at -40°C over a period of six months.

^{1}H NMR (300 MHz, C$_6$D$_6$, 293 K): δ =7.07 (s, 1H; m-CH$_{Mes}$), 6.65 (d, $^3J_{HH}$=1.8 Hz, 1H; CH$_{imid}$), 6.48 (s, 1H; m-CH$_{Mes}$), 6.16 (d, $^3J_{HH}$=1.8 Hz, 1H; CH$_{imid}$), 4.60 (s, 1H; TaCH^{t}Bu), 3.29 (d, $^2J_{HH}$=13.1 Hz, 1H; NCH$_2$), 3.03 (d, $^2J_{HH}$=13.1 Hz, 1H; NCH$_2$), 2.41 (d, $^2J_{HH}$=13.6 Hz, 1H; Ta-CH$_2$-Ar), 2.13 (s, 3H; o-CH$_{3,Mes}$), 1.98 (s, 3H; p-CH$_{3,Mes}$), 1.85 (d, $^2J_{HH}$=13.6 Hz, 1H; Ta-CH$_2$^{t}Bu), 1.58 (d, $^2J_{HH}$=13.7 Hz, 1H; Ta-CH$_2$-Ar), 1.54 (s, 9H; CH$_2$^{t}Bu), 1.25 (d, $^2J_{HH}$=13.7 Hz, 2H; Ta-CH$_2$-^{t}Bu), 1.18 (s, 3H; CH$_3$), 1.14 (s, 3H; CH$_3$), 1.05 ppm (s, 9H; CH^{t}Bu);

^{13}C{^{1}H} NMR (101 MHz, C$_6$D$_6$,293 K): δ =252.2 (Ta=CH^{t}Bu), 205.2 (Ta=C$_{imid}$), 148.4 (C$_{Ar}$), 137.4 (C$_{Ar}$), 133.2 (C$_{Ar}$), 127.4 (C$_{Ar}$), 126.0 (CH$_{Ar}$), 125.9 (CH$_{Ar}$), 121.4 (CH$_{imid}$), 119.6 (CH$_{imid}$), 83.6 (Ta-*C*H$_2$^{t}Bu), 76.9 (OC), 61.1 (NCH$_2$), 60.4 (Ta-CH$_2$Ar), 44.4 (Ta-CH*C*(Me)$_3$), 36.7 (C(*C*H$_3$)$_3$), 34.7 (C(*C*H$_3$)$_3$), 34.6 (Ta-CH$_2$*C*(Me)$_3$), 28.9 (CH$_3$), 28.2 (CH$_3$), 21.2 (CH$_{3,Mes}$), 19.6 ppm (CH$_{3,Mes}$);

DRIFT (25°C, KBr solid solution under argon): $\tilde{\nu}$ =3188.3 (w, ν$_{C-H}$), 3140.2 (w, ν$_{C-H}$), 3018.7 (w, ν$_{C-H}$), 2965.8 (s, ν$_{C-H}$), 2947.0 (s, ν$_{C-H}$), 2930.3 (s, ν$_{C-H}$), 2889.9 (s, ν$_{C-H}$), 2848.3 (s, ν$_{C-H}$), 2806.3 (m, ν$_{C-H}$), 2751.3 (w, ν$_{C-H}$), 2737.7 (w, ν$_{C-H}$), 1600.4 (w), 1589.2 (w), 1559.8 (w), 1549.2 (w), 1478.9 (s), 1468.7 (s), 1456.9 (s), 1413.2 (m), 1394.9 (w), 1380.1 (m), 1367.6 (m), 1352.6 (s), 1336.0 (m), 1303.3 (w), 1283.0 (w), 1244.4 (m), 1214.3 (s), 1193.4 (m), 1171.5 (w), 1145.4 (m), 1110.8 (m), 1089.5 (w), 1038.4 (m), 1012.8 (m), 1004.1 (m), 985.7 (s), 958.5 (s), 930.4 (w), 905.5 (w), 882.5 (w), 843.0 (m), 827.2 (w), 804.8 (m), 790.4 (w), 775.4 (w), 737.9 (w), 725.3 (s), 690.0 (m), 665.2 (w), 625.3 (m), 617.0 (m), 607.4 (m), 560.9 cm^{-1} (w);

Elemental analysis calculated (%) for $C_{26}H_{41}N_2OTa$: C 53.98, H 7.14, N 4.84; found: C 53.81, H 7.16, N 4.87.

Synthesis of tantalum imido alkylidene complex [Ta(L)(CH^{t}Bu)(CH$_2$^{t}Bu)$_2$]:

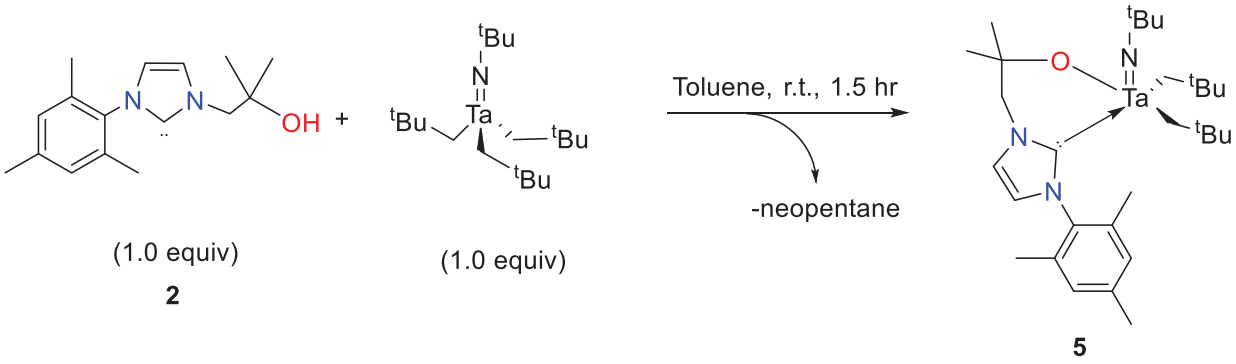

(1.0 equiv) **2** (1.0 equiv) **5**

A 8 mL toluene suspension of HL (**2**) (300 mg, 1.16 mmol, 1 eq.) was added dropwise to a 10 mL toluene solution of Ta(N^{t}Bu)(CH$_2$^{t}Bu)$_3$ (540 mg, 1.16 mmol, 1 eq.). The reaction mixture was stirred at room temperature for 90 min., yielding a yellow solution. The volatiles were removed *in vacuo* and the solid residue was extracted with 2 mL pentane, filtered and stored at -40°C for 16h. This produced yellow crystals that were recovered, washed with 0.4 mL pentane and dried *in vacuo* to yield Ta(L)(N^{t}Bu)(CH$_2$^{t}Bu)$_2$ (**3**) as pale yellow crystalline solid (562 mg, 0.86 mmol, 74 %). Single crystals suitable for X-ray diffraction were grown in a similar fashion.

^{1}H NMR (400 MHz, C_6D_6, 293K): δ = 6.71 (s, 2H, *m*-CH$_{Mes}$), 6.03 (d, $^3J_{HH}$ = 1.7 Hz, 1H, CH$_{imid}$), 5.88 (d, $^3J_{HH}$ = 1.7 Hz, 1H, CH$_{imid}$), 3.52 (s, 2H, NCH$_2$), 2.11 (s, 3H, *p*-CH$_{3Mes}$), 1.93 (s, 6H, *o*-CH$_{3Mes}$), 1.54 (s, 9H, N^{t}Bu), 1.38 (s, 18H, CH$_2$^{t}*Bu*), 1.12 (s, 6H, CH$_3$), 0.94 (d, $^3J_{HH}$ = 13.7 Hz, 2H, TaC*H*$_2$), 0.80 (d, $^3J_{HH}$ = 13.7 Hz, 2H, TaC*H*$_2$). ^{1}H NMR (300 MHz, THF-d_8, 293K) δ = 7.34 (d, $^3J_{HH}$ = 1.6 Hz, 1H, CH$_{imid}$), 7.00 (d, $^3J_{HH}$ = 1.6 Hz, 1H, CH$_{imid}$), 6.97 (s, 2H, *m*-CH$_{Mes}$), 4.15 (s, 2H, NCH$_2$), 2.30 (s, 3H, *p*-CH$_{3Mes}$), 2.03 (s, 6H, *o*-CH$_{3Mes}$), 1.27 (s, 9H, N^{t}Bu), 1.20 (s, 6H, CH$_3$), 0.91 (s, 18H, CH$_2$^{t}*Bu*), 0.47 (d, $^2J_{HH}$ = 13.7 Hz, 2H, TaC*H*$_2$), 0.38 (d, $^2J_{HH}$ = 13.7 Hz, 2H, TaC*H*$_2$).

^{13}C{^{1}H} NMR (101 MHz, C_6D_6, 293K): δ = 196.7 (Ta=*C*$_{imid}$), 139.0 (*C*$_{Ar}$), 136.9 (*C*$_{Ar}$), 135.1 (*C*$_{Ar}$), 129.5 (*C*H$_{Ar}$), 122.1 (*C*H$_{imid}$), 121.4 (*C*H$_{imid}$), 88.0 (Ta-*C*H$_2$^{t}Bu), 74.9 (O*C*), 65.9 (N*C*(CH$_3$)$_3$), 64.8 (N*C*H$_2$), 36.2 (Ta-CH$_2$*C*(CH$_3$)$_3$), 35.2 (Ta-CH$_2$*C*(CH$_3$)$_3$), 34.6 (NC(*C*H$_3$)$_3$), 27.5 (*C*H$_3$), 20.9 (*C*H$_{3Mes}$), 18.1 (*C*H$_{3Mes}$).

DRIFT (25°C, KBr solid solution under argon): 3164.9 (w, ν$_{C-H}$), 3132.9 (w, ν$_{C-H}$), 2967.7 (s, ν$_{C-H}$), 2948.5 (s, ν$_{C-H}$), 2934.9 (s, ν$_{C-H}$), 2892.9 (m, ν$_{C-H}$), 2860.4 (m, ν$_{C-H}$), 2794.7 (m, ν$_{C-H}$), 1609.5 (w), 1546.9 (w), 1489.4 (m), 1452.3 (m), 1405.3 (m), 1372.1 (m), 1356.3 (s), 1351.7 (s), 1333.1 (w),

1278.6 (s), 1252.9 (m), 1221.6 (s), 1213.4 (s), 1205.7 (s), 1185.5 (m), 1167.7 (w), 1135.7 (m), 1098.1 (m), 1007.9 (s), 998.2 (s), 957.9 (m), 932.3 (w), 852.7 (m), 794.3 (m), 770.1 (w), 743.9 (w), 726.8 (s), 682.5 (m), 645.4 (w), 583.3 (m), 573.5 (m).

Elemental analysis for $C_{30}H_{52}N_3OTa$: C, 55.29; H, 8.04; N, 6.45. Found: C, 55.30; H, 8.09; N, 6.41.

Synthesis of [Rh(HL)(cod)(Cl)]:

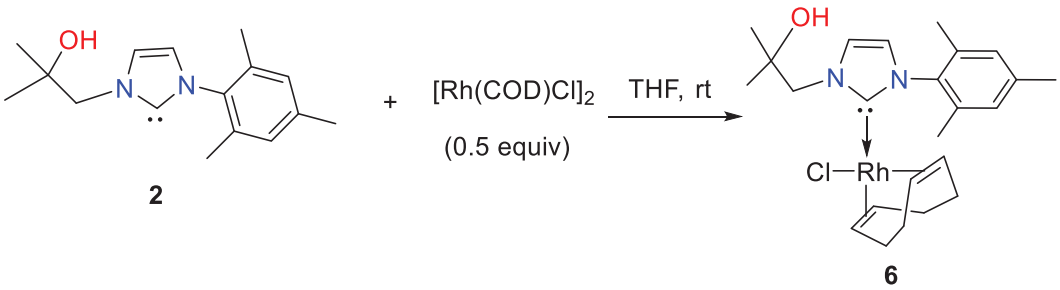

In a 20 mL vial NHC (300 mg, 1.18 mmol, 2.0 equiv) was dissolved in 9 ml of THF to yield a yellow color solution. In another 20 mL vial Rhodium precursor (0.286 g, 0.59 mmol, 1.0 equiv) was dissolved in 8 ml of THF. The NHC solution was added drop-wise to the Rhodium metal precursor solution by a 2.0 ml glass pipette. The reaction was allowed to stir over the weekend inside the glovebox. The reaction mixture was concentrated to half of its volume i.e., approximately 8 mL. A two layer recrystallization with Pentane (6 mL) at -40°C yielded the desired complex as yellow powder (0.481 g, 0.88 mmol, 75.27 % yield). Single crystals suitable for recrystallization were also grown in similar fashion.

^{1}H NMR (300 MHz, $CDCl_3$, 293 K): δ =7.35 (d, $^3J_{HH}$=1.6 Hz, 1H; CH_{imid}), 7.00 (s, 2H; m-CH_{Mes}), 6.75 (d, $^3J_{HH}$=1.6 Hz, 1H; CH_{imid}), 4.87 (s, 2H; N_{CH_2}), 4.83 (s, 2H; cod), 3.22 (s, 2H; cod), 3.17 (s, 1H; OH), 2.37 (s, 3H; p-$CH_{3,Mes}$), 2.13 (s, 6H; o-$CH_{3,Mes}$), 2.10–1.60 (brm, 8H; cod), 1.41 ppm (s, 6H; CH_3);

^{13}C{^{1}H} NMR (101 MHz, $CDCl_3$, 293 K): δ = 181.9 (d, J_{Rh-C}=52 Hz, Rh-$C_{carbene}$), 138.6 (CAr), 136.1 (CAr), 135.7 (CAr), 128.8 (CHAr), 122.9 (CH_{imid}), 122.2 (CH_{imid}), 97.1 (d, J_{Rh-C}=7 Hz, CH_{cod}), 70.2 (OC), 68.3 (d, J_{Rh-C} = 14 Hz, CH_{cod}), 61.4 (NCH_2), 32.7 ($CH_{2,cod}$), 28.5 (CH_3), 28.4 ($CH_{2,cod}$), 21.0 (o-$CH_{3,Mes}$), 18.6 ppm (p-$CH_{3,Mes}$);

DRIFT (25°C, KBr solid solution under argon): $\tilde{\nu}$ =3367.8 (s, ν_{O-H}), 3178.5 (w, ν_{C-H}), 3140.5 (m, ν_{C-H}), 3110.2 (w, ν_{C-H}), 3023.6 (w, ν_{C-H}), 2992.2 (m, ν_{C-H}), 2965.3 (s, ν_{C-H}), 2933.4 (s, ν_{C-H}), 2916.2 (s, ν_{C-H}), 2879.3 (s, ν_{C-H}), 2830.0 (m, ν_{C-H}), 1606.8 (w), 1570.6 (w), 1522.8 (w), 1489.2 (s),

1475.7 (s), 1435.6 (s), 1402.1 (s), 1377.9 (s), 1362.2 (m), 1339.9 (m), 1296.3 (m), 1252.4 (s), 1219.7 (s), 1203.6 (s), 1175.9 (s), 1168.9 (s), 1146.9 (s), 1105.3 (w), 1082.0 (m), 1027.3 (m), 1005.1 (w), 992.9 (m), 976.0 (m), 966.5 (m), 931.6 (m), 914.3 (m), 896.0 (s), 888.3 (s), 859.5 (s), 838.0 (m), 815.2 (s), 773.3 (s), 766.9 (m), 743.3 (s), 735.0 (s), 702.3 (s), 685.5 (w), 642.9 (w), 611.3 (w), 592.2 (s), 574.8 cm^{-1} (s);

Elemental analysis calculated (%) for $C_{24}H_{34}ClN_2ORh$: C 57.09, H 6.79, N 5.55; found: C 56.84, H 7.26, N 5.62.

Generation of Rhodium Cationic species: ***Note the reaction is performed in dark conditions***

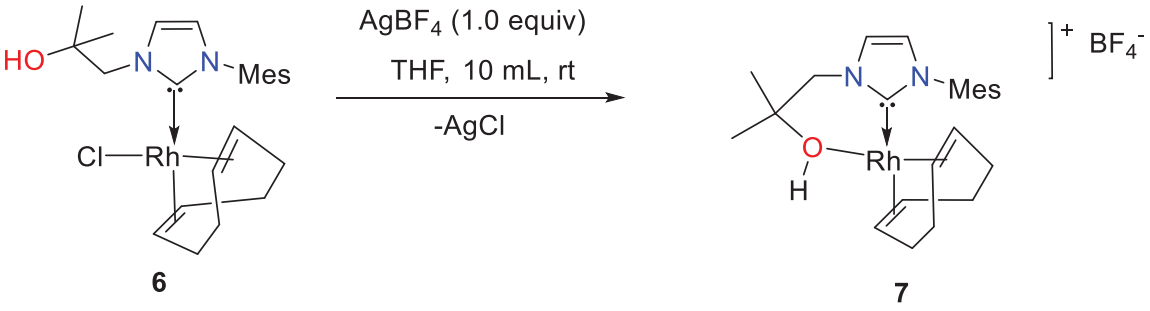

6 7

The Rhodium NHC precursor [Rh(HL)(COD)(Cl)] (480 mg, 0.95 mmol, 1.0 equiv) was mixed with Silver tetrafluoroborate (184.9 mg, 0.95 mmol, 1.0 equiv) and 10 mL of THF was added to it. Formation of white precipitate is observed. The reaction mixture is stirred for 1.0 hr at room temperature. After that the ppt. was removed by filtration. The resultant yellow filtrate was concentrated, filtered and stored at -40°C. This yielded yellow crystals which were recovered and dried in vacuo to give $[Rh(HL)(COD)]^+BF_4^-$ as yellow crystalline solid (408 mg, 0.73 mmol, 77%). Single crystals suitable for X-Ray diffraction were grown in same manner.

^{1}H NMR (400 MHz, $CDCl_3$, 298K): δ= 7.08 (d, $^3J_{HH}$ = 1.76 Hz, 1H; CH_{imid}), 7.03 (s, 2H; m-CH_{mes}), 6.78 (d, $^3J_{HH}$ = 1.76 Hz, 1H; CH_{imid}), 5.75 (s, 1H; OH), 4.84 (s, 2H; COD), 4.33 (s, 2H; NCH_2), 3.17-3.12 (br m, 2H; COD), 2.37 (s, 3H; *p*-$CH_{3,mes}$), 2.29-2.19 (br m, 2H; COD), 2.16 (s, 6H; *o*-$CH_{3,mes}$), 2.05-1.95 (br m, 2H; COD), 1.81-1.73 (br m, 2H; COD), 1.70-1.63 (br m, 2H; COD), 1.30 (s, 6H; CH_3);

^{13}C{^{1}H} NMR (100 MHz, $CDCl_3$, 298K): δ = 174.58 (d, J_{Rh-C} = 52 Hz; Rh-$C_{carbene}$), 139.88 (C_{Ar}), 135.42 (C_{Ar}), 135.21 (C_{Ar}), 129.37 (CH_{Ar}), 123.36 (CH_{imid}), 122.92 (CH_{imid}), 99.95 (d, J_{Rh-C} = 7 Hz, CH_{COD}), 72.25 (OC), 68.14 (THF), 67.91 (d, J_{Rh-C} = 16 Hz, CH_{COD}), 61.33 (NCH_2), 32.97 ($CH_{2,COD}$), 28.10 (CH_3), 25.78 (THF), 24.95 ($CH_{2,COD}$), 21.26 (*o*-$CH_{3,mes}$), 18.51 (*p*-$CH_{3,mes}$);

$^{19}F\{^1H\}$ NMR (376.45 MHz, $CDCl_3$, 299 K): δ = -150.27 ppm (s, $^{10}BF_4^-$), -150.32 (s, $^{11}BF_4^-$); $^{11}B\{^1H\}$ NMR (96.29 MHz, $CDCl_3$, 293 K): δ = -1.05 ppm (s);

DRIFT (25°C, KBr solid solution under Argon): $\tilde{\nu}$ = 3349.4 (s, ν_{O-H}), 3157.7 (m, ν_{C-H}), 3132.2 (m, ν_{C-H}), 2973.5 (s, ν_{C-H}), 2935.1 (s, ν_{C-H}), 2922.9 (s, ν_{C-H}), 2874.3 (s, ν_{C-H}), 2829.3 (s, ν_{C-H}), 1608.7 (w), 1490.1 (s), 1450.9(s), 1412.7 (s), 1392.0 (s), 1373.3 (m), 1348.5 (w), 1305.3 (w), 1259.1 (w), 1224.6 (m), 1192.4 (m), 1142.7 (s), 1111.8 (s), 1084.1 (s), 967.9 (s), 912.9 (w), 887.2 (m), 865.6 (m), 775.7 (m), 762.5 (s), 703.2 (w), 587.2 (w), 518.8 (m), 494.2 cm^{-1} (m);

Elemental analysis calculated (%) for $C_{24}H_{34}N_2ORhBF_4$: C 51.82, H 6.16, N 5.04; found: C 51.93, H 6.25, N 5.12.

Chemistry of Rhodium cationic species with Potassium bis (trimethylsilyl) amide {KHMDS}:

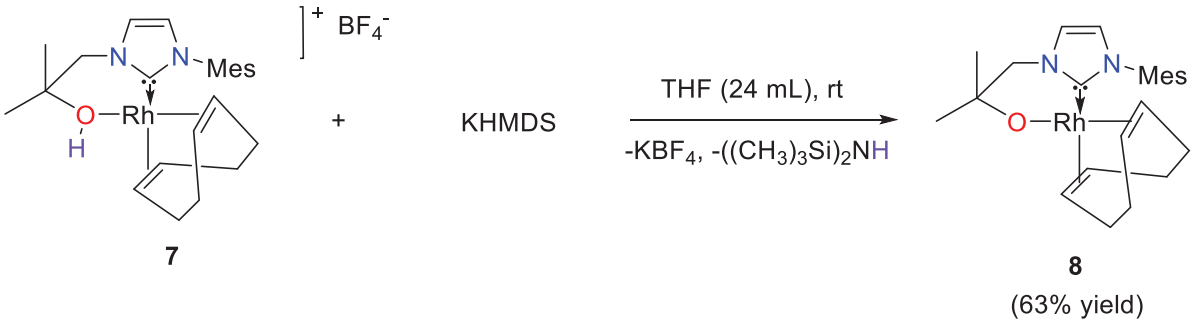

A colorless THF solution (6 mL) of KHMDS (47.33 mg, 0.237 mmol, 1.0 equiv) was added drop-wise to a stirring yellow THF solution (16 mL) of $[Rh(HL)(COD)]^+BF_4^-$ (132 mg, 0.237 mmol, 1.0 equiv). The color of the reaction mixture changes to greenish yellow instantaneously. The reaction mixture was stirred at room temperature for 1.0 hr. After that the solution was evaporated to give yellow powder. It was then dissolved in minimum amount of THF (4 mL), layered with pentane (10 mL) and stored at -40°C. This yielded shiny rectangular shaped yellow crystals which were dried in vacuo to produce RhLCOD (70 mg, 0.15 mmol, 63%). Single crystals suitable for X-Ray diffraction were grown by the diffusion of Pentane (10.0 mL) into a concentrated THF solution of the compound (4.0 mL) at -40°C.

^1H NMR (500 MHz, $CDCl_3$, 298K): δ= 6.97 (s, 2H; m-CH_{mes}), 6.89 (d, $^3J_{HH}$ = 1.7 Hz, 1H; CH_{imid}), 6.64 (d, $^3J_{HH}$ = 1.7 Hz, 1H; CH_{imid}), 4.60 (s, 1H; COD), 4.05 (s, 2H; NCH_2), 2.64 (s, 2H; COD), 2.34 (s, 3H; *p*-$CH_{3,mes}$), 2.19 (s, 6H, o-$CH_{3,mes}$), 2.15-2.10 (br m, 2H, COD), 2.06-1.98 (br m, 2H, COD), 1.72-1.62 (br m, 4H; *COD*), 0.99 (s, 6H, CH_3),

$^{13}C\{^1H\}$ NMR (125 MHz, $CDCl_3$, 298K): δ = 179.75 (d, J_{Rh-C} = 56 Hz; Rh-$C_{carbene}$), 138.60 (C_{Ar}), 136.36 (C_{Ar}), 135.55 (C_{Ar}), 128.76 (CH_{Ar}), 121.74 (CH_{imid}), 120.88 (CH_{imid}), 97.62 (d, J_{Rh-C} = 8 Hz, CH_{COD}), 67.98 (s, THF), 67.79 (OC), 67.01 (NCH_2), 63.12 (d, J_{Rh-C} = 13Hz, CH_{COD}), 33.46 ($CH_{2,COD}$), 34.12 (s, Pentane), 29.07 (CH_3), 28.32 ($CH_{2,COD}$), 25.62 (s, THF), 22.34 (s, Pentane), 21.09 (*o*-$CH_{3,mes}$), 16.82 (*p*-$CH_{3,mes}$); 14.07 (s, Pentane);

DRIFT (25°C, KBr solid solution under Argon): $\tilde{\nu}$ = 3158.9 (m, ν_{C-H}), 3128.4 (s, ν_{C-H}), 3010.9 (w, ν_{C-H}), 2970.0 (s, ν_{C-H}), 2957.3 (s, ν_{C-H}), 2942.1 (s, ν_{C-H}), 2932.1 (s, ν_{C-H}), 2919.8 (s, ν_{C-H}), 2907.6 (s, ν_{C-H}), 2872.8 (s, ν_{C-H}), 2863.0 (s, ν_{C-H}), 2853.7 (m, ν_{C-H}), 2925.6 (s, ν_{C-H}), 1641.4 (w), 1538.5 (m), 1519.8 (w), 1492.7 (s), 1466.8 (s), 1448.8 (m), 1443.0 (m), 1403.9 (s), 1384.7 (s), 1362.2 (s), 1344.3 (m), 1322.3 (m), 1271.1 (s), 1214.2 (s), 1204.6 (s), 1175.5 (s), 1142.4 (s), 1099.9 (w), 1080.4 (m), 1043.2 (w), 1033.8 (m), 1000.6 (m), 982.1 (s), 951.7 (s), 983.9 (s), 875.3 (m), 865.3 (m), 851.9 (m), 817.0 (m), 775.3 (s), 721.4(s), 717.4 (s), 694.2 (m), 683.1 (m), 640.6 (m), 608.3 (m), 596.1 (s), 587.9 cm^{-1} (s);

Elemental analysis calculated (%) for $C_{24}H_{33}N_2ORh$: C 61.52, H 7.10, N 5.98; found: C 61.47, H 7.24, N 5.93.

Chemistry of Rhodium cationic species with Tantalum schrock:

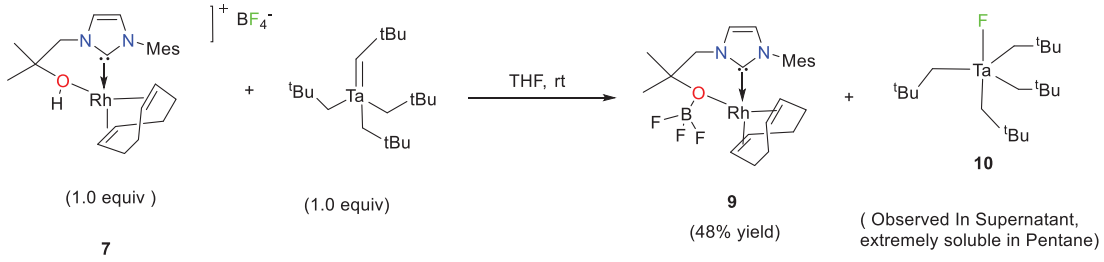

A light yellow suspension of Rhodium cationic precursor $[Rh(HL)(COD)]^+BF_4^-$ (250 mg, 0.449 mmol, 1.0 equiv) in 16.0 mL THF was added drop-wise to a stirring dark orange solution of Tantalum trisneopentyl neopentylidene complex (208 mg, 0.449 mmol, 1.0 equiv) in 8.0 mL. The reaction mixture was stirred at room temperature for 6.5 hr. After that the solution was concentrated, filtered and stored at -40°C. This yielded yellow powder which was dried in vacuo to give $RhLCODBF_3$ (115 mg, 0.21 mmol, 48%). Single crystals suitable for X-Ray diffraction were grown by the diffusion of Diethyl ether (5.0 mL) into a concentrated DCM solution of the compound (2.0 mL) at -40°C.

^1H NMR (300 MHz, $CDCl_3$, 296K): δ= 7.11 (s, 1H; m-CH_{mes}), 7.03 (d, $^3J_{HH}$ = 1.75 Hz, 1H; CH_{imid}), 6.91 (s, 1H; m-CH_{mes}), 6.73 (d, $^3J_{HH}$ = 1.75 Hz, 1H; CH_{imid}), 5.50 (d, $^2J_{HH}$ = 14 Hz, 1H; NCH_2), 5.40 (s, 1H; COD), 5.23 (s, 1H, OH), 5.27 (s, 1H; COD), 3.95 (d, $^2J_{HH}$ = 14 Hz, 1H; NCH_2), 3.35 (s, 1H,

COD), 2.65 (s, 1H, COD), 2.48 (br s, 1H, COD), 2.37 (s, 3H; *p*-$CH_{3,mes}$), 2.35 (s, 3H, o-$CH_{3,mes}$), 2.04-1.99 (br m, 4H; COD), 1.88 (s, 3H; *o*-$CH_{3,mes}$), 1.76 (br m, 1H, COD), 1.61 (s, 3H, CH_3), 1.44 (br m, 2H; COD), 1.21 (s, 3H; CH_3),

$^{13}C\{^1H\}$ NMR (125 MHz, THF-d_8, 297K): δ = 179.12 (d, J_{Rh-C} = 51 Hz; Rh-$C_{carbene}$), 139.42 (C_{Ar}), 137.71 (C_{Ar}), 136.40 (C_{Ar}), 134.79 (C_{Ar}), 130.04 (CH_{Ar}), 128.88 (CH_{Ar}), 123.39 (CH_{imid}), 123.10 (CH_{imid}), 102.41 (d, J_{Rh-C} = 90 Hz, COD), 72.09 (OC), 64.98 (s, N-CH_2), 63.21 (d, J_{Rh-C} = 17 Hz, CH_{COD}), 61.73 (d, J_{Rh-C} = 17 Hz, CH_{COD}), 34.94 ($CH_{2,COD}$), 31.49 (s, $CH_{2,COD}$), 29.56 (s, $CH_{2,COD}$), 26.84 (s, $CH_{2,COD}$), 26.34 (s, CH_3), 24.50 (s, CH_3), 20.90 (*o*-$CH_{3,mes}$), 19.25 (*o*-$CH_{3,mes}$), 17.60 (*p*-$CH_{3,mes}$);

$^{19}F\{^1H\}$ NMR (282.38 MHz, $CDCl_3$, 296 K): δ = -141.15 ppm (q 1:1:1:1, $^2J_{B-F}$=9.7 Hz); $^{11}B\{^1H\}$ NMR (96.29 MHz, $CDCl_3$, 297 K): δ = -0.53 ppm (q, $^2J_{F-B}$=11 Hz);

DRIFT (25°C, KBr solid solution under Argon): $\tilde{\nu}$ = 3172.2 (m, ν_{C-H}), 3142.7 (m, ν_{C-H}), 2971.0 (s, ν_{C-H}), 2930.0 (s, ν_{C-H}), 2872.3 (m, ν_{C-H}), 2829.2 (m, ν_{C-H}), 1608.7 (w), 1489.1 (s), 1474.7 (w), 1437.7 (m), 1412.9 (s), 1385.6 (s), 1366.6 (w), 1350.2 (w), 1333.3 (w), 1306.1 (w), 1271.4 (w), 1236.9 (m), 1224.7 (s), 1186.1 (s), 1146.1 (s), 1091.7 (s), 1057.7 (s), 1039.1 (s), 984.2 (s), 968.5 (s), 915.6 (s), 866.0 (m), 812.3 (w), 751.6 (m), 727.6 (m), 698.9 (m), 587.1 (w), 509.5 cm^{-1} (m);

Elemental analysis calculated (%) for $C_{24}H_{33}N_2ORhBF_3$: C 53.72, H 6.20, N 5.22; found: C 53.63, H 6.30, N 5.14.

Synthesis of trimetallic complex along with the desired bimetallic complex in toluene:

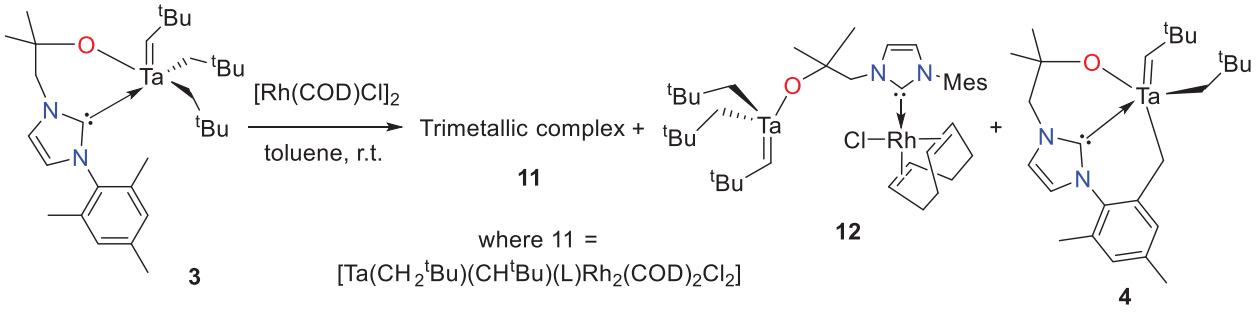

A 6 mL yellow toluene solution of $[Rh(COD)Cl]_2$ (151 mg, 0.31 mmol, 0.5 equiv) was added dropwise to an orange stirring solution of complex Ta(L)(CH^{t}Bu)($CH_2{}^t$Bu) **1** (400 mg, 0.6 mmol, 1.0 equiv) in 6 ml of toluene. The reaction mixture was stirred at room temperature for 4h, yielding a brown solution which was evaporated to dryness. Analysis of the crude reaction mixture by ^1H NMR reveals the formation of a mixture of species containing **11, 12 and 4**. Fractional recrystallization of the solid residue from saturated pentane solutions at -40°C

yielded a solid containing a mixture of **11** and **12**. Unfortunately, all attempts to further separate these species were unsuccessful since feature similar solubilities and co-crystallize in the same conditions. NMR data:

^{1}H NMR (500 MHz, C_6D_6, 296K): δ = 7.29 (d, $^{3}J_{HH}$ = 1.9 Hz, 1H, CH_{imid}), 6.89 (s, 1H, *m*-CH_{Mes}), 6.68 (s, 1H, *m*-CH_{Mes}), 6.00 (d, $^{3}J_{HH}$ = 1.9 Hz, 1H, CH_{imid}), 5.78 (d, $^{2}J_{HH}$ = 14.3 Hz, 1H, NCH_2), 5.41 (m, 1H, COD), 5.31 (m, 1H, COD), 4.65 (d, $^{2}J_{HH}$ = 14.3 Hz, 1H, NCH_2), 3.93 (s, 1H, Ta=C*H*^{t}Bu), 3.51 (m, 1H, COD), 3.19 (m, 1H, COD), 2.69 (s, 3H, *o*-CH_{3Mes}), 2.16 (s, 3H, *o*-CH_{3Mes}), 2.28 (br m, 1H, COD), 2.11 (br m, 1H, COD), 1.98 (br m, 1H, COD), 1.71 (s, 3H, *p*-CH_{3Mes}), 1.80 (br m, 1H, COD), 1.69 (br m, 2H, COD), 1.57 (s, 6H, CH_3), 1.51 (br m, 2H, COD), 1.33 (s, 9H, CH^{t}*Bu*), 1.42 (d, $^{3}J_{HH}$ = 13.3 Hz, 1H, TaCH_2), 1.37 (d, $^{3}J_{HH}$ = 13.3 Hz, 1H, TaCH_2), 1.21 (s, 9H, $CH_2{}^{t}$*Bu*), 1.20 (s, 9H, $CH_2{}^{t}$*Bu*), 0.61 (d, $^{3}J_{HH}$ = 13.3 Hz, 1H, TaCH_2), 0.51 (d, $^{3}J_{HH}$ = 13.3 Hz, 1H, TaCH_2).

^{13}C{^{1}H} NMR (125.7 MHz, C_6D_6, 296K): δ = 238.2 (s, Ta=C), 184.5 (d, $^{1}J_{Rh\text{-}C}$ = 52 Hz, Rh-$C_{carbene}$), 138.8 (C_{Ar}), 138.0 (C_{Ar}), 137.0 (C_{Ar}), 134.5 (C_{Ar}), 130.1 (CH_{Ar}), 128.6 (CH_{Ar}), 122.9 (CH_{imid}), 122.3 (CH_{imid}), 97.1 (d, $^{1}J_{Rh\text{-}C}$ = 14 Hz, CH_{COD}), 95.1 (Ta-$CH_2{}^{t}$Bu), 94.8 (Ta-$CH_2{}^{t}$Bu), 85.3 (O*C*), 68.0 (d, $^{1}J_{Rh\text{-}C}$ = 14 Hz, CH_{COD}), 62.5 (NCH_2), 46.2 (^{t}Bu), 35.0 (^{t}Bu), 34.9 (^{t}Bu), 34.8 (^{t}Bu), 34.3 (CH_{2COD}), 34.1 (^{t}Bu), 32.5 (CH_{2COD}), 30.9 (CH_3), 30.1 (CH_3), 29.2 (CH_{2COD}), 28.9 (CH_{2COD}), 28.4 (o-CH_{3Mes}), 20.3 (o-CH_{3Mes}), 17.8 (p-CH_{3Mes}).

Synthesis of the trimetallic species 11 in THF:

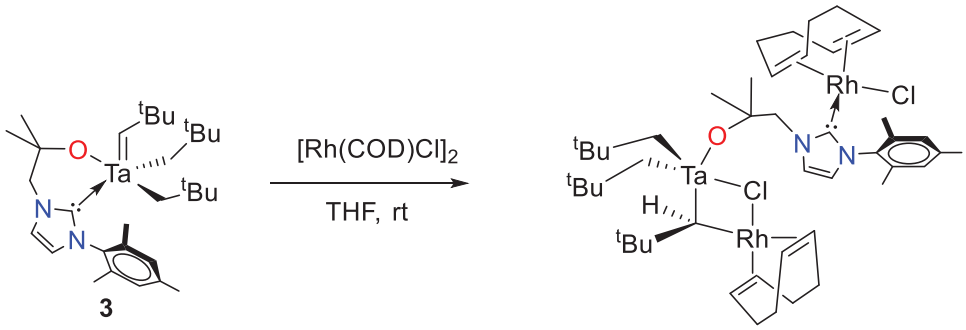

3 **11**

(79.6% yield)

Reaction of with [Rh(COD)Cl]$_2$: A yellow 4 ml THF solution of [Rh(COD)Cl]2 (94.7 mg, 0.19 mmol, 1.0 equiv) was added at once to a 4 ml dark orange THF solution of tantalum precursor [Ta(L)CHtBu(CH2tBu)2] (125 mg, 0.19 mmol, 1.0 equiv). The color of the reaction mixture changes instantaneously to brown from dark orange. The reaction mixture was stirred at room temperature for 4 hr. Following which the solvent was removed under vacuum to yield yellow

powder. The crude compound was recrystallized from a two layer diffusion of pentane (1.5 ml) into THF (3 ml) at -40°C. The recrystallized compound was under vacuum to yield complex (175 mg, 0.15 mmol, 79.6 % yield).

^{1}H NMR (500 MHz, C_6D_6, 296K): δ = 6.89 (s, 2H, *m*-CH_{Mes}), 6.68 (s, 2H, *m*-CH_{Mes}), 6.62 (d, $^3J_{HH}$ = 1.7 Hz, 1H, CH_{imid}), 6.62 (d, $^3J_{HH}$ = 1.7 Hz, 1H, CH_{imid}), 6.16 (d, $^2J_{HH}$ = 13.7 Hz, 1H, NCH_2), 6.12 (d, $^2J_{HH}$ = 13.7 Hz, 1H, NCH_2), 5.94 (d, $^3J_{HH}$ = 1.7 Hz, 1H, CH_{imid}), 5.93 (d, $^3J_{HH}$ = 1.7 Hz, 1H, CH_{imid}), 5.38 (m, 2H, COD), 5.30 (m, 4H, COD), 5.12 (m, 2H, COD), 4.82 (s, 1H, Ta=C*H*^{t}Bu), 4.78 (s, 1H, Ta=C*H*^{t}Bu), 4.55 (d, $^2J_{HH}$ = 13.7 Hz, 1H, NCH_2), 4.50 (d, $^2J_{HH}$ = 13.7 Hz, 1H, NCH_2), 3.90 (m, 2H, COD), 3.81 (m, 2H, COD), 3.59 (m, 2H, COD), 3.14 (d, $^2J_{HH}$ = 9.7 Hz, 1H, TaCH_2), 3.14 (d, $^2J_{HH}$ = 9.7 Hz, 1H, TaCH_2), 3.08 (m, 2H, COD), 2.71 (br m, 2H, COD), 2.70 (s, 3H, *o*-CH_{3Mes}), 2.69 (s, 3H, *o*-CH_{3Mes}), 2.45 (br m, 2H, COD), 2.37 (br m, 2H, COD), 2.21 (br m, 2H, COD), 2.15 (s, 6H, *o*-CH_{3Mes}), 2.07 (br m, 4H, COD), 1.97 (br m, 6H, COD), 1.91 (d, 1H, TaCH_2), 1.90 (d, 1H, TaCH_2), 1.88 (br m, 2H, COD), 1.87 (d, 1H, TaCH_2), 1.86 (d, 1H, TaCH_2), 1.85 (d, 1H, TaCH_2), 1.84 (s, 3H, CH_3), 1.8s (s, 3H, CH_3), 1.81 (d, 1H, TaCH_2), 1.66 (s, 3H, *p*-CH_{3Mes}), 1.65 (s, 3H, *p*-CH_{3Mes}), 1.65 (s, 6H, CH_3), 1.64 (s, 6H, CH_3), 1.58 (s, 9H, C*H*^{t}*Bu*), 1.55 (s, 9H, C*H*^{t}*Bu*), 1.49 (s, 9H, C*H*^{t}*Bu*), 1.47 (s, 9H, C*H*^{t}*Bu*), 1.47 (s, 9H, CH_2^{t}*Bu*), 1.45 (s, 9H, CH_2^{t}*Bu*).

^{13}C{^{1}H} NMR (125.7 MHz, C_6D_6, 296K): δ = 184.6 (d, $^1J_{Rh\text{-}C}$ = 53 Hz, Rh-$C_{carbene}$), 170.2 (d, $^1J_{Rh\text{-}C}$ = 22 Hz, Ta=C), 170.0 (d, $^1J_{Rh\text{-}C}$ = 22 Hz, Ta=C), 138.9 (C_{Ar}), 138.0 (C_{Ar}), 137.1 (C_{Ar}), 134.6 (C_{Ar}), 134.5 (C_{Ar}), 130.0 (CH_{Ar}), 122.8 (CH_{imid}), 122.8 (CH_{imid}), 122.7 (CH_{imid}), 122.7 (CH_{imid}), 105.6 (Ta-CH_2), 105.4 (Ta-CH_2), 97.8 (d, $^1J_{Rh\text{-}C}$ = 6 Hz, CH_{COD}), 97.7 (d, $^1J_{Rh\text{-}C}$ = 6 Hz, CH_{COD}), 97.5 (d, $^1J_{Rh\text{-}C}$ = 6 Hz, CH_{COD}), 97.4 (d, $^1J_{Rh\text{-}C}$ = 6 Hz, CH_{COD}), 97.3 (d, $^1J_{Rh\text{-}C}$ = 6 Hz, CH_{COD}), 97.2 (d, $^1J_{Rh\text{-}C}$ = 6 Hz, CH_{COD}), 96.5 (d, $^1J_{Rh\text{-}C}$ = 6 Hz, CH_{COD}), 96.3 (d, $^1J_{Rh\text{-}C}$ = 6 Hz, CH_{COD}), 92.5 (Ta-CH_2), 92.3 (Ta-CH_2), 86.0 (O*C*), 85.9 (O*C*), 76.4 (d, $^1J_{Rh\text{-}C}$ = 18 Hz, CH_{COD}), 75.8 (d, $^1J_{Rh\text{-}C}$ = 18 Hz, CH_{COD}), 69.6 (d, $^1J_{Rh\text{-}C}$ = 15 Hz, CH_{COD}), 69.4 (d, $^1J_{Rh\text{-}C}$ = 15 Hz, CH_{COD}), 68.6 (m, 4 CH_{COD}), 62.4 (NCH_2), 62.35 (NCH_2), 43.8 (^{t}Bu), 43.6 (^{t}Bu), 37.5 (^{t}Bu), 37.4 (^{t}Bu), 37.0 (^{t}Bu), 36.2 (^{t}Bu), 36.0 (^{t}Bu), 36.0 (^{t}Bu), 35.9 (^{t}Bu), 35.5 (^{t}Bu), 35.0 (CH_{2COD}), 34.9 (CH_{2COD}), 34.8 (CH_{2COD}), 34.6 (CH_{2COD}), 31.9 (CH_3), 31.8 (CH_3), 29.8 (CH_3), 29.8 (CH_3), 29.7 (CH_{2COD}), 29.6 (CH_{2COD}), 29.4 (CH_{2COD}), 29.3 (CH_{2COD}), 29.1 (CH_{2COD}), 28.8 (CH_{2COD}), 28.5 (CH_{2COD}), 28.2 (o-CH_{3Mes}), 28.2 (CH_{2COD}), 27.7 (o-CH_{3Mes}), 21.1 (o-CH_{3Mes}), 20.4 (o-CH_{3Mes}), 17.7 (p-CH_{3Mes}), 17.6 (p-CH_{3Mes}).

Anal. calcd for $C_{47}H_{77}N_2OCl_2Rh_2Ta$: C, 49.35; H, 6.79; N, 2.45; Cl, 6.20, Rh, 17.9; Ta, 15.8. Found: C, 49.46; H, 6.80; N, 2.51; Cl, 6.03, Rh, 17.5; Ta, 15.8.

m/z (ESI): 1148.35 [M-Cl+ CH_3CN]$^+$; 1107.3320 [M-Cl]$^+$; 964.3490 (M+); 879.3741 (M+); 469.1717 [**4**-Cl]$^+$

Synthesis of tantalum-rhodium heterobimetallic complex Ta(μ-L)(N^{t}Bu)(CH$_2$^{t}Bu)$_2$Rh(COD)(Cl) :

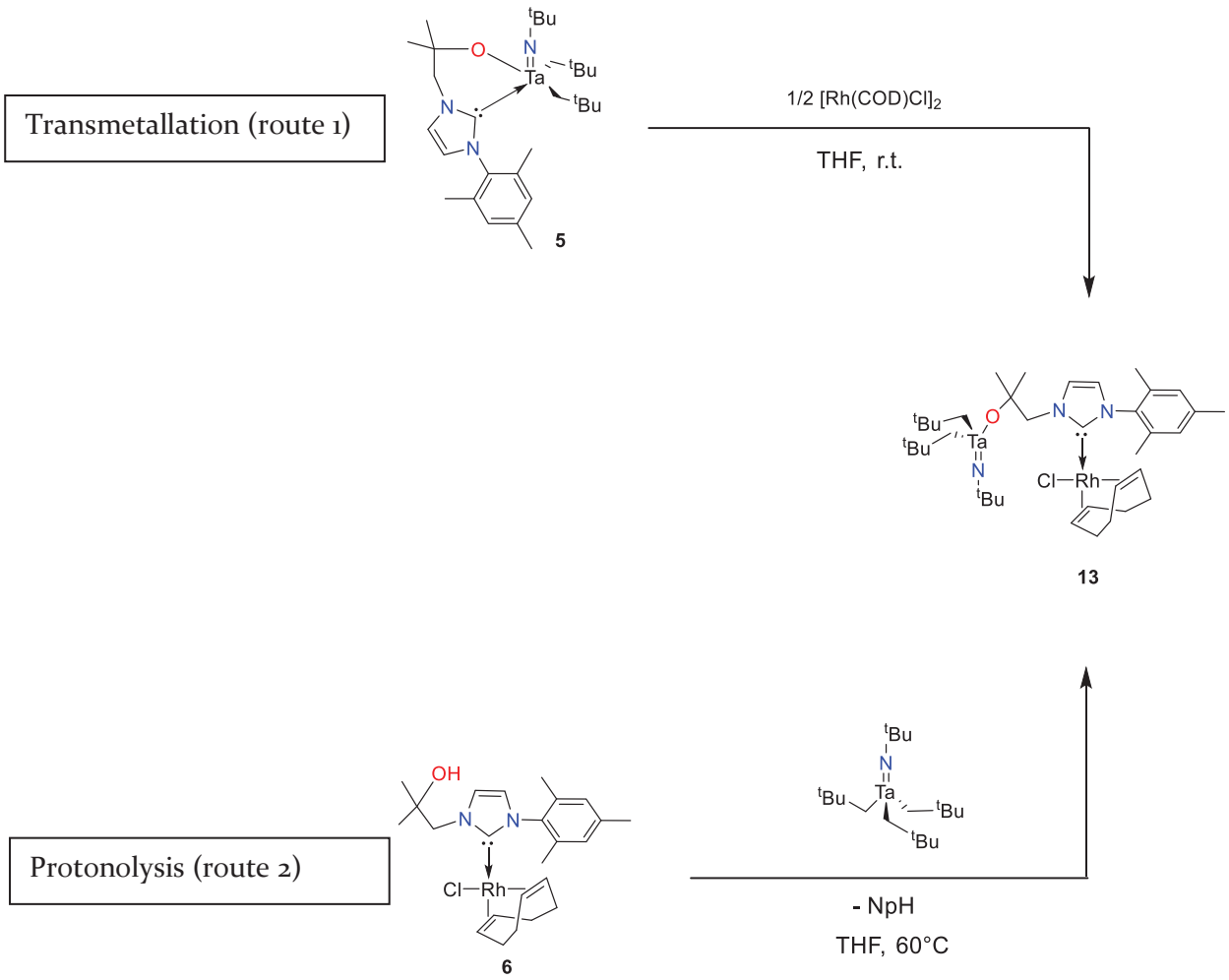

Route 1) A 3 mL THF solution of Ta(L)(N^{t}Bu)(CH$_2$^{t}Bu)$_2$ (**3**) (100 mg, 0.15 mmol, 1 eq.) was added to a 3 mL yellow THF solution of [Rh(COD)Cl]$_2$ (37.8 mg, 0.08 mmol, 0.5 eq.). The reaction mixture was stirred at room temperature for 2h, yielding a yellow solution that was evaporated to dryness. The residue was extracted in 2 mL pentane, filtered and stored at -40°C. This produced yellow-green crystalline material that was recovered and dried *in vacuo* to yield Ta(μ-L)(N^{t}Bu)(CH$_2$^{t}Bu)$_2$Rh(COD)(Cl) (**13**) (98 mg, 0.10 mmol, 68%). Single crystals suitable for X-ray diffraction were grown in a similar fashion.

^{1}H NMR (400 MHz, THF-d_8, 293K): δ = 7.58 (d, $^3J_{HH}$ = 1.9 Hz, 1H, CH_{imid}), 7.11 (s, 1H, *m*-CH_{Mes}), 7.05 (d, $^3J_{HH}$ = 1.9 Hz, 1H, CH_{imid}), 6.95 (s, 1H, *m*-CH_{Mes}), 5.47 (d, $^2J_{HH}$ = 14.3 Hz, 1H, NCH_2), 4.82 (m, 1H, COD), 4.70 (m, 1H, COD), 4.49 (d, $^2J_{HH}$ = 14.3 Hz, 1H, NCH_2), 3.41 (m, 1H, COD), 2.97 (m, 1H, COD), 2.43 (s, 3H, *o*-CH_{3Mes}), 2.36 (s, 3H, *o*-CH_{3Mes}), 2.32 (br m, 1H, COD), 2.14 (br m, 1H, COD), 1.93 (br m, 1H, COD), 1.85 (s, 3H, *p*-CH_{3Mes}), 1.81 (br m, 1H, COD), 1.69 (br m, 2H, COD), 1.65 (s, 3H, CH_3), 1.56 (s, 3H, CH_3), 1.50 (br m, 2H, COD), 1.48 (s, 9H, N^{t}Bu), 1.25 (d, $^3J_{HH}$ = 13.2 Hz, 1H, TaCH_2), 1.20 (d, $^3J_{HH}$ = 13.2 Hz, 1H, TaCH_2), 1.13 (s, 9H, $CH_2{}^tBu$), 1.07 (s, 9H, $CH_2{}^tBu$), 0.83 (d, $^3J_{HH}$ = 13.2 Hz, 1H, TaCH_2), 0.69 (d, $^3J_{HH}$ = 13.2 Hz, 1H, TaCH_2).

^{13}C{^{1}H} NMR (101 MHz, THF-d_8, 293K): δ = 184.0 (d, $J_{Rh\text{-}C}$ = 52 Hz, Rh-$C_{carbene}$), 139.1 (C_{Ar}), 138.0 (C_{Ar}), 137.5 (C_{Ar}), 135.3 (C_{Ar}), 130.0 (CH_{Ar}), 128.6 (CH_{Ar}), 123.9 (CH_{imid}), 122.8 (CH_{imid}), 96.5 (d, $J_{Rh\text{-}C}$ = 7 Hz, CH_{COD}), 96.4 (d, $J_{Rh\text{-}C}$ = 7 Hz, CH_{COD}), 92.9 (Ta-$CH_2{}^t$Bu), 91.8 (Ta-$CH_2{}^t$Bu), 81.8 (O*C*), 68.4 (d, $J_{Rh\text{-}C}$ = 14 Hz, CH_{COD}), 68.4 (d, $J_{Rh\text{-}C}$ = 14 Hz, CH_{COD}), 66.7 (N*C*$(CH_3)_3$), 63.0 (NCH_2), 35.4 (Ta-$CH_2C(CH_3)_3$), 35.3 (Ta-$CH_2C(CH_3)_3$), 35.2 (Ta-$CH_2C(CH_3)_3$), 35.0 (Ta-$CH_2C(CH_3)_3$), 34.4 (NC$(CH_3)_3$), 34.3 (CH_{2COD}), 32.5 (CH_{2COD}), 31.0 (CH_3), 30.0 (CH_3), 29.4 (CH_{2COD}), 28.9 (CH_{2COD}), 20.9 (o-CH_{3Mes}), 20.0 (o-CH_{3Mes}), 17.8 (p-CH_{3Mes}).

DRIFT (25°C, KBr solid solution under argon): 3163.4 (w, $\nu_{C\text{-}H}$), 3127.6 (w, $\nu_{C\text{-}H}$), 3097.0 (w, $\nu_{C\text{-}H}$), 2946.3 (s, $\nu_{C\text{-}H}$), 2866.0 (s, $\nu_{C\text{-}H}$), 2829.5 (m, $\nu_{C\text{-}H}$), 1609.0 (w), 1521.0 (w), 1487.7 (m), 1462.0 (m), 1439.4 (m), 1404.5 (m), 1380.2 (m), 1355.9 (m), 1332.6 (w), 1277.8 (s), 1247.7 (m), 1230.6 (m), 1212.7 (s), 1187.7 (m), 1166.7 (m), 1136.9 (s), 1083.6 (w), 993.3 (s), 968.7 (m), 931.6 (w), 891.3 (w), 851.9 (m), 806.5 (m), 765.1 (w), 731.5 (m), 701.3 (m).

Elemental analysis for $C_{38}H_{64}ClN_3ORhTa$: C, 50.81; H, 7.18; N, 4.68. Found: C, 51.33; H, 7.27; N, 4.47.

Route 2) A 0.5 mL THF-d_8 solution of Ta(N^{t}Bu)$(CH_2{}^tBu)_3$ (10 mg, 0.02 mmol, 1 eq.) was added at r.t. to a 0.5 mL THF-d_8 solution of Rh(HL)(COD)(Cl) (**4**) (10.8 mg, 0.02 mmol, 1 eq.). 1,2,4,5-tetramethylbenzene (5.8 mg, 0.04 mmol, 1 eq.) is added as an internal standard. The reaction mixture is heated at 60°C for 24h, yielding a yellow solution that was analyzed by ^{1}H NMR, revealing that complex **11** was formed quantitatively together with one equivalent of neopentane.

Further data (^{1}H, ^{13}C NMR, IR and X-ray crystallographic) studies are reported in appendix 2.

Chapter 4

Development of POSS based homogeneous molecular model of the bimetallic complex and the synthesis of silica-supported early-late heterobimetallic complexes

4.1) INTRODUCTION

4.1.1) Recent advances in silica-supported heterobimetallic complexes

Recent advances in bimetallic chemistry have focused both on a) harnessing the cooperative activity between two metals and b) grafting bimetallic complex over surfaces to achieve enhanced reactivity. Initially the focus was on grafting homo-bimetallic complexes of Pd,[1] Ir,[2] Cr,[3] Ti,[4] W[5] etc. over silica. The general strategy for the synthesis of the supported complexes usually involves the reaction between homobimetallic metal complexes and dehydroxylated silica surfaces. The reaction process involves the elimination of a leaving group upon grafting, most of the time as a result of a protonolysis reaction. In recent years, a few examples of supported heterobimetallic complexes emerged. Franck Rataboul and co-workers reported a Zr-Ta heterobimetallic complex supported over silica.[6] The strategy to synthesize the bimetallic complex is a two-step process. The first step is to graft a zirconium peralkyl species over silica surface followed by treatment of the latter with H_2 to convert the alkyl species into a Zr monohydride derivative, and then addition of N_2O to convert the hydride ligand into a hydroxyl group (**Scheme 4.1**). The last step involves the addition of the tantalum *tris*(neopentyl)neopentylidene precursor over the silica supported Zr-OH species to yield the desired heterobimetallic complex (**Scheme 4.1**). The amount of neopentane released during the reaction process is calculated by gas chromatography which shows 1.1 equivalent of neopentane released during the grafting process, in agreement with the proposed structure.

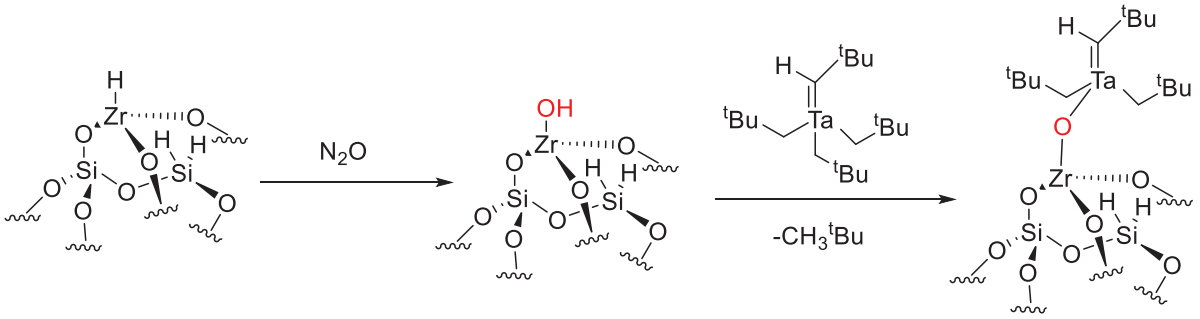

Scheme 4.1: A novel synthetic procedure to synthesis heterobimetallic complex has been reported by Rataboul et al. They used the silica supported tri-podal Zr-H and converted it to Zr-OH by passing N2O. Corresponding bimetallic complex is synthesized with the grafting the tantalum precursor with simultaneous release of neopentane.

The grafted complex is characterized by IR spectroscopy, solid state ^{13}C CP-MAS NMR (cross-polarization at magic angle spinning), EXAFS and elemental analysis. The IR spectroscopy study shows the disappearance of the Zr-OH (3785 cm^{-1}) stretching frequency with

concomitant appearance of $\tilde{\nu}_{C\text{-}H}$ (3000-2800 cm^{-1}) and δ_{CH_2} (1500-1300 cm^{-1}) stretching frequencies. The ^{13}C CP-MAS NMR spectrum of the complex shows the characteristic tantalum-alkylidene peak at 243 ppm which is similar to what has been reported for silica grafted tantalum alkylidene complexes [(≡SiO)Ta(=CH^{t}Bu)(CH$_2$^{t}Bu)$_2$].[7–10] The Zr-Ta bimetallic complex is then converted to the corresponding hydride species by heating it under a dihydrogen atmosphere at 150°C. The grafted bimetallic hydride shows superior reactivity (100 turnover numbers) in propane metathesis* when compared to the monometallic Ta-H complex (58 TON). It is reasoned that the bimetallic hydride complex is more stable and reactive than the monometallic Ta-H complex which leads to higher catalytic activity. It is also observed that the monometallic silica supported Zr-H species is inactive towards propane metathesis. This clearly establishes that cooperativity between both the metals lead to increased catalytic reactivity. Later Basset and coworkers reported silica-supported W-Ti[11] and W-Zr[12] bimetallic materials. Their synthetic strategy involved a) the grafting of 0.5 equivalent of a monometallic tungsten complex over silica first which leaves remaining Si-OH free to react with the second metal complex and b) addition of the second monometallic complex over the remaining silica surface silanols (**Scheme 4.2**). They used 2D HETCOR (Heteronuclear chemical shift correlation) studies to establish the fact that both the grafted monometallic complexes interacted with each other. This research group reported that the bimetallic complexes depicted enhanced catalytic activity for alkane metathesis (TON = 1436) as compared to the monometallic tungsten complex (TON = 650).

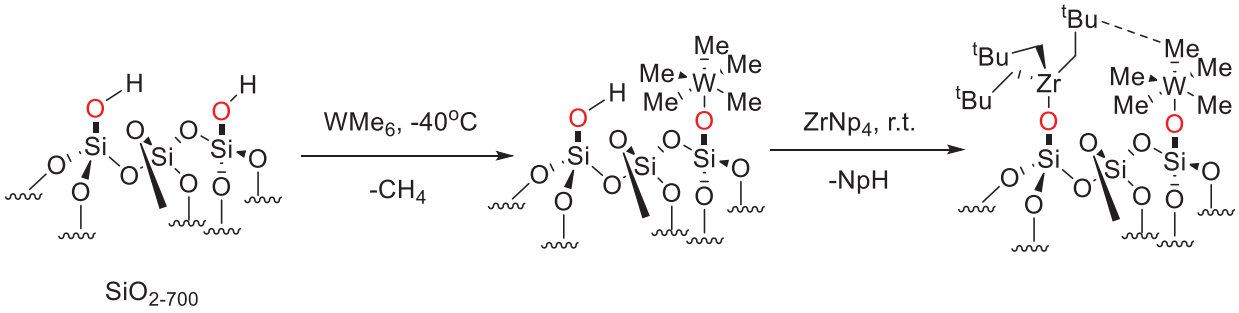

Scheme 4.2. Basset and coworkers have been recently focusing on early-early transition metals bimetallic complexes for alkane metathesis. In the scheme, a tungsten complex is grafted over silica at very low temperature followed by addition of a zirconium precursor at room temperature to yield the desired bimetallic material.[12]

---

*__Alkane metathesis__ is a chemical reaction to convert alkanes into higher and lower homologues. For example, propane metathesis in the current case leads to methane, ethane, butane, pentane and hexane.

The improved catalytic activity of the grafted heterobimetallic complexes as compared with monometallic complexes prompted us to explore the chemistry of heterobimetallic complexes over silica. As discussed in the above examples, the bimetallic complexes prepared to date involved solely early metal complexes (Zr-Ta, W-Ti or W/Zr). In our group, we wish to explore the chemistry of early late heterobimetallic complexes supported on silica and exploit the catalytic activity of the resulting grafted complexes (**Figure 4.1**). As mentioned in the general introduction (Chapter 1), our group was able to prepare well-defined Ta/Ir species with excellent catalytic activity for H/D exchange reactions. In this work we wish to extend this research area through the use of the bifunctional NHC ligand strategy presented in chapters 2 and 3. As silica support, we chose a mesoporous silica dehydroxylated at 700°C ($SBA_{15\text{-}700}$) which contains isolated silanols (Si-OH groups).

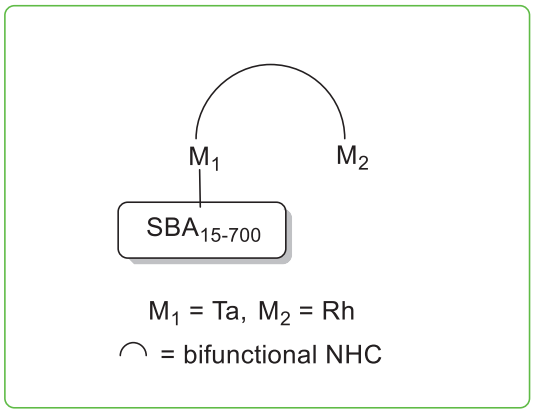

Figure 4.1. Targeted structure of the silica grafted tantalum-rhodium heterobimetallic complex. The two metals are assembled through the bifunctional N-heterocyclic carbene which is already reported in Chapter 2 of the thesis.

However, as mentioned in the introductory chapter of this thesis that synthesizing and characterizing silica supported complexes is a challenging process. This is due to the complex nature of data obtained from the characterization techniques which is relatively difficult to comprehend. Hence there is a need to complement the data collected from solid samples with the data obtained from a homogeneous solution sample. Moreover, the synthesis of silica and its dehydroxylation to obtain isolated silanols is a multistep process and hence it is necessary to optimize the synthetic pathway using the homogeneous molecular analogues of silica. Hence, we decided to develop POSS based homogeneous analogue of the bimetallic complex.

4.1.2) Two different routes to synthesize the grafted bimetallic complex

We hypothesized two different synthetic routes to explore the synthesis of supported heterobimetallic complexes, as shown on **Scheme 4.3**.

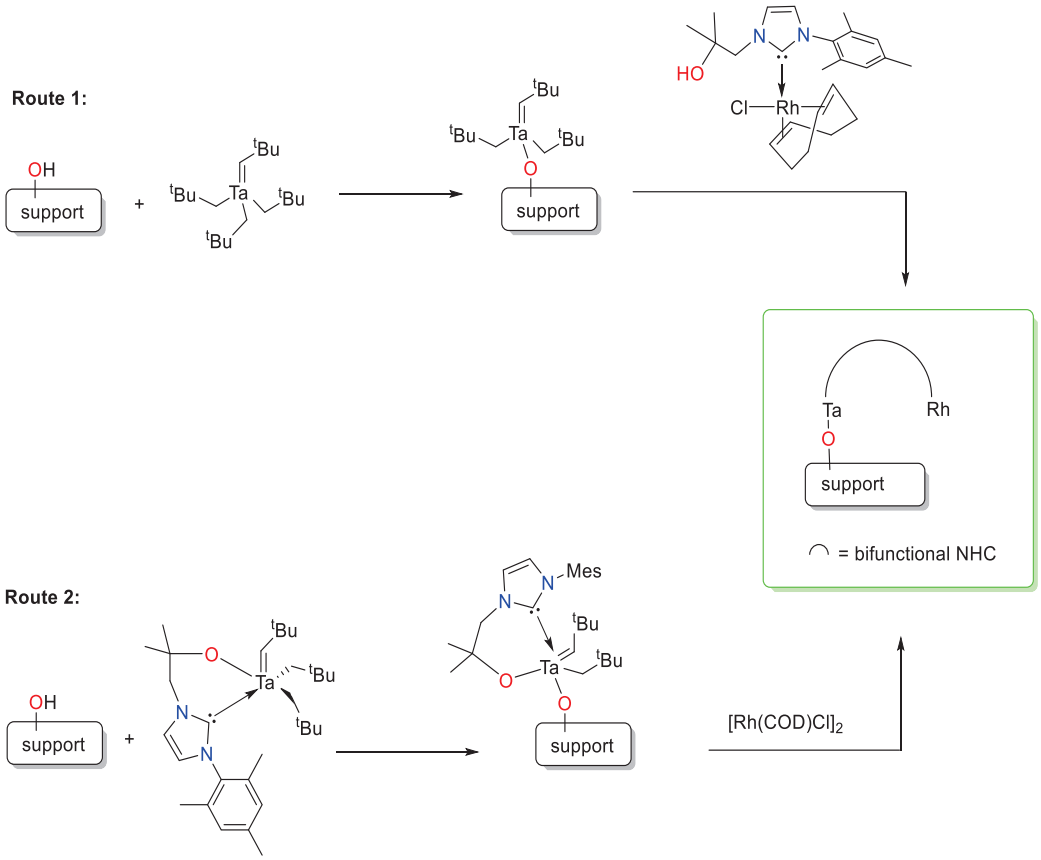

Scheme 4.3: The scheme depicts two different routes to immobilize the alcoxy-NHC heterobimetallic complex.

In both approaches the support is first functionalized with a tantalum derivative, and the rhodium center is incorporated in a second step. Route 1 involves the grafting of the tantalum *tris*-alkyl alkylidene complex on the hydroxyl-containing support followed by the addition of the hydroxyl-NHC functionalized rhodium complex to yield the desired supported species through protonolysis. Route 2 involves the addition of the tantalum-NHC complex to the support to yield a grafted Ta-NHC complex as intermediate, which upon transmetallation with a rhodium precursor would yield the targeted heterobimetallic complex. This chapter will discuss first the synthesis of homogeneous molecular models of the Ta-Rh bimetallic complex based on molecular silanols (POSS and *tris*-tertbutoxysilanol). Upon streamlining the

synthetic procedure with the help of these molecular models, we will report the synthesis and characterization of silica grafted heterobimetallic complexes.

4.2) RESULTS AND DISCUSSION

4.2.1) Synthesis and characterisation of POSS based heterobimetallic complexes

The polyhedral oligomeric silsesquioxane (POSS) derivative (c-$C_5H_9)_7Si_8O_{12}(OH)$ [POSS-OH] is synthesized following the established literature procedure by Feher *et al.*[13] The synthetic protocol is a multistep process which involves the reaction of (c-$C_5H_9)_7Si_7O_9(OH)_3$ with 1.0 equivalent of $SiCl_4$ and 3.0 equivalent of NEt_3 to yield the chlorinated silsesquioxane molecule (c-$C_5H_9)_7Si_8O_{12}Cl$. The hydrolysis of this chloro-capped silsesquioxane species in a (2:1) THF/H_2O mixture (reflux, 48 h) yields the desired mono-silanol molecule (c-$C_5H_9)_7Si_8O_{12}(OH)$, **14**, as shown on **Scheme 4.4**.

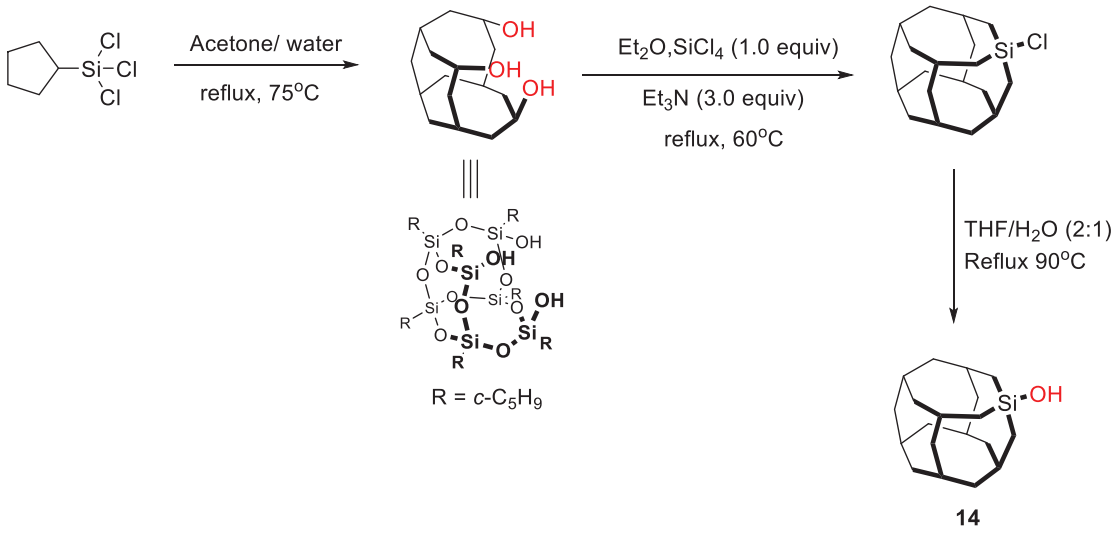

Scheme 4.4. Synthetic protocol to obtain the POSS-OH molecule (c-$C_5H_9)_7Si_8O_{12}(OH)$, **14**.

The ^1H NMR spectrum the molecule **14** (Figure S1) recorded in $CDCl_3$ solution shows a signal corresponding to the hydroxyl group at δ = 2.01 ppm. The ^1H and ^{13}C NMR signals are in agreement with those reported in literature for this molecule.

Complex [(c-$C_5H_9)_7Si_7O_{12}$SiO-Ta(=CH^{t}Bu)($CH_2{}^t$Bu)$_2$], **15**, (see **Scheme 4.5**) is synthesized following the established literature procedure.[7] A toluene solution of the POSS-OH is added to the tantalum *tris*-alkyl alkylidene precursor which yields complex **15**.

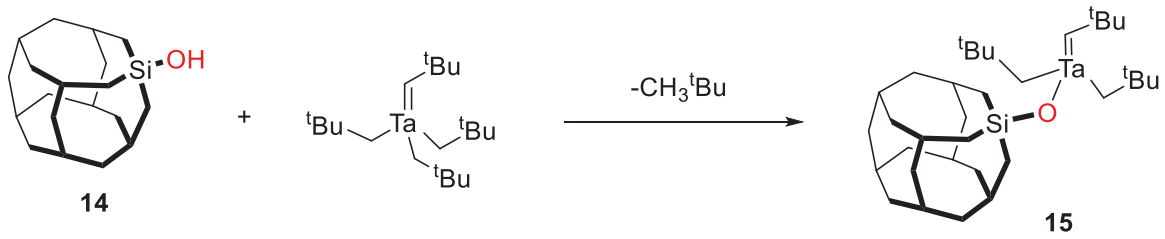

Scheme 4.5. Complex **15** was synthesized following an established literature procedure which involves the addition of Ta(CH^{t}Bu)(CH$_2$^{t}Bu)$_3$ precursor to the POSS-OH molecule **14**.

The ^{1}H NMR of complex **15** (Figure S3) shows the signal corresponding to the tantalum alkylidene proton at δ = 4.79 ppm in C_6D_6 solution, as expected. The alkyl protons signals of the complex get merged with the POSS cyclopentyl protons signals which appear as broad multiplets in the alkyl region. These observations are in agreement with the data reported for the POSS based tantalum complex [(c-C_5H_9)$_7$$Si_7O_{12}$SiO-Ta(=CH^{t}Bu)(CH$_2$^{t}Bu)$_2$].[8]

In order to synthesize the targeted heterobimetallic species, complex **15** is treated with one equivalent of the rhodium-NHC complex **6**. The reaction did not occur at room temperature. The temperature of the reaction mixture is therefore increased to 50°C but no reaction is observed between the precursors. The reaction mixture was thus heated to 70°C, but unfortunately this leads to the formation of an intractable mixture of compounds (**Scheme 4.6**).

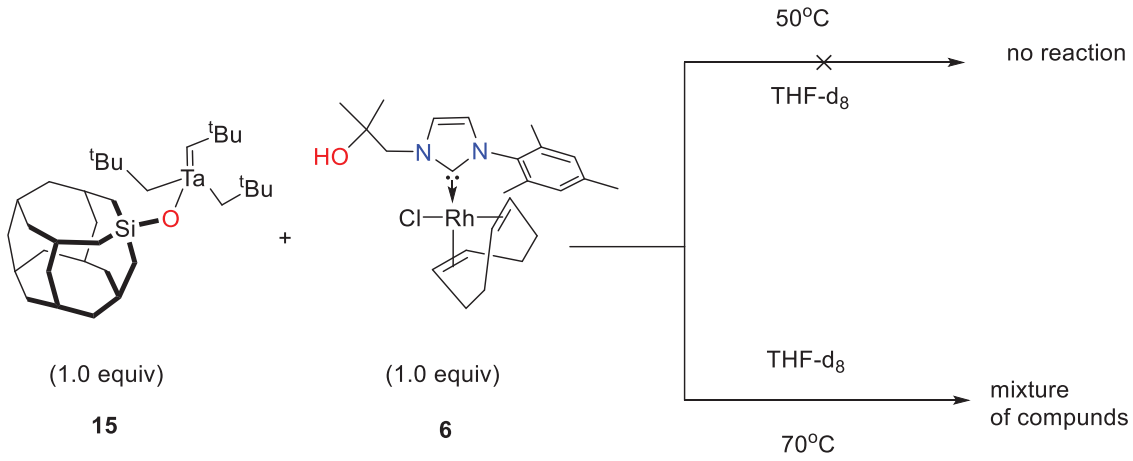

Scheme 4.6. Synthetic route 1. The reaction between the hydroxyl-NHC rhodium complex **6** with the POSS-supported Ta precursor **15** does not occur at low temperature (20-50°C). A further increase in the temperature to 70°C leads to observation of a mixture of unidentifiable compounds.

One possible reason for the observation of mixture of compounds could be different modes of reaction between the ligand hydroxyl proton and the tantalum derivative. Indeed, the hydroxyl proton can react with the alkylidene center as well as with the neopentyl groups. This result rules out route 1 to synthesize the targeted bimetallic complex. Thus, a second route has been investigated, which involves the preparation of a POSS-supported tantalum alcoxy-NHC derivative, followed by the incorporation of rhodium, in a two-step process. In the first step a colorless pentane suspension of POSS-OH was added drop-wise to a stirring orange pentane solution of the tantalum NHC complex **3** (**Scheme 4.7**). Instantaneously the color of the solution changes from dark orange to pale yellow. The proton NMR spectrum of the crude compound (Figure S4) in C_6D_6 does not contain the peak corresponding to the alkylidene proton of the tantalum-NHC complex **3** (which was present at δ = 4.85 ppm) and does not exhibit resonances for the POSS hydroxyl proton. Therefore this indicates that the projected addition reaction between the alkylidenic carbon of the tantalum-NHC precursor and the hydroxyl group of the POSS-OH ligand indeed occurred (Scheme 4.7). The NHC backbone protons are observed as doublets ($^3J_{HH}$ = 1.27 Hz) at δ = 6.59 and 6.57 ppm respectively integrating to one proton each. The *meta* mesityl proton is observed as a singlet at δ = 6.81 ppm integrating to two protons. The cyclopentyl protons of the POSS ligand are also observed as broad multiplets in the region 2.5 – 1.0 ppm. This NMR signal overlaps with that of the neopentyl groups. ^{1}H NMR monitoring does not show any evolution of neopentane during the reaction which is generally observed at 0.9 ppm in C_6D_6. This reaction is in contrast with the reported synthesis of compound **15**[7,8] since in that case, after 1,2 addition, the restoration of the alkylidene carbon occurs through an alpha-H elimination process which releases one neopentane molecule (See above). The IR spectrum of complex **16** (Figure S17) shows the $\tilde{\nu}_{CH}$ stretching frequency in the 3130-2870 cm^{-1} region, corresponding to the cyclopentyl groups as well as the metalloligand framework.

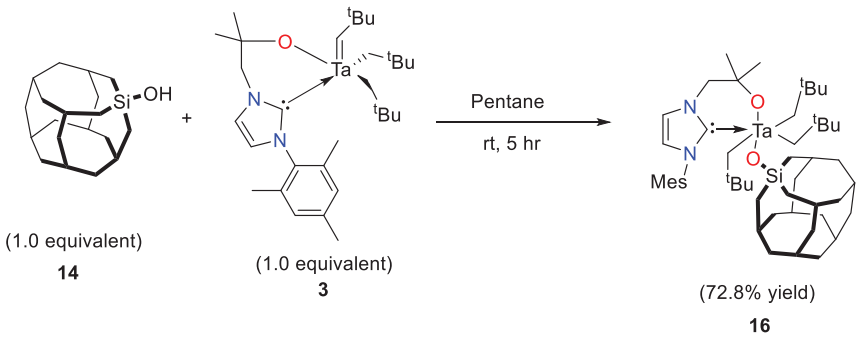

Scheme 4.7. 1,2-addition of POSS-OH to the alkylidene moiety of the tantalum NHC precursor **16.**

Multiple attempts to recrystallize this complex at -40°C proved futile due to the high solubility of complex **16** in hydrocarbon solvents, which prevented the isolation of single crystals suitable for X-ray diffraction studies. However, to explore the second step of synthetic route 2, we utilized the crude compound **16**, since it is of sufficient purity based on NMR studies. The incorporation of rhodium metal is achieved by treatment of compound **16** with a toluene solution of $[Rh(COD)Cl]_2$ (**Scheme 4.8**).

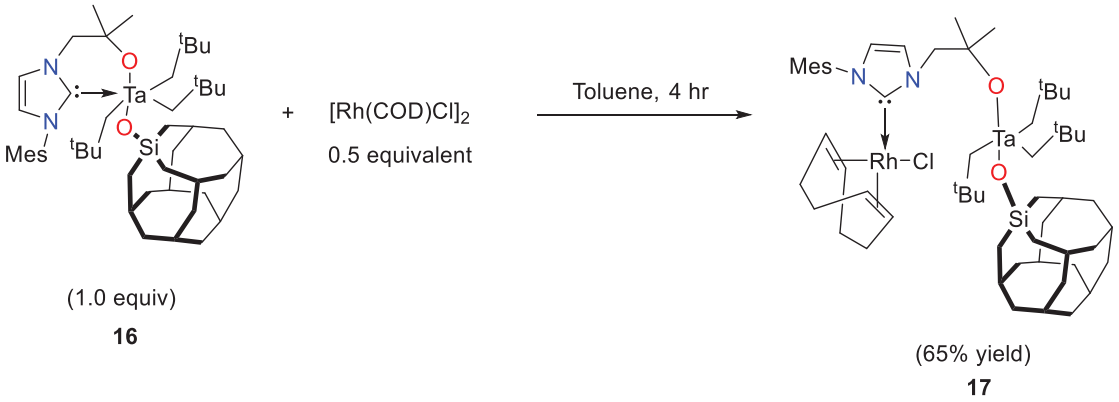

(1.0 equiv)
16

(65% yield)
17

Scheme 4.8. Synthetic route 2. The addition of $[Rh(COD)Cl]_2$ to complex **16** at room temperature leads to transmetallation of the NHC motif from Ta to Rh, and allows the incorporation of the rhodium metal center into the complex.

The color of the reaction mixture changes from creamy yellow (starting material) to dark yellow during the progress of reaction. The solvent is removed under vacuum to yield the projected compound as a yellow powder (65% yield). The ^1H NMR spectrum of the complex **17** in C_6D_6 (Figure S5) shows the appearance of two broad peaks at δ = 5.4 and 3.6 ppm attributed to the cyclooctadiene sp^2 protons, which supports the incorporation of the Rh-COD motif into the complex. The remaining signals for the sp^3 protons of the cyclooctadiene group are overlapping with the broad POSS signals. The two equivalent meta protons of the mesityl ring of complex **16** (observed at 6.8 ppm) are now observed as two separate peaks at δ = 6.95 and 5.95 ppm respectively in complex **17** which reflects the asymmetric nature of complex. The N-CH_2 protons of the NHC ligand are also observed as two distinct doublets at δ = 6.4 and 4.4 ppm respectively instead of a singlet as observed in the precursor complex **16**, as shown on **Figure 4.2** below. This again supports the observation that after the incorporation of rhodium metal into complex **16** an asymmetric species, **17**, is formed. To gain more insight into the structure of complex **17**, multiple attempts were made to recrystallize the compound with the hope of getting single crystals suitable for XRD characterization. Unfortunately, the

compound did not recrystallize, again because of the high solubility of the compound in hydrocarbon solvents.

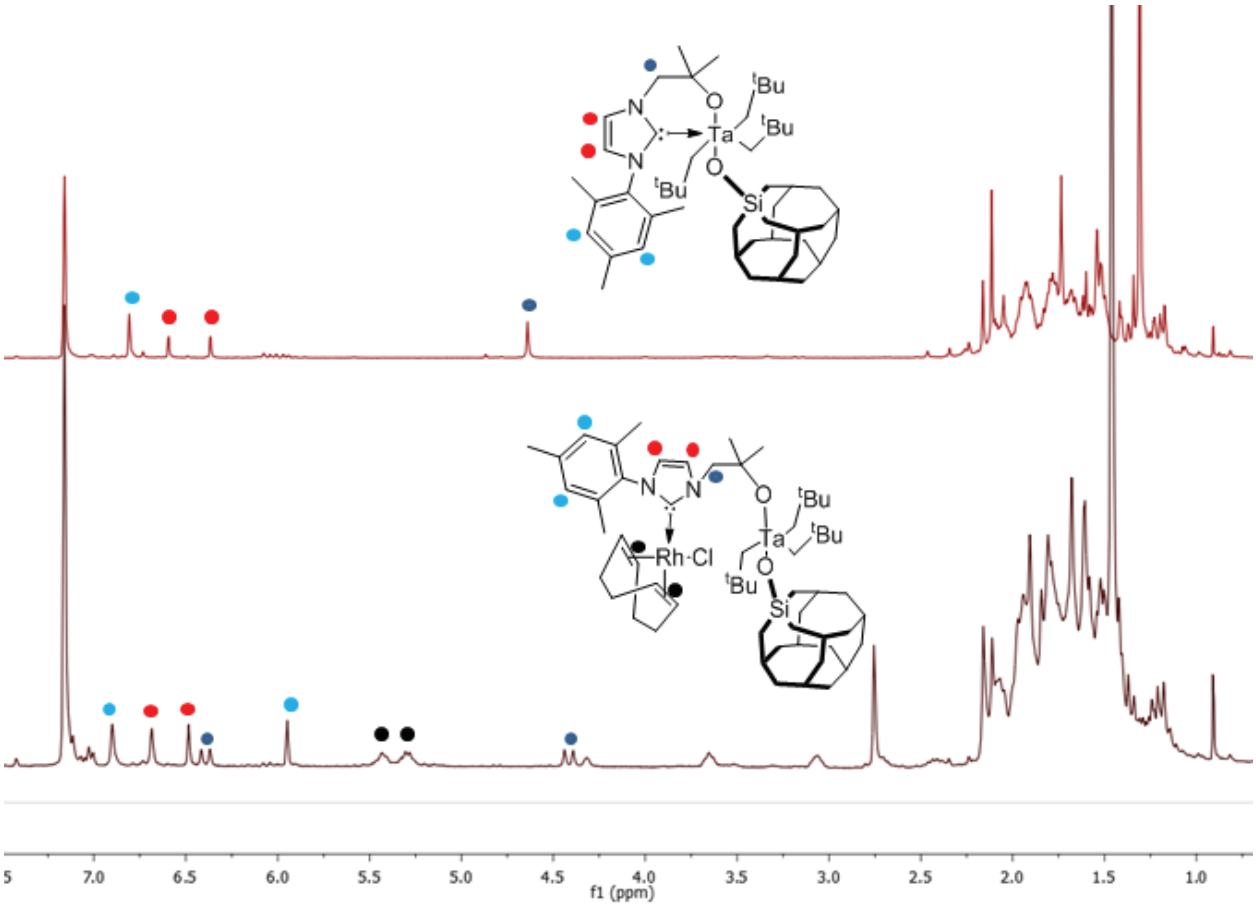

Figure 4.2. Comparison of the ^{1}H NMR spectra of the POSS supported tantalum monometallic complex **16** (below) and tantalum-rhodium bimetallic complex **17** (above), recorded in C_6D_6 solution.

In summary, the above discussion on the synthesis of POSS based heterobimetallic complexes establishes that route **1** leads to unidentifiable mixture of substances at 60°C, but appreciatively route **2** yields the desired bimetallic complex (**Figure 4.3**). We also studied the reaction between the trimetallic complex (Rh_2Ta) **11** and POSS-OH which did not proceed at room temperature. On further elevating the temperature of the mixture to 60°C, this leads to decomposition of the trimetallic compound to yield unidentified mixture of substances (**Figure 4.3** bottom row).

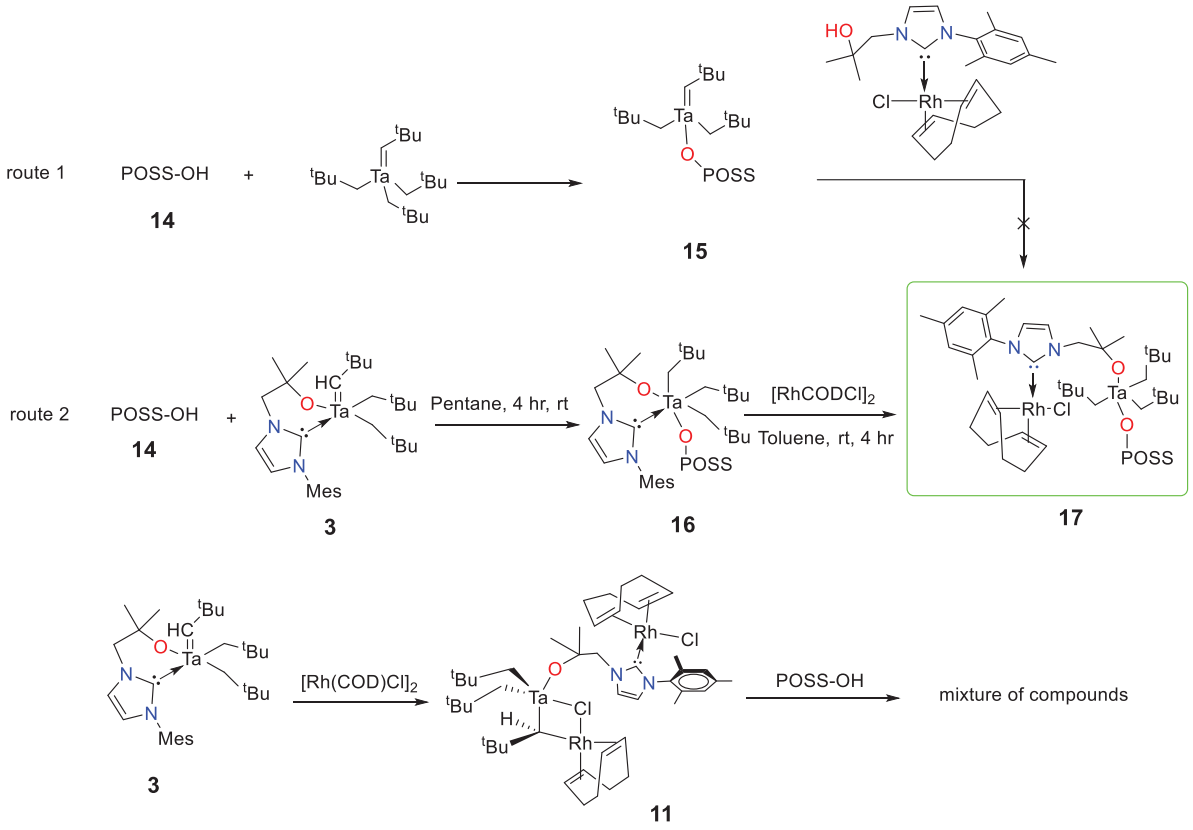

Figure 4.3: The figure shows that only route 2 is appropriate to synthesize a POSS based tantalum-rhodium bimetallic complex. Route 1 leads to mixture of products at elevated temperatures whereas route 3 did not yield the desired molecular bimetallic complex but a trimetallic one, and its reaction with POSS-OH is ill-defined.

4.2.2) Synthesis, characterization and reactivity of tris(tert-butoxy) silanol based heterobimetallic complexes

Since the elaborate POSS derivatives could not be structurally characterized, we turned our attention to simpler silanols as molecular models of the surface silanols groups of silica supports. Tris(tert-butoxy)silanol [(^{t}BuO)$_3$SiOH] is a commercially available and bulky silanol which has also been used as a silica mimicking molecular model[14] and a wide range of tris(tert-butoxy) silanolate derivatives have been synthesized and recrystallized.[15–20] Following an analogous synthetic route (as developed for POSS) the tris(tert-butoxy)siloxy tantalum-NHC derivative, **18**, is isolated.(**Scheme 4.9**) The ^{1}H NMR monitoring of the reaction in C_6D_6 (figure S6) shows disappearance of the alkylidene proton from the tantalum precursor and no evolution of neopentane during the reaction process, in agreement with a 1,2 addition of the hydroxyl group to the alkylidene moiety, as seen in the case of the POSS chemistry described

above. Complex **18** features good thermal stability (up to 110°C) and is fully characterized through ^{1}H, ^{13}C NMR and IR spectroscopy and elemental analysis. The ^{1}H NMR and the ^{13}C NMR spectra of complex **18** in C_6D_6 does not contain signals corresponding to alkylidenic proton/carbon of a putative Ta=CH(^{t}Bu) motif which is in accordance with a formal 1,2-addition of the silanol hydroxyl onto the tantalum neopentylidene fragment. The ^{13}C NMR spectrum of **18** (figure S7) depicts a characteristic signal at δ = +219.4 ppm corresponding to the carbenic carbon of the NHC ligand. Such a downfield shift of this signal (as compared to corresponding $\delta(^{13}C_{NHC})$ = 203.1 ppm in complex tantalum-NHC complex[21] **3** is evocative of free carbenes which are not interacting with transition metal centers (typical range: 210-220 ppm).[22–24] Accordingly, the NHC moiety in **18** is most likely not interacting with the Ta, as represented in **Scheme 4.9**.

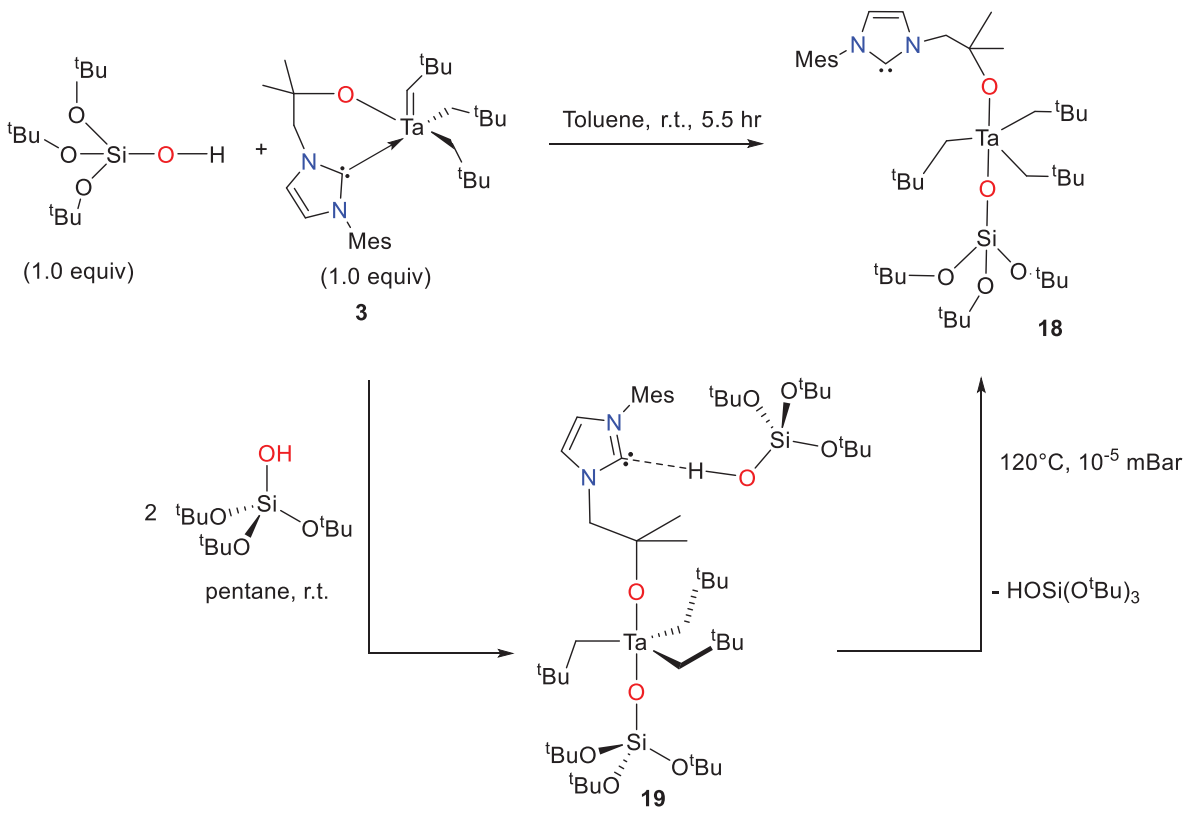

Scheme 4.9. Synthesis of the *tris*(tert-butoxy)siloxy tantalum-NHC complex **18**. Addition of 2 equivalents of silanol leads to an unusual silanol-NHC adduct **19**.

Interestingly, we discovered that addition of two equivalents of $HOSi(O^{t}Bu)_3$ onto **3** affords an unanticipated silanol-NHC adduct, $\{HOSiO^{t}Bu_3\}\{Ta(L)[OSi(O^{t}Bu)_3](CH_2{}^{t}Bu)_3\}$ **19** in **Scheme 4.9**. The ^{1}H NMR spectrum for **19** (Figure S8) exhibits a highly shifted singlet resonance for the

hydroxyl proton at δ = 7.78 ppm. The ^{13}C NMR spectrum for **19** (Figure S9) is particularly diagnostic. The ^{13}C carbene resonance is shifted upfield in comparison with that of **18** (δ = +206.8 versus +219.4 ppm respectively), which indicates that the carbene is engaged into electronic donation to the hydroxyl proton. Similar behavior was previously reported for the free hydroxyl-carbene 1-mesityl-3-(2-hydroxyisobutyl) imidazol-2-ylidene ligand, as described in Chapter 2. This behavior is also reported for *N,N'*-bis(mesityl)imidazol-2-ylidene (IMes) in the presence of methanol, whose ^{13}C carbenic resonance is shifted from δ = 219.7 ppm[25] in the absence of methanol to δ = 203.9 ppm[26] in the IMes-methanol H-bonded adduct. The solid-state structure of **19**, which is reproduced in **Figure 4.4**, is a rare example of a silanol-carbene hydrogen-bonded adduct. The measured distance between the hydroxyl oxygen and the NHC carbon is short (2.782(5) Å) and is consistent with hydrogen bonding. The silanol-carbene formulation proposed for **19** is confirmed by the values of the C1-N_{imid} bond lengths (1.357(5) and 1.358(5) Å) and the N1-C1-N2 ring angle (102.9(3)°) (typical range for NHCs: 1.35-1.37 Å and 101-105°).[21,23] In the putative symmetrically opposite siloxy-imidazolium situation, a shortening of the C-N_{imid} bond lengths and a relaxation of the NCN ring angle would have been expected (typical range for imidazoliums: 1.31-1.34 Å and 107-110°). The formation of **19** further suggests that the NHC moiety in **18** is most likely unbound to Ta, or at least highly labile and available for further reactivity. This behavior was unexpected since treatment of Ta-alkyl derivatives with silanols usually leads to protonolysis and formation of Ta siloxides with release of alkane.[7,8,27] The thermal treatment (120°C) of **19** under vacuum (10^{-5} mBar) does not trigger protonolysis of a Ta-neopentyl moiety either. Instead, the free NHC species **18** is quantitatively restored, through sublimation of the hydrogen-bonded $HOSi(O^tBu)_3$ molecule. The lability of the carbenic carbon with respect to the tantalum center in complex **18** is exploited in the transmetallation reaction with rhodium. Complex **18** was treated with 0.5 equivalents of $[Rh(COD)Cl]_2$ in THF at room temperature to selectively afford the desired heterobimetallic complex $\{Ta(\mu\text{-}L)[OSi(O^tBu)_3](CH_2{}^tBu)_3Rh(COD)(Cl)\}$, **20**, in 85% yield (**Scheme 4.10**).

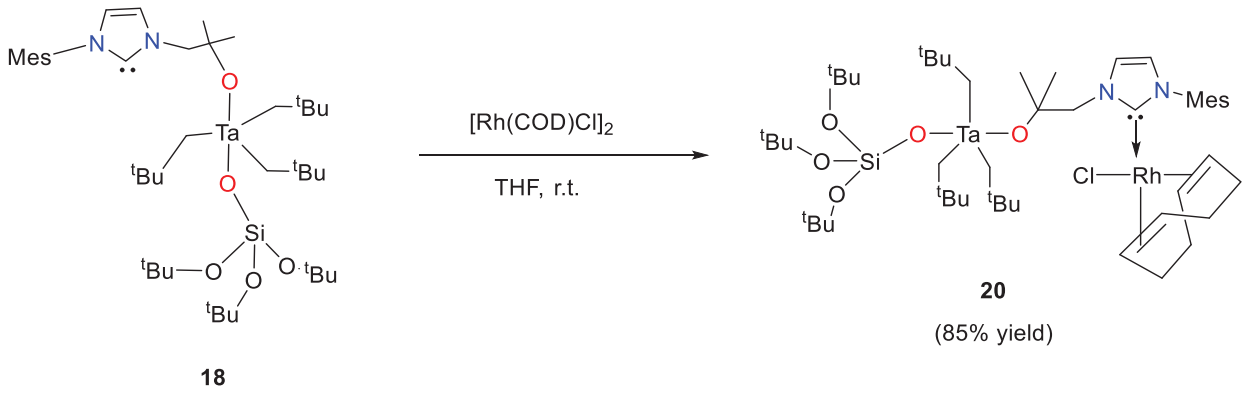

Scheme 4.10: Synthesis of the Ta/Rh heterobimetallic complex **20**.

The rhodium coordination to the NHC moiety in solution is confirmed by the ^{13}C NMR spectrum (Figure S11) of complex **20** in C_6D_6 which displays a characteristic resonance at δ = +184 ppm, strongly shifted downfield when compared to **18**, with a $^{1}J_{Rh\text{-}C}$ coupling constant of 52 Hz which is distinctive of a Rh-$C_{carbene}$ interaction.[28,29] The coordination of COD to rhodium is confirmed by the ^{1}H NMR spectrum of complex **20** (Figure S10) which shows characteristic signals at δ = 4.92, 4.70, 2.87 and 2.46 ppm corresponding to the Rh-bound sp^2 protons of the cyclooctadiene ligand. As a result of Rh ligation, the alkoxy-NHC ligand backbone adopts a more rigid conformation, which is reflected notably by the N-CH_2 ^{1}H NMR signal (singlet integrating for 2H at δ = 4.80 ppm in **18**) which splits into two doublets at δ = 6.12 and 4.34 ppm ($^{2}J_{HH}$ = 14.0 Hz) in **20**. Finally the formula of **20** is supported by elemental analysis and its solid-state structure as determined by X-ray crystallography. A view of the structure is reproduced on **Figure 4.4** and confirms that Rh is indeed coordinated to the NHC moiety.

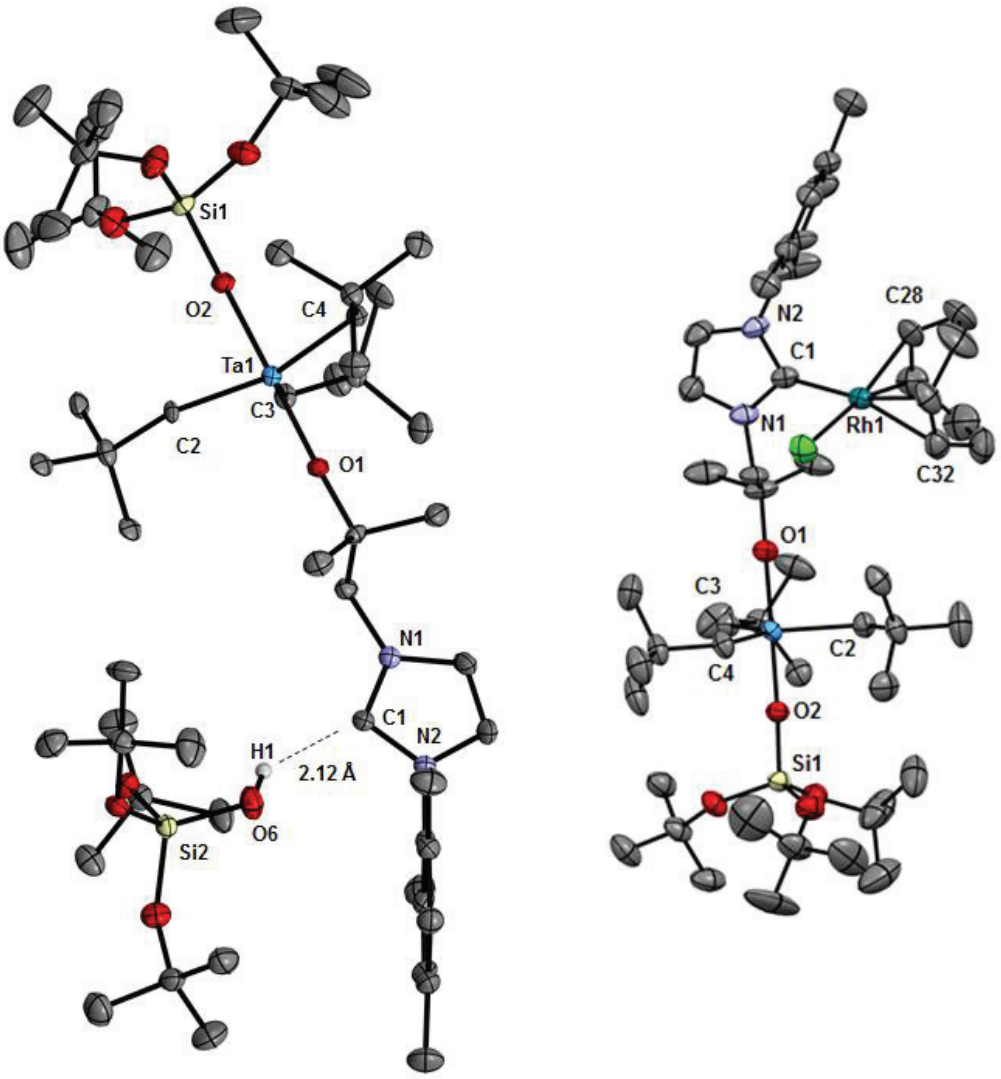

Figure 4.4. Solid-state molecular structures of **19** (left) and **20** (right) (50% probability ellipsoids). Hydrogen atoms, except that of the silanol group in **19** (H1) have been omitted for clarity. Selected bond distances (Å) and angles (°) for **19**: Ta1-O1 1.883(3); Ta1-O2 1.921(3); Ta1-C2 2.162(4); Ta1-C3 2.150(3); Ta1-C4 2.165(4); O6···C1 2.782(5); N1-C1 1.357(5); N2-C1 1.358(5); O1-Ta1-O2 179.0(1); N1-C1-N2 102.9(3); O6-H1···C1 137.8(3). For **20**: Ta1-O1 1.882(4); Ta1-O2 1.912(4); Ta1-C2 2.165(6); Ta1-C3 2.184(6); Ta1-C4 2.163(7); Rh1-C1 2.033(7); Rh1-Cl1 2.3740(18); Rh1-C27 2.090(8); Rh1-C28 2.101(7); Rh1-C31 2.162(8); Rh1-C32 2.182(8); N1-C1 1.364(8); N2-C1 1.362(8); O1-Ta1-O2 178.2(2); N1-C1-N2 102.7(6); C1-Rh1-Cl1 85.52(19).

As in **19**, the tantalum atom adopts trigonal bipyramid coordination geometry with the neopentyl ligands in equatorial position and the two oxygen donors in apical position. The Ta-C and Ta-O bond distances are as expected.[30] The rhodium center adopts a pseudo square-planar geometry, which is characteristic of d^8 Rh(I) species. The NHC ring is tilted with respect to the pseudo-D_{4h} plane (dihedral angle 68.1(2)°), and the Rh-C_{NHC} bond distance (2.033(7) Å) is in the range of reported values for related Rh-NHC complexes.[31–34] The Rh-C_{COD}

bond distances in trans position with respect to the NHC ligand (2.162(8) and 2.182(8) Å) are slightly elongated compared to that trans to the chloride (2.090(8) and 2.101(7) Å), which is in agreement with the strong sigma donation of the NHC. Both metals lie far away from one another and are separated by 6.6997(8) Å.

After synthesis and characterization of complex **20**, its reactivity with dry dihydrogen was explored as shown in **Scheme 4.11.**

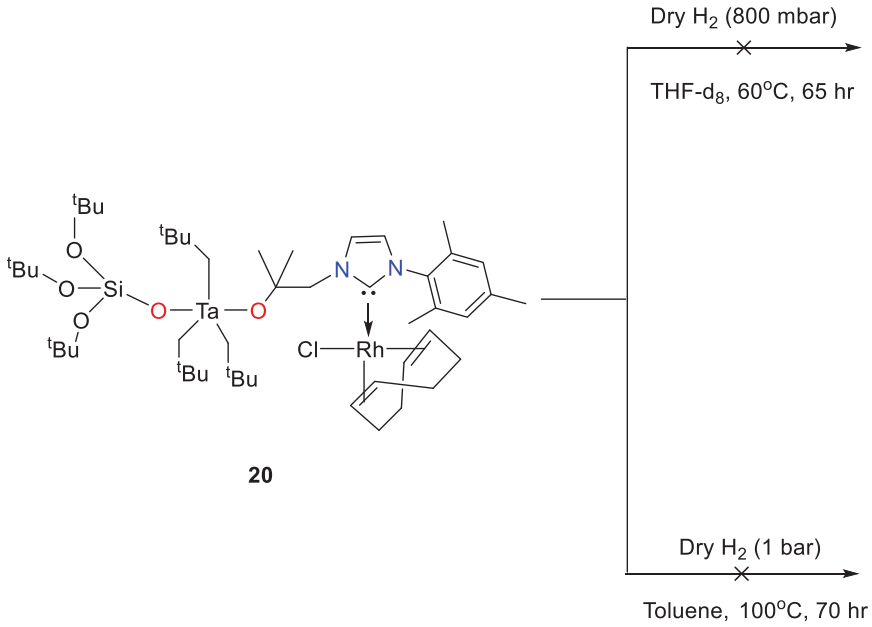

Scheme 4.11. Dihydrogen is introduced in a reaction vessel containing a yellow solution heterobimetallic complex **20** and the reaction mixture is heated at different temperatures. However neither the formation of metal hydride species nor the release of either cyclooctane or neopentane is observed.

Dihydrogen (800 mbars) is introduced in a reaction vessel containing a yellow THF-d_8 solution of the heterobimetallic complex **20**. ^{1}H NMR monitoring of the reaction shows the presence of a dihydrogen resonance as a singlet at δ = 4.59 ppm. The reaction mixture is heated to 60°C but no reaction is observed at this temperature, therefore the reaction is performed again in toluene-d_8. The toluene-d_8 solution of complex **20** is heated at 100°C for 70 hours in the presence of H_2 (1 bar). Even at this temperature no reaction between the both reagents is observed which reflects the chemical and thermal stability of complex **20**. Harsher conditions (higher H_2 pressure or temperature) are probably required to trigger the formation of metal hydride species through the release of cyclooctane or neopentane, but we did not explored this range of experimental conditions with the homogeneous complex. Instead we developed

silica-supported analogues and explored the reactivity of these materials with H_2 in a gas-solid reaction, as described below.

4.2.3) Surface OrganoMetallic Chemistry

4.2.3.1) Synthesis and characterization of the silica support: $SBA_{15\text{-}700}$

Mesoporous silica is chosen as silica support due to its high surface area (approx. 1000 $m^2.g^{-1}$) which in turn will provide higher quantity of surface silanols to graft the organometallic complex. Having a good loading of active sites is extremely important for characterization purposes, notably by solid-state NMR, to have a better signal/noise ratio, especially since we work at low density of sites (see below). The most popular and commonly used mesoporous silicas for SOMC are SBA-15 (Santa Barbara amorphous-15) and MCM-41 (Mobil crystalline material-41). We opted for SBA-15 as the silica support for grafting the organometallic complexes since it features a thermal stability up to 700°C, with no collapse of the mesostructure and contains high surface area.[17,35] Compared to MCM-41, SBA-15 also displays larger pore size (c.a. 8 nm in the present case) which avoids diffusion issues during catalytic processes.[35,36] SBA-15 is synthesized using a sol-gel process.[37–40] Pluronic P123 [symmetric triblock copolymer constituted of poly(ethylene oxide)$_{20}$-poly(propylene oxide)$_{70}$-poly(ethylene oxide)$_{20}$] is used as a structure directing agent (template) to ensure uniform pore size. Tetraethoxysilane (TEOS) is dissolved in acidic distilled water (pH = 2.0) in the presence of NaF catalyst and the template to yield the well-structured mesoporous silica material. The structure directing agent is removed by calcination at 200°C under the continuous flow of dry air. The calcined SBA-15 is then dehydroxylated to a final temperature of 700°C (by gradually increasing the temperature) under high vacuum (10^{-5} mbar), yielding a material (namely $SBA\text{-}15_{700}$) which is stored under inert atmosphere. This last step of the process is extremely important to control the surface chemistry of the material and to obtain a support with low density of isolated surface hydroxyl groups (ca. 0.6 ≡Si-OH groups *per* nm^2), required for ensuring sites-isolation. The Diffuse Reflection Infrared Fourier Transform (DRIFT) spectrum of $SBA\text{-}15_{700}$ (*i.e.* after dehydroxylation) is particularly diagnostic since it features only the characteristic sharp IR band at 3747 cm^{-1} corresponding to isolated surface silanols[41] (**Figure 4.5** blue trace), while the spectrum of the material before dihydroxylation (SBA-15) shows a broad distribution of bands in the range 3100-3800 cm^{-1} arising from the several types of surface hydroxyl groups (vicinal, geminal and isolated surface silanols) as well

as physisorbed water, which is reflected by the presence of the δ_{OH} vibration at 1628 cm^{-1} (**Figure 4.5** red trace).

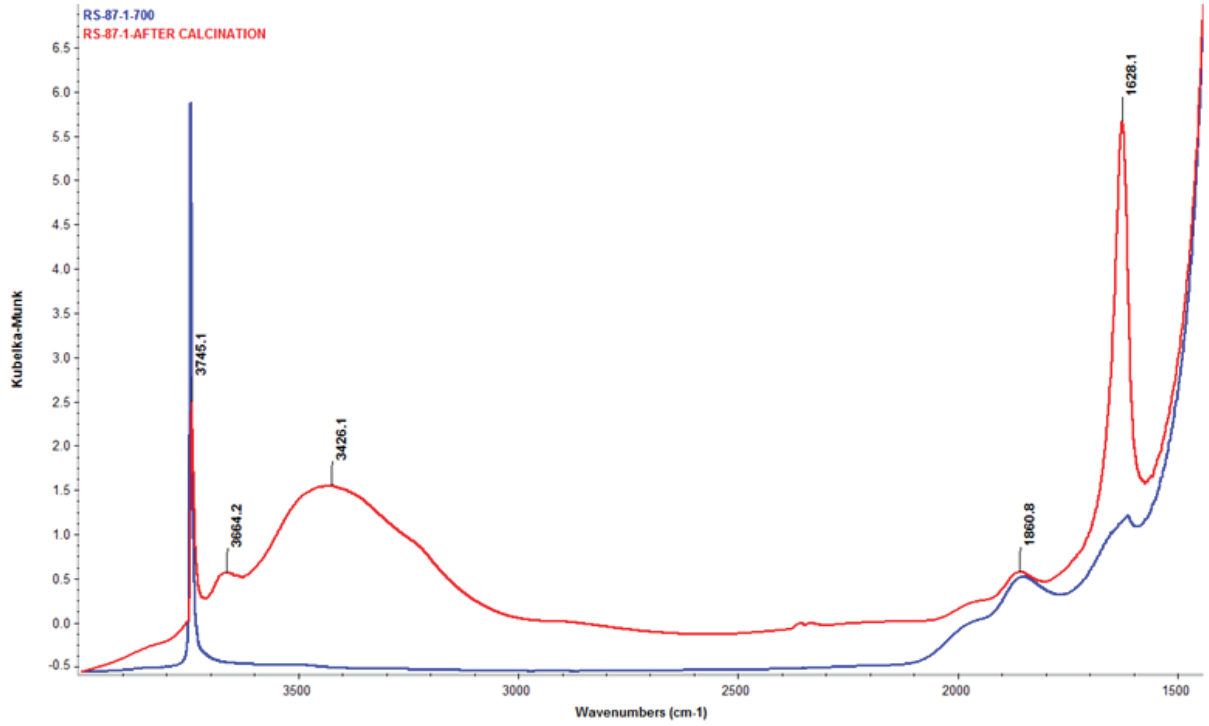

Figure 4.5: DRIFT spectra of SBA-15 after calcination (red color) and after dehydroxylation at 700°C under high vacuum (blue color). The sharp peak at 3747 cm^{-1} corresponds to the stretching vibration of the hydroxyl groups arising from isolated surface silanols (Si-OH) units.

This SBA-15_{700} support still contains high loadings of reactive surface silanols *per* gram (c.a. $5x10^{20}$ sites.g^{-1}) due to the high surface area of this mesoporous silica (895 $m^2.g^{-1}$), as determined by N_2 adsorption-desorption studies. The resulting material contains an ordered hexagonal network of rod-shaped mesopores, as expected for this type of material and observed by TEM. The existence of single distribution of mesopores was also confirmed by N_2 adsorption-desorption studies (Figure S12).

4.2.3.2) Synthesis and characterization of silica-supported tantalum-NHC species

The grafting of complex **3** was performed upon treatment of SBA15_{700} with a diethyl ether solution of **3** in a two-sided Schlenk reaction vessel equipped with a sintered glass filter. The reaction mixture was stirred at room temperature for 5.0 hours. After the reaction the

supernatant is filtered away from the solid, and the solid is washed with fresh solvent to ensure removal of unreacted **3**, if any. The volatile components are then condensed in a 6.7 liters round bottom flask under high vacuum and the gas phase is injected into GC which revealed that 0.1-0.2 equivalent of neopentane is released *per* grafted Ta (quantified against propane used as internal standard). The low amount of released neopentane is attributed to the partial decomposition of complex **3** (leading to **4**, as described in chapter 3) during the course of reaction. The DRIFT spectrum of the isolated material (**Figure 4.6**) shows the disappearance the sharp IR band at 3747 cm^{-1} corresponding to isolated surface silanols. New signals attributed to $\nu(C_{sp3}\text{-}H)$ stretches from the alkyl groups of the ligands are observed in the region 3000-2850 cm^{-1}. $\nu(C_{sp2}\text{-}H)$ stretches from the mesityl group as well as the NHC backbone are observed as a weak broad peak around 3142 cm^{-1}. The δ_{CH} frequencies are observed in the region 1620-1300 cm^{-1}. These analyses are consistent with the chemical grafting of the precursor onto silica *via* the 1,2-addition of the Ta alkylidene group to surface silanols.

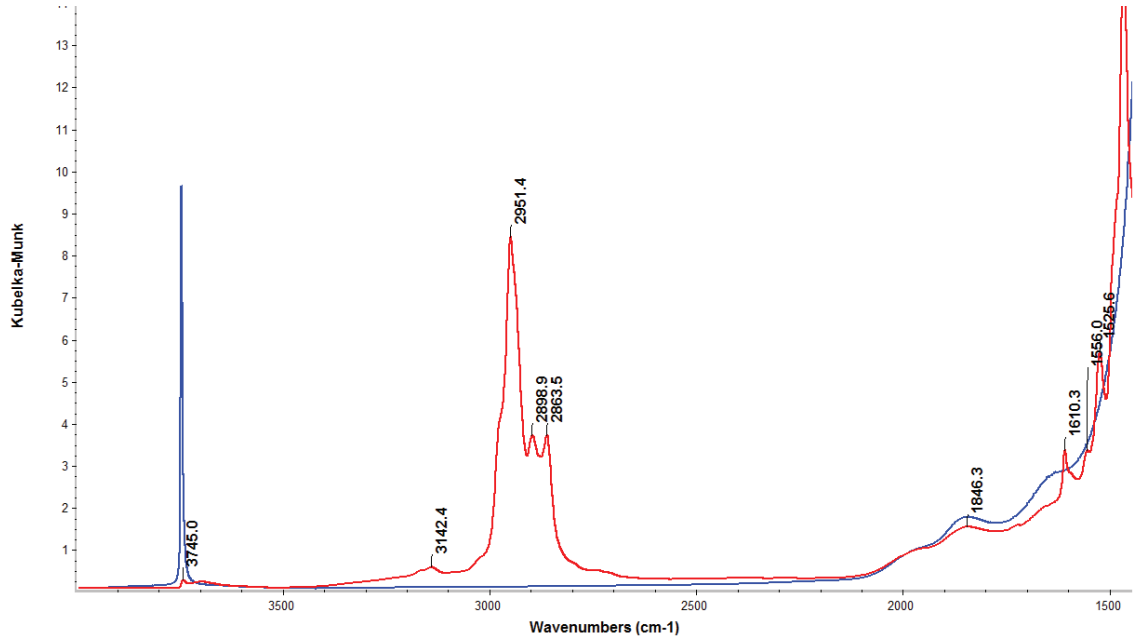

Figure 4.6: DRIFT spectra of SBA-15_{700} (blue line) and material **21** (red line) recorded on powder materials under argon.

The elemental analysis of the grafted complex **21** (Expected wt. %: Ta, 8.59; C, 17.67; H, 2.53; N, 1.32. Found: Ta, 8.59; C, 15.98; H, 2.53; N, 1.60s) is in excellent agreement with the expected elemental composition.

The ^{13}C CP-MAS (Cross Polarisation - Magic Angle Spinning) Solid State NMR spectrum of material **21** is recorded to gain more details into the structure of the grafted complex. The

spectrum, shown in **Figure 4.7,** shows the expected ligand signals, with aromatic carbon resonances corresponding to the mesityl group in the region 140-120 ppm and a signal at 120 ppm corresponding to the imidazole backbone. The Ta-CH_2 moieties are observed at δ = 90 and 80 ppm and the N-CH_2 and –OC moieties are found at 61.93 and 76.93 ppm respectively. Signals observed in the alkyl region correspond to tert-butyl groups and the methyl groups from the ligand framework. No signal corresponding to a putative tantalum alkylidene carbon was located, which indicates that that it has been consumed during the reaction, in agreement with the solution studies reported in the first section of this chapter.

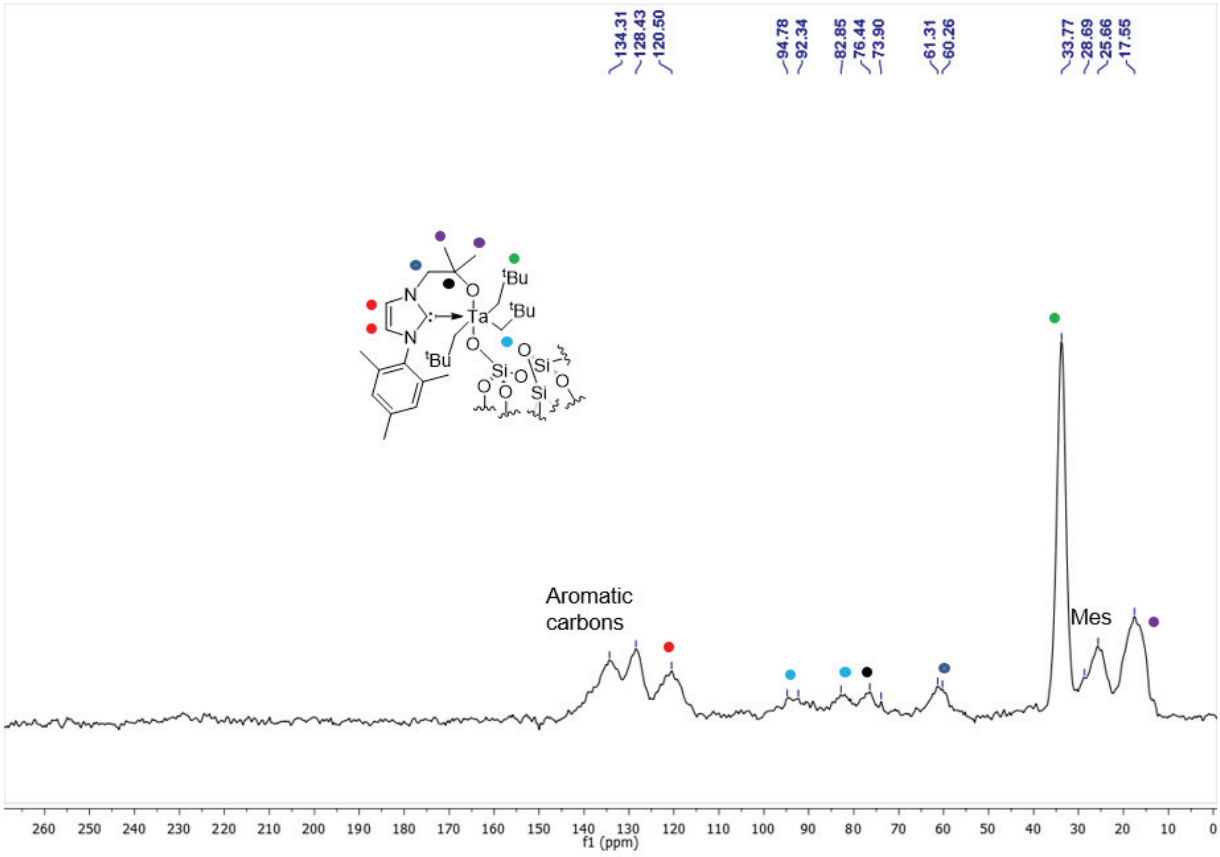

Figure 4.7: ^{13}C CPMAS SS NMR spectrum of material **21**.

Unfortunately the signal corresponding to the carbenic carbon could not be observed in the ^{13}C CP MAS SSNMR. This is due to the low sensitivity of ^{13}C NMR, which is amplified by the transfer of polarisation from hydrogen atoms attached to the carbon atoms in CP experiments, but this does not apply to the carbenic carbon which does not have hydrogens attached. Hence the ^{13}C labelled version of complex **3** (labelled at the carbene position using ^{13}C formaldehyde) is synthesized and grafted over silica surface using a similar procedure.

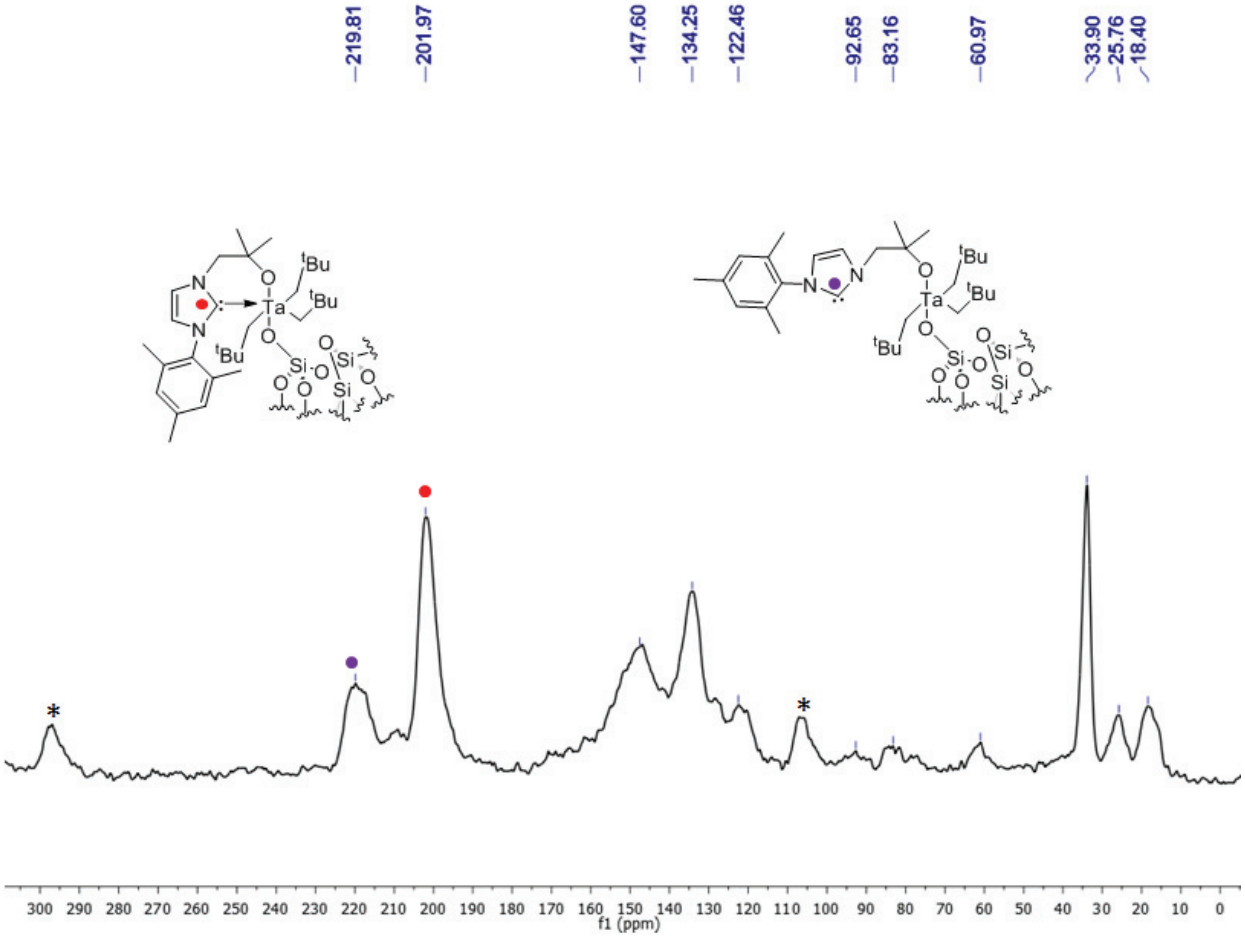

Figure 4.8: ^{13}C CP-MAS SSNMR of the ^{13}C labelled tantalum-NHC complex grafted over $SBA15_{700}$. The peaks labelled by an asterisk (*) correspond to satellite bands.

The ^{13}C CP-MAS SS NMR spectrum of the ^{13}C labelled material **21**, reproduced on **Figure 4.8,** displays two signals corresponding to the $NHC_{carbene}$. The medium intensity signal at 219.81 ppm corresponds to a free carbene[24] which is not interacting with the tantalum centre. This observation is similar to that found in the case of the *tris*(tertbutoxy)siloxy Ta-NHC complex **18** (carbene signal at 219 ppm) as discussed in section 4.2.2. In addition, an intense carbene signal is also observed at 201.97 ppm, and corresponds to a tantalum bound NHC moiety.[21,24,42] Based on the SSNMR data we can conclude that material **21** contains two different Ta surface species: the major component, complex **21**, in which the NHC ligand is bound to Ta, and a minor species, complex **21'**, in which the NHC ligand remains unbound, as proposed in **Scheme 4.12**.

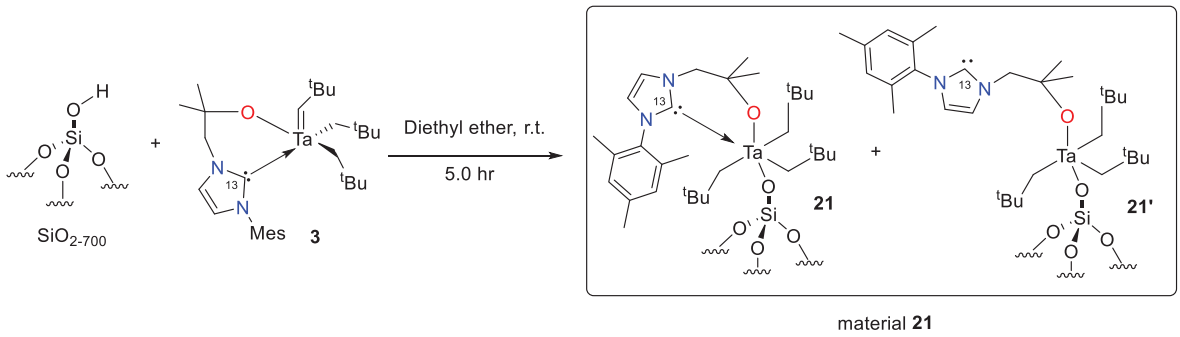

Scheme 4.12. Preparation of the silica-supported Ta-NHC species leading to material **21** which contains two type of Ta surface species, **21** and **21'**.

4.2.3.3) Preparation and characterization of silica-supported Ta/Rh heterobimetallic species

Material **21**, containing the ^{13}C labelled ligand, is then treated with a THF solution of the rhodium dimer $[Rh(COD)Cl]_2$ (0.5 equivalents) in order to get the silica-supported Ta/Rh heterobimetallic species. When the reaction is carried out at room temperature for 5.0 hours material **22** is obtained as a light yellow powder after workup (**Scheme 4.13**). GC analysis of the volatile components showed no release of neopentane and cyclooctadiene, as anticipated. The DRIFT spectrum of material **22**, as shown in **Figure 4.9**, is very similar to that of material **21**, which is expected. Therefore the IR data cannot prove rhodium incorporation in the material.

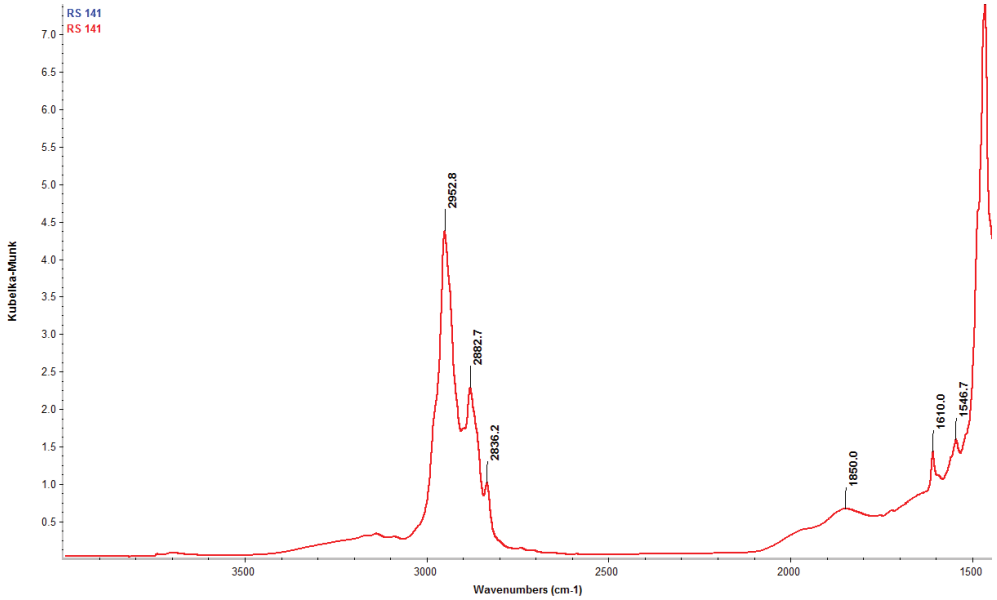

Figure 4.9: DRIFT spectrum of material **22** recorded under argon atmosphere.

The ^{13}C CP-MAS SSNMR of material **22** (**Figure 4.10**) shows a carbenic resonance at 184 ppm which is characteristic of the Rh-NHC species[33,43,44] and validates the incorporation of rhodium metal into the complex. The corresponding COD sp^2 C-H carbons are observed overlapping with the Ta-CH_2 moieties and SSNMR sidebands (labelled with * on **Figure 4.10**) in the region 100-80 ppm. However, although species **21'** is fully reacted, it is also observed that some unreacted species **21** is remaining on the surface, depicted by the residual peak at 201.97 ppm. This is attributed to the easier metalation of species **21'**, in which the NHC moiety is free, in comparison to species **21**, in which the NHC is bound to Ta and requires transmetallation from Ta to Rh to lead to **22**.

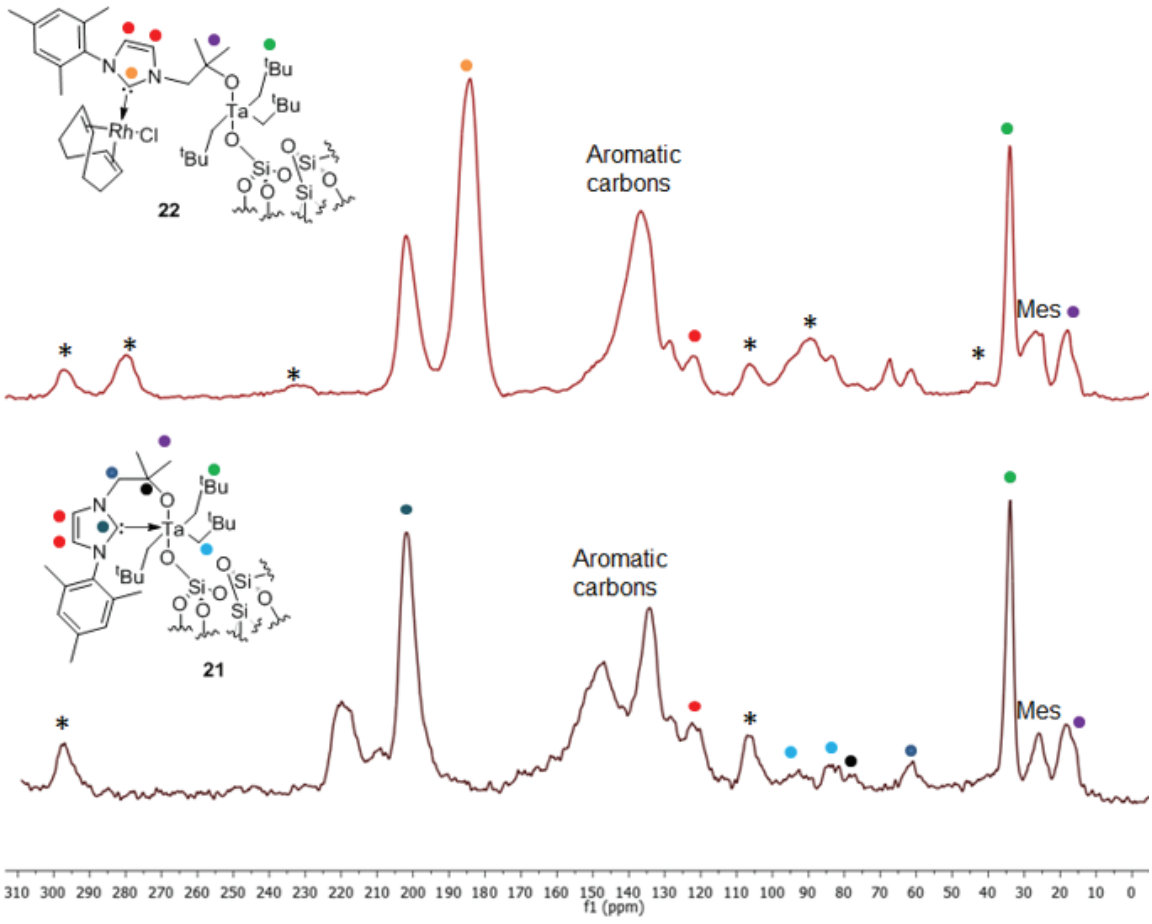

Figure 4.10. The ^{13}C CP-MAS SS NMR spectra of material **22** (above) and material **21** (below). The comparison of the two spectra clearly shows the NHC coordination to rhodium in material **22** (characteristic signal at 184 ppm). The peaks labelled by an asterisk * correspond to satellite bands.

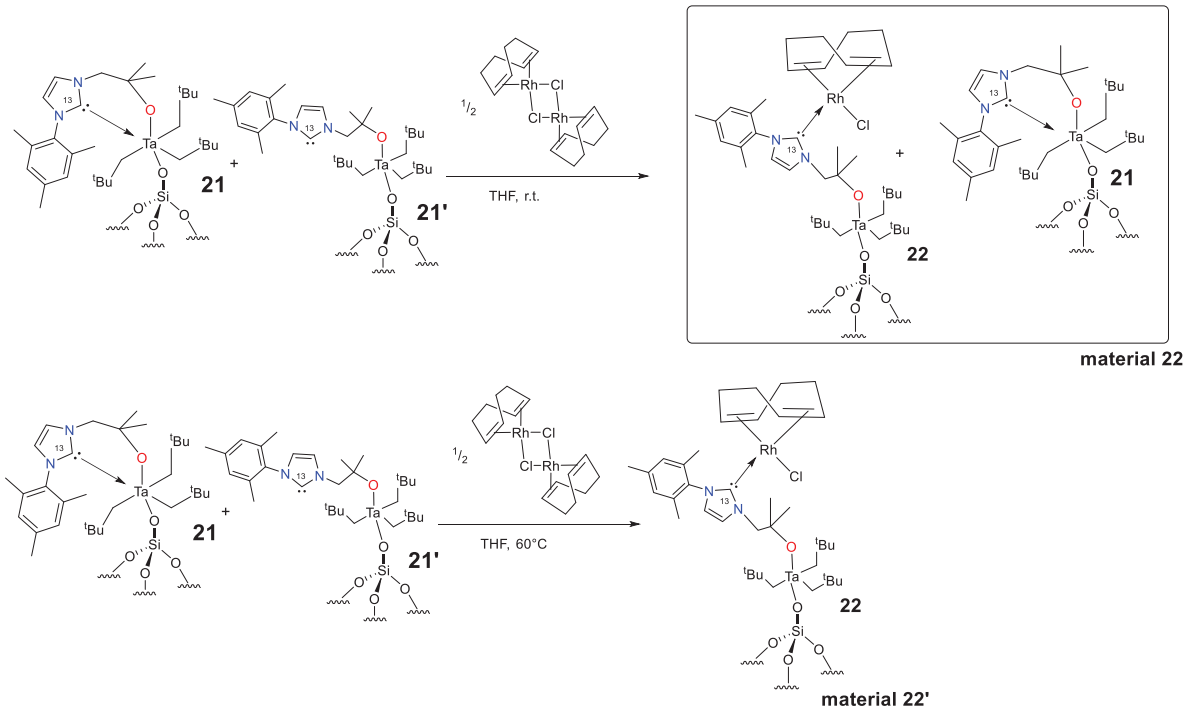

Scheme 4.13. The scheme shows the preparation of the silica-supported Ta/Rh heterobimetallic species **22**.

The reaction conditions is therefore optimized to ensure maximum conversion of complex **21** into **22**. It is observed that the heating the reaction mixture at 60°C strongly improves transmetallation of the carbene ligand from tantalum to rhodium (**Figure 4.11**). This conversion is evident from the disappearance of the residual Ta-$NHC_{carbene}$ signal at 201 ppm in the ^{13}C SSNMR spectrum. However, heating the sample at 60°C also leads to partial decomposition of product **22** as evidenced by the release of 0.15 equivalent of neopentane. In addition an increase of the ^{13}C NMR signal at 140 ppm is also observed. The aromatic carbons from the mesityl substituent of the NHC ligand appear at this chemical shift. But, as reported in chapter 2 of the thesis, the ^{13}C NMR resonance of the imidazolic carbon arising from the imidazolium species are also observed in this region (enhanced due to ^{13}C labelling at this position). Therefore this could point towards the partial formation of imidazolium species on the surface.

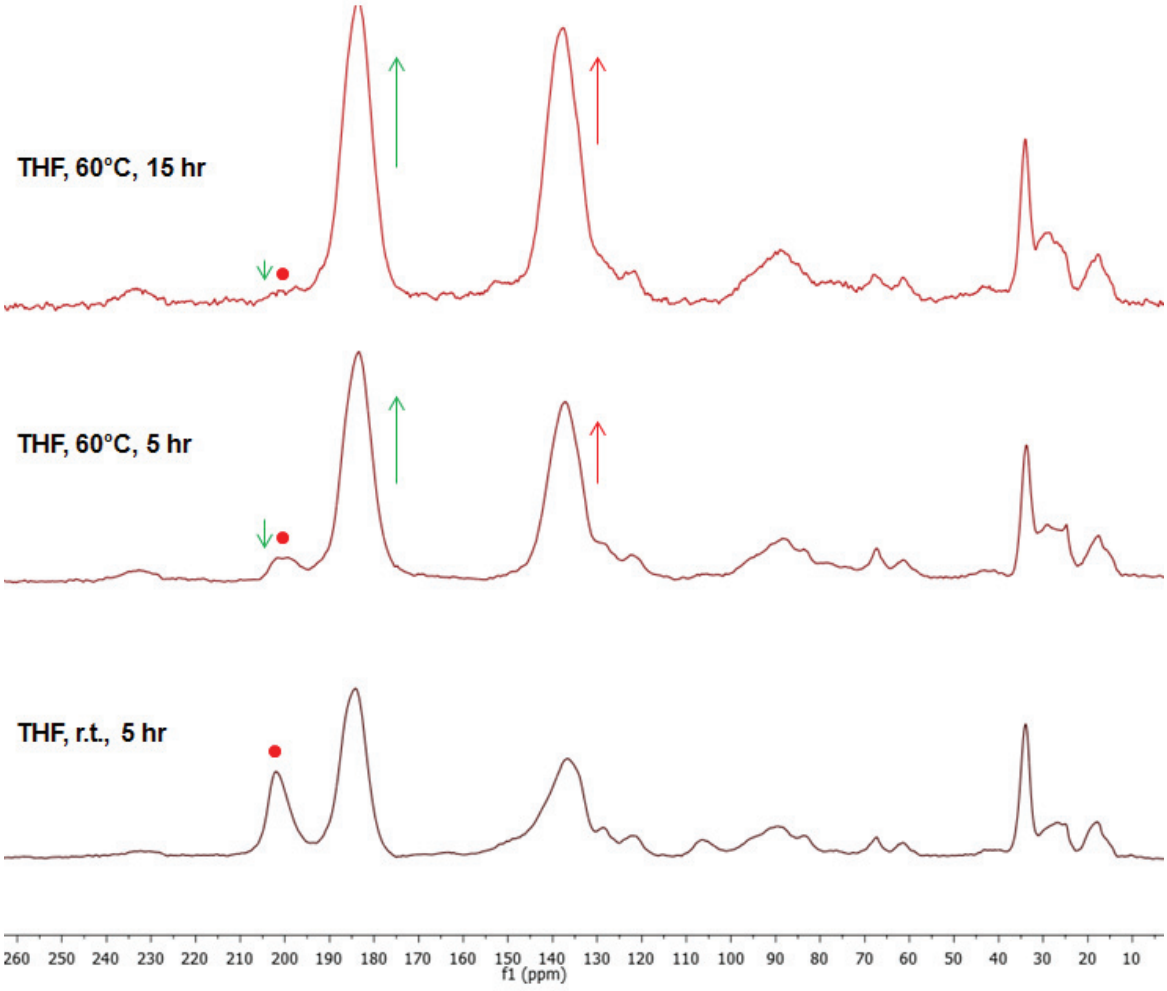

Figure 4.11. The figure shows that increasing the reaction temperature and duration leads to complete transmetallation of the Ta-$NHC_{carbene}$ to Rh-$NHC_{carbene}$ as evident by solid state ^{13}C NMR.

The elemental analysis of the silica-supported heterobimetallic species (material **22'**) gives an Rh/Ta ratio of 0.85. The carbon, nitrogen and hydrogen loadings are 16.36, 1.39 and 2.29 weight % respectively. The elemental analysis result fits with the expected elemental composition (see SI) except that the concentration of chlorine is far lower than expected (expected 1.3 weight%, received 0.1 weight%). We do not have a clear explanation for this abnormally low chlorine concentration.

We then studied the thermal stability of the supported heterobimetallic species. For this purpose a 30 mg pellet of material **22'** is prepared, mounted on a sample holder and transferred into a glass reactor featuring CaF_2 windows to monitor the reactivity by FTIR spectroscopy **(Figure 4.12)**. The sample is then heated at different temperatures under 10^{-5} mbar vacuum. The amount of neopentane released during the reaction is estimated by the

integration of the ν_{C-H} peak, and is also detected by gas chromatography. It is observed by FTIR spectroscopy as well as GC that heating the compound under vacuum at 100°C for 22 hr leads to the release of 1.0 equivalent of neopentane. Note that elevating the temperature to 150°C leads to partial decomposition of the imidazole backbone which is evident from the change in the FTIR spectrum in the region 3050-3200 cm^{-1}.

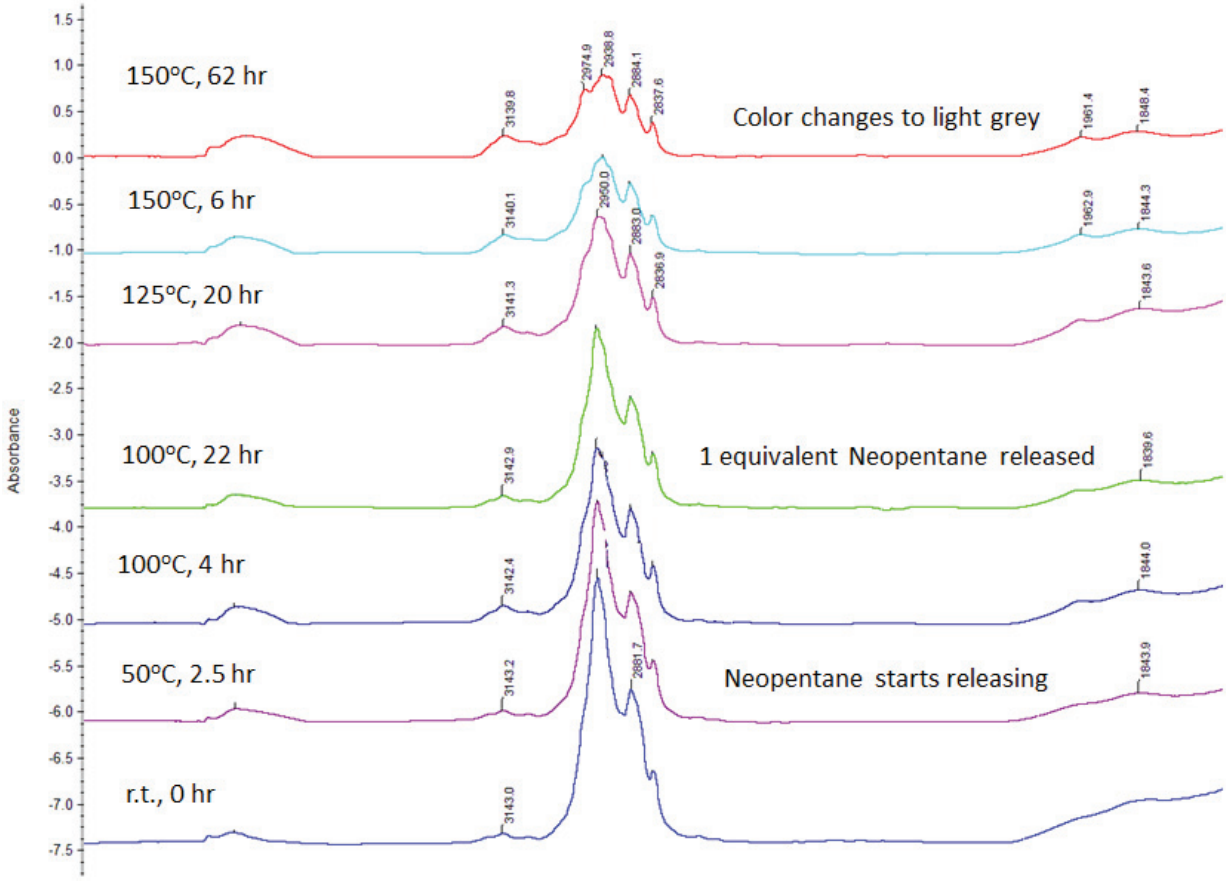

Figure 4.12. FTIR absorbance spectra of material **22'** heated under vacuum at different temperatures shows a decrease in intensity of the CH stretches at 3050-2800 cm^{-1} with increasing temperature.

We also studied the reaction of dihydrogen with the grafted bimetallic complex **22'** in order to synthesize metallic hydrides. For this purpose material **22'** is transferred to a DRIFT cell equipped with KBr windows. The DRIFT cell has a inlet to pass dry dihydrogen gas and a outlet which is connected to a GC-MS apparatus to monitor the gas phase. Dry dihydrogen is passed (1 bar pressure) under countinuous flow (5 ml/min) on the powder and heated at 125°C for 6hr (ramp of 2°C/min from 25-125°C). It is observed that 0.7 equivalent of cyclooctane

(calculated by the area under the curve in Graph 4.1) is released, which is in agreement with the Rh amount determined by elemental analysis; along with neopentane (Graph 4.1). The amount of neopentane released cannot be calculated since no source of neopentane was available to calibrate the GC-MS for its quantification.

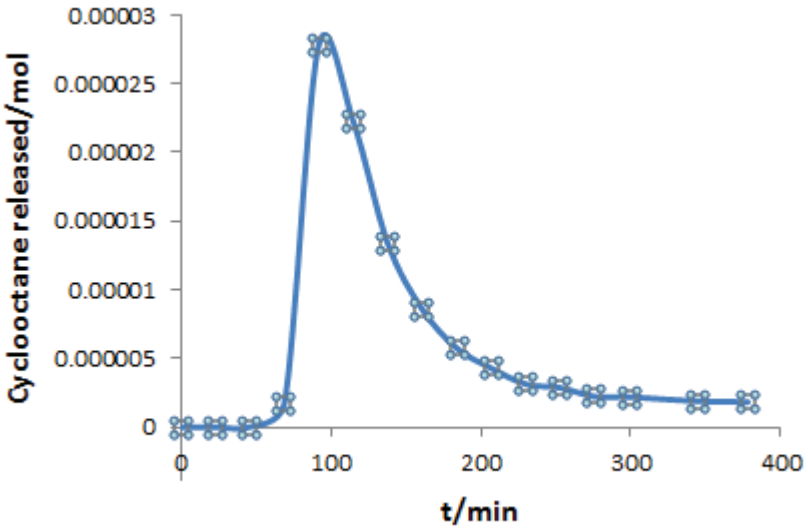

Graph 4.1. Cyclooctane released (in mol) w.r.t. time (in min.).

The IR spectrum of the sample shows the intensity of alkyl C-H stretching frequency (in the region 3200-2800 cm^{-1}) decreasing with time implying the loss of carbon containing compounds.

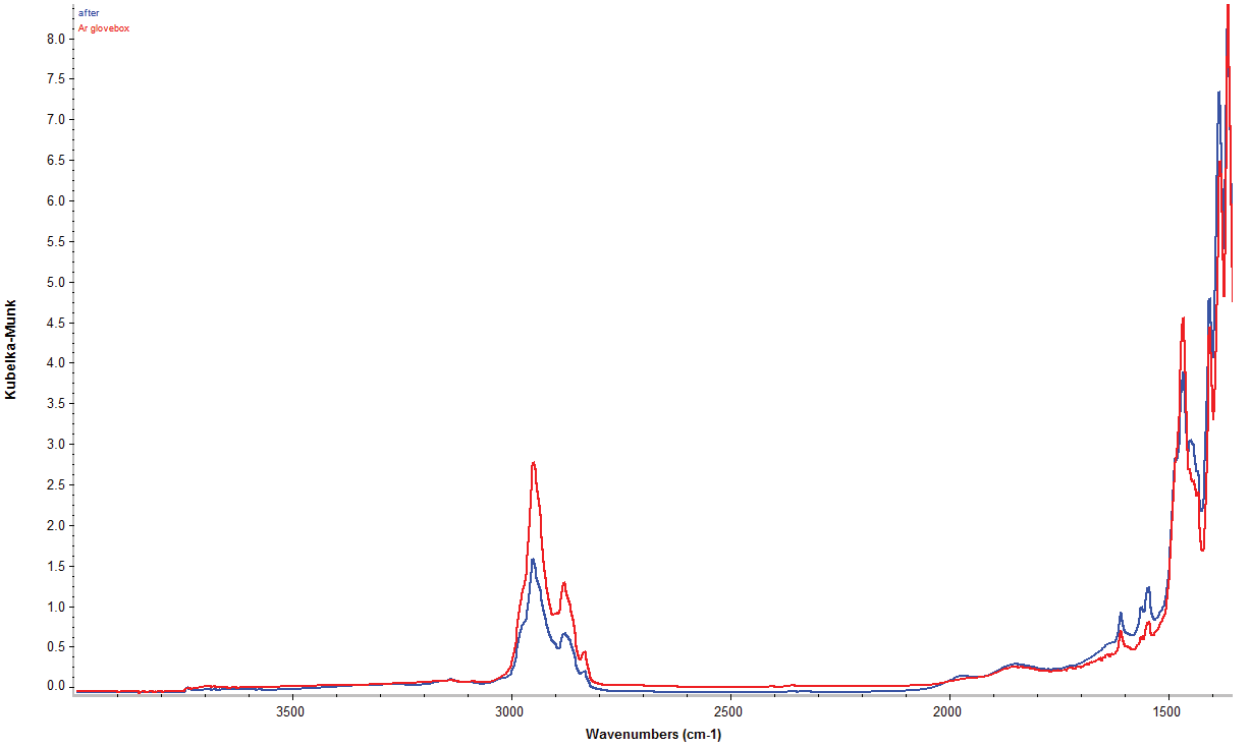

Figure 4.13. FTIR spectra of material **22'** before (in red) and after (in blue) passing hydrogen heating at 125°C.

However, no peaks corresponding to Ta-H (around 1800 cm^{-1})[41,45] or Rh-H (region 2000 cm^{-1})[46] stretches is observed in the IR spectrum (**Figure 4.13**). This experiment shows the presence of cyclooctadiene in the grafted bimetallic complex **22'** which is released as cyclooctane by passing dry dihydrogen and heating the sample at 125°C. Future work is required to fully elucidate the nature of the species generated after H_2 treatment.

CONCLUSION

Molecular silanols [POSS (Polyhedral Oligosilsesquioxane) and $HOSi(O^tBu)_3$] are used as silica mimicking molecular analogues to explore various possible pathways to immobilize the desired alkoxy-NHC Ta/Rh heterobimetallic complex. These studies shows that a stepwise approach is viable, consisting first in grafting the monometallic tantalum-NHC alkylidene motif over silica through a 1,2 addition of the silanol hydroxyl group onto the alkylidene ligand, followed then by the incorporation of rhodium onto the NHC moiety. The ^{13}C NMR spectra of the monometallic tantalum-NHC siloxy species displays a downfield signal around 219 ppm which suggests that the carbenic center does not interact with Ta in these species. The unbound nature of the carbene is also confirmed by the addition of one additional equivalent of $HOSi(O^tBu)_3$ which leads to the reversible formation of a carbene-silanol adduct through hydrogen bonding. Gratifyingly, the targeted Ta/Rh heterobimetallic species are accessed by the addition of $[Rh(COD)Cl]_2$ onto the siloxy-supported Ta-NHC monometallic derivatives, and the crystal structure of the bimetallic complex is elucidated. This important proof-of-concept result validates the methodology postulated in this thesis.

Once the proposed synthetic strategy is optimized in solution, these results are translated at the surface of silica. The monometallic Ta-NHC complex is successfully grafted over $SBA15_{700}$ to yield a monopodal species whose composition is established by elemental analysis results and GC titration. Interestingly, ^{13}C CP-MAS NMR studies performed on the ^{13}C labelled version of the complex demonstrates that a mixture of two species is obtained: a major one (about 80%) in which the NHC is bound to Ta (contrary to what seen in solution), and a minor one in which the NHC center remains unbound to Ta. Treatment of the silica-supported monometallic Ta species with $[Rh(COD)Cl]_2$ leads to the incorporation of rhodium to the NHC ligand. As expected, the rhodium metallation of the supported species containing a free carbene is easier than that of the Ta-bound NHC, but optimization of the reaction condition by heating at 60°C overnight ensured maximum conversion to the silica-supported Ta/Rh heterobimetallic species. The ^{13}C CP-MAS NMR confirms the incorporation of rhodium species which displays the characteristic rhodium-carbene signal at 185 ppm. However some uncertainties remain regarding the precise nature of this species, and its stability. An increase of signal in the ^{13}C NMR data might indicate the formation of imidazolium minor species, which might explain why the Ta:Rh ratio is slightly below 1 (0.85). In addition the amount of chlorine, as determined by elemental analysis, is unexpectedly low. Finally preliminary reactivity data indicates that this species is not thermally stable since neopentane is evolved upon heating, possibly through α-H elimination at the Ta center. Treatment under hydrogen

shows that the cyclooctadiene ligand can be eliminated to generate an active species, but further studies are necessary to elucidate the structure and the reactivity of the complex generated after H_2 treatment.

REFERENCES

1 M. K. Richmond, S. L. Scott and H. Alper, *J. Am. Chem. Soc.*, 2001, **123**, 10521–10525.

2 F. Héroguel, D. Gebert, M. D. Detwiler, D. Y. Zemlyanov, D. Baudouin and C. Copéret, *J. Catal.*, 2014, **316**, 260–269.

3 M. F. Delley, G. Lapadula, F. Núñez-Zarur, A. Comas-Vives, V. Kalendra, G. Jeschke, D. Baabe, M. D. Walter, A. J. Rossini, A. Lesage, L. Emsley, O. Maury and C. Copéret, *J. Am. Chem. Soc.*, 2017, **139**, 8855–8867.

4 R. L. Brutchey, B. V Mork, D. J. Sirbuly, P. Yang and T. D. Tilley, *J. Mol. Catal. A Chem.*, 2005, **238**, 1–12.

5 T. Alphazan, A. Bonduelle-Skrzypczak, C. Legens, A. S. Gay, Z. Boudene, M. Girleanu, O. Ersen, C. Copéret and P. Raybaud, *ACS Catal.*, 2014, **4**, 4320–4331.

6 F. Rataboul, C. Copéret, L. Lefort, A. de Mallmann, J. Thivolle-Cazat, J.-M. Basset, *Dalt. Trans.*, 2007, **417**, 923–927.

7 E. Le Roux, M. Chabanas, A. Baudouin, A. De Mallmann, C. Copéret, E. A. Quadrelli, J. Thivolle-Cazat, J. M. Basset, W. Lukens, A. Lesage, L. Emsley and G. J. Sunley, *J. Am. Chem. Soc.*, 2004, **126**, 13391–13399.

8 M. Chabanas, E. A. Quadrelli, B. Fenet, C. Copéret, J. Thivolle-Cazat, J.-M. Basset, A. Lesage and L. Emsley, *Angew. Chemie Int. Ed.*, 2001, **40**, 4493.

9 P. Avenier, M. Taoufik, A. Lesage, X. Solans-Monfort, A. Baudouin, A. De Mallmann, L. Veyre, J. M. Basset, O. Eisenstein, L. Emsley and E. A. Quadrelli, *Science*, 2007, **317**, 1056–1060.

10 C. Copéret, D. P. Estes, K. Larmier and K. Searles, *Chem. Rev.*, 2016, **116**, 8463–8505.

11 M. K. Samantaray, S. Kavitake, N. Morlans, E. Abou-Hamad, A. Hamieh, R. Dey and J. M. Basset, *J. Am. Chem. Soc.*, 2017, **139**, 3522–3527.

12 M. K. Samantaray, R. Dey, S. Kavitake, E. Abou-Hamad, A. Bendjeriou-Sedjerari, A. Hamieh and J. M. Basset, *J. Am. Chem. Soc.*, 2016, **138**, 8595–8602.

13 F. J. Feher, T. A. Budzichowski, R. L. Blanski, K. J. Weller and J. W. Ziller, *Organometallics*, 1991, **10**, 2526–2528.

14 C. Copéret, M. Chabanas, R. Petroff Saint-Arroman and J.-M. Basset, *Angew. Chemie*, 2003, **115**, 164–191.

15 G. Lapadula, M. P. Conley, C. Copéret and R. A. Andersen, *Organometallics*, 2015, **34**, 2271–2277.

16 K. L. Fujdala and T. Don Tilley, *Chem. Mater.*, 2004, **16**, 1035–1047.

17 C. Copéret, A. Comas-Vives, M. P. Conley, D. P. Estes, A. Fedorov, V. Mougel, H. Nagae, F. Núnez-Zarur and P. A. Zhizhko, *Chem. Rev.*, 2016, **116**, 323–421.

18 O. Cooper, C. Camp, J. Pécaut, C. E. Kefalidis, L. Maron, S. Gambarelli and M. Mazzanti, *J. Am. Chem. Soc.*, 2014, **136**, 6716-6723.

19 Y. S. Choi, E. G. Moschetta, J. T. Miller, M. Fasulo, M. J. McMurdo, R. M. Rioux and T. D. Tilley, *ACS Catal.*, 2011, **1**, 1166–1177.

20 S. Lysenko, C. G. Daniliuc, P. G. Jones and M. Tamm, *J. Organomet. Chem.*, 2013, **744**, 7–14.

21 R. Srivastava, R. Moneuse, J. Petit, P.-A. Pavard, V. Dardun, M. Rivat, P. Schiltz, M. Solari, E. Jeanneau, L. Veyre, C. Thieuleux, E. A. Quadrelli and C. Camp, *Chem. - A Eur. J.*, 2018, **24**, 4361–4370.

22 A. J. Arduengo, J. R. Goerlich and W. J. Marshall, *Angew. Chem., Int. Ed. Engl*, 1995, **117**, 2518.

23 A. J. Arduengo, V. Rasika Dias, R. L. Harlow and M. Kline, *J. Am. Chem. Soc.*, 1992, **114**, 5530-5534.

24 D. Tapu, D. A. Dixon and C. Roe, *Chem. Rev.*, 2009, **109**, 3385–3407.

25 J. A. Cowan, J. A. C. Clyburne, M. G. Davidson, R. L. W. Harris, J. A. K. Howard, P. Küpper, M. A. Leech and S. P. Richards, *Angew. Chemie Int. Ed.*, 2002, **41**, 1432–1434.

26 M. Movassaghi and M. A. Schmidt, *Org. Lett.*, 2005, **7**, 2453–2456.

27 D. P. Estes, G. Siddiqi, F. Allouche, K. V. Kovtunov, O. V. Safonova, A. L. Trigub, I. V. Koptyug and C. Copéret, *J. Am. Chem. Soc.*, 2016, **138,** 14987-14999.

28 M. V. Jiménez, J. J. Pérez-Torrente, M. I. Bartolomé, V. Gierz, F. J. Lahoz and L. A. Oro, *Organometallics*, 2008, **27**, 224–234.

29 P. Gigler, B. Bechlars, W. A. Herrmann and F. E. Kühn, *J. Am. Chem. Soc.*, 2011, **133**, 1589–1596.

30 T. Watanabe, T. Matsuo and H. Kawaguchi, *Angew. Chem., Int. Ed*, 2000, **37**, 6580.

31 I. Peñafiel, I. M. Pastor, M. Yus, M. A. Esteruelas and M. Oliván, *Organometallics*, 2012, **31**, 6154–6161.

32 G. Mancano, M. J. Page, M. Bhadbhade and B. A. Messerle, *Inorg. Chem.*, 2014, **53**, 10159-10170.

33 J. P. Morales-Cerón, P. Lara, J. López-Serrano, L. L. Santos, V. Salazar, E. Álvarez and A. Suárez, *Organometallics*, 2017, **36**, 2460–2469.

34 G. Lázaro, M. Iglesias, F. J. Fernández-Alvarez, P. J. SanzMiguel, J. J. Pérez-Torrente and L. A. Oro, *Chem.Cat.Chem.*, 2013, **5**, 1133–1141.

35 R. Anwander, *Chem. Mater.*, 2001, **13**, 4419–4438.

36 M. C. Bacariza, I. Graça, S. S. Bebiano, J. M. Lopes and C. Henriques, *Chem. Eng. Sci.*, 2018, **175**, 72–83.

37 Abdelhamid Sayari, and Bao-Hang Han and Y. Yang, 2004, **126**, 14348-14349.

38 A. Galarneau, H. Cambon, F. Di Renzo, R. Ryoo, M. Choi and F. Fajula, *New J. Chem.*, 2003, **27**, 73–79.

39 M. Choi, W. Heo, F. Kleitz and R. Ryoo, *Chem. Commun.*, 2003, 1340–1341.

40 J. P. Thielemann, F. Girgsdies, R. Schlögl and C. Hess, *Beilstein J. Nanotechnol.*, 2011, **2**, 110–118.

41 S. Soignier, M. Taoufik, E. Le Roux, G. Saggio, C. Dablemont, A. Baudouin, F. Lefebvre, A. De Mallmann, J. Thivolle-Cazat, J. M. Basset, G. Sunley and B. M. Maunders, *Organometallics*, 2006, **25**, 1569–1577.

42 L. P. Spencer, C. Beddie, M. B. Hall and M. D. Fryzuk, *J. Am. Chem. Soc.*, 2006, **128**, 12531–12543.

43 M. T. Zarka, M. Bortenschlager, K. Wurst, O. Nuyken and R. Weberskirch, *Organometallics*, 2004, **23**, 4817–4820.

44 F. Aznarez, P. J. Sanz Miguel, T. T. Y Tan and F. Ekkehardt Hahn, *Organometallics*, 2016, **35**, 410-419.

45 S. Lassalle, R. Jabbour, P. Schiltz, P. Berruyer, T. K. Todorova, L. Veyre, D. Gajan, A. Lesage, C. Thieuleux and C. CAMP, *J. Am. Chem. Soc.*, 2019, jacs.9b08311.

46 D. G. Holah, A. N. Hughes and B. C. Hui, *Can. J. Chem.*, 2005, **50**, 3714-3718.

EXPERIMENTAL SECTION

All the manipulations were performed under purified argon atmosphere unless mentioned. Either schlenk line technique or an MBraun glovebox was used to provide the inert argon atmosphere. All the glassware, cannulae, silica filters, glass syringes and needles were dried overnight (15 hr) at 110°C in the oven and assembled while hot under vacuum to perform the reaction. Pentane, toluene, tetrahydrofuran (THF) and diethyl ether were collected from Solvent purification system (SPS). Here all these solvents were already pre-dried by a passage through the activated alumina column. Then the solvents were dried over Na/benzophenone until the color changes to dark purple. Following which they were distilled under vacuum and then degassed to yield ready-to-use dry solvents. Dichloromethane (DCM) was dried over CaH_2 and vacuum distilled and degassed. Deuterated solvents like THF-d_8, C_6D_6, toluene-d_8 were dried over Na/benzophenone, vacuum distilled and degassed before using. $CDCl_3$ and CD_2Cl_2 were dried over CaH_2, vacuum distilled and then degassed prior to using them for NMR spectrum acquisition. Tantalum precursor was prepared according to available literature procedures. All other reagents used were commercially available and they were used as received. Bruker AV-300, AVQ-400 and AV-500 spectrometers were used to record the NMR. All the chemical shifts were measured relative to the corresponding residual peak of the deuterated solvents; which in turn were assigned relative to an external TMS standard set at 0.00 ppm. ^{1}H, ^{13}C, COSY, HSQC and HMBC NMR spectrum were thoroughly analyzed to assign the ^{1}H and ^{13}C peaks. IR spectrum was recorded using a Nicolet 6700 FT-IR spectrometer. Samples for recording IR spectrum were prepared in a DRIFT cell equipped with KBr dome under argon atmosphere. Samples were either send to the school of Human sciences, Science centre, London Metropolitan University or to Mikroanalytisches Labor Pascher, Germany for elemental analysis. X-Ray diffraction was performed at Centre de Diffractometrie Henri Longchambon-ISA, Université de Lyon. All the details regarding X-Ray diffraction are provided in the supporting information.

Synthesis of **16**

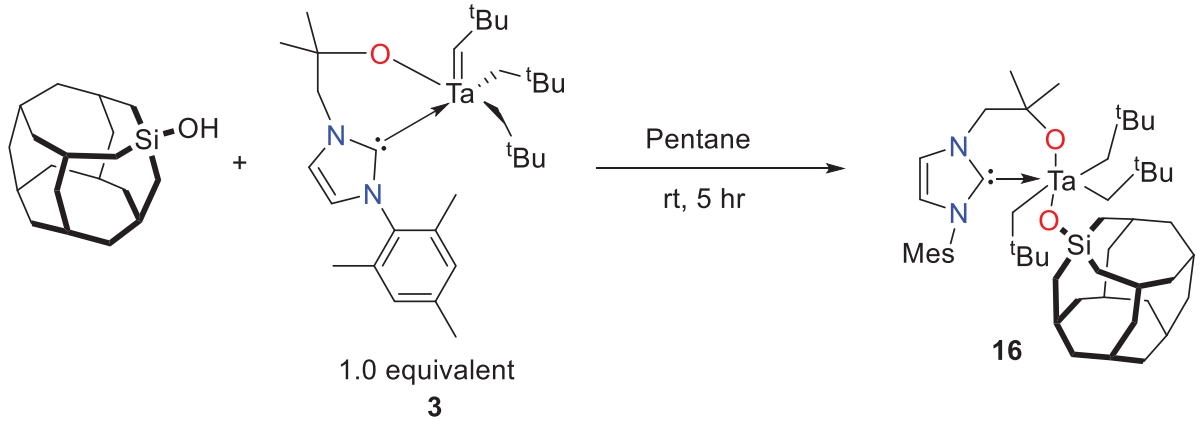

A white suspension of POSS-OH (157.59 mg, 172 µmol) in pentane was added dropwise to the orange solution of Ta-NHC (112mg, 1.0 equiv) to give light yellow solution. The resultant mixture was stirred for 3.0 hr, filtered, concentrated and kept in -40°C freezer for recrystallization. After seeing no recrystallized product; solvent was evaporated to give complex **16** as creamy powder. (196 mg, 72.8%)

^{1}H NMR (300 MHz, C6D6, 293 K): δ = 6.81 (s, 2H, m-CH_{Mes}), 6.59 (d, $^3J_{HH}$ = 1.25 Hz, 1H, CH_{imid}), 6.37 (d, $^3J_{HH}$ = 1.25 Hz, 1H, CH_{imid}), 4.64 (s, 2H, NCH_2), 2.16 (s, 3H, *p*-CH_{3Mes}), 2.11 (s, 6H, *o*-CH_{3Mes}), rest of the alkyl region contains broad peak from 2.0 ppm to 1.0 ppm containing the POSS protons as well as remaining alkyl groups of the complex.

Synthesis of complex 17

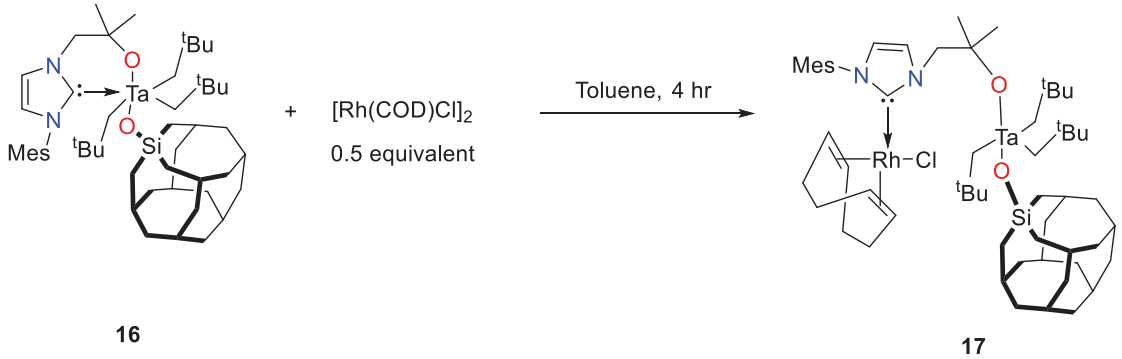

A 1.5 ml yellow solution of Rh-COD in toluene was added dropwise to a dark orange solution of POSS derivative of Tantalum-NHC in toluene. The reaction mixture was stirred for 4.0 hr and then evaporated to give dark yellow powder 17.

^{1}H NMR (300 MHz, C_6D_6, 293K): δ = 6.90 (d, $^3J_{HH}$ = 1.8 Hz, 1H, CH_{imid}), 6.98 (s, 1H, CH_{Mes}), 6.48 (d, $^3J_{HH}$ = 1.8 Hz, 1H, CH_{imid}), 6.41 (d, $^2J_{HH}$ = 14.0 Hz, 1H, NCH_2), 5.95 (s, 1H, CH_{Mes}), 5.4 (m,

2H, COD), 5.3 (m, 2H, COD), 4.42 (d, $^{2}J_{HH}$ = 14.0 Hz, 1H, NCH_2), 3.6 (m, 1H, COD), 3.05 (m, 1H, COD), 2.75 (s, 3H, *o*-CH_{3Mes}), 2.41 (m, 1H, COD), rest of the alkyl region contains broad peak from 2.25 ppm to 1.0 ppm containing the POSS protons as well as remaining alkyl groups of the complex.

Synthesis of complex 18

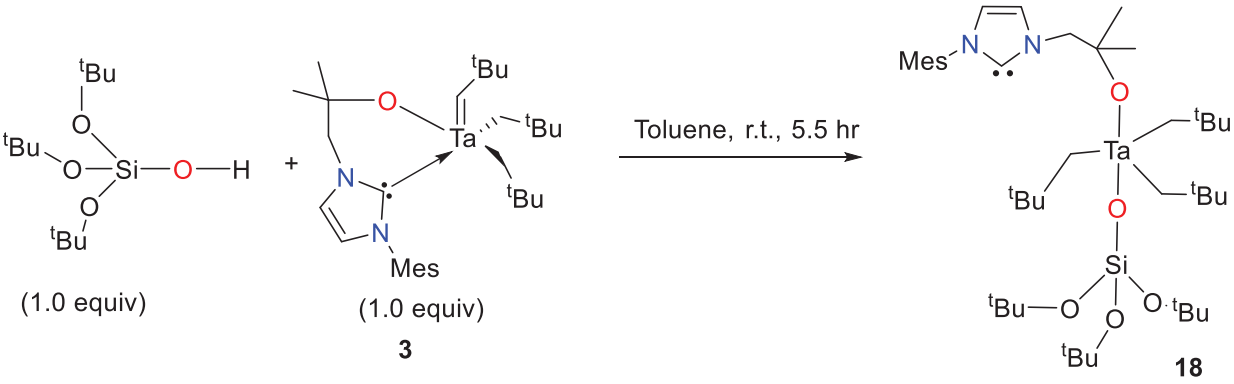

A 4 mL colorless toluene solution of tris(tert-butoxy) silanol (54 mg, 0.21 mmol, 1.0 equiv) was added dropwise to an orange stirring solution of complex Ta(L)(CH^{t}Bu)($CH_2{}^t$Bu) **3** (135 mg, 0.21 mmol, 1.0 equiv) in 6 mL of toluene. The color of the solution turned light cream instantaneously. The reaction mixture was stirred at room temperature for 3h, and then the volatiles evaporated to dryness to yield complex **18** (167 mg, 0.18 mmol, 87% yield).

^{1}H NMR (400 MHz, C_6D_6, 296K): δ = 6.81 (s, 2H, m-CH_{Mes}), 6.66 (d, $^{3}J_{HH}$ = 1.5 Hz, 1H, CH_{imid}), 6.39 (d, $^{3}J_{HH}$ = 1.5 Hz, 1H, CH_{imid}), 4.80 (s, 2H, NCH_2), 2.16 (s, 3H, *p*-CH_{3Mes}), 2.11 (s, 6H, *o*-CH_{3Mes}), 1.84 (s, 6H, CH_3), 1.53 (s, 6H, Ta-CH_2), 1.50 (s, 27H, O^{t}Bu), 1.34 (s, 27H, $CH_2{}^t$Bu).

^{13}C{^{1}H} NMR (100.6 MHz, C_6D_6, 296K): δ = 219.5 (s, C_{NHC}), 139.3 (CAr), 137.0 (CAr), 135.5 (CAr), 129.1 (CAr), 128.0 (CHAr), 127.9 (CHAr), 120.7 (CH_{imid}), 120.2 (CH_{imid}), 90.4 (Ta-$CH_2{}^t$Bu), 84.8 (O*C*$(CH_3)_2(CH_2N)$), 73.4 (O*C*$(CH_3)_3$), 61.4 (NCH_2), 35.9 (OC(*C*$H_3)_3$), 34.6 (Ta-$CH_2C(CH_3)_3$), 32.4 (Ta-$CH_2C(CH_3)_3$), 27.3 (CH_3), 21.0 (*p*-CH_{3Mes}), 18.1 (*o*-CH_{3Mes}).

DRIFT (25°C, KBr solid solution under argon): 2972.6 (s, ν_{C-H}), 2955.0 (s, ν_{C-H}), 2897.7 (m, ν_{C-H}), 2859.4 (m, ν_{C-H}), 1495.2 (w), 1469.5 (m), 1391.0 (m), 1364.4 (s), 1241.0 (s), 1215.5 (m), 1190.0 (m), 1158.3 (m), 1079.4 (m), 1066.5 (s), 1031.3 (m), 976.2 (m), 945.1 (s), 854.1 (w), 828.3 (w), 799.1 (m), 713.1 (m), 695.1 (m), 583.8 (w), 570.4 (w).

Anal. Calcd for $C_{43}H_{81}N_2O_5SiTa$: C, 56.44; H, 8.92; N, 3.06. Found: C, 56.29; H, 9.02; N, 3.05.

Synthesis of complex 19.

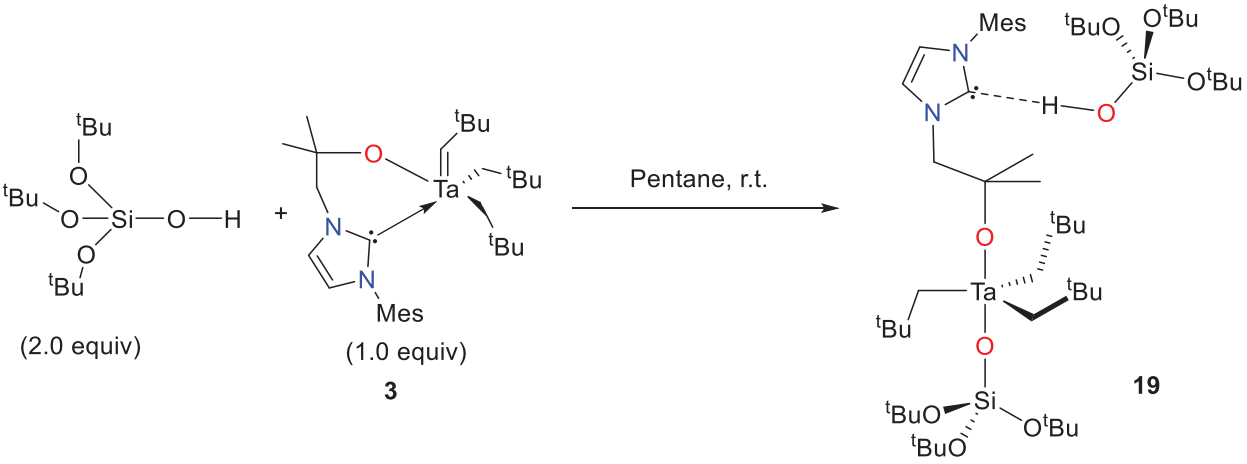

A 4 mL colorless pentane solution of tris(tert-butoxy) silanol (243 mg, 0.92 mmol, 2.0 equiv) was added dropwise to an orange stirring solution of complex Ta(L)(CH^{t}Bu)(CH$_2$^{t}Bu) **3** (300 mg, 0.46 mmol, 1.0 equiv) in 16 mL of pentane. The color of the reaction turned gradually from yellow to pale cram. The reaction mixture was stirred at room temperature for 3h, and then the volatiles evaporated to dryness. The solid residue was extracted with 10 mL pentane; filtered and stored at -40°C for 2 days to yield adduct **19** as a white crystalline solid (448 mg, 0.38 mmol, 83% yield). Single crystals of **19** suitable for X-ray diffractions were grown from a saturated THF solution at -40°C.

^{1}H NMR (500 MHz, C_6D_6, 296K): δ = 7.78 (s, 1H, SiOH), 6.82 (s, 2H, m-CH$_{Mes}$), 6.67 (s, 1H, CH$_{imid}$), 6.25 (s, 1H, CH$_{imid}$), 4.77 (s, 2H, NCH$_2$), 2.18 (s, 3H, *p*-CH$_{3Mes}$), 2.10 (s, 6H, *o*-CH$_{3Mes}$), 1.85 (s, 6H, CH$_3$), 1.52 (s, 6H, Ta-CH$_2$), 1.50 (s, 27H, O^{t}Bu), 1.44 (s, 27H, O^{t}Bu), 1.34 (s, 27H, CH$_2$^{t}Bu).

^{13}C{^{1}H} NMR (125.7 MHz, C_6D_6, 296K): δ = 206.8 (s, C$_{NHC}$), 138.1 (CAr), 137.8 (CAr), 135.3 (CAr), 129.2 (CHAr), 121.5 (CH$_{imid}$), 120.3 (CH$_{imid}$), 90.2 (Ta-*C*H$_2$^{t}Bu), 84.8 (O*C*(CH$_3$)$_2$(CH$_2$N)), 73.4 (O*C*(CH$_3$)$_3$), 71.9 (O*C*(CH$_3$)$_3$), 61.0 (NCH$_2$), 35.9 (OC(*C*H$_3$)$_3$), 34.6 (Ta-CH$_2$*C*(CH$_3$)$_3$), 32.4 (Ta-CH$_2$C(*C*H$_3$)$_3$), 31.9 (OC(*C*H$_3$)$_3$), 27.5 (CH$_3$), 21.0 (*p*-CH$_{3Mes}$), 18.1 (*o*-CH$_{3Mes}$).

DRIFT (25°C, KBr solid solution under argon): 3164.7 (w, ν_{C-H}), 3130.3 (w, ν_{C-H}), 2972.6 (s, ν_{C-H}), 2953.1 (s, ν_{C-H}), 2898.0 (m, ν_{C-H}), 2858.9 (m, ν_{C-H}), 1468.3 (m), 1385.4 (m), 1364.1 (s), 1239.3 (s),

1221.3 (m), 1192.3 (s), 1160.8 (m), 1061.6 (s), 1026.9 (m), 975.1 (m), 954.8 (s), 934.6 (m), 848.6 (w), 825.3 (m), 797.9 (w), 747.2 (m), 695.5 (m), 627.1 (w), 571.5 (m).

Anal. calcd for $C_{55}H_{109}N_2O_9Si_2Ta$: C, 56.00; H, 9.31; N, 2.37. Found: C, 55.99; H, 9.34; N, 2.35.

Synthesis of complex 20.

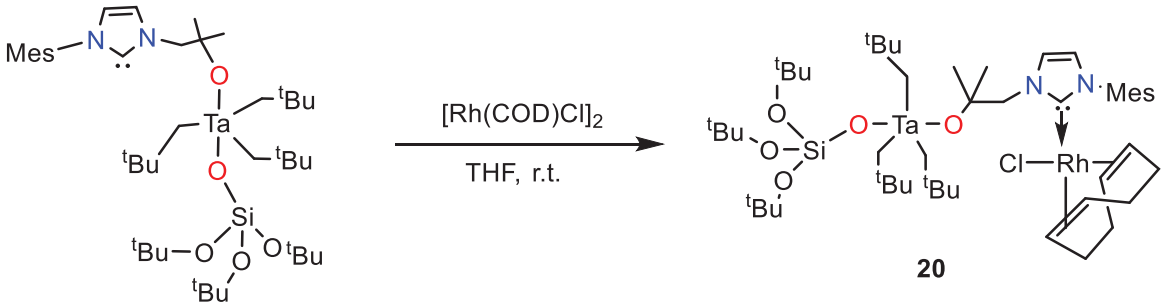

18 **20**

An orange THF solution (6 mL) of the $[Rh(COD)Cl]_2$ dimer (108.4 mg, 0.22 mmol, 0.5 equivalent) was added dropwise to the creamy THF solution (6 mL) of complex **18** (354 mg, 0.38 mmol, 1.0 equivalent) at room temperature. The reaction mixture was stirred for 14 hr at r.t. and then the volatiles were removed under vacuum to yield a yellow powder. The solid was dissolved in 4 mL THF and then let to crystallize at -40°C to yield 20 as yellow microcrystalline solid (486 mg, 0.38 mmol, 85% yield). Single crystals suitable for X-ray diffraction were grown in a similar fashion.

^{1}H NMR (500 MHz, THF-d_8, 296K): δ = 7.37 (d, $^3J_{HH}$ = 1.8 Hz, 1H, CH_{imid}), 7.15 (s, 1H, CH_{Mes}), 7.07 (d, $^3J_{HH}$ = 1.8 Hz, 1H, CH_{imid}), 6.96 (s, 1H, CH_{Mes}), 6.12 (d, $^2J_{HH}$ = 14.0 Hz, 1H, NCH_2), 4.92 (m, 1H, COD), 4.70 (m, 1H, COD), 4.34 (d, $^2J_{HH}$ = 14.0 Hz, 1H, NCH_2), 2.87 (m, 1H, COD), 2.53 (s, 3H, *o*-CH_{3Mes}), 2.46 (m, 1H, COD), 2.37 (s, 3H, *o*-CH_{3Mes}), 2.09 (br m, 2H, COD), 1.94 (s, 3H, *p*-CH_{3Mes}), 1.89 (br m, 1H, COD), 1.86 (s, 3H, CH_3), 1.84 (s, 3H, CH_3), 1.79 (br m, 2H, COD), 1.51 (br m, 1H, COD), 1.47 (s, 27H, O*t*Bu), 1.40 (s, 6H, $TaCH_2$), 1.30 (br m, 1H, COD), 1.25 (s, 27H, $CH_2(CH_3)_3$).

^{13}C{^{1}H} NMR (125.7 MHz, THF-d_8, 296K): δ = 184.7 (d, $^1J_{Rh\text{-}C}$ = 52 Hz, Rh-C_{NHC}), 139.3 (CAr), 138.2 (CAr), 138.0 (CAr), 135.6 (CAr), 130.0 (CHAr), 128.5 (CHAr), 124.1 (CH_{imid}), 123.9 (CH_{imid}), 97.6 (d, $^1J_{Rh\text{-}C}$ = 7.6Hz, COD), 95.0 (d, $^1J_{Rh\text{-}C}$ = 7.6Hz, COD), 90.3 (Ta-$CH_2C(CH_3)_3$), 84.1 (OC), 73.8 (Ta-$CH_2C(CH_3)_3$), 66.6 (d, $^1J_{Rh\text{-}C}$ = 14 Hz, COD), 69.4 (d, $^1J_{Rh\text{-}C}$ = 14 Hz, COD), 62.0 (NCH_2), 36.1 (Ta-$CH_2C(CH_3)_3$), 35.3 (Ta-$CH_2C(CH_3)_3$), 35.0 (Ta-$CH_2C(CH_3)_3$), 32.5 (Ta-$CH_2C(CH_3)_3$), 31.3

(COD), 30.5 (COD), 28.0 (CH_3), 27.9 (CH_3), 27.5 (COD), 25.7 (COD), 20.9 (*o*-CH_{3Mes}), 20.2 (*o*-CH_{3Mes}), 17.6 (*p*-CH_{3Mes}).

DRIFT (25°C, KBr solid solution under argon): 2973.4 (s, ν_{C-H}), 2952.8 (s, ν_{C-H}), 2898.5 (m, ν_{C-H}), 2876.8 (m, ν_{C-H}), 2830.8 (m, ν_{C-H}), 1469.8 (m), 1404.3 (w), 1387.1 (m), 1363.5 (s), 1322.0 (w), 1291.4 (w), 1239.1 (m), 1230.3 (m), 1189.5 (m), 1159.3 (m), 1139.3 (w), 1063.0 (s), 1027.9 (w), 974.2 (w), 941.2 (s), 851.6 (w), 826.4 (w), 799.7 (m), 747.1 (w), 725.0 (w), 696.7 (m), 568.0 (w).

Anal. calcd for $C_{51}H_{93}ClN_2O_5SiTaRh$: C, 52.71; H, 8.07; N, 2.41. Found: C, 52.62; H, 8.20; N, 2.55

Synthesis of silica supported monometallic complex 21

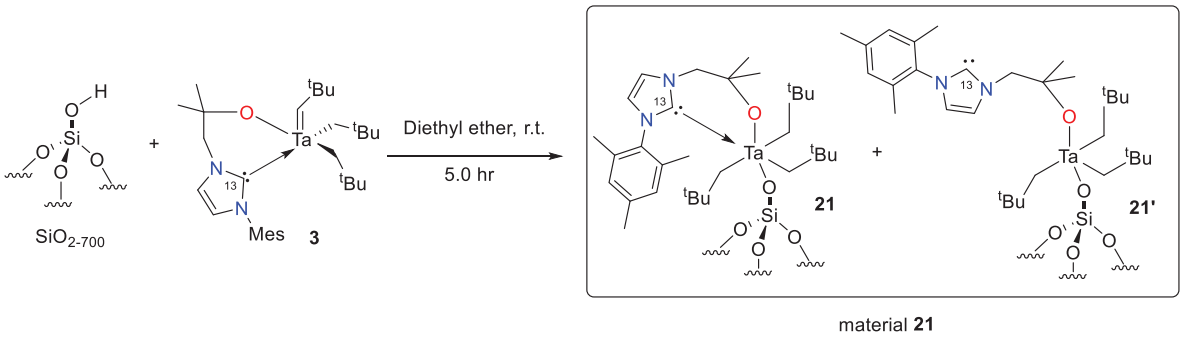

material **21**

200 mg of tantalum-NHC complex **3** was dissolved in 8 mL of diethyl ether and transferred to the other arm of double schlenk containing 200 mg of silica dehydroxylated at 700°C. The reaction mixture was stirred at room temperature for 5 hr. Following which the unreacted tantalum-NHC complex was removed by multiple washings with diethyl ether. The solvent was transferred to 6.945 L of balloon and 742 mbar of propane was transferred to it. The solid powder was dried overnight under high vacuum to give 238 mg of creamy colored powdery complex. The gas quantification of the solution phase shows 0.25 equivalents of neopentane released during the grafting reaction.

^{13}C NMR (100.6 MHz, C_6D_6, 296K): δ = 134.3 (CAr) , 128.4 (CHAr), 120.5 (CH_{imid}), 94.7 (Ta-$CH_2{}^t$Bu), 82.8 (Ta-$CH_2{}^t$Bu), 76.4 ($OC(CH_3)_2(CH_2N)$), 61.3 (NCH_2), 33.7 (Ta-$CH_2C(CH_3)_3$), 28.7 (CH_{3Mes}), 17.3 (CH_3). Anal. Calcd for C31H53N2OTa expected: Ta, 8.59; C, 17.67; H, 2.53; N, 1.32. Found: Ta, 8.59; C, 15.98; H, 2.53; N, 1.60.

Anal. Calcd for ^{13}C labelled $C_{31}H_{53}N_2Ta$: Ta, 7.77; C, 15.99; H, 2.29; N, 1.20. Found: Ta, 7.81; C, 14.89; H, 2.13; N, 1.52.

Synthesis of silica supported bimetallic complex **22**

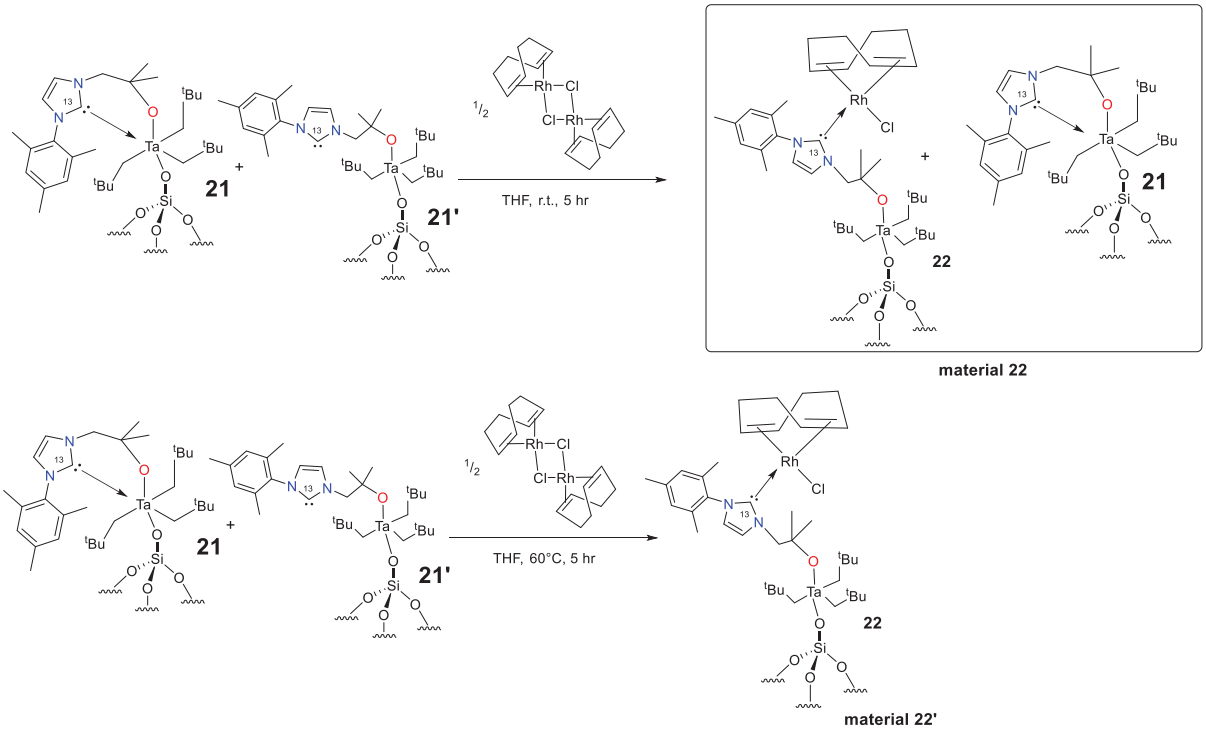

102 mg, 2.5 equivalents of rhodium precursor was dissolved in 8 ml of diethyl ether and added to 175 mg, 0.083 mmol silica supported Ta-NHC complex. The reaction was stirred at room temperature for 5 hr. Following which the excess rhodium precursor was removed by multiple washings. The solvent was transferred to a balloon of 6.495 L and 714 mbar of pentane was transferred to it. The compound was dried under vacuum to give 160 mg of yellow complex **22.** The gas quantification of the solution phase shows no neopentane released during the process. No elemental analysis was recorded for this sample. For the reaction at 60°C, THF was transferred to the reaction mixture inside the glovebox and then the reaction was heated for 15 hr. The ^{13}C NMR and elemental analysis of this material is reported below:

^{13}C NMR (100.6 MHz, C_6D_6, 296K): δ = 184.9 (s, $C_{Rh\text{-}NHC}$), 138.3 (CAr), 130.4 (CHAr), 122.5 (CH_{imid}), 33.0 (Ta-$CH_2C(CH_3)_3$), 28.0 (CH_{3Mes}), 18.3 (CH_3).

Anal. Calcd. for $C_{39}H_{65}N_2OTaRh$: Ta, 7.02; Rh, 3.99; C, 18.18; H, 2.58; N, 1.08; Cl, 1.37. Found: Ta, 7.09; Rh, 3.41; C, 16.36; H, 2.39; N, 1.39; Cl, 0.1<.

Further data (^1H, ^{13}C, IR and X-ray crystallographic studies) are reported in appendix 3.

Chapter 5

N_2 activation to NH_3: Computational studies using bimetallic complex

5.1) INTRODUCTION

5.1.1) General introduction on N_2 activation to outline different molecular mechanisms

Surface organometallic chemistry, which aims at developing well-defined surface species, can also be steered toward exploring unprecedented reactivity with few or no counterparts in homogeneous and heterogeneous catalysis.[1–3] For example, the silica-supported tantalum hydrides $(SiO)_2Ta(H)_x$ [where x= 1-3], which have been discussed in detail in chapter 1, are reported to catalyze alkane metathesis reactions. (**Scheme 5.1**).[4–8]

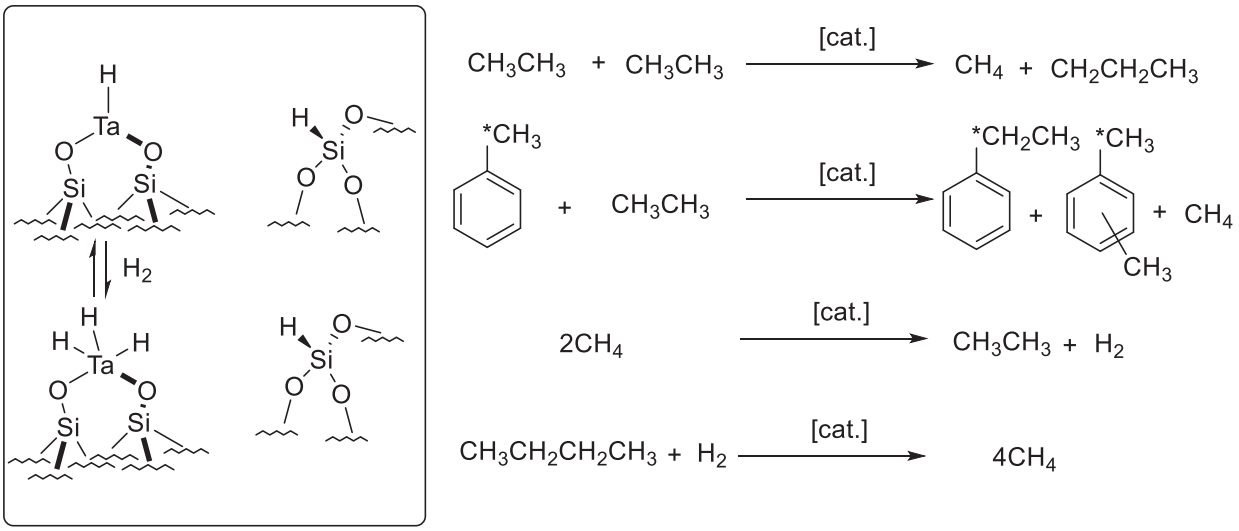

Scheme 5.1: Examples of catalytic application of silica-supported tantalum hydrides in C-H and C-C activation of hydrocarbons.

A further field where such $(SiO)_2Ta(H)_x$ have shown particular activity is N_2 activation. Quadrelli and coworkers[9] reported the application of well-defined silica supported tantalum hydride species to carry out stoichiometric N_2 activation to tantalum imido and amido species, which are also the final product of the tantalum hydride reaction with NH_3[10] (**Scheme 5.2**).

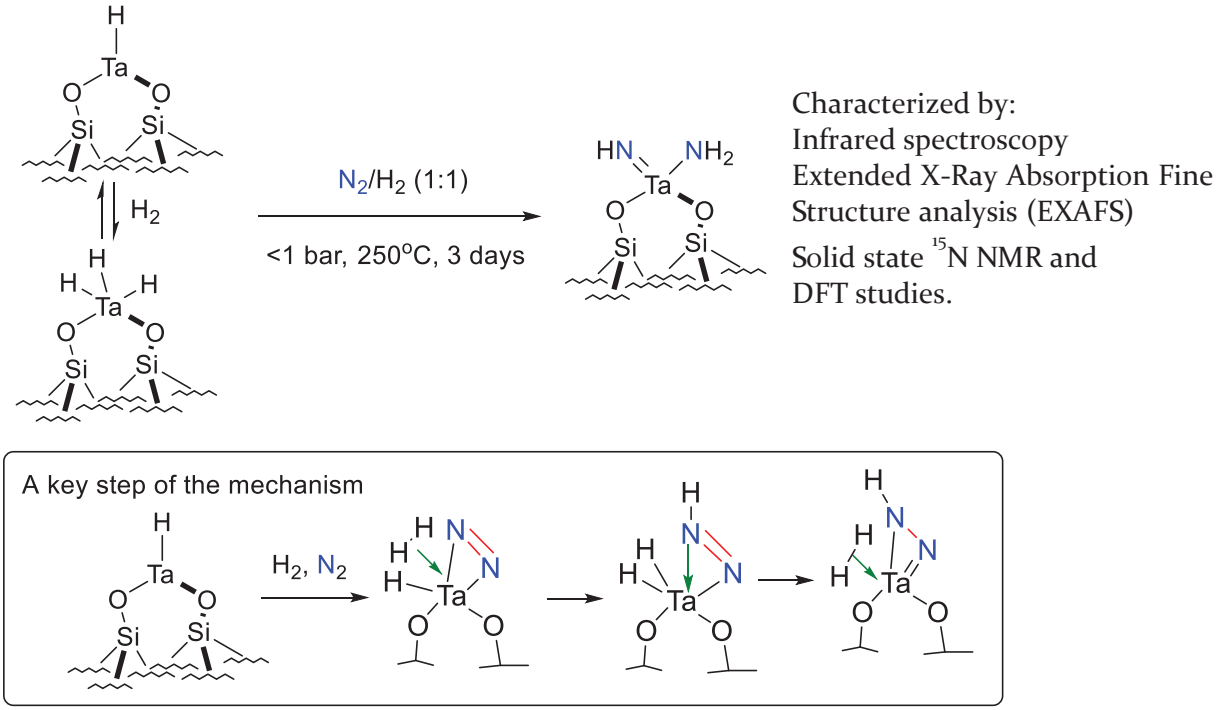

Scheme 5.2. N_2 activation by a silica supported Ta-H species leading to the formation of $[(\equiv SiO)_2Ta(=NH)(NH_2)]$.[11,12]

At 250°C, the chemically inert triple bond of the dinitrogen molecule is cleaved by the silica supported tantalum hydride to yield a Ta^V amido imido complex $[(\equiv SiO)_2Ta(=NH)(NH_2)]$. More insight into the mechanistic aspects of this N_2 activation was provided by DFT calculations and experiments carried out with competent reactants like N_2H_2, N_2H_4 and NH_3 with $(SiO)_2Ta(H)_x$ species, to isolate and characterize possible reaction intermediates.[12,13] It is observed that the first step of the N_2 activation begins on the monohydride with η^2 coordination of N_2 molecule which is energetically favorable and lays -80 kJ.mol^{-1} lower in energy. The next step involves the addition of a H_2 molecule to tantalum to yield a η^2-H_2 moiety. This intermediate can also be accessed from the starting Ta(V) trihydride and dinitrogen. Successive hydrogen cleavage and transfer of hydrides in multiple steps to the η^2 bonded N_2 leads to the dinitrogen cleavage at the tantalum center yielding Ta=NH and Ta-NH_2 moieties. The amido imido moiety lays 400 kJ.mol^{-1} lower in energy than the starting tantalum hydride species. The mechanistic pathway proposed and established by Quadrelli *et al* for N_2 activation is a novel route which distinguishes itself from all the metallic heterogeneous or homogeneous counterparts reported in literature. In particular the ability of the tantalum hydrides species to bind with dihydrogen molecule in a η^2 fashion and

subsequent bifunctional activation across metal-nitrogen bond is the unprecedented mechanistic step.

At the same time, the N_2 activation by silica-supported tantalum hydride species finds an interesting overlap with enzymatic mechanism for catalytic reduction of N_2 to NH_3 in presence of protons and ferredoxin-shuttled electrons. In nature the dinitrogen conversion to ammonia is catalyzed by enzyme nitrogenase which has been represented in **Scheme 5.3**. The nitrogenase enzyme consists of two proteins. The majority of the reaction involving nitrogen conversion to ammonia occurs on the molybdenum-iron (MoFe) protein where the electron transfer for the reduction of dinitrogen takes place at the bimetallic iron-molybdenum cofactors (FeMocos.)[14] Overall $8H^+$ and $8e^-$ are required to produce 2 equivalents of NH_3. The spectroscopic studies on the first few steps of the reaction mechanism shows that the remaining $2H^+$ and $2e^-$ are transitional in nature and stored as hydrides in two bridging [Fe–(μ-H)–Fe] hydride ligands.[15] The coordination of N_2 released the dihydrides as dihydrogen molecule explaining the surplus $2e^-$. These two electrons are utilized in the reduction of dinitrogen. There are obvious, fundamental and very large differences between the two systems discussed here: the nitrogenase and the silica-supported tantalum hydrides; like biological activation by nitrogenase enzyme is catalytic whereas the silica-supported catalyst does stoichiometric activation, the biological activation occurs at room temperature (r.t.) vs 250°C by silica-supported catalyst, biological activation is multimetallic vs. monometallic system in silica-supported complex etc. At the same time, the existing mechanistic connections between the two systems suggests that the SOMC –based mechanism with H_2 can also work with H^+/e^- supply, thus providing an original route to H_2-free N_2 reduction.

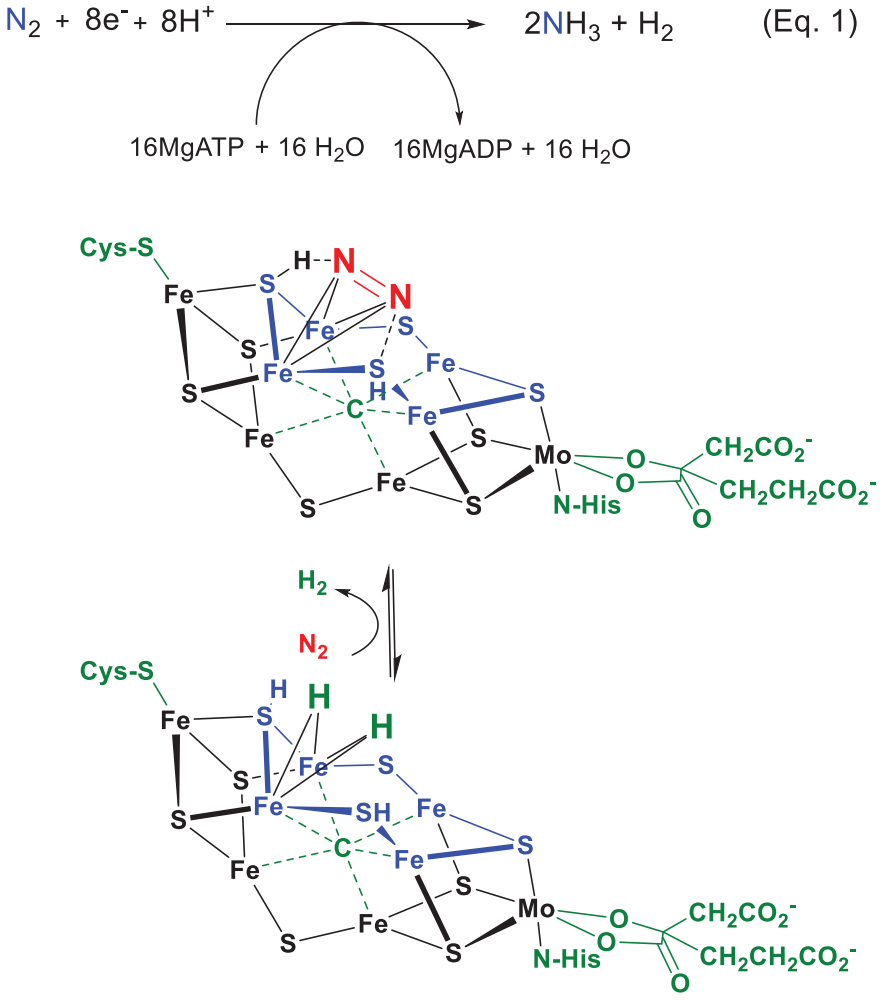

Scheme 5.3: The N_2 activation to NH_3 carried out by enzyme nitrogenase and a crucial mechanistic step.[12,14]

Industrially ammonia is produced by well-known Haber-Bosch process (HBP). The current tonnage are 140 million ton annually,[16] the process utilizes about 1-2% of the world energy consumption and has a similary very large share in overall greenhouse gas CO_2 footprint of industrial processes.[17] The main source of such heavy footprint, is mainly connected to H_2 production which is dominated by steam reforming of coal/natural gas and water gas shift reaction which produces CO_2 in the process.

$$N_2 + 3H_2 \underset{P = 150\text{-}200\ atm}{\overset{T = 300\text{-}500^oC}{\rightleftharpoons}} 2NH_3 \qquad \text{(Eq. 2)}$$

The biological activation of N_2 to NH_3 by nitrogenase enzyme utilizing H^+ and e^- source to reduce N_2 provides an alternative option to molecular dihydrogen (obtained from steam reforming process) and thus it can be utilized in similar N_2 activation reactions carried out on silica-supported complexes. We therefore found this problem an interesting avenue to study where multimetallic (bifunctional) activation can possibly lead to a new mechanistic pathway for N_2 activation.

5.1.2) State of the art for the activation of N_2 molecule by homogeneous bimetallic complexes

Tantalum is a protagonist of N_2 activation in molecular chemistry.[18–21] Seminal work by Fryzuk and coworkers reported dinitrogen activation by a ditantalum tetrahydride complex, $([NPN^{Si}]Ta)_2(\mu\text{-}H)_4$, yielding an unusual side-on end-on bound dinitrogen complex $\{[NPN^{Si}]Ta)_2(\mu\text{-}\eta^1\text{:}\eta^2\text{-}N_2)(\mu\text{-}H)_2\}$ (**Figure 5.1**). The N-N bond length in this species is 1.319 Å which is consistent with a strongly activated N_2 moiety.[19,21–23] Quite appealingly, the N_2 bridge is functionalized by hydroborating and hydrosilylating reagents. However, the release of the functionalized dinitrogen moiety from the bimetallic complex cannot be achieved.

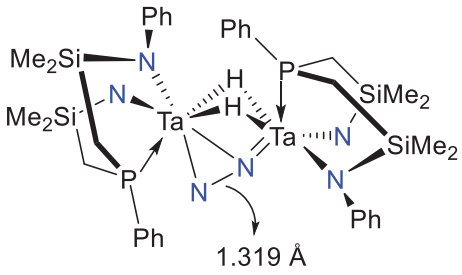

Figure 5.1. Structure of $\{[NPNSi]Ta)_2(\mu\text{-}\eta^1\text{:}\eta^2\text{-}N_2)(\mu\text{-}H)_2\}$, a complex resulting from N_2 activation by a ditantalum tetrahydride complex, reported by Fryzuk and coworkers.[20]

The most efficient homogeneous catalyst reported till date for N_2 reduction is based on molybdenum and is developed by Nishibayashi *et al.* This catalytic system exhibits the highest equivalent of NH_3 production (415 NH_3 equivalents based on Mo atom).[24,25] As we shall see in the catalytic cycle (**Scheme 5.4**), the dinitrogen activation pathway involves a dimolybdenum intermediate in which the nitrogen molecule is bound to both metal centers in an end-on fashion. Upon subsequent cleavage and series of protonation and reduction steps the N_2

molecule is converted to ammonia. Computational studies shows that the N_2 bridged bimetallic complex is converted into the molybdenum nitride complex through an exothermic step. The transition state for such conversion lays 21.8 kcalmol^{-1} higher than the bridging complex. The presence of two metal centers is therefore required in this process.

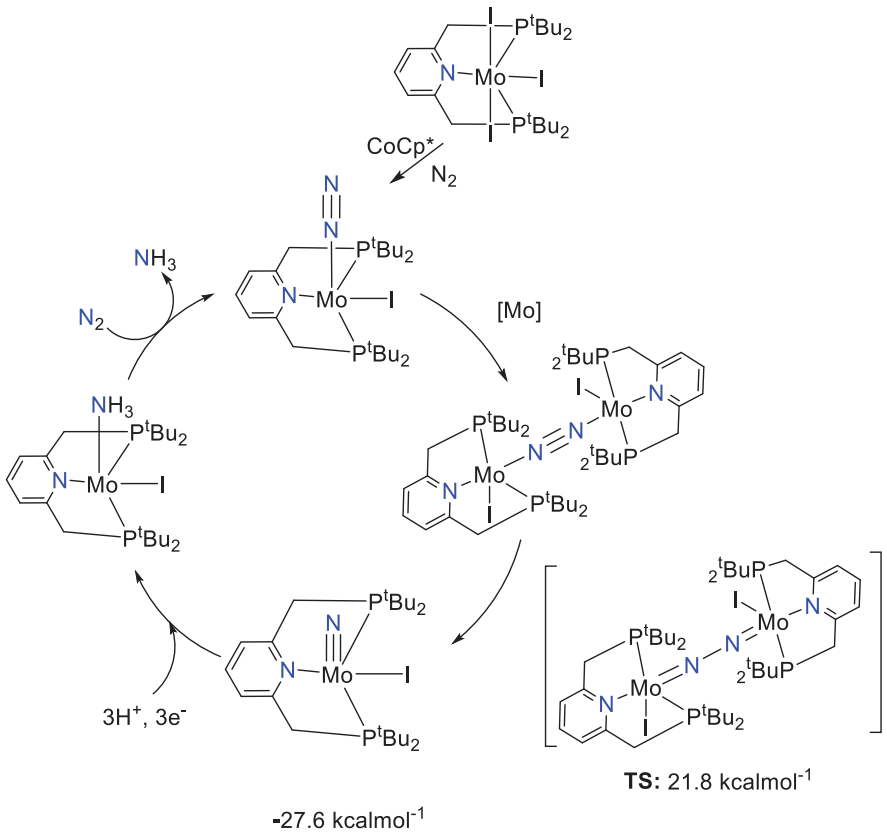

Scheme 5.4. The catalytic cycle proposed by Nishibayashi *et al* for the N_2 activation to NH_3.

Interestingly, Zr-Zr,[18] Nb-Nb,[26] Nb-Mo,[27] W-Rh,[28] Ru-Mo[29] and Re-Mo[30] based (hetero)bimetallic complexes have also been explored both in laboratory and computationally for dinitrogen activation. Hidai and coworkers[31–34] reported the seminal work on N_2 activation to NH_3 by bimetallic complexes. They employed Ru based complex trans-$[RuCl(dppp)_2]BF_4^-$ together with cis-$[W(N_2)_2(PMe_2\text{-}Ph)_4]$ in a 10:1 stoichiometry under 1 atm of H_2 at 55°C for dinitrogen activation to ammonia (in 55% yield). The complete reaction mechanism is not yet clear but based on experimental evidence the authors showed that the process starts with the coordination and subsequent cleavage of dihydrogen at Ru center to yield Ru dihydride moieties. The next step consists of transfer of hydrides to cis-$[W(N_2)_2(PMe_2\text{-}Ph)_4]$ to yield tungsten hydrazido complex which upon further protonation yields NH_3.

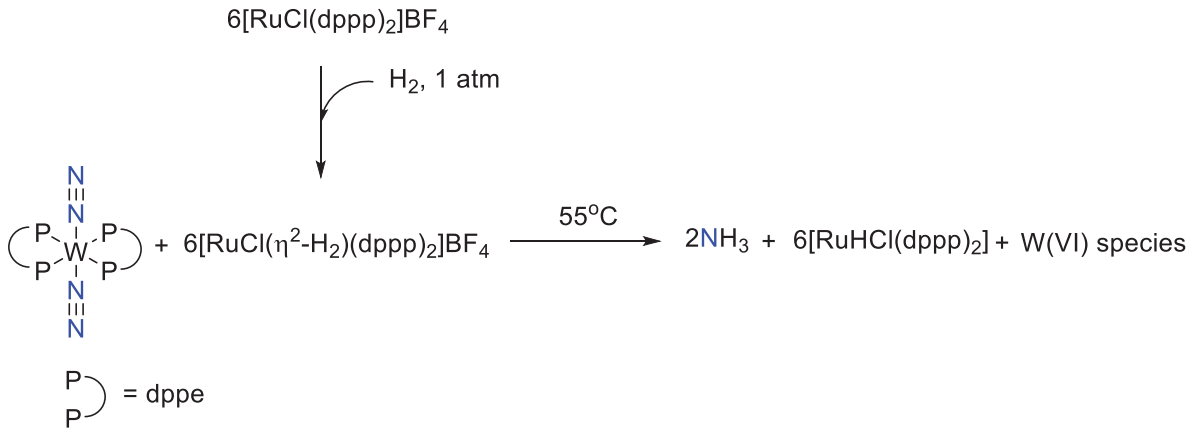

Scheme 5.5: N_2 activation by W-Ru bimetallic complex proposed by Hidai *et al*.

Similarly, Hölscher *et al* have harnessed cooperative reactivity between two metal centers to achieve N_2 reduction to NH_3. They conceptualized a Lewis base - Lewis acid catalytic system based on a W-Rh bimetallic system where the tungsten acriphos dinitrogen complex [W(acriphos)$(N_2)_3$] [acriphos=4,5-bis-(di-tert-butyl-phosphanyl)acridine] is used as a Lewis base and the cationic rhodium complex $[Rh(Cp^*)(phpy)(MeCN)]^+$ (Cp*=pentamethylcyclo-pentadienyl; phpy=2-phenylpyridyl) was employed as the Lewis acid.[35] The closed catalytic cycle is computed with an energy span of 39 kcalmol^{-1} (**Figure 5.2**).

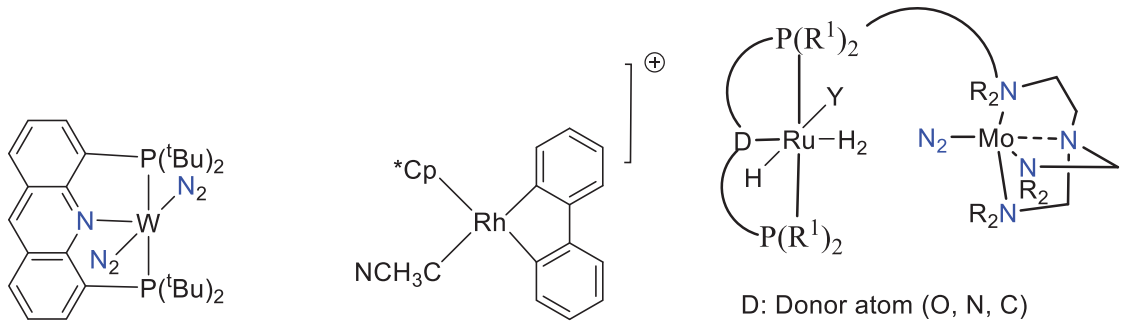

Figure 5.2. Hölscher *et al* proposed an original bifunctional activation of N_2 using two metal centers.

In this system, the rhodium center acts as the potential hydride donor whereas the nitrogen reduction to ammonia occurs at the tungsten center. They also explored an analogous Ru-Mo bimetallic system where the nitrogen reduction occurs at the Mo center with the Ru site acting as the prominent center for dihydrogen cleavage and hydride delivery to Mo bound dinitrogen.[29] The highest energy barrier of the computed catalytic cycle is 30 kcalmol^{-1}.

Well defined early-late heterobimetallic complexes also present potential avenues for small molecules activation. Thomas and co-workers reported a Ti-Co bimetallic complex (**Scheme 5.6**) which is active in the disproportionation of hydrazine into NH_3 and N_2 with a turn over number of 17.[36] The reaction mechanism, supported by DFT calculations, shows that both metal atoms are involved in the bifunctional activation of the hydrazine molecule.[37]

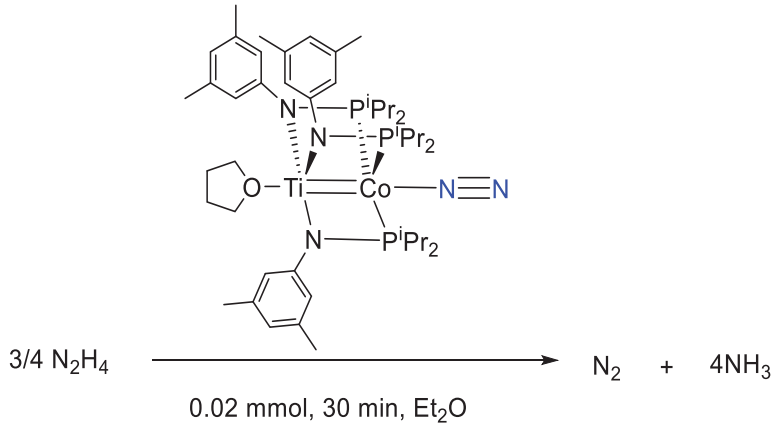

Scheme 5.6. Thomas *et al* reported a Ti-Co bimetallic complex supported by a tris phosphinoamide ligand. The complex shows a TON of 17 for hydrazine disproportionation.

Recently Crimmin and co-workers reported a ruthenium based heterobimetallic complex where the second metal is either of Al, Zn or Mg.[38] The computational and spectroscopic data suggests that with the decrease in electronegativity (Al>Zn>Mg) the metal-metal bond becomes more polar and as a result more electrons occupy the frontier orbitals of ruthenium. This leads to increased electron donation to the Ru-bound dinitrogen molecule and thus weakening of the N≡N bond. The bond weakening is confirmed by IR spectroscopy, which shows a $\tilde{\nu}_{N\equiv N}$ in the region 2160-2130 cm^{-1} as against free N≡N Raman stretching frequency of 2361 cm^{-1}.

The above examples establish the role of bimetallic complexes in dinitrogen activation and present a potential way forward to develop alternatives to the Haber-Bosch catalytic system.

5.1.3) Aim of the chapter

Inspired by the potential of early-late heterobimetallic complexes and the available literature on N_2 activation by tantalum species, we postulated that the Ta-Rh bimetallic complex shown in **Figure 5.3** may constitute an interesting reaction manifold for undertaking N_2 activation. The hypothesis was that the interaction of small molecules with both metal centers could lead to the polarization of the molecule and thus increasing the reactivity of the molecule.

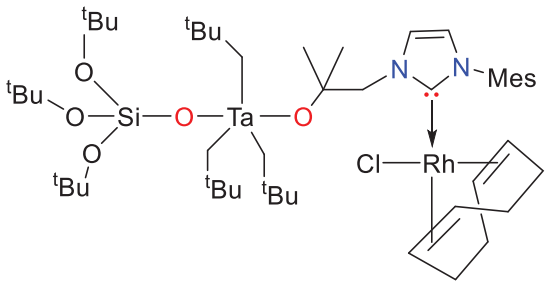

Figure 5.3. The Ta-Rh heterobimetallic complex developed in this thesis is used as a catalytic precursor to study the N_2 conversion to NH_3.

The aim of the computational study is to identify potential steps involved in the dinitrogen conversion to ammonia by the heterobimetallic complex and scrutinize the energy requirements of each step. The focus will be on establishing the idea that two extreme metals can interact with each other to lower the energy demand of such conversion. The computational study which has been carried out at RWTH Aachen University as part of mobility in the cotutelle work will also focus on the reactivity of other late transition metals for dinitrogen conversion to ammonia.

The computational study will be performed by using B97D3-BJ dispersion corrected hybrid functional and split valence basis set (def2-SVP). The B97D3 hybrid functional developed by Grimme *et al* has been used because of its accurate energy calculations of large molecules and relatively less computer time requirement.[39] The B97D3 is also reported to have low error spread and mean absolute deviation in case of transition metal complexes.[40,41]

5.2) RESULTS AND DISCUSSION

5.2.1) Structure optimisation of tris(tertiary-butoxy) silanolate derivative of bimetallic complex

For the simplicity of the calculation the three neopentyl groups at the tantalum center are replaced by the methyl group. The bimetallic complex is optimized to obtain the desired minimum energy structure**.** It is observed that the bimetallic complex adopts the same structure as obtained by the crystal structure. (**Figure 5.4**)

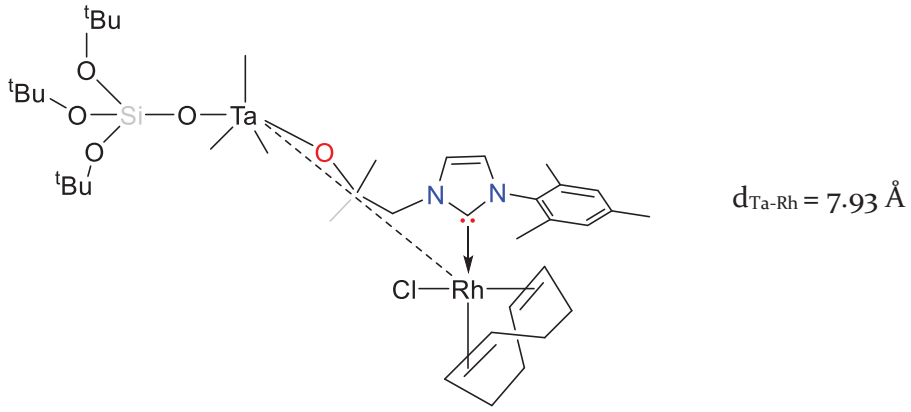

Figure 5.4: The optimized minima observed showed that the bimetallic complex adopts the similar orientation as shown in the crystal structure. Tantalum rhodium distance is too high for a close cooperation.

The distance between the two metal atoms is 7.93 Å which is too long to allow chemical interaction between both the metals in this orientation. Hence we proceeded with the dinitrogen activation at rhodium center to study the behavior of the complex for N_2 conversion. The first step of the catalytic cycle began with the addition of dihydrogen and dinitrogen to the rhodium center of the bimetallic complex with the simultaneous release of cyclooctane. The addition of H_2 and N_2 can lead to the formation of different species for example η^2H_2:η^2N_2 (**2'**), η^2H_2:η^2N_2 (**3'**), η^2H_2: end-onN_2 (**4'**), H_2: η^2H_2 (**5'**), η^2N_2:η^2N_2 (**6'**) among others. Hence computational calculation is performed on these different structures to obtain the molecule with lowest energy possible. **(Figure 5.5)** It is observed that the rhodium complex **4'** with η^2H_2:N_2 is the lowest in energy. However multiple attempts to locate the transition state for the transfer of hydride from rhodium to nitrogen atom failed. Hence the rhodium complex **5'** with η^2H_2:H_2 is taken as the starting initial complex.

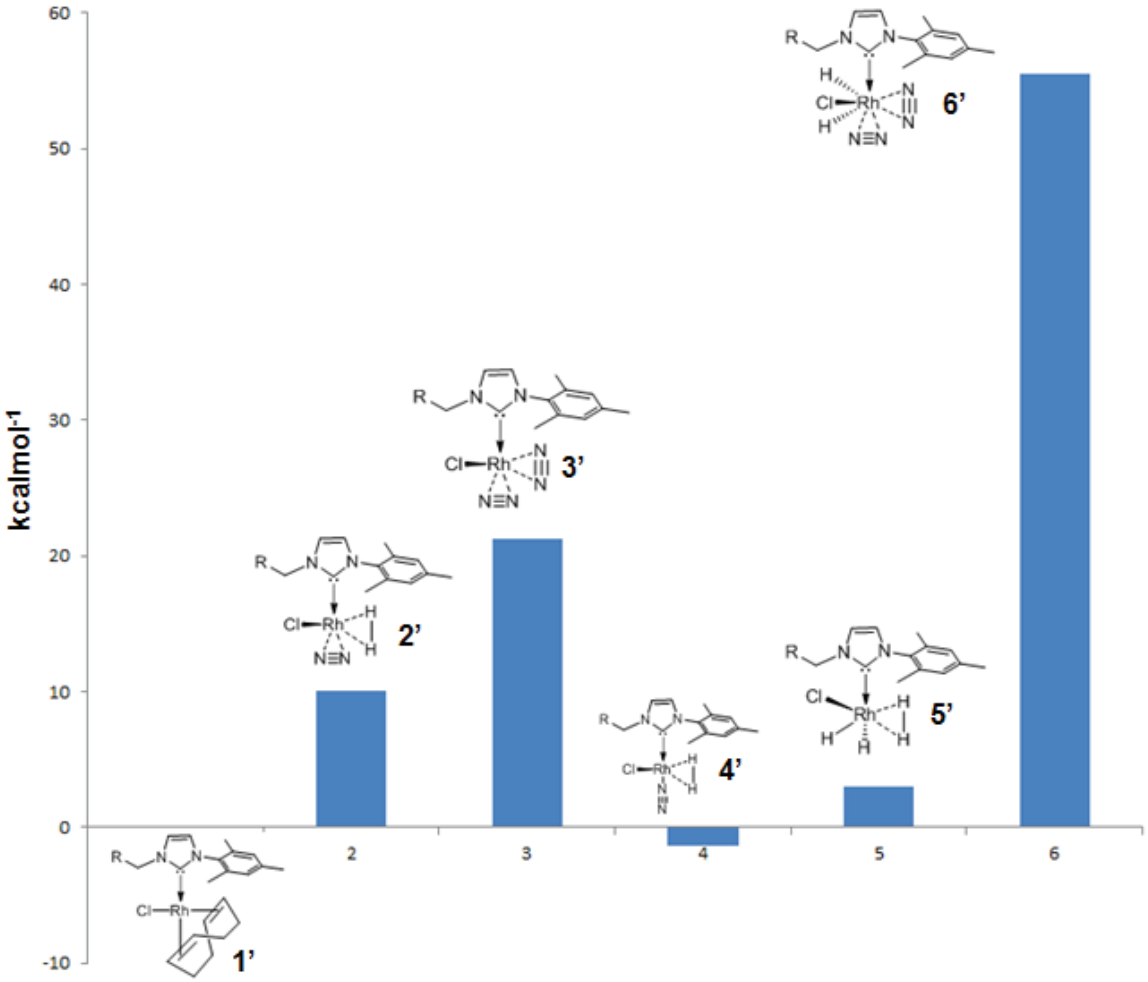

Figure 5.5: Gibbs free energies calculated for different possible complexes after the addition of H_2 and N_2 to complex 1 in the gas phase. The calculation is done using the B97D3-BJ functional and def2-SVP basis set.

The generation of $RhLH_2(\eta^2\text{-}H_2)$ **5'** (where L= metalloligand framework) molecule is endergonic in nature and requires 3.0 kcalmol^{-1} of energy. The rhodium center in the molecule adopts a trigonal bipyramidal structure where the classical dihydrogen molecule occupies the apical position (trans to the NHC) and the equatorial positions are occupied by the dihydride and chlorine atom. (**Scheme 5.7**) The rhodium-dihydrogen distance (1.64 Å), H···H distance (0.83 Å) and the rhodium hydride bond length (1.55 Å) compares well with those reported for the $RhH_2(\eta^2\text{-}H_2)$ systems.[42] The tantalum center in such a complex is located at 6.5 Å away from the rhodium center indicating that no possible interaction can be achieved between both the metal centers in the molecule.

5.2.3) Computation of catalytic cycle for dinitrogen conversion to ammonia using rhodium as late metal

The catalytically active molecule **1** is obtained by the addition of dinitrogen molecule to the complex **5'**. This addition is endergonic in nature and requires 8.9 kcalmol^{-1} of energy. (**Scheme 5.7**)

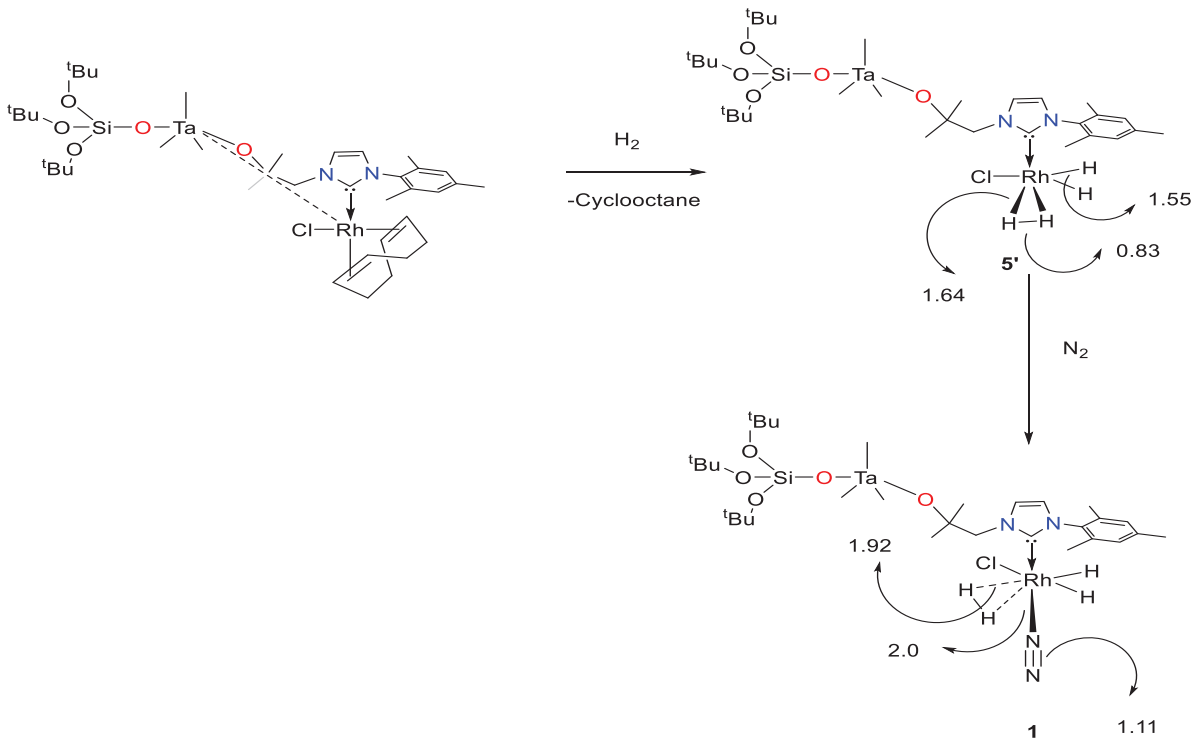

Scheme 5.7: General scheme showing the first two step of the reaction which leads to the formation of catalytically active complex with dinitrogen bonded in an end-on fashion.

After the addition of the dinitrogen molecule, the complex **1** $RhLN_2H_2(\eta_2\text{-}H_2)$ adopts an octahedral structure at the rhodium center. The nitrogen molecule is trans to NHC carbene and binds in an end-on fashion with the rhodium center with $d_{Rh\text{-}N}$ being 2.0 Å which is more on the longer side of the reported bond distances for late transition metal dinitrogen complexes.[43] This depicts a weak rhodium nitrogen interaction which is also reflected by the fact that the N···N bond distance is 1.11 Å (the distance is 1.09 Å in free dinitrogen molecule). The octahedral plane is occupied by the dihydrogen molecule, dihydride and the chlorine atom. The rhodium dihydrogen bond distance increased to 1.92 Å as compared to 1.64 Å in the precursor molecule depicting the weakening of the rhodium dihydrogen interaction after the coordination of the dinitrogen molecule. But the corresponding H···H bond distance in the classical dihydrogen molecule slightly decreases to 0.80 Å as compared to 0.83 Å in the

precursor complex. The Rh····Cl distance increases to 2.49 Å from the corresponding distance of 2.40 Å in the precursor complex. The next step in the catalytic cycle will be the transfer of rhodium bound hydride to one of the nitrogen atoms of the dinitrogen molecule to generate the complex **2**. (**Figure 5.7**) However to transfer the hydride the reaction step passed through a transition state (**TS1-2)** which lays 46 kcalmol^{-1} higher in the energy profile than the starting complex **1**. The transition state (**TS1-2)** was characterized by the formation of four member ring with the simultaneous elongation of Rh-N, N-N (the stretching frequency of N-N bond decreases to 1950 cm^{-1}) and Rh-H bond. The Rh-N1-N2 angle is almost 90° in the transition state implying that the dinitrogen molecule has to bend by 90° to come in close proximity of the hydride for the transfer to take place. The Rh····H bond in the transition state elongates to 1.86 Å as compared to 1.55 Å in the starting molecule **1**. The Rh····H bond distance of the classical dihydrogen molecule decreases to 1.82 Å as compared to the corresponding bond length of 1.97 Å in the complex **1**. After passing through the transition state the molecule reaches the local minimum **2**. The step **1-2** is endergonic and requires 36 kcalmol^{-1} of energy. The molecule **2** adopts a square pyramidal orientation with all the groups (except the NHC carbene) at rhodium center occupying the plane of the square pyramid. While the bond lengths of the hydride and the dihydrogen molecule is almost similar to that of complex **1**; the Rh-N bond length is considerably reduced from 2.0 Å in **1** to 1.87 Å in **2**. This indicated the strengthening of the bond post hydride transfer.

The succeeding step of the cycle involves the transfer of another rhodium bound hydride to the distal NH group to yield complex **3**. The transition state (**TS2-3)** (+61 kcalmol^{-1}) leading to the complex **3** is very much similar in orientation to that of (**TS1-2)** with the simultaneous oxidative addition of the dihydrogen molecule. However the energy required for passing through the transition state is very high and poses a challenge to realize the reaction in laboratory. The complex **3** adopts a trigonal bipyramidal orientation at the rhodium center with the –N=NH$_2$ group occupying the apical position. The overall energy requirement to reach local minima **3** is 31 kcalmol^{-1} which is 5 kcalmol^{-1} more stable than that of local minima **2**.

The next step involves the addition of one more hydrogen molecule to complex **3** in order to give the local minimum **4**. The addition of dihydrogen to complex **3** is endergonic in nature and requires approximately 8 Kcalmol^{-1} of energy. After the addition of dihydrogen molecule the complex **4** once again adopts the octahedral structure. The activation barrier for the transformation of **4** to **5** is 23 kcalmol^{-1} and local minima **5** is 1 kcalmol^{-1} is higher in energy

than **4**. The reaction step involves the transfer of hydride from rhodium to the inner nitrogen atom directly bonded to the rhodium center in order to generate NH-NH_2 unit. This step passes through the transition state (**TS4-5)** (63 kcalmol^{-1}) which was again a very high energy barrier to achieve in laboratory conditions.

The succeeding step in the catalytic cycle proceeds by the transfer of another hydride to the –NH_2 group in order to form complex **6** with the simultaneous release of NH_3 molecule. The transformation from **5** to **6** is exergonic and releases 2 kcalmol^{-1} of energy. The transition state (**TS5-6)** (59 kcalmol^{-1}) is a four membered ring where the Rh-N bond is 2.13 Å which is considerably longer than the corresponding bond in the complex **5**. The activation barrier from **5** to **6** is 18 kcalmol^{-1} higher in energy than the local minimum **5**. Succeeding further the reaction profile involves the oxidative addition of the dihydrogen molecule to the rhodium center to form the dihydride complex **7**. This oxidative addition is endergonic in nature and requires 9 kcalmol^{-1} of energy.

The next step proceedes by the transfer of hydride from rhodium to the =NH group to yield the local minimum **8**. The local minimum **8** (1 kcalmol^{-1}) is situated at a very low energy. The transformation from **7** to **8** is highly exergonic in nature and releases 47 kcalmol-1 of energy in the process. However the reaction step passes through the transition state (**TS7-8)** which is 1 kcalmol^{-1} lower in Gibbs free energy than the local minima **7**. To ascertain that indeed the **TS7-8** connects the complexes **7** and **8**, we performed intrinsic reaction coordinate calculation (IRC). (**Figure 5.6**)

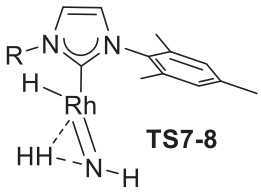

TS7-8

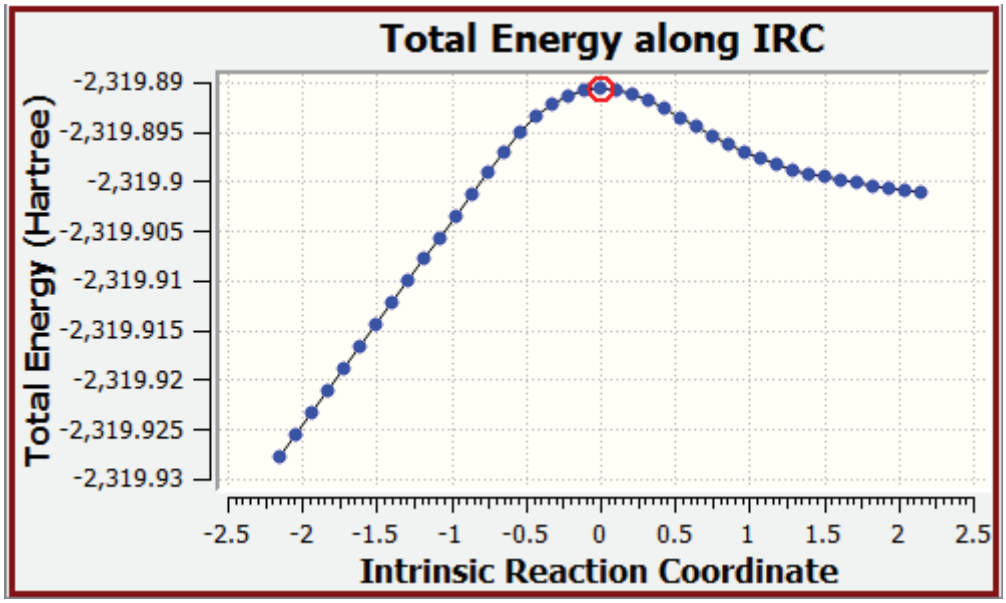

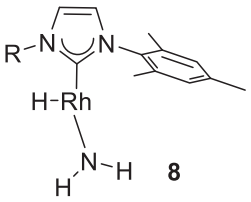

8

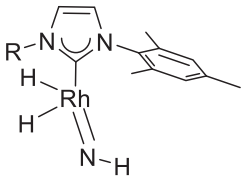

7

Figure 5.6: The IRC calculation is done starting with TS 7-8 and then moving forward and backward for ten steps. The structures obtained at the end of the IRC calculation are optimized to minima again to yield the complex 7 and 8. This confirmed the observation that TS 7-8 is indeed a transition state.

Following this hydride transfer another hydrogen molecule is added in a η^2 fashion to the complex **8** leading to local minimum **9**. The transformation is endergonic in nature and requires 10 kcalmol^{-1} of energy. The next step in the cycle is transfer of the hydride to the $-NH_2$ group to generate local minima **10**. The NH_3 molecule is interacting to the rhodium center with the Rh-NH_3 distance at 2.18 Å. The transformation of the complex **9** to **10** is highly exergonic in nature (36 kcalmol^{-1}) and it is -27 kcalmol^{-1} lower in the energy profile as compared to the starting complex. The next step is the addition of H_2 and N_2 molecule to generate the starting complex again which completes the catalytic cycle. (**Figure 5.7**)

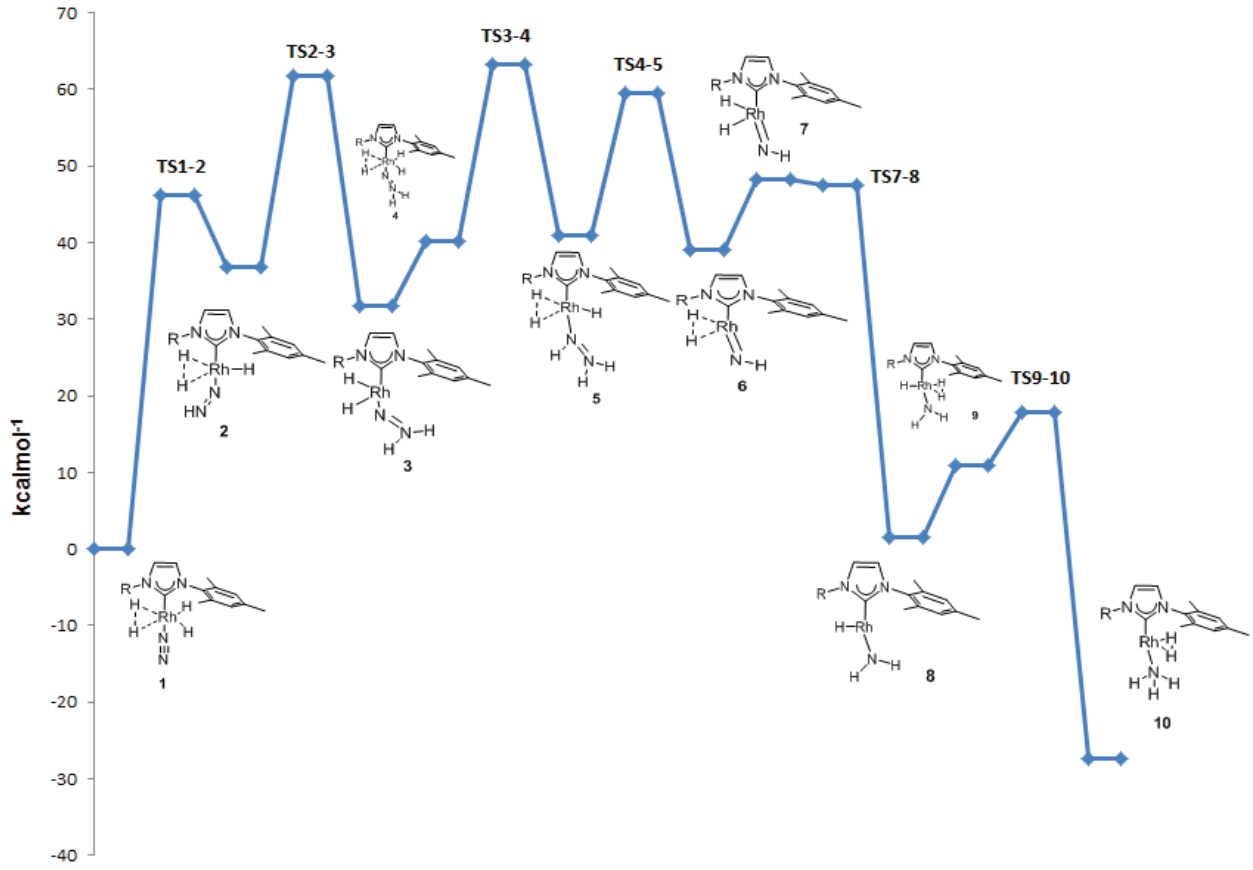

Figure 5.7: Gibbs energy profiles (B97D3-BJ/def2-SVP) computed with catalyst system **1** in the gas phase.

It can be observed that the some of the transitions states are too high in energy barrier that it will be impossible for the dinitrogen conversion to ammonia to happen practically in the laboratory.

5.2.4) Computation of catalytic cycle for dinitrogen conversion to ammonia using cobalt as late metal

Cobalt complexes are known to activate dinitrogen to a large extent. Recently Deng *et al* synthesized cobalt-NHC complex $[(ICy)_3CoCl]$ and showed that the complex is able to activate dinitrogen to a large extent.[44] The infra-red stretching frequency of N···N bond is reduced considerably to 1800 cm^{-1}. Kuriyama *et al* reported Co-PNP pincer complex which is able to reduce dinitrogen to ammonia producing 4.2 $\pm$ 1 equivalents of ammonia.[45] The low turnover number of this catalytic reaction promises further exploration of cobalt complexes for N_2 activation. Therefore we replaced the rhodium metal with cobalt to generate Ta-Co bimetallic system. The Ta-Co catalytic cycle started with the addition of the hydrogen and nitrogen

molecule to the starting complex. This leads to the formation of $CoN_2H_2(\eta^2\text{-}H_2)$ **1** which adopts an octahedral structure at the cobalt center. The nitrogen atom is bonded in trans position to the NHC-carbene in an end-on fashion. The cobalt-nitrogen bond length is 1.82 Å which shows that cobalt dinitrogen binding strength is stronger than the rhodium dinitrogen interaction (2.0 Å). It is also observed that the N···N bond length weakens to 1.12 Å as compared to corresponding to bond length for rhodium dinitrogen complex.

The transition state for the transfer of hydride center from rhodium to the distal nitrogen atoms requires crossing an activation barrier of 42 kcalmol^{-1}. Transformation of **1** to **2** is endergonic in nature and the local minimum **2** is 25 kcalmol^{-1} higher in energy. However the energy of local minimum **2** is 11 kcalmol^{-1} lower as compared to the corresponding minimum of rhodium complex. The whole catalytic cycle is computed following the similar chemical pathway as established for rhodium. (**Figure 5.8**)

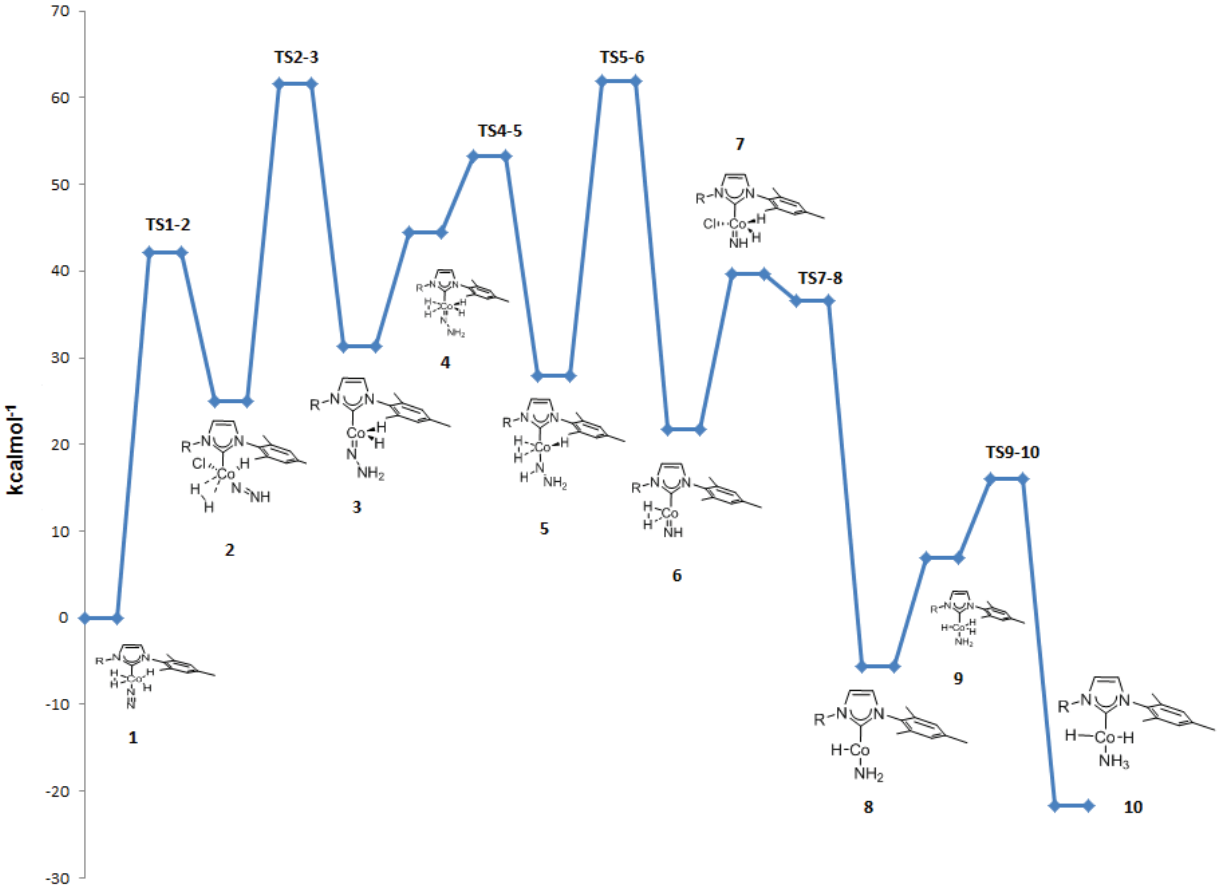

Figure 5.8: Gibbs energy profile (B97D3-BJ/def2-SVP) for the cycle computed with tantalum-cobalt bimetallic complex. Some of the local minima and transition states were lower in energy as compared to tantalum-rhodium system.

It can be seen that many local minima are lower in energy as compared to corresponding minima in rhodium catalyzed cycle. However **TS2-3**, **TS4-5** and **TS5-6** are still higher in energy and need more stabilization of the transition state.

5.2.4) Computation of catalytic cycle for dinitrogen conversion to ammonia using iridium as late metal

The corresponding iridium analogue of bimetallic complex is also explored and the transition state energy barriers for first few steps are calculated. As could be seen that even iridium analogue requires crossing the energy barrier of 52, 69 and 63 kcalmol^{-1} respectively for the first three transition states. (**Figure 5.9**)

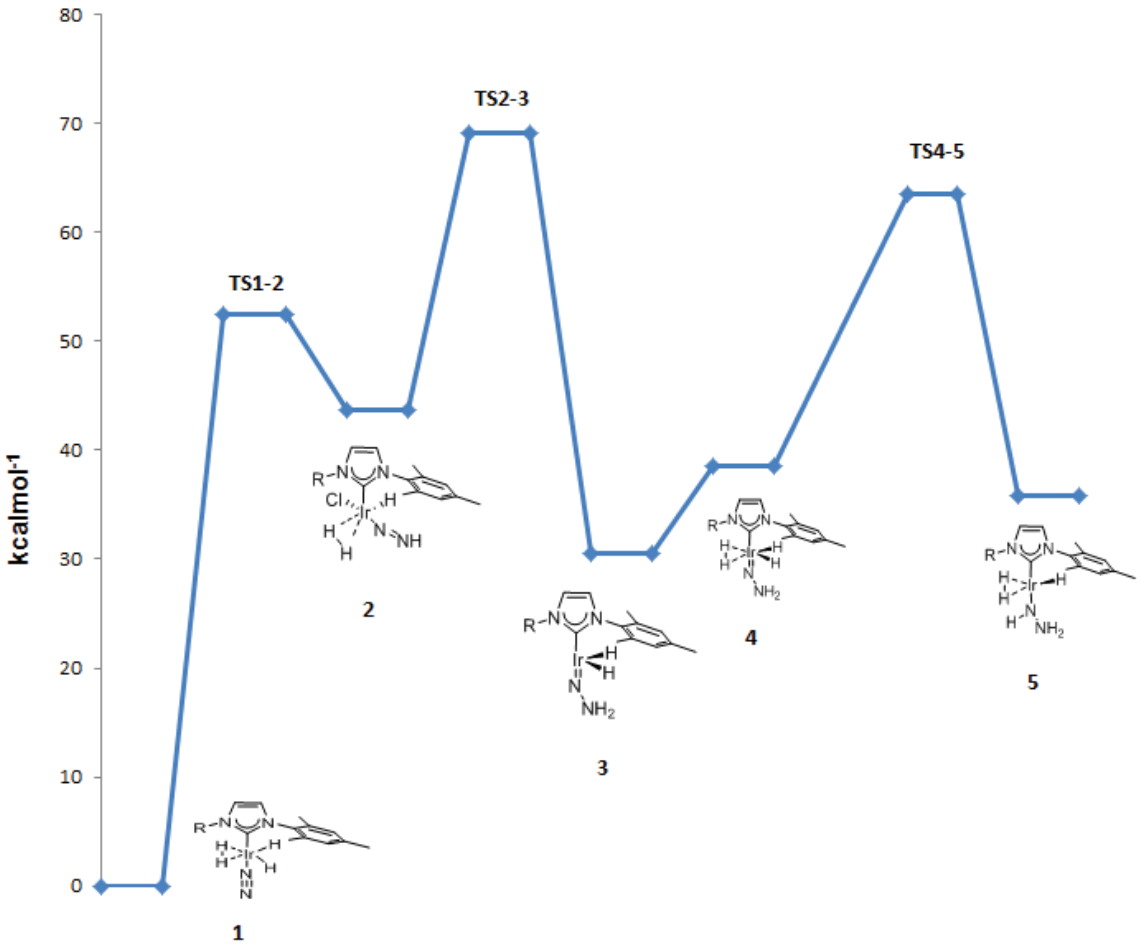

Figure 5.9: Gibbs energy profile (B97D3-BJ/def2-SVP) of the catalytic system with tantalum-iridium bimetallic complex. The transition states were too high in energy to be realized practically.

It can be observed from above discussion that changing the late metal from Rh to either Co or Ir does not lower the transition states comprehensively. It can also be seen that none of the

above mentioned structures involves the interaction of tantalum and late metal center. This is due to the presence of three methyl groups around tantalum center which provides steric hindrance to the rhodium metal center to approach closer to tantalum atom.

5.2.5) Computation of catalytic cycle for dinitrogen conversion to ammonia at tantalum center and replacing tris(tert-butoxy) silanol with POSS molecule

The tris(tert-butoxy) silanol molecule is replaced with POSS molecule and silicon atoms are saturated with fluorine atoms. This will match the electronegativity of the POSS moiety with silica surface. Saturation with fluorine is also important as it removes the erstwhile cyclopentyl groups which may interact with the metal center and change the chemical behavior of the complex.[46] Samantaray and co-workers have reported that the siloxane bridge of the silica surface interacts with the metal center and stabilizes it[47] which is why we chose to replace the tris(tert-butoxy) silanol with POSS molecule expecting the reduction in transition state energy barrier. However, no interaction of the POSS siloxane bridge with the metal center is observed in our case due to steric hindrance produced by the metalloligand framework. The three methyl groups attached to the tantalum center are removed by adding H_2 and N_2 which leads to the formation of Ta-H species shown below with dinitrogen bonded in a side on η^2 fashion to the tantalum center (seminal work by Quadrelli and co-workers on N2 activation). (**Figure 5.10**)

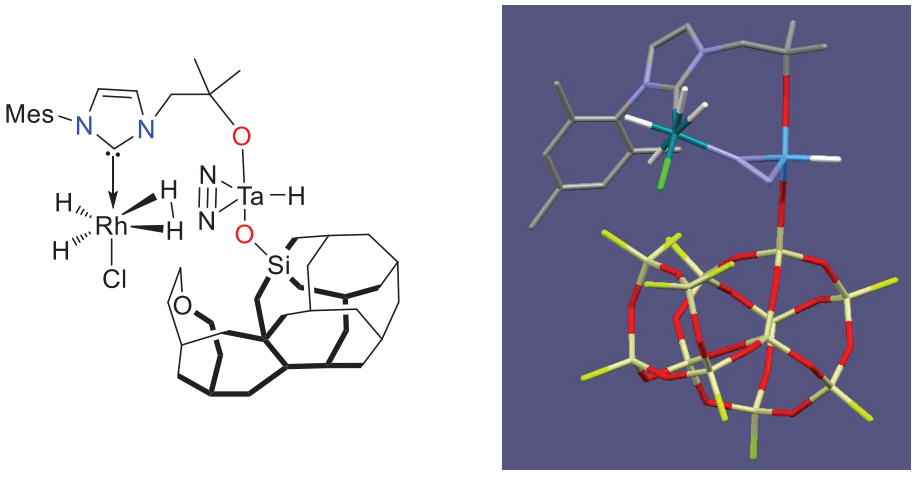

Figure 5.10: The POSS based Ta-Rh bimetallic complex proposed for N_2 activation to NH_3. The Ta center will act as the nitrogen reduction site whereas the hydrides will be transferred from the rhodium center.

The Ta-η^2N_2 bond distances are 2.09 and 2.03 Å. The N-N bond distance is 1.23 Å which is longer than the observed N-N bond distance in Rh-N_2 complex reported earlier. The rhodium center possesses the dihydride and the classical dihydrogen molecule. The bond length for Rh-H and Rh-η^2H_2 is similar to what has been reported earlier in the chapter. The Ta-Rh bond distance is 3.88 Å which is far lower than the observed Ta-Rh distance (7.93 Å) reported for starting complex in section 5.2.3. The first step of the catalytic cycle involves the transfer of hydride from rhodium center to the nitrogen atom. The hydride transfer is exergonic in nature and releases -4.87 kcalmol^{-1} of energy to yield complex **2**. The N-N bond distance in complex **2** is 1.36 Å which is considerably longer w.r.t. complex **1**. The Ta-N and Rh-N bond distances are 1.79 and 2.06 Å respectively. Multiple attempts to locate the transition state for the hydride transfer cannot be obtained. The transfer of another hydride from rhodium to the –NNH group gives complex **3**. This step is exergonic too and lays -12.76 kcalmol^{-1} lower in energy profile when compared with complex **1**. The transition state **TS23** for the hydride transfer is located and it lays 17.85 kcalmol^{-1} higher in energy profile as compared to complex **1**. The next step of the cycle is addition of one more hydrogen molecule at the rhodium center. (**Figure 5.11**)

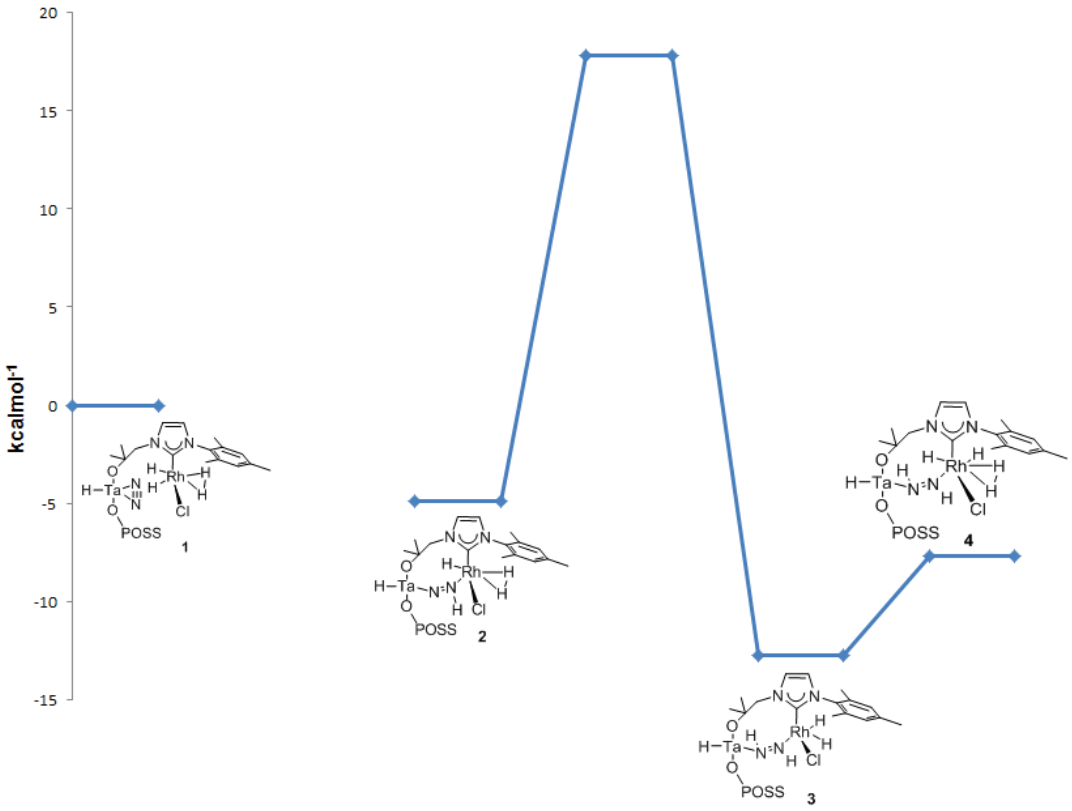

Figure 5.11: Gibbs energy profile (B97D3-BJ/def2-SVP) of the POSS based bimetallic complex with the nitrogen molecule bonded with tantalum centre. The calculations are still going to locate the transition state TS1-2 whereas TS2-3 lays 17.85 kcalmol-1 higher than the complex 1.

It can be seen from **figure 5.11** that the reaction profile involves local minima and transition states at far lower energy level when compared to dinitrogen activation at rhodium center. The work is still going on to compute TS1-2 and other local minima to complete the catalytic cycle.

5.3) CONCLUSION:

NH_3 is synthesized from N_2 by both biological and industrial processes. Both, the natural activation by nitrogenase enzyme and industrial activation by Haber-Bosch process involves the interplay of multiple elements to carry out the dinitrogen activation. However, the reaction conditions employed during HBP are very harsh and the H_2 required in the reaction is obtained from steam reforming of coal/natural gas which itself produces greenhouse gas CO_2 in the process. Hence, scientific work in this field had focused on the development of organometallic complexes to carry out N_2 activation to NH_3 in mild conditions. The Ta-Rh heterobimetallic complex offers a viable alternative to the existing homogeneous complexes for N_2 activation to NH_3 through bifunctional activation of small molecules. The structure optimization of the homogeneous bimetallic complex proposed by us reveals that the tantalum and rhodium centers are approximately 7.93 Å away from each other. At such high distance no cooperative activity could be expected. And indeed, computational study reveals that the transition states are too high in energy to practically realize the dinitrogen conversion to ammonia using the bimetallic complex. Cobalt and iridium based bimetallic complexes have also been explored to observe the effect of same group elements on the energy of transition states. It is observed that tantalum-cobalt bimetallic complex based catalytic pathway involves low energy minimum and lower transition states energy barrier. However, the energy required to cross the activation barrier is still very high. We then explored the dinitrogen reduction at tantalum atom with the hydride transfer from the rhodium center. Indeed it is observed that the transition state barrier is lowered with this molecular set up. We will compute the full catalytic cycle to study the overall energy barrier.

REFERENCES:

1 C. Copéret, F. Allouche, K. Wing Chang, M. Conley, M. F. Delley, A. Fedorov, I. Moroz, V. Mougel, M. Pucino, K. Searles, K. Yamamoto, P. Zhizhko, K. Wing Chan, M. P. Conley, I. B. Moroz and P. A. Zhizhko, *Angew. Chem. Int. Ed. Angew. Chem*, 2018, **57**, 6398-6440.

2 E. Le Roux, M. Chabanas, A. Baudouin, A. De Mallmann, C. Copéret, E. A. Quadrelli, J. Thivolle-Cazat, J. M. Basset, W. Lukens, A. Lesage, L. Emsley and G. J. Sunley, *J. Am. Chem. Soc.*, 2004, **126**, 13391–13399.

3 M. K. Samantaray, S. Kavitake, N. Morales, E. Abou-Hamad, A. Hamieh, R. Dey and J. M. Basset, *J. Am. Chem. Soc.*, 2017, **139**, 3522–3527.

4 C. Copéret, M. Chabanas, R. Petroff Saint-Arroman and J. M. Basset, *Angew. Chem. - Int. Ed.*, 2003, **42**, 156–181.

5 Y. Chen, E. Abou-Hamad, A. Hamieh, B. Hamzaoui, L. Emsley and J. M. Basset, *J. Am. Chem. Soc.*, 2015, **137**, 588–591.

6 D. Soulivong, S. Norsic, M. Taoufik, C. Copéret, J. Thivolle-Cazat, S. Chakka and J. M. Basset, *J. Am. Chem. Soc.*, 2008, **130**, 5044–5045.

7 J. D. A. Pelletier and J. M. Basset, *Acc. Chem. Res.*, 2016, **49**, 664–677.

8 Y. Chen, S. Ould-Chikh, E. Abou-Hamad, E. Callens, J. C. Mohandas, S. Khalid and J.-M. Basset, *Organometallics*, 2014, **33**, 51.

9 P. Avenier, M. Taoufik, A. Lesage, X. Solans-Monfort, A. Baudouin, A. de Mallmann, L. Veyre, J.-M. Basset, O. Eisenstein, L. Emsley and E. A. Quadrelli, *Science,* 2007, **317**, 1056–1060.

10 Priscilla Avenier, Anne Lesage, Mostafa Taoufik, Anne Baudouin, Aimery De Mallmann, Steven Fiddy, Manon Vautier, Laurent Veyre, Jean-Marie Basset, Lyndon Emsley and Elsje Alessandra Quadrelli, *J. Am. Chem. Soc.,* 2007, **129**, 176-186.

11 P. Avenier, M. Taoufik, A. Lesage, X. Solans-Monfort, A. Baudouin, A. De Mallmann, L. Veyre, J. M. Basset, O. Eisenstein, L. Emsley and E. A. Quadrelli, *Science*, 2007, **317**, 1056–1060.

12 H.-P. Jia and E. A. Quadrelli, *Chem. Soc. Rev.*, 2014, **43**, 547–564.

13 X. Solans-Monfort, C. Chow, E. Gouré, Y. Kaya, J.-M. Basset, M. Taoufik, E. A. Quadrelli and O. Eisenstein, *Inorg. Chem.*, 2012, **51**, 7237–7249.

14 R. D. Duda, R. D. Milton, S. Maheshwari, S. D. Minteer, S. L. Foster, S. I. P. Bakovic, L. F. Greenlee, M. J. Janik and J. N. Renner, *Nat. Catal.*, 2018, **1**, 490–500.

15 B. M. Hoffman, D. Lukoyanov, D. R. Dean and L. C. Seefeldt, *Acc. Chem. Res.*, 2013, **46**, 587–595.

16 S. F. McWilliams, E. Bill, G. Lukat-Rodgers, K. R. Rodgers, B. Q. Mercado and P. L. Holland, *J. Am. Chem. Soc.*, 2018, **140**, 8586–8598.

17 V. Kyriakou, I. Garagounis, A. Vourros, E. Vasileiou and M. Stoukides, *Joule*, 2020, **4**, 1–17.

18 M. D. Fryzuk, T. S. Haddad, M. Mylvaganam, D. H. McConville and S. J. Rettig, *J. Am. Chem. Soc.*, 1993, **115**, 2782–2792.

19 R. J. Burford and M. D. Fryzuk, *Nat. Rev. Chem.*, 2017, **1**, 0026.

20 M. D. Fryzuk, B. A. MacKay and B. O. Patrick, *J. Am. Chem. Soc.*, 2003, **125**, 3234–3235.

21 R. J. Burford, L. Castro, L. Maron, J. E. Hein and M. D. Fryzuk, *Dalt. Trans.*, 2018, **47**, 7983–7991.

22 R. J. Burford, A. Yeo and M. D. Fryzuk, *Coord. Chem. Rev.*, 2017, 334, 84–99.

23 B. Cheng, W. Liu and Z. Lu, *J. Am. Chem. Soc.*, 2018, **140**, 5014–5017.

24 K. Arashiba, A. Eizawa, H. Tanaka, K. Nakajima, K. Yoshizawa and Y. Nishibayashi, *Bull. Chem. Soc. Jpn.*, 2017, **90**, 1111–1118.

25 Y. Nishibayashi, *Inorg. Chem.*, 2015, **54**, 9234–9247.

26 F. Akagi, T. Matsuo and H. Kawaguchi, *Angew. Chemie - Int. Ed.*, 2007, **46**, 8778–8781.

27 G. Christian and R. Stranger, *Dalt. Trans.*, 2004, **16**, 2492–2495.

28 V. Moha, W. Leitner and M. Hölscher, *Chem. - A Eur. J.*, 2016, **22**, 2624–2628.

29 M. Hölscher and W. Leitner, *Chem. - A Eur. J.*, 2017, **23**, 11992–12003.

30 S. B. Seymore and S. N. Brown, *Inorg. Chem.*, 2006, **45**, 9540–9550.

31 Y. Nishibayashi, S. Iwai and M. Hidai, *Science*, 1998, **279**, 540–542.

32 M. Hidai, S. In Molybdenum Enzymes·, S. Ed, John Wiley, George, T. A. Pignolet, L. H. Ed, J. R. Dilworth, R. L. Richards, J. Chatt, R. A. Head, G. J. Leigh and C. J. Pickett, Pergamon Press, 1992, **114**, 5429-5432.

33 Y. Ishii, M. Kawaguchi, Y. Ishino, T. Aoki and M. Hidai, *Organometallics*, 1994, **13**, 5062-5071.

34 M. Hidai and Y. Mizobe, 1993, 346–362.

35 V. Moha, W. Leitner and M. Hölscher, *Chem. - A Eur. J.*, 2016, **22**, 2624–2628.

36 B. Wu, K. M. Gramigna, M. W. Bezpalko, B. M. Foxman and C. M. Thomas, *Inorg. Chem.*, 2015, **54**, 10909–10917.

37 B. Wu, K. M. Gramigna, M. W. Bezpalko, B. M. Foxman and C. M. Thomas, *Inorg. Chem.*, 2015, **54**, 10909–10917.

38 S. Lau, A. J. P. White, I. J. Casely and M. R. Crimmin, *Organometallics*, 2018, **37**, 4521–4526.

39 S. Grimme, *J. Comput. Chem.*, 2006, **27**, 1787–1799.

40 R. Grüber and P. Fleurat-Lessard, *Theor. Chem. Acc.*, 2014, **133**, 1533.

41 L. Liu Zeonjuk, P. St. Petkov, T. Heine, G.-V. Röschenthaler, J. Eicher and N. Vankova, *Phys. Chem. Chem. Phys.*, 2015, **17**, 10687–10698.

42 R. Gelabert, M. Moreno, J. M. Lluch and A. Lledós, *Organometallics*, 2002, **16**, 3805–3814.

43 K. W. Huang, J. H. Han, C. B. Musgrave and E. Fujita, *Organometallics*, 2007, **26**, 508–513.

44 Y. Gao, G. Li and L. Deng, *J. Am. Chem. Soc.*, 2018, **140**, 2239–2250.

45 S. Kuriyama, K. Arashiba, H. Tanaka, Y. Matsuo, K. Nakajima, K. Yoshizawa and Y. Nishibayashi, *Angew. Chem. Int. Ed.*, 2016, **55**, 14291–14295.

46 M. P. Conley, M. F. Delley, G. Siddiqi, G. Lapadula, S. Norsic, V. Monteil, O. V Safonova and C. Cop??ret, *Angew. Chem. Int. Ed.*, 2014, **53**, 1872–1876.

47 M. K. Samantaray, J. Alauzun, D. Gajan, S. Kavitake, A. Mehdi, L. Veyre, M. Lelli, A. Lesage, L. Emsley, C. Copéret and C. Thieuleux, *J. Am. Chem. Soc.*, 2013, **135**, 3193–3199.

CONCLUDING REMARKS

This doctoral research work has embarked on an ambitious project which cuts across a wide range of research domains. During this process it has offered solutions and opened new dimensions at each step of its progression. This progression is reflected in the series of novel molecular and surface-bound organometallic complexes which revolve around a common and original architectural unit: a bifunctional ligand for early-late heterobimetallic assemblies by design.

The core element of this project is the bifunctional N-heterocyclic carbene (NHC) containing a pendant alkoxy functionality. Its purpose is assembling two metal atoms in close proximity with each other yet with chemically different reactivity: the "soft" ligand-NHC is designed to coordinate the late metal while the harder alkoxy group is introduced to coordinate the oxophilic early metal. The two moieties are connected by a tether designed to be sufficiently long and flexible for allowing the two metals to come in proximity of each other, to form the targeted early-late heterobimetallic (ELHB) complexes. Building up on the previously reported work on bifunctional alkoxy-NHC ligands which were utilized solely for the synthesis of monometallic complexes (see introduction chapter), we reported a straightforward, scalable synthetic process of the bifunctional alkoxy-NHC ligand. We utilized the ligand for the successful assembly of a novel tantalum-rhodium heterobimetallic complex. The Ta-Rh ELHB complex assembled through the bifunctional NHC has the potential to be a trail opener for a larger family of complexes, since there is no foreseeable reason such ligand should be restricted to the (Ta,Rh) couple. For example, the bifunctional NHC has already been utilized in our laboratory to report Mn- and Al- based (Camp *et al Dalton Trans*. 2018, 47, 10429-10433) monometallic-NHC complexes and its application will be extended further to assemble other earth-abundant monometallic-NHC complexes. The choice of earth abundant metals is also to contribute to the ongoing push in catalysis toward such metals where no strain exist in the current supply chain of the metal ore, not in its disposal circuit. Regarding the application to catalysis, in this thesis we have started exploring the catalytic properties of these new complexes bearing the NHC-OH ligand. We have been able to observe that a series of monometallic Rh-NHC complexes are active catalysts for alkene hydrosilylation reaction. The preliminary results suggest that the Rh-NHC complexes are catalytically active (with a low catalyst loading of 0.1 mol %) for both terminal and internal alkenes. Going forward other challenging catalytic transformations would be explored with the hetero-bimetallic Ta/Rh-NHC complexes. So far, the most straightforward attempts to probe a unique reactivity for the bimetallic Ta-Rh assembly have not been found. For example, a reaction between the *tris*(ter-butoxy) silanolate derivative of the Ta-Rh bimetallic complex and molecular dihydrogen (1

bar) at elevated temperatures (100°C) have not yielded the desired bimetallic hydride complexes. The stability and saturation of the coordination sphere around the two metals can in part contribute to this lack of reactivity.

A successful strategy to have access to very reactive organometallic moieties, that have little to no parallel in homogeneous catalysis, is the grafting on surfaces by the surface organometallic chemistry (SOMC) approach, possibly followed by post-treatment such as hydrogenation that can increase the steric accessibility and reactivity of resulting surface –bound moieties. We therefore tackled the second domain of the work: achieving Ta-Rh silica supported species, whose spatial relative position is ensured by the NHC-OH bifunctional ligand. The underlying belief is that surface–bound complexes will not only lead to isolated organometallic moieties devoid of any intermolecular interactions but will also lead to an increase in the reactivity of these species under different reaction conditions like high temperature and pressure, solventless reactions etc.

The development of the Polyhedral Oligosilsesquioxanes (POSS) Ta-Rh bimetallic molecular model has been a stepping stone toward silica-supported species. Namely, this study has revealed that the straightforward reaction of a preassembled [Ta-(O-NHC)-Rh] complex with the surface is not appropriate and suggested a successful stepwise synthetic route to the desired model. Indeed, an attempt to synthesize a well-defined Ta-Rh bimetallic molecular complex led to the formation of a trimetallic complex of nuclearity Rh_2Ta instead; owing to the reactivity of tantalum alkylidene precursor. The pre-settlement of the POSS molecule in the tantalum coordination sphere proved to be the right synthetic strategy in order to suppress the reactivity of the alkylidene precursor and ultimately leading to the formation of POSS based Ta-Rh bimetallic complex. The two-step synthetic process developed over POSS molecule has been extended to the silica surface in order to synthesize bimetallic species over silica. However, the development of silica-grafted bimetallic complex has not been as straightforward and its elemental composition is not as expected which is reflected in far lower concentration of chlorine (observed 0.1 weight%) rather than the expected 1.3 weight%. This is due to the partial protonation of the free $NHC_{carbene}$ *in situ* to yield imidazolium salt whereas the probable counter anion chlorine is washed away during the work-up. A possible way forward could be direct grafting of *tris*(ter-butoxy) silanolate derivative of the Ta-Rh bimetallic complex [$(^tBuO)_3SiO$-Ta(O-NHC)-Rh] over the silica surface to avoid imidazolium formation. This challenge, as well as the current inability to obtain surface metal hydrides

(that have been the cornerstone of many SOMC success in catalysis), will be addressed in later studies.

A natural "playing ground" for novel unique surface organometallic moieties is catalysis. An interesting topic is to undercover if bimetallic surface moieties could unlock unique molecular mechanisms toward N_2 reduction that could ultimately help bypass environmentally-burdensome H_2 utilization, in the footstep of the unique mechanism that has been previously observed in our laboratories for a SOMC-derived monometallic tantalum hydride, but still non catalytic. Not completely disjoined from the current synthetic challenge of disposing of the targeted surface bound Ta-Rh(NHC-O) moiety, the potential catalytic activity of the surface supported species has been explored *in silico*. We decided to explore the reactivity of the supported bimetallic complex for N_2 activation reaction, which is a very energy challenging process from a mechanistic point of view, mostly owing to the inertness of the N≡N bond. The calculations suggest that the heterolytic cleavage of both N_2 and H_2 molecules across the two metals of the chemically diverse (and hence potentially bifunctional) bimetallic core is not accessible. Conversely a new mechanistic route can be proposed which involves the role of a late metal center for hydrogen cleavage and subsequent hydride transfer; while the early metal center acts as the nitrogen reduction site. This synergistic role of both the metals in N_2 activation, established as of now computationally, corroborates the founding hypothesis for this doctoral work: the unique chemical ability of the early-late bimetallic complexes to open new chemical pathways to desired chemical transformations. It could also open up the path for development of ELHB complexes to realize chemical transformations which have yet no precedent with monometallic complexes.

In conclusion, this thesis has reported for the first time, the assembly of an early-late heterobimetallic complex in solution and over silica with the help of a bifunctional NHC ligand. Even though the exact nature of the surface species has not been determined yet and its catalytic reactivity has not been explored in laboratory; the synthetic protocol established for the assembly of the bimetallic complex could be exploited to assemble a wider range of bimetallic complexes. The bifunctional NHC ligand forms an important constituent of this thesis which holds promising future applications. The growing role of NHC ligands as a replacement of phosphines due to their easy synthesis and superior chemical properties (which is illustrated in Grubbs 2nd generation *vs* Grubbs 1st generation catalysts) could lead to the design of chemically diverse range of monometallic and bimetallic NHC complexes. The scientific research in the field of silica supported bimetallic complexes has not used bridging

ligands for assembling two metals till date. If in future the scientific community decides to harness the growing potential of NHCs to report surface supported bimetallic species, the current work could be a beacon.

ACKNOWLEDGEMENT

I am highly thankful to SINCHEM program for providing me the opportunity to work in reputed universities with state of the art facilities. I extend my sincere gratitude to Dr. Stefania Albonetti; the SINCHEM coordinator at University of Bologna, Italy for putting into place a planned organizational setup for the smooth conduct of the program. I also thank her for organizing yearly SINCHEM autumn and winter schools which not only provided us an opportunity to discuss the research work with other SINCHEM fellows but also gave us a platform to share our administrative and cultural experiences. I would like to thank my supervisors Dr. Alessandra Quadrelli at CPE Lyon and Prof. Walter Leitner at RWTH Aachen University for their scientific inputs at regular intervals. I extend my deep gratitude to my co-supervisors Dr. Clément Camp and Dr. Markus Hölscher with whom I had continuous interactions regarding the progress of the project. It was a unique experience to be the first PhD student of Dr. Clément Camp who not only helped me in understanding laboratory aspects of organometallic chemistry during my initial days but also provided me his administrative and scientific support throughout the PhD.

I would also like to thank various instrument-in-charges for their continuous help in acquisition and analysis of the data. I would like to thank Mrs. Christine Lucas, Anne Boudouin and Mr. Emmanuel Chefdeville for their help in NMR data acquisition. I thank Mr. Erwann Jeanneau for his help in X-ray crystallographic data acquisition. I also thank Mr. Laurent Veyre and Madam Nesrine Oueslati for their assistance in the laboratory. I extend my gratitude to human resources department of the university of Lyon as well as RWTH Aachen for their help in administrative paperwork throughout the PhD. Especially; I thank Mrs. Emmanuelle Fouilhe and Ms. Stephanie Mersmann for their help.

My stay in France and Germany would not have been possible without my labmates. If I could sustain three years in the European society, it was because of my colleagues from both the universities. I would like to thank my friends and ex-colleagues Tapish Saboo and Pooja Gaval for their continuous help during the PhD. Particularly, their help was instrumental in completing various administrative paperwork required for my stay in Europe. I miss the discussions that I used to have with them relating to Indian culture, society, language, food, politics etc. I thank my colleague and friend Sebastein Lasalle for all the funny discussions that we had while working together with the glovebox. I also thank him for inviting me to his home and showing me the fields and the gardens of the countryside which reminded me of my own home in India. God, I miss my home. I also thank my friend Clement Demarcy for all kind of discussions that we had related to work, food, visiting cities etc., thanks to his office place

which is just besides me. I also thank him for inviting me to his grandmother's house in the countryside. It was a memorable trip where we hiked, ate, and visited around. I would like to thank my senior colleagues Walid Darwich and Marc Renom for their help in the laboratory. I thank Marc for his insight in my research work and Walid for teaching me to dance on the Lebanese songs. I would like to thank David Kuß, my friend and colleague from RWTH Aachen who helped me in understanding each and every concept of computational chemistry. It was due to his continuous assistance that I could learn and perform computational calculations. I thank my friends and colleagues from C2P2; Matthieu Cavallies, Iurii Suleimanov, Paul-Alexis, Julien Petit, Leon Escomel, Vincent Dardun, Lisa Lou, Isis N'dala Louika, Pauline Schlitz, Noor Nawaz, Martin Jakoobi, Alexandre Verchere for the time we spent together. I also thank Gregor Voit, Anne- Kristine, Martin Schwarzer and Niklas We from RWTH Aachen for my memorable stay in Aachen. I am thankful to my dear friends Amit Dahiya and Akash Kaithal for all the memories that we made together in Aachen. Amit Dahiya, I will miss the spicy food prepared by you. I wholeheartedly thank my SINCHEM colleagues for all the memories that we made together during SINCHEM schools.

I wholeheartedly thank my parents and brothers for their support throughout my PhD. This thesis would not have been possible without their moral support. Thanks Mammi, thank you Papa, thanks Avinash, Saurabh and Vivek. I also thank my cousin brothers and sisters and my relatives for supporting me during my PhD years. These three years were memorable; these three years were a unique experience. I will remember my European years. Au revoir!

ANNEXURE

APPENDIX 1: Supporting information on chapter 2

Figure S1. ^{1}H NMR spectrum (293K, 300 MHz, CD_2Cl_2) of the imidazolium salt **1**.

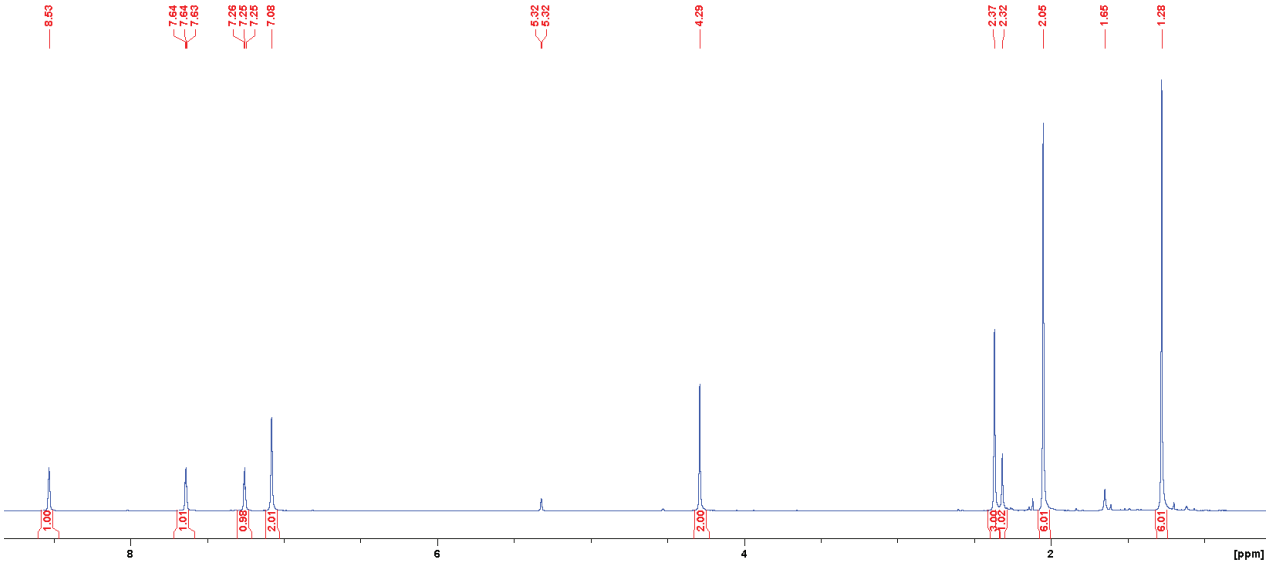

Figure S2. $^{13}C\{^{1}H\}$ NMR spectrum (293K, 101 MHz, CD_2Cl_2) of the ^{13}C labelled species **1-^{13}C**.

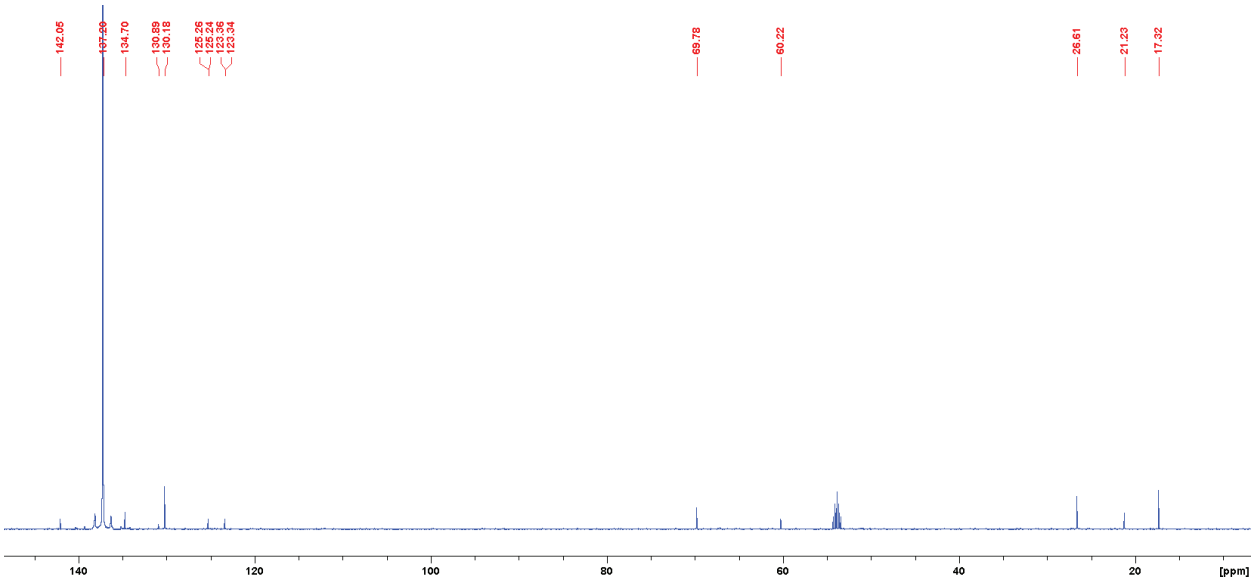

Figure S3. ^{1}H NMR spectrum (293K, 300 MHz, THF-d_8) of the bifunctional NHC ligand **2**.

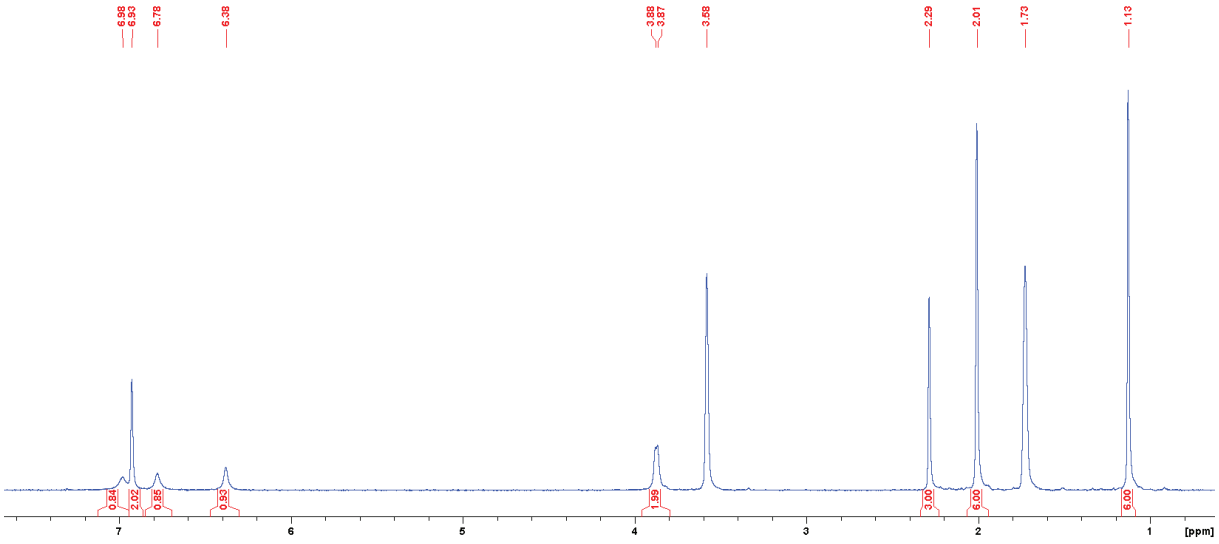

Figure S4. ^{13}C{^{1}H} NMR spectrum (293K, 75 MHz, THF-d_8) of the ^{13}C labelled ligand HL **2**-^{13}**C**.

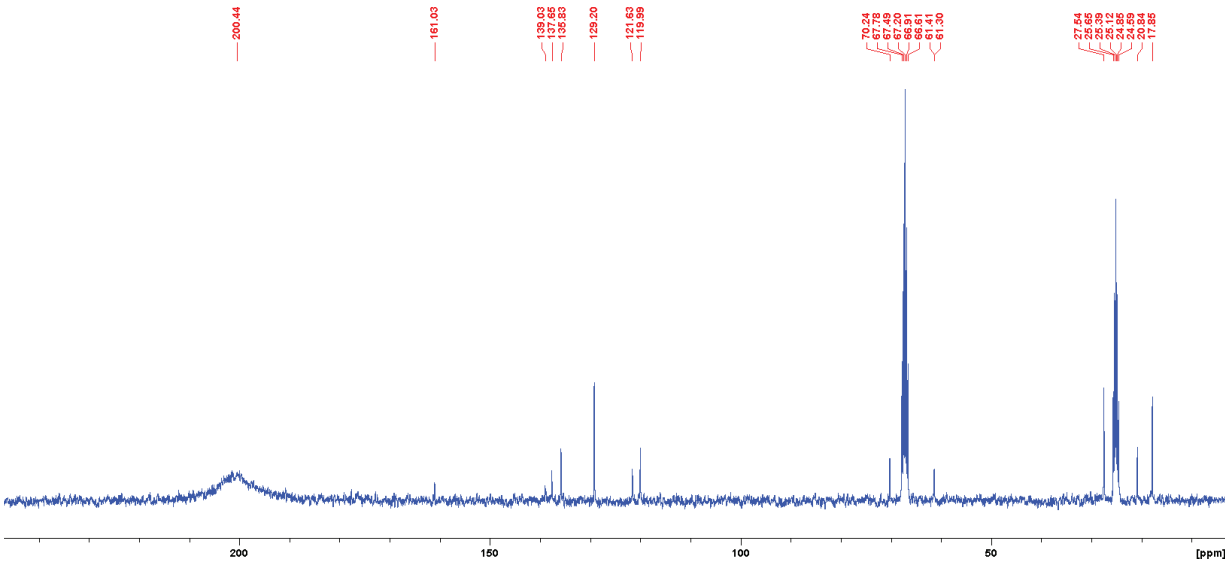

Figure S5: DRIFT spectrum (25°C, KBr solid solution under argon) for the free NHCcarbene.

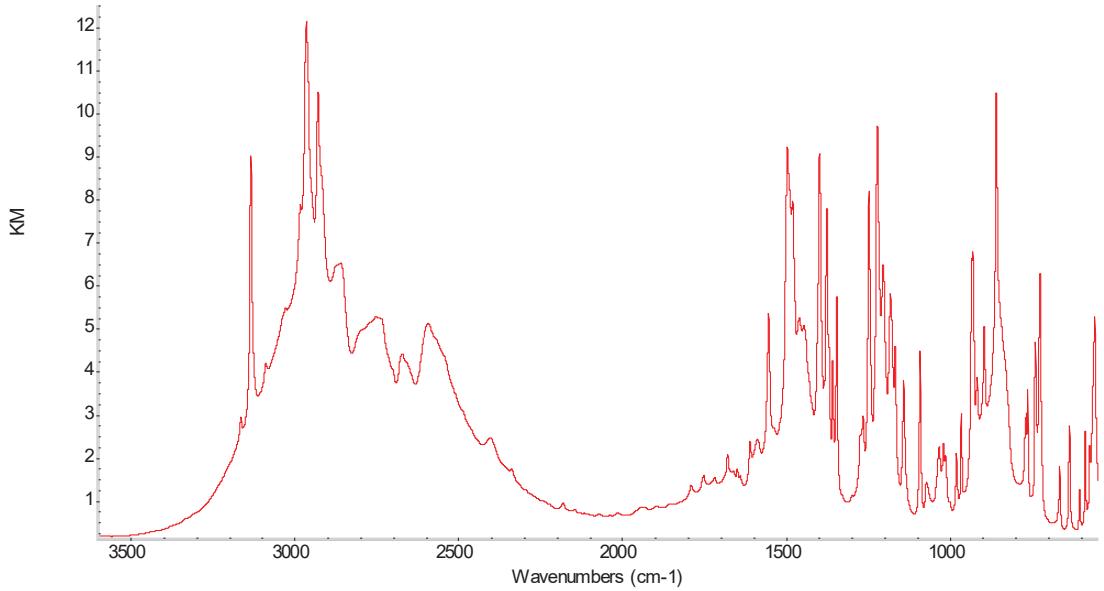

X-Ray Crystallography

X-ray structural determinations were performed at the centre de diffractométrie Henri Longchambon, Université de Lyon. A suitable crystal coated in Parabar oil was selected and mounted on a Gemini kappa-geometry diffractometer (Rigaku Oxford Diffraction) equipped with an Atlas CCD detector and using Cu (λ= 1.54184 Å) for compounds **1** and **2**. Intensities were collected at 150 K by means of the CrysalisPro software. Reflection indexing, unit-cell parameters refinement, Lorentz-polarization correction, peak integration and background determination were carried out with the CrysalisPro software. An analytical absorption correction was applied using the modeled faces of the crystal. The resulting set of hkl was used for structure solution and refinement. The structures were solved by direct methods with SIR97and the least-square refinement on F2 was achieved with the CRYSTALS software. All non-hydrogen atoms were refined anisotropically. The hydrogen atoms were all located in a difference map, but those attached to carbon atoms were repositioned geometrically. The H atoms were initially refined with soft restraints on the bond lengths and angles to regularize their geometry (C---H in the range 0.93--0.98 Å, O---H =0.82 Å) and Uiso(H) (in the range 1.2-1.5 times Ueq of the parent atom), after which the positions were refined with riding constraints.

Compound	**1**	**2**
Formula	$C_{16}H_{23}F_6N_2OP$	$C_{16}H_{22}N_2O$
cryst syst	Orthorhombic	Monoclinic
space group	P b c a	C2/c
volume (Å^3)	3844.7(5)	3082.9(4)
a (Å)	15.3460(11)	14.7860(12)
b (Å)	14.8717(12)	9.6249(8)
c (Å)	16.8465(13)	21.8567(17)
α (deg)	90	90
β (deg)	90	97.641(7)
γ (deg)	90	90
Z	8	8
formula weight (g/mol)	404.33	258.37
density (g cm^{-3})	1.397	1.113
absorption coefficient (mm^{-1})	1.867	0.546
F(000)	1680	1120
temp (K)	150.0(1)	150.0(1)
total no. reflections	26486	69860
unique reflections [R(int)]	3393 [0.0486]	6468 [0.028]
Final R indices [I > 2σ(I)]	R1 = 0.0298, wR2 = 0.0745	R1 = 0.0122, wR2 = 0.0291
Largest diff. peak and hole (e.A^{-3})	0.345 and -0.427	0.315 and -0.346
GoF	1.0326	1.082

APPENDIX 2: Supporting information on chapter 3

NMR spectroscopic data

Figure S1: ^{1}H NMR spectrum (293K, 300 MHz, C_6D_6) of Ta(L)(CH^{t}Bu)(CH$_2$^{t}Bu)$_2$ **3.**

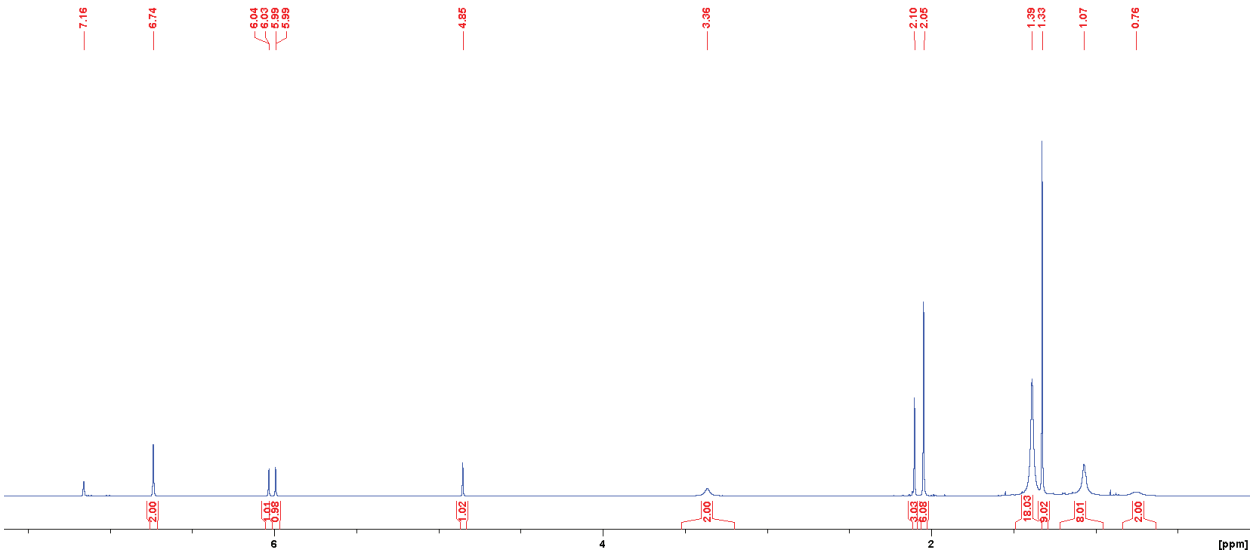

Figure S2: $^{13}C\{^{1}H\}$ NMR spectrum (293K, 101 MHz, C_6D_6) of Ta(L)(CH^{t}Bu)(CH$_2$^{t}Bu)$_2$ **3.**

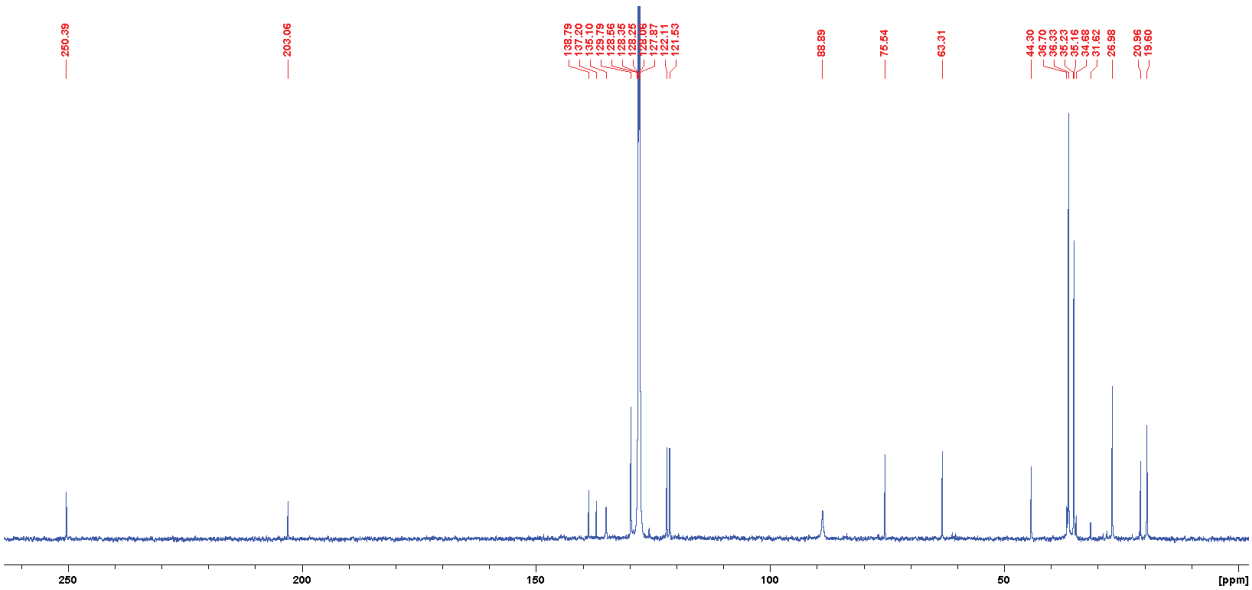

Figure S3. ^{1}H NMR spectrum (293K, 300 MHz, C_6D_6) of Ta(L*)(CH^{t}Bu)(CH$_2$^{t}Bu) **4**.

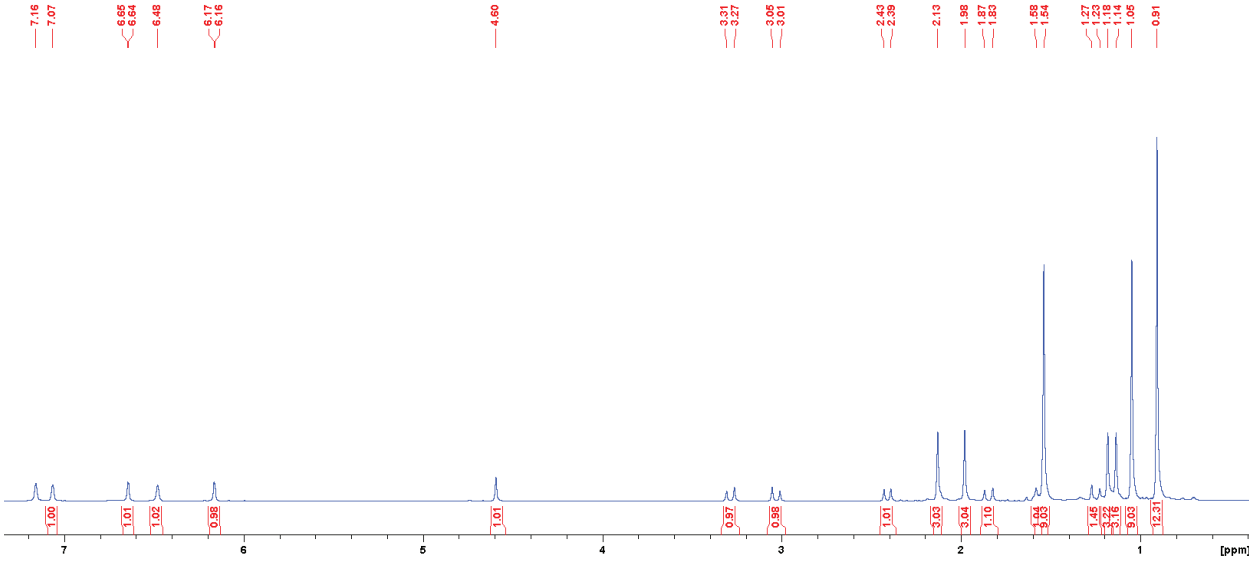

Figure S4. $^{13}C\{^{1}H\}$ NMR spectrum (293K, 101 MHz, C_6D_6) of Ta(L*)(CH^{t}Bu)(CH$_2$^{t}Bu) **4**.

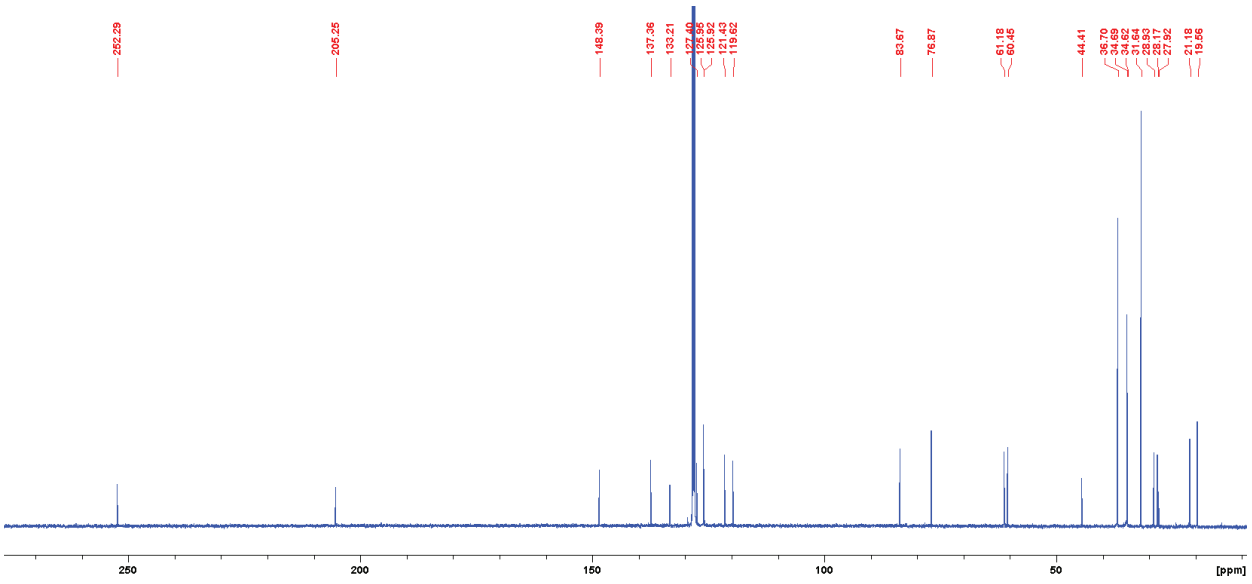

Figure S5. Kinetic monitoring of the transformation of **3** into **4** at 45°C over 6h by ^{1}H NMR (298K, 300 MHz, C_6D_6): plot of $\ln([\mathbf{3}]/[\mathbf{3}]_0)$ *versus* time (min) showing a linear trend, in agreement with a 1st order in **3** (k = 0.0073 min^{-1} at 45°C).

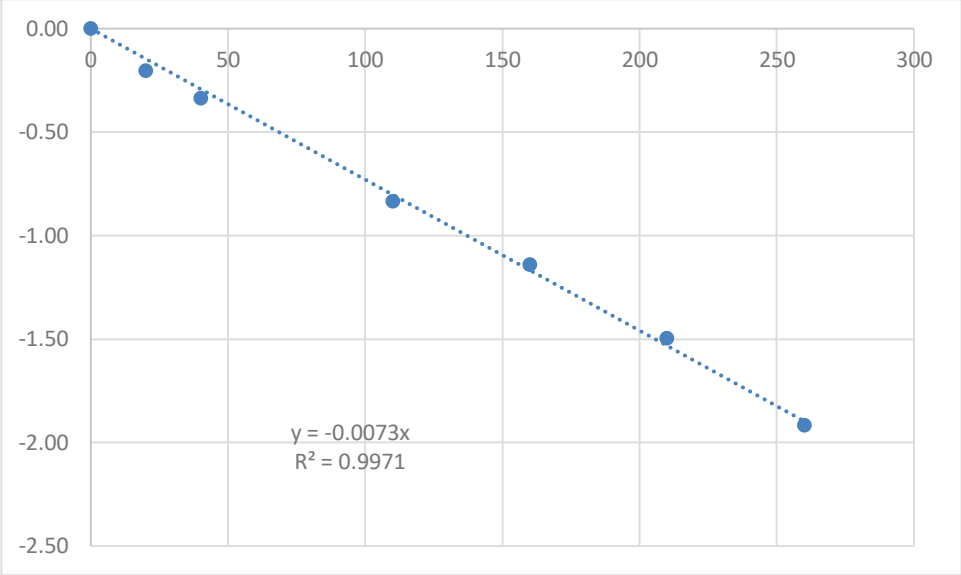

Figure S6. ^{1}H NMR spectrum (293K, 300 MHz, C_6D_6) of Ta(L)(N^{t}Bu)(CH$_2$^{t}Bu)$_2$ **5**.

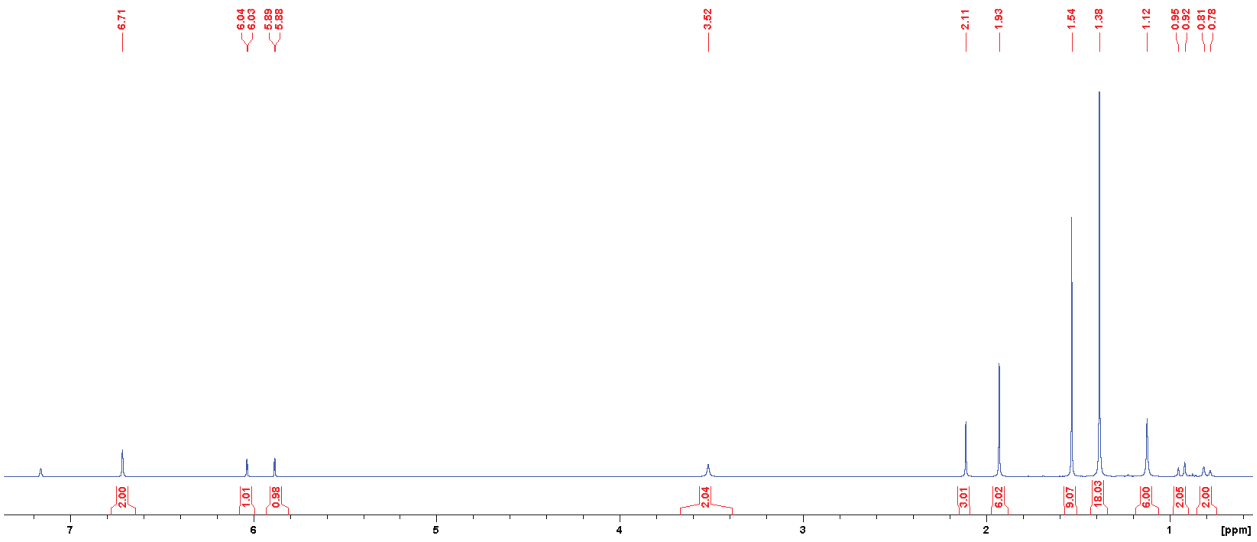

Figure S7. $^{13}C\{^{1}H\}$ NMR spectrum (293K, 101 MHz, C_6D_6) of Ta(L)(N^{t}Bu)(CH$_2$^{t}Bu)2 **5**.

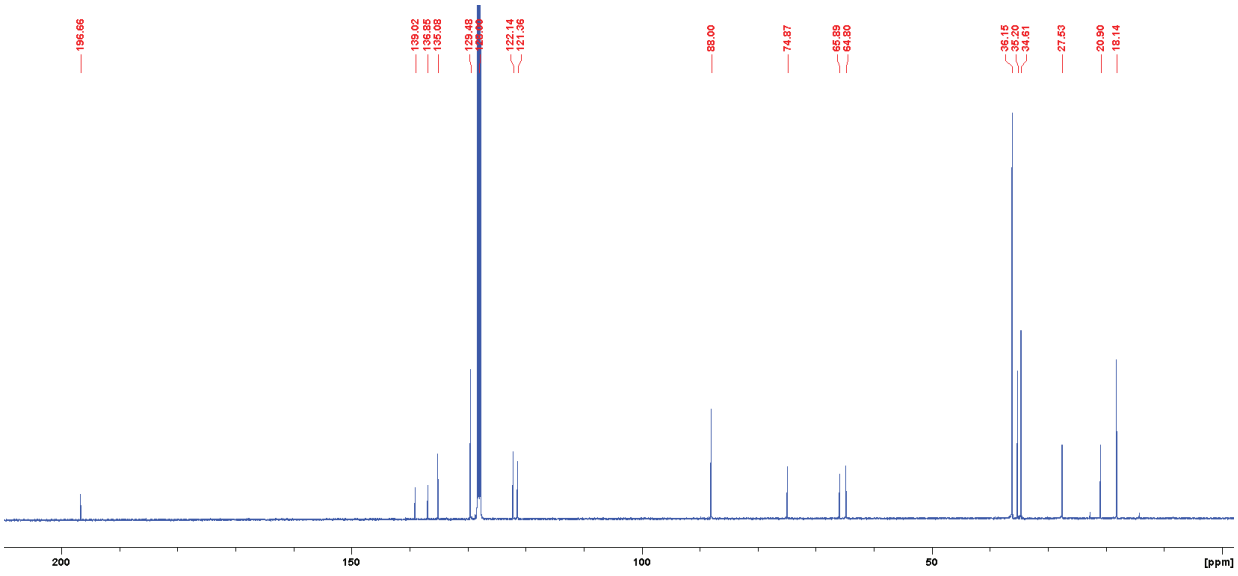

Figure S8. ^{1}H NMR spectrum (293K, 101 MHz, $CDCl_3$) of Rh(HL)(COD)(Cl) **6**.

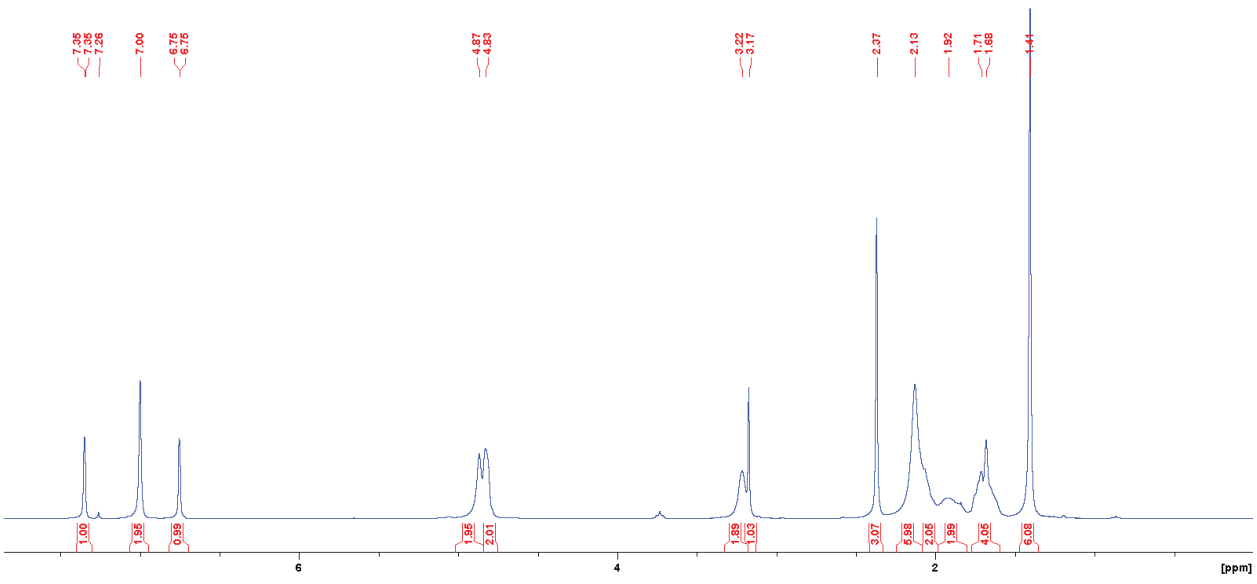

Figure S9. $^{13}C\{^{1}H\}$ NMR spectrum (293K, 101 MHz, $CDCl_3$) of Rh(HL)(COD)(Cl) **6**.

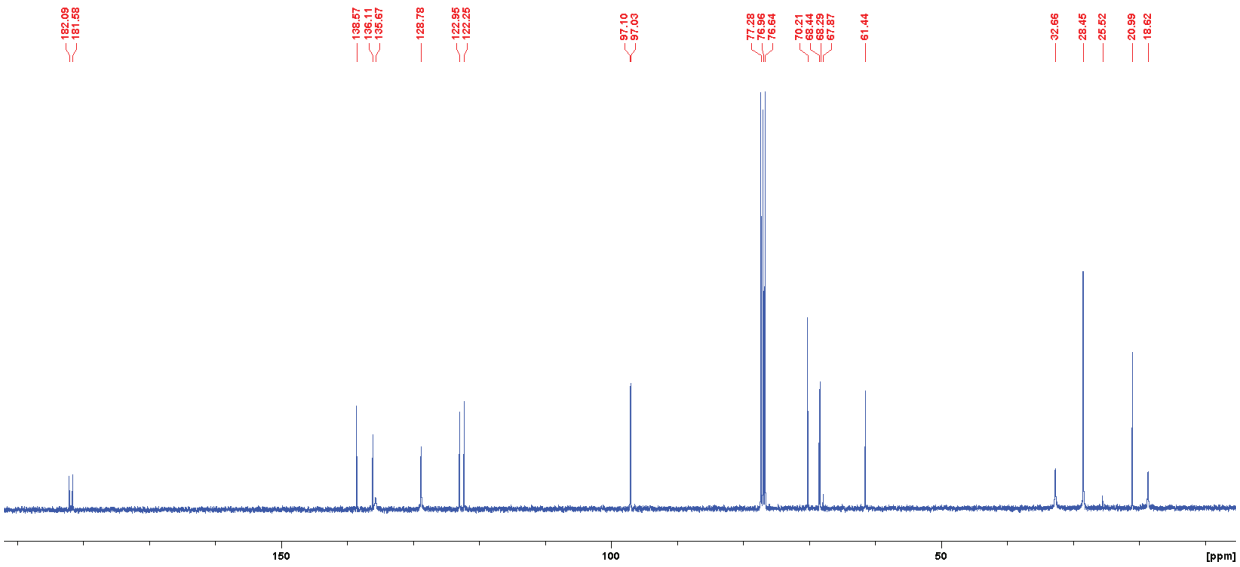

Figure S10. ^{1}H NMR spectrum (293K, 300 MHz, $CDCl_3$) of complex **7**.

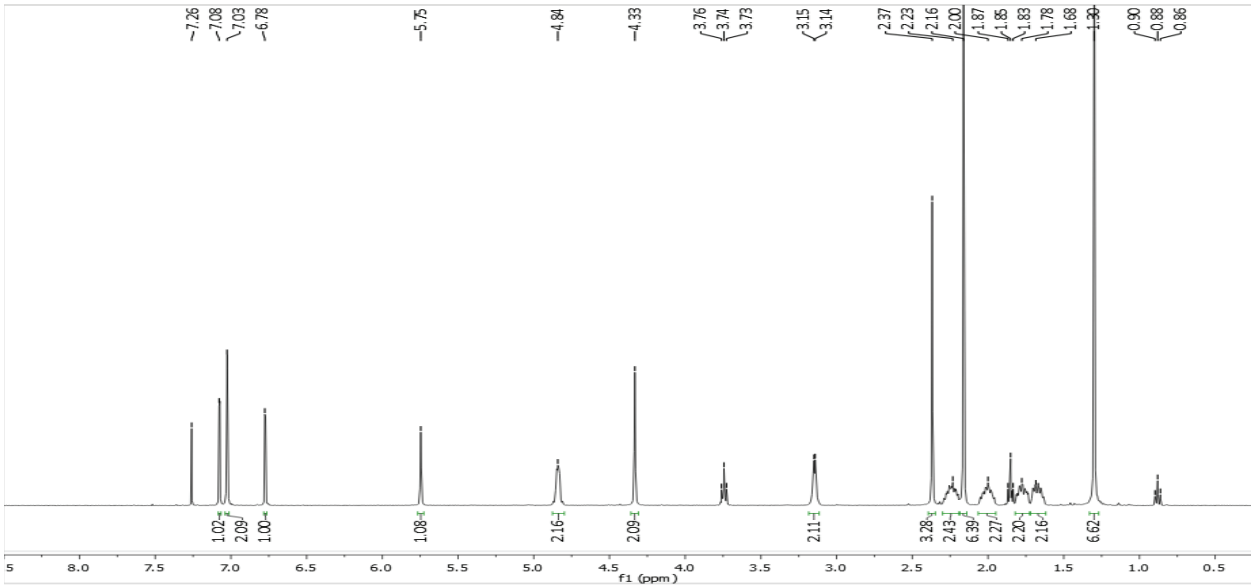

Figure S11. ^{13}C {^{1}H} NMR spectrum (293K, 101 MHz, $CDCl_3$) of complex **7**.

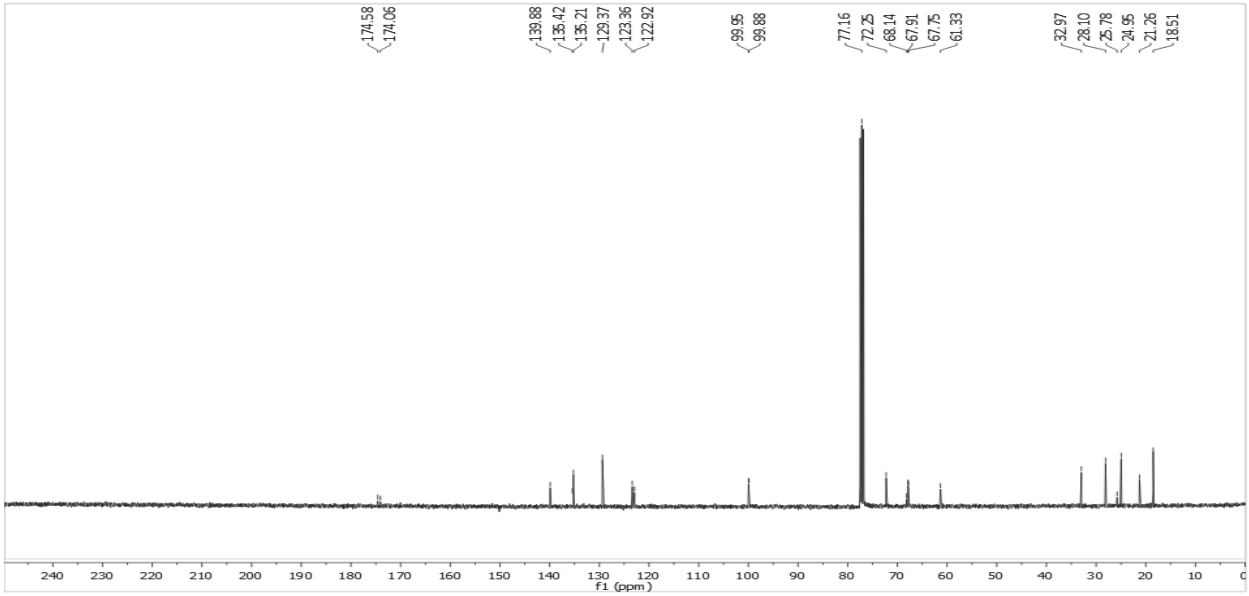

Figure S12. ^{19}F NMR spectrum (299K, 376 MHz, $CDCl_3$) of complex **7**.

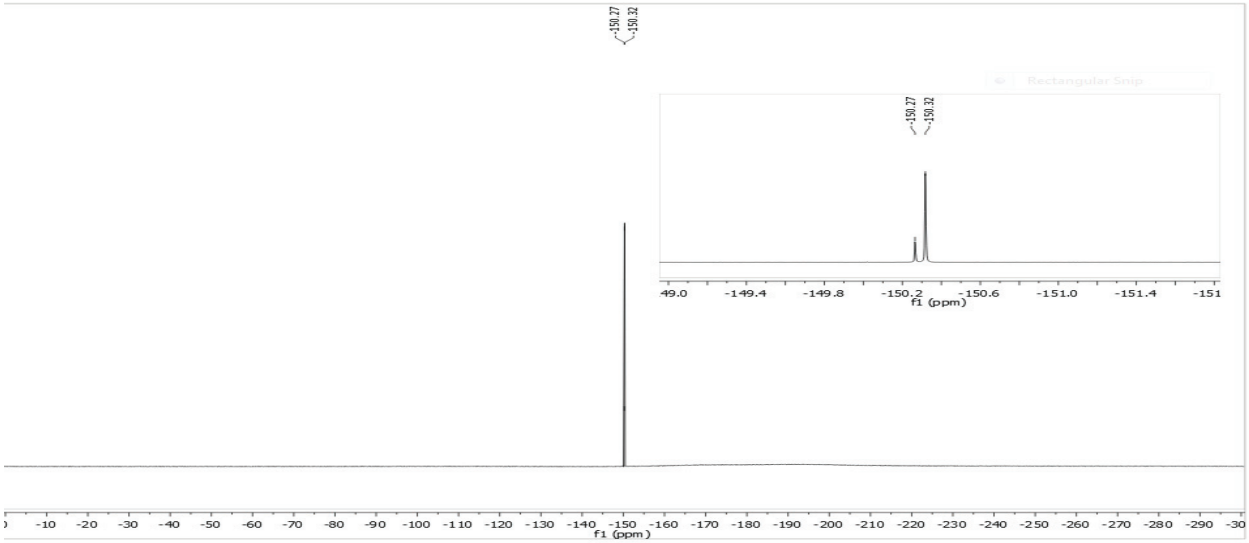

Figure S13. ^{11}B NMR spectrum (293K, 96 MHz, $CDCl_3$) of **7**.

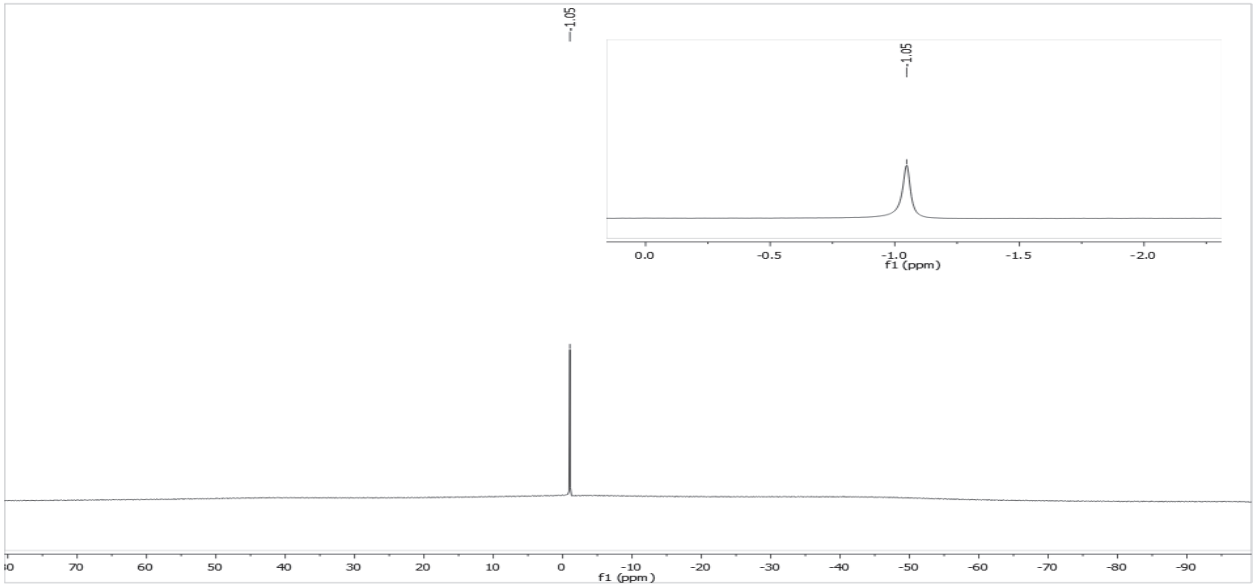

Figure S14. ^{1}H NMR spectrum (297K, 500 MHz, $CDCl_3$) of the complex **8.**

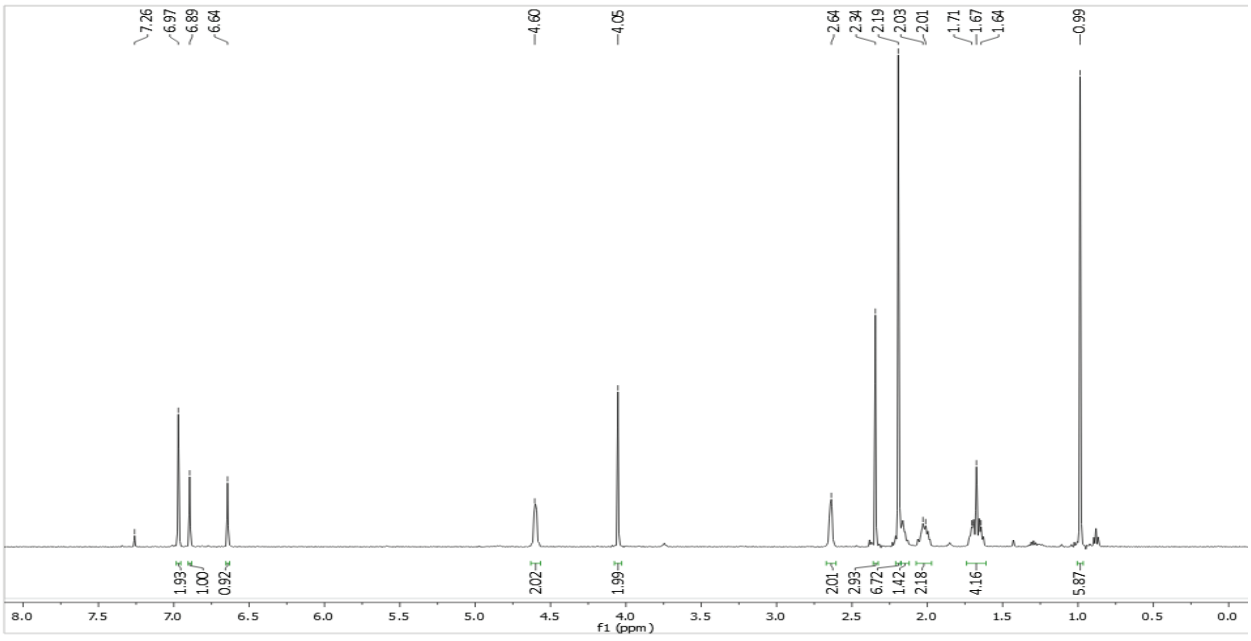

Figure S15. ^{13}C {^{1}H} NMR spectrum (297K, 125 MHz, $CDCl_3$) of the complex **8**.

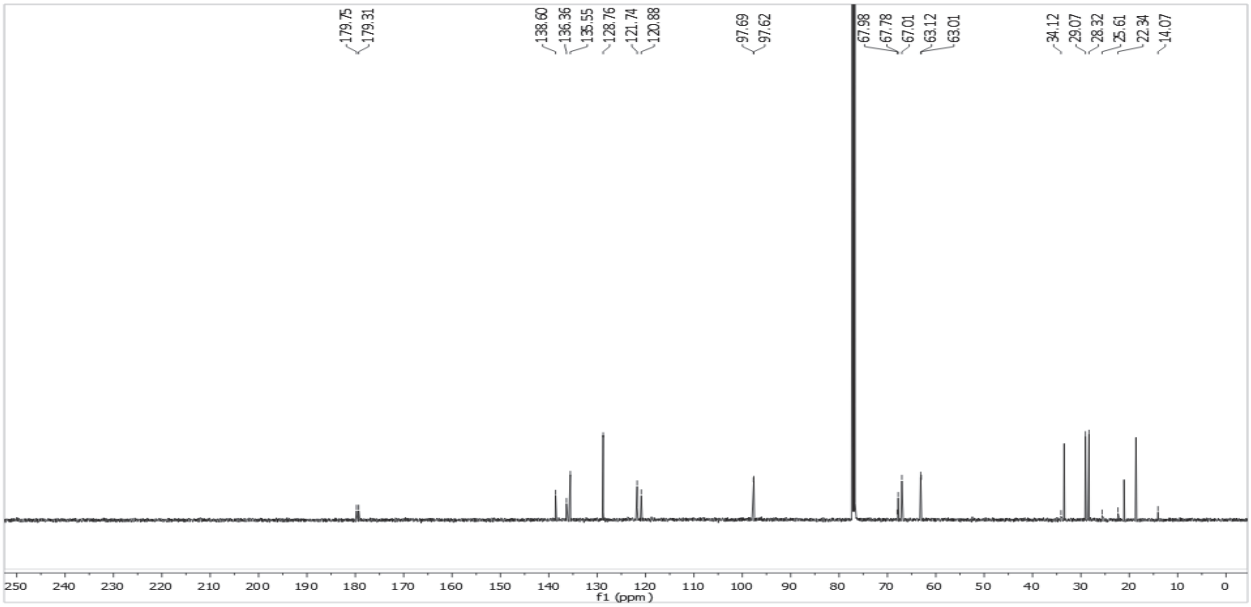

Figure S16. ^{1}H NMR comparison spectrum (296K, 300 MHz, THF-d_8) of the complex **5** vs complex **8+BF3.THF**.

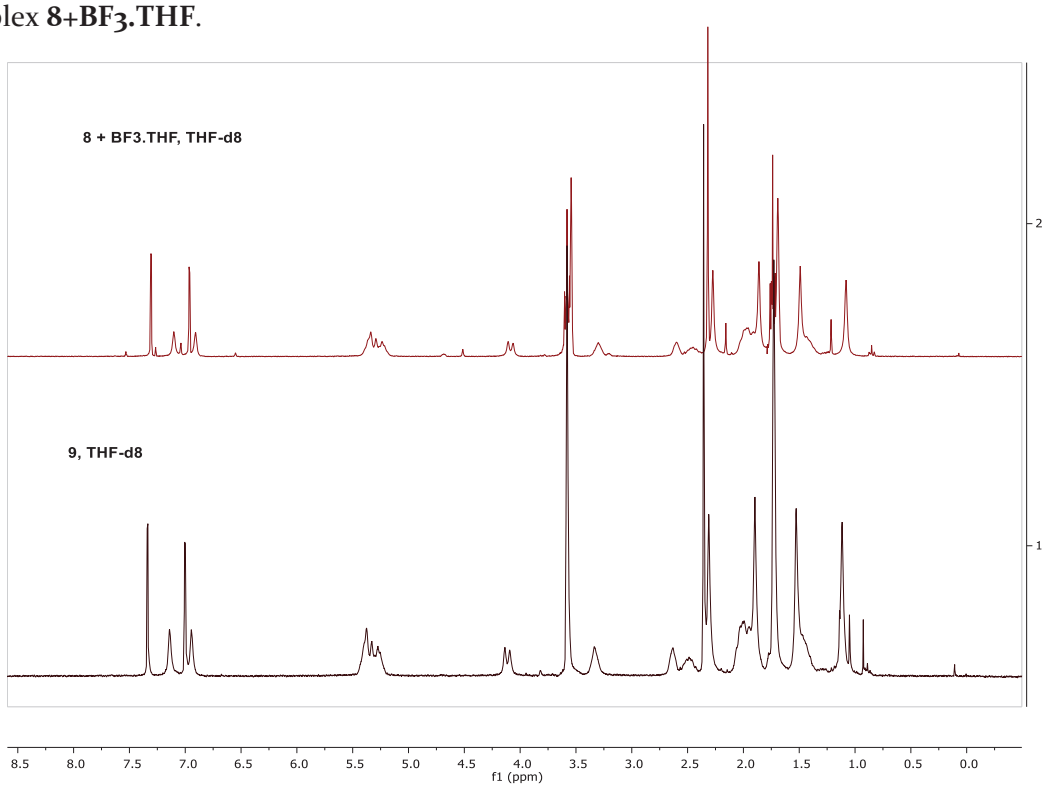

Figure S17. ^{1}H NMR spectrum (296K, 300 MHz, THF-d_8) of the complex **9**.

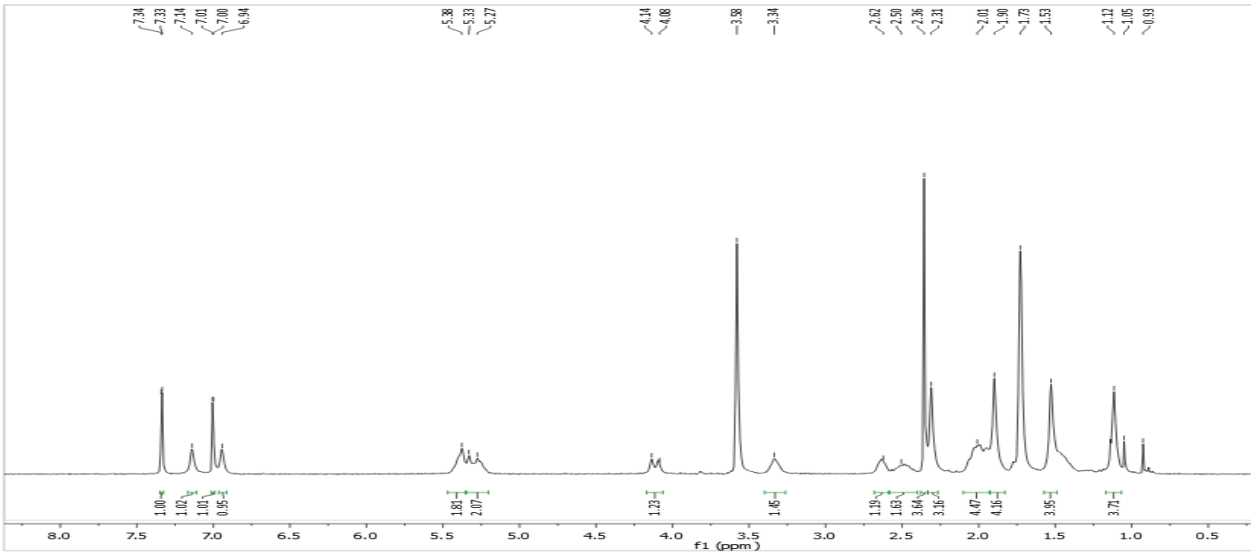

Figure S18. ^{13}C {^{1}H} NMR spectrum (297K, 125 MHz, THF-d_8) of the complex **9**.

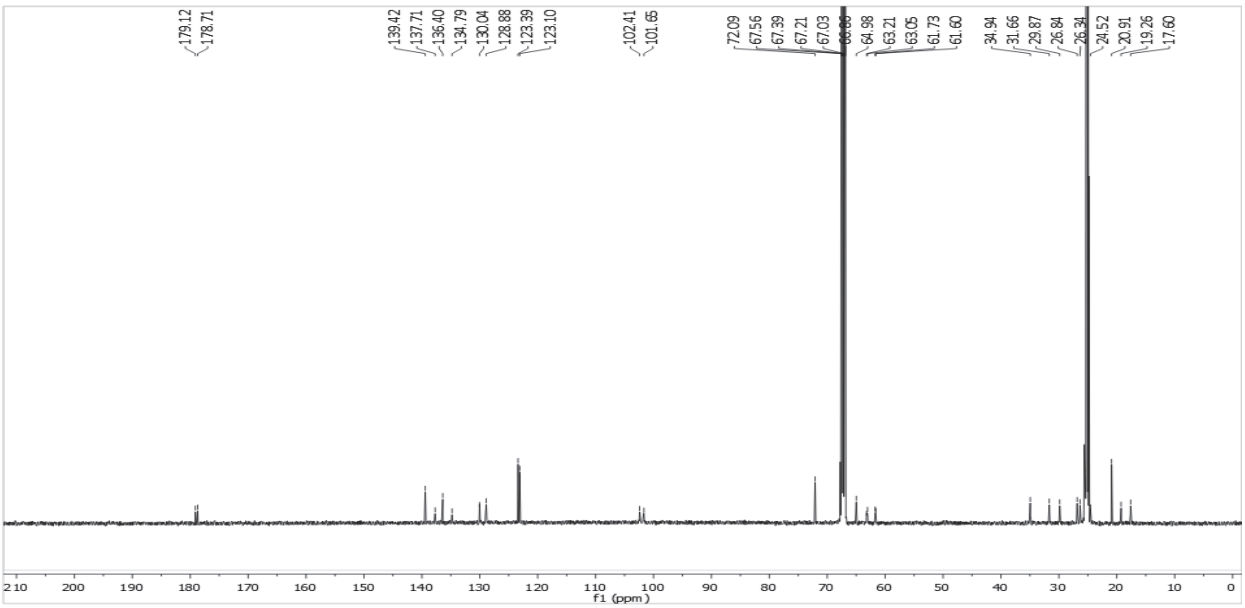

Figure S19. ^{19}F NMR spectrum (297K, 470 MHz, THF-d_8) of the complex **9**.

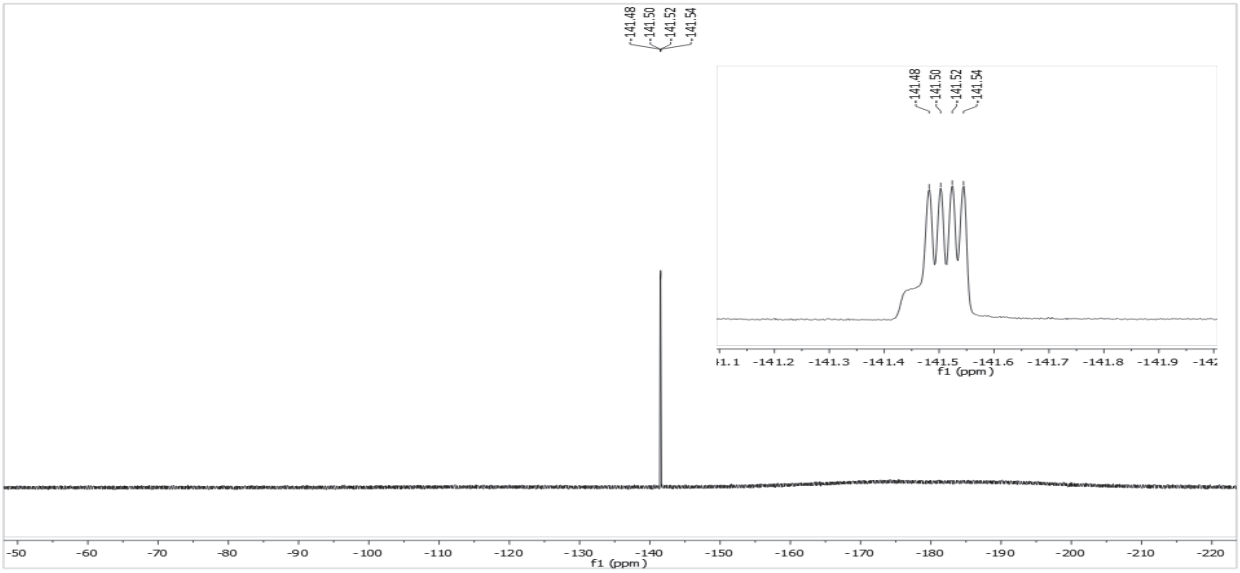

Figure S20. ^{11}B NMR spectrum (297K, 470 MHz, THF-d_8) of the complex **9**.

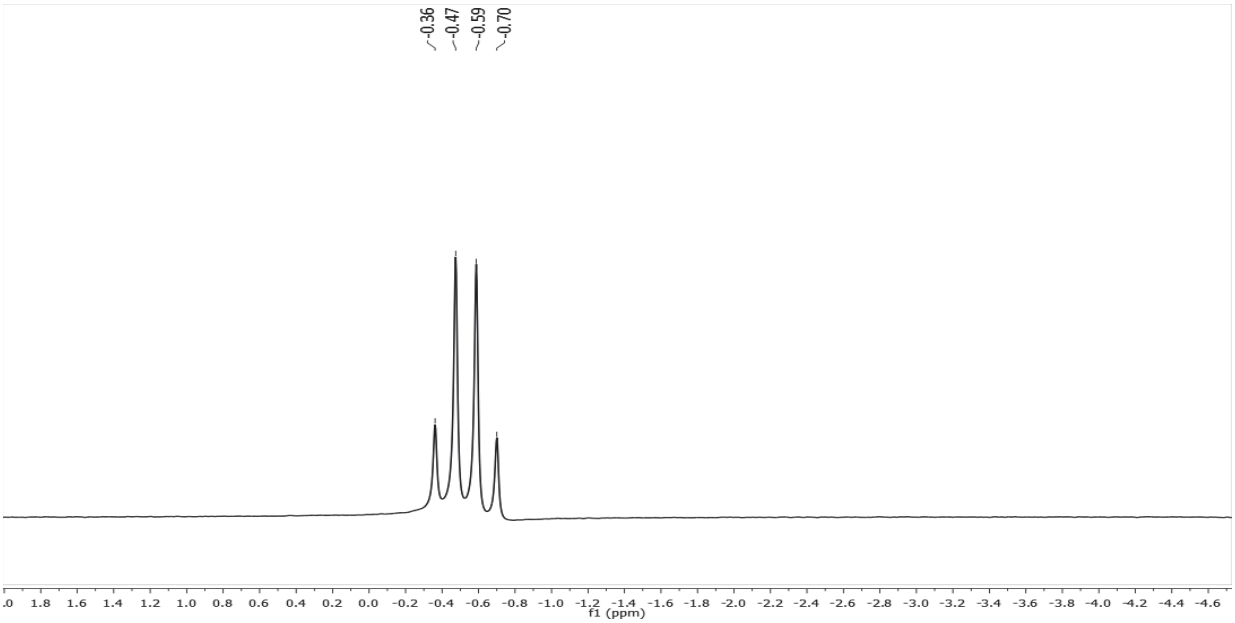

Figure S21. ^{19}F NMR spectrum (296K, 282 MHz, THF-d_8) of supernatant establishing the existence of Ta-F bond.

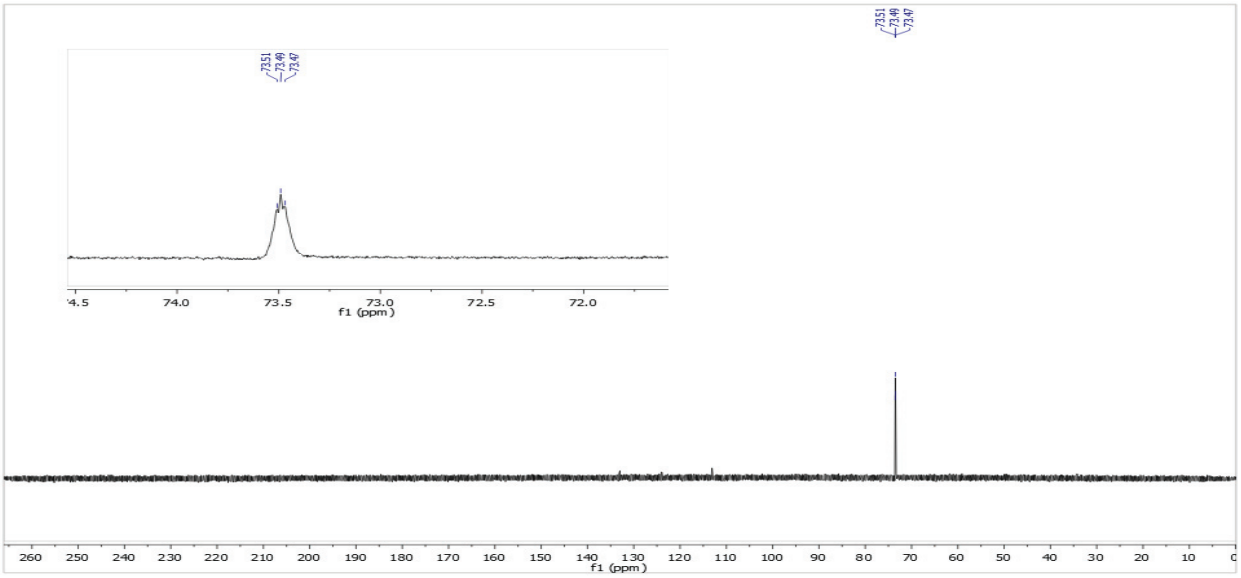

Figure S22: ^{1}H NMR spectrum (294K, 300 MHz, C_6D_6) of reaction mixture with Ta:[Rh(COD)Cl]2 = 1:0.5.

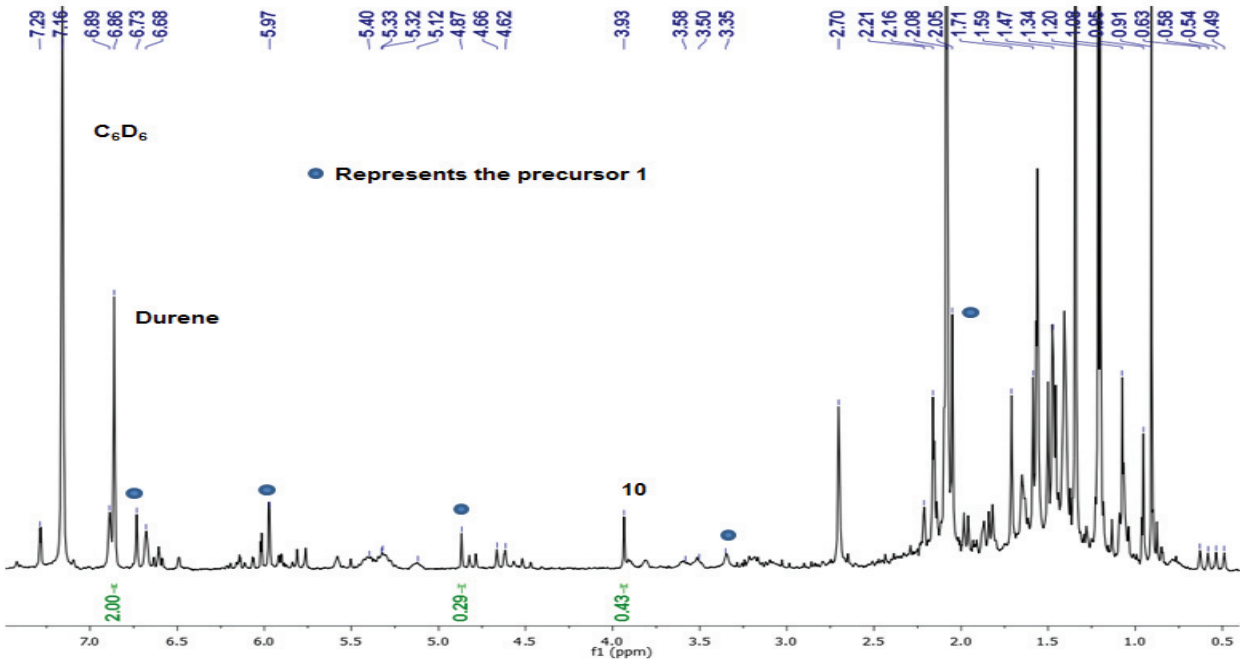

Figure S23: ^{1}H NMR spectrum (294K, 300 MHz, C_6D_6) of reaction mixture with Ta:[Rh(COD)Cl]2 = 1:1

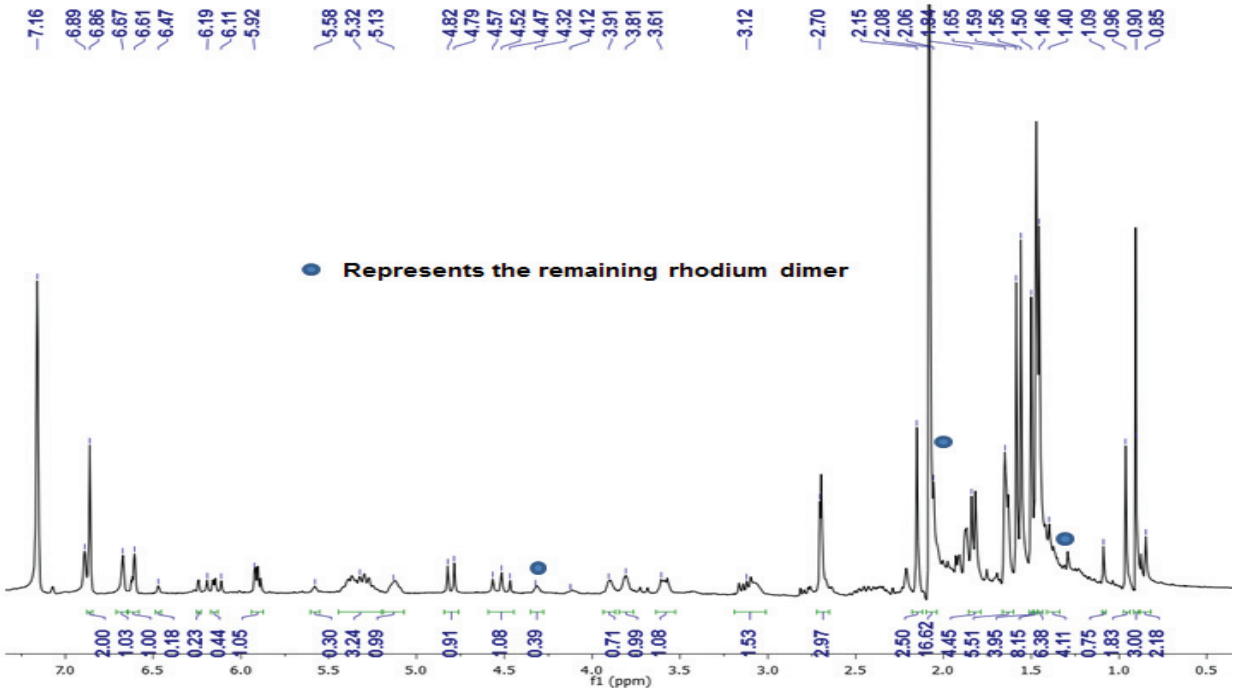

Figure S24: ^{1}H NMR spectrum (294K, 300 MHz, C_6D_6) of reaction mixture with Ta:[Rh(COD)Cl]2 = 1:0.75.

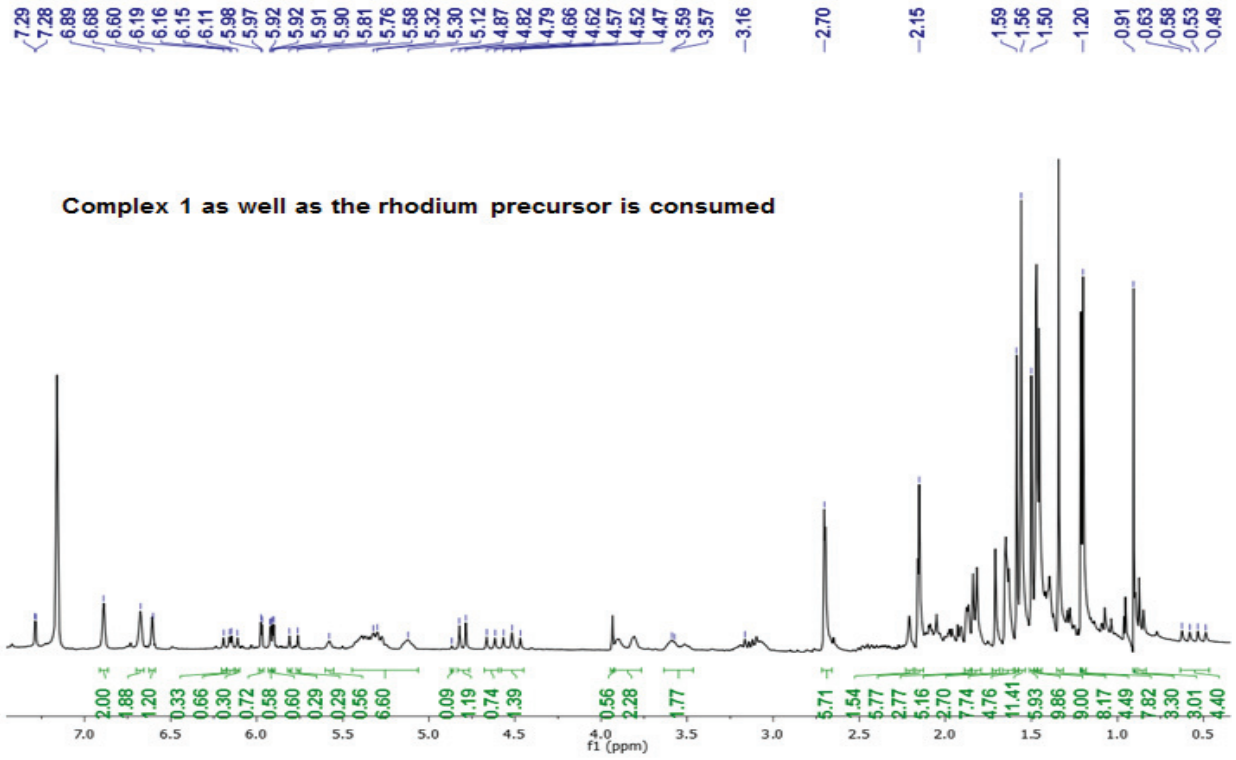

Figure S25. ^{1}H NMR spectrum of a 1:1 co-crystallized mixture of complexes **11** (.) and **12** (*) (500 MHz, C_6D_6, 296 K).

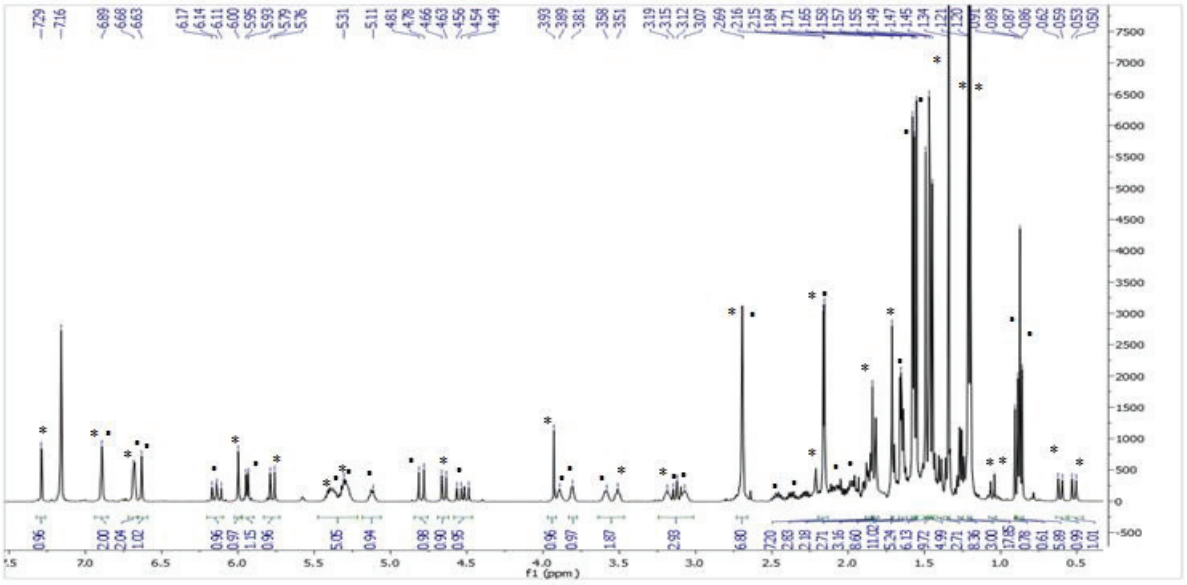

Figure S26. 13C {^{1}H} NMR spectrum (293K, 500 MHz, C_6D_6) of the mixture of complexes.

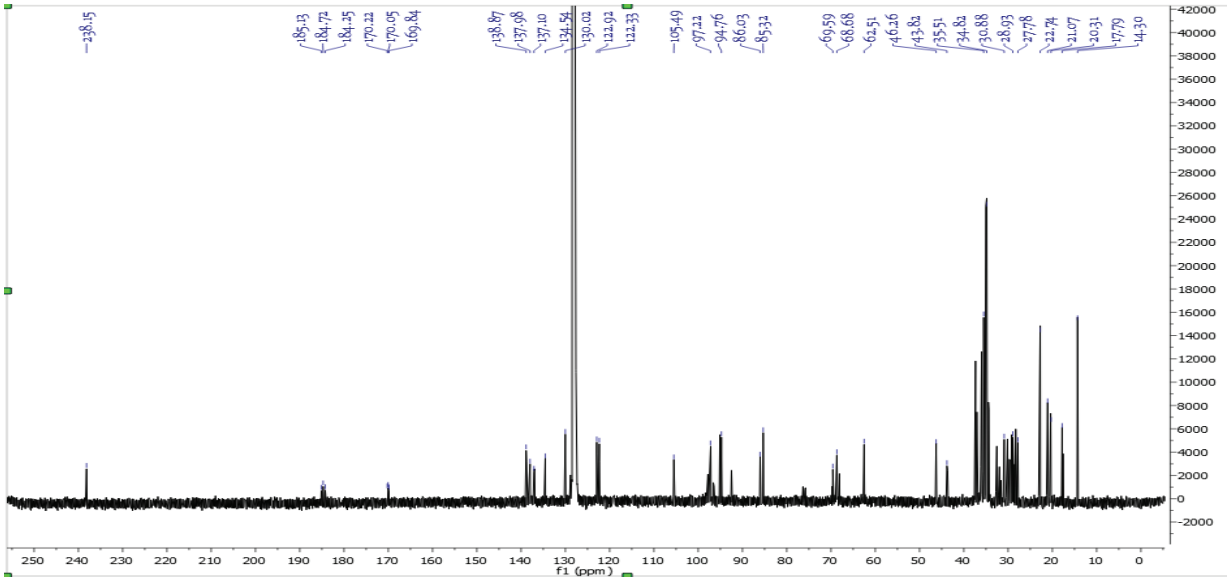

Figure S27. 13C {^{1}H}-1H HSQC NMR spectrum (296K, 500 MHz, C_6D_6) of mixture of complexes.

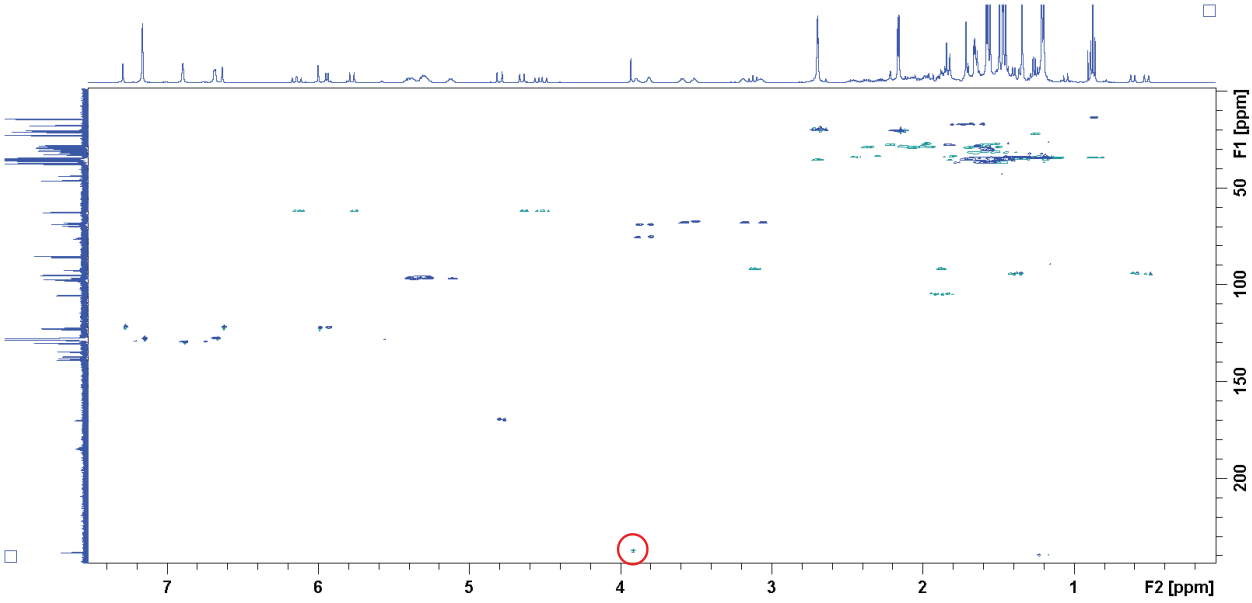

Figure S28. ^{1}H NMR spectrum (298K, 400 MHz, C_6D_6) of trimetallic complex **11**.

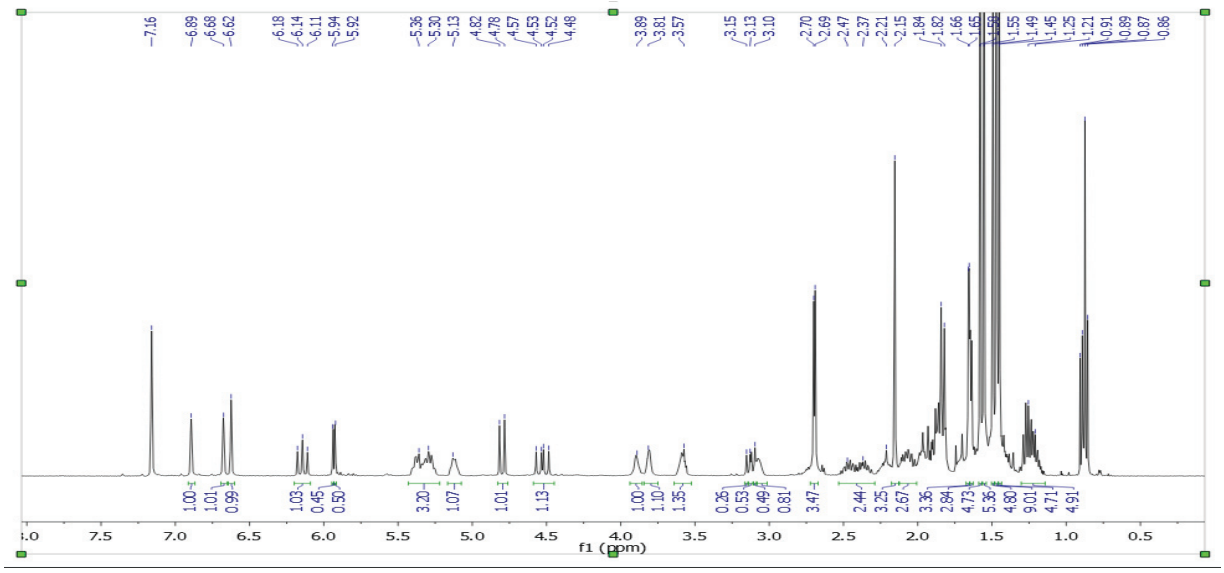

Figure S29. ^{13}C {^{1}H} NMR spectrum (296K, 100 MHz, C_6D_6) of trimetallic complex **11**.

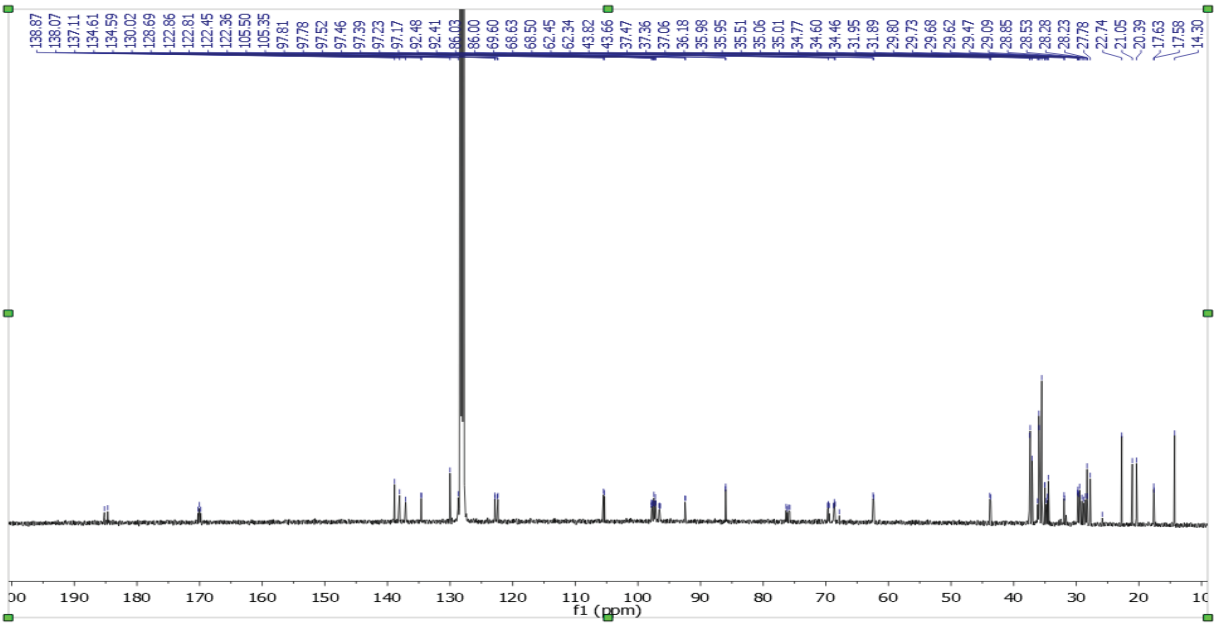

Figure S30. ^{13}C {^{1}H}-1H HSQC NMR spectrum (296K, 100 MHz, C_6D_6) of trimetallic complex **11**.

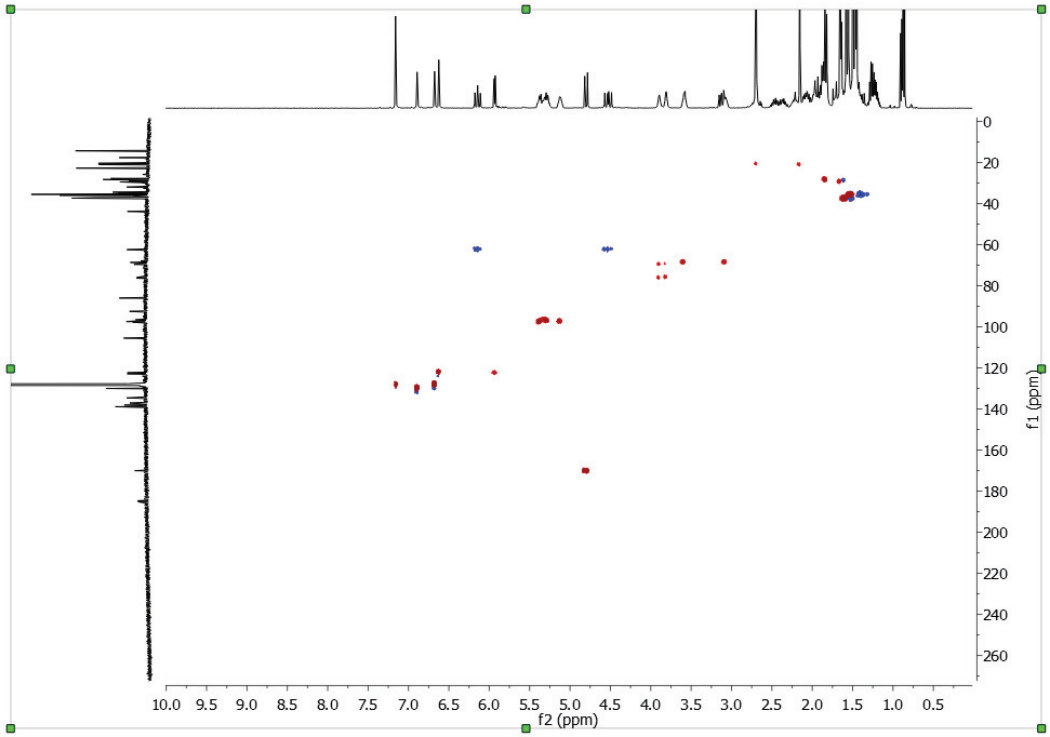

Figure S31: HRMS-ESI spectrum of the trimetallic complex **11.**

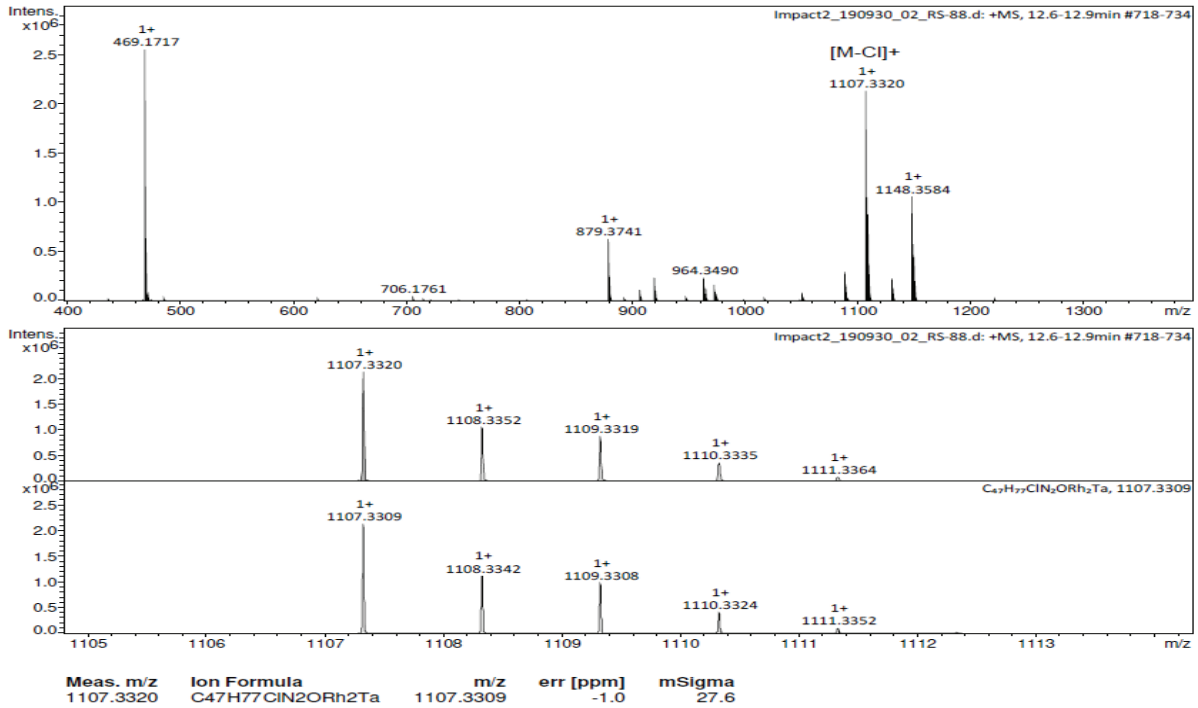

Figure S31: ^{1}H NMR spectrum (293K, 400 MHz, THF-d_8) of Ta(μ-L)(N^{t}Bu)(CH$_2$^{t}Bu)$_2$Rh(COD)(Cl) **13**.

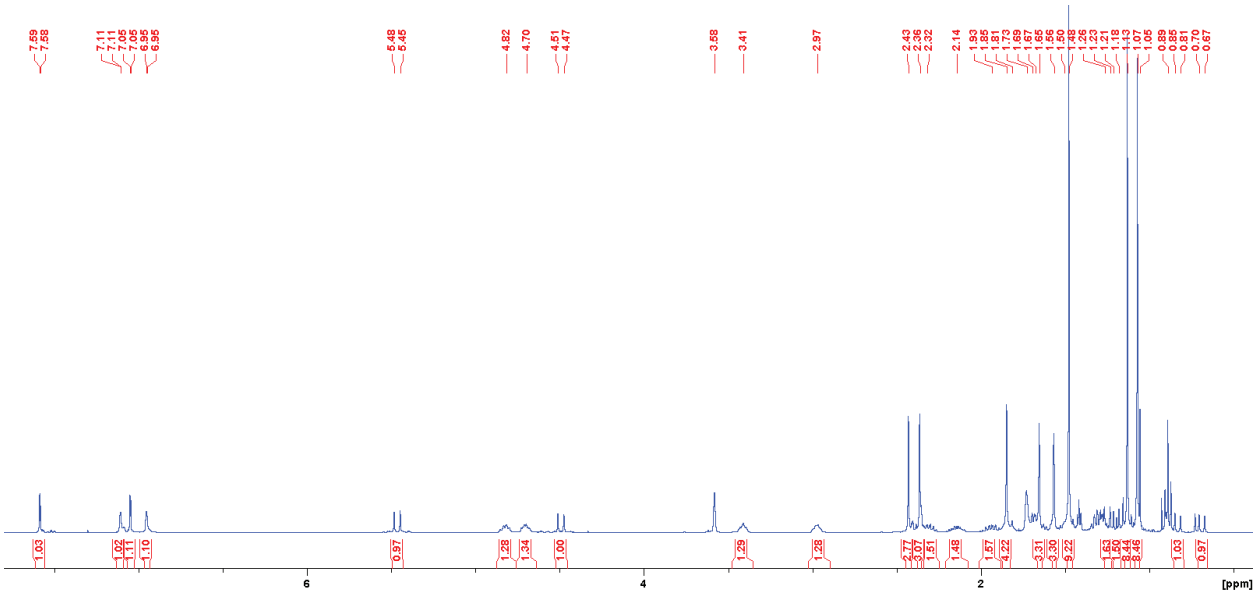

Figure S32: $^{13}C\{^{1}H\}$ NMR spectrum (293K, 101 MHz, THF-d_8) of Ta(μ-L)(N^{t}Bu)(CH$_2$^{t}Bu)$_2$Rh(COD)(Cl) **13**.

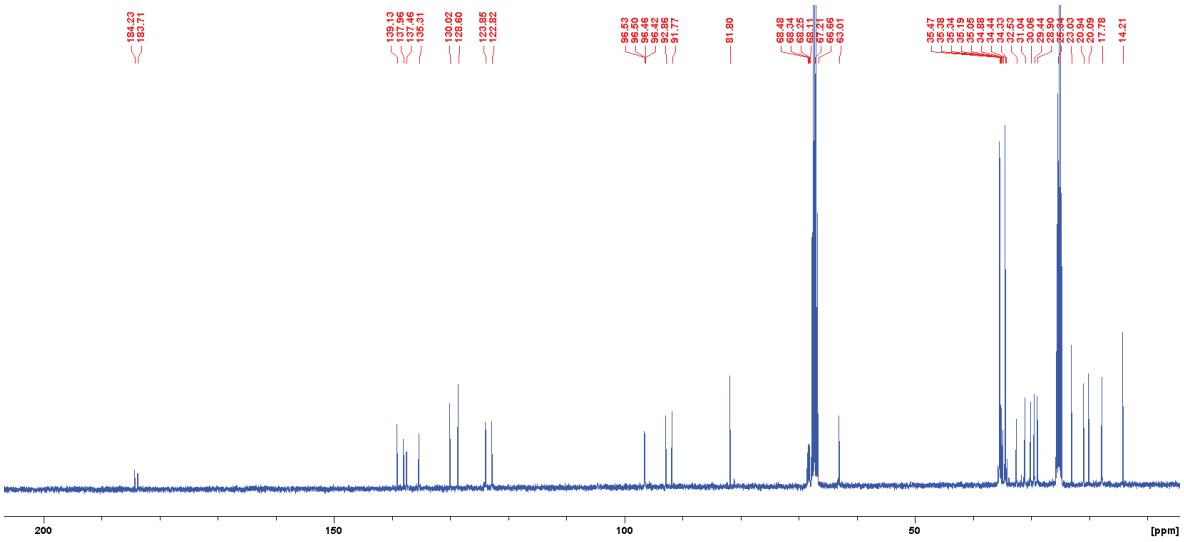

Figure S33: ^{1}H NMR monitoring of the reaction between Ta(=N^{t}Bu)(CH$_2$^{t}Bu)$_3$ (1 eq.) and Rh(HL)(COD)(Cl) **6** (1 eq.) with durene as internal standard (2 eq.) (293K, 300 MHz, C_6D_6), leading to the clean formation of Ta(μ-L)(N^{t}Bu)(CH$_2$^{t}Bu)$_2$Rh(COD)(Cl) **11** and neopentane.

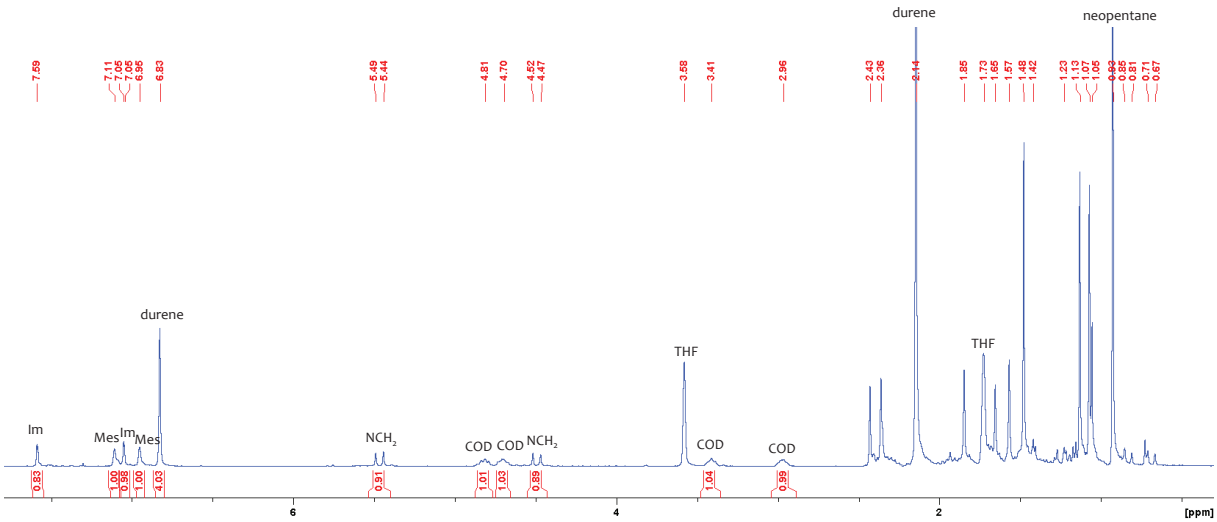

IR spectroscopic data

Figure S34. DRIFT (25°C, KBr solid solution under argon) spectrum for tantalum-NHC complex **3**.

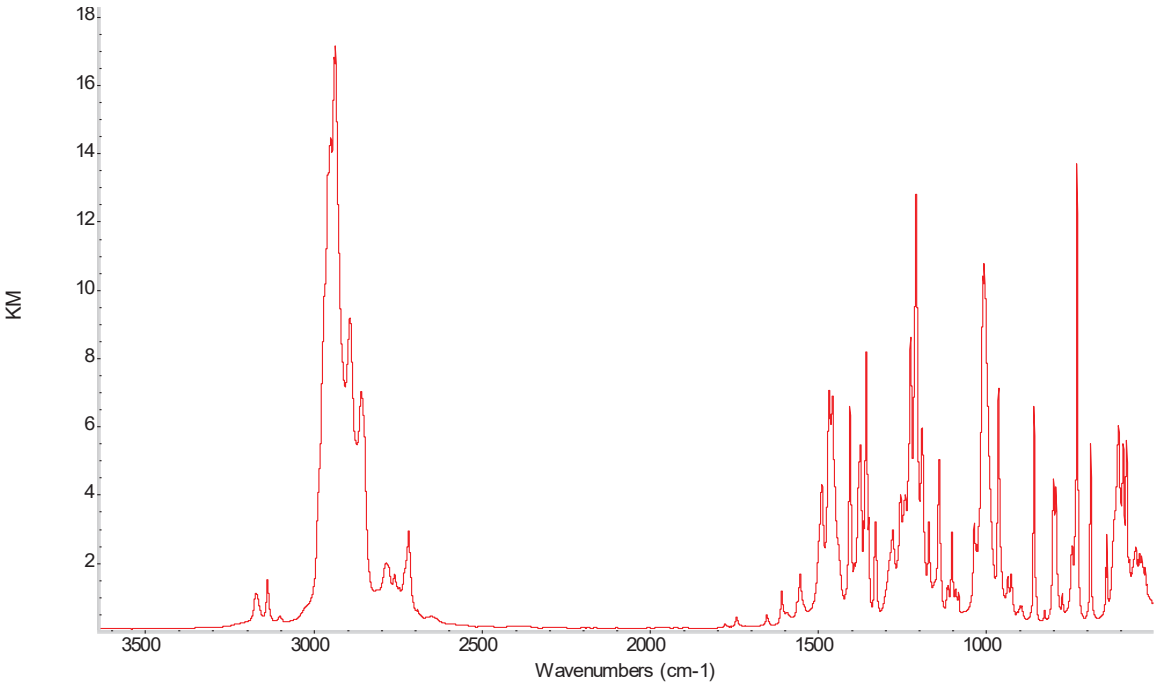

Figure S35. DRIFT (25°C, KBr solid solution under argon) spectrum for decomposed tantalum-NHC complex **4**.

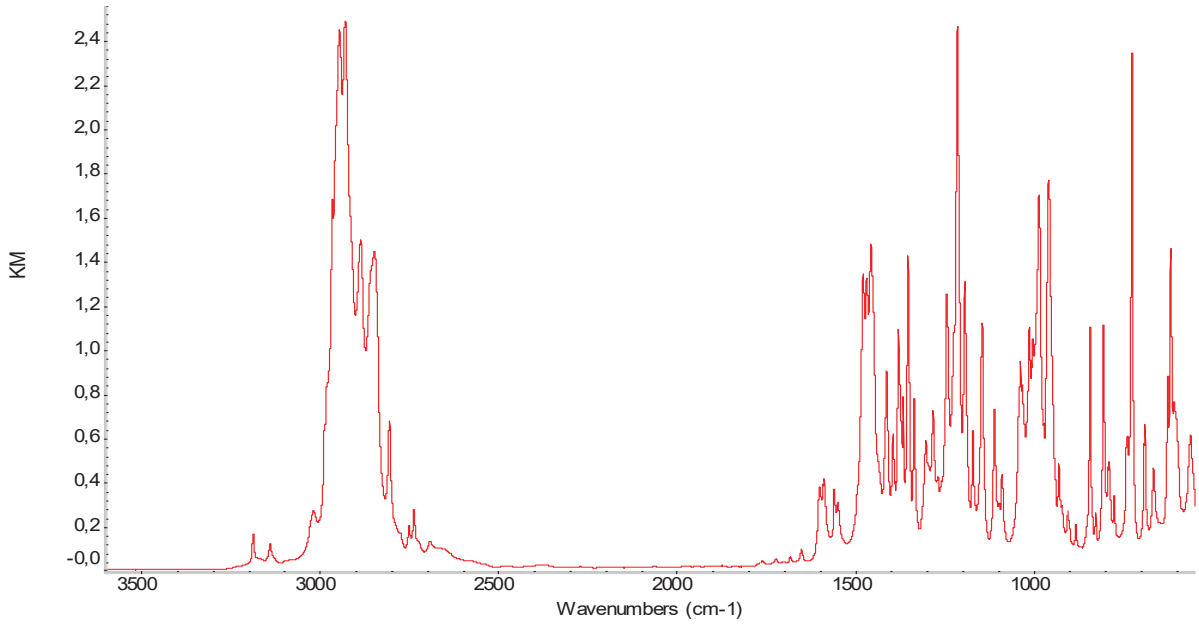

Figure S36: DRIFT (25°C, KBr solid solution under argon) spectrum for tantalum-imido alkylidene NHC complex **5**.

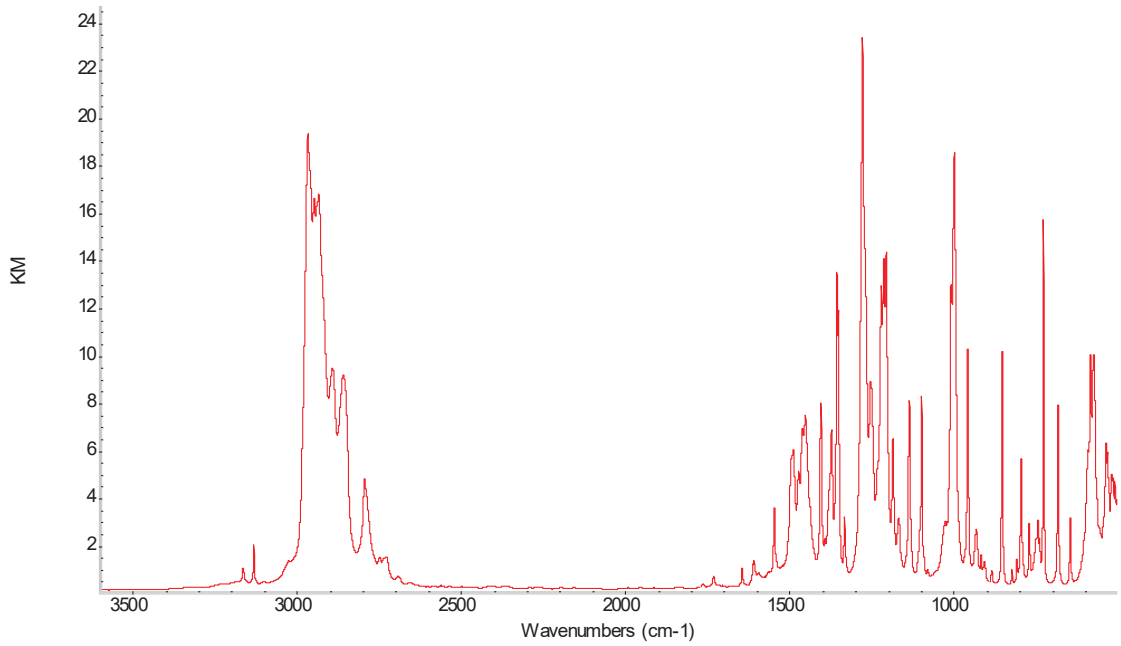

Figure S37. DRIFT (25°C, KBr solid solution under argon) spectrum for Rhodium-NHC complex **6**.

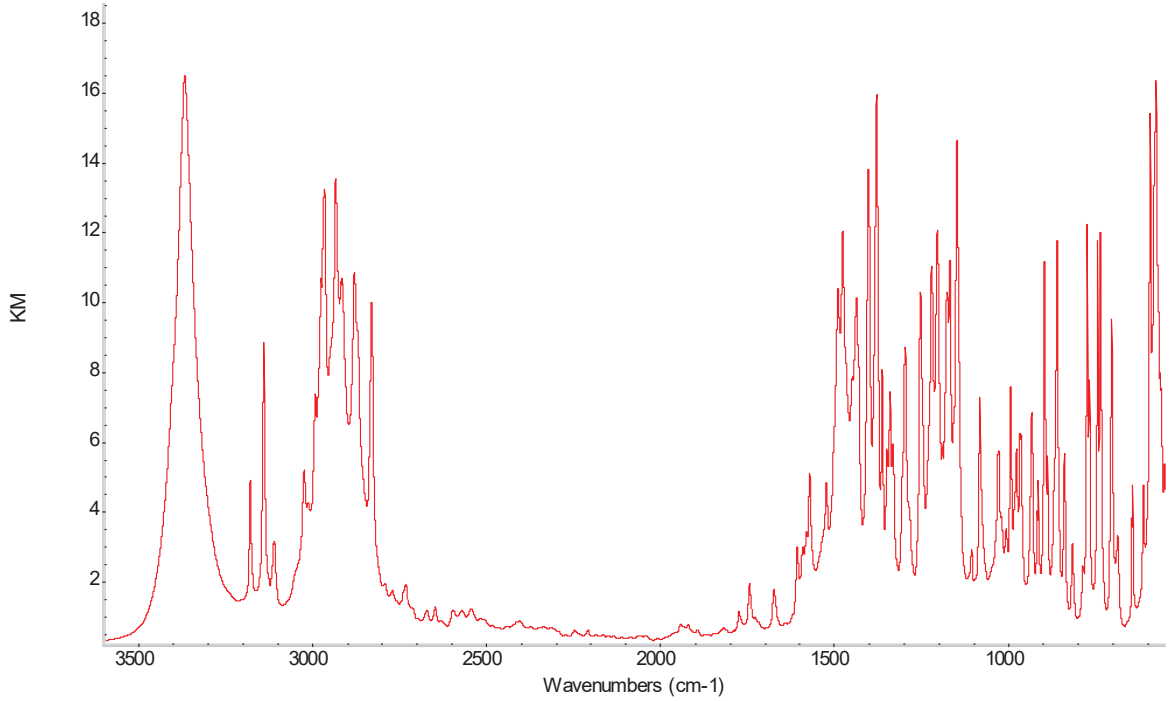

Figure S38. DRIFT (25°C, KBr solid solution under argon) spectrum for **7.**

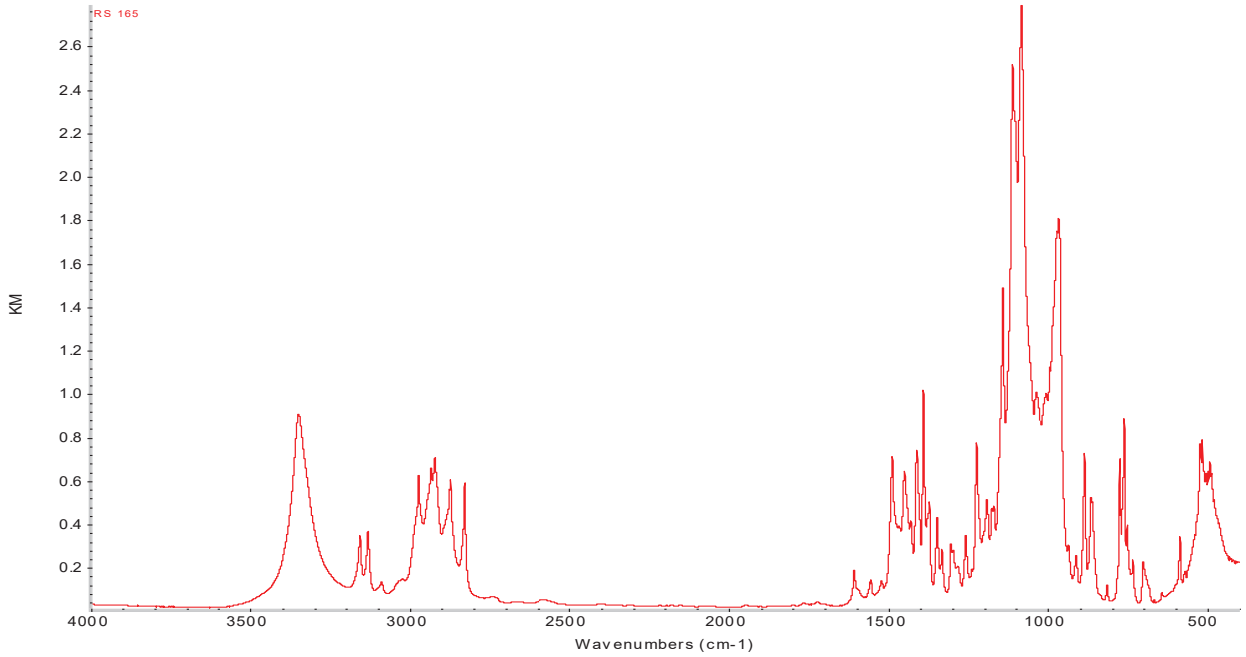

Figure S40. DRIFT (25°C, KBr solid solution under argon) spectrum for **8.**

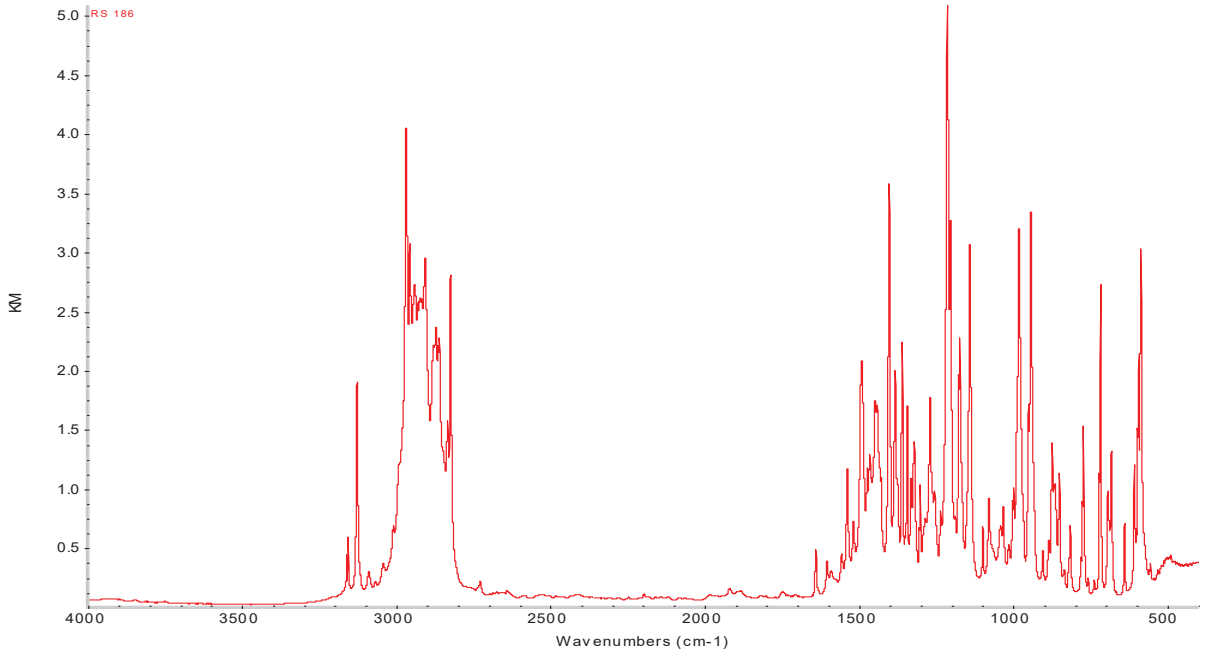

Figure S39. DRIFT (25°C, KBr solid solution under argon) spectrum for **9.**

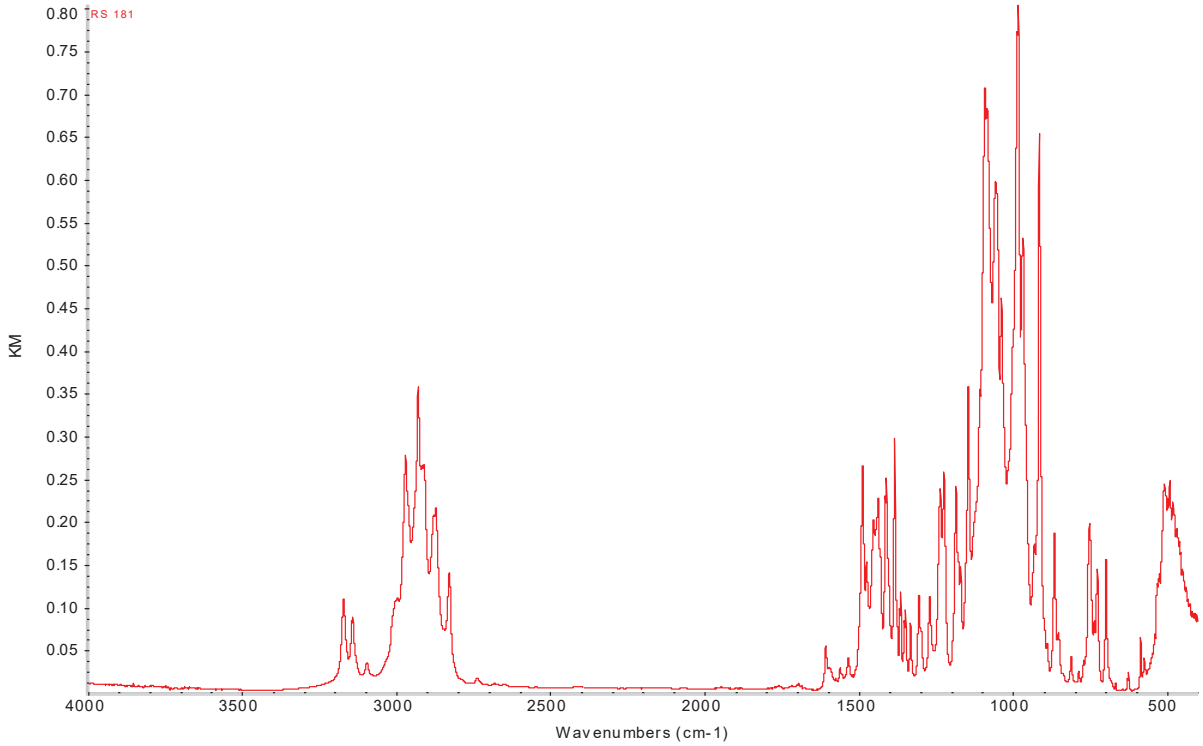

Figure S41. DRIFT (25°C, KBr solid solution under argon) spectrum for mixture of complexes.

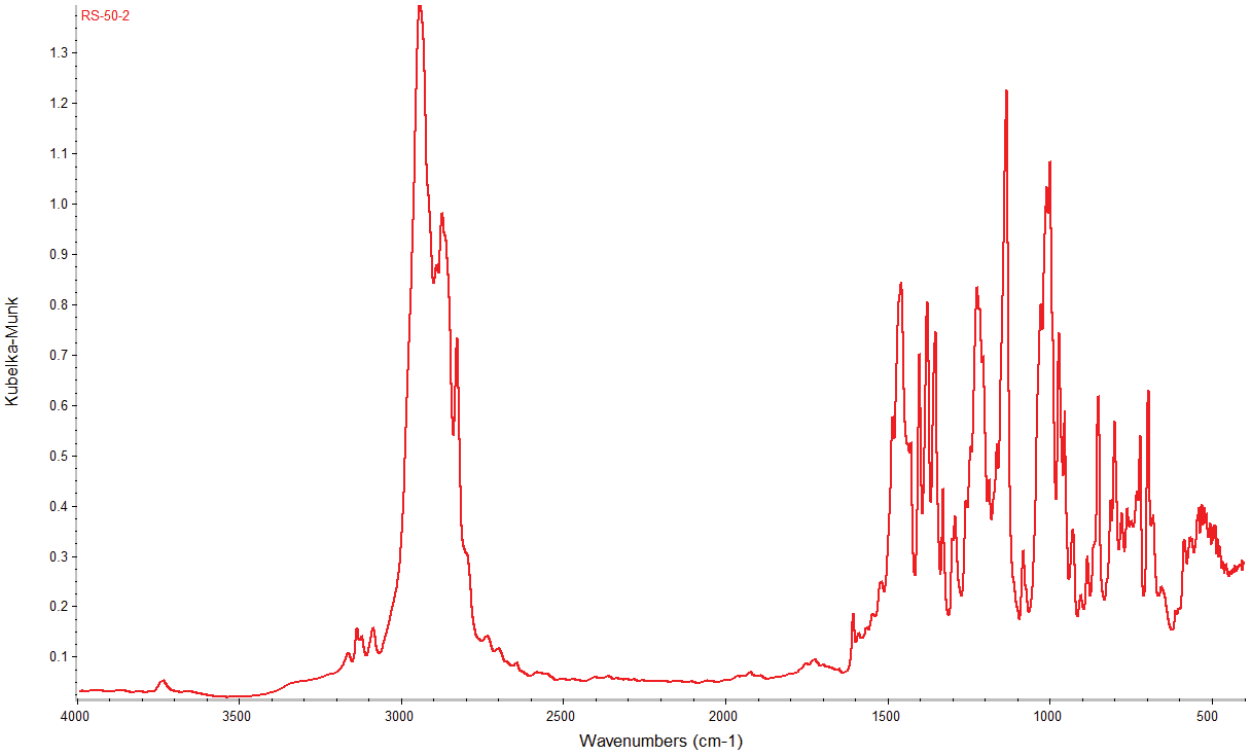

Figure S42. DRIFT (25°C, KBr solid solution under argon) spectrum for trimetallic complex **11**.

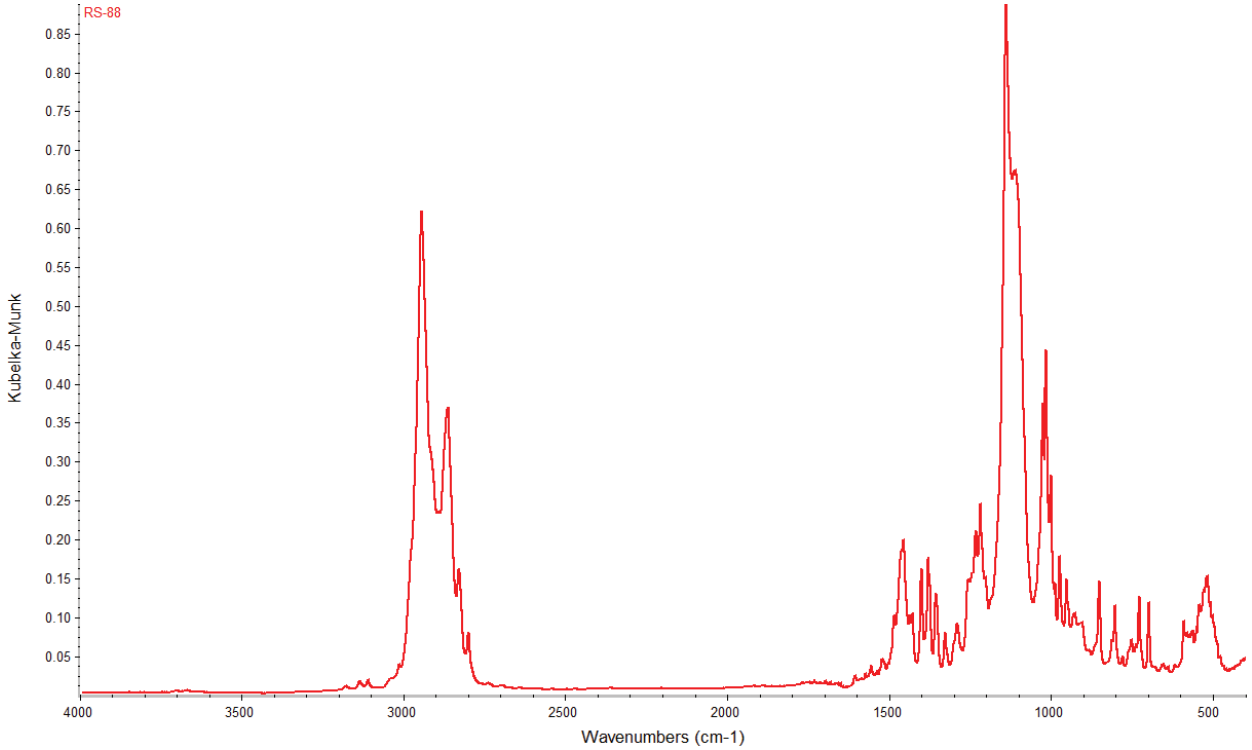

Figure S43: DRIFT (25°C, KBr solid solution under argon) spectrum for heterobimetallic complex **13**.

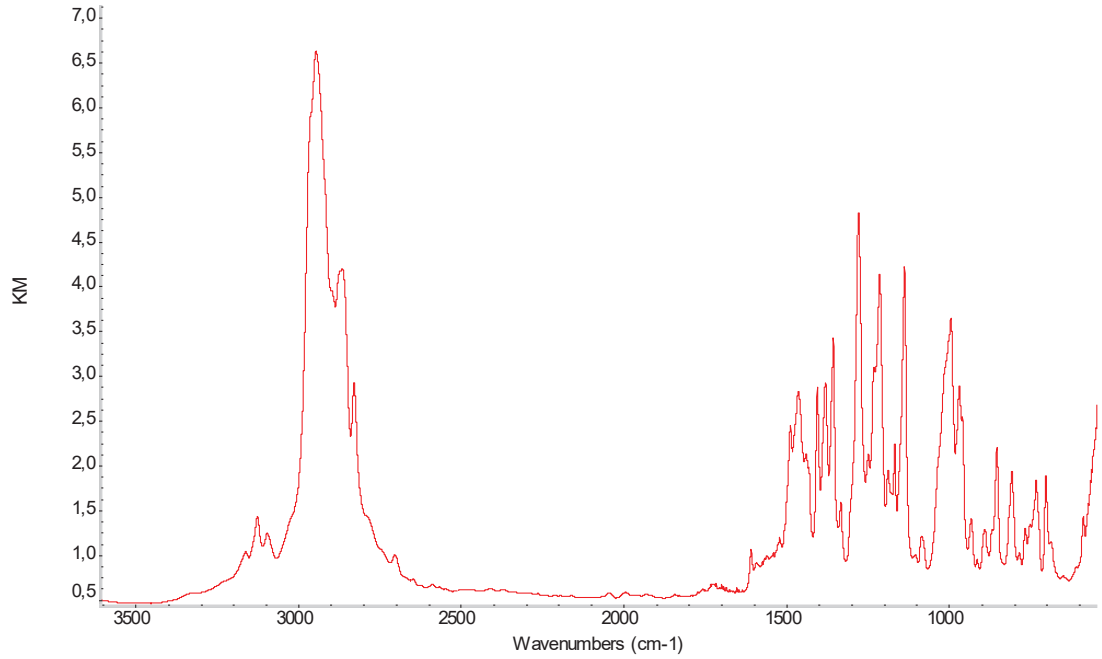

Crystallographic data for compounds

Compound	**3**	**4**	**[6]$_2$.(pentane)**	**7**
Formula	$C_{31}H_{53}N_2OTa$	C26H41N2OTa	$[C_{24}H_{34}ClN_2ORh]_2$, C_5H_{12}	$C_{24}H_{34}N_2ORh{\cdot}BF_4$
cryst syst	Monoclinic	Triclinic	Monoclinic	Monoclinic
space group	$P2_1/n$	P-1	$P2_1/n$	C2/c
volume (Å^3)	3218.9(3)	1297.2(4)	2596.8(5)	5787(3)
a (Å)	11.4036(6)	8.6557(7)	9.6069(10)	41.765(7)
b (Å)	17.0630(10)	10.8781(7)	18.1953(18)	7.8159(6)
c (Å)	16.5497(10)	15.8244(11)	15.2750(19)	24.836(4)
α (deg)	90	71.346(6)	90	90
β (deg)	91.630(6)	75.611(7)	103.453(11)	134.45(3)
γ (deg)	90	68.301(7)	90	90
Z	4	2	2	8
formula weight (g/mol)	650.72	578.57	1081.93	556.25
density (g cm^{-3})	1.343	1.48	1.384	1.397
absorption coefficient (mm^{-1})	3.437	4.255	0.781	0.630
F(000)	1336	1226	1132	2288
temp (K)	150.0(1)	150.0(1)	150.0(1)	150.0(1)
total no. reflections	105474	30768	81467	61738
unique reflections [R(int)]	22101 [0.085]	6555 [0.068]	81467 [0.033]	3393 [0.056]
GoF	1.040	0.9970	1.032	1.0326

Compound	**8**	**9**	**12**	**13**
Formula	$C_{24}H_{33}N_2ORh$	$C_{24}H_{33}BF_3N_2ORh$	C_{39} H_{65} Cl_1 N_2 O_1 Rh_1 Ta_1	$C_{38}H_{64}ClN_3ORh$ Ta
cryst syst	Trigonal	Triclinic	monoclinic	Triclinic
space group	*R*3	*P*-1	$P2_1/n$	P-1
volume (Å^3)	9813.7 (19)	1192.33(17)	4129.9(5)	2207.6(4)
a (Å)	32.883 (3)	7.6521(6)	10.0011(7)	11.1252(11)
b (Å)	32.883 (3)	12.0807(9)	15.523(1)	13.4090(14)
c (Å)	10.4799 (11)	14.3701(10)	26.6754(19)	15.4178(14)
α (deg)	120	65.159(7)	90	98.636(8)
β (deg)	120	82.202(6)	94.253(6)	100.883(8)
γ (deg)	120	83.726(7)	90	96.769(8)
Z	18	2	4	2
formula weight (g/mol)	468.43	536.24	897.24	1541.41
density (g cm^{-3})	1.364	1.494	1.443	1.351
absorption coefficient (mm^{-1})	0.80	0.758	3.141	2.939
F(000)	4392	552	820	912
temp (K)	100.0(1)	100.01(10)	150.0(1)	150.0(1)
total no. reflections	26484	42172	56886	69860
unique reflections [R(int)]	22799 [0.062]	6468 [0.0792]	10862 [0.097]	6468 [0.028]
GoF	1.026	1.125	1.0076	1.082

APPENDIX

We also wanted to explore the catalytic activity of these monometallic rhodium complexes. Complex **7**, **8** and **9** were used as catalysts to compare their catalytic properties for alkene hydrosilylation. For this purpose, 0.45 mmol each of the 3,3-dimethylbut-1-ene alkene and MD'M Silane were taken and 1 mol% of the all the catalysts were used in a NMR scale reaction. (**See scheme below**)

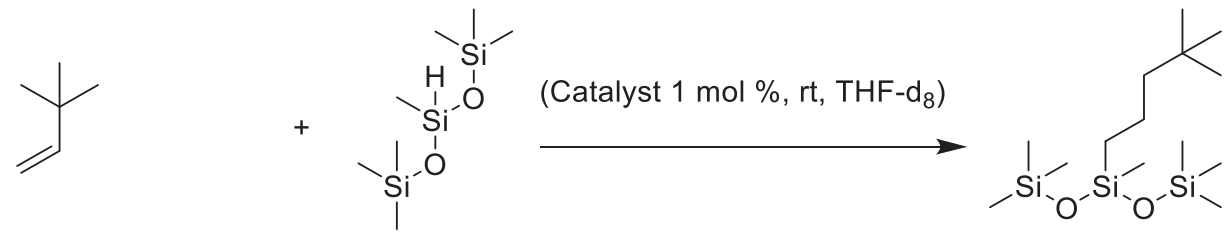

(0.45 mmol) (0.45 mmol)

S.No.	Catalyst	Reaction time (t/hr) for 100% conversion
1	7	5.0 hr
2	8	0.25 hr
3	9	40 hr
4	6	20 hr @50 °C

The results show that the complex **8** has highest reactivity among them for the hydrosilylation reaction. The optimisation of the catalytic reaction parameters were done to achieve the optimum reaction conditions for maximum catalytic activity using catalyst 10. The first step was to optimize the catalytic loading for the hydrosilylation reaction. Hence, two NMR scale reactions were set up using 0.1 and 0.01 mol% of the catalyst respectively. 3,3-dimethylbut-1-ene alkene and MD'M as Silane was used to optimize the effective catalyst loading (**as scheme above**). The reaction was performed at room temperature in THF-d_8. The progress of the reaction was monitored by ^{1}H NMR using Durene as internal; standard. The kinetic profile of

the reaction is shown below. We can observe maximum conversion (94%) of the silane to the hydrosilylated product within 6.5 hr with 0.1 mol% of the catalytic loading. After that there is a plateau in the reaction profile suggesting no further progress of the reaction. Expectedly the kinetic profile with 0.01 mol% lies below against that of 0.1 mol% loading line. It takes 49 hr with 0.01 mol% catalytic loading to reach maximum conversion of 94%. Then further a plateau is observed in the reaction profile as well.

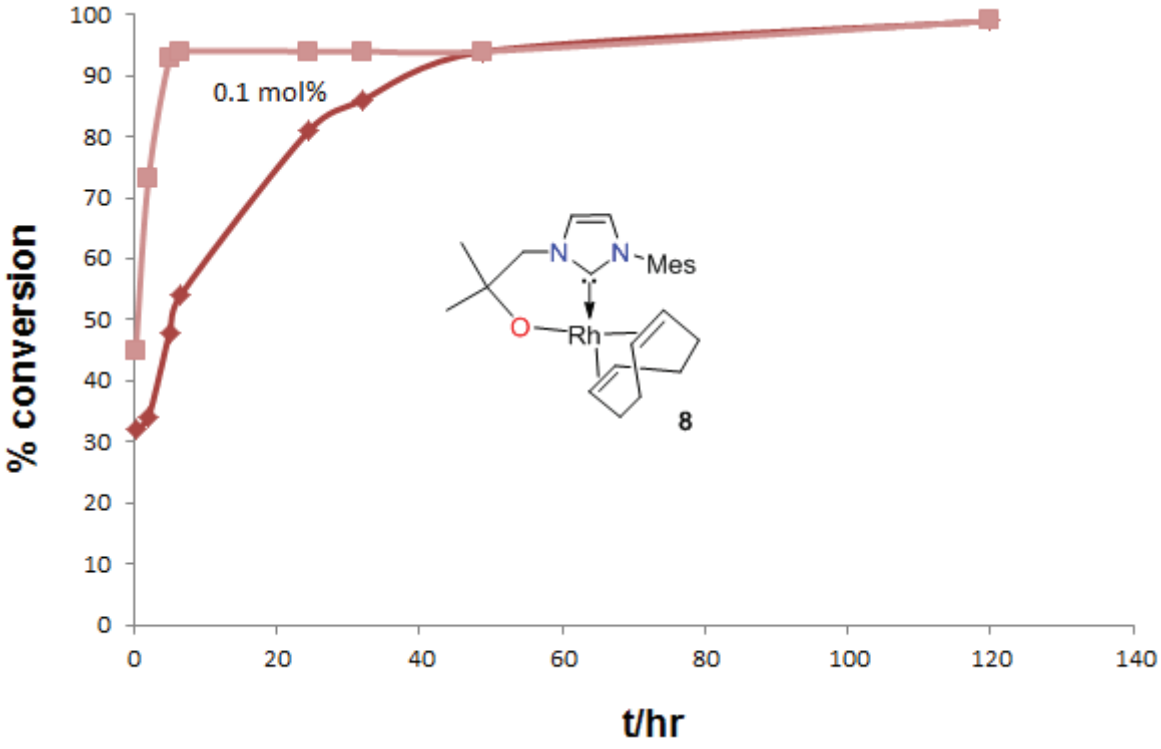

Figure: The kinetic profile of the reaction with 0.1 and 0.01 mol% of catalytic loading for the hydrosilylation of 3,3-dimethylbut-1-ene at room temperature. The reaction is followed by ^{1}H NMR.

Catalytic screening:

With the optimisation of catalytic loading we performed preliminary screening on variety of alkenes for catalytic hydrosilylation. The table below represents the preliminary results:

S.No.	silane	alkene	Time	Results
1	MD'M 1eq, 0.1 mol% catalyst loading (Unless specified)	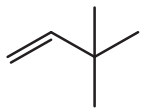	NMR at t=0, t=3h, t=5h	Reaction over in 5 hr Reaction over in 24 hr (0.01 mol% cat)
2		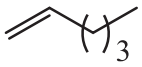	NMR at t=0, t=3h, t=5h, t=24 h	Reaction over in 24 hr
3		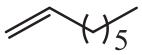		Reaction over in 15 minutes (***1 mol% catalyst loading***)
4		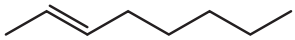	Heating at 50°C	Silane disappears after heating, no reaction
5		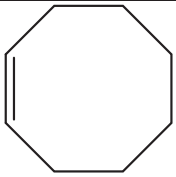	Heated at 50°C for 19 hr	No reaction
6		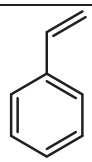	Heated at 55°C for 19 hr	Starting material consumed completely, reaction works

7		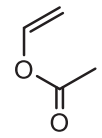	5 hr, rt	Reaction is over in 5 hr ***(1 mol% catalyst loading)***
8		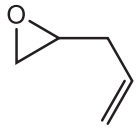	24 hr, rt	Reaction over in 24 hr ***(1 mol % catalyst loading)***

APPENDIX 3: Supporting information on chapter 4

Figure S1: ^{1}H NMR spectrum of the POSS-OH [(c- $C_5H_9)_7Si_7O_{12}$-SiOH] (300 MHz, C_6D_6, 297 K).

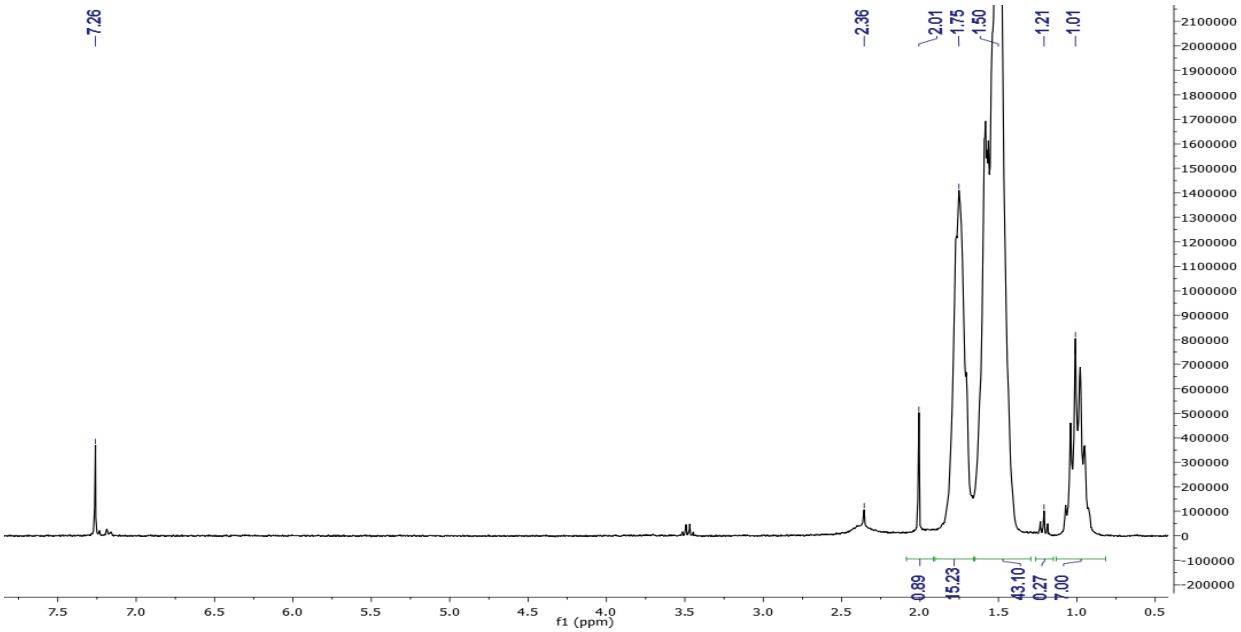

Figure S2: ^{13}C NMR spectrum of the POSS-OH [(c- $C_5H_9)_7Si_7O_{12}$-SiOH] (75 MHz, C_6D_6, 298 K).

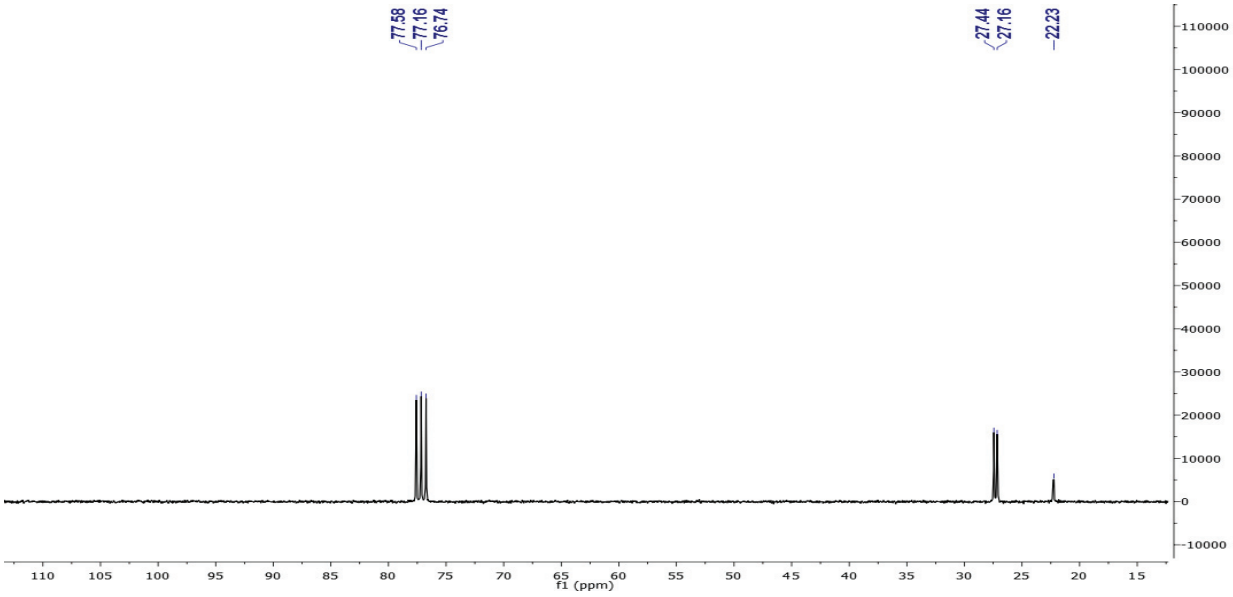

Figure S3: ^{1}H NMR spectrum of the POSS tantalum complex **15** [(c- $C_5H_9)_7Si_7O_{12}$-SiO-Ta(CH^tBu)($CH_2{}^tBu)_2$] (300 MHz, C_6D_6, 296 K)

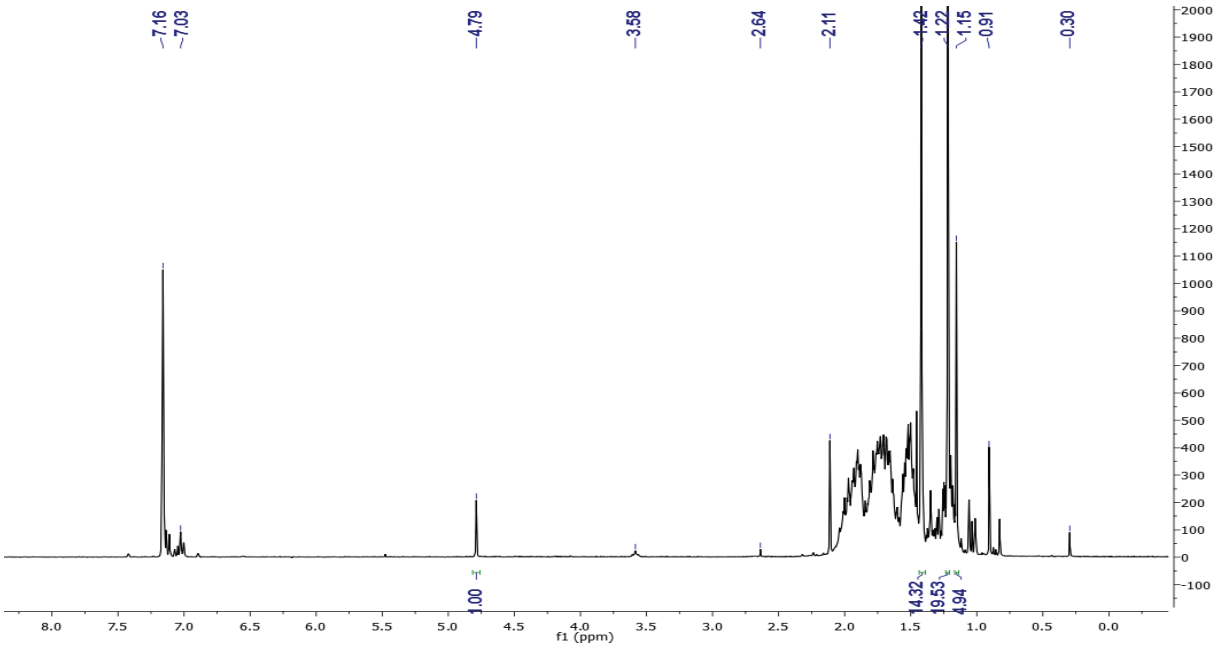

Figure S4: ^{1}H NMR spectrum of the POSS tantalum-NHC complex **16** [(c- $C_5H_9)_7Si_7O_{12}$-SiO-TaNHC] (300 MHz, C_6D_6, 293 K)

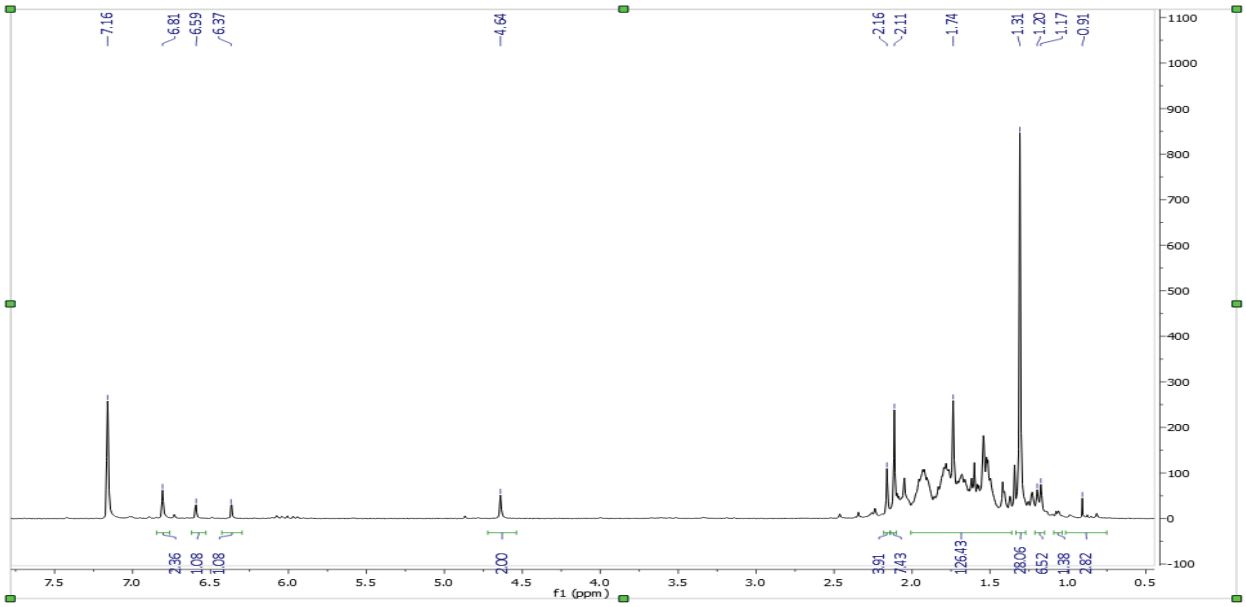

Figure S5: ^{1}H NMR spectrum of the POSS tantalum-NHC-Rh(COD)Cl complex **17** [(c-$C_5H_9)_7Si_7O_{12}$-SiO-TaNHC-Rh(COD)Cl] (300 MHz, C_6D_6, 293 K)

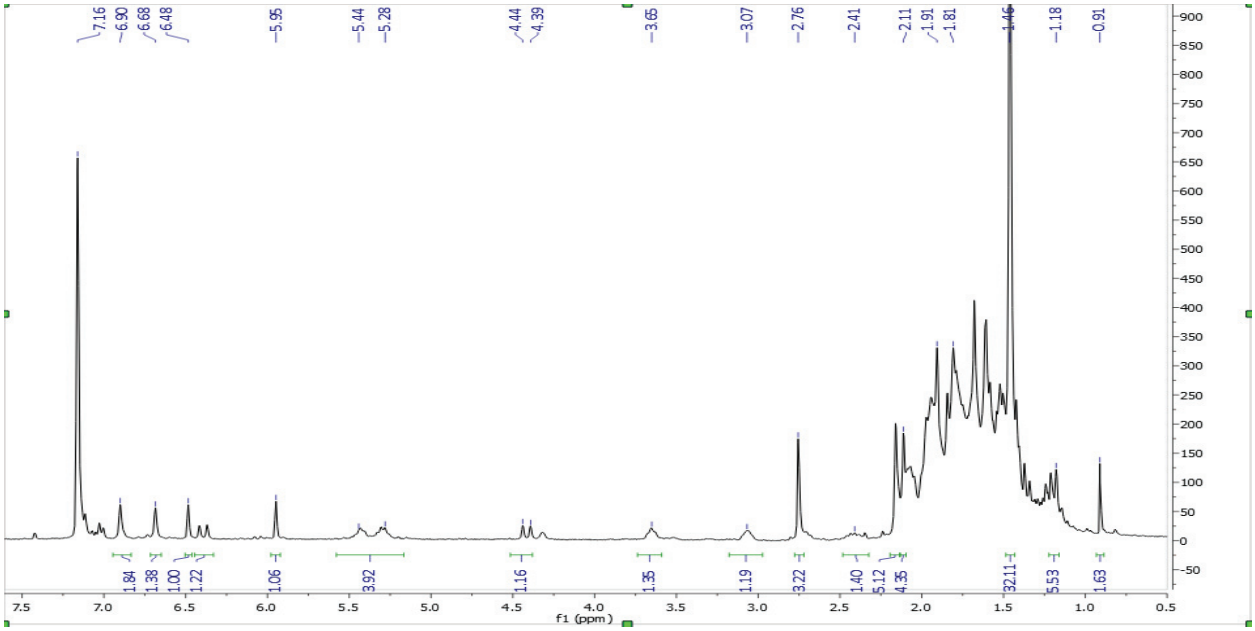

Figure S6: ^{1}H NMR spectrum of the tris(tert-butoxy) silanolate tantalum-NHC complex **18** [$(tBuO)_3$-SiO-TaNHC] (400 MHz, C_6D_6, 296 K)

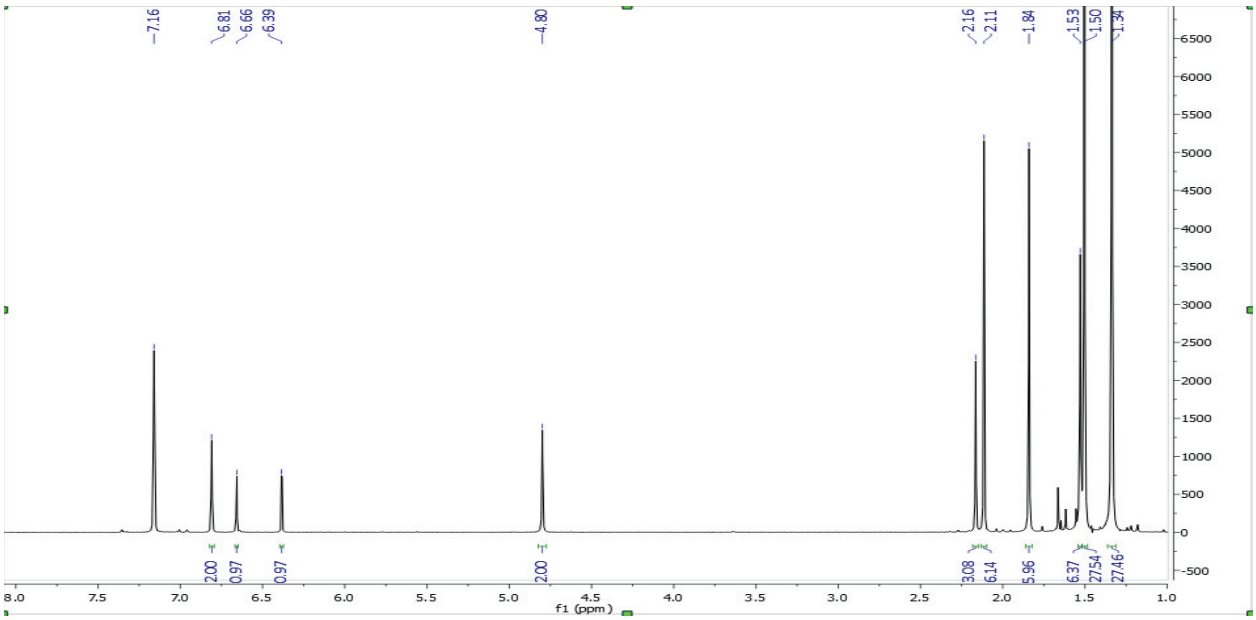

Figure S7: ^{13}C {^{1}H} NMR spectrum of the tris(tert-butoxy) silanolate tantalum-NHC complex **18** [$(tBuO)_3$-SiO-TaNHC] (100 MHz, C_6D_6, 297 K)

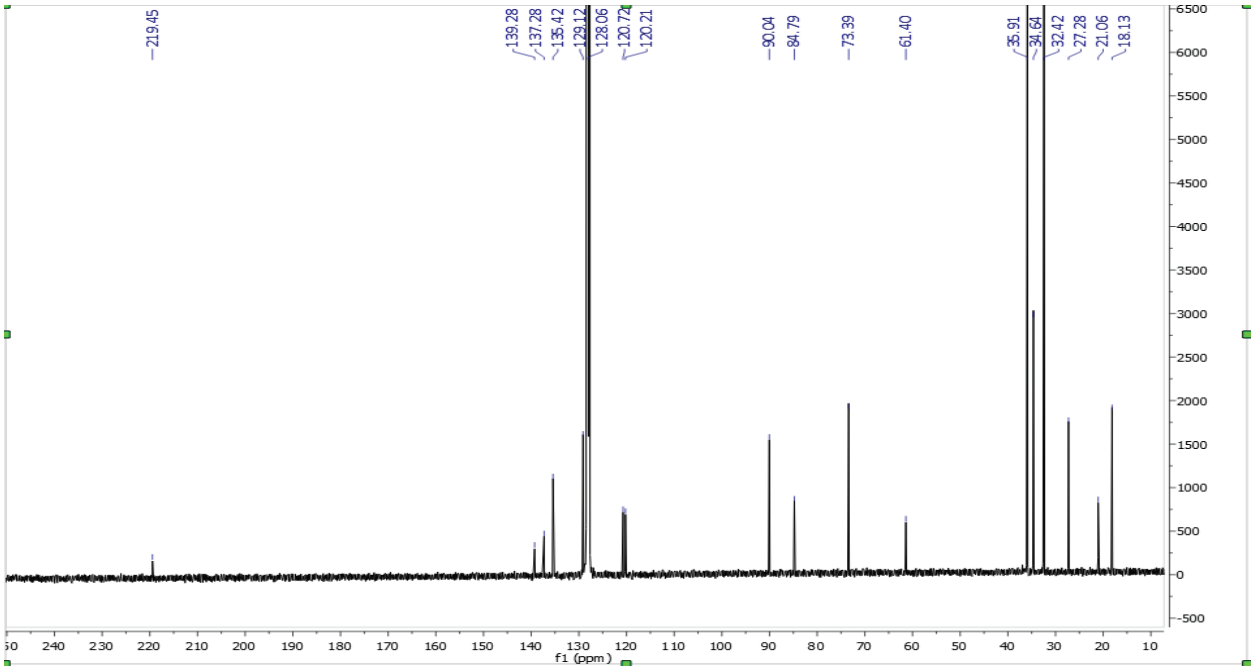

Figure S8: ^{1}H NMR spectrum of the tris(tert-butoxy) silanolate tantalum-NHC-OH-Si(^{t}BuO)3 complex **19** [$(tBuO)_3$-SiO-TaNHC] (400 MHz, C_6D_6, 296 K)

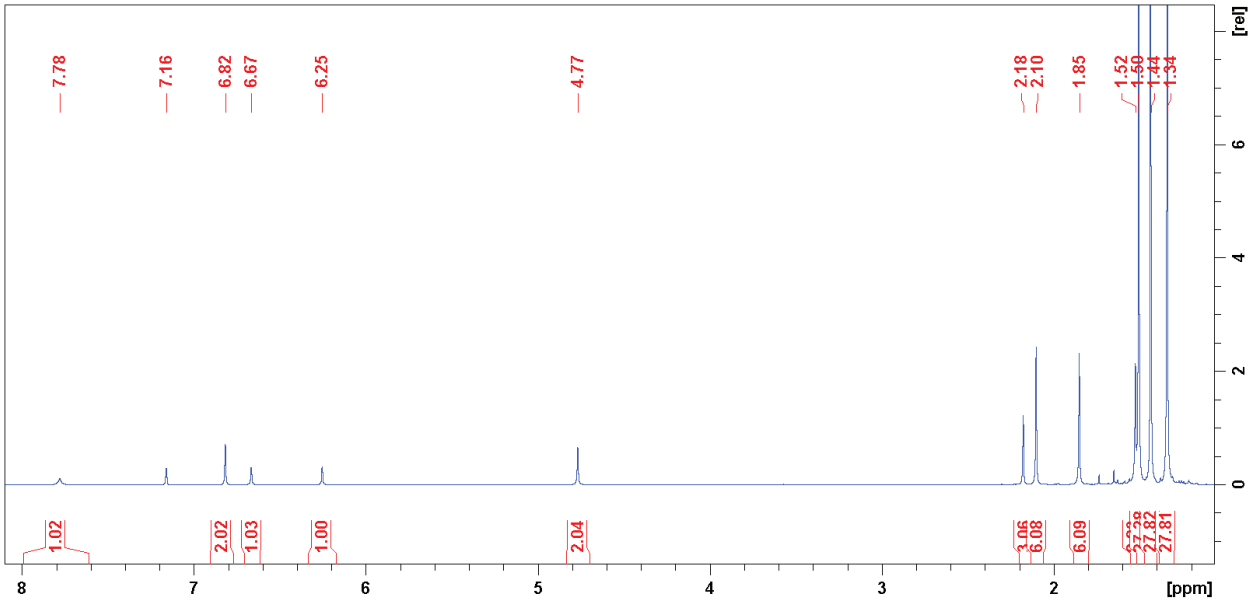

Figure S9: ^{13}C {^{1}H} NMR spectrum of the tris(tert-butoxy) silanolate tantalum-NHC-OH-Si(^{t}BuO)3 complex **19** [(tBuO)$_3$-SiO-TaNHC-OH-Si(^{t}BuO)$_3$] (400 MHz, C_6D_6, 296 K)

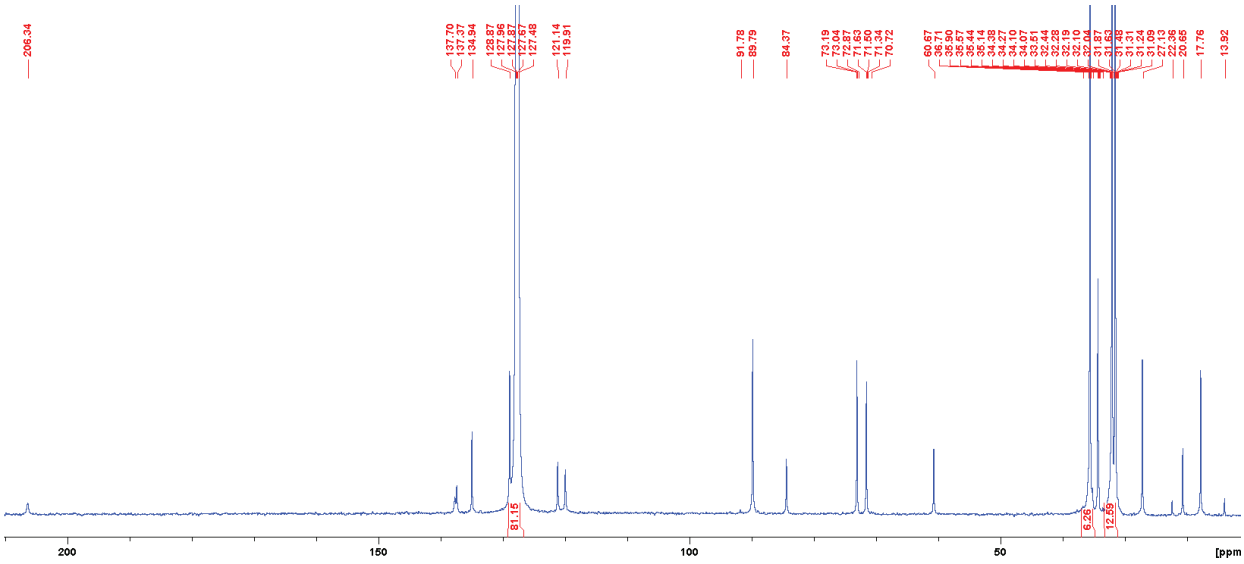

Figure S10: ^{1}H NMR spectrum of the tris(tert-butoxy) silanolate tantalum-NHC-Rh(COD)Cl complex **20** [(tBuO)$_3$-SiO-TaNHC-Rh(COD)Cl] (500 MHz, THF-d_8, 297 K)

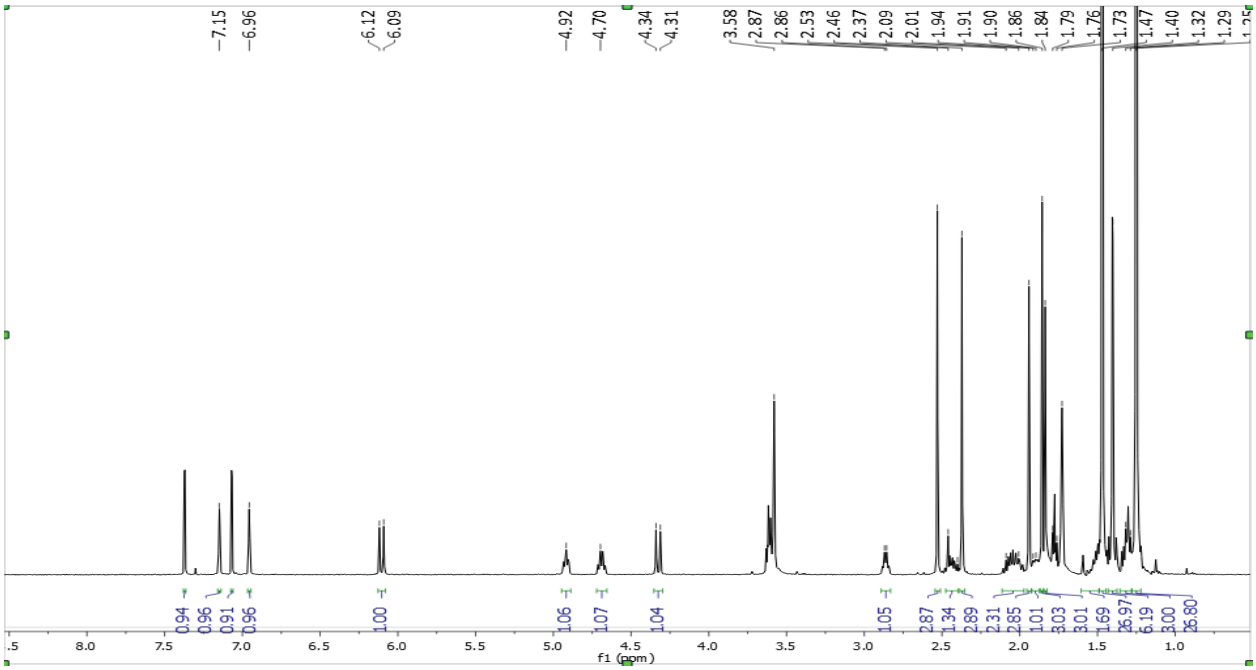

Figure S11: ^{13}C $\{^{1}H\}$ NMR spectrum of the tris(tert-butoxy) silanolate tantalum-NHC-Rh(COD)Cl complex **20** [$(tBuO)_3$-SiO-TaNHC-Rh(COD)Cl] (75 MHz, THF-d_8, 296 K)

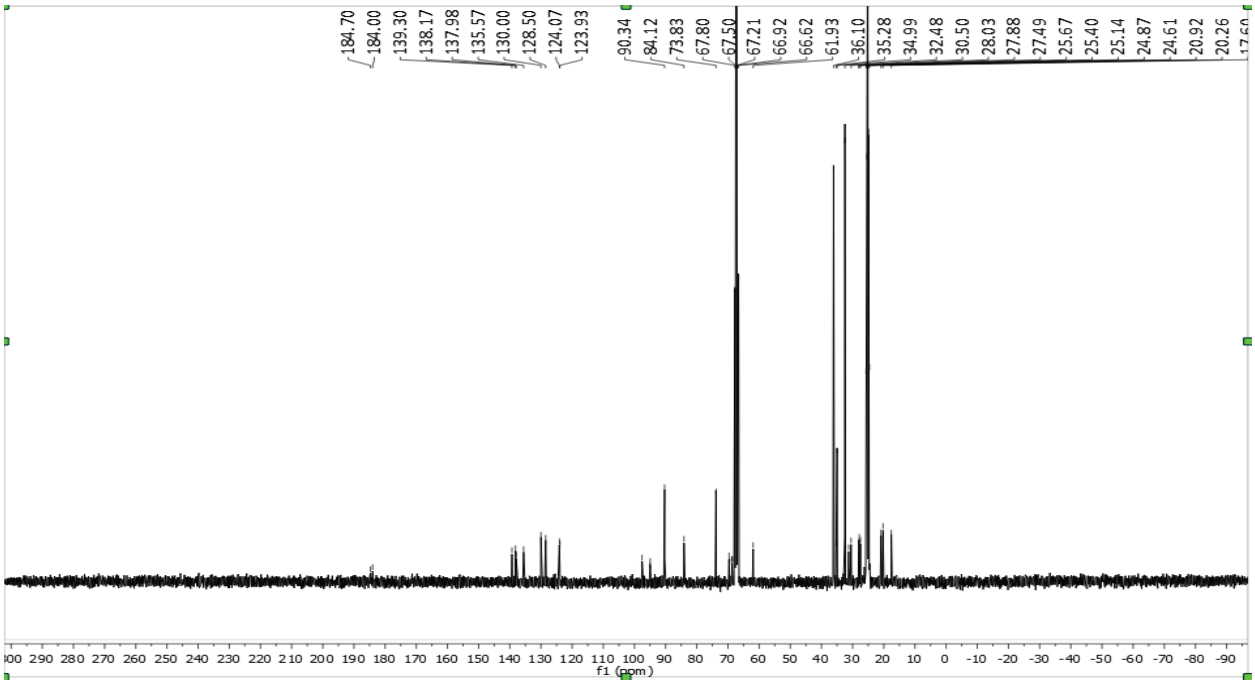

Figure S12: The figure shows the BET N_2 adsorption-desorption isotherm for SBA15-700 to determine the surface area of the mesoporous solid.

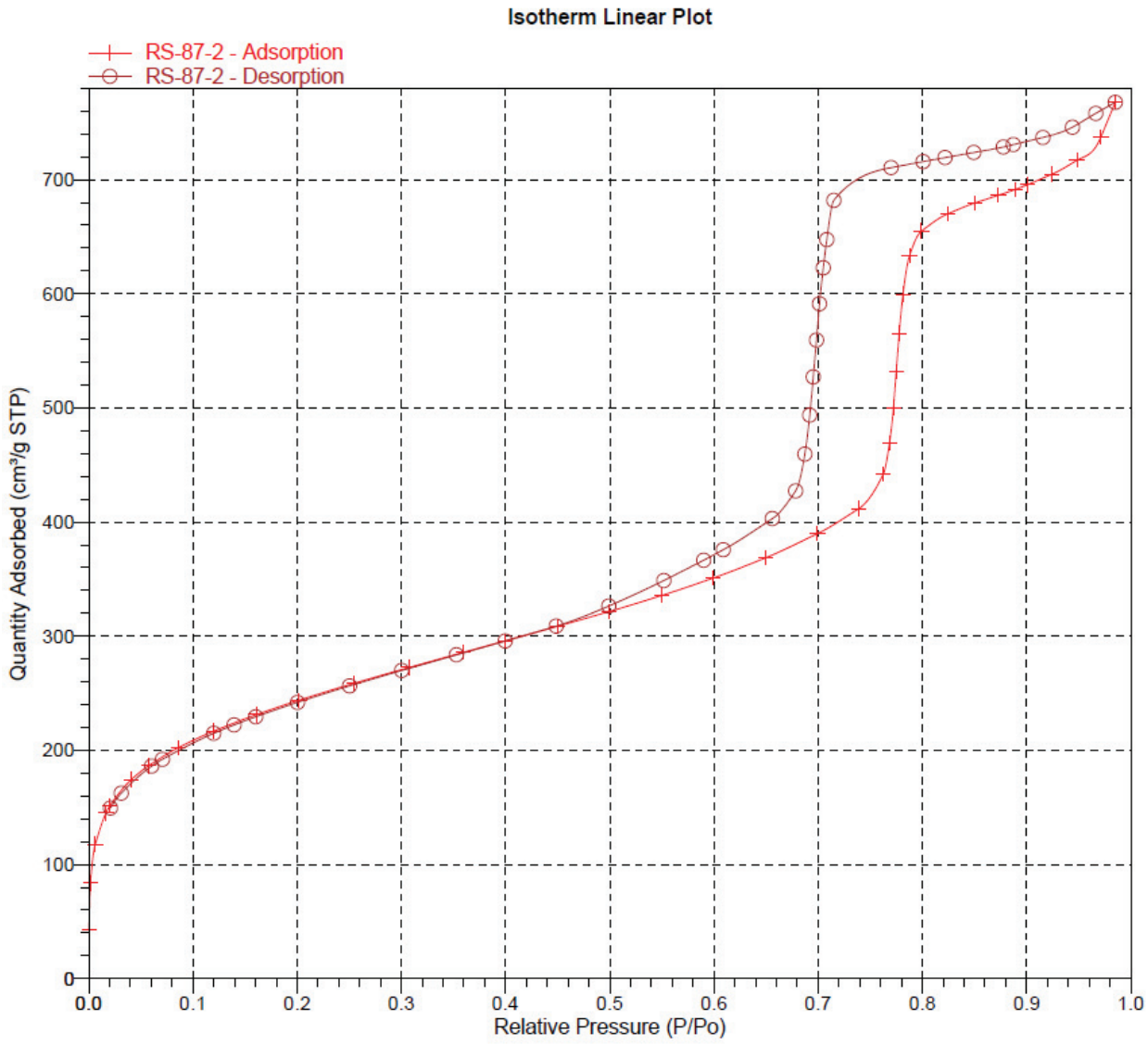

Figure S13: The BJH plot (in green) shows the distribution of different pore sizes for SBA15-700. Most of the pores have an average pore diameter of 9.5 nm.

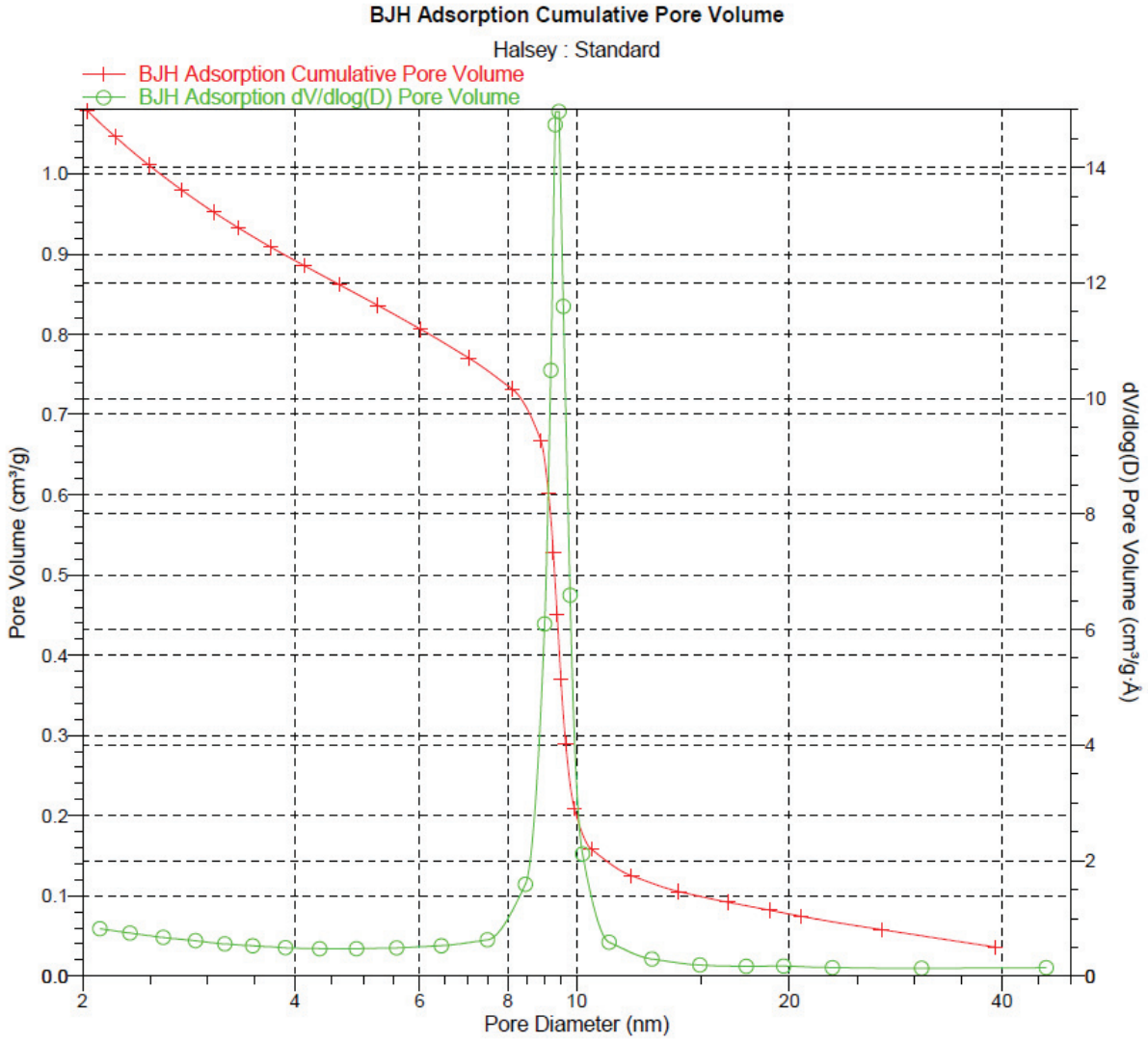

Figure S14: ^{13}C CP-MAS SSNMR spectrum of the silica supported material **21** (500 MHz, 12 KHz)

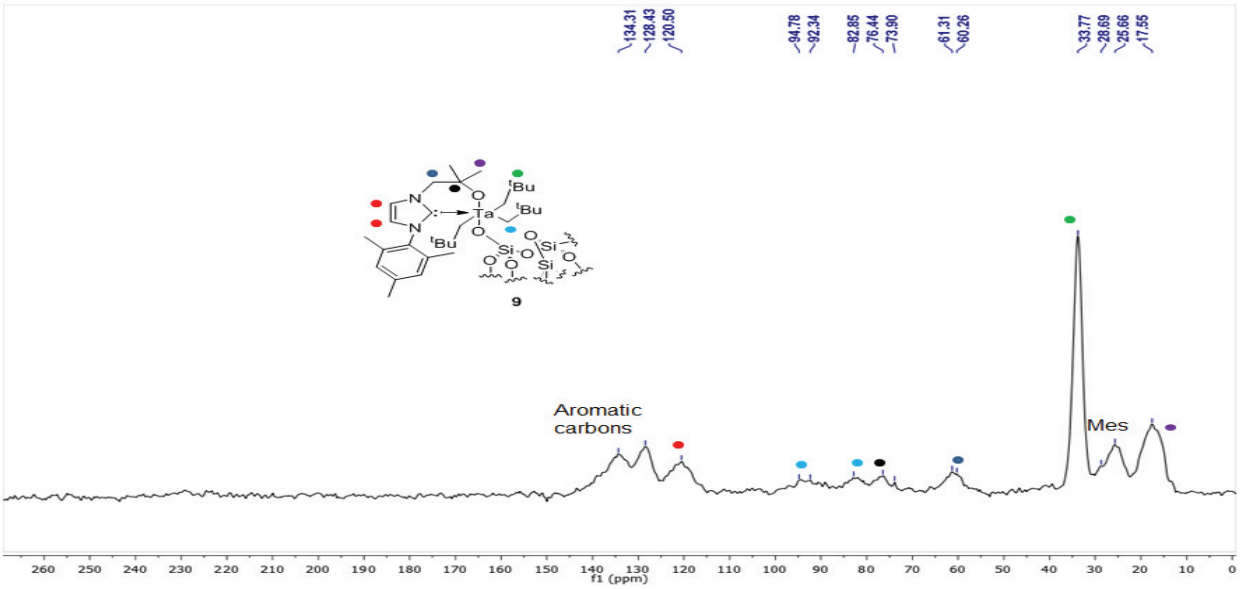

Figure S15: ^{13}C CP-MAS SSNMR spectrum of the ^{13}C labelled silica supported material **21** (500 MHz, 12 KHz

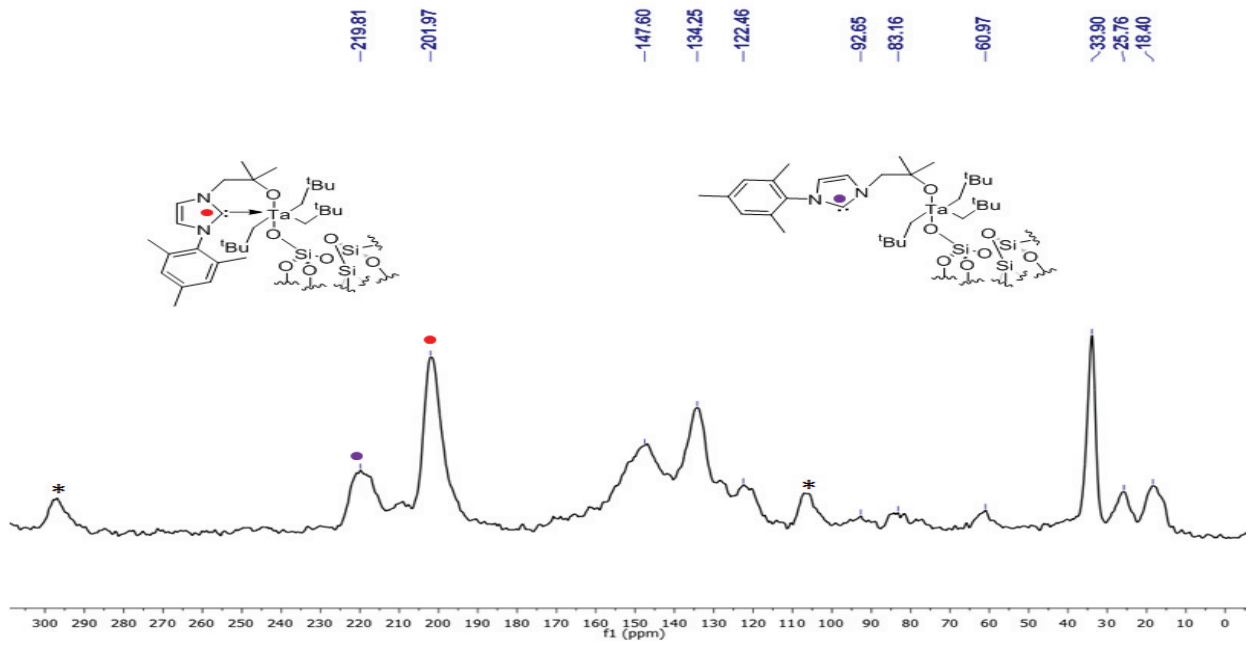

Figure S16: ^{13}C CP-MAS SSNMR spectrum of the silica supported material **22** (500 MHz, 12 KHz)

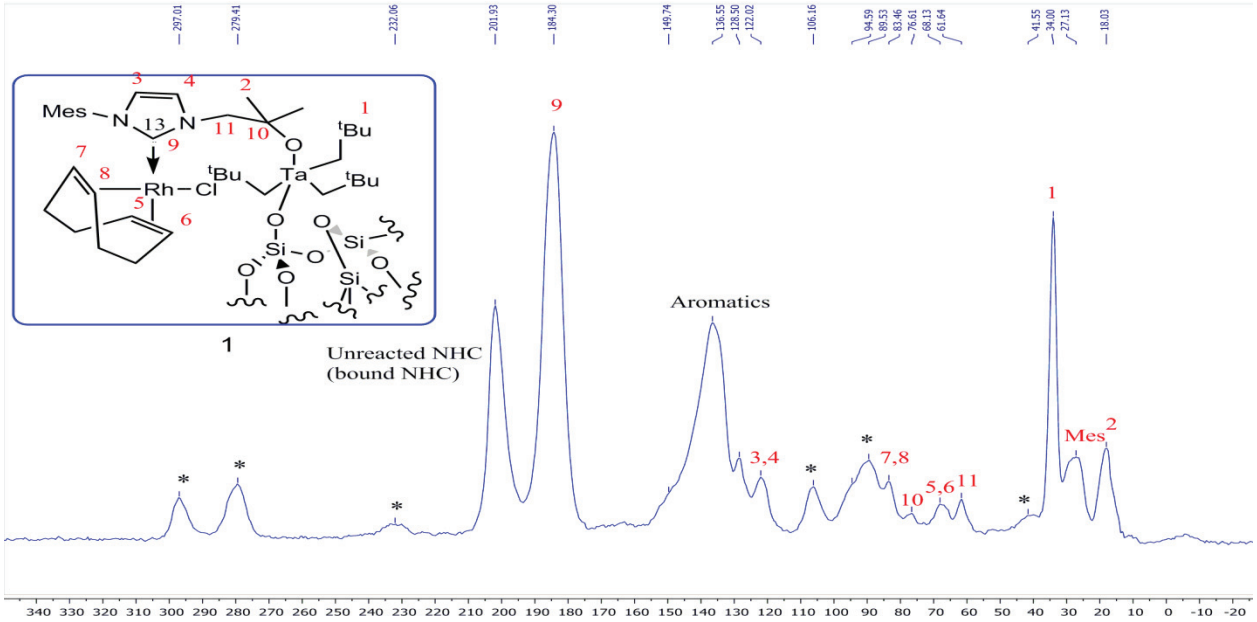

IR Spectroscopy

Figure S17: DRIFT spectrum (25°C, KBr solid solution under argon) of the POSS tantalum-NHC complex **16**.

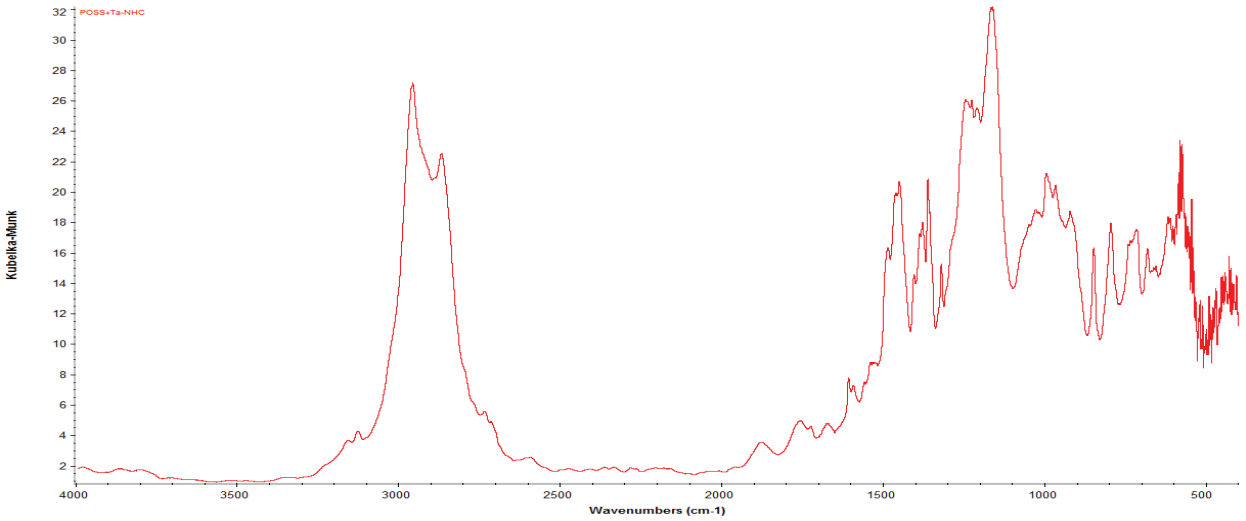

Figure S18: DRIFT spectrum (25°C, KBr solid solution under argon) of the tris (tert-butoxy) silanolate tantalum-NHC complex **18** [$(tBuO)_3$-SiO-TaNHC]

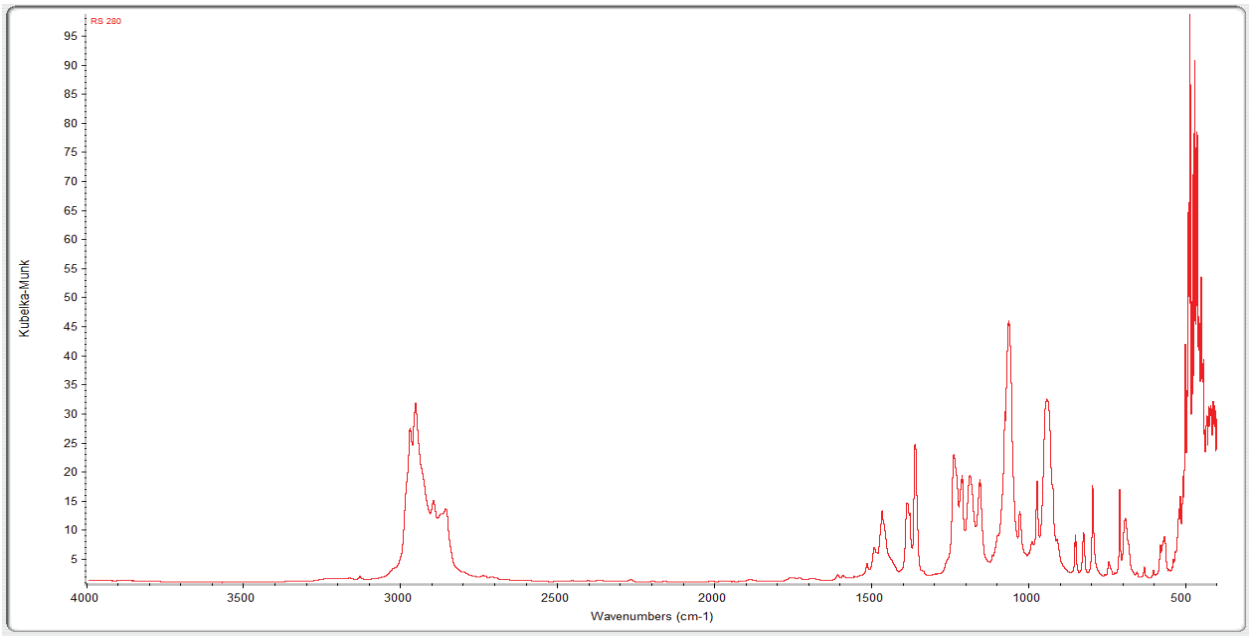

Figure S19: DRIFT spectrum (25°C, KBr solid solution under argon) of the complex **19** [$(tBuO)_3$-SiO-TaNHC]. [$(tBuO)_3$-SiOH

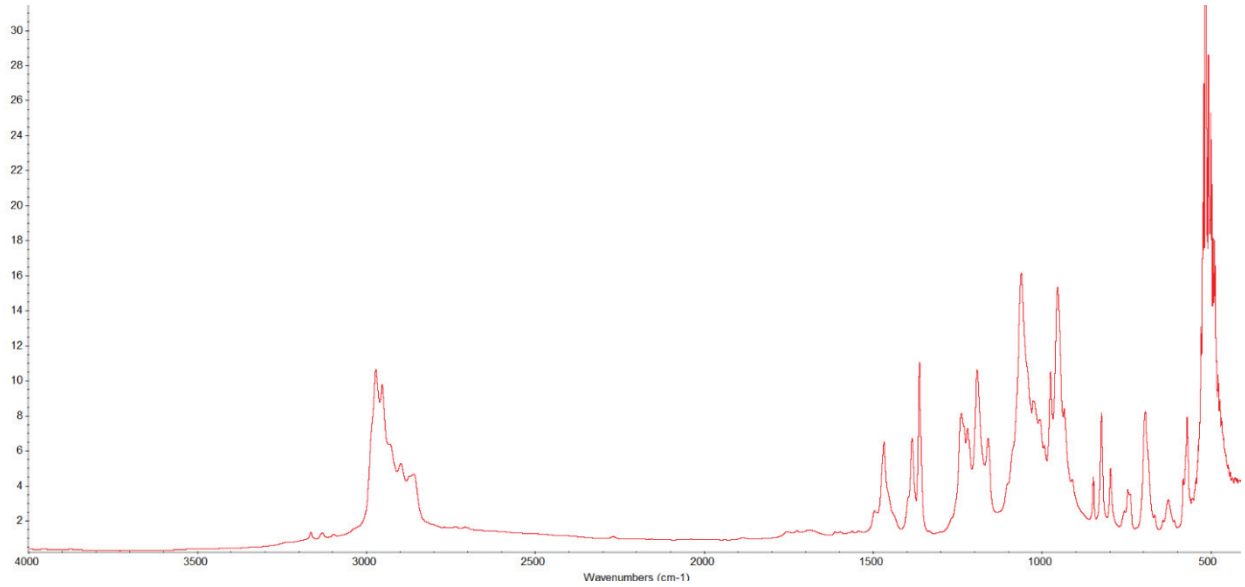

Figure S20: DRIFT spectrum (25°C, KBr solid solution under argon) of the tris (tert-butoxy) silanolate tantalum-NHC-Rh(COD)Cl complex **20** [$(tBuO)_3$-SiO-TaNHC-Rh(COD)Cl]

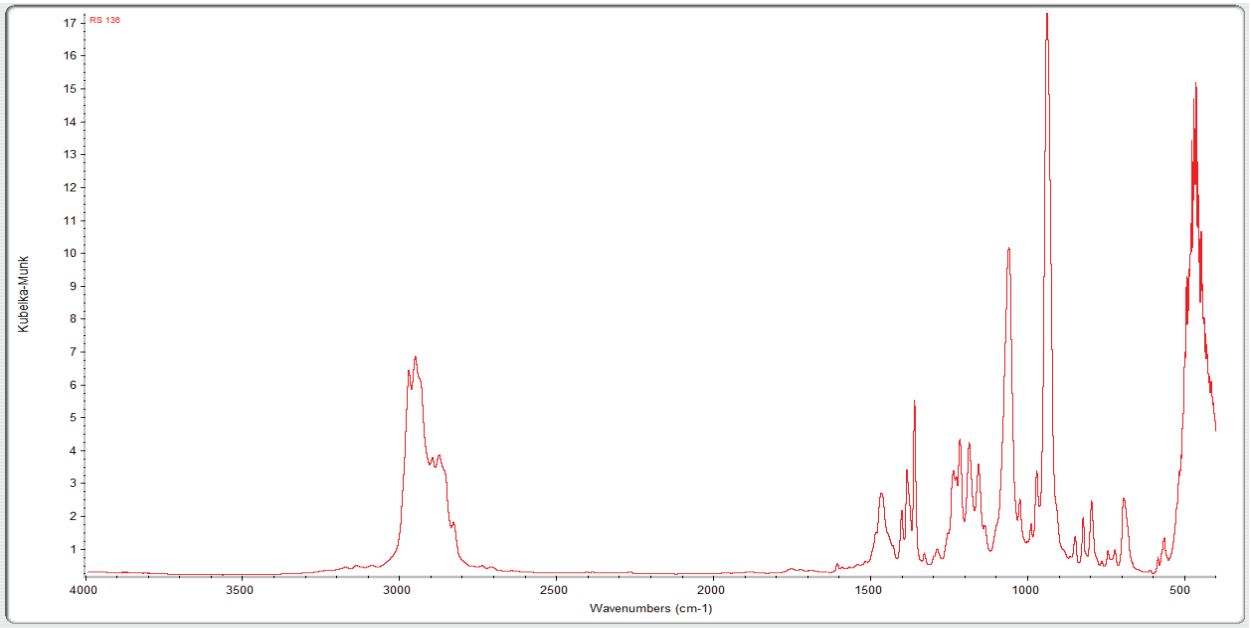

Figure S21: DRIFT spectrum (25°C, KBr solid solution under argon) of the silica supported material **21.**

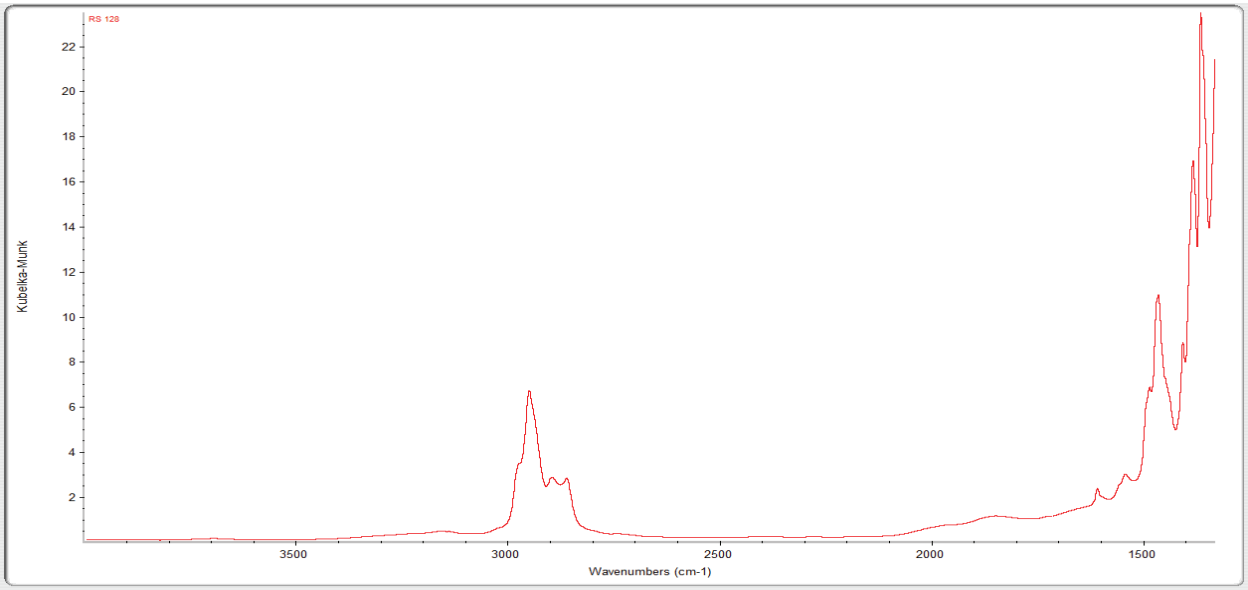

Figure S22: DRIFT spectrum (25°C, KBr solid solution under argon) of the silica supported material **22.**

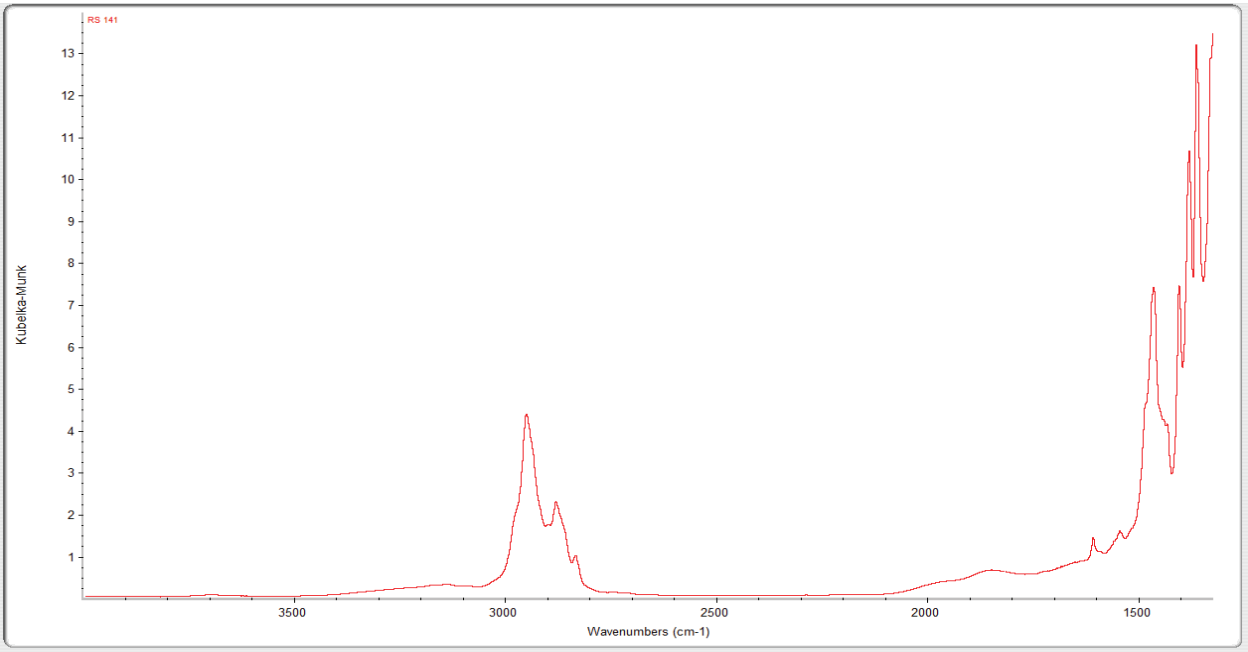

APPENDIX 4: Supporting information on chapter 5

All calculations were carried out using the Guassiano9 program. Unless and otherwise mentioned all the structures are optimized in gas phase, at T= 298.15 K and under atmospheric pressure (p= 1 atm). The B97D3-BJ dispersion corrected density functional and def2-SVP basis set was used to perform the calculations. The effective core potential (ECP) model potential was used in place f the core electrons of the metal centers. The nature of all stationary points was verified by frequency calculations proving the existence of zero and one imaginary frequency for minima and transition states, respectively.

Table 5.1: The table depicts the energies of optimized structures with the Tantalum-Rhodium bimetallic system corresponding to figure 5.7.

Reference	Electronic energy	Zero point Electronic energy	Enthalpy	Gibbs energy	Δgrxnhart	ΔGrxn /Kcal
1.out	-2375.263759	-2374.650881	-2374.600302	-2374.739267	0	0
TS1-2.out	-2375.181801	-2374.574473	-2374.523545	-2374.665704	0.073563	46.16148135
2.out	-2375.198738	-2374.585867	-2374.534282	-2374.680646	0.058621	36.7852344
TS2-3.out	-2375.156149	-2374.545949	-2374.4947	-2374.640862	0.098405	61.75007235
3.out	-2375.212702	-2374.596043	-2374.545022	-2374.688705	0.050562	31.72813534
4.out	-2376.395365	-2375.761412	-2375.709843	-2375.855041	0.064013	40.16876562
TS4-5.out	-2376.35927	-2375.72769	-2375.676877	-2375.818228	0.100826	63.26927285
5.out	-2376.397316	-2375.760274	-2375.708584	-2375.853803	0.065251	40.94562238
TS5-6.out	-2376.367692	-2375.732721	-2375.681693	-2375.824288	0.094766	59.46656528
6.out	-2319.901818	-2319.302019	-2319.252029	-2319.39415	0.062361	39.13211993
7.out	-2319.889684	-2319.2892	-2319.239825	-2319.37967	0.076841	48.21845749
TS7-8.out	-2319.890626	-2319.291479	-2319.24223	-2319.380827	0.075684	47.492429
8.out	-2319.966742	-2319.361894	-2319.312203	-2319.453929	0.002582	1.620229529
9.out	-2321.149479	-2320.529068	-2320.478501	-2320.618909	0.017389	10.9117627
TS9-10.out	-2321.138044	-2320.518906	-2320.469045	-2320.607752	0.028546	17.91288619
10.out	-2321.209212	-2320.584926	-2320.533734	-2320.679992	-0.043694	-27.41840009

Table 5.2: The table depicts the energies of optimized structures with the tantalum-cobalt bimetallic system corresponding to figure 5.8.

Reference	Electronic energy	Zero point Electronic energy	Enthalpy	Gibbs energy	Δgrxnhart	ΔGrxn /Kcal
1.out	-3647.602683	-3646.988028	-3646.937271	-3647.078183	0	0
TS1-2.out	-3647.529026	-3646.920787	-3646.870277	-3647.011019	0.067164	42.14605
2.out	-3647.56249	-3646.949401	-3646.898707	-3647.038465	0.039718	24.92342
TS2-3.out	-3647.497262	-3646.887098	-3646.836149	-3646.979905	0.098278	61.67038
3.out	-3647.553757	-3646.936023	-3646.885339	-3647.028385	0.049798	31.24872
4.out	-3648.729213	-3648.092731	-3648.04124	-3648.18721	0.07076	44.40257
TS4-5.out	-3648.154589	-3648.102548	-3648.043575	-3648.17308	0.08489	53.26927
5.out	-3648.764342	-3648.123072	-3648.072195	-3648.21353	0.04444	27.88652
TS5-6.out	-3648.703482	-3648.068707	-3648.017923	-3648.159263	0.098707	61.93958
6.out	-3592.269928	-3591.669285	-3591.619659	-3591.760749	0.034678	21.76077
7.out	-3592.242436	-3591.642157	-3591.592846	-3591.732201	0.063226	39.67492
TS7-8.out	-3592.248507	-3591.649349	-3591.60032	-3591.737062	0.058365	36.62459
8.out	-3592.317139	-3591.712677	-3591.663079	-3591.804428	-0.009	-5.64821
9.out	-3593.496438	-3592.875771	-3592.825542	-3592.964088	0.011126	6.981671
TS9-10.out	-3593.481999	-3592.86212	-3592.812656	-3592.949667	0.025547	16.03099
10.out	-3593.539972	-3592.915904	-3592.86498	-3593.0098	-0.03459	-21.703

Table 5.3: The table depicts the energies of optimized structures with the tantalum-iridium bimetallic system corresponding to figure 5.9.

References	EE	Ezpe	Ethermalenthalpy	Egibbsenergy	Δghart	Δgkcal
1.out	-2369.092017	-2368.478089	-2368.427684	-2368.567066	0	0
TS1-2.out	-2368.999418	-2368.391363	-2368.340527	-2368.483516	0.08355	52.42842
2.out	-2369.020278	-2368.405896	-2368.354982	-2368.49755	0.069516	43.62195
TS2-3.out	-2368.97379	-2368.362573	-2368.311674	-2368.456956	0.11011	69.09507
3.out	-2369.042789	-2368.424475	-2368.373419	-2368.518515	0.048551	30.46621
4.out	-2370.226392	-2369.591512	-2369.540094	-2369.685363	0.06149	38.58556
TS4-5.out	-2370.188878	-2369.556067	-2369.505501	-2369.645733	0.10112	63.45376
5.out	-2370.235281	-2369.596462	-2369.545028	-2369.689769	0.057084	35.82075

Table 5.3: The table depicts the energies of optimized structures with the tantalum-iridium bimetallic system corresponding to figure 5.11.

Reference	EE	Ezpe	Enthalpy	Gibbs energy	Δghart	Δgkcal
1.out	-7546.213679	-7545.689737	-7545.614145	-7545.802469	0	0
2.out	-7546.232768	-7545.701992	-7545.628613	-7545.810218	-0.00775	-4.86257
TS2-3.out	-7546.1921	-7545.664936	-7545.591571	-7545.774016	0.028453	17.85453
3.out	-7546.245749	-7545.714015	-7545.639973	-7545.822816	-0.02035	-12.7679
4.out	-7547.43441	-7546.8857	-7546.811011	-7546.994564	-0.01231	-7.72339